8-7-2007

Hot Stars with Disks

Erika Dawn Grundstrom

Hot Stars With Disks

by

Erika D. Grundstrom

Under the Direction of Douglas R. Gies

Abstract

The evolutionary paths of the massive O and B type stars are often defined by angular momentum transformations that involve circumstellar gas disks. This circumstellar gas is revealed in several kinds of observations, and here I describe a series of investigations of the hydrogen line emission from such disk using detailed studies of five massive binaries and a survey of 128 Be stars. By examining three sets of spectra of the active mass-transfer binary system RY Scuti, I determined masses of 7.1 ± 1.2 $M_{\odot}$ for the bright supergiant and 30.0 ± 2.1 $M_{\odot}$ for the massive companion that is hidden by an accretion torus. I also present a cartoon model of the complex mass flows in the system. Using optical spectroscopy and X-ray flux data, I investigated the mass transfer processes in four massive X-ray binaries (a massive B star with mass flowing onto a compact, neutron star companion). The B-supergiant system LS I +65 010 transfers mass via stellar winds. I find the X-ray flux modulates with the orbital period. In the other three X-ray binary systems (LS I +61 303, HDE 245770, and X Per), an outflowing circumstellar disk is responsible for the mass transfer, and in all three systems, the disk appears to be truncated by gravitational interactions with the compact companion. The disk in the microquasar system LS I +61 303 is limited in radius by the periastron separation and an increase in both Hα equivalent width

and X-ray flux following periastron may be due to a density wave in the disk induced by tidal forces. Observations of HDE 245770 document what appears to be the regeneration of a circumstellar disk. The disk of X Per appears to have grown to near record proportions and the X-ray flux has dramatically increased. Tidal interaction may generate a spiral density wave in the disk and cause an increase in Hα equivalent width and mass transfer to the compact companion. During the course of the analysis of the X-ray binaries, I developed numerical models for estimating the size of the Be star disks using just the Hα equivalent width. Finally, I present the results of a three year spectroscopic survey of both the Hα and Hγ regions of 128 Be stars. I find that the median fractional variation in the equivalent width of the disk emission lines is 15% over a two year period. I also find that two-thirds of the sample displays evidence of Fe II emission or absorption resulting from surrounding circumstellar material. Many candidates for non-radial pulsation and binary systems are also found. Spectra and notes for all of the sample stars are presented in an appendix.

Index Words: spectroscopy – circumstellar matter – stars: emission-line, Be – stars: winds, outflows – stars: early type – binaries: spectroscopic

Hot Stars With Disks

by

Erika D. Grundstrom

A Dissertation

Presented in Partial Fulfillment of Requirements for the Degree of

Doctor of Philosophy

in the College of Arts and Sciences

Georgia State University

2007

Hot Stars With Disks

by

Erika D. Grundstrom

Major Professor:	Douglas R. Gies
Committee:	Gary Hastings
	Todd J. Henry
	Harold A. McAlister
	Geraldine J. Peters
	David W. Wingert

Electronic Version Approved:

Office of Graduate Studies
College of Arts & Sciences
Georgia State University
August 2007

Dedication

To my family:

my mother DorRayne, my father Don,
and my siblings Tyan, Ian, and Svaya

You have always been there for me, supporting me
and giving me that kick in the pants when I needed it!

Acknowledgments

There are so many people I'd like to thank and acknowledge, people who have helped shape me into who I am today, and people who have helped make this whole process of education a joy.

First and foremost, I'd like to thank my parents and my siblings. They have always been there for me and we always have such fun and interesting experiences. Throughout my life, they've always encouraged my schooling and my odd little interests and all of the activities I do. Plus, they love to brag about me and that's always nice! My extended family has always been supportive and curious about what I do and that's the kind of encouragement a budding young scientist needs.

I'd also like to thank my advisor extraordinaire, Dr. Douglas R. Gies. He has always encouraged me to be a whole person and not chained to my desk (even if he may have wanted me to be ;)) and has been extraordinarily supportive of my interest in education and education research.

A big thanks to my committee, Gary, Todd, Hal, Gerrie, Dave, and of course, Doug, for reading this! I hope you like it!

MissAngela has been my roommate, officemate, best friend, and belly dance partner for years now and that I'll never forget and always cherish :)

The faculty and students at the University of Minnesota, especially my undergrad advisor, Dr. Larry Rudnick, prepared me so well for graduate school and I thank them. While at the U of M, I was an undergraduate mentee of graduate student Andrew Young and he's been a friend and mentor throughout grad school, so I'd really like to thank him too.

Of course, a girl can't be slaving away all the time so many thanks to all my swing dancing, belly dancing, booty-shakin', and band-going friends in both Atlanta and Minnesota for helping keep me active and in the loop.

Many people at Georgia State have helped me along the way, teaching classes, making templates, going on observing trips, doing preliminary research... Many thanks to Alvin Das for the GSU dissertation template - it worked like a charm! Dr. David Wingert, Stephen Williams, and Tabby Boyajian have all gone on observing runs with me and we've had a great time and learned a great deal in the process. Dr. Ginny McSwain, former roommate, now collaborator, has been a great friend and resource, plus she got me more telescope time! I'd also like to thank all of the graduate students in Doug's Stellar Spectroscopy class for doing the preliminary work on the X-ray binaries, it was a great help. I'd especially like to thank the two undergraduates I have advised, John Helsel and Diana Gudkova - they have both done great work and it's been so helpful!

As everyone at GSU knows, without the tireless work of the systems administrators, none of us would be able to do our work. Rajesh Deo has kept things running in tip-top shape for the last few years and John McFarland and Dave Berger did before that. Thanks also to over-arching sysadmin Duke Windsor.

I'd also really like to thank Daryl Willmarth (Coudé Feed guru!) and the staff of KPNO for their assistance in making these observations possible.

Now for the official acknowledgements.

This research has made extensive use of the SIMBAD database, operated at CDS, Strasbourg, France, of NASA's Astrophysics Data System Bibliographic Services, and of the Washington Double Star Catalog maintained at the U.S. Naval Observatory. The X-ray results were provided by the *RXTE*/ASM teams at MIT and at the *RXTE* SOF and GOF at NASA's GSFC. The *IUE* data presented in this dissertation were obtained from the Multimission Archive at the Space Telescope Science Institute (MAST). STScI is operated by the Association of Universities for Research in Astronomy, Inc., under NASA contract NAS5-26555. Support for MAST for non-HST data is provided by the NASA Office of Space Science via grant NAG5-7584 and by other grants and contracts. The Green Bank Interferometer is a facility of the National Science Foundation operated by the NRAO in support of NASA High Energy Astrophysics programs. This work was supported by the National Science Foundation under grants AST-0205297, AST-0506573 and AST-0606861. Institutional support has been provided from the GSU College of Arts and Sciences and from the Research Program Enhancement fund of the Board of Regents of the University System of Georgia, administered through the GSU Office of the Vice President for Research.

Contents

Tables

Figures

Abbreviations and Acronyms

AAVSO	American Association of Variable Star Observers
ASM	All-Sky Monitor on the *Rossi X-ray Timing Explorer*
BeXRB	Be X-ray Binary
CCD	Charged Coupled Device
CCF	cross-correlation function
FWHM	full-width at half-maximum
FWSM	full-width of the second moment at half-maximum
HJD	Heliocentric Julian Date
HWHM	half-width at half-maximum
IDL	Interactive Data Language
IR	infrared
IRAF	Image Reduction and Analysis Facility
IUE	*International Ultraviolet Explorer*
JD	Julian Date
KPNO	Kitt Peak National Observatory
keV	kiloelectron-volts

LTE	local thermodynamic equilibrium
MAST	Multimission Archive at Space Telescope
NASA	National Aeronautic and Space Administration
NOAO	National Optical Astronomy Observatory
NRP	non-radial pulsation
pc	parsec
RXTE	*Rossi X-ray Timing Explorer*
RV	radial velocity
S/N	signal-to-noise ratio
XRB	X-ray Binary

– 1 –

Introduction

1.1 Massive Stars

The stars with O and B-type spectral classifications are much hotter, brighter, and more massive than our Sun. They evolve very quickly compared to cooler, less massive stars. Because they have short lifetimes, O and B stars are usually found in groups in star-forming regions and at a variety of stages in the evolutionary track of a star. Due to their intrinsic brightness, their groupings, and their short lifetimes, these massive stars provide excellent laboratories for studying stellar evolution.

Throughout this dissertation, I will be focusing on B type stars, and therefore I will first describe the properties of the B stars. They have masses between 3 and 20 $M_{\odot}$, temperatures of 10000 to 30000 K, radii between 2.5 and 6 $R_{\odot}$ (for the unevolved, "main sequence" stars), and lifetimes of 6 million to 600 million years (the more massive, the shorter the lifetime). For comparison, our Sun's lifetime is 10 billion years. The hottest B stars are B0 and are often called "early"-type in the literature while the coolest B stars, B9, are called "late"-type. Another part of a star's classification is its luminosity class. From brightest to dimmest, the classes are

I, II, III, IV, and V. The class V (dwarf) stars are the unevolved main sequence stars and are the most plentiful. Class I stars are supergiants, II are bright giants, III are giants, and IV are subgiants.

The lifetime quoted above is the main sequence lifetime. A star on the main sequence is fusing hydrogen into helium in its core. Once the star has exhausted its fuel supply and can no longer fuse hydrogen, the radiation and gas pressure that kept the star from collapsing due to gravity is gone and the stellar core begins to collapse. This heats the core and makes it denser, which provides an environment for fusion of helium. Helium starts fusing and the star expands. This cycle of fusion, exhaustion, collapse, and fusion of a new element continues until either the collapse of the core cannot restart fusion or until the core has fused to iron. Iron is the "magic" element, as fusion of iron does not release energy, it requires energy. For stars with masses of about 3 to about 9 $M_{\odot}$, fusion stops at carbon, oxygen, and nitrogen and the remnant of this star is a white dwarf (supported by electron degeneracy pressure). Above 9 $M_{\odot}$, the core can fuse until iron forms, then fusion stops and there is no more pressure to keep the star from collapsing completely, and the star experiences a core-collapse supernova event. For stars with masses of about 9 to 30-40 $M_{\odot}$, the remnant is a neutron star (supported by neutron degeneracy pressure). For stars with masses greater than 30-40 $M_{\odot}$ (i.e., O stars), the remnant is a black hole.

The path of stellar evolution outlined above is for a single star; however, many B stars are part of close binary systems and the interaction between the two stars alters the path dramatically. Both tidal interactions and mass transfer play large roles. When two stars are near each other, their zones of gravitational dominance are defined by a Roche lobe. A Roche lobe is the surface around a star where a freely released particle would be gravitationally bound to the star. A diagram of the Roche lobes in a binary system is shown in Figure 1.1. Let us say we have two stars, one

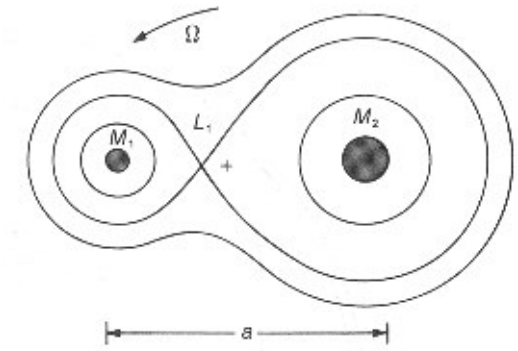

Figure 1.1: Diagram illustrating gravitational equipotential contours around two stars with masses M_1 and M_2 that are a distance a apart. They are rotating around the center of mass (the *plus sign*) with an angular velocity Ω. The two parts of the *lopsided figure-eight* are the respective Roche lobes and where they join is the inner Lagrangian point (L_1). Image from Bowers & Deeming (1984).

with twice the mass of the other. The more massive star will evolve faster. In the course of its evolution, should this more massive star become equal to the size of its Roche lobe, it cannot get any bigger as material outside of the Roche lobe will move toward the other star (as the gravitational attraction of the companion will now be greater than that of the lobe-filling star). This is when mass starts transferring onto the smaller companion star. The Roche lobe-filling star keeps evolving and therefore keeps transferring mass onto the companion as the outer portions of the large star do not affect the inner fusion. Eventually, much of the mass that is not in the fusing core of the more evolved star will be transferred to the companion. This evolved star may still experience a supernova explosion and become a remnant (a neutron star or black hole). Meanwhile, the companion has been "rejuvenated" by the mass transfer, and it evolves as a star of its new higher mass. This rejuvenated star, due to all of the transferred mass and angular momentum, may be spinning so fast that material starts lifting off of its equator and forms an outflowing disk. This process is illustrated in Figure 1.2. Not all close binaries have B stars with outflowing disks and neutron star companions, but this process is a good example of three such systems discussed

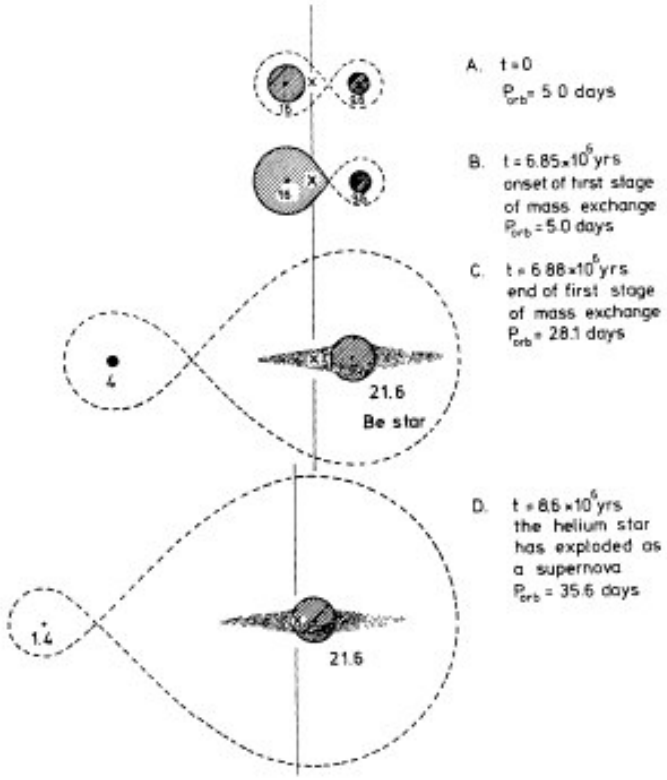

Figure 1.2: The evolution of a close binary system into a Be X-ray binary system. Image from Rappaport & van den Heuvel (1982).

in later chapters. Material from the outflowing disk may transfer back onto the now remnant companion and an accretion disk will form. This accretion disk can get hot enough to produce X-rays.

1.2 Observational Techniques in Spectroscopy

Besides pointing a telescope at a star and simply collecting the light and counting how many photons there are, an observer may collect the light, disperse it, and *then* count the photons as a function of wavelength. A spectrum is the result of dispersing light so wavelengths are separated in space. The dispersing instrument is either a prism or a diffraction grating. Should the light source be a source of all visible wavelengths (a blackbody), the spectrum will be continuous, all colors of the rainbow, with no

deviations in intensity. Should the light source be behind a cool gas, the electrons in that cool gas will absorb photons of certain wavelengths (the photons corresponding to the energy required to move said electron to a higher energy level) creating an absorption spectrum. Should the light source be a hot (i.e., energized), thin gas, it will emit photons at the wavelengths corresponding to the energy released when electrons move to a lower energy level, creating an emission spectrum. As no two elements have the same energy levels for their electrons, no two elements have the same spectral signature.

The spectrum of a star is an absorption spectrum as the source of light (produced by fusion at the core) is surrounded by a cooler gas (the stellar atmosphere). There are many different gas species in the atmosphere of a star andtherefore many spectral signatures are superposed on one another. The most important spectral lines in my study of hot stars are produced by hydrogen, helium, carbon, oxygen, nitrogen, silicon, and iron.

The spectral lines of hydrogen that are at optical wavelengths are called the Balmer lines. These lines are produced by electrons going into and out of energy level 2 from and to higher energy levels. Hα (a red line) is produced by the electron transition between levels 2 and 3 (absorption is from 2 to 3, emission from 3 to 2). Hβ (a blue-green line) is the transition between 2 and 4, and Hγ (a violet line) is between levels 2 and 5. Throughout this dissertation, I rely heavily on the Hα and Hγ lines.

1.2.1 Absorption Line Studies

By studying the absorption lines in a spectrum, we as observers may gather information about the temperature, gravity, chemical composition, rotational velocity, and orbital motion of a star. Through knowledge of how an element reacts at certain temperatures and comparisons of one star to another, we can discern the tempera-

ture of a star. For instance, in B stars, the depths of the hydrogen absorption lines change a great deal with temperature – the hotter the star, the smaller (i.e., narrower and shallower) the lines (so B9 stars have very deep and broad hydrogen lines while B0 stars have relatively small hydrogen lines). Other lines also display temperature sensitivity – Mg II gets stronger the cooler the star is, Si III and He II start appearing at hotter temperatures, and He I gets stronger, peaks, and gets weaker with increasing temperature. Therefore, if one knows the patterns, one may estimate the temperature, which is considered a fundamental parameter of a star.

The gravitational force at the photospheric surface of the star is measured as $\log g$ (g expressed in cgs units of $cm\ s^{-2}$). The bigger the number, the more surface gravity there is. More gravitational pressure will cause atoms to collide more, which will broaden the spectral line. For supergiant stars, $\log g$ is small, about 3.0 (as the surface of the star is far from the gravitational center of the star) and the spectral lines are not broad. For main sequence stars, $\log g$ is relatively high (about 4.0 or 5.0) so the lines will look broader. The value of $\log g$ is also considered a fundamental parameter of a star because it is linked to mass, the most fundamental of all stellar characteristics.

If one examines the spectrum of superposed spectral lines of different elements, one may determine the chemical composition of the star. The chemical composition of a star is measured relative to the solar abundance (as the Sun is the best studied star). Should the relative size of the absorption line of, say, helium be stronger than hydrogen for the temperature of the star, then we would say the star is helium enriched (or perhaps hydrogen deficient, depending on the abundances derived from other lines).

Stars do not just sit, unmoving, in space. Among many other motions, stars rotate. This rotational motion affects the light observed from the star in the form

of Doppler shifting. When a light source moves toward (away from) an observer, the wavelength of the light is shifted blueward (redward). Using the amount of shift in the wavelength, one may determine the velocity at which the light source is moving. The non-relativistic version of the Doppler formula is

$$v = \frac{\lambda - \lambda_0}{\lambda_0} c \tag{1.1}$$

where v is the velocity of the light source, λ is the observed wavelength, λ_0 is the rest wavelength, and c is the speed of light. As a star rotates, part of it is moving toward the observer and part is moving away, so some of the light is shifted blueward and some is shifted redward. This shifting due to rotation will broaden any stellar spectral feature. The left side of Figure 1.3 illustrates how Doppler-shifted light from segments of a stellar surface can combine to make a broadened composite. The portions of the star in regions I and V are moving the fastest so they provide the most shifted light. On the right side of Figure 1.3, the effects of rotational broadening are shown for a computed profile on the top and then in the lower two panels, two stars of the same type but different rotation speeds (the slower one is on the bottom). The projected rotational velocity $V \sin i$ is another fundamental parameter of a star.

Another characteristic of a star one can determine from spectroscopy results from the fact that stars are not always single – they may be found in pairs, triples, and more. Pairs of stars, called binary systems, are the most common. There are seven orbital elements used to describe the orbit of a binary star system - P, i, T, e, a, ω, and Ω. P is the period of orbital revolution, basically how long it takes the stars to orbit each other. Common units are days (if the period is less than about 3 years) and years. The element i is the inclination of the plane of the binary orbit to the plane of the sky, where $i = 0°$ is for an orbit that is face-on to the observer and $i = 90°$ is edge-on. T is the epoch of periastron passage and is given as a date. This date is exactly

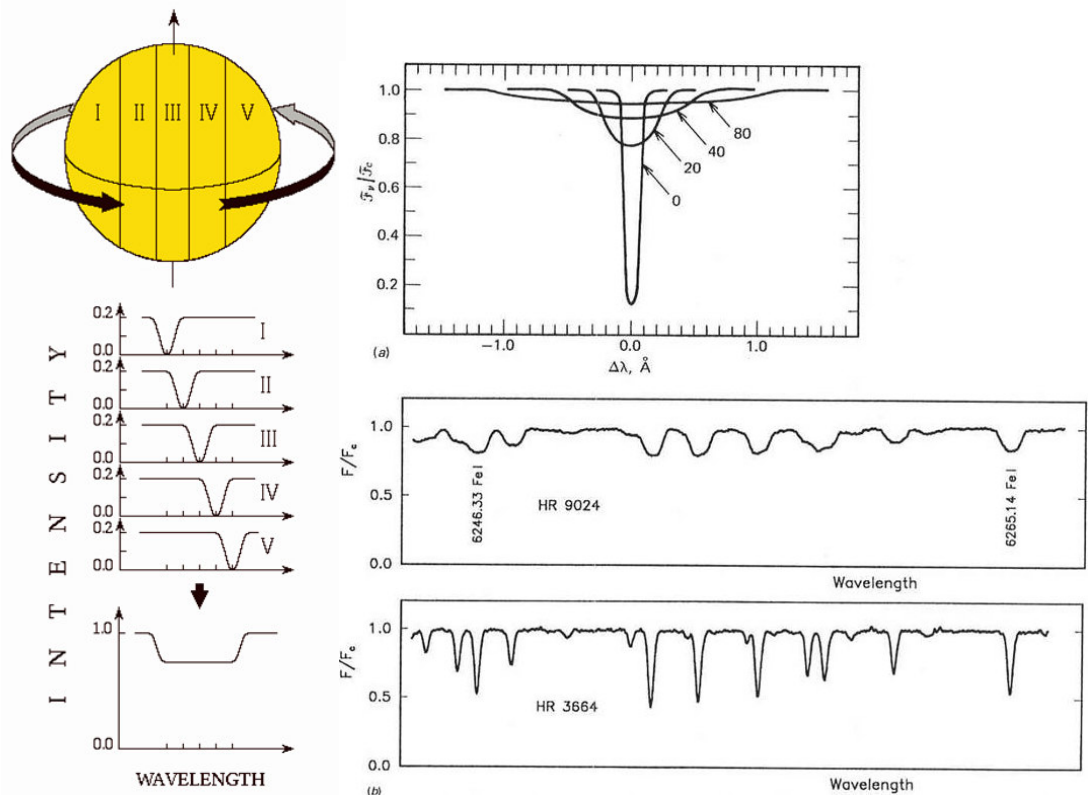

Figure 1.3: Left: Illustration showing how the addition of all areas of a rotating star contribute to the broadening of a spectral line (from http://www.konkoly.hu/staff/kovari/research.html). Right: Diagram from Gray (1992). The top panel shows computed profiles to illustrate broadening by rotation and the labels denote the rotation speed in $\mathrm{km\,s^{-1}}$. The bottom two panels show two stars of the same spectral type but HR 9024 rotates faster.

when the two stars are closest in their orbits. This value can be different depending on when the star was observed, as it is used as a starting point to determine where a star is in the binary orbit at the actual time of observation. Orbital phase is defined as the fractional part of $\phi = (t - T)/P$ for any given time t. The fourth element is the eccentricity e. Eccentricity is a measure of how non-circular (or "elliptical") an orbit is, where $e = 0$ is a perfect circle and $e = 1$ is a straight line (the circle is completely "squished"). Denoting the semi-major axis of the orbit, the fifth element a is often given in astronomical units and is measured in the plane of the orbit. The quantity $a \sin i$ is the semi-major axis projected onto the plane of the sky. The sixth element is

ω, the longitude of periastron, and it is the angle measured in the orbital plane from the point where the star crosses the plane of the sky to the periastron position. The final element is Ω, the longitude of the nodes, the nodes being where orbital plane crosses the plane of the sky (thus there are two). This angle is measured in the plane of the sky from north to a node (should be less than 180° unless one can determine which one corresponds to the star moving away from the observer).

Should the binary system have enough spectroscopic information regarding shifts in spectral features from a "rest" wavelength (radial velocities), one may make a radial velocity curve. If a star is moving quickly around it's companion, spectral features will be shifted according to the Doppler formula above. There are two parameters that characterize the radial velocity curve, K and γ. K is the semi-amplitude of the curve in $\mathrm{km\,s^{-1}}$. The faster a star orbits, the larger K is. The center-of-mass (or systemic) velocity is denoted by γ. If this number is positive, the binary system is moving away from the observer, if negative, toward. If one has radial velocity curves for both components of the binary, one may also determine the mass ratio q by taking the inverse ratio of the K measurements (as the more massive one will have a smaller semi-amplitude and vice versa).

1.2.2 Emission Line Studies

Because emission lines are formed by hot, excited gas, the study of them in relation to stars is the study of circumstellar material. This circumstellar material can be in the form of a stellar wind, a circumstellar disk or torus, a nebula, or a nearby cloud of gas. My studies focus on winds and disks. One may generally assume that the more emission there is, the more circumstellar material there is. The shapes of emission lines give information about the circumstellar gas (e.g., if there is more density in one area than another, how fast the gas is moving). Also, emission lines may be used

(together with absorption lines) to study the radial velocity shifts of the star or of the circumstellar gas itself.

1.3 Studies Presented Here

In this dissertation, I will present a variety of spectroscopic studies of hot stars with disks. First, I will discuss RY Scuti, an interacting binary observed during a rapid mass transfer phase (Ch. 2). This system contains disks around the mass gainer and around the entire binary. Then I will discuss four cases of binaries with a neutron star companion (massive X-ray binaries). In one case, the mass transfer occurs via stellar winds (LS I +65 010, Ch. 3) while in the remaining three cases, mass transfer results from the outflowing disk of a rapidly rotating star (LS I +61 303 in Ch. 5, HDE 245770 and X Per in Ch. 6). During that discussion, I will also present a model for determining the size of such an outflowing disk (Ch. 4). In Chapter 7, I describe a survey of Be stars and discuss the variability of the outflow disks. Finally, in Chapter 8, I will present some concluding remarks regarding my research and what avenues I will pursue in future work.

– 2 –

Mass Transfer in the Roche Lobe Overflow Binary RY Scuti

Abstract

The massive interacting binary RY Scuti is an important representative of an active mass-transferring system that is changing before our eyes and which may be an example of the formation of a Wolf-Rayet star through tidal stripping. Utilizing new and previously published spectra, we[1] present examples of how a number of illustrative absorption and emission features vary during the binary orbit. We identify spectral features associated with each component, calculate a new, double-lined spectroscopic binary orbit, and find masses of 7.1 ± 1.2 $M_{\odot}$ for the bright supergiant and 30.0 ± 2.1 $M_{\odot}$ for the hidden massive companion. Through tomographic reconstruction of the component spectra from the composite spectra, we confirm the O9.7 Ibpe spectral class of the bright supergiant and discover a B0.5 I spectrum associated with the hidden massive companion; however, we suggest that the latter is actually the spectrum of the photosphere of the accretion torus immediately surrounding the

[1]Grundstrom, E. D.; Gies, D. R.; Hillwig, T. C.; McSwain, M. V.; Smith, N.; Gehrz, R. D.; Stahl, O.; Kaufer, A. - published as Grundstrom et al. (2007d)

massive companion. We describe the complex nature of the mass loss flows from the system based upon recent hydrodynamical models and find RY Scuti has matter leaving the system in two ways: 1) a bipolar outflow from winds generated by the hidden massive companion, and 2) an outflow from the bright O9.7 Ibpe supergiant in the region near the L2 point to fill out a large, dense circumbinary disk. This circumbinary disk (radius $\approx$ 1 AU) may feed the surrounding double-toroidal nebula (radius $\approx$ 2000 AU).

2.1 Introduction

RY Scuti (HD 169515) is a distant (1.8 $\pm$ 0.1 kpc; Smith et al. 2002) and massive eclipsing binary system with an orbital period of 11.12445 days (Kreiner 2004). Analysis of the light curve indicates that at least one of the components fills its Roche lobe. The present configuration may be semi-detached (Cowley & Hutchings 1976), overcontact (Milano et al. 1981; Djurašević et al. 2001), or one with the more massive component embedded in an opaque, optically thick disk (King & Jameson 1979; Antokhina & Kumsiashvili 1999). The binary appears to be in an advanced stage of evolution, and it has ejected gas into a young ($\sim$130 year old; Smith, Gehrz, & Goss 2001), double-toroidal emission nebula. The $\approx$ 2000 AU nebula is angularly resolved in radio images (Gehrz et al. 1995), infrared images (Gehrz et al. 2001), and in *Hubble Space Telescope* Hα images (Smith et al. 1999, 2001, 2002). Because the nebula is so young and the star system is still in an active Roche-lobe overflow phase, RY Scuti is a powerful laboratory for studying non-spherical mass and angular momentum loss in interacting binaries.

Only one of the component stars is readily visible in optical spectra, and it has a spectral classification of O9.7 Ibpe var (Walborn 1982). We will refer to this com-

ponent as the "supergiant." The other star appears to be enshrouded as it is very difficult to detect in the spectrum. Most investigators agree that this second star is the more massive of the two, and we will refer to the second component as the "massive companion." However, the actual masses of the stars in this system are debatable. The radial velocity curve of the supergiant is reasonably well established, but the results for the massive companion depend critically on what spectral features one assumes are associated with that star. As these features are difficult to observe and interpret, the estimated mass range has been huge. For example, Popper (1943) arrived at a total system mass in excess of 100 $M_{\odot}$. Later investigators found lower values: Cowley & Hutchings (1976) estimated masses of 36 and 46 $M_{\odot}$, Skul'Skii (1992) found 8 and 26 $M_{\odot}$, and Sahade, West, & Skul'Skii (2002) estimated 9 and 36 $M_{\odot}$ (for the supergiant and massive companion, respectively, in each case). There are a number of important photometric studies (e.g., ranging from the discovery by Gaposchkin & Shapley 1937 through photoelectric investigations by Giuricin & Mardirossian 1981 and Milano et al. 1981, and up to the most recent multi-color work by Djurašević et al. 2001); however the results differ with regard to the assumed binary configuration and depend sensitively on the mass ratio adopted from spectroscopy.

This unique system is representative of the short-lived, active mass transfer stage in the evolution of massive binaries. Theoretical models (Petrovic, Langer, & van der Hucht 2005) indicate most of the mass transfer occurs during a brief ($\approx 10^4$ yr), and thus rare, phase in which the mass donor transfers most of its mass to the mass gainer star. Mass transfer will shrink the orbital dimensions until the mass ratio is reversed (and the gainer becomes the more massive star), and then the system will enter a slower (and longer lived) mass transfer phase as the binary expands. The massive binaries that are just emerging from the rapid mass transfer phase probably

belong to the observed class of W Serpentis binaries (Tarasov 2000). Only the mass donor star is visible in the spectra of these binaries, and the more massive gainer star is hidden in a thick accretion disk (one source of emission lines in the spectra). The mass transfer process is complex and leaky, and a significant fraction of the mass loss leaves the system completely (as described by Harmanec 2002 for the best known object of the class, β Lyr). The mass donor may eventually lose its entire hydrogen envelope and emerge as a Wolf-Rayet star. Therefore, a system like RY Scuti may be the progenitor of a WR+O binary system (Giuricin & Mardirossian 1981; Antokhina & Cherepashchuk 1988; Smith et al. 2002).

In a prior paper (Smith et al. 2002), several of us presented a detailed study of the spectral features formed in the surrounding double-toroidal nebula through an examination of a set of high-dispersion spectra obtained with the ESO FEROS spectrograph. Here we use the same set of spectra supplemented by additional optical spectra to explore the spectral features associated with the central binary and its immediate circumstellar environment. Our primary goal is to determine how the binary ejects the gas that ultimately flows into the dense outer double-toroidal nebula. We describe our observations and data reduction methods in §2.2, and we present in §2.3 many examples of the orbital phase-related spectral variations we observed. The radial velocity curve and a new orbital solution for the supergiant mass donor are described in §2.4. In §2.5 we review the spectral clues about the nature of the enshrouded mass gainer, and we present a preliminary radial velocity curve and orbital solution for this massive companion. Both radial velocity curves are used in §2.6 to make a Doppler tomographic reconstruction of the optical spectra of the individual components. We describe in §2.7 a model for the mass outflows in RY Scuti that is based upon recent hydrodynamical simulations and explains many of the observed spectral variations. Our results are summarized in §2.8.

2.2 Observations and Reductions

Our analysis is based upon spectra collected from three telescopes. The highest dispersion spectra (17 in number) were obtained in 1999 with the Fiber-fed Extended Range Optical Spectrograph (FEROS) mounted on the 1.52 m telescope of the European Southern Observatory (ESO) at La Silla, Chile (see Smith et al. 2002). Also in 1999, we obtained 40 moderate dispersion spectra (in the red region surrounding Hα) using the Kitt Peak National Observatory coudé feed 0.9 m telescope. Finally, in 2004 we used the CTIO 1.5 m telescope[2] and Cassegrain spectrograph to obtain ten blue spectra of moderate resolution covering one orbital period. Table 2.1 contains run number, dates, spectral coverage, spectral resolving power, number of spectra, telescope, spectrograph grating, and CCD detector used in each case. Exposure times were generally limited to 30 minutes or less. Each set of observations was accompanied by numerous bias, flat-field, and ThAr comparison lamp calibration frames. Furthermore, we obtained multiple spectra each night of the rapidly rotating A-type star ζ Aql for removal of atmospheric water vapor and O_2 bands in the red spectra made with the KPNO coudé feed.

Table 2.1: Journal of Spectroscopy

Run Number	Dates (HJD-2,450,000)	Range (Å)	Resolving Power ($\lambda/\triangle\lambda$)	Number of Spectra	Observatory/Telescope/ Spectral Grating/CCD
1	1354.7 – 1354.8	6431 – 6785	5440	2	KPNO/0.9m/RC181/TI5
2	1355.7 – 1364.9	5405 – 6743	3950	32	KPNO/0.9m/RC181/F3KB
3	1373.7 – 1394.6	3600 – 9200	48000	17	ESO /1.5m/FEROS/EEV 2 × 4K
4	1421.8 – 1429.7	5397 – 6735	4050	6	KPNO/0.9m/RC181/F3KB
5	3152.9 – 3164.9	4068 – 4738	2430	10	CTIO/1.5m/#47II/Loral 1K

The spectra from all the telescopes were extracted and calibrated using standard routines in IRAF[3]. All the spectra were rectified to a unit continuum by fitting line-

[2]operated by the SMARTS consortium

[3]IRAF is distributed by the National Optical Astronomical Observatory, which is operated by the Association of Universities for Research in Astronomy, Inc. (AURA), under cooperative agreement with the National Science Foundation.

free regions. We removed the atmospheric lines from the red coudé feed spectra by creating a library of ζ Aql spectra from each run, removing the broad stellar features from these, and then dividing each target spectrum by the modified atmospheric spectrum that most closely matched the target spectrum in a selected region dominated by atmospheric absorptions. In a few cases this resulted in the introduction of spectral discontinuities near the atmospheric telluric lines, and these were excised by linear interpolation. We did not attempt any removal of atmospheric lines for the FEROS spectra, but some problem sections in the echelle-overlap regions were excised via linear interpolation. The spectra were then transformed to a common heliocentric wavelength grid for each of the FEROS, KPNO coudé feed, and CTIO 1.5 m runs. We show several examples of the final spectra in the next section.

2.3 Spectral Variations with Orbital Phase

The optical spectrum of RY Scuti is very complex and time variable, and in this section we describe the appearance and orbital phase-related variations of several representative line features. A depiction of the time-average of all the FEROS spectra in the range from 3600 to 9200 Å appears in Smith et al. (2002) (their Fig. 16). This illustration is ideal for identifying the many sharp, quadruple-peaked, emission lines formed in the surrounding double-toroidal nebula, but photospheric lines appear broad and shallow as the average was made over the full range of orbital Doppler shifts. A large fraction of the circumstellar emission lines are species that do not have a stellar absorption counterpart (such as [Fe III] and many other forbidden lines), but there are several emission lines that are superimposed upon important stellar spectral features (for example, in the H Balmer and He I lines). As the nebular features are analyzed in great detail elsewhere (Golovatyi & Skulskii 1992; Skul'Skii & West 1993; Smith

et al. 2002), we will not discuss them here. We will focus on those spectral features formed in the photospheres of the stellar components and in the rapidly moving gas immediately surrounding them. Here we introduce the different kinds of patterns of variability observed, and in the following sections we analyze in detail the Doppler velocity shifts related to features associated with the supergiant (§2.4) and its massive companion (§2.5).

We begin with some examples from the high resolution FEROS spectra. The Si IV λ4088 absorption feature is one of only a small number of spectral lines formed in the photosphere of the supergiant that is not filled in or affected by nebular emission. We show the orbital phase variations of this line (and the nearby N III λ4097 and Hδ lines) in Figure 2.1 as a function of heliocentric radial velocity for Si IV λ4088. In this and the next figures we adopt the orbital period from Kreiner (2004) of $P = 11.12445$ d and the epoch of phase zero as the supergiant superior conjunction at T_{SC} = HJD $2,451,396.71$ (derived in §2.4). The upper portion of Figure 2.1 shows the Si IV profiles with their continua aligned with the phase of observation (increasing downwards) while the lower portion shows the spectra as a gray-scale image interpolated in phase and velocity. Features moving with the radial velocity curve of the supergiant will have a characteristic "S" shape in this image. The break in the continuity of the "S" curve near phase $\phi = 0.35$ is due to the unfortunate gap in our phase coverage near there and to the simplicity of the interpolation scheme. The Si IV λ4088 feature appears to be useful for the radial velocity measurement of the supergiant, although we find that the depth of the line varies with phase, weakening at $\phi = 0.0$ and strengthening at $\phi = 0.5$. There is no obvious evidence of a reverse "S" feature that would correspond to the motion of the massive companion (although a weak feature is present; §2.6).

The orbital variations in two helium lines, the He I λ4387 singlet and the He I

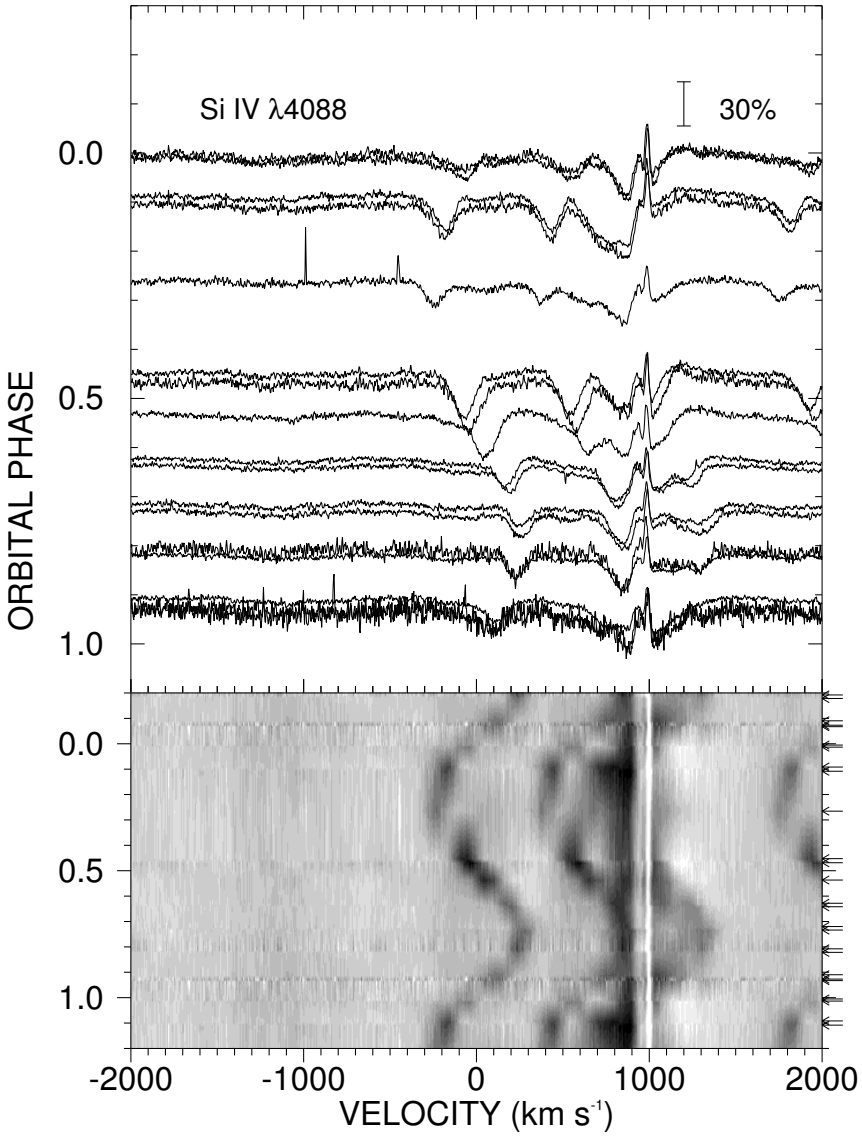

Figure 2.1: The orbital phase variations in the Si IV $\lambda 4088$ absorption line in the FEROS spectra of RY Scuti are shown in linear plots (*top panel*) and as a gray-scale image (*lower panel*). The intensity in the gray-scale image is assigned one of 16 gray levels based on its value between the minimum (dark) and maximum (bright) observed values. The intensity between observed spectra is calculated by a linear interpolation between the closest observed phases (shown by arrows along the right axis). The feature centered at 0 km s^{-1} is Si IV $\lambda 4088$, and to the right is N II $\lambda 4097$, Hδ $\lambda 4101$ (exhibiting both photospheric absorption and nebular emission features), and Si IV $\lambda 4116$ (far right edge).

$\lambda 4471$ triplet, are illustrated in Figures 2.2 and 2.3, respectively. Both features show sharp nebular emission peaks from the surrounding double-torus (Smith et al. 2002)

superimposed on the stellar absorption feature. Both lines show an absorption component that follows the radial velocity curve of the supergiant. However, the He I λ4387 feature strengthens at both conjunctions and almost disappears at phase $\phi = 0.25$. It also shows a blueshifted absorption feature that appears at $\phi = 0.5$ and lasts for nearly half the orbit. Other He I singlets ($\lambda\lambda 4009, 4143, 4921$ shown in Figs. 2.4, 2.5, and 2.6 respectively) exhibit the same behavior. On the other hand, the He I λ4471 triplet displays a much stronger blueshifted component between $\phi = 0.5 - 0.8$ that develops into a very sharp and blueshifted (≈ -200 km s^{-1}) absorption line that lasts for greater than half the orbit. The other He I triplets ($\lambda\lambda 4026, 4713$ shown in Figs. 2.4 and 2.7) also show these same features.

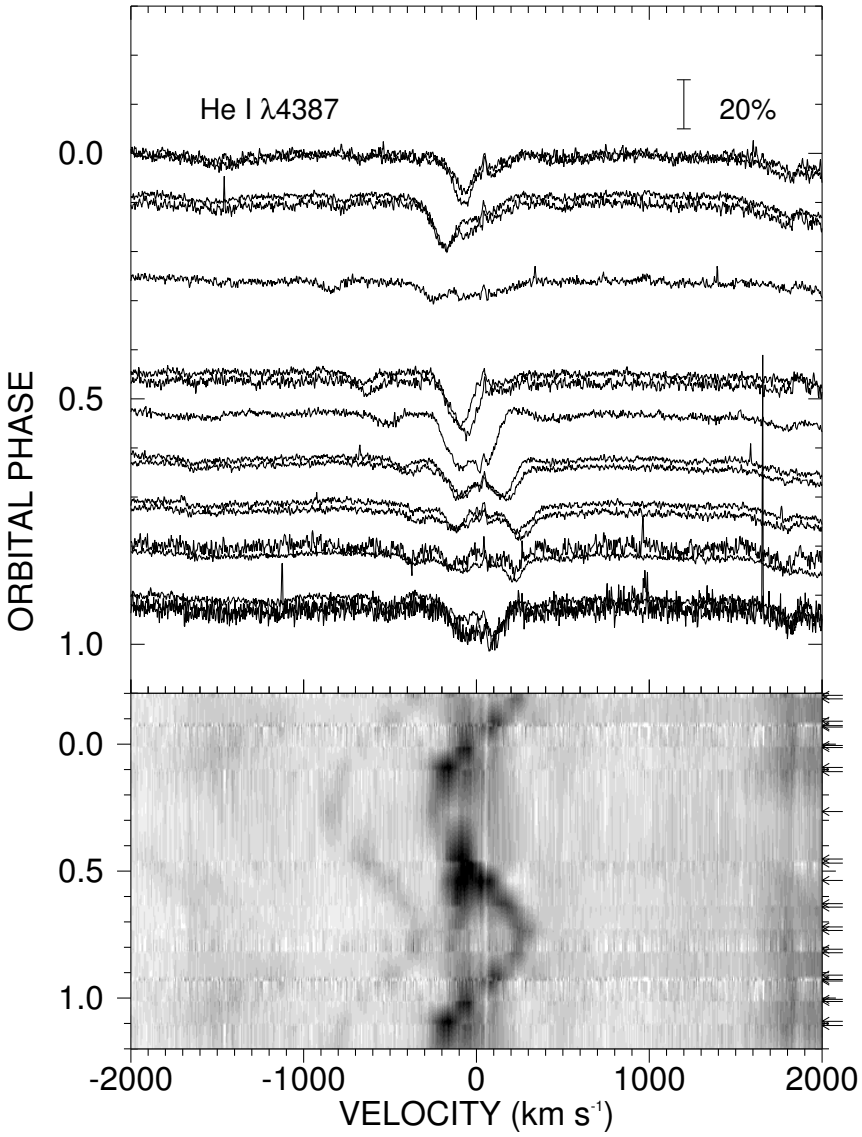

Figure 2.2: The orbital phase variations in the He I $\lambda 4387$ singlet shown in the same format as Fig. 2.1. This feature strengthens at conjunctions and develops a blueshifted absorption feature after $\phi = 0.5$. Traces of the radial velocity curve of the fainter massive companion are seen especially after $\phi = 0.5$, however, this feature is not used in the radial velocity analysis due to the aforementioned blueshifted absorption feature. The fainter absorption feature just to the left is N III $\lambda 4379$.

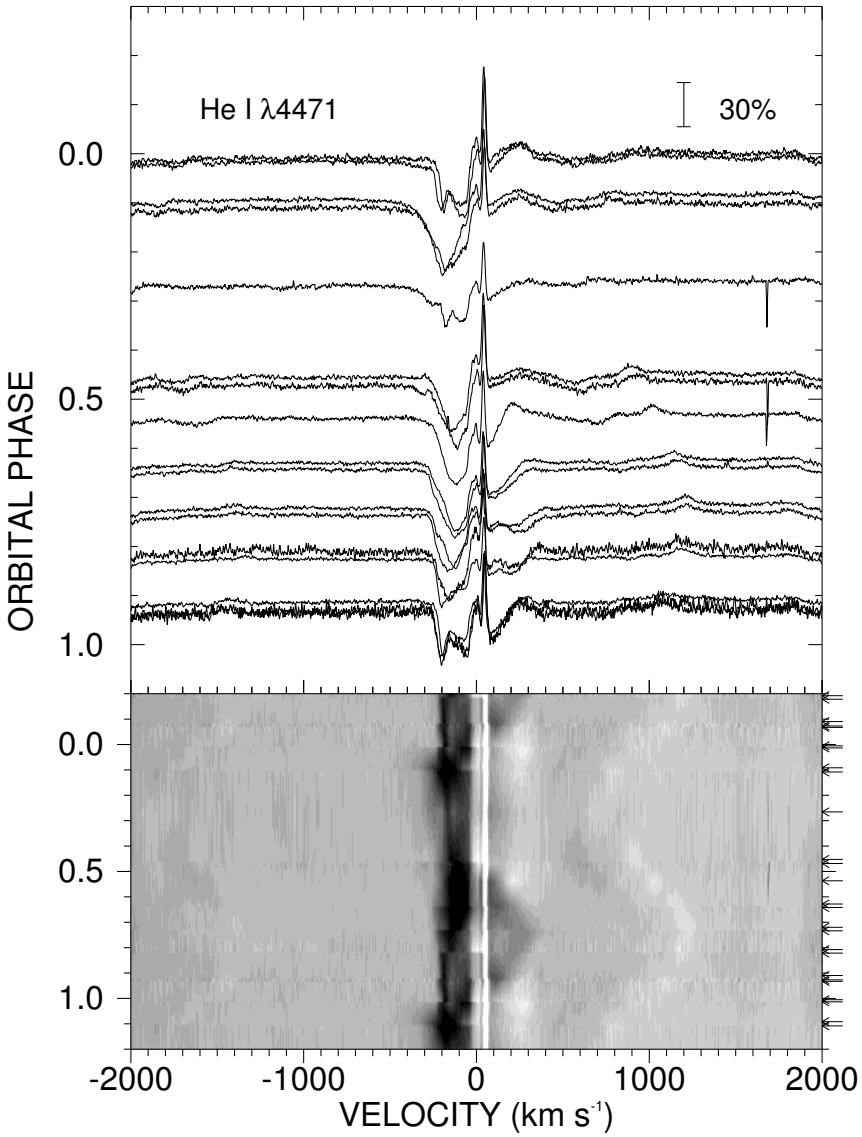

Figure 2.3: The orbital phase variations in the He I $\lambda 4471$ triplet shown in the same format as Fig. 2.1. This line has a stronger blueshifted absorption feature after $\phi = 0.5$ that transforms into a narrow and long-lived absorption line. There is also some evidence of redward emission at the conjunctions that hints at a P Cygni profile shape.

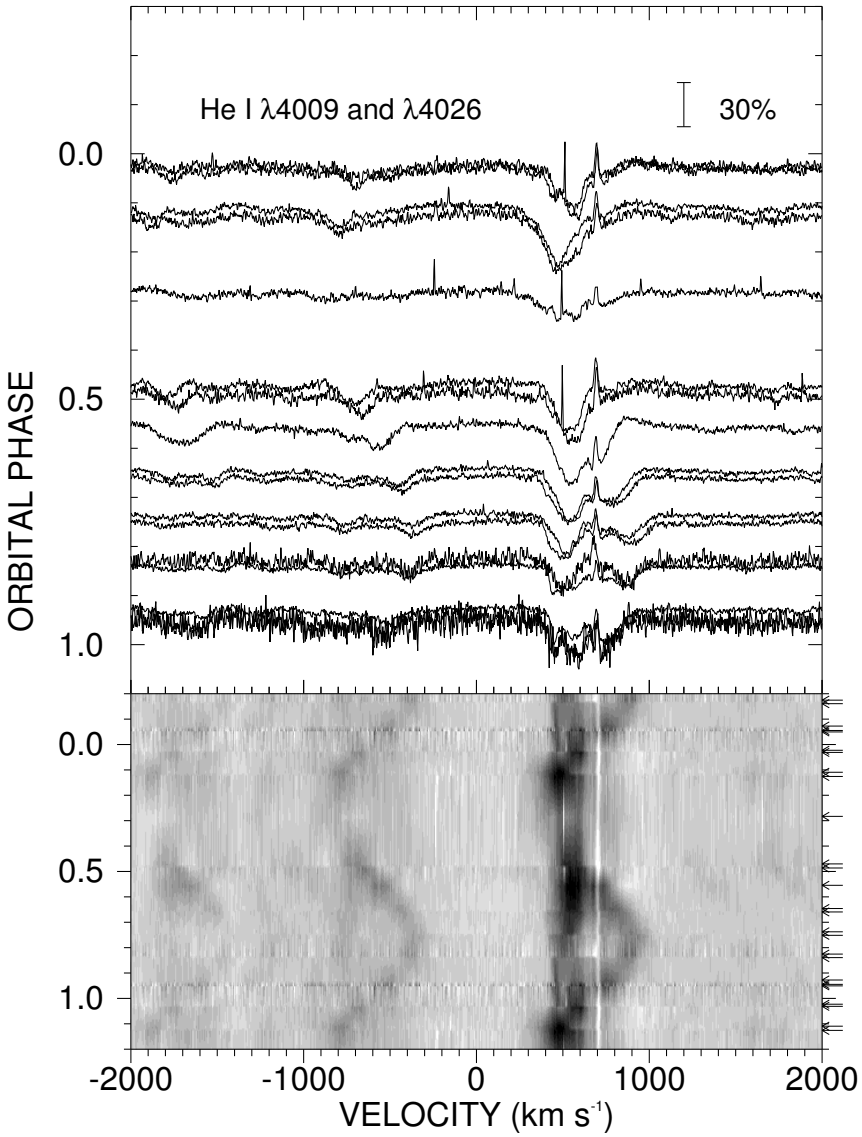

Figure 2.4: The orbital phase variations in the He I $\lambda 4009$ singlet (at -634 km s^{-1}) and the He I $\lambda 4026$ triplet (at $+634$ km s^{-1}) shown in the same format as Fig. 2.1. He I $\lambda 4009$ exhibits the same behavior as He I $\lambda 4387$ (also a singlet). He I $\lambda 4026$ behaves like He I $\lambda 4471$ (also a triplet).

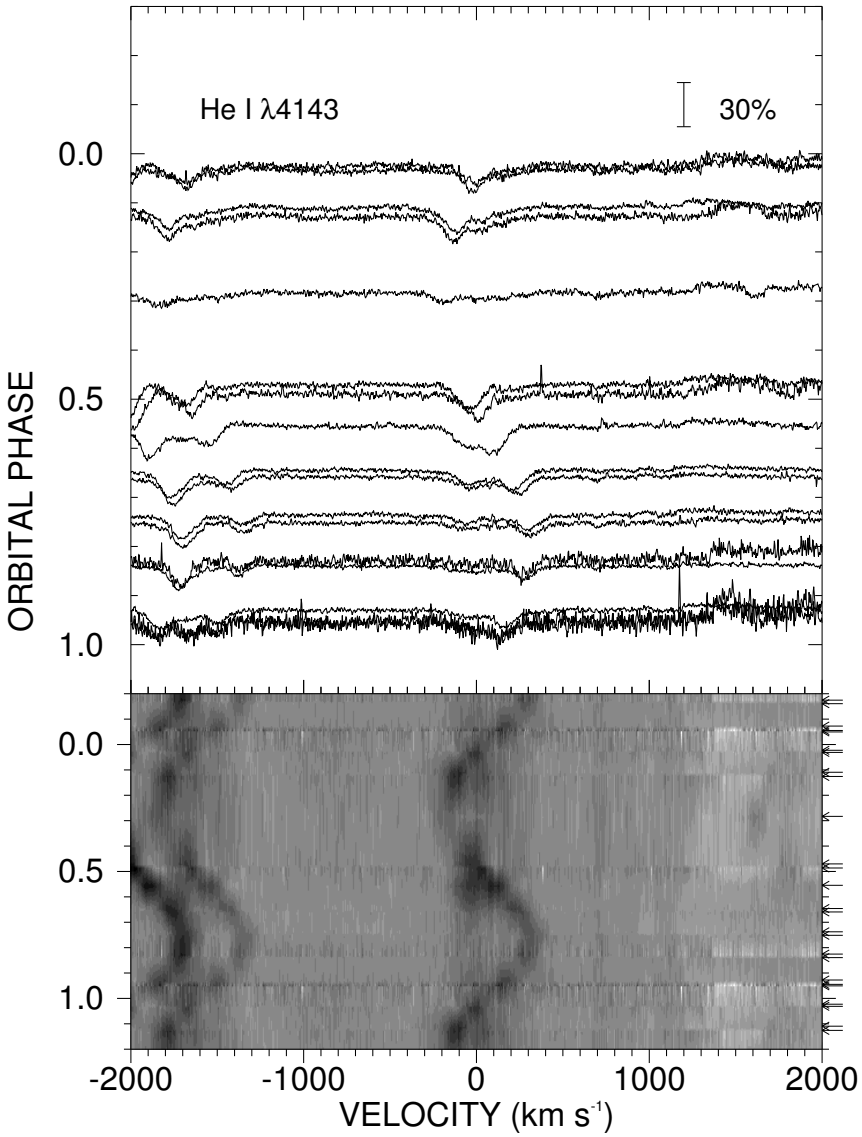

Figure 2.5: The orbital phase variations in the He I $\lambda 4143$ singlet shown in the same format as Fig. 2.1. It behaves as the He I $\lambda 4387$ singlet does. The two absorption features at -1953 and -1591 km s^{-1} are Si IV $\lambda 4116$ and He I $\lambda 4121$ (this helium feature is also a singlet). The emission-like features redward of 1300 km s^{-1} are induced by echelle overlap.

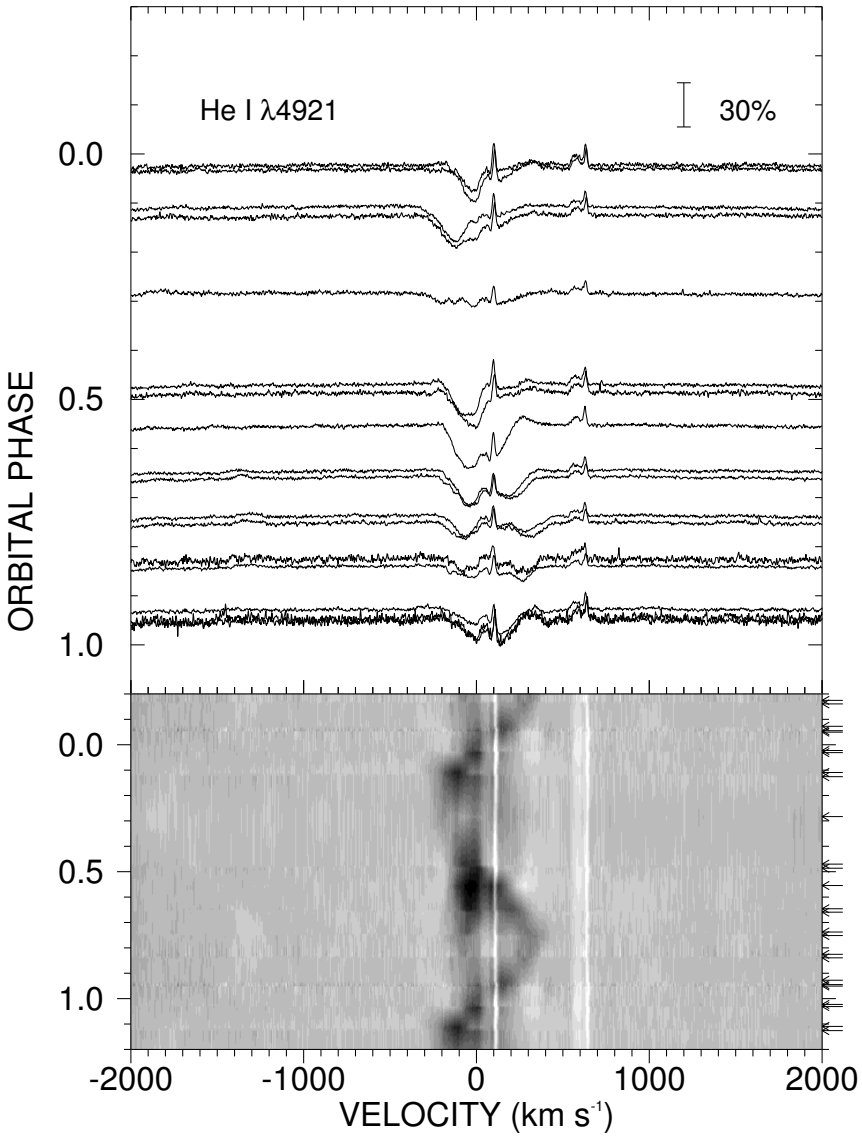

Figure 2.6: The orbital phase variations in the He I $\lambda 4921$ triplet shown in the same format as Fig. 2.1. This line behaves in the same manner as the He I $\lambda 4471$ triplet. The feature at $+600$ km s^{-1} is a [Fe II] nebular emission feature.

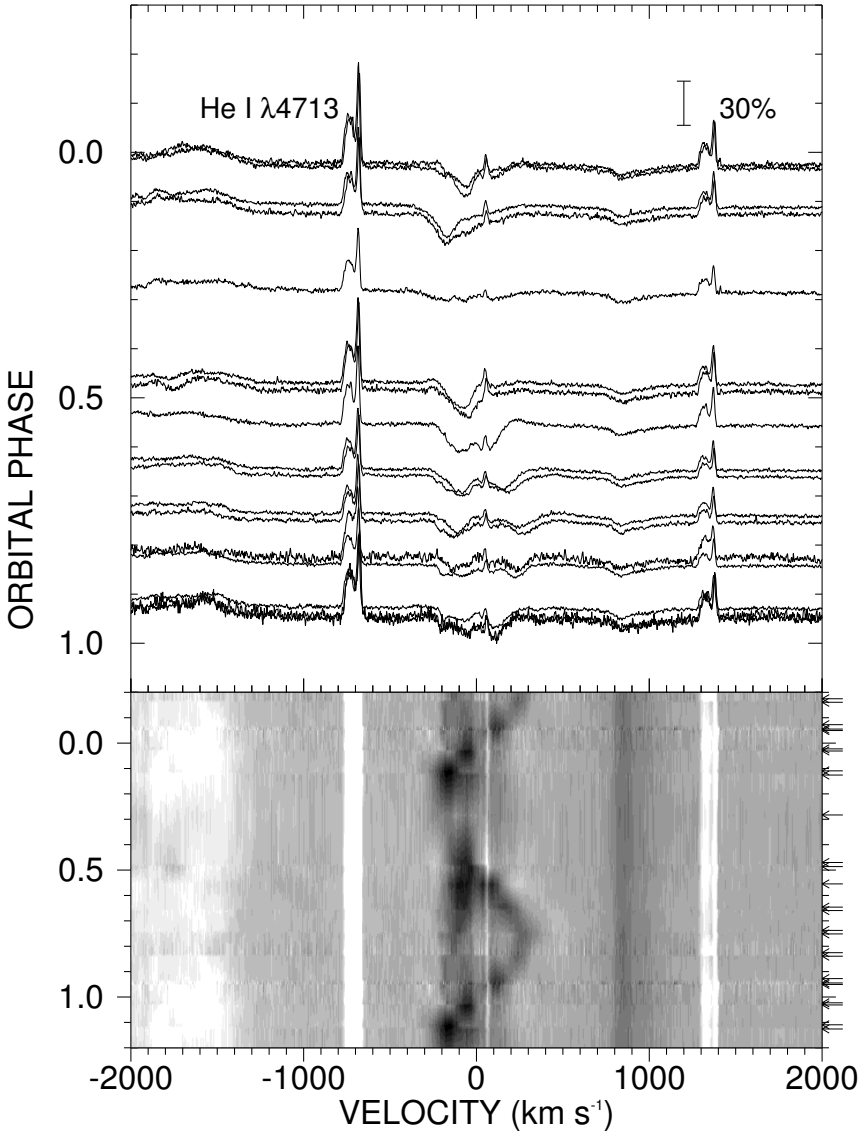

Figure 2.7: The orbital phase variations in the He I $\lambda 4713$ triplet shown in the same format as Fig. 2.1. This line behaves in the same manner as the He I $\lambda 4471$ triplet. The broad emission feature on the left is He II $\lambda 4686$ which is discussed further in Fig. 2.13. Strong [Fe II] nebular emission features are present at -810 and $+1450$ km s^{-1}. The faint absorption at $+840$ km s^{-1} is a diffuse interstellar band.

Figure 2.8 shows the orbital variations in the triplet Si III $\lambda\lambda 4552, 4567, 4574$ in the velocity frame of Si III $\lambda 4552$. The supergiant component appears to be present and undergoes the same kind of strengthening at conjunctions seen in the He I lines. However, each of the triplet members also shows a broad shallow feature that moves in the manner expected for the massive companion. Thus, our observations confirm the detection of this second component that was discovered by Skul'Skii (1992).

There are several weak and narrow emission lines that appear to follow the supergiant's motion. These lines are likely formed in its atmosphere. In Figure 2.9, we show an example of just such a line.

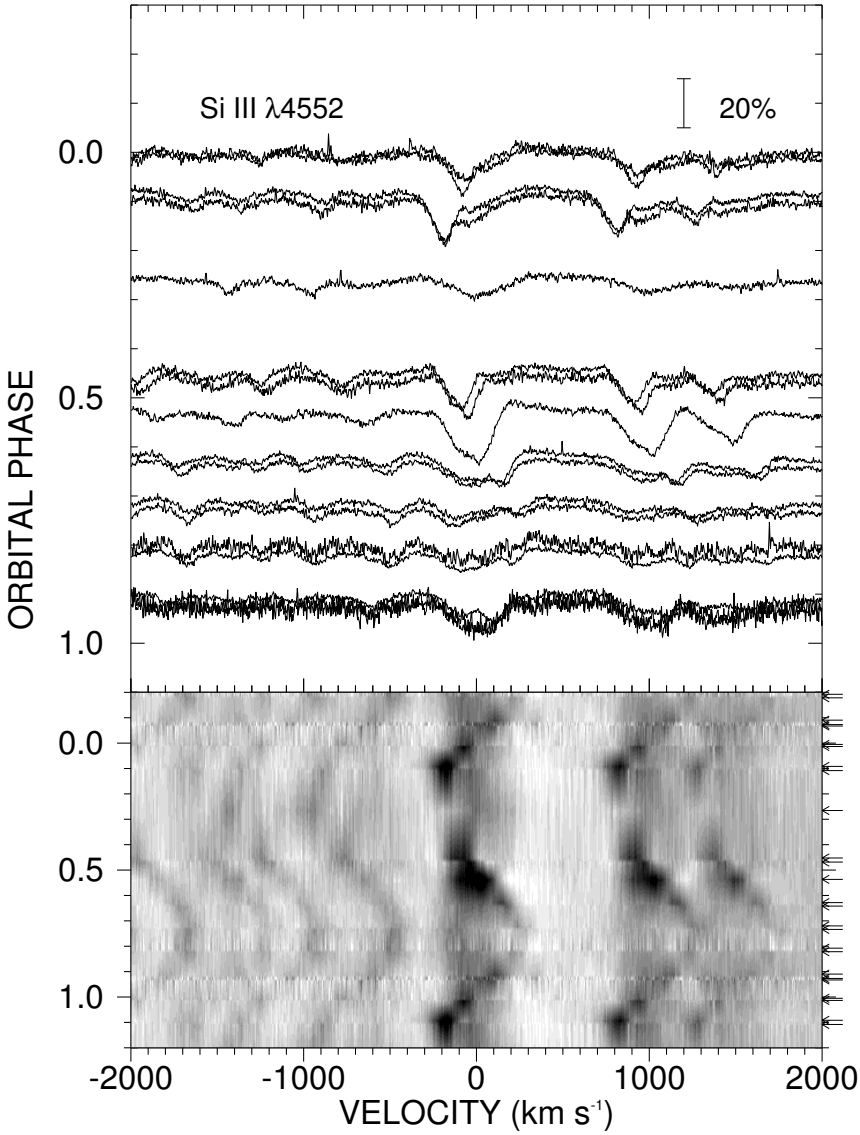

Figure 2.8: The orbital phase variations in the Si III $\lambda 4552$ line in the same format as Fig. 2.1. All of the triplet Si III $\lambda 4552, 4567, 4574$ (at 0, 1004, and 1459 km s^{-1}, respectively) components show dramatic strengthening at the conjunctions and display a broad, shallow feature moving in anti-phase as expected for the massive companion. The absorption feature at -726 km s^{-1} is He II $\lambda 4541$.

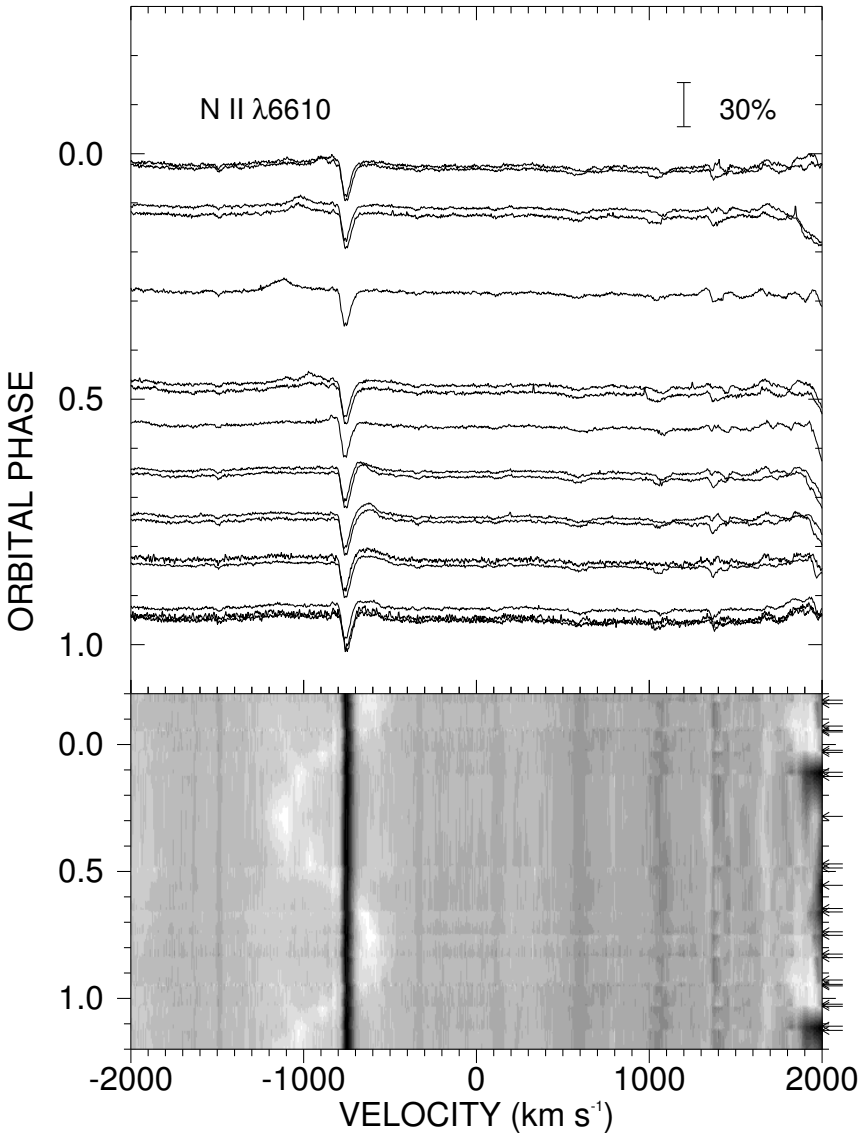

Figure 2.9: The orbital phase variations in the emission feature of N II $\lambda 6610$ shown in the same format as Fig. 2.1 although the plot is not centered on the feature as the very strong Hα and [N II] features are nearby. The dark absorption line at -725 km s^{-1} is the diffuse interstellar band at 6613 Å . To the far right is the wing of He I $\lambda 6678$.

There are two very broad emission lines present that are important to the study of this binary system, Hα λ6563 and He II λ4686 (Sahade et al. 2002). The Hα feature consists of a broad emission feature that is spatially coincident with the central binary plus a strong but narrow component formed in the double-toroidal nebula (Smith et al. 2002). Therefore, in order to isolate the emission component near the binary, we had to remove the nebular components of Hα and the nearby [N II] $\lambda\lambda 6548, 6583$ lines. This removal process was done by scaling the [N II] λ6583 line in each spectrum to the appropriate size (of either Hα or [N II] λ6548) using the equivalent widths of these lines from Smith et al. (2002), shifting the rescaled line to the location of the line to be removed, and then subtracting it from the spectrum. This process was done interactively and included small adjustments in the scaling and shifting parameters to optimize the subtraction. This procedure was carried out using the IDL program *subcs-v3.pro* given in Appendix B. An example of the spectrum before and after subtraction is given in Figure 2.10. The resulting subtracted Hα profiles, based upon the large set of KPNO coudé feed spectra, are illustrated as a function of orbital phase in the left panel of Figure 2.11. We also show the one spatially resolved *HST* spectrum of the central binary from the work of Smith et al. (2002) (which has no nebular emission present) that verifies that our line subtraction technique creates difference profiles with the appropriate shape. The emission strength appears to be much stronger at the conjunction phases, but this is due mainly to the drop in the continuum flux at those eclipse phases and our normalization of the emission strength to this varying continuum level. The right panel in Figure 2.11 shows a representation of the Hα profiles relative to a constant flux continuum we made by rescaling the emission flux by a factor

$$f/f(\text{quadrature}) = 10^{-0.4(V-9.03)}$$

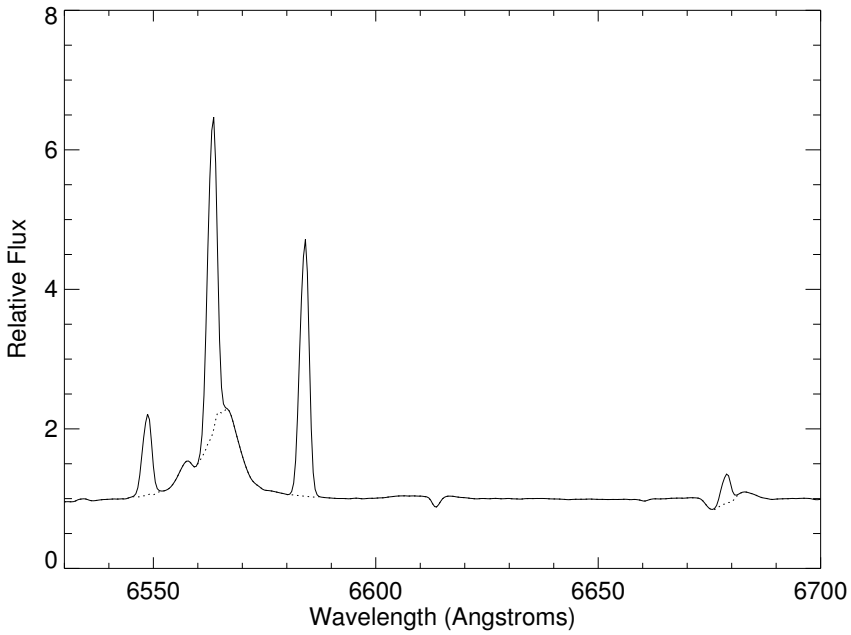

Figure 2.10: Diagram showing the remainder from the subtraction of the nebular lines in Hα and He I $\lambda 6678$ and of the [N II] $\lambda\lambda 6548, 6583$ lines for the data set from the KPNO coudè feed. The *solid line* is the original, unaltered spectrum, and the *dotted line* is the spectrum with the nebular features removed.

where V is the V-band magnitude at the orbital phase of observation (found by interpolation in the light curve data from Djurašević et al. 2001) and $V = 9.03$ corresponds to the maximum brightness of the system at quadrature phases. The Hα emission feature appears broad (spanning over 1000 km s^{-1}) and approximately constant in strength and position in this version. There is often a weak, blueshifted absorption component present (with a radial velocity of ≈ -150 km s^{-1}) that gives the profile a P Cygni appearance. Similar results were seen in the Hα difference profiles formed from the smaller set of FEROS spectra using using the IDL program *subcsFEint.pro* given in Appendix B. The orbital phase variations are shown in Figure 2.12.

Finally, we show in Figure 2.13 the orbital phase variations in the weak He II $\lambda 4686$ emission line observed in the FEROS spectra that we smoothed with a Gaussian of

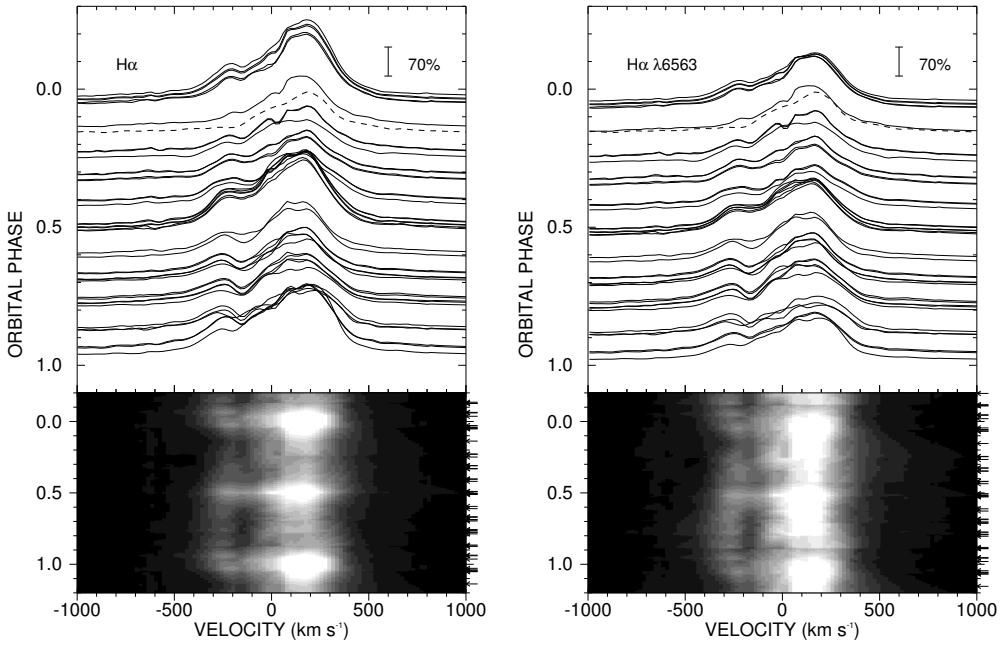

Figure 2.11: The orbital variations in the Hα profiles after subtraction of the nebular component (based upon the KPNO coudé feed set of spectra). The dashed line at $\phi = 0.15$ is a single *HST* spectrum of the central binary exclusive of the surrounding nebula, and the good match to our spectra at that phase indicates that the nebular subtraction method is reliable. The left hand panel shows the profiles normalized to the observed continuum (lower near $\phi = 0.0$ and $\phi = 0.5$) while the right hand panel shows the emission rescaled to a constant reference continuum. The net Hα profile is approximately stationary and has high velocity wings that move in anti-phase to the supergiant's radial velocity curve.

FWHM = 45 km s^{-1} to improve the otherwise noisy appearance. This feature is found only in very hot plasmas, and there is no corresponding nebular feature in this case. The He II λ4686 emission is almost as broad as the net Hα emission, but is significantly weaker. The wings of the line appear to exhibit a slight anti-phase motion that was documented by Sahade et al. (2002).

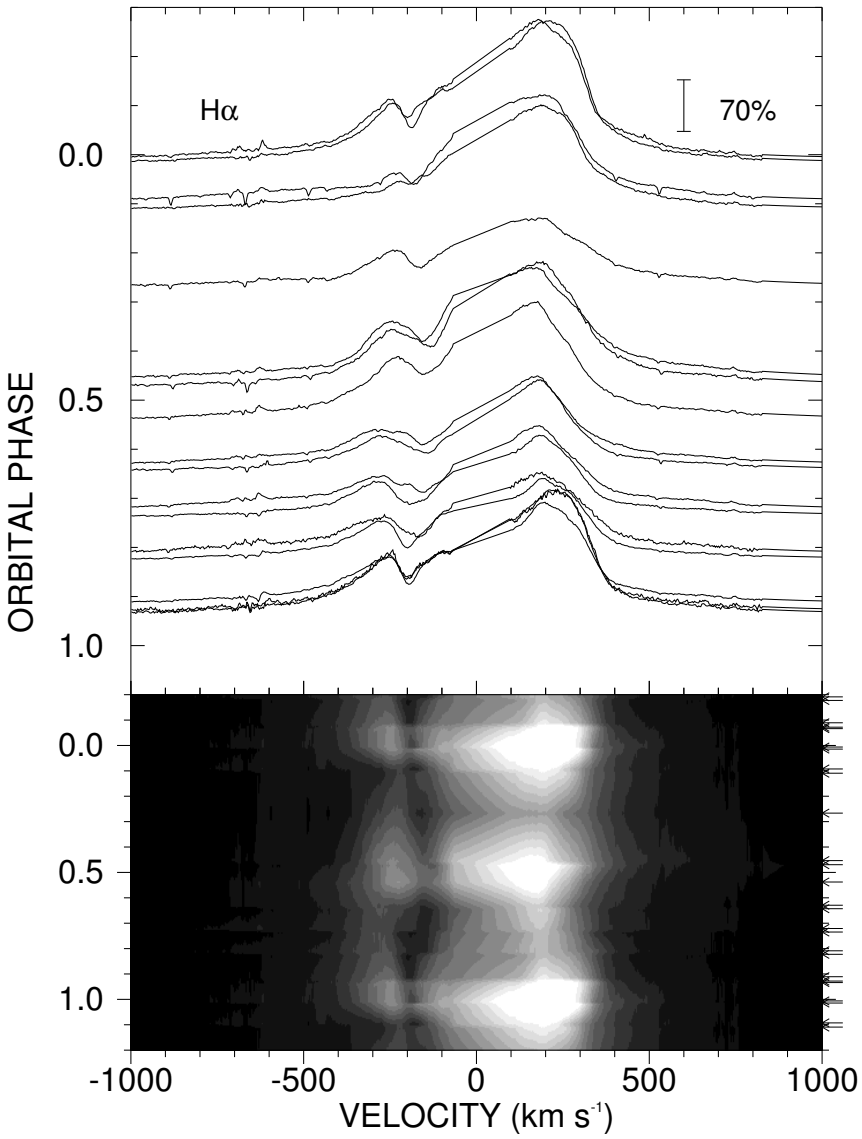

Figure 2.12: The orbital variations in the Hα profiles after excising the nebular component (based upon the FEROS set of spectra). It shows the same behavior as the coudé feed set (Fig. 2.11)

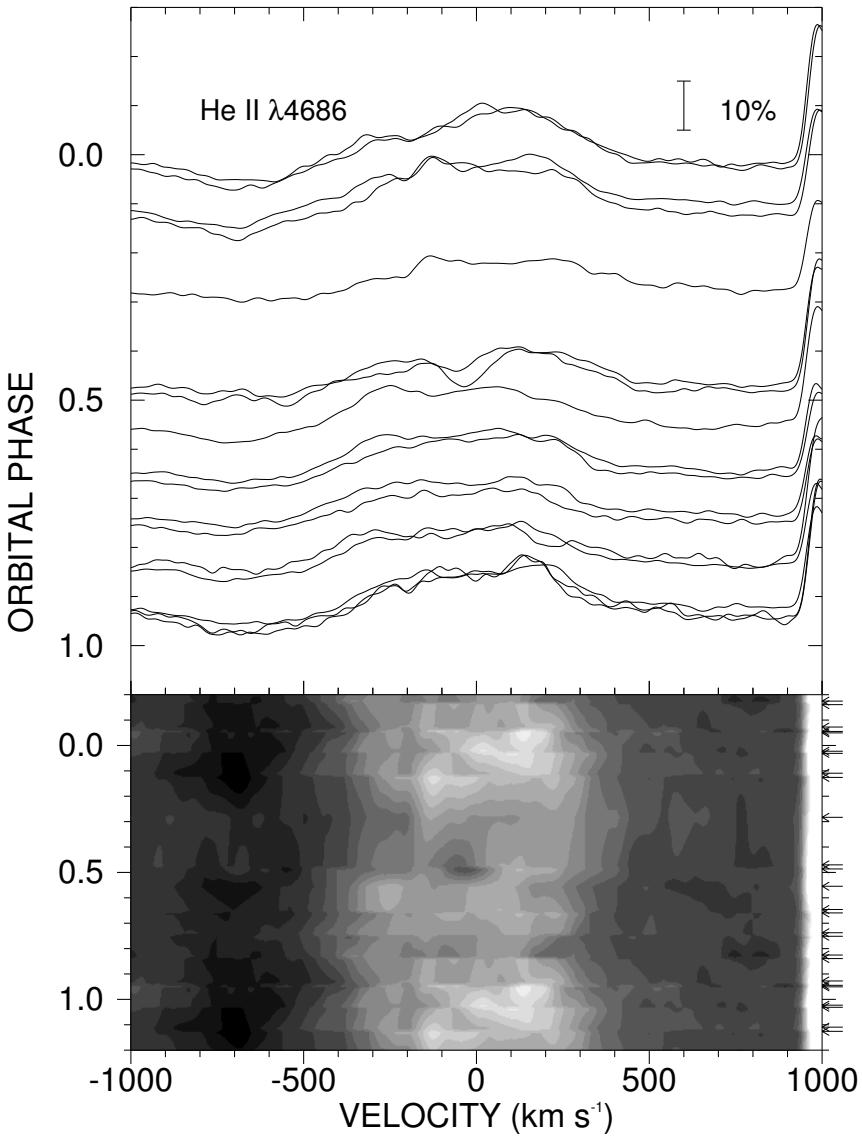

Figure 2.13: The orbital phase variations of the broad and weak He II $\lambda 4686$ emission line. It appears brighter at $\phi = 0.0$ and shows a hint of the anti-phase motion associated with the massive companion. The nebular emission feature at 1000 km s^{-1} is [Fe III] $\lambda 4702$.

2.4 Radial Velocity Curve of the Supergiant

The radial velocity shifts of the supergiant are readily apparent in many lines, and given the quality and number of the new spectra we decided to measure the radial velocities and reassess the orbital elements. We measured relative radial velocities by cross-correlating each spectrum with a template spectrum. For the FEROS and CTIO spectra, this template spectrum was generated from the non-LTE, line-blanketed model atmosphere and synthetic spectra grid from Lanz & Hubeny (2003) using $T_{\rm eff}$ = 30000 K and $\log g$ = 3.0, which are appropriate values for an O9.7 Ib star (Herrero et al. 1995). This template was rotationally broadened (§2.5) and also smoothed to the instrumental resolution of the FEROS or CTIO spectra. First, we removed certain interstellar features by forming an average interstellar spectrum from the mean of the entire set and then dividing each spectrum by the average interstellar spectrum. Because the spectrum of RY Scuti contains so many stationary nebular lines and possible features from the massive companion, we restricted the wavelength range for the cross-correlation to regions surrounding a set of absorption lines that appeared to be free of line blending and that were clearly visible throughout the orbit. The main features in the selected regions are summarized in Table 2.2.

Table 2.2: Supergiant Radial Velocity Line Sample

Telescope Run	Line Regions
ESO 1.5 m	Si IV λ4088; Si IV λ4116, He I λ4121; N III $\lambda\lambda$4510, 4514, 4518;
CTIO 1.5 m	Si IV λ4088; Si IV λ4116, He I λ4121; N III $\lambda\lambda$4510, 4514, 4518;
KPNO CF	N II λ6610 (em.); Si IV λ6701 (em.)

For the KPNO coudé feed spectra, we selected one spectrum from the set of 40 to serve as the template as the Lanz & Hubeny models did not match the emission

lines we measured (Table 2.2). This spectrum (made on HJD 2451425.784) has relatively high signal-to-noise, exhibits well-defined spectral features, and was made near quadrature when the supergiant Doppler shifts are large and the features reasonably well separated from any component from the massive companion. Once again, we first removed interstellar features, then selected regions free from nebular lines for the cross-correlation. Once we performed the cross-correlation, we determined the absolute radial velocity of the template spectrum by fitting the core of the emission lines (N II λ6610 and Si IV λ6701) with a parabola and determined the shift from the rest wavelengths. We added the radial velocity of the template to all the relative velocities to place them on an absolute scale.

Because the velocities from the different runs are based upon measurements of different lines in the template and individual spectra, we anticipated that there might be systematic differences in the zero-points of each set. We began by making independent circular orbital fits for each set, and indeed we found the systemic velocity γ for the FEROS set was offset by -20.6 km s^{-1} from the resulting systemic velocities for the KPNO and CTIO sets. As the latter were closer to the nebular systemic velocity (20 ± 3 km s^{-1}; Smith et al. 2002) and based upon more observations, we arbitrarily adjusted the FEROS measurements by adding 20.6 km s^{-1} to bring them into consistency with the other measurements. Note that this decision adds an additional uncertainty to the real error in the final determination of the systemic velocity but otherwise has no effect on the other orbital elements. Our final radial velocities are collected in Table 2.3 that lists the date of observation, orbital phase (see below), radial velocity, calculated error in radial velocity, observed minus calculated residual, and the telescope where the spectrum was acquired (Table 2.1). The quoted radial velocity error for the blue spectra is the standard deviation of the cross-correlation measurements from the three line regions. We measured only two line regions in the

red spectra, so the velocity error is estimated as the larger of the difference between the two measurements or the mean value of $|V_i - V_{i+1}|/\sqrt{2}$ from closely spaced pairs of observations.

Table 2.3: Supergiant Radial Velocity Measurements

HJD (−2,450,000)	Orbital Phase	V_r (km s^{-1})	σ (km s^{-1})	$O-C$ (km s^{-1})	Telescope
1354.781 ...	0.231	−221.6	11.6	14.6	KPNO CF
1354.803 ...	0.233	−218.0	9.6	18.5	KPNO CF
1355.674 ...	0.312	−217.2	30.0	2.2	KPNO CF
1355.701 ...	0.314	−207.2	11.3	10.8	KPNO CF
1355.914 ...	0.333	−215.4	16.9	−10.8	KPNO CF
1355.935 ...	0.335	−212.4	27.4	−9.3	KPNO CF
1356.722 ...	0.406	−116.8	20.1	10.9	KPNO CF
1356.744 ...	0.408	−122.4	25.1	2.6	KPNO CF
1356.910 ...	0.423	−122.0	28.7	−17.0	KPNO CF
1357.691 ...	0.493	−30.1	12.2	−30.5	KPNO CF
1357.712 ...	0.495	−7.8	10.1	−11.1	KPNO CF
1357.832 ...	0.506	8.5	13.4	−11.7	KPNO CF
1357.853 ...	0.507	25.2	34.2	2.0	KPNO CF
1357.912 ...	0.513	21.5	9.7	−9.9	KPNO CF
1357.933 ...	0.515	29.7	9.6	−4.7	KPNO CF
1358.861 ...	0.598	127.5	9.6	−28.1	KPNO CF
1359.663 ...	0.670	232.0	26.9	2.0	KPNO CF
1359.709 ...	0.674	214.8	9.8	−18.3	KPNO CF
1359.889 ...	0.691	213.2	13.3	−30.4	KPNO CF
1359.911 ...	0.692	223.3	15.7	−21.4	KPNO CF
1360.664 ...	0.760	251.5	10.7	−8.8	KPNO CF
1360.730 ...	0.766	248.9	17.6	−10.6	KPNO CF
1360.860 ...	0.778	238.7	25.9	−18.3	KPNO CF
1360.881 ...	0.780	242.1	27.4	−14.4	KPNO CF
1361.872 ...	0.869	209.2	20.6	14.7	KPNO CF
1361.953 ...	0.876	199.8	10.0	13.2	KPNO CF
1362.661 ...	0.940	142.8	9.6	39.1	KPNO CF
1362.706 ...	0.944	120.8	15.2	22.9	KPNO CF
1363.684 ...	0.032	0.8	9.6	38.5	KPNO CF
1363.807 ...	0.043	−43.5	9.6	11.0	KPNO CF
1363.839 ...	0.046	−61.5	9.6	−2.6	KPNO CF
1363.925 ...	0.053	−70.6	9.6	−0.1	KPNO CF
1363.946 ...	0.055	−75.4	9.6	−2.1	KPNO CF
1364.900 ...	0.141	−191.6	31.9	−10.1	KPNO CF
1373.693 ...	0.931	112.4	12.0	−3.3	ESO 1.5 m
1373.758 ...	0.937	103.7	8.6	−3.7	ESO 1.5 m
1374.655 ...	0.018	−53.7	7.3	−37.3	ESO 1.5 m
1375.709 ...	0.113	−161.2	6.5	−10.6	ESO 1.5 m
1379.718 ...	0.473	−16.1	7.4	14.6	ESO 1.5 m
1381.646 ...	0.646	214.1	11.5	4.4	ESO 1.5 m
1382.668 ...	0.738	272.0	3.9	11.9	ESO 1.5 m
1383.645 ...	0.826	252.3	8.5	19.4	ESO 1.5 m
1384.625 ...	0.914	140.1	6.8	0.5	ESO 1.5 m
1385.687 ...	0.010	−53.4	10.9	−49.9	ESO 1.5 m
1386.650 ...	0.096	−161.5	6.9	−31.5	ESO 1.5 m
1388.583 ...	0.270	−215.0	3.4	20.9	ESO 1.5 m
1390.664 ...	0.457	−49.4	8.9	5.8	ESO 1.5 m
1391.602 ...	0.541	78.5	12.8	3.2	ESO 1.5 m
1392.619 ...	0.633	194.5	10.4	−1.6	ESO 1.5 m
1393.638 ...	0.724	272.4	7.1	14.9	ESO 1.5 m
1394.615 ...	0.812	253.2	1.4	11.2	ESO 1.5 m
1421.765 ...	0.253	−230.9	9.6	6.9	KPNO CF
1425.784 ...	0.614	165.2	9.6	−9.9	KPNO CF
1426.745 ...	0.700	236.6	29.3	−12.1	KPNO CF
1427.748 ...	0.790	244.5	27.8	−8.2	KPNO CF
1428.718 ...	0.878	179.7	24.1	−5.0	KPNO CF
1429.713 ...	0.967	98.4	21.3	35.8	KPNO CF
3152.930 ...	0.871	195.5	13.9	3.0	CTIO 1.5 m
3153.825 ...	0.951	83.9	22.5	−3.0	CTIO 1.5 m
3154.927 ...	0.050	−118.3	46.0	−52.4	CTIO 1.5 m
3156.922 ...	0.229	−216.3	15.4	19.5	CTIO 1.5 m

Continued on Next Page...

Table 2.3 – Continued

HJD (−2,450,000)	Orbital Phase	V_r (km s^{-1})	σ (km s^{-1})	$O-C$ (km s^{-1})	Telescope
3157.932 ...	0.320	−204.4	17.0	9.6	CTIO 1.5 m
3158.928 ...	0.410	−128.2	2.5	−5.9	CTIO 1.5 m
3161.915 ...	0.678	239.7	14.6	3.8	CTIO 1.5 m
3162.914 ...	0.768	254.1	11.2	−5.0	CTIO 1.5 m
3163.892 ...	0.856	206.1	17.7	−1.4	CTIO 1.5 m
3164.903 ...	0.947	83.5	19.6	−9.5	CTIO 1.5 m

We determined revised orbital elements using the the nonlinear, least-squares, fitting code of Morbey & Brosterhus (1974). Because the errors associated with each run are different, we assigned each measurement a weight proportional to the inverse square of the measurement error. The orbital period was fixed at $P = 11.12445$ days as found by Kreiner (2004) from contemporary eclipse timing observations over a long time base. We made both eccentric and circular orbital solutions, but we think the eccentric solution, while formally statistically significant according to the test of Lucy & Sweeney (1971), is probably spurious. Harmanec (1987) found that gas streams and circumstellar matter (both present in RY Scuti) can distort spectroscopic features in mass-transferring binaries because they add emission to said features in non-symmetric ways. Such distortions can lead to skewed radial velocity results and thus artificial eccentricities (Lucy 2005). A zero eccentricity is consistent with predictions for Roche lobe overflow systems where the tidal effects are expected to circularize the orbit and synchronize the rotational and orbital periods. The final orbital elements from both the circular and eccentric solutions are presented in Table 2.4 together with solutions from Sahade et al. (2002) and Skul'Skii (1992). The epoch T_{SC} refers to the time of supergiant superior conjunction (close to the time of photometric minimum light) while T is the epoch of periastron in the eccentric solution. The radial velocities and orbital velocity curves are plotted in Figure 2.14. Our results are in reasonable agreement with earlier determinations of the elements, with the possible exception of the larger non-zero eccentricity found by Sahade et al.

(2002). We suspect the difference is due to the lack of orbital phase coverage in the observations of Sahade et al. (2002) in the ascending portion of the velocity curve.

Table 2.4: Orbital Elements for RY Scuti

Element	Circular	Elliptical	Sahade et al. (2002)	Skul'skii (1992)
P (days)	11.12445[a]	11.12445[a]	11.124646[a]	11.1250[a]
T_{SC} (HJD–2,400,000)	51396.71 ± 0.02	···	···	44777.9 ± 1.0
T (HJD–2,400,000) ..	···	51395.68 ± 0.40	45107.74	···
e	0	0.05 ± 0.01	0.16 ± 0.04	0
ω (deg)	···	57 ± 13	345 ± 15	···
K_{SG} (km s^{-1})	249 ± 3	247 ± 3	273 ± 14	235 ± 3
K_{MC} (km s^{-1})	59 ± 9	···	71 ± 9	71 ± 2
γ_{SG} (km s^{-1})	11 ± 2	12 ± 2	17 ± 5	9 ± 2
γ_{MC} (km s^{-1})	-20 ± 9	···	···	11 ± 2
r.m.s.$_{SG}$ (km s^{-1}) ...	19	17	···	···
r.m.s.$_{MC}$ (km s^{-1}) ..	25	···	···	···
a ($R_\odot$)	69.9 ± 2.3	···	77 ± 4	68
$q = M_{MC}/M_{SG}$	4.2 ± 0.7	···	3.9 ± 0.5	3.3 ± 0.1
M_{SG} ($M_\odot$)	7.1 ± 1.2	···	10.2 ± 1.7	8
M_{MC} ($M_\odot$)	30.0 ± 2.1	···	39 ± 4	26

[a] Fixed

2.5 Nature of the Massive Companion

Very little is known about the massive companion because it is difficult to find its associated features in the spectrum (probably because the massive companion is enshrouded in a thick accretion disk; §2.7). We can make an approximate estimate for the expected semiamplitude of motion for the massive companion using a geometrical argument to find the mass ratio, $q = M_{MC}/M_{SG}$. Let us assume the supergiant is filling its Roche lobe and is synchronously rotating (reasonable in the case of RY Scuti where we see so much spectroscopic evidence of active mass transfer). Gies & Bolton (1986) showed that for such Roche-filling stars, the projected rotational velocity $V \sin i$ provides a measure of the stellar radius while the semiamplitude K is related to the mass ratio and semimajor axis a, and the ratio of these quantities is a

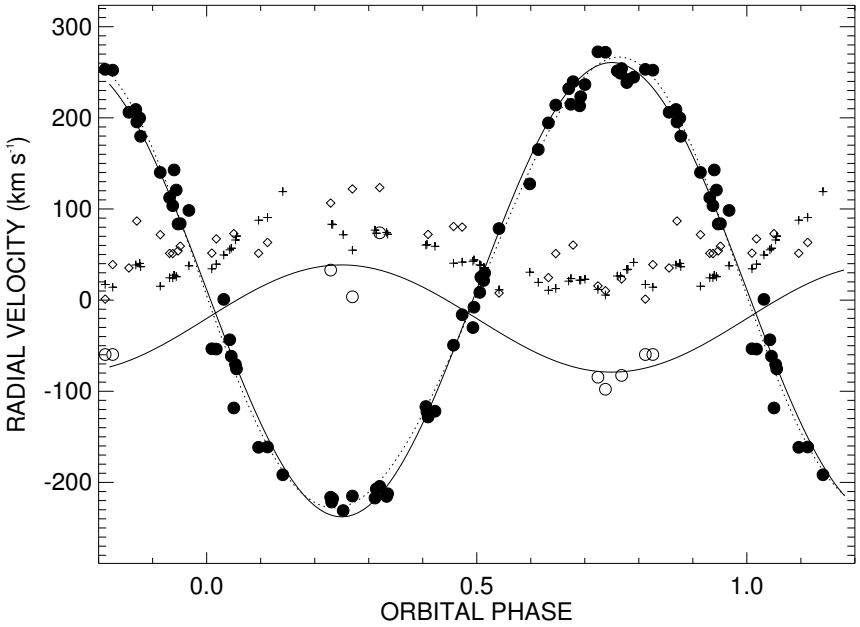

Figure 2.14: The radial velocity curve and measurements for several spectral components (where $\phi = 0.0$ corresponds to supergiant superior conjunction). The *filled circles* represent radial velocities of the supergiant (with typical errors of 10 km s^{-1}) while the large amplitude *solid line* shows the derived velocity curve for the circular solution and the elliptical solution is shown by the *dotted curve* (Table 2.4). The *open circles* illustrate the radial velocities for Si III λ4552 (with typical errors of 30 km s^{-1}) which represents the massive companion and the smaller amplitude *solid line* shows the constrained fit (Table 2.7). The *diamonds* represent the radial velocities for the broad He II λ4686 emission (with typical errors of 50 km s^{-1}) while the *plus signs* indicate radial velocities for the Hα wings (with typical errors of 2 km s^{-1}).

function that solely depends on the mass ratio,

$$\begin{aligned} V \sin i / K &= \frac{\Omega R_{SG} \sin i}{\Omega a_{SG} \sin i} \\ &= \left(1 + \frac{M_{SG}}{M_{MC}}\right) \frac{R_{SG}}{a} = (1+Q)\, f(Q) \end{aligned}$$

where Ω is the orbital angular rotation speed, $Q = 1/q = M_{SG}/M_{MC}$, and $f(Q)$ is the fractional Roche filling radius (Eggleton 1983). Thus, a measurement of the supergiant's projected rotational velocity leads directly to an estimate of the mass ratio. We show below that this geometrical mass ratio estimate is consistent with the

mass ratio derived from orbital velocity measurements for both components.

We determined $V \sin i$ for the supergiant through a comparison of the photospheric line width with models for a grid of projected rotational velocity. For this purpose, we selected the Si IV λ4088 line because it is free of nebular emission and line blending with other features and its shape is dominated by rotational broadening. We measured the FWHM of Si IV λ4088 in three of the FEROS spectra obtained near supergiant maximum velocity (to avoid the unusual strengthening seen at conjunctions and any line blending problems with absorption from the massive companion). We then used the model profiles from the non-LTE, line blanketed models of Lanz & Hubeny (2003) that were rotationally broadened by a simple convolution of the zero-rotation model profiles with a rotational broadening function (Gray 1992) using a linear limb-darkening coefficient from the tables of Wade & Rucinski (1985). From the Lanz & Hubeny grid, we selected a model profile for $T_{\rm eff} = 30000$ K and $\log g = 3.0$ and adopted a linear limb darkening coefficient at this wavelength of $\epsilon = 0.38$. Finally, the resulting models were convolved with an instrumental broadening function to match the resolution of the FEROS spectra. The projected rotational velocity for the supergiant derived from the resulting $(V \sin i, FWHM)$ relation is $V \sin i = 80 \pm 5$ km s^{-1}. The error represents the standard deviation of $V \sin i$ as derived from the three measurements of line width and does not account for any systematic errors associated with the choice of model atmosphere parameters.

We caution that this is actually an upper limit for $V \sin i$ because the line may also be broadened by macroturbulence in the stellar atmosphere (Ryans et al. 2002). If we include an estimate of $V_{macro} = 30$ km s^{-1} (a mid-range value for B-supergiants; Ryans et al. 2002), then we find $V_{eq} \sin i = 74^{+7}_{-13}$ km s^{-1} (where the error range accounts for the derived error in $V \sin i$ and a range in macroturbulent velocity from 10 to 50 km s^{-1}). Thus, using the $V \sin i/K$ method described above, we find an

estimate of the mass ratio, $q = 4.9^{+2.9}_{-0.9}$. We can use this mass ratio estimate to offer some guidance about the expected orbital semiamplitude of the massive companion, $K_{MC} = K_{SG}/q = 31 - 61$ km s^{-1}.

Previous researchers (Popper 1943; Cowley & Hutchings 1976; Skul'Skii 1992; Sahade et al. 2002) have associated a variety of spectral features with the massive companion, and we inspected the orbital variations of all these proposed lines in the FEROS spectra (examples shown in Fig. 2.1 – 2.8). Many of these lines have complicating factors related to nebular emission and blending with other features. For example, a number of the He I lines appear to show a blueshifted absorption feature in the phase range $\phi = 0.6 - 0.9$ where we would expect to find the absorption component from the massive companion, but these blueshifted features first appear at $\phi = 0.5$ when any gas leaving the supergiant in the L2 region would also appear blueshifted (§2.7). Consequently, an identification of these features with the massive companion is ambiguous.

Only three of the proposed spectral features for the massive companion clearly fit the mass ratio argument described above and display the expected anti-phase velocity shifts: Hα, He II λ4686 and Si III λ4552. Here we present radial velocity measurements for each of these. The Hα emission profile is not Gaussian in shape (see Fig. 2.11) and therefore could not be measured as such. Instead we determined the radial velocity of the line wings (which represent the fastest-moving gas and are unaffected by nebular emission) based upon a bisector position found using the method of Shafter, Szkody, & Thorstensen (1986). We sampled the line wings using oppositely signed Gaussian functions and determined the mid-point position between the wings by cross-correlating these Gaussians with the profile. We used Gaussian functions with FWHM = 137 km s^{-1} at sample positions in the wings of $\pm$382 km s^{-1} for spectra from both the coudé feed and the FEROS instrument. An inspection of

radial velocity measurements closely spaced in time ($\delta t > 0.5$ d) indicates an average error of 1.7 km s^{-1}. Our results are given in column 3 of Table 2.5, and the values are plotted as a function of orbital phase in Figure 2.14.

Table 2.5: Hα Wing Velocities and Equivalent Widths

Date (HJD−2,450,000)	Orbital Phase	V_r (km s^{-1})	W_λ (Å)
1354.781	0.231	83.3	−13.4
1354.803	0.233	82.9	−13.4
1355.674	0.312	76.8	−12.9
1355.701	0.314	73.4	−13.2
1355.913	0.333	74.2	−13.2
1355.935	0.335	72.3	−12.7
1356.722	0.406	60.3	−14.8
1356.744	0.408	61.0	−14.8
1356.910	0.423	59.0	−14.6
1357.691	0.493	42.6	−21.9
1357.712	0.495	44.1	−22.8
1357.832	0.506	38.8	−23.0
1357.853	0.507	38.0	−23.0
1357.912	0.513	35.7	−20.5
1357.933	0.515	35.4	−19.6
1358.861	0.598	30.6	−14.5
1359.663	0.670	20.8	−12.5
1359.709	0.674	23.7	−13.4
1359.889	0.691	21.9	−12.1
1359.911	0.692	21.8	−12.3
1360.664	0.760	26.4	−13.6
1360.730	0.766	26.3	−14.0
1360.860	0.778	33.4	−13.0
1360.881	0.780	33.8	−12.7
1361.872	0.869	38.5	−13.8
1361.953	0.876	40.2	−12.1
1362.661	0.940	27.3	−18.8
1362.706	0.944	25.7	−19.5
1363.684	0.032	49.5	−21.9
1363.807	0.043	55.2	−21.3
1363.839	0.046	56.9	−21.1
1363.925	0.053	66.0	−18.6
1363.946	0.055	70.3	−18.0
1364.900	0.141	119.1	−13.6
1373.693	0.931	24.4	−18.4
1373.758	0.937	24.4	−19.2
1374.655	0.018	39.5	−21.5
1375.709	0.113	90.6	−15.1
1379.718	0.473	41.7	−19.7
1381.646	0.646	12.7	−12.7
1382.668	0.738	5.5	−11.5
1383.645	0.826	14.2	−12.4
1384.625	0.914	15.2	−15.1
1385.687	0.010	34.4	−21.3
1386.650	0.096	87.7	−16.1
1388.583	0.270	54.8	−11.8
1390.664	0.457	40.5	−19.0
1391.602	0.541	11.3	−18.7
1392.619	0.633	10.8	−13.2
1393.638	0.724	11.7	−13.1
1394.615	0.812	17.2	−13.0
1421.765	0.253	71.7	−12.1
1425.784	0.614	19.5	−14.3
1426.745	0.700	22.9	−12.4
1427.748	0.790	41.3	−12.4
1428.718	0.878	36.7	−13.1
1429.713	0.967	37.7	−20.9

The He II λ4686 emission profile is also broad (FWHM $\approx$ 850 km s^{-1}) and not Gaussian-shaped. Therefore, we used spectral templates and cross-correlation functions to measure radial velocities. We formed templates from the averages of the entire run for the respective FEROS and CTIO data sets as the He II λ4686 emission strength may have changed between 1999 (FEROS) and 2004 (CTIO). We then transformed the relative velocities to an absolute scale by adding the radial velocity derived by fitting each template with a broad Gaussian. Our results are given in column 4 of Table 2.6 and are plotted in Figure 2.14. Based on visual estimates of the goodness of the fit of this very broad line, we estimate errors in the velocities are $\approx$ 50 km s^{-1}.

Table 2.6: Features Associated with the Massive Companion

Date (HJD−2,450,000)	Orbital Phase	V_r(Si III) (km s^{-1})	V_r(He II) (km s^{-1})	W_λ(He II) (Å)
1373.693	0.931	···	51.3	−0.93
1373.758	0.937	···	51.1	−0.92
1374.655	0.018	···	67.2	−0.99
1375.709	0.113	···	63.3	−0.95
1379.718	0.473	···	80.2	−0.63
1381.646	0.646	···	51.1	−0.77
1382.668	0.738	−97.8	10.3	−0.63
1383.645	0.826	−59.7	39.0	−0.74
1384.625	0.914	···	71.8	−0.74
1385.687	0.010	···	51.6	−0.95
1386.650	0.096	···	51.4	−0.96
1388.583	0.270	3.6	122.0	−0.66
1390.664	0.457	···	80.8	−0.60
1391.602	0.541	···	7.8	−0.74
1392.619	0.633	···	24.7	−0.81
1393.638	0.724	−84.6	15.6	−0.78
1394.615	0.812	−59.7	1.1	−0.58
3152.930	0.871	···	86.8	−0.59
3153.825	0.951	···	59.2	−0.70
3154.928	0.050	···	72.9	−0.71
3156.922	0.229	33.0	106.5	−0.29
3157.932	0.320	73.9	123.5	−0.34
3158.928	0.410	···	72.1	−0.58
3161.915	0.678	···	60.4	−0.34
3162.914	0.768	−82.6	23.2	−0.51
3163.892	0.856	···	35.3	−0.52
3164.903	0.947	···	54.0	−0.66

We also measured equivalent widths for both these emission lines by a direct numerical integration (over the range 6536.3 − 6595.0 Å for Hα and 4675.3 − 4694.5 Å for He II λ4686). Our results for Hα are given in column 4 of Table 2.5 and for He II

are given in column 5 of Table 2.6. Errors in Hα measurements are $\approx$0.5 Å based upon examining results closely spaced in time. The He II equivalent width errors are 0.02 Å for the FEROS data but are about three times worse for the CTIO data (due to the lower resolution of the CTIO spectra). The orbital variations of these equivalent widths are discussed below (§2.7).

The absorption line Si III λ4552 displays narrow and broad components that move with the expected orbital Doppler shifts of the supergiant and massive component, respectively (Fig. 2.8). In order to avoid any line blending problems between these components, we selected a subset of FEROS and CTIO spectra observed near the quadrature phases where the the broad component could be measured unambiguously, and we made Gaussian fits to determine the radial velocities. Using a visual estimate of goodness of fit to this broad, shallow line, we estimate errors in these velocities are $\approx$ 30 km s^{-1}. Our results are given in column 3 of Table 2.6 and are plotted in Figure 2.14.

The plots of the radial velocities in Figure 2.14 show that all three features exhibit the anti-phase motion expected for the massive companion. We made circular fits of each set by fixing the orbital period and epoch from the solution for the supergiant (Table 2.4) and then solving for the semiamplitude K_{MC} and systemic velocity γ_{MC}. The results are listed in Table 2.7. The semiamplitudes for each feature are within the expected range, however, the values for the two emission lines are smaller than that for the Si III λ4552 absorption line. Furthermore, the systemic velocities for the two emission lines are larger than that found for the supergiant and the nebular emission. We suspect this is due to the P Cygni shape of both features that will bias an emission line velocity measurement to a larger value. We argue below (§2.7) that these emission features are probably formed in gas flows and are thus probably less representative of the orbital motion of the massive companion.

Table 2.7: Summary of Radial Velocity Fits

Element	V_r(Si III)	V_r(He II λ4686)	V_r(Hα wings)
K (km s^{-1})	59 ± 5	36 ± 6	30 ± 3
γ (km s^{-1})	-20 ± 5	64 ± 4	49 ± 2
r.m.s. (km s^{-1})	22	21	13

Thus, if we adopt the Si III λ4552 velocity fits as the most representative of the massive companion, we can make a double-lined solution of the spectroscopic masses, $M \sin^3 i$, using eq. 2.52 in Hilditch (2001),

$$M_{1,2} \sin^3 i = (1.0361 \times 10^{-7})(1 - e^2)^{3/2}(K_1 + K_2)^2 K_{2,1} P \; M_\odot,$$

where K is the semiamplitude in km s^{-1} and P is the period in days. Furthermore, if we set the orbital inclination equal to that for the double-toroidal nebula, then $i = 75°6 \pm 1°7$ (Smith et al. 1999) (in substantial agreement with the light curve solutions; Milano et al. 1981; Djurašević et al. 2001), and we can estimate the component masses directly. We find the masses of the components are $M_{SG} = 7.1 \pm 1.2 \; M_\odot$ and $M_{MC} = 30.0 \pm 2.1 \; M_\odot$. The former is very low for a normal O-supergiant (Martins, Schaerer, & Hillier 2005a), but we should bear in mind this star is in the process of losing its outer envelope to the massive companion and therefore its properties will be very different from those of a single star of comparable temperature and gravity. The mass of the massive companion is like that of a hot O-dwarf or an evolved B-supergiant and we will explore these and other possibilities in the next sections. Our mass results are quite similar to those first obtained by Skul'Skii (1992) but are lower than those determined by Sahade et al. (2002) (given in Table 2.4).

2.6 Tomographic Reconstruction of Spectra

Once the orbital solution for RY Scuti was found, we used a tomographic reconstruction technique (Bagnuolo et al. 1994) with the FEROS data to separate the individual spectra of the components. Tomographic reconstruction is an iterative scheme that uses the combined spectra and their associated radial velocities to determine the appearance of each star's spectrum. RY Scuti presents a special difficulty due to the stationary sharp nebular features. Therefore, before reconstruction, all nebular features listed by Smith et al. (2002) were excised via linear interpolation. We also removed the interstellar lines from each spectrum prior to reconstruction to avoid creating spurious reconstructed features in their vicinity. The reconstruction was based upon a subset of seven FEROS spectra that were obtained near the velocity extrema at the quadrature phases so that we might avoid introducing artifacts due to the line strengthening at the conjunctions and any eclipse effects. Figures 2.15 and 2.16 show plots of the reconstructed spectra in two different regions along with identifications of the principal lines. Also plotted are two comparison spectra from the Valdes et al. (2004) *Indo-U.S. Library of Coudé Feed Stellar Spectra* that have a lower resolving power ($R \approx 3600$) than that of the FEROS spectra ($R \approx 48000$).

The supergiant has a classification of O9.7 Ibpe var (Walborn 1982) and we see the spectrum of the normal single star, HD 188209 (O9.5 Iab; Walborn 1976), provides a reasonably good match. The He II $\lambda\lambda 4199, 4541, 4686$ features appear to be slightly weaker in the RY Scuti supergiant, which is consistent with its subtype difference in spectral type. We used the ratios of the equivalent widths of several weaker He I lines for the RY Scuti supergiant and HD 188209 spectra to set the monochromatic flux ratio for the RY Scuti binary components, and we find the supergiant contributes $\approx 57 \pm 13\%$ of the total flux. The error is based on scatter between the results from

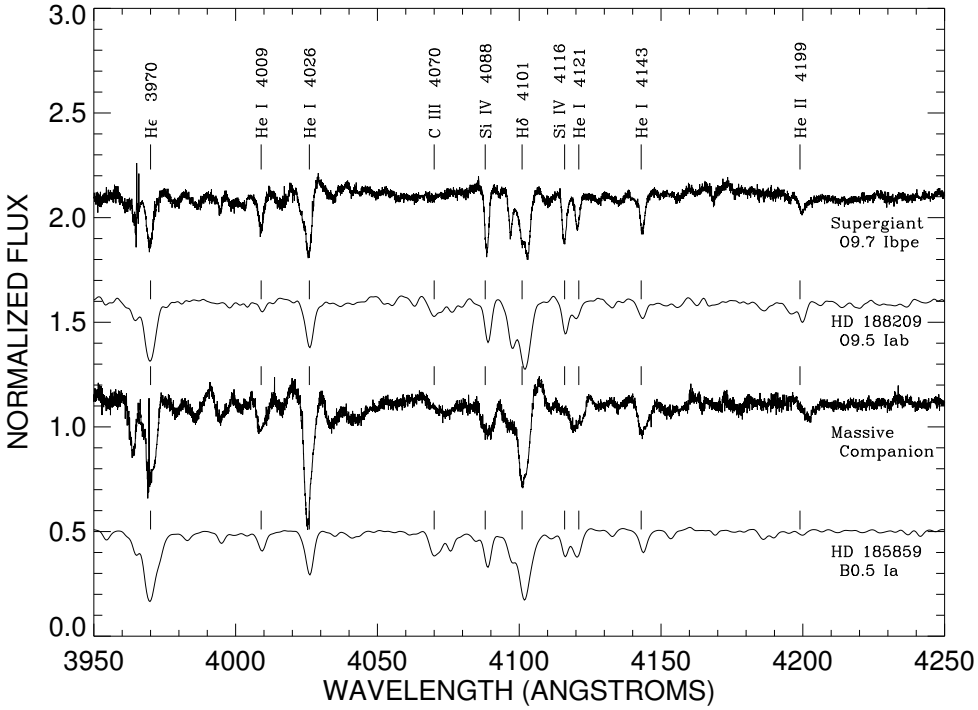

Figure 2.15: Tomographically reconstructed spectra for the supergiant and the environment of the massive companion in the spectral range $3950 - 4250$ Å plotted using normalized flux. These are compared with two single star spectra from the atlas of Valdes et al. (2004). The spectra are offset in flux for clarity. The reconstructed spectra display some "rippling" near some strong features due to residual emission with non-orbital motions.

different spectral features. The reconstructed spectra are plotted in Figures 2.15 and 2.16 normalized to their respective continuum fluxes, so individual lines appear deeper than in the composite spectra, where each is diluted by the flux of the other star. There are several obvious differences between the supergiant component and single star spectrum in some of the stronger lines, such as Hϵ λ3970 and Hδ λ4101, but we do not ascribe any particular significance to these as such features are clearly distorted by emission from circumstellar gas. On the other hand, there does appear to be a significant weakness in the C lines and an enhancement in the N lines in the spectrum of the RY Scuti supergiant compared to that of HD 188209. For example, the C III $\lambda\lambda 4070, 4647$ lines that are present in the spectrum of HD 188209 are conspicuously

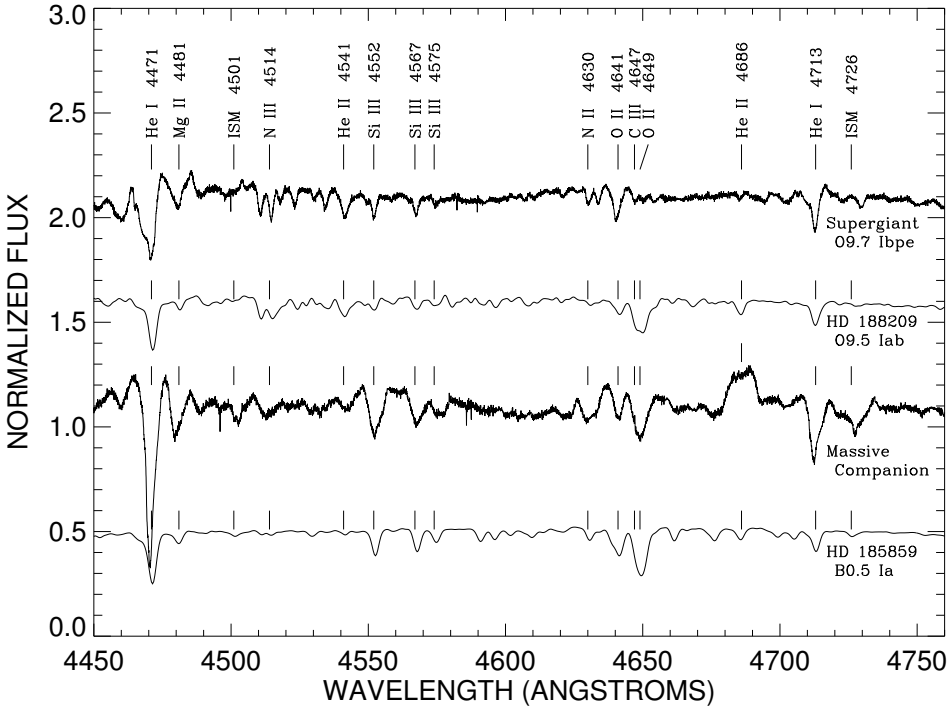

Figure 2.16: Tomographically reconstructed spectra in the range of $4450 - 4750$ Å (in the same format as Fig. 2.15).

absent in the RY Scuti supergiant's spectrum. This suggests the atmosphere of the supergiant is enhanced with CNO-processed gas (as is the surrounding nebula; Smith et al. 2002). Perhaps this is not surprising given that a large portion of the supergiant's mass must have already been lost to reveal gas from deeper layers closer to the source of core H-fusion. This result suggests that the bright O9.7 supergiant is the ultimate source of the processed gas that now forms the outer double-toroidal nebula.

Skul'Skii (1992) suggested the spectral features moving with Doppler shifts of the massive companion have the appearance of a B2 star. We find the lines in the reconstruction for the orbital shifts of the massive companion more closely resemble that of the B0.5 Ia star, HD 185859 (Morgan, Code, & Whitford 1955). However,

there are several features in the reconstruction that make us caution against assuming this spectrum forms in the photosphere of a supergiant star. First, the luminosity sensitive lines of Si IV $\lambda\lambda 4088, 4116$ and Si III $\lambda\lambda 4552, 4567, 4574$ appear very strong in the reconstructed spectrum relative to those in HD 185859, which would imply the lines form in a very low density plasma (like those in the photospheres of the most luminous stars; Walborn & Fitzpatrick 1990). Second, if we suppose that the gravity of a B0.5 Ia star is $\log g = 3.0$ (see the case of the similar star κ Ori; McErlean, Lennon, & Dufton 1999), then using our derived mass, the massive companion star would have a radius of $\approx 29\ R_{\odot}$, which is 83% of its Roche radius. A radius this big would have two observational consequences: first, the flux from this component would be twice the flux from the bright O9.7 supergiant, and second, a star this large would cause the spectral lines of the bright O9.7 supergiant to weaken or disappear during primary eclipse ($\phi = 0.0$). Neither of these two predictions are seen: the massive companion flux is less than that of the supergiant and the supergiant's absorption lines do not weaken at primary eclipse (Fig. 2.1 – 2.8). Also, we estimated the projected rotational velocity of the massive companion spectrum by measuring the widths of the Si III $\lambda 4552$ feature in five FEROS spectra where the feature was well separated from any component of the bright supergiant. We used these widths to obtain $V \sin i = 194 \pm 18$ km s^{-1} in the same way as described above for the primary (§2.5) by comparing them with rotationally broadened model spectra for $T_{\rm eff} = 27500$ K, $\log g = 3.0$, and a limb darkening coefficient $\epsilon = 0.34$. This result is unreasonably large as Ryans et al. (2002) find that no early B-type supergiant has a $V \sin i$ greater than 60 km s^{-1}. Therefore, we suggest these characteristics are best explained if we place the origin of the spectrum in the photosphere of a thick accretion disk surrounding the massive companion rather than in the photosphere of the star itself and we explore this idea further in the next section. Note that the very broad He II $\lambda 4686$ emission is assigned

to the massive companion in the reconstruction, but we argue below that its site of origin may not be exactly co-spatial with that of the absorption line spectrum.

2.7 Mass Outflows in RY Scuti

Many of the spectral features discussed above originate in gas outflows from the binary, and in this section we explore their sites of origin with reference to recent hydrodynamical simulations of gas flows in Roche lobe overflow binaries. The luminous supergiant in RY Scuti can potentially be losing mass by a radiatively driven wind and/or tidal streams along the axis joining the stars. Friend & Castor (1982) show that a continuum of states can exist between these idealized cases. When a luminous star has a radius that is significantly smaller than the critical Roche lobe, the wind will be fast and spherically symmetric (as for single stars). As the ratio of stellar to Roche radius increases, the star becomes tidally distorted and its wind becomes asymmetric with a higher mass loss rate and slower outflow along the axis joining the stars (a "focused wind"). Finally, once the star essentially attains a size filling the Roche surface, most of the mass loss will occur in slow outflows directed along the axis joining the stars. All of the photometric light curve studies confirm the supergiant is very tidally distorted and must therefore be close to Roche filling. Thus, we will explore the consequences of tidally formed outflows in reviewing the observational clues about the mass loss.

The discussion begins with the dimensions of the system, and in Figure 2.17 we present a cartoon illustration of the cross section of the system as viewed from above the orbital plane. The direction of the observer at different orbital phases is indicated by numbers in the periphery of the diagram. As before, we assume the supergiant fills its critical Roche surface and thus has an equivalent volume radius of

approximately $R_{SG} = 18\ R_{\odot}$ (Eggleton 1983). The supergiant is depicted on the left side of Figure 2.17. If we assume the massive companion is a main sequence star (that happens to be surrounded by a thick accretion disk), then for its derived mass we expect it is an O6.5 V star with a polar radius of approximately 9.6 $R_{\odot}$ (see Table 4 in Martins et al. 2005a). The equatorial radius could be significantly larger if the star is rapidly rotating, but we assume it is a spherical star in its depiction on the right hand side of Figure 2.17. Either way, the radius of the massive companion is probably significantly less than its critical Roche radius, and therefore we begin our analysis assuming that the system is semi-detached.

The kinds of gas outflows expected in systems like RY Scuti are explored in a series of recent papers by Nazarenko & Glazunova (2003, 2006a,b). They present hydrodynamical simulations in two and three-dimensions to model the case of the interacting binary β Lyr (Harmanec et al. 1996; Harmanec 2002). RY Scuti and β Lyr share many of the properties common to the W Serpentis class, and we can obtain considerable insight about the gas flows in RY Scuti from these papers (although we caution that the stars in RY Scuti are both hotter and more massive than those in β Lyr). These numerical models assume the mass donor is a low gravity object that fills its Roche surface, and the authors use the models to follow the time evolution of the gas flows until they reach a semi-static configuration. There are several features of these models that are relevant to the case at hand. First, Nazarenko & Glazunova find that the donor loses mass through both the inner L1 region and the outer L2 region (facing away from the companion). Because the gas is so loosely bound to the donor, these gas streams are not compressed into a classical stream but instead fan out across a significant portion of the stellar surface facing towards and away from the companion. The approximate ranges of these outflows are indicated by the dashed lines to the left and right of the supergiant in Figure 2.17 and are based upon simple

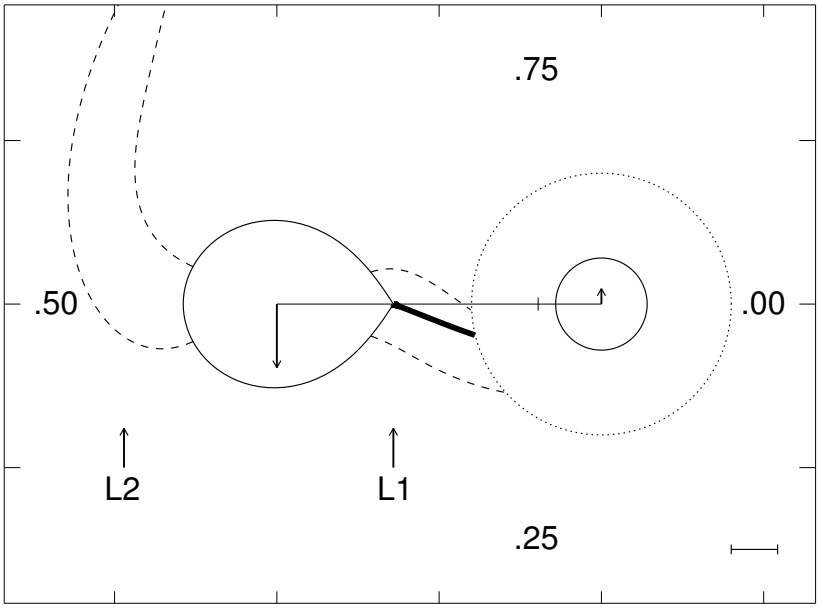

Figure 2.17: Cartoon model of the system as seen from above the orbital plane with the observer's orbital phases noted on the periphery and a scale bar denoting 10 $R_\odot$ in the lower right of the diagram. The Roche-filling supergiant appears on the left while the massive companion is shown on the right surrounded by a dense accretion disk with the outer boundary shown as the dotted line. The mass loss from the supergiant primarily occurs in two regions: the L1 region between the stars and the L2 region on the left side of the supergiant. These are delineated by the dashed lines. The thick solid line represents the classical Roche lobe overflow stream from L1 to the disk. The tick mark on the axis joining the centers of the two stars marks the center of mass, and the arrows at the centers of both stars indicate their orbital velocities. The L1 and L2 points lie along the axis joining the two stars at the points indicated. The L3 point lies off the plot to the right (62 $R_\odot$ from the center of the massive companion).

ballistic trajectories. The thicker line to the right of the supergiant indicates the classical L1 gas trajectory (Lubow & Shu 1975). The models also show an accretion disk does form but that gas may be lost from the binary near the outer L3 point (to the right of the massive companion in Fig. 2.17). We have simply illustrated the disk in Figure 2.17 assuming it extends to 80% of the Roche radius of the massive companion ($R_{Roche} \approx 35\ R_\odot$). The three-dimensional models (Nazarenko & Glazunova 2006a,b) show the inner portions of the disk attain a significant height above and below the orbital plane, and therefore the gas structure is referred to as a torus rather than

a disk. If the massive companion is a main sequence star, then the height of the torus may well exceed the stellar radius and block it from view for all but extremely low orbital inclinations. Finally, Nazarenko & Glazunova (2006b) consider the effect that a stellar wind from the mass gainer will have on the surrounding torus. They find the wind breaks out in bipolar outflows and that the hottest gas temperatures occur where the wind strikes the inner torus. Such a bipolar outflow may explain the elongated radio emission surrounding β Lyr (Umana et al. 2000). If the massive companion in RY Scuti is an O6.5 V star, then we expect it will be hot and luminous (perhaps exceeding the luminosity of normal dwarfs due to the addition of accretion luminosity), and thus it will be a source of a significant radiatively-driven wind.

We will use the framework of gas features illustrated in Figure 2.17 to offer a plausible origin for some of the spectral features discussed in earlier sections. We begin with the expected outflows from the supergiant towards L1 and L2. Most of the absorption lines associated with the supergiant appear to strengthen considerably in depth at the conjunction phases and this change is particularly striking in the case of the He I lines illustrated in Figures 2.2 and 2.3. The absorption preferentially strengthens on the blue side of the profile, and in the case of supergiant inferior conjunction ($\phi = 0.5$), remains blueshifted for a while longer. For triplet transitions like He I λ4471 (Fig. 2.3), the blueshifted component transforms from a broad feature into a narrow, almost nebular absorption line that lasts for more than half the orbit. We suggest these changes are best explained by absorption from the outflows from the supergiant that emerge in the L1 and L2 directions. The blueshifts we observe with projected speeds of ≈ 200 km s^{-1} are consistent with an outflow towards L1 (at $\phi = 0.0$) and towards L2 (at $\phi = 0.5$). The disappearance of the broad absorption shortly after $\phi = 0.0$ is expected as this flow terminates only a short distance from the supergiant where the gas strikes the accretion disk. On the other hand, the gas

leaving the L2 region forms a long trailing plume that may occult the supergiant for a considerable time following $\phi = 0.5$ and thus may account for the presence of blueshifted absorption until $\phi \approx 0.8$. The appearance of the narrow blueshifted absorption in the He I triplets may be due to low optical depth gas associated with the L2 outflow that extends well above and below the orbital plane.

The gas that enters the accretion disk from the L1 outflow is probably very dense and extended from the orbital plane. In such a situation, the massive companion may be wholly obscured from our point of view and its photospheric spectrum will be invisible. However, we noted in §2.5 and §2.6 that there are a number of spectral features that do display radial velocity patterns opposite to those of the supergiant and may plausibly be associated with the immediate environment of the massive companion. In particular, we suggest the Si III and other lines found in the spectral reconstruction for orbital motion of the massive companion (§2.6) are probably formed in the extended accretion disk "photosphere" surrounding the massive companion. These features are very broad (indicative of the large Keplerian motions in the disk) and appear similar to those in early B-supergiants (suggesting a gas density that is relatively low compared to most stellar photospheres). Furthermore, the fact that this spectral component appears slightly cooler (like a B0.5 I star) than the supergiant (O9.7 Ibpe) is consistent with idea that the gas has cooled slightly since leaving the supergiant and is shielded from the flux from the presumably hot massive companion by the denser regions of the accretion disk. Similar kinds of disk photospheric features have recently been detected in the spectrum of β Lyr (Ak et al. 2007).

According to the recent ephemeris from Kreiner (2004), minimum light occurs at spectroscopic phase $\phi = 0.980 \pm 0.008$ (Table 2.4). The fact that the deeper eclipse occurs when the supergiant is behind the massive component is consistent with the somewhat cooler disk photosphere we find from the line patterns in the reconstructed

spectrum.

The large mass of the massive companion suggests the star probably has a vigorous radiatively-driven stellar wind. Hydrodynamical models for β Lyr indicate the radiatively-driven wind of the mass gainer will break out of the accretion torus in bipolar flows that are the suspected source of the Hα emission in β Lyr (Harmanec et al. 1996; Ak et al. 2007). If bipolar wind outflows are also the source of some of the Hα emission in RY Scuti, then they should extend far away from the orbital plane and be minimally eclipsed at conjunction phases. We may test this idea by comparing the orbital phase variations in the Hα equivalent width (W_λ) with the V-band light curve. We measure the total emission flux relative to a time variable continuum flux and if the emission flux is constant, then the product of the emission equivalent width and continuum flux will also be constant (i.e., the measured equivalent width will vary inversely as the continuum flux). In Figure 2.18, we show the orbital phase variations in W_λ(Hα) normalized to their mean at the quadrature phases. We see the measured W_λ increases during the decreases in flux that occur surrounding the times of eclipse at $\phi = 0.0$ and 0.5. We also show in Figure 2.18 the inverse continuum flux variation derived from the V-band observations of Djurašević et al. (2001) and transformed by the equation described in §2.3. The fact the broad Hα equivalent width variations follow the inverse light curve so closely indicates the Hα emission source is not substantially eclipsed by either the supergiant or the accretion disk, and therefore probably forms over a volume that is either very large and/or extended far from the orbital plane (we discuss this further below). We showed in §2.5 that the bisector velocities of the Hα emission wings (corresponding to the fastest moving gas) show approximately the same velocity pattern as expected for the massive companion and this anti-phase velocity pattern is seen in Figure 2.11. The combined evidence of orbital motion and the lack of eclipses suggests the emission line wings of the Hα

feature (and probably part of the main core) form in the bipolar outflows from the disk-constrained wind of the massive companion. The highest projected speeds observed ($\approx$ 500 km s^{-1}) are consistent with outflow velocities normal to the orbital plane of $\approx$ 2000 km s^{-1}, a typical value among O-dwarf winds.

The central part of the Hα profile appears as a quasi-P Cygni profile (with an emission peak at redshifted velocities and a weak absorption at blueshifted velocities) that usually implies a gas outflow. This part of the Hα profile is generally stationary, showing neither the motion associated with the supergiant nor that of the massive companion. This is very different from the case of the wind emission of the comparable supergiant in the massive X-ray binary system Cygnus X-1, where the Hα emission is much weaker and follows the Doppler motions of the supergiant (Gies et al. 2003). Furthermore, the wind emission in single OB-supergiants is generally an order of magnitude weaker than observed in RY Scuti (Morel et al. 2004), which indicates that the dense outflow in RY Scuti occurs over a volume much larger than that in the region immediately surrounding the supergiant. The lack of any orbital velocity variation suggests either the source is close to the center of mass or the flux originates far from the center of mass where any orbital motions disappear due to conservation of angular momentum. The first possibility appears to be ruled out by the fact that the main core shows no evidence of eclipses (Fig. 2.18). Taken together, these properties suggest that a large fraction of the emission flux originates in outflowing gas that surrounds the binary as a whole. This circumbinary disk is probably fed by the gas flows leaving the binary in the vicinity of the L2 and L3 regions. These broad flows may have sufficient vertical extent to account for the blueshifted absorption observed at the quadrature phases. The absence of any substantial decrease in emission flux around $\phi = 0.0$ (Fig. 2.18) suggests that the inner radius of the circumbinary disk is larger than $a_{SG}+R_{SG}/\cos i = 131\ R_{\odot}$, i.e., approximately twice the binary separation.

On the other hand, because the gas density will decline with increasing radius and because the Hα emission depends on gas density squared, we expect that most of the emission comes from the inner part of the circumbinary disk. Thus, the Hα emitting region of the circumbinary disk probably has a characteristic radius of approximately 1 AU. The circumbinary disk flux contribution appears to decline as expected among the profiles of the higher members of the Balmer sequence (see Fig. 16 in Smith et al. 2002). We note for completeness that the broad asymmetrical shape of the Hα emission from the inner circumbinary disk appears somewhat like a velocity-expanded version of the profile from the outer double-toroidal nebula (Smith et al. 2002). As the latter is due to a spatial gas asymmetry in the outer expanding ring, it is possible that there may also be asymmetries in the mass loss into the inner circumbinary disk.

The He II λ4686 emission found in the spectrum of RY Scuti has a radial velocity curve that is similar to that of the massive companion (Fig. 2.14) and this suggests it is formed in the same vicinity. Furthermore, the equivalent width variations of the He II λ4686 emission (Fig. 2.18) indicate a drop in relative emission strength at $\phi = 0.5$ when the supergiant is in the foreground, consistent with an origin near the massive companion. The hydrodynamical models (Nazarenko & Glazunova 2006b) suggest that the hottest gas is located at the place where some of the incoming gas stream through L1 climbs over the accretion torus vertical extensions and collides with the high speed wind from the massive companion. Thus, the hot gas is predicted to have a velocity curve for a position slightly offset from the centroid of the massive companion towards the binary center of mass. This appears to be consistent with the He II λ4686 velocity curve (Fig. 2.14) that has a slightly smaller semiamplitude than that for the Si III lines that probably form in the disk photosphere (which is approximately centered on the massive companion).

Our results indicate the mass outflow from RY Scuti has at least two components,

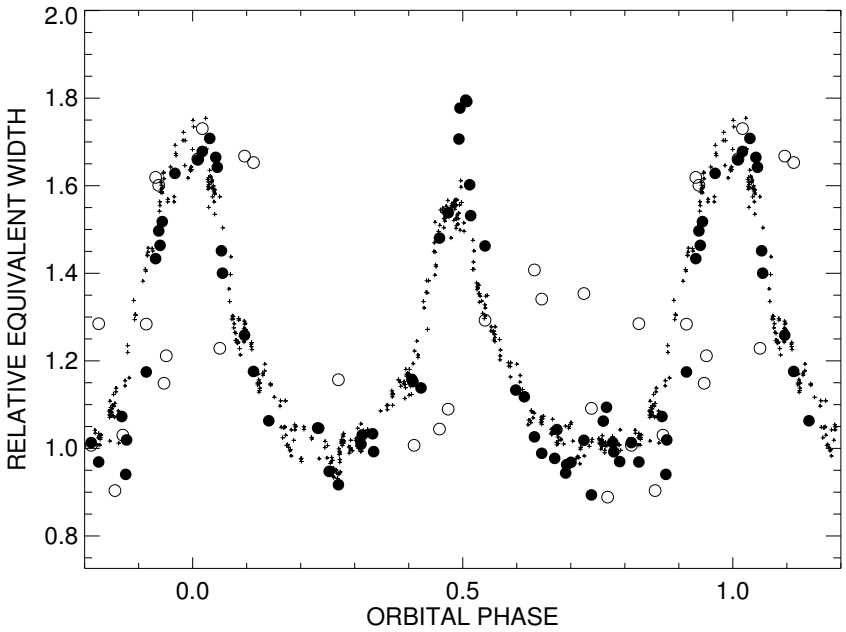

Figure 2.18: A representation of the apparent increases in equivalent width due to the changing continuum levels in the eclipsing binary. The small plus signs mark the inverse fluxes in the V-band from Djurašević et al. (2001), and these show the predicted trend in equivalent width for any uneclipsed emission source. The filled circles show the normalized variation in Hα equivalent width that appears to follow the predicted curve (indicating that the Hα source is not significantly eclipsed). The open circles show the same for He II λ4686. In this case, the absence of brightening at $\phi = 0.5$ suggests that the He II emission is partially occulted/eclipsed then. Conservative estimates of the relative equivalent width errors for Hα are 4% and those for He II λ4686 are between 4% and 10%.

a bipolar outflow of hot stellar wind gas from the massive companion and an equatorial outflow of cooler gas fed by the plume from the L2 region and disk leakage from the L3 region. There is no direct evidence of the high-speed, bipolar outflow in Hα images made with *HST* (shown in Smith et al. 1999), but future optical and radio emission maps made with much higher angular resolution may reveal these jet-like features. We suspect most of the cool gas outflow in the orbital plane ends up in a circumbinary disk that slowly transports mass and angular momentum away from the binary and may eventually be a source of gas for the outer double-toriodal nebula. This draining of angular momentum from the binary may explain the observed shortening of the orbital

period and shrinkage of the semimajor axis (Šimon 1999). It is possible the density and spatial extent of the circumbinary disk are sufficient to become a significant opacity source blocking the ionizing flux from the central binary. We speculate that this may be one of the reasons why the surrounding H II double-toroidal nebula seen in *HST* images has a darker equatorial zone (shaded from ionizing radiation by the intervening circumbinary disk).

2.8 Conclusions

Our spectroscopic investigation of RY Scuti has led to a reassessment of the component masses, a new understanding of the properties of the spectral features related to each star, and a sketch of how the binary is ejecting gas from the system. Our new radial velocities and orbital elements for the supergiant improve upon past work and we argue that the orbit is probably circular as expected for Roche-filling systems. We determined radial velocities for the Si III λ4552 absorption line, a feature that is probably formed in the vicinity of massive companion, and by combining the semiamplitudes of the supergiant and this feature, we estimate the mass ratio is $M_{MC}/M_{SG} = 4.2 \pm 0.7$. If we adopt an orbital inclination from that for the surrounding double-toroidal nebula, then the stellar masses are $M_{SG} = 7.1 \pm 1.2\ M_{\odot}$ and $M_{MC} = 30.0 \pm 2.1\ M_{\odot}$. These are consistent with the idea that the massive companion is an O-star hidden within a dense accretion disk and that the mass-losing supergiant is destined to become a Wolf-Rayet star. In the distant future, this system may resemble the well known O + WR binary γ^2 Vel that has component masses of $M(O) = 28.5 \pm 1.1\ M_{\odot}$ and $M(WR) = 9.0 \pm 0.6$ (North et al. 2007).

We used a Doppler tomographic reconstruction scheme to separate the component optical spectra of the stars. The line patterns of the the supergiant dominate

the combined spectrum and a comparison with a similarly classified star indicates that the supergiant contributes about 57% of the visible flux. The optical spectrum of the supergiant displays unusually weak carbon lines, suggesting the photosphere (like the surrounding nebula) contains CNO-processed gas. The reconstructed spectrum for the massive companion has a superficial resemblance to that of a rapidly rotating B-supergiant, but we argue this spectrum probably forms in the accretion disk photosphere surrounding the massive companion.

We found several lines of evidence indicating mass loss from the binary. The apparent strengthening of blueshifted parts of many absorption lines at both conjunctions, and especially following supergiant inferior conjunction, suggests that the supergiant is losing mass in broad streams directed both towards and away from the massive companion. The strong Hα feature appears as a broad P Cygni line, indicating outflow. The radial velocity curve of the Hα wings indicates the highest velocity emission originates near the massive companion, probably in a bipolar outflow where the stellar wind of the massive companion breaks out of the thick surrounding accretion disk. The core Hα emission is stationary and uneclipsed, and we suggest it forms mainly in an outflowing equatorial region (a circumbinary disk). The other important emission line, He II λ4686, also has a radial velocity curve consistent with an origin near the massive companion, and we suggest it forms in hot regions where gas from the L1 stream flows over the thicker portions of the disk and strikes the fast wind from the massive companion.

We argue that the gas lost from the supergiant through the outer L2 region and also lost from the outer parts of the accretion disk near L3 ends up in a relatively cool and dense circumbinary disk with a characteristic Hα emitting radius of 1 AU. We suspect this disk gas will continue to flow outwards and may help channel gas into the surrounding double-toroidal nebula. Smith et al. (2001) studied the proper motions

of the outer double-torus nebula and they conclude the gas in this H II region was probably ejected from the central binary around the year 1876 ± 20. It is possible this time corresponded to an epoch with an especially high binary mass transfer rate and associated outflow into the circumbinary disk. We note, for example, that the first light curve for the binary from Gaposchkin & Shapley (1937) (covering the years 1924 to 1934) shows a secondary minimum that is only 0.3 mag deep compared to the current day observed 0.5 mag drop (Djurašević et al. 2001) while the primary eclipse depth is the same. This suggests the disk surrounding the massive companion was cooler in the early part of the last century, which would be consistent with the presence of a thicker, more extended disk resulting from a higher mass transfer rate. Finally, we note that the mass loss into the circumbinary disk removes angular momentum from the central binary, consistent with the observation that the orbital period is decreasing (Šimon 1999). Thus, contrary to the predictions of conservative mass transfer models, the components of RY Scuti are continuing to be drawn together even after the mass ratio reversal has occurred. We may therefore expect that an episode of more intense interaction and mass transfer and mass loss lies in the immediate future for RY Scuti, and continuing observations will be vital in documenting this key stage in the evolution of massive binaries.

– 3 –

Wind Transfer in the B-Supergiant System LS I +65 010 = 2S 0114+650

Abstract

We[1] report on a three year spectroscopic monitoring program of the Hα emission in the massive X-ray binary LS I +65 010 = 2S 0114+650, which consists of a B-supergiant and a slowly rotating X-ray pulsar. We present revised orbital elements that yield a period of $P = 11.5983 \pm 0.0006$ d and confirm that the orbit has a non-zero eccentricity $e = 0.18 \pm 0.05$. The Hα emission profile is formed in the base of the wind of the B-supergiant primary, and we show how this spectral feature varies on timescales that are probably related to the rotational period of the B-supergiant. We also examine the X-ray fluxes from the *Rossi X-ray Timing Explorer* All-Sky Monitor instrument, and show that the X-ray orbital light curve has a maximum at periastron and a minimum at the inferior conjunction of the B-supergiant. We also show that

[1]Grundstrom, E. D.; Blair, J. L.; Gies, D. R.; Huang, W.; McSwain, M. V.; Raghavan, D.; Riddle, R. L.; Subasavage, J. P.; Wingert, D. W.; Levine, A. M.; Remillard, R. A. - published as Grundstrom et al. (2007a)

the wind emission strength and the high energy X-ray flux appear to vary in tandem on timescales of approximately a year.

3.1 Introduction

Massive X-ray binaries consist of a massive, luminous star with a neutron star or black hole companion with an orbital separation small enough to power an accretion-driven X-ray source. The mass donor is often a rapidly rotating Be star, and the neutron star companion accretes gas from the slowly outflowing circumstellar disk of the Be star (Coe 2000). A second kind of massive X-ray binary contains an OB supergiant as the mass donor, and mass transfer occurs by a Roche lobe overflow stream or stellar wind capture (Kaper 1998). In both cases the mass transfer rate can be time variable and lead to large variations in the X-ray flux. The gas in the immediate vicinity of the mass donor will generally be dense and hot enough to be a source of Hα emission. Our goal here is to investigate how the mass loss fluctuations at the source (as observed in Hα) are related to the X-ray variations, particularly as measured with the All-Sky Monitor (ASM) instrument aboard the *Rossi X-ray Timing Explorer (RXTE)* satellite (Levine et al. 1996). We present similar investigations of such co-variations in the Be X-ray binaries LS I +61 303 (Chapter 5) and HDE 245770 = A 0535+26 and X Per (Chapter 6), as well as in the black hole binary Cyg X-1 = HDE 226868 (Gies et al. 2003) (not part of this thesis).

Our subject here is the massive X-ray binary system 2S 0114+650 (4U 0114 + 65) whose optical counterpart is LS I +65 010 (V662 Cas; HIP 6081; ALS 6517). The characteristics of the mass donor star in this system were determined in a spectroscopic and photometric study by Reig et al. (1996). They show that the star is a supergiant with a spectral classification of B1 Ia. They also suggest that the Hα

emission present in the spectrum forms in the stellar wind of the supergiant and that the expected wind parameters and accretion rate are consistent with the observed X-ray properties. The orbital elements were first determined by Crampton, Hutchings, & Cowley (1985) who found that the orbit has a small eccentricity and a period of 11.6 d. The orbital period is also found in the X-ray flux variations (Farrell, Sood, & O'Neill 2006; Wen, Levine, Corbet, & Bradt 2006) along with two other periodic signals: a super-orbital period of 30.7 d (possibly related to the precession of the disk surrounding the neutron star; Farrell et al. 2006) and the pulsar spin period of 2.7 hr (Finley, Belloni, & Cassinelli 1992; Hall, Finley, Corbet, & Thomas 2000; Koenigsberger, Canalizo, Arrieta, Richer, & Georgiev 2003; Bonning & Falanga 2005). This is the longest spin period of any known X-ray pulsar, and Li & van den Heuvel (1999) argue that the pulsar was probably born with a huge magnetic field (as a magnetar) in order to have spun down sufficiently within the lifetime of the mass donor star.

Here we outline the results of an Hα monitoring program on LS I +65 010 that spanned the years 1998–2000. We describe the spectroscopy in §3.2 and present revised orbital elements in §3.3. We discuss the properties and temporal variations of the Hα emission in §3.4, and in §3.5 compare them with the X-ray variations observed by *RXTE*/ASM.

3.2 Observations

We obtained 100 optical spectra of LS I +65 010 with the Kitt Peak National Observatory 0.9 m coudé feed telescope during six observing runs between 1998 August and 2000 December. The details of the spectrograph arrangement for each run are listed in Table 3.1. All the spectra cover the region surrounding Hα, but they were made using two different spectral dispersions. During the first, fifth, and sixth runs,

we used grating B (316 grooves mm^{-1} with a blaze wavelength of 6000 Å in second order) and obtained a resolving power of $R = \lambda/\delta\lambda \approx 9500$. The spectra from the other three runs were made with the lower dispersion RC181 grating (316 grooves mm^{-1} with a blaze wavelength of 7500 Å; made in first order with a GG495 filter to block higher orders), which yielded an average resolving power of $R = 4100 - 4400$. Exposure times were usually 30 minutes, and the spectra generally have a S/N ≈ 100 pixel^{-1} in the continuum.

Table 3.1: Journal of Optical Spectroscopy

Dates (HJD-2,400,000)	Spectral Range (Å)	Resolving Power ($\lambda/\triangle\lambda$)	Number of Spectra
51053 – 51065	6313 – 6978	9530	23
51421 – 51429	5397 – 6735	4050	11
51464 – 51469	5400 – 6736	4100	14
51491 – 51497	5545 – 6881	4400	14
51817 – 51830	6440 – 7105	9500	16
51890 – 51901	6443 – 7108	9500	22

The spectra were extracted and calibrated using standard routines in *IRAF*[2], and then each continuum rectified spectrum was transformed onto a uniform heliocentric wavelength grid for analysis. The removal of atmospheric lines was done by creating a library of spectra from each run of the rapidly rotating A-star ζ Aql, removing the broad stellar features from these, and then dividing each target spectrum by the modified atmospheric spectrum that most closely matched the target spectrum in a selected region dominated by atmospheric absorptions.

[2]IRAF is distributed by the National Optical Astronomy Observatory, which is operated by the Association of Universities for Research in Astronomy, Inc., under cooperative agreement with the National Science Foundation.

3.3 Orbital Radial Velocity Curve

The spectra from different runs cover different portions of the red spectrum (Table 3.1), but all record both the Hα emission line and the He I λ6678 absorption line. Thus, we will concentrate on these common features in the analysis. We measured radial velocities by cross-correlating each spectrum with a standard template that was formed by averaging all the spectra from the fifth run (2000 October). The spectral range for the cross-correlation was generally limited to the immediate vicinity of the He I λ6678 line, but we also included the region surrounding He I λ7065 for the spectra from the final two runs (2000 October and December). The positions of these two features in the template spectrum were measured by parabolic fits to the lower portions of the profiles, and we added their mean radial velocity, -52.8 ± 0.4 km s^{-1}, to each relative velocity to place them on an absolute scale. We note that there are known line-to-line velocity differences in the spectrum that are related to line formation at different depths in the expanding atmosphere (Crampton et al. 1985; Koenigsberger et al. 2003), and velocities based on the strong He I lines are probably systematically more negative than those from lines formed deeper in the atmosphere. We also made cross-correlation measurements of the strong interstellar line at 6613 Å that we used to monitor the radial velocity stability of our spectra. Our results are summarized in Table 3.2, which lists the mid-point heliocentric Julian date of observation, the orbital phase, radial velocity, observed minus calculated residual from the fit, the measured velocity difference of the 6613 Å interstellar line from its position in the template spectrum, and the equivalent width of the Hα emission (§3.4). The typical stellar radial velocity errors are about $\pm$1.7 km s^{-1} for the high dispersion spectra and about twice that value for the lower dispersion spectra (based upon the differences of closely spaced pairs of observations).

Table 3.2: Radial Velocity and Equivalent Width Measurements

Date (HJD−2,400,000)	Orbital Phase	V_r (km s^{-1})	$(O-C)$ (km s^{-1})	$\triangle V_{\rm ISM}$ (km s^{-1})	W_λ(Hα) (Å)
51053.803	0.481	−70.8	−4.5	−1.8	−2.05
51053.824	0.483	−66.8	−0.5	−0.4	−2.01
51055.810	0.655	−55.1	1.1	0.6	−1.98
51055.832	0.656	−56.3	−0.2	0.7	−2.10
51055.917	0.664	−53.9	1.8	3.9	−2.02
51056.826	0.742	−56.1	−6.0	2.4	−1.70
51056.850	0.744	−54.4	−4.5	2.3	−1.68
51056.871	0.746	−57.0	−7.3	2.2	−1.74
51057.810	0.827	−50.5	−5.8	1.0	−1.53
51057.831	0.829	−49.7	−5.2	2.0	−1.59
51057.852	0.831	−49.7	−5.3	2.1	−1.66
51058.801	0.912	−47.0	−4.4	3.6	−1.15
51058.822	0.914	−49.8	−7.1	2.8	−1.16
51058.844	0.916	−49.2	−6.5	2.4	−1.28
51061.800	0.171	−61.0	5.0	−2.0	−1.77
51061.821	0.173	−57.6	8.6	−0.1	−1.77
51061.843	0.175	−59.2	7.1	2.3	−1.73
51063.887	0.351	−73.2	−2.9	2.0	−1.11
51063.908	0.353	−71.4	−1.0	1.7	−1.13
51063.930	0.355	−74.6	−4.3	0.5	−1.17
51065.811	0.517	−71.5	−6.9	0.5	−1.54
51065.835	0.519	−66.0	−1.5	−0.5	−1.63
51065.856	0.521	−64.4	0.0	0.7	−1.75
51421.915	0.220	−69.0	−0.2	−3.2	−0.98
51423.896	0.391	−75.5	−5.9	−3.2	−1.30
51425.898	0.563	−68.8	−6.7	−6.6	−1.27
51425.919	0.565	−67.4	−5.4	−7.9	−1.28
51426.879	0.648	−61.4	−4.7	−0.4	−0.82
51426.901	0.650	−60.9	−4.3	−0.2	−0.85
51427.879	0.734	−56.3	−5.7	1.2	−0.86
51428.838	0.817	−48.2	−3.1	−1.8	−0.79
51428.860	0.819	−48.7	−3.6	−1.1	−0.82
51429.836	0.903	−46.1	−3.5	−1.5	−0.93
51429.857	0.905	−46.4	−3.8	1.0	−0.90
51464.760	0.914	−44.5	−1.8	−0.3	−1.43
51464.783	0.916	−41.9	0.9	1.0	−1.17
51465.814	0.005	−57.9	−9.7	−3.8	−1.57
51465.835	0.007	−56.0	−7.6	−5.6	−1.63
51465.858	0.009	−57.5	−8.8	−4.0	−1.50
51466.772	0.087	−56.0	1.9	−8.4	−1.28
51466.794	0.089	−57.1	1.1	−5.2	−1.26
51466.816	0.091	−59.0	−0.6	−3.4	−1.35
51467.855	0.181	−72.7	−5.9	−0.4	−1.03
51467.876	0.183	−70.7	−3.9	−2.2	−1.19
51468.812	0.263	−70.9	−0.7	1.3	−1.46
51468.834	0.265	−65.4	4.8	0.8	−1.49
51469.829	0.351	−67.6	2.8	−6.1	−1.28
51469.850	0.353	−70.5	−0.2	−2.1	−0.72
51491.753	0.241	−56.9	12.7	−2.9	−1.56
51491.775	0.243	−58.0	11.7	···	−1.64
51492.713	0.324	−64.2	6.5	3.0	−1.70
51492.734	0.326	−69.8	0.8	−0.8	−1.66
51493.696	0.409	−71.9	−2.8	3.0	−1.46
51493.717	0.411	−73.0	−3.9	3.4	−1.43
51494.708	0.496	−60.3	5.4	−2.3	−1.14
51494.730	0.498	−58.9	6.7	−4.5	−1.22
51495.765	0.587	−62.5	−1.9	1.1	−0.91
51495.787	0.589	−58.9	1.6	1.1	−0.89
51496.757	0.673	−66.3	−11.3	−4.3	−0.95
51496.778	0.675	−66.2	−11.3	−4.1	−0.46
51497.718	0.756	−55.6	−6.5	−2.5	−0.87
51497.739	0.757	−56.4	−7.4	−1.6	−0.81
51817.702	0.344	−69.6	0.8	−1.0	−1.13
51817.739	0.348	−70.3	0.2	−1.9	−1.20
51818.722	0.432	−64.1	4.2	−1.0	−1.16
51818.746	0.434	−68.3	−0.0	0.3	−1.14
51819.693	0.516	−59.7	5.0	1.0	−1.10
51819.716	0.518	−59.9	4.7	−2.4	−1.02
51820.735	0.606	−56.3	3.2	−0.0	−1.21
51821.698	0.689	−52.1	1.7	−0.6	−1.20
51821.720	0.691	−52.5	1.2	−1.5	−1.24

Continued on Next Page...

Table 3.2 – Continued

Date (HJD−2,400,000)	Orbital Phase	V_r (km s^{-1})	$(O-C)$ (km s^{-1})	$\triangle V_{\rm ISM}$ (km s^{-1})	W_λ(Hα) (Å)
51822.710	0.776	−24.2[a]	23.5	1.3	−1.21
51823.692	0.861	−22.2[a]	21.1	0.2	−1.65
51823.713	0.863	−21.0[a]	22.2	0.7	−1.56
51824.687	0.947	−42.9	0.8	3.7	−1.32
51824.708	0.949	−43.8	0.1	4.1	−1.30
51830.713	0.466	−64.5	2.5	−1.2	−1.89
51830.735	0.468	−65.0	1.9	0.2	−1.75
51890.622	0.632	−65.4	−7.6	−2.0	−1.81
51890.643	0.633	−66.2	−8.5	0.8	−1.86
51892.613	0.803	−45.3	0.6	−2.9	−1.86
51892.635	0.805	−45.1	0.8	−1.4	−1.76
51893.642	0.892	−43.0	−0.4	−0.3	−1.39
51893.664	0.894	−43.0	−0.4	0.0	−1.34
51894.640	0.978	−51.1	−5.4	−2.0	−1.42
51894.661	0.980	−51.5	−5.5	−0.5	−1.33
51895.620	0.063	−60.5	−5.5	−0.7	−1.51
51895.642	0.064	−59.4	−4.2	−0.1	−1.49
51896.662	0.152	−70.3	−5.7	−0.5	−1.07
51896.683	0.154	−70.9	−6.2	0.5	−1.24
51897.664	0.239	−67.1	2.5	−1.5	−1.15
51897.685	0.241	−69.6	0.0	−0.6	−1.10
51898.667	0.325	−72.0	−1.4	−1.6	−1.47
51898.688	0.327	−72.6	−2.0	−1.4	−1.50
51899.670	0.412	−73.0	−4.0	0.3	−1.70
51899.691	0.413	−74.5	−5.5	−1.0	−1.74
51900.664	0.497	−55.9	9.7	1.0	−1.67
51900.685	0.499	−54.2	11.3	1.6	−1.64
51901.649	0.582	−44.9	16.0	1.2	−1.31
51901.671	0.584	−48.4	12.5	−1.1	−1.45

[a] Assigned zero weight in the orbital solution.

We determined orbital elements from these velocities using the non-linear least-squares fitting program of Morbey & Brosterhus (1974). We initially determined elements for both the new data and the archival measurements from Crampton et al. (1985), and while most of the elements were in good agreement, we found the systemic velocity γ for the new set was 2.5 km s^{-1} lower than that based on the data from Crampton et al. (1985). This is not surprising given the existence of systematic line-to-line velocity differences and that Crampton et al. (1985) measured a different set of lines in the blue. Consequently, we subtracted this value from all the archival velocities, and then made a new fit of the merged velocities. The revised elements are presented in Table 3.3, and the radial velocity curve is shown in Figure 3.1. The revised orbital elements are in reasonable agreement with the original values from Crampton et al. (1985), also listed in Table 3.3. The main differences are a factor

of 5 improvement in the accuracy of the orbital period and a modest decrease in the orbital semiamplitude K.

Table 3.3: Orbital Elements

Element	Crampton et al. (1985)	This Work
P (days)	11.588 ± 0.003	11.5983 ± 0.0006
T (HJD–2,400,000)	44134.9 ± 0.7	51825.3 ± 0.5
e	0.16 ± 0.07	0.18 ± 0.05
ω (deg)	11 ± 11	51 ± 17
K (km s^{-1})	17 ± 1	14.0 ± 0.7
γ (km s^{-1})	-57 ± 1	-58.2 ± 0.5
$f(m)$ ($M_\odot$)	0.006 ± 0.001	0.0032 ± 0.0005
$a_1 \sin i$ ($R_\odot$)	3.9 ± 0.2	3.16 ± 0.16
r.m.s. (km s^{-1}) ...	6.8	6.4

Crampton et al. (1985) were unable to decide between circular and elliptical solutions, but it is now clear that a non-zero eccentricity is required. We made fits assuming both circular and elliptical parameters, and the improvement in the residuals in the elliptical case would only occur by random chance with a probability of 0.8% according to the test of Lucy & Sweeney (1971). Thus, the eccentricity is significantly different from zero, and we report only the elliptical solution in Table 3.3. The residuals from the fit (rms = 6.4 km s^{-1}) are larger than those associated with the measurement errors (1.7 – 3.4 km s^{-1}), and, in fact, we zero-weighted three measurements that had exceptionally large deviations (Fig. 3.1). We suspect that this scatter is due to the microvariablility inherent to the atmospheres of early-type supergiants (Gies & Bolton 1986).

3.4 Hα Variations

The Hα feature has always appeared in emission in past observations (Reig et al. 1996; Liu & Hang 1999; Koenigsberger et al. 2003) and emission was consistently

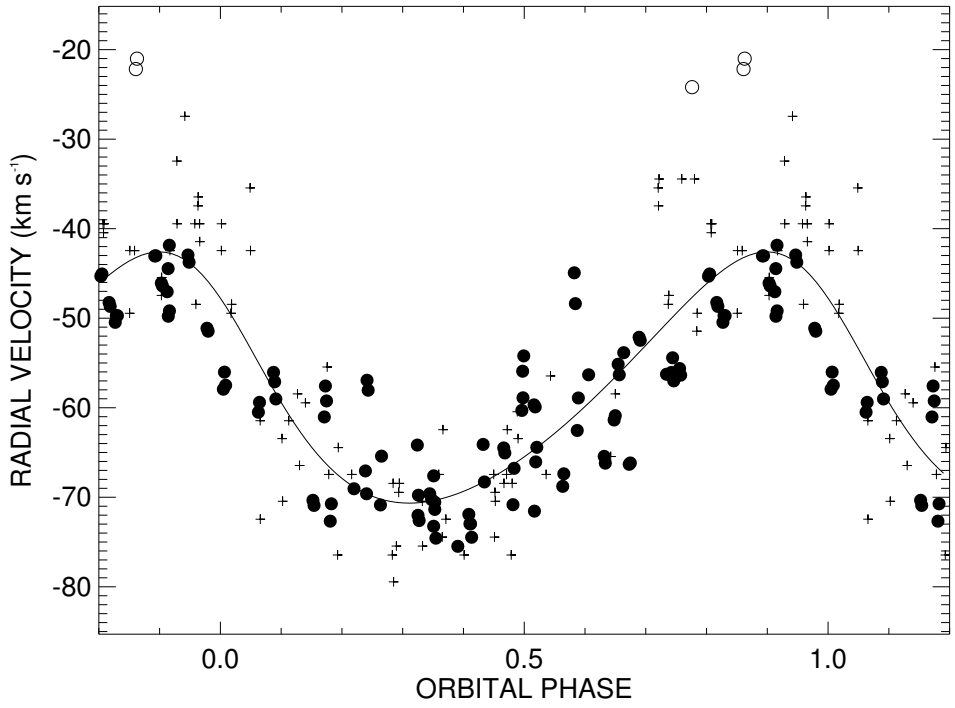

Figure 3.1: Calculated radial velocity curve (*solid line*) for LS I +65 010. The measured radial velocities are shown as filled circles. Open circles mark the measurements that were assigned zero weight (§3.3), and plus signs indicate the measurements from Crampton et al. (1985).

present in our spectra as well. However, the shape and strength of the profile varied on a timescale of days. We show in Figure 3.2 two example time sequences from our best sampled runs. A red-shifted emission peak is generally present and in about half of the spectra a blue-shifted absorption trough is also visible. There are indications in several cases of absorption features that appear to migrate bluewards to velocities of ≈ -400 km s^{-1}. These kinds of variations are common among B-supergiants (Fullerton et al. 1997; Markova & Valchev 2000) and probably result from transient structures in the wind. Similar kinds of blueward absorption variations were also observed in the He I λ5876 line in the spectrum of LS I +65 010 by Koenigsberger et al. (2003). Liu & Hang (1999) interpreted episodes of double-peaked Hα emission as evidence of a second emission component from the vicinity of the neutron star

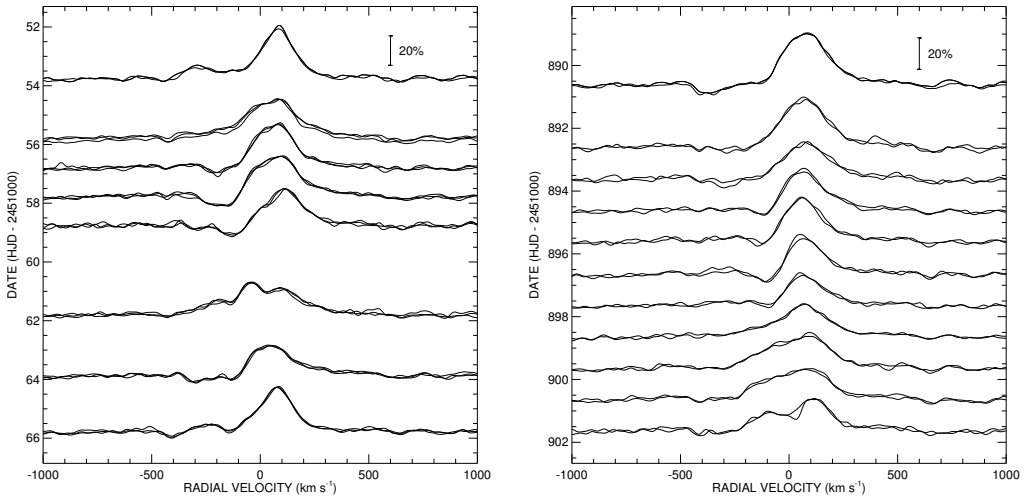

Figure 3.2: Temporal variations in the Hα profile. The left panel shows the profiles from 1998 August while the right panel shows the variations in 2000 December. The vertical bar at upper right indicates the spectral intensity scale relative to a unit continuum. The spectra were smoothed with a Gaussian filter with FWHM = 30 km s^{-1}.

companion, but our time sequences suggest that they are instead the result of varying stellar wind absorption.

We measured emission equivalent widths for Hα by making a simple numerical integration of line flux above the continuum, and our results are listed in the final column of Table 3.2. The typical measurement errors are approximately $\pm$0.05 Å for the higher dispersion spectra and about twice that for the lower dispersion spectra. The resulting equivalents widths fall within the range reported in the past (Reig et al. 1996; Liu & Hang 1999). We searched for any periodic signals in the time variations of the Hα equivalent widths using the discrete Fourier transform and CLEAN algorithm[3] (Roberts, Lehar, & Dreher 1987). These results are summarized for each observing season and for the entire data set in Figure 3.3. Most of the temporal variability appears to occur on timescales around 10 d (frequency of 0.1 cycles d^{-1}). We found no compelling evidence of periodic variability at either the orbital (11.6 d) or super-

[3]Written in the Interactive Data Language by A. W. Fullerton

orbital period (30.7 d), and the 1σ upper limits for such cyclic variations are $< 4\%$ and $< 10\%$ for these two periods, respectively (based upon sinusoidal fits at these fixed periods). The strongest signal in the power spectrum (among a number of candidate periods in the range between 6 and 12 d) occurs at a period of 9.72 ± 0.02 d. The false alarm probability that this peak is due to noise is small, $p_0 \approx N \exp(-z_0) = 0.0002$ where $z_0 = 15.6$ is the ratio of the power peak to the variance and $N = 1000$ is the number of quasi-independent frequencies tested over the range in physically interesting timescales between 0 and 1 cycle d^{-1} (Scargle 1982). Although Hα variations occurred during each run on such timescales, there were large differences in the mean equivalent width between runs and in the detailed profile shape variations within runs that indicate the importance of other timescales as well. We suggest that this 10 d timescale represents a characteristic recurrence time for ephemeral structures to appear in a wind that is subject to longer term variations in mass loss rate. If the structures are azimuthally distributed with respect to the star's spin axis, then this characteristic time may correspond to the stellar rotation period (see the case of the B-supergiant HD 64760 discussed by Fullerton et al. 1997 and the models for rotational modulation presented by Harries 2000). We can estimate the rotational period very approximately using the projected rotational velocity $V \sin i = 96 \pm 20$ km s^{-1} and radius estimate $R/R_\odot = 37 \pm 15$ (Reig et al. 1996) plus the probable inclination range (see Fig. 3.6 below). The timescale for the Hα variations falls within the derived range of rotational period of 9 to 15 d.

3.5 X-ray Variations

The 2S 0114+650 system is one of some hundred targets that have been under continuous surveillance since 1996 March by the All-Sky Monitor on the *Rossi X-ray*

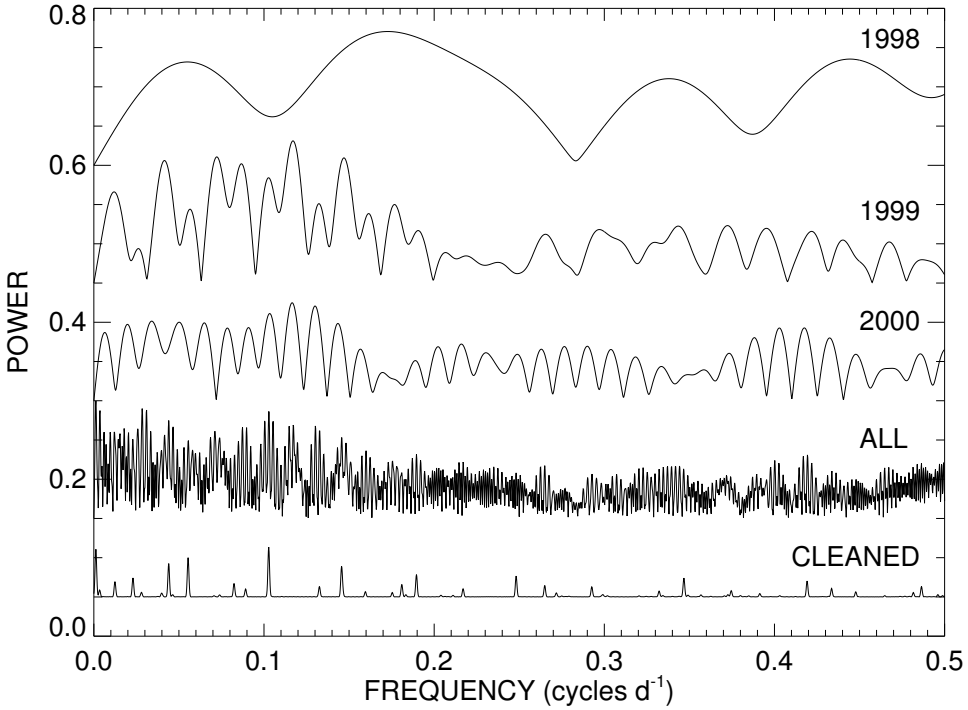

Figure 3.3: Periodograms of the Hα equivalent width variations for data from 1998, 1999, 2000, and all years (*top to bottom*, with offsets of 0.6, 0.45, 0.3, and 0.15, respectively). The lower plot shows the CLEANed periodogram (offset by 0.05) derived from a deconvolution of the full sample periodogram.

Timing Explorer (Levine et al. 1996). This instrument records the X-ray flux across three energy bands in 90 s observation segments. We extracted the flux measurements from 1996 March through 2006 May from the quick-look results provided by the *RXTE*/ASM team[4]. The source is relatively weak and there is a significant amount of scatter among the individual measurements. However, because there are currently over 60,000 measurements available for 2S 0114+650, we can achieve a significant increase in S/N by averaging the fluxes into temporal or orbital-phase bins of interest.

We first consider the long term variations in X-ray flux. We show in the upper

[4]http://xte.mit.edu/

panel of Figure 3.4 the high energy band fluxes for the duration of the *RXTE* mission binned into intervals equivalent to 12 binary orbits (139 d) as 12 looked nice. Each symbol shows the mean and standard deviation of the mean of the flux in the time bin. These means and errors were taken from measurements made only with the Scanning Shadow Camera (SSC) 2 and SSC3, as there is some indication of a long term trend of uncertain origin in the results from SSC1 for this particular source (possibly related to the calibration of gain changes in the proportional counter associated with SSC1). The lower panel illustrates the Hα equivalent width measurements over the same dates (but with much more restricted time coverage). There is a significant range in observed equivalent width during each run (§3.4), but it appears that mean strength was largest in 1998 ($\sim$ HJD 2,451,060), smallest in 1999 ($\sim$ HJD 2,451,460), and intermediate in 2000 ($\sim$ HJD 2,451,860). The binned X-ray fluxes in the top panel also show a similar kind of variation, which is suggestive that the time-averaged Hα emission and X-fluxes appear to vary together. Taken at face value, this indicates that long term variations in the B-supergiant mass loss rate are reflected in the X-ray accretion flux. A similar result was found for the massive X-ray binary and microquasar LS 5039 (Reig et al. 2003; McSwain et al. 2004).

Next we binned the ASM fluxes according to orbital phase from our spectroscopic solution (Table 3.3), and the light curves for the three energy bands are plotted in Figure 3.5. The orbital light curve is best defined in the 5 – 12 keV band where the observed counts are highest (top panel of Fig. 3.5; compare with the earlier light curve presented in Fig. 1 of Hall et al. 2000). We see that there is a clear maximum when the stars are closest near periastron (phase 0.0). At that point in the orbit, the neutron star will encounter the densest and slowest portions of the supergiant's wind, and the wind accretion rate will attain a maximum (Lamers, van den Heuvel, & Petterson 1976). The highest 5 – 12 keV flux average actually occurs for the bin centered at

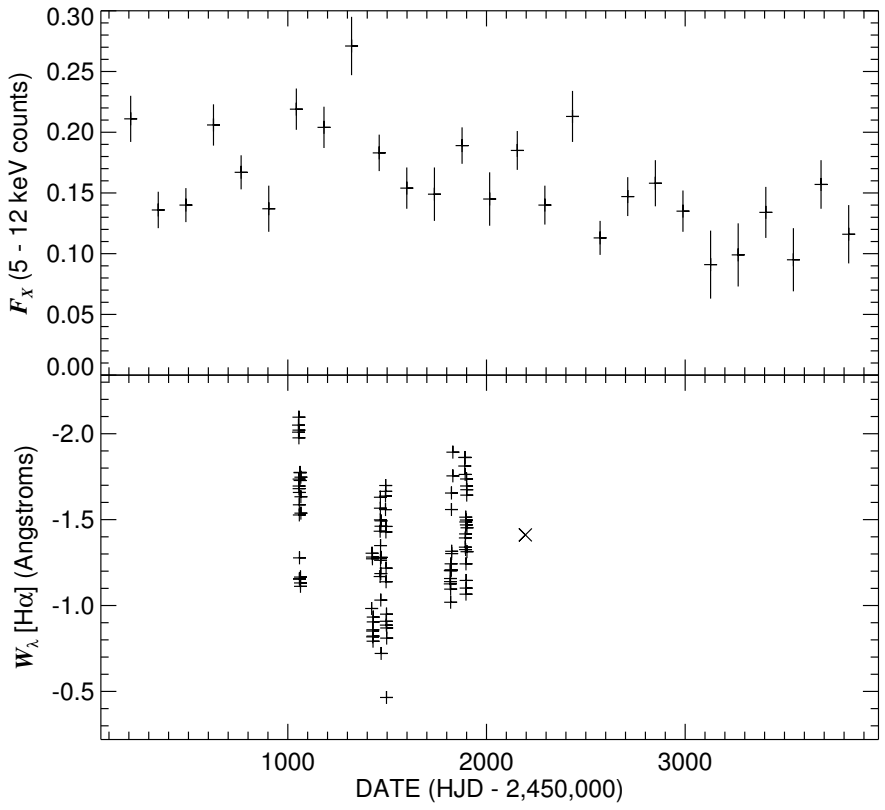

Figure 3.4: The long term variations in the *RXTE*/ASM high energy flux and Hα equivalent width. The top panel shows the ASM counts binned into intervals of 139 d (12 orbital periods) while the lower panel illustrates the Hα emission strength. The plus signs indicate our measurements while the single $\times$ sign is based on the observation from Koenigsberger et al. (2003).

phase 0.08, corresponding to a time some 22 hours after periastron. This may indicate the interval between accretion and heating to X-ray emitting temperatures or it may represent the transit time for a wind density enhancement created by tidal effects at periastron to reach the vicinity of the neutron star.

The minimum in the X-ray light curve appears near phase 0.63, which is very close to the predicted phase of supergiant inferior conjunction at phase 0.65 ± 0.06. The 5 – 12 keV X-ray flux does not vanish at this minimum, so we suspect that we are observing an atmospheric rather than a total eclipse (Hall et al. 2000). For example,

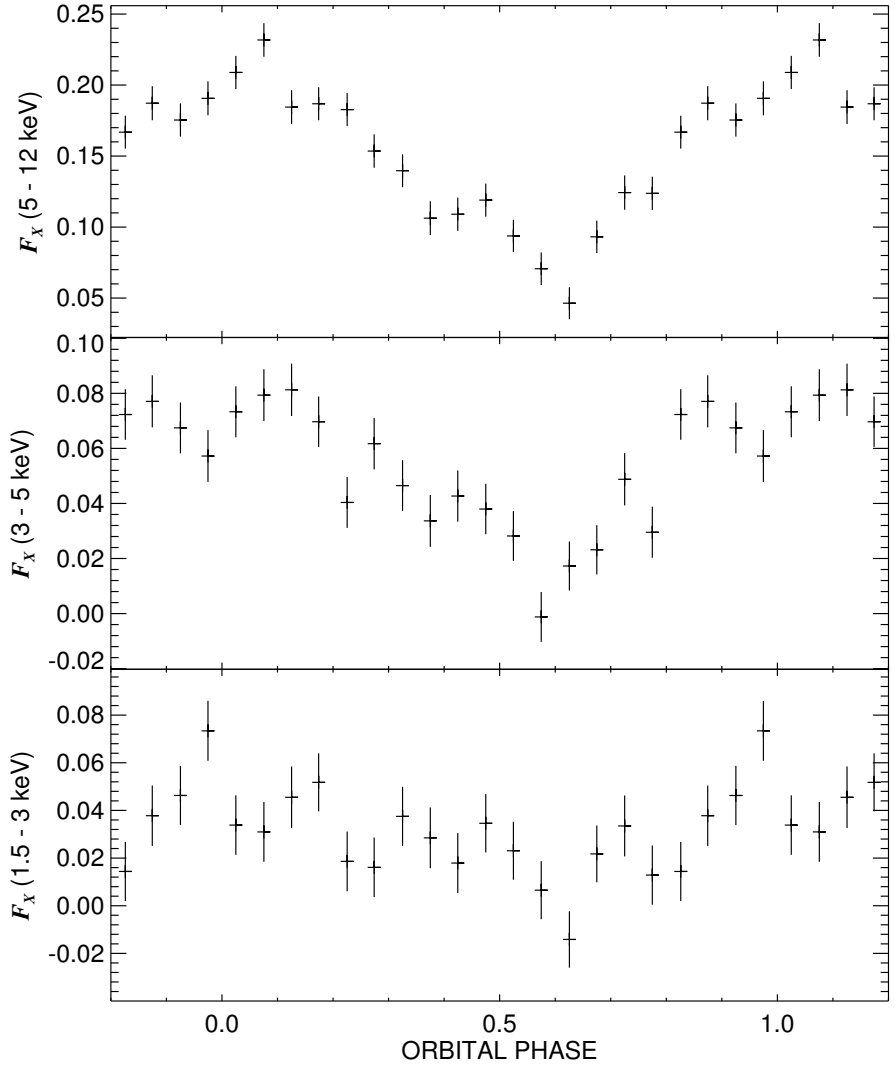

Figure 3.5: The *RXTE*/ASM fluxes binned according to orbital phase (phase 0.0 for periastron). The panels show the bin mean and standard deviation of the mean of ASM counts for each of the three energy bands.

Wen et al. (1999) show that in the case of Cyg X-1, the decrease in X-ray flux observed when the supergiant is in the foreground is well explained by the attenuation of the X-ray flux by the wind of the supergiant. We suspect that the same explanation applies to the case of the LS I +65 010 = 2S 0114+650 system as Hall et al. (2000)

find evidence of an increase in column density near X-ray minimum.

The kind of analysis made by Wen et al. (1999) of the wind attenuation as a function of orbital phase would also be profitable in this case and would presumably help place limits on the orbital inclination. We show in Figure 3.6 the constraints on the masses of the two components in the mass plane diagram. The solid lines show the mass relations for given values of orbital inclination that are derived from the mass function ($f(m)$ given in Table 3.3). Reig et al. (1996) estimate that the supergiant mass and radius are $16 \pm 5\ M_{\odot}$ and $37 \pm 15\ R_{\odot}$, respectively, based upon their analysis of the optical and near-IR spectrum. Note that this supergiant radius is much smaller than the star's Roche radius for the full range of acceptable inclination and mass ratio. The limiting line for the absence of full eclipses is shown by the dashed line in Figure 3.6 (derived from the radius given above and the projected semimajor axis $a_1 \sin i$ listed in Table 3.3). Finally, we can place a weak constraint on a minimum inclination angle of $i = 20^{\circ}$ by assuming that the supergiant rotates no faster than the critical rate (based on the given radius and observed projected rotational velocity $V \sin i = 96 \pm 20$ km s^{-1}; Reig et al. 1996). This is a weak constraint because it is based upon the assumption that the supergiant's spin inclination is the same as the orbital inclination, but these inclinations could differ if the neutron star suffered an asymmetric kick at the time of the supernova explosion (Brandt & Podsiadlowski 1995). The shaded region in Figure 3.6 shows the probable B-supergiant mass range together withthe observed range in neutron star mass (van Kerkwijk, van Paradijs, & Zuiderwijk 1995), and a plus sign marks the nominal position for a Chandrasekhar mass neutron star ($1.4\ M_{\odot}$). This best estimate solution has an inclination of $i = 45^{\circ}$, just below eclipse limit near $i = 50^{\circ}$, and this orientation is probably consistent with the atmospheric eclipse seen in the X-ray light curve. A realistic model of the X-ray attenuation by the wind of the B-supergiant would provide a reliable estimate of the

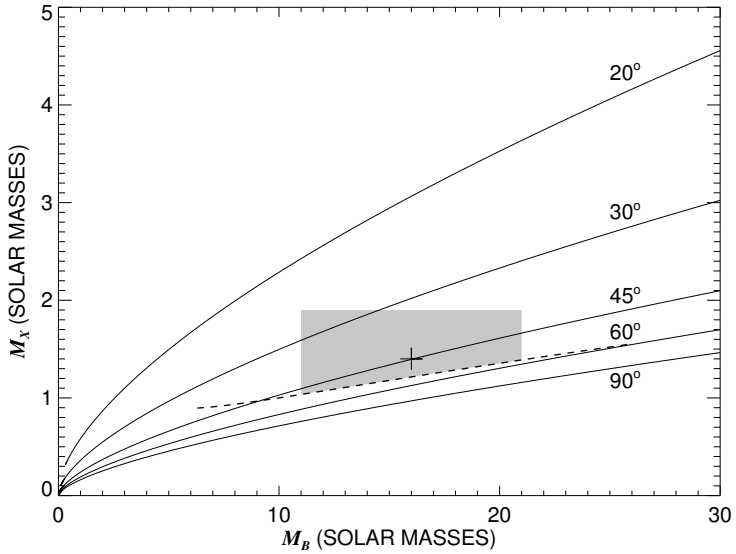

Figure 3.6: The relations between the supergiant mass M_B and neutron star mass M_X for LS I +65 010. Lines of constant orbital inclination are constructed from the mass function and are labeled at the right hand side. The dashed line indicates the upper limit on inclination and the lower limit on X-ray source mass based upon the lack of eclipses. The shaded region shows the probable solution space with the plus sign marking the favored solution.

inclination and better constraints on the masses of both stars.

– 4 –

Estimating the Size of Be Star Disks

Abstract

We[1] present numerical models of the circumstellar disks of Be stars, and we describe the resulting synthetic Hα emission lines and maps of the wavelength-integrated emission flux projected onto the sky. We demonstrate that there are monotonic relationships between the emission line equivalent width and the ratio of the angular half-width at half maximum of the projected disk major axis to the radius of the star. These relationships depend mainly upon the temperatures of the disk and star, the inclination of the disk normal to the line of sight, and the adopted outer boundary for the disk radius. We show that the predicted Hα disk radii are consistent with those observed directly through long baseline interferometry of nearby Be stars (especially once allowance is made for disk truncation in binaries and for dilution of the observed Hα equivalent width by continuum disk flux in the V-band). These models are used in the two following chapters.

[1]Grundstrom, E. D.; Gies, D. R. - published as Grundstrom & Gies (2006)

4.1 Hα Spectral and Spatial Emission Models

Be stars are rapidly rotating B-type stars that lose mass into an equatorial, circumstellar disk (Porter & Rivinius 2003). The disk flux is observed in emission lines (especially the hydrogen Hα line), an infrared excess, and the polarization of starlight scattered in the disk. It is now possible to investigate the actual extent and geometry of the circumstellar disks through optical long baseline interferometry of nearby Be stars (Stee et al. 1995; Quirrenbach et al. 1997; Chesneau et al. 2005; Tycner et al. 2005, 2006). Most of these investigations have focused on the angular resolution of the disks in a narrow spectral band centered on the Hα emission line. The long baseline interferometric observations are limited to the nearby sample of Be stars at present, so we need other indirect methods to help estimate the sizes of Be star disks in more distant targets.

Here we explore how the disk radius may be estimated from measurements of the disk Hα emission flux. We begin with an idealized case to illustrate some of the important parameters that define the relationship between equivalent width and radius. Suppose that the disk is isothermal and geometrically thin, and that the line emission is dominated by an inner optically thick region that appears as an ellipse projected onto the plane of the sky. We also make the simplifying assumption that the specific intensity of the disk emission I_λ^d is isotropic. Then the wavelength integrated Hα flux will depend on the product of the surface flux, the wavelength range where Hα is optically thick, and the projected solid angle,

$$F(\mathrm{H}\alpha) = \pi I_\lambda^d < \triangle\lambda > \cos i \left(\frac{R_d}{D}\right)^2 \tag{4.1}$$

where $< \triangle\lambda >$ is the wavelength interval over which the line is optically thick (averaged over the visible disk), i is the disk normal inclination angle, R_d is the boundary

radius of the optically thick disk, and D is the distance to the star. We measure this flux through the emission equivalent width W_λ, which is given in wavelength units relative to the local continuum flux,

$$F(\mathrm{H}\alpha) = |W_\lambda|(1+\epsilon)\pi I_\lambda^s \left(\frac{R_s}{D}\right)^2 \tag{4.2}$$

where ϵ is the ratio of disk continuum flux to stellar flux in the Hα region, I_λ^s is the stellar specific intensity near Hα (assumed isotropic), and R_s is the radius of the star. We can then equate these two expressions to find the predicted relationship between the ratio of disk to stellar radius and Hα emission equivalent width,

$$\frac{R_d}{R_s} = \sqrt{\frac{I_\lambda^s}{I_\lambda^d} \frac{W_\lambda(1+\epsilon)}{< \triangle\lambda > \cos i}}. \tag{4.3}$$

This special case is characterized by a disk radius that varies as the square root of the emission equivalent width, and this expectation is supported by the interferometric observations of Tycner et al. (2005) who find that the emitted Hα flux scales with the square of the disk radius. However, the coefficient of the relationship also depends on the ratio of the stellar to disk specific intensities that is dependent upon the stellar and disk temperatures. Furthermore, there is an inclination dependence in both the $\cos i$ projection factor and the $< \triangle\lambda >$ term (through the range in velocities and Doppler shifts viewed through the disk). The $< \triangle\lambda >$ term also depends upon the assumed disk density as the optical depth is based on the product of neutral hydrogen density and the emission line profile. Finally, there must also be some emission contribution from the optically thin outer disk that is ignored in the expression above. Thus, in order to predict accurately the relationship between equivalent width and disk radius, we need a more complete model that accounts for the specific dependences on disk temperature, inclination, and density.

We have adopted the Be disk model approach of Hummel & Vrancken (2000)

that is based upon models developed by Horne & Marsh (1986) and Horne (1995) for accretion disks in cataclysmic variables. The disk is assumed to be axisymmetric and centered over the equator of the underlying star, and the gas density varies as

$$\rho(R,Z) = \rho_0 R^{-n} \exp\left[-\frac{1}{2}\left(\frac{Z}{H(R)}\right)^2\right] \tag{4.4}$$

where R and Z are the radial and vertical cylindrical coordinates (in units of stellar radii), ρ_0 is the base density at the stellar equator, n is a radial density exponent, and $H(R)$ is the disk vertical scale height. The neutral hydrogen population within the disk is found by equating the photoionization and recombination rates (Gies et al. 2007). In stellar radius units, the disk vertical scale height at radius R is

$$H(R) = \frac{C_s}{V_K} R^{3/2}$$

where the sound speed $C_s = \sqrt{\gamma R_g T_d}$ ($\gamma = 5/3$ for mono-atomic gases and R_g is the universal gas constant) and the local Keplerian velocity is $V_K = \sqrt{(GM)/R}$ (for concentric circular orbits). The disk gas is assumed to be isothermal and its temperature T_d is related to the stellar effective temperature $T_{\rm eff}$ by $T_d = 0.6 T_{\rm eff}$ (Carciofi & Bjorkman 2006).

The numerical model represents the disk by a large grid of azimuthal and radial surface elements, and the equation of transfer is solved along a ray through the center of each element according to

$$I_\lambda = S_\lambda^L (1 - e^{-\tau_\lambda}) + I_\lambda^s e^{-\tau_\lambda} \tag{4.5}$$

where I_λ is the derived specific intensity, S_λ^L is the source function for the disk gas (taken as the Planck function for the disk temperature T_d), I_λ^s is the specific intensity for a uniform disk star (taken as the product of the Planck function for $T_{\rm eff}$ and an Hα photospheric absorption line derived from the grid of Martins et al. 2005a), and τ_λ is the integrated optical depth along the ray (we assume Keplerian rotation).

For each surface element of the disk, the line of sight intersects the disk's midplane at an inclination angle i that is radius R from the disk center and azimuth angle ϕ measured counter-clockwise from the near side of the disk. Hummel & Vrancken (2000) (following Horne & Marsh 1986) show in their equation 7 that

$$\tau_\lambda = \frac{W\,(R)}{\cos i}\frac{\lambda_0}{\sqrt{2\pi}\Delta V}\exp\left[-\frac{1}{2}\left(\frac{V - V_d(0)}{\Delta V}\right)^2\right]. \tag{4.6}$$

The leading constant is

$$W(R) = \frac{\pi e^2}{mc}\ f\ \Sigma(R)$$

where e, m, and c are the charge of the electron, the mass of the electron, and the speed of light, respectively. The oscillator strength of the atomic transition producing the line is denoted by f and the surface density of the disk is

$$\Sigma(R) = \rho_0 R^{-n}\sqrt{2\pi}H(R)R_*$$

where R_* is the radius of the star. The term ΔV in equation 4.6 is the line profile width

$$\Delta V = \sqrt{\Delta V_{th}^2 + V_{sh}^2}$$

where ΔV_{th} is the thermal velocity dispersion and the velocity shear is

$$V_{sh} = -\frac{3}{2}\frac{H}{R}V_{Kep}\sin i\tan i\sin\phi\cos\phi \tag{4.7}$$

following equation 4 in Horne (1995). The term $V_d(0)$ in equation 4.6 is the velocity of the disk at $R = 0$ which is equivalent to the radial velocity of the star itself.

The first term in equation 4.5 applies to all disk area elements unocculted by the star. Hummel & Vrancken (2000) determine that the boundary of the occulted region is (their equation 12)

$$R_o\,(\phi) = \frac{\sec i}{\sqrt{\cos^2\phi + \sin^2\phi\sec^2\phi}} \tag{4.8}$$

where R_o is the radius of the region occulted by the star and i and ϕ are again the inclination angle and azimuthal angle, respectively. The second term in equation 4.5 applies to all elements that correspond to the projected photospheric disk of the star. The absorption line adopted in I_λ^s is Doppler shifted according to solid body rotation for the photospheric position in a star that is rotating at 90% of the critical value.

The model code calculates a synthetic line profile over the range from -2000 to $+2000$ km s^{-1} at 10 km s^{-1} intervals by summing the product of projected area and specific intensity over the disk grid. We then integrate the line profile relative to the continuum to form a predicted equivalent width (taken as positive for net absorption or negative for net emission). The model also forms a synthetic image of the star plus disk in the plane of the sky by summing the intensity over a 2.8 nm band centered on Hα. We collapsed this image along the projected major axis to get the summed spatial intensity, and then we determined the radius where the summed intensity drops to half its maximum value (excluding the spatial range corresponding to photospheric intensity). We adopt this half-maximum summed intensity radius as the effective disk radius in the following discussion.

We need to specify the stellar mass and radius in the code in order to determine the disk Keplerian velocities (stellar radius provides the inner limit), and we adopted these as a function of stellar effective temperature (or spectral subtype) using the eclipsing binary results for B-stars from Harmanec (1988). We determined the relationship between model equivalent width and disk radius by running a sequence of models defined by the spectral subtype of the star, the disk inclination, the disk radial density exponent n, and the selected value for the outer boundary of the disk. The final variable for any sequence is the base density ρ_0, and we computed models over a range in ρ_0 that corresponds to Hα profiles with no visible emission up to strong emission cases with $|W_\lambda| > 50$ Å.

We show the predicted relationship between the disk radius and Hα equivalent width in Figure 4.1 for the case of a B2 Ve star ($T_{\rm eff}$ = 23100 K) assuming n = 3.0 and an outer boundary at 100 R_s. The lower solid line shows the pole-on case ($i = 0°$). At higher inclination angles ($i = 50°$ and $i = 80°$ for the middle and top lines, respectively) the projected disk area is smaller ($\propto \cos i$), and consequently the emission equivalent width is smaller for a given disk radius. We do not show the $i = 90°$ case because the shear broadening approximation for the emission profile width breaks down for an edge-on orientation (Horne & Marsh 1986). The symbols along each sequence indicate positions of fiducial base density values. Note that all three curves show the expected square root dependence predicted for the simple case (eq. [4.3] above).

The three dashed lines in Figure 4.1 show the corresponding inclination cases for a B8 Ve star ($T_{\rm eff}$ = 11600 K) again made assuming $n = 3.0$ and an outer boundary at 100 R_s. These curves are all shifted to the left relative to the B2 Ve sequences because the photospheric absorption component is larger in cooler B-stars. The model profiles of the B8 Ve sequence have less Hα emission at a given disk radius than their B2 Ve counterparts because at this lower temperature the disk-to-star intensity ratio, the vertical scale height, and the thermal emission line broadening are all smaller.

The dotted line in Figure 4.1 shows how the Hα equivalent width is reduced when the outer boundary for the disk grid is moved inwards from 100 R_s to 25 R_s for the case of a B2 Ve star with a disk inclination of 80° and a disk density exponent of n = 3.0. The outer disk region contains low brightness, optically thin gas, and although the emission contribution from any particular outer radius area element is small, the projected area of such elements increases with radius so that the selection of the outer boundary condition is important. We found that increasing the outer boundary from 100 R_s to 200 R_s for this parameter set increased the equivalent widths

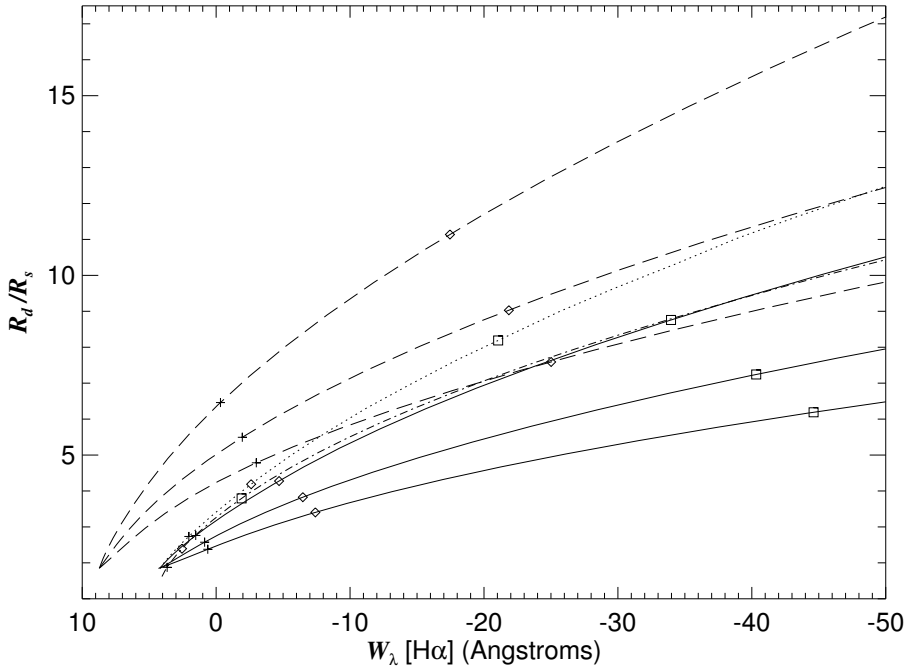

Figure 4.1: Plots of the predicted Hα equivalent width and disk half-maximum radius for several model sequences. The solid lines show the relationships for models with a B2 Ve central star, an outer boundary of $100\ R_s$, and inclinations of $0°$ (*bottom*), $50°$ (*middle*), and $80°$ (*top*). The three dashed lines show the results from models with the same inclinations but with a B8 Ve star. The dotted line shows how the relation changes for a model with a B2 Ve star and disk inclination of $80°$ when the outer boundary is reduced to $25\ R_s$. The dot-dashed line shows that the relation is almost identical for a model with a B2 Ve star, $i = 80°$, and $100\ R_s$ boundary when the disk density exponent is changed from $n = 3.0$ to 3.5. Disk base density values of $\rho_0 = 1 \times 10^{-12}$, 2×10^{-12}, and 5×10^{-12} g cm^{-3} are indicated along sequences by a plus sign, diamond, and square, respectively.

by only 10%, so we adopted the 100 R_s boundary as our nominal choice. The selection of the boundary radius will mainly be important for Be stars in binary systems where the outer disk will be truncated by the gravitational influence of the companion.

Finally, the dot-dashed line in Figure 4.1 shows another sequence for the same B2 Ve, $i = 80°$, and 100 R_s boundary case, but calculated this time with a larger disk density exponent of $n = 3.5$ (i.e., a steeper drop off in density). The overall shape of this curve is almost the same as the one for $n = 3.0$ (although the fiducial base density points have very different locations), and this suggests that the particular choice of

density law is not important for the derived equivalent width – radius relationships. Investigations of the infrared flux excess in Be stars suggest that the exponent falls in the range $n = 2 - 4$ (Porter & Rivinius 2003). We caution that the results become more sensitive to the outer disk boundary for $n < 3$ where the emission from the optically thin, outer regions assumes more significance.

We have constructed such model sequences for subtypes B0, B2, B4, B6, and B8 Ve, for inclinations $i = 0°$, $50°$, and $80°$, and for outer boundary radii of 17 R_s, 25 R_s, 50 R_s, and 100 R_s. These numerical results, an interpolation program, and our code are available to interested readers at our Web site[2]. Relevant code is also included in Appendix B.

4.2 Comparison with Disk Radii from Interferometry

We can test the predictions of the model with the interferometric observations of nearby Be stars for which the projected disk shape and size in the sky are known. The long baseline interferometric observations in the narrow band surrounding Hα are fit with an elliptical Gaussian, and the reported diameter $\theta^d_{\rm mj}$ is the FWHM of the Gaussian fit to the major axis. We list in Table 4.1 the observed and adopted parameters for the Be stars with Hα interferometric observations from Quirrenbach et al. (1997) and Tycner et al. (2005, 2006). The columns of Table 4.1 list the star name, a contemporaneous measurement of W_λ and a code for the data source, adopted effective temperature (Zorec, Frémat, & Cidale 2005), the stellar angular diameter determined from flux fitting methods (Underhill et al. 1979; Ochsenbein & Halbwachs 1982), the interferometric disk radius, ratio of the projected minor to major axis r, and a code for the data source, an estimate of the disk inclination, and finally the

[2]http://www.chara.gsu.edu/~gies/Idlpro/BeDisk.tar

ratio R_d/R_s from interferometry and from W_λ (plus the adopted outer boundary for the calculation of the latter).

Table 4.1: Be Stars with Interferometric Hα Measurements

Star Name	W_λ (Å)	Ref. C2	$T_{\rm eff}$ (kK)	$\theta^\star$ (mas)	$\theta^d_{\rm mj}$ (mas)	r	Ref. C6,7	i (deg)	R_d/R_s (interf.)	R_d/R_s (Hα)	R_d/R_s (bound)
γ Cas	-29.1	1	30.2	0.45	3.47	0.70	2	49	7.7 ± 1.2	6.3 ± 0.9	27
γ Cas	-22.5	3	30.2	0.45	3.67	0.79	3	42	8.2 ± 1.2	5.3 ± 0.7	27
γ Cas	-31.2	4	30.2	0.45	3.59	0.58	5	58	8.0 ± 1.2	6.9 ± 1.1	27
ϕ Per	-35.0	1	28.8	0.26	2.67	0.46	2	67	10.1 ± 0.8	8.3 ± 1.4	22
ϕ Per	-42.6	4	28.8	0.26	2.89	0.27	5	79	10.9 ± 0.4	10.2 ± 1.9	22
ψ Per	-33.7	1	16.8	0.35	3.26	0.47	2	66	9.3 ± 0.7	9.2 ± 1.5	100
η Tau	-6.9	6	12.4	0.72	2.65	0.95	2	21	3.7 ± 0.2	5.2 ± 0.5	100
η Tau	-4.3	3	12.4	0.72	2.08	0.75	3	44	2.9 ± 0.3	5.4 ± 0.7	100
48 Per	-22.3	1	16.7	0.39	2.77	0.89	2	31	7.2 ± 1.5	7.4 ± 1.1	18
ζ Tau	-19.4	6	20.1	0.43	4.53	0.28	2	78	10.5 ± 1.2	8.6 ± 1.5	24
ζ Tau	-20.6	3	20.1	0.43	3.14	0.31	3	75	7.3 ± 0.5	8.7 ± 1.5	24
β CMi	-3.3	3	12.1	0.73	2.13	0.69	3	49	2.9 ± 0.7	5.5 ± 0.7	100

1. Hummel & Vrancken (1995); 2. Quirrenbach et al. (1997); 3. Tycner et al. (2005); 4. Gies et al. (2007); 5. Tycner et al. (2006); 6. Apparao et al. (1993).

We determined the ratio R_d/R_s for each of the observations listed in Table 4.1 by interpolating in the model sequences for W_λ, $T_{\rm eff}$, i, and outer disk boundary. We estimated the disk inclination angle by equating the predicted value of the projected minor to major axis with the observed value,

$$r \approx \cos i + \frac{C_s}{V_{\rm K}} \sqrt{\frac{R_d}{R_s}} \sin i \tag{4.9}$$

where the disk vertical dimension is evaluated at radial distance R_d, C_s is the speed of sound, and $V_{\rm K}$ again is the Keplerian velocity at $R = R_s$. The ratio $C_s/V_{\rm K}$ is ≈ 0.022 among main sequence B-stars for the temperatures, masses, and radii given by Harmanec (1988). We assumed an outer disk boundary of $100R_s$ for all but the known binary stars where we adopted the Roche radius of the primary star instead (Hubert et al. 1997; Gies et al. 2007).

The model disk radii predicted from W_λ are listed in Table 4.1 and compared to the interferometric radii in Figure 4.2. The predicted radii are generally in reasonable agreement with the observed radii, however, the model tends to overestimate the radii

for a given equivalent width (or to underestimate the equivalent width for a given radius) for the weaker emission and cooler stars, η Tau and β CMi. Furthermore, the predicted radii of the stronger emission stars appear to be systematically lower than observed. We suspect that this latter problem is due to an underestimation of the true emission equivalent width in very active Be stars. If Be star disks contribute a fraction of the continuum flux in the V-band spectrum of $\epsilon = F_\lambda^d / F_\lambda^s$, then we need to renormalize the equivalent widths to $(1+\epsilon)W_\lambda$ in order to compare them with the model results where the equivalent width is referred to the stellar continuum alone. We lack direct information on the value of ϵ for the targets in Table 4.1, but we can approximately estimate the renormalization factor from the work of Dachs, Kiehling, & Engels (1988) who found that $(1+\epsilon) \approx (1 - 0.003W_\lambda)^{-1}$ based upon fits of the spectral energy distributions in a sample of Be stars (see their eq. [40]). The revised radii including this correction (*open squares* in Fig. 4.2) are in better agreement with the interferometric radii. Thus, the predictions of the models appear to be generally consistent with the available interferometric data.

The method outlined above offers a new way to estimate disk radius for distant Be stars that is based only upon the Hα equivalent width and estimates of spectral subtype, inclination, and outer disk boundary. It should prove to be a useful addition to the traditional method from Huang (1972) that is based upon measurements of the separation between double peaks of the Hα profile and upon an assumed mass. We caution readers that the derived radii for individual targets are probably only accurate to within $\pm$30% at the moment (percentage standard deviation of the residuals for the dilution corrected radii in Fig. 4.2) and that higher precision will require detailed modeling of the spectral energy distribution and emission lines. Such models will probably need a more detailed physical description of the disk (Carciofi & Bjorkman 2006) with attention paid to possible asymmetries in the disk gas (Porter & Rivinius

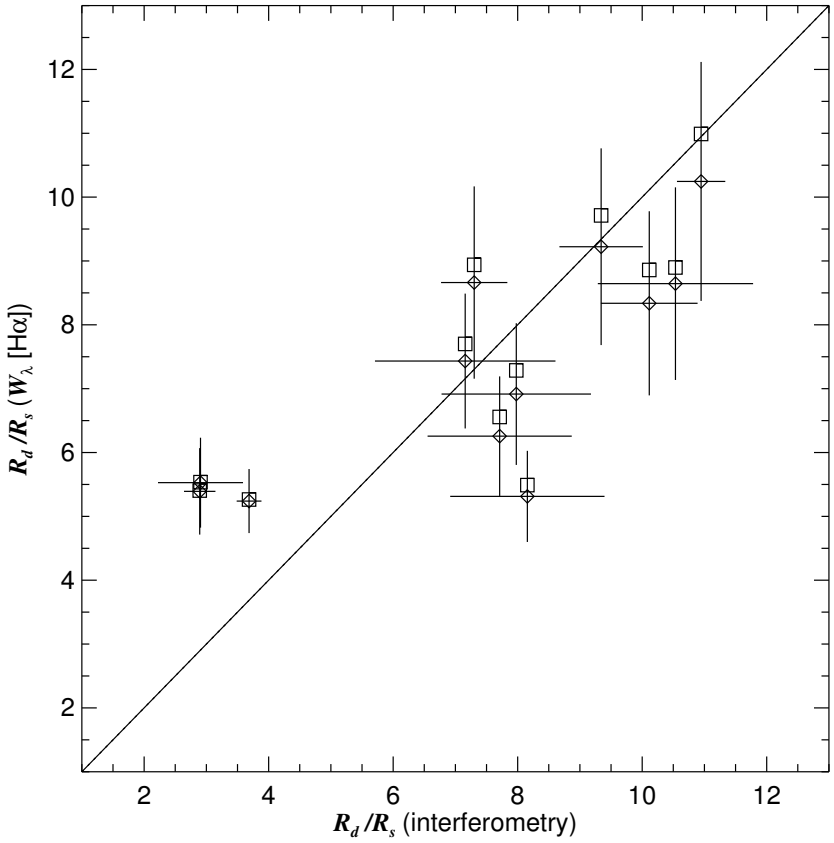

Figure 4.2: A comparison of the Hα disk radii obtained directly from interferometry with those predicted by the models using the Hα equivalent width (*diamonds* centered on the errors bars). The solid line shows the expected one-to-one correspondence. The open squares show how the predicted radii increase if the equivalent widths are renormalized to account for dilution by the disk continuum V-band flux (Dachs et al. 1988).

2003). The effort involved is certainly merited in studies of selected Be stars, but the simpler approach presented here may be valuable in surveys of Be stars where observations are limited to low resolution spectroscopic measurements of the Hα equivalent width (or a photometric counterpart; McSwain & Gies 2005). The method will also be useful for planning future interferometric observations.

In fact, this model is used in the next two chapters which discuss three different Be X-ray binaries.

– 5 –

The Be X-ray Binary and Microquasar LS I +61 303

Abstract

We[1] present the results of an Hα monitoring campaign on the BeXRB and microquasar system LS I +61 303. We use radial velocity measurements of He I lines in our spectra to re-evaluate the orbital elements and to better establish the time of periastron. We list equivalent widths and other parameters for the Hα emission line and discuss the orbital phase related variations observed. We call attention to a dramatic episode of emission weakening that occurred in less than a day that probably resulted from exposure to a transient source of ionizing radiation. We argue that the increase in Hα and X-ray emission following periastron probably results from the creation of an extended density wave in the disk created by tidal forces. We also discuss estimates of the size of the disk from the Hα equivalent width measurements, and we suggest that the disk radius from the average equivalent width corresponds to a resonant truncation radius of the disk while the maximum equivalent width corre-

[1]Grundstrom, E. D.; Caballero-Nieves, S. M.; Gies, D. R.; Huang, W.; McSwain, M. V.; Rafter, S. E.; Riddle, R. L.; Williams, S. J.; Wingert, D. W. - published as Grundstrom et al. (2007c)

sponds to a radius limited by the separation of the stars at periastron. We note that a nearby faint companion is probably an unrelated foreground object.

5.1 Introduction

The remarkable binary system LS I +61 303 is one of the best studied microquasars in the sky (Massi 2004). It consists of a rapidly rotating Be star surrounded by a dense circumstellar disk and a compact companion that is a source of both orbital phase modulated X-ray (Paredes et al. 1997; Leahy 2001; Wen et al. 2006) and radio flux (Taylor et al. 1992; Gregory 2002). High angular resolution observations suggest that the system has precessing, relativistic radio jets (Massi et al. 2004), and these jets may be the source of variable and very high energy, γ-ray emission (Albert et al. 2006). The companion is generally considered to be a magnetic neutron star, but it may be a black hole (Punsly 1999). The orbital parameters were recently reanalyzed by Casares et al. (2005) who confirmed the high eccentricity of the system and discussed the possible mass range. Their work shows that the orbital phases of the X-ray and radio maxima do not occur at periastron but are curiously delayed by a significant fraction of the orbital period. The disk that feeds the companion is a strong source of Hα emission, and there is a well established record of the emission line variations over the past decade (Paredes et al. 1994; Zamanov et al. 1999; Liu et al. 2000; Zamanov et al. 2001; Liu & Yan 2005). Zamanov et al. (1999) demonstrated that some of the emission line properties vary with the orbital period, presumably as the result of the companion's varying gravitational pull.

Here we present the results of a new observational effort on the Hα variations in LS I +61 303 that we launched to investigate the co-variations with the X-ray flux as recorded by the All-Sky Monitor (ASM) instrument aboard the *Rossi X-ray Timing*

Explorer (RXTE) satellite. It follows similar investigations of LS I +65 010 (Ch. 3), HDE 245770 = A 0535+26 and X Per (Ch. 6), and Cyg X-1 (Gies et al. 2003). We first describe radial velocity measurements and a re-evaluation of the orbital elements in §5.2. Then we turn in §5.3 to the temporal variations observed in the Hα profile on rapid, orbital, and long term timescales. We discuss the results in the context of the disk truncation model of Okazaki et al. (2002) in §5.4.

5.2 Radial Velocities and Orbital Elements

We obtained a set of 100 spectra of LS I +61 303 between 1998 August and 2000 December. The observations were made with the Kitt Peak National Observatory 0.9 m coudé feed telescope during six runs. We used two spectrograph arrangements to record the red spectral region around Hα with resolving powers of $R = \lambda/\triangle\lambda = 4100$ and 9500. The details about the spectra and their reduction are given in Chapter 3 on LS I +65 010. We also recorded the spectrum of a nearby visual companion, and we discuss its properties in §5.5.

All the spectra record the Hα emission line and the He I λ6678 feature. The He I λ6678 line appears in most spectra as a weak and narrow absorption core flanked by emission wings (compare the upper and lower spectra in Fig. 5.2, below). We suspect that this line is a composite of a partial photospheric absorption line with wing emission and central absorption that originates in the inner disk. We assume that the radial velocity variations of this composite profile represent the motion of the Be star as the line formation probably occurs very close to the photosphere of the Be star. We note in passing that the half-width at half-minimum in the absorption core of He I λ6678 is 101 km s^{-1} in most of our spectra. This is similar to the projected rotational velocity $V \sin i = 113$ km s^{-1} reported by Casares et al. (2005), but much

smaller than that found earlier by Hutchings & Crampton (1981) of $V \sin i = 360 \pm 25$ km s^{-1}. This suggests that some of the blue spectral lines measured by Casares et al. (2005) may also have been affected by weak emission in the line wings that made the absorption cores appear more narrow.

We measured radial velocities by cross-correlating each spectrum with a template spectrum formed from the average of 24 spectra from our run in 2000 December. The cross-correlation was made over the spectral region in the immediate vicinity of He I λ6678, although we also included the region surrounding He I λ7065 for the spectra from the 2000 October and December runs that also recorded this line. These relative velocities were transformed to an absolute scale by adding the radial velocity of the template spectrum, -43.1 km s^{-1}, found by parabolic fitting of the cores of He I $\lambda\lambda 6678, 7065$. We also obtained cross-correlation velocities of the interstellar line at 6613 Å to monitor the radial velocity stability of our measurements. All these results are reported in Table 5.1, which lists the heliocentric Julian date of mid-exposure, orbital phase, radial velocity, observed minus calculated residual from the fit, and the interstellar line offset (plus columns describing the Hα profile discussed in §5.3). The typical measurement error is ± 2.1 km s^{-1} based upon the scatter between pairs of observations at closely spaced times.

Many recent papers on the orbital properties of LS I +61 303 adopt an arbitrary zero-phase at HJD 2,443,366.775 (Taylor & Gregory 1982) and an orbital period of 26.4960 ± 0.0028 d, which was determined by Gregory (2002) after his careful study of the radio flux curve. Here we adopt the same convention for orbital phase that we denote by ϕ(TG).

Table 5.1: Radial Velocity and Hα Measurements

Date (HJD−2,400,000)	ϕ(TG)	V_r (km s^{-1})	$(O-C)$ (km s^{-1})	$\triangle V_{\rm ISM}$ (km s^{-1})	W_λ (Å)	$V_r(W)$ (km s^{-1})	$V_r(V)$ (km s^{-1})	$V_r(R)$ (km s^{-1})	$W_\lambda(V)$ / $W_\lambda(R)$	V/R	FWHM(V) (Å)	FWHM(R) (Å)
51053.860	0.122	−34.7	4.3	−1.2	−11.01	−8.5	−202.5	144.9	0.75	0.96	4.29	5.45
51053.881	0.123	−31.4	7.6	−0.7	−11.29	−10.1	−202.0	144.5	0.73	0.95	4.21	5.43
51055.855	0.198	−40.6	−9.2	1.6	−11.65	−16.2	−197.8	143.7	0.82	0.93	4.70	5.30
51055.877	0.199	−37.1	−5.9	0.5	−11.76	−18.5	−195.3	145.3	0.83	0.89	4.77	5.14
51055.941	0.201	−39.2	−8.2	2.1	−11.75	−17.2	−197.9	143.3	0.85	0.91	4.84	5.16
51056.902	0.237	−23.5	3.5	0.3	−11.29	−18.6	−196.3	148.7	0.88	0.89	5.12	5.16
51056.923	0.238	−32.7	−5.8	0.6	−11.36	−20.7	−197.4	149.0	0.86	0.88	5.05	5.19
51056.945	0.239	−21.8	5.0	0.4	−11.67	−19.2	−197.3	146.0	0.82	0.91	4.85	5.40
51057.880	0.274	−21.5	5.5	1.6	−11.82	−30.8	−201.2	149.1	0.91	0.90	5.37	5.33
51057.901	0.275	−12.7	14.4	−0.4	−11.21	−29.1	−196.0	148.4	0.87	0.89	5.13	5.26
51057.922	0.276	−16.6	10.7	−1.0	−11.60	−26.8	−195.7	149.2	0.87	0.90	5.20	5.36
51058.869	0.312	−38.4	1.0	0.5	−11.11	−33.5	−203.2	145.2	0.82	0.90	5.09	5.60
51058.892	0.312	−40.8	−1.0	1.6	−10.80	−32.1	−201.8	150.1	0.86	0.88	5.38	5.55
51058.913	0.313	−33.4	6.8	−1.6	−10.91	−33.5	−199.6	149.4	0.87	0.91	5.29	5.55
51061.882	0.425	−30.9[a]	33.1	−2.0	−12.77	−37.8	−200.8	140.3	0.93	0.92	6.53	6.48
51061.903	0.426	−27.6[a]	36.5	−0.9	−13.56	−41.9	−201.0	137.3	0.95	0.93	6.63	6.54
51061.924	0.427	−30.4[a]	33.7	−1.9	−12.86	−39.3	−191.1	150.8	1.27	0.99	7.60	5.89
51065.882	0.576	−68.2	−5.7	1.0	−11.35	−29.1	−225.8	129.4	0.64	0.77	4.64	5.61
51065.903	0.577	−67.0	−4.4	−0.3	−11.30	−29.1	−226.2	130.6	0.63	0.77	4.66	5.65
51065.946	0.579	−67.1	−4.6	−0.6	−11.65	−29.2	−225.2	126.5	0.61	0.79	4.44	5.72
51066.756	0.609	−60.2	1.5	−0.9	−11.60	−13.7	−217.3	132.9	0.59	0.76	4.67	5.96
51066.778	0.610	−66.9	−5.2	1.0	−12.30	−22.1	−215.8	128.7	0.57	0.77	4.41	6.01
51066.800	0.611	−66.9	−5.2	−1.3	−12.24	−16.5	−214.4	129.8	0.57	0.78	4.43	6.01
51421.937	0.014	−49.0	−2.5	−0.2	−9.16	−23.0	−209.5	136.7	0.66	0.69	4.79	5.01
51425.943	0.165	−34.8	0.1	−3.6	−10.74	−15.2	−207.8	150.7	0.89	0.92	5.60	5.75
51425.964	0.166	−36.4	−1.5	−3.5	−10.72	−25.3	−209.9	135.6	0.74	0.82	4.95	5.50
51427.933	0.241	−44.8	−18.1	−1.3	−9.34	−5.8	−205.6	149.5	0.84	0.85	6.20	6.32
51428.882	0.276	−42.7	−15.4	6.8	−9.07	−24.3	−212.6	146.4	0.63	0.69	5.17	5.60
51428.903	0.277	−41.8	−14.4	−0.8	−9.46	−25.1	−214.2	139.7	0.60	0.70	4.84	5.64
51429.880	0.314	−43.4	−2.9	−1.2	−9.69	−38.7	−202.4	138.5	0.67	0.72	4.94	5.32
51429.901	0.315	−37.5	3.4	−3.4	−9.42	−39.4	−202.0	138.3	0.68	0.75	4.90	5.41
51464.828	0.633	−58.4	2.6	1.0	−12.35	12.8	−218.0	149.1	0.51	0.71	4.35	6.09
51464.850	0.634	−57.8	3.3	0.2	−12.29	15.5	−217.9	148.0	0.49	0.70	4.33	6.13
51464.930	0.637	−62.4	−1.5	−4.1	−12.28	14.7	−222.6	142.7	0.48	0.69	4.31	6.18
51465.890	0.673	−70.5	−10.6	−3.6	−13.29	22.4	−220.5	143.1	0.49	0.74	4.38	6.60
51465.911	0.674	−62.2	−2.4	−3.2	−13.37	22.1	−222.1	140.9	0.48	0.72	4.47	6.77
51466.840	0.709	−62.4	−3.6	−3.7	−12.00	11.7	−221.2	143.6	0.46	0.80	4.06	7.08
51466.861	0.710	−62.0	−3.2	−3.8	−12.16	14.3	−220.4	142.5	0.45	0.79	4.05	7.11
51466.884	0.711	−63.0	−4.2	−11.5	−12.26	9.7	−223.0	139.1	0.45	0.79	4.05	7.04
51467.899	0.749	−83.6[a]	−26.1	−14.8	−1.11	51.6	−200.5	96.3	0.20	0.30	3.07	4.49
51467.920	0.750	−79.9[a]	−22.4	−12.3	−0.92	81.2	−225.3	91.9	0.14	0.20	3.28	4.70
51468.862	0.785	−82.2[a]	−25.9	−7.0	−1.31	49.2	−225.3	74.0	0.12	0.35	2.11	6.02
51468.883	0.786	−79.0[a]	−22.7	−4.3	−1.11	−9.1	−246.5	78.9	0.11	0.36	1.55	5.36
51469.872	0.823	−79.9[a]	−25.0	−11.3	−1.05	−4.2	−230.1	83.5	0.18	0.41	2.53	5.68
51469.893	0.824	−81.8[a]	−26.9	−8.0	−1.57	−23.3	−226.9	86.9	0.13	0.31	2.52	5.95
51491.798	0.651	−63.5	−2.9	−5.3	−12.80	4.0	−220.5	145.4	0.52	0.84	4.39	7.05
51491.820	0.652	−62.2	−1.7	−4.0	−12.79	4.0	−222.4	144.6	0.52	0.84	4.39	7.13
51492.757	0.687	−58.0	1.4	0.1	−11.51	15.8	−221.3	152.9	0.51	0.86	4.44	7.43

Continued on Next Page...

Table 5.1 – Continued

Date (HJD−2,400,000)	ϕ(TG)	V_r (km s^{-1})	$(O-C)$ (km s^{-1})	$\triangle V_{\rm ISM}$ (km s^{-1})	W_λ (Å)	$V_r(W)$ (km s^{-1})	$V_r(V)$ (km s^{-1})	$V_r(R)$ (km s^{-1})	$W_\lambda(V)$ / $W_\lambda(R)$	V/R	FWHM(V) (Å)	FWHM(R) (Å)
51492.779	0.688	−56.4	3.1	0.5	−11.06	12.7	−224.6	152.6	0.52	0.86	4.45	7.35
51493.740	0.724	−62.6	−4.3	4.6	−10.53	14.6	−218.3	140.2	0.48	0.92	3.82	7.28
51493.761	0.725	−57.2	1.1	2.0	−10.90	14.6	−219.4	140.1	0.49	0.93	3.87	7.38
51494.752	0.762	−56.0	1.0	−2.5	−10.27	11.6	−211.5	142.8	0.48	0.78	4.21	6.87
51494.773	0.763	−56.4	0.6	0.8	−10.06	11.2	−213.0	141.8	0.48	0.79	4.17	6.84
51495.809	0.802	−52.6	3.1	−5.6	−10.72	−4.8	−212.9	138.4	0.64	0.76	4.92	5.84
51495.830	0.803	−52.8	2.8	−5.5	−10.63	−1.5	−211.4	137.1	0.62	0.79	4.67	5.92
51496.800	0.840	−54.1	0.3	−4.1	−10.00	−19.2	−212.5	138.5	0.67	0.75	5.12	5.77
51496.821	0.840	−49.4	5.0	−0.1	−10.08	−15.2	−209.6	138.0	0.67	0.77	5.09	5.84
51497.765	0.876	−60.2	−7.2	−1.3	−10.06	−14.4	−215.1	145.5	0.65	0.74	5.23	5.96
51497.786	0.877	−56.8	−3.9	−3.5	−10.23	−11.2	−216.8	146.5	0.64	0.75	5.23	6.14
51817.802	0.955	−62.0	−12.5	−0.4	−8.63	−23.8	−219.1	139.6	0.61	0.72	4.21	4.92
51817.850	0.957	−60.0	−10.6	−0.1	−8.53	−25.9	−218.1	138.7	0.62	0.72	4.18	4.87
51818.830	0.994	−58.5	−10.9	1.2	−8.85	−23.8	−221.4	140.5	0.65	0.71	4.30	4.73
51818.851	0.994	−58.7	−11.1	0.8	−8.29	−16.7	−221.7	142.0	0.63	0.71	4.23	4.74
51819.817	0.031	−53.2	−7.7	2.0	−8.87	−12.6	−216.3	142.6	0.60	0.79	4.35	5.68
51819.840	0.032	−51.9	−6.4	−0.4	−9.16	−13.6	−215.3	143.0	0.61	0.72	4.53	5.33
51820.827	0.069	−51.5	−8.4	2.9	−9.30	−23.2	−215.9	133.3	0.55	0.73	4.00	5.30
51821.770	0.105	−44.5	−4.0	−0.6	−9.51	−31.8	−212.4	131.4	0.66	0.86	4.00	5.19
51821.792	0.105	−45.0	−4.5	0.8	−9.41	−25.8	−213.9	135.7	0.64	0.86	3.98	5.29
51822.812	0.144	−38.1	−1.0	1.9	−9.91	−23.8	−212.5	136.0	0.68	0.91	4.04	5.38
51822.834	0.145	−39.6	−2.5	1.1	−9.73	−22.2	−211.8	136.7	0.69	0.93	4.00	5.38
51823.762	0.180	−40.5	−7.0	−0.1	−10.90	−35.1	−215.8	137.7	0.80	0.93	4.60	5.35
51823.783	0.181	−37.0	−3.7	2.0	−10.75	−36.0	−213.7	136.2	0.79	0.92	4.56	5.32
51824.765	0.218	−25.0	4.0	5.7	−10.59	−25.8	−204.2	147.4	0.76	0.89	4.61	5.37
51824.786	0.218	−28.1	0.8	3.4	−10.43	−26.5	−202.6	146.9	0.80	0.86	4.79	5.16
51830.779	0.445	−59.6	4.7	0.4	−10.44	−43.1	−221.7	121.9	0.61	0.76	4.60	5.78
51830.801	0.445	−61.4	3.0	1.4	−10.18	−39.5	−220.5	122.2	0.59	0.77	4.44	5.84
51889.762	0.671	−53.2	6.8	1.2	−9.43	−27.5	−219.8	132.1	0.72	1.09	4.02	6.05
51889.783	0.671	−50.8	9.2	−1.5	−9.73	−25.8	−220.3	133.3	0.71	1.09	3.96	6.04
51890.669	0.705	−31.9[a]	27.0	−1.4	−9.76	−13.5	−216.9	145.8	0.74	1.13	4.03	6.14
51890.690	0.706	−38.9[a]	20.0	0.2	−9.54	−14.2	−215.2	144.1	0.74	1.14	3.96	6.13
51892.658	0.780	−42.8	13.7	−0.9	−10.76	−7.3	−216.1	142.3	0.68	1.02	4.24	6.37
51892.682	0.781	−43.6	12.9	−1.7	−10.96	−10.3	−215.8	138.0	0.66	1.00	4.20	6.39
51893.686	0.819	−51.6	3.5	−2.4	−11.15	−1.1	−210.1	120.8	0.51	0.89	3.90	6.80
51893.707	0.820	−52.7	2.4	−0.4	−11.42	−5.2	−208.8	121.1	0.54	0.91	3.91	6.66
51894.684	0.856	−52.9	0.8	0.7	−9.31	−13.6	−208.2	128.4	0.58	0.84	4.02	5.86
51894.705	0.857	−53.1	0.6	−0.8	−9.35	−11.8	−206.7	130.5	0.59	0.83	4.08	5.80
51895.733	0.896	−51.5	0.6	0.7	−9.88	−11.8	−203.9	131.6	0.58	0.78	4.36	5.84
51895.754	0.897	−48.1	4.0	−0.9	−9.77	−11.0	−201.9	132.5	0.59	0.79	4.25	5.68
51896.706	0.933	−42.5	8.1	−0.4	−8.73	−13.5	−203.7	144.9	0.68	0.84	4.21	5.19
51896.727	0.934	−41.1	9.4	−1.0	−8.56	−9.2	−201.7	146.8	0.66	0.83	4.12	5.23
51897.707	0.971	−46.7	2.1	0.2	−8.02	−19.4	−206.4	140.4	0.66	0.89	3.77	5.08
51897.728	0.971	−43.1	5.7	−1.1	−7.97	−18.3	−206.7	139.0	0.67	0.90	3.83	5.11
51898.711	0.008	−42.6	4.3	−0.7	−8.24	−21.9	−207.4	143.1	0.77	0.92	4.23	5.04
51898.732	0.009	−45.5	1.2	−0.6	−8.28	−21.8	−206.7	144.4	0.79	0.91	4.34	5.00
51899.713	0.046	−31.9	12.7	0.2	−8.52	−19.2	−207.1	145.7	0.72	0.89	4.24	5.26
51899.734	0.047	−36.0	8.6	−0.1	−8.54	−16.0	−208.2	145.0	0.72	0.90	4.26	5.29
51900.708	0.084	−35.1	7.0	2.0	−9.23	−10.5	−200.3	137.5	0.68	0.90	4.21	5.52
51900.729	0.085	−36.3	5.7	1.0	−9.56	−12.5	−200.7	139.0	0.69	0.90	4.24	5.52

Continued on Next Page...

Table 5.1 – Continued

Date (HJD−2,400,000)	ϕ(TG)	V_r (km s^{-1})	$(O-C)$ (km s^{-1})	$\triangle V_{\rm ISM}$ (km s^{-1})	W_λ (Å)	$V_r(W)$ (km s^{-1})	$V_r(V)$ (km s^{-1})	$V_r(R)$ (km s^{-1})	$W_\lambda(V)$ / $W_\lambda(R)$	V/R	FWHM(V) (Å)	FWHM(R) (Å)
51901.693	0.121	−35.8	3.4	0.7	−9.18	−12.3	−200.1	134.4	0.72	0.92	4.23	5.36
51901.714	0.122	−35.6	3.4	1.3	−9.63	−11.9	−201.5	134.3	0.72	0.88	4.34	5.34

[a] Assigned zero weight.

We determined orbital elements using the non-linear, least-squares program of Morbey & Brosterhus (1974). We also included the radial velocity data from the recent study by Casares et al. (2005), but we found that our velocities are systematically lower than theirs by -9.4 km s^{-1} so we added this value to their measurements for ease of comparison. Our first fit using all the available velocities is shown as the dotted line in Figure 5.1, and the resulting orbital elements are listed in column 4 of Table 5.2. The r.m.s. of this fit is 10.4 km s^{-1}, which is about five times larger than the estimated measurement error. This large scatter is caused by temporal changes in the shape of the He I λ6678 profile. For example, the six very low velocity measurements shown in Figure 5.1 were made during a remarkable episode of reduced Hα emission strength (§5.3) when the He I emission wings disappeared and the absorption core became broader. Thus, we selectively zero-weighted these six measurements and five other very discrepant points that also appeared to display profile shape changes. The fit resulting from this edited set of velocities is shown as a solid line in Figure 5.1, and the corresponding orbital elements are given in column 5 of Table 5.2.

Our results are generally in good agreement with earlier determinations of the elements by Hutchings & Crampton (1981) and Casares et al. (2005) (given in columns 2 and 3 of Table 5.2, respectively). The largest range in results is found for the orbital eccentricity e, and unfortunately the paucity of measurements in the orbital phase range 0.4 – 0.5 limits the accuracy of the estimate in our work. Our final result of $e = 0.55 \pm 0.05$ is somewhat lower than the estimate of $e = 0.8 \pm 0.1$ from fits of the IR light curve (Martí & Paredes 1995). Models for the accretion flux variations indicate an eccentricity in the range $e = 0.3$ (Leahy 2001) to $e = 0.6$ (Taylor et al. 1992). Periastron occurs at phase $\phi(\mathrm{TG}) = 0.301 \pm 0.011$. This is in reasonable agreement with the expectation from the radio model of Gregory (2002) that places the phase of periastron in the range $\phi(\mathrm{TG}) = 0.33 - 0.40$.

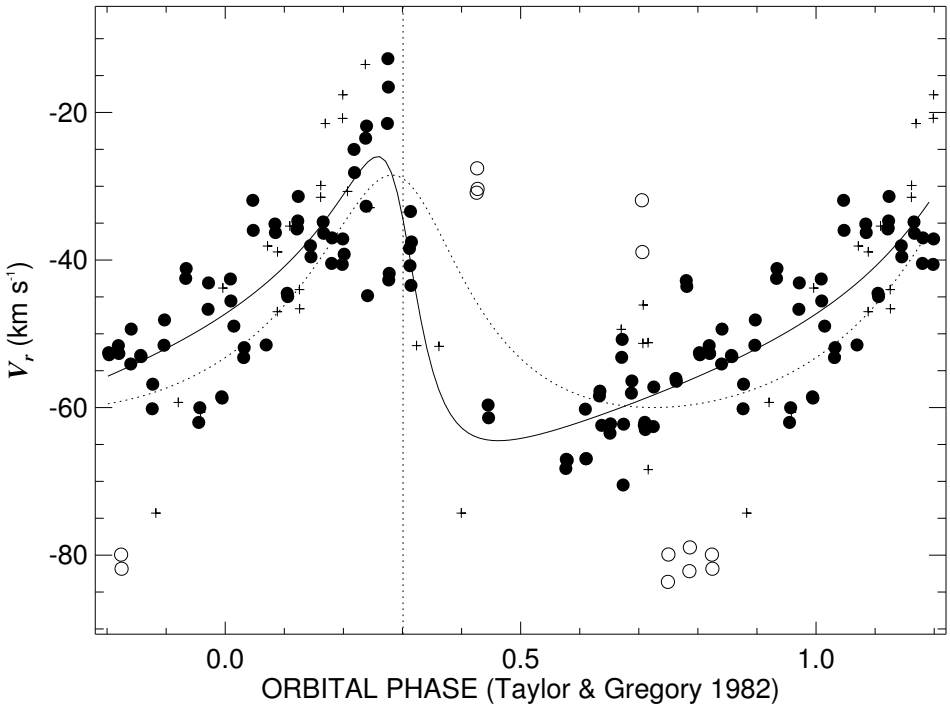

Figure 5.1: Calculated radial velocity curve (*solid line*) for LS I +61 303. The measured radial velocities are shown as filled circles. Open circles mark the measurements that were assigned zero weight, and plus signs indicate the measurements from Casares et al. (2005). The curved dotted line shows the orbital solution that results when the discrepant measurements are included in the fit. The vertical dotted line indicates periastron phase.

Table 5.2: Orbital Elements

Element	Hutchings & Crampton (1981)	Casares et al. (2005)	All Measures	Edited Set
P^a (d)	26.51	26.4960	26.4960	26.4960
T (HJD–2,400,000)	43559 ± 1	43372.9 ± 0.5	51057 ± 1	51058.6 ± 0.3
Periastron (ϕ(TG))	0.25 ± 0.04	0.23 ± 0.02	0.24 ± 0.04	0.301 ± 0.011
e	0.60 ± 0.13	0.72 ± 0.15	0.34 ± 0.08	0.55 ± 0.05
ω (deg)	46 ± 23	21 ± 13	15 ± 17	57 ± 9
K (km s^{-1})	24 ± 6	23 ± 6	15.8 ± 1.4	19.3 ± 1.5
γ (km s^{-1})	-57 ± 3	-40.2 ± 1.9	-49 ± 1	-51.0 ± 0.8
$f(m)$ ($M_\odot$)	0.019 ± 0.015	0.011 ± 0.012	0.009 ± 0.003	0.011 ± 0.003
$a_1 \sin i$ ($R_\odot$)	10 ± 3	8 ± 3	7.8 ± 0.7	8.4 ± 0.8
r.m.s. (km s^{-1}) ...	15.6	8.5	10.4	7.5

[a] Fixed.

5.3 Hα Variations

The Hα emission line is formed in the circumstellar disk of the Be star, and here we examine the temporal variations in the profile to investigate how the changes in the disk are related to changes in the accretion flux from the vicinity of the companion. The Hα profile appears as a double-peaked emission line in most of our spectra, and we made a number of measurements to characterize the shape and strength of the emission. These measurements are summarized in Table 5.1. Column 6 of Table 5.1 lists the numerical integration of the line flux that includes the full extent of the line wings. Because the emitting gas in the disk probably experiences Keplerian rotation (Porter & Rivinius 2003), the high velocity wings are formed closest to the Be star. We measured the radial velocity of the wings based upon a bisector position determined using the method of Shafter, Szkody, & Thorstensen (1986) as described in Appendix A. We used Gaussian functions with FWHM = 200 km s^{-1} at sample positions in the wings of $\pm$390 km s^{-1}. The resultant radial velocities are given in column 7 of Table 5.1. Zamanov et al. (1999) advocated making fits of the double-peaked Hα profile using Gaussian functions to match the violet V and red R peaks, and we have followed their approach for consistency. These double-Gaussian fits were restricted to the inner part of the profile ($|\triangle\lambda| < 7$ Å) as the wings are much more extended that those of Gaussian functions. The remaining columns in Table 5.1 list the parameters for these fits: radial velocity of the V peak (col. 8), radial velocity of the R peak (col. 9), ratio of the equivalent widths of the V and R components (col. 10), V/R peak intensity ratio (col. 11), FWHM for the V peak (col. 12), and FWHM for the R peak (col. 13).

We find evidence for temporal variations on timescales of days and longer. The most dramatic change in the Hα profile that we observed occurred in 1999 October

(starting HJD 2,451,467). During the first three nights of this run the Hα profile appeared at normal strength (top plot in Fig. 5.2), but in the course of 24 hours or less the emission strength declined by about a factor of ten (lower plot in Fig. 5.1). The equivalent width over the next two days stayed at record low values relative to existing measurements (Paredes et al. 1994; Zamanov et al. 1999; Liu et al. 2000; Zamanov et al. 2001; Liu & Yan 2005). At the same time the emission in the wings of He I λ6678 also disappeared revealing a broader and deeper photospheric line. Liu & Yan (2005) obtained a spectrum six days after our last weak emission observation, and by that time the emission equivalent width was back to normal levels. We measured a projected rotational velocity for the weak emission spectra of $V \sin i = 104 \pm 5$ km s^{-1} from a comparison of the width of He I λ6678 with that in model profiles (Lanz & Hubeny 2003) convolved with a rotational broadening function. This is close to the value obtained by Casares et al. (2005), but we caution that this is probably only a lower limit as the He I profile (like Hα) is still probably affected by emission components even during this weak emission phase.

It is hard to imagine any process that would change the density properties of the Be star's disk so significantly in such a short time span. We suggest instead that the neutral hydrogen in the disk was almost totally ionized at that time by exposure to energetic radiation from the vicinity of the companion. We show in Figure 5.3 the contemporary variations of the radio flux as observed with the NRAO Green Bank Interferometer[2] (Ray et al. 1997), the daily averaged 5 – 12 keV X-ray flux observed with *RXTE*/ASM[3] (Levine et al. 1996), and the Hα equivalent width. Although there is no evidence of any X-ray flare at that time, a secondary radio brightening did occur about the time of the Hα decline. However, because the Hα strength appeared

[2]ftp://ftp.gb.nrao.edu/pub/fghigo/gbidata/gdata/00README
[3]http://xte.mit.edu

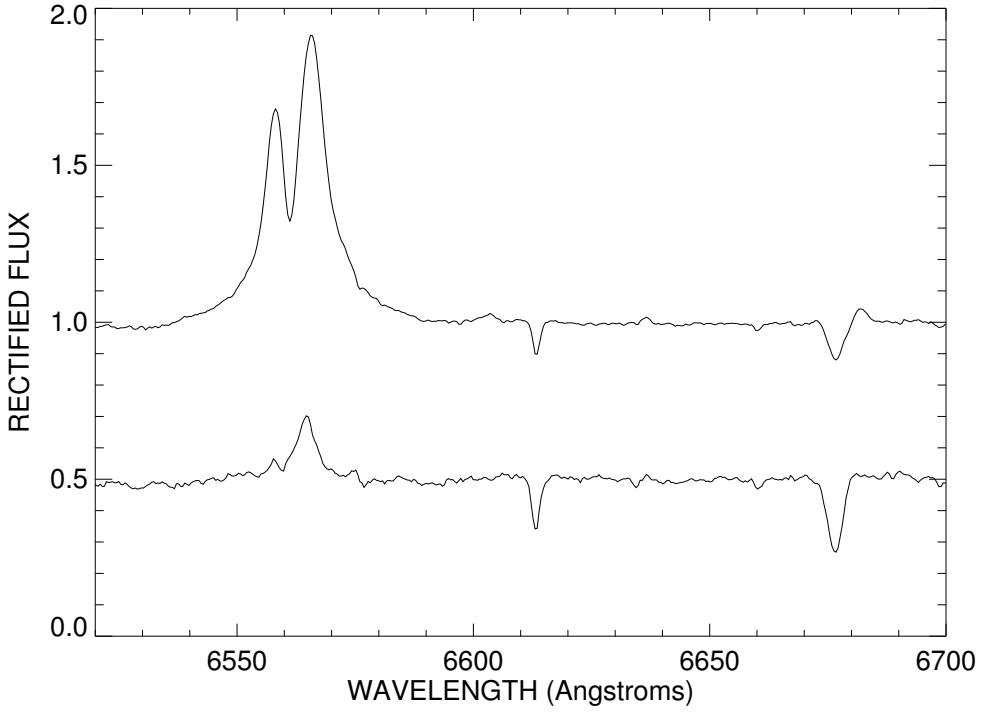

Figure 5.2: Average spectra of LS I +61 303 from 1999 October. The top plot shows the average from the first three nights when the Hα emission strength was normal, while the bottom plot (offset by -0.5 in rectified flux for clarity) shows the average from the next three nights when the emission strength plummeted. The other spectral features shown are the interstellar 6613 Å line and He 1 λ6678.

relatively normal during other radio bursts, it is not clear how or if this secondary maximum is related to the Hα weakening event. If the radio emission forms in the relativistic jets, then it is possible that the secondary radio maximum originated at positions further away from the orbital plane where the inner Be star disk was more directly illuminated by jet emission. We note that the emission weakening event occurred near apastron, an orbital phase where Liu & Yan (2005) also observed rapid variations in the Hα profile.

We next turn to Hα variations related to the orbital period. Zamanov et al. (1999) demonstrated that the variations in the relative strengths of the V and R peaks are least partially related to orbital phase (see their Fig. 3), and our results

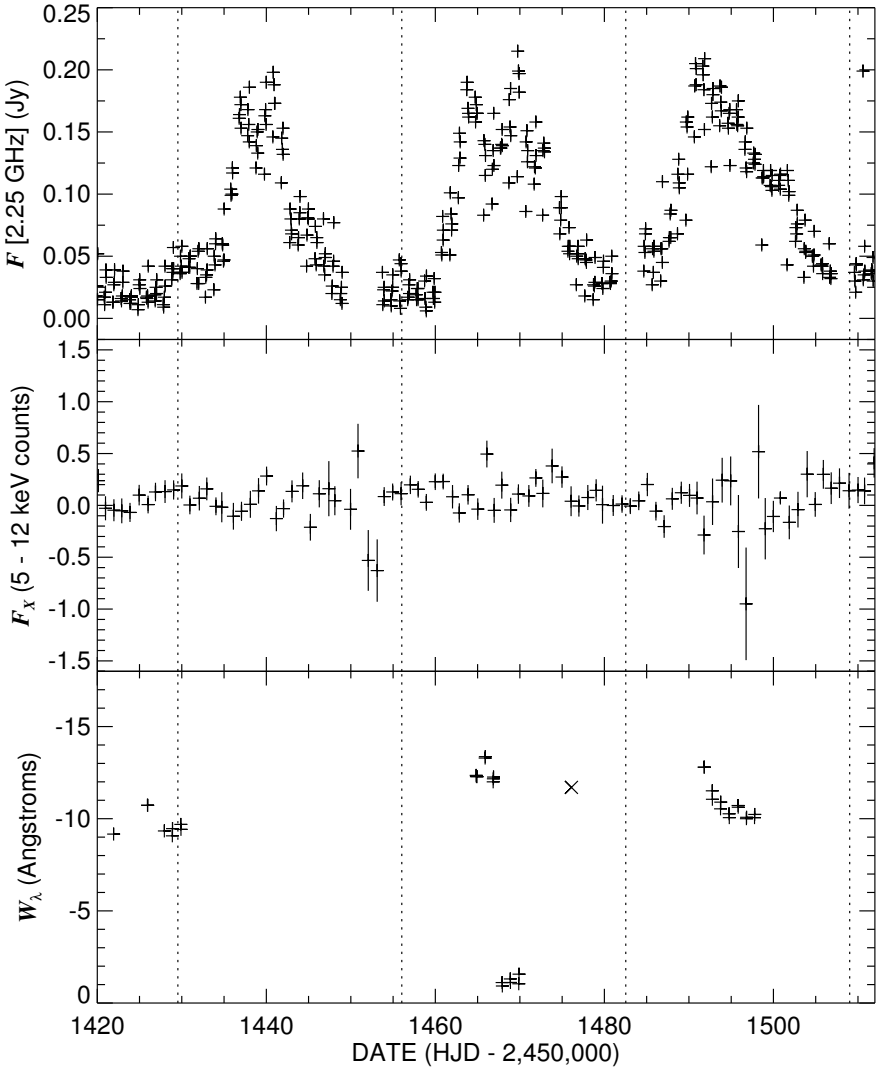

Figure 5.3: The time variations in radio flux (*top panel*), X-ray emission (*middle panel*), and Hα emission equivalent width (*lower panel*) around the time of the Hα emission decline. The X symbol in the lower plot represents an equivalent width measurement from Liu & Yan (2005). The dotted lines indicate times of periastron.

appear to support their conclusion. We show in the lower panel of Figure 5.4 the ratio of the equivalent widths of the V and R fitted components (Table 5.1) plotted as a function of the orbital phase. We see that the V peak appears to strengthen relative to the R peak around periastron, $\phi(\mathrm{TG}) = 0.30$. This strengthening of the short

wavelength side of the profile also appears to shift the wing radial velocity to lower values. The top panel of Figure 5.4 shows how the wing velocity attains a minimum near periastron with a velocity curve that is markedly different from the orbital one (shown as a dotted line). The middle panel shows the average radial velocity of the V and R peaks that show no evidence of orbital motion.

We compare in Figure 5.5 the Hα equivalent width variations with orbital phase to those observed in the radio and X-ray fluxes. The lower panel shows our equivalent width measurements combined with 159 other published measurements (Paredes et al. 1994; Zamanov et al. 1999; Liu et al. 2000; Zamanov et al. 2001; Liu & Yan 2005) that we have binned into ten phase groups (after omitting the six unusually low measurements from the 1999 October decline). We see that when averaged over many cycles there appears to be a coherent cyclic variation in emission strength that attains a maximum near $\phi(\mathrm{TG}) = 0.55$. A similar kind of variation is seen in the orbital phase binned X-ray fluxes from *RXTE*/ASM (Paredes et al. 1997; Leahy 2001). The top panel of Figure 5.5 shows the binned radio curve from the Green Bank Interferometer. Note that the radio brightenings from cycle to cycle show significant variation in the shape of the light curve and phase of maximum (Gregory 2002).

Finally we show in Figure 5.6 these same three fluxes over the period of active observation. The top panel shows the Green Bank Interferometer flux density observations at 2.25 GHz that we averaged by binning into time intervals equal to three orbital periods (bins of 79.5 d), and the middle panel illustrates the *RXTE*/ASM X-ray fluxes binned in the same way. The lower panel shows the individual Hα equivalent widths from our measurements (*plus signs*) and from other published measurements (*X signs*). Gregory (2002) reported evidence of a long (1167 d) periodicity in the radio measurements, and Zamanov & Martí (2000) showed that a comparable timescale is found in the Hα properties. There are two maxima visible that are sepa-

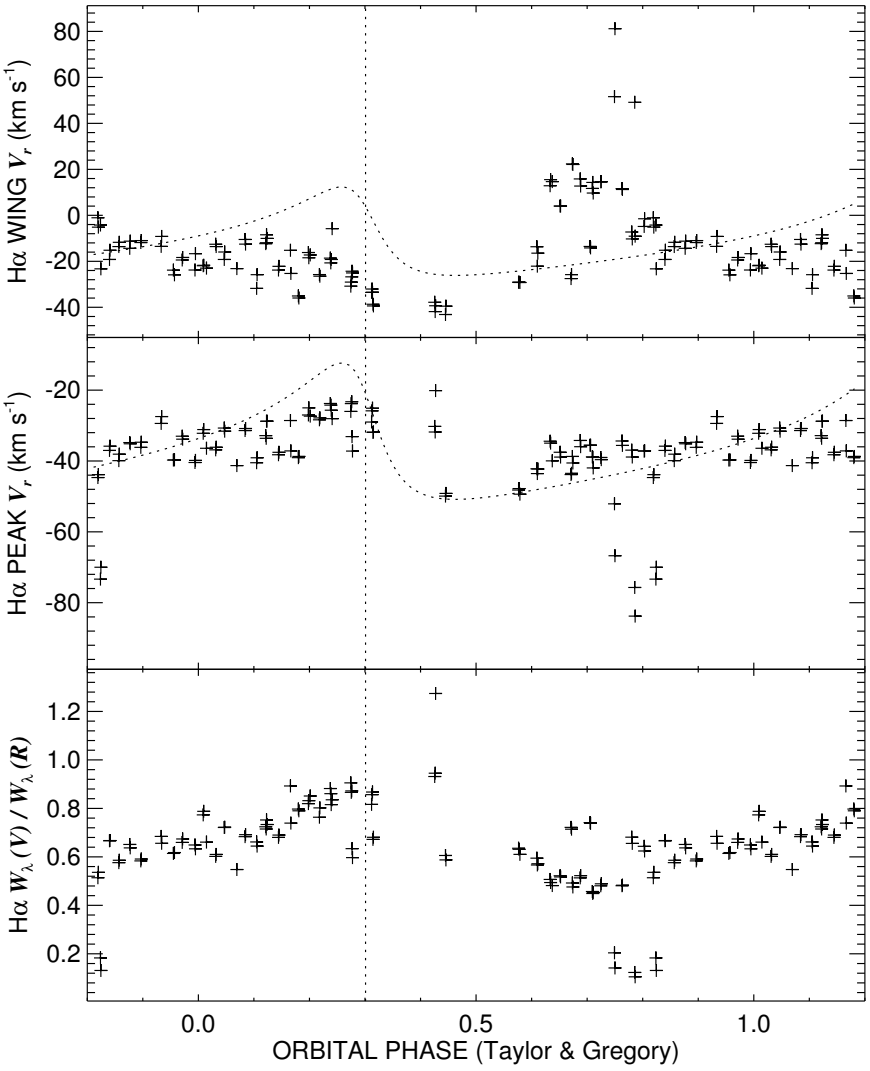

Figure 5.4: The orbital phase variations in the Hα wing radial velocity (*top*), the mean Hα peak radial velocity (*middle*), and the ratio of the equivalent widths of the V and R components (*bottom*). The curved dotted lines in the upper two panels show the orbital radial velocity curve translated to the mean velocity of the sample in each case. The vertical dotted line indicates periastron phase.

rated by about 1200 d in the Hα time series, but the coverage is too sparse to verify whether other cyclic maxima are present.

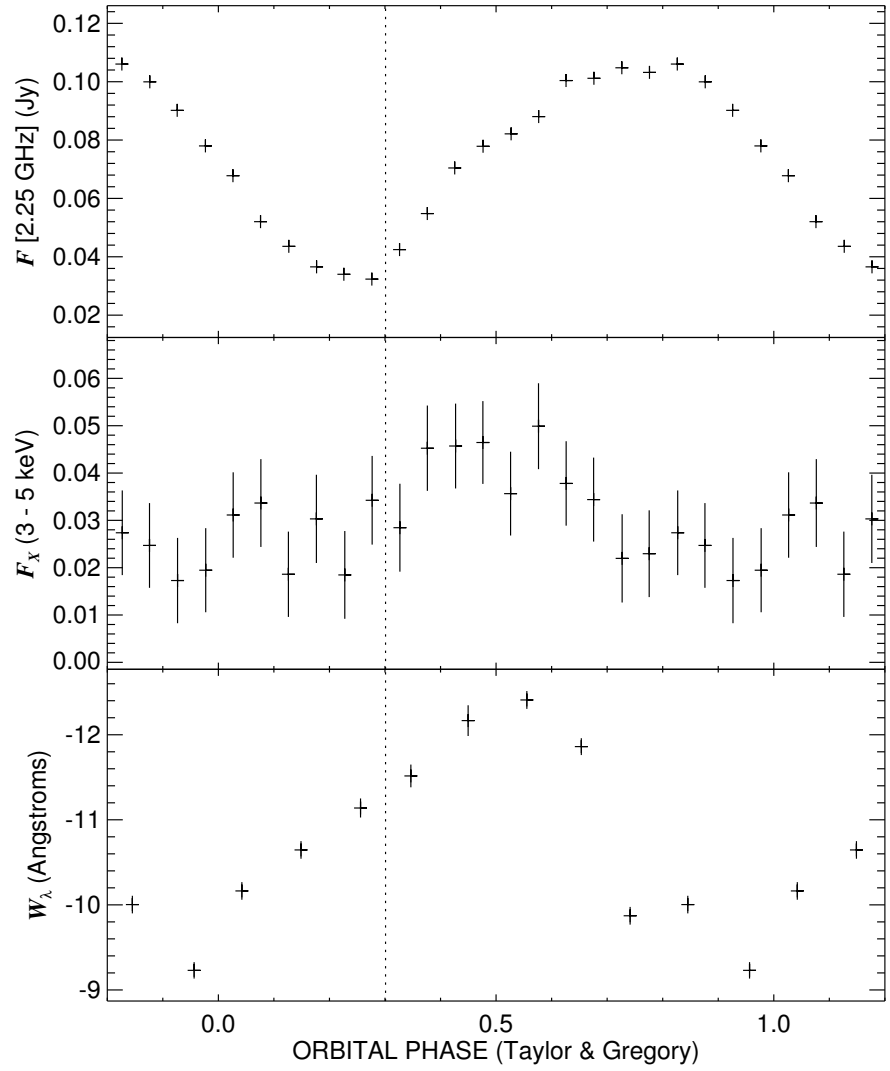

Figure 5.5: The variations in radio flux (*top panel*), X-ray emission (*middle panel*), and Hα emission equivalent width (*lower panel*) binned and plotted as a function of orbital phase. The vertical bars through each point express the standard deviation of the mean in the phase bin. The vertical dotted line indicates periastron phase.

5.4 Discussion

The circumstellar disks of the BeXRBs are comparable in many ways to those of other Be stars, but their outer radii are probably limited by the gravitational influence of

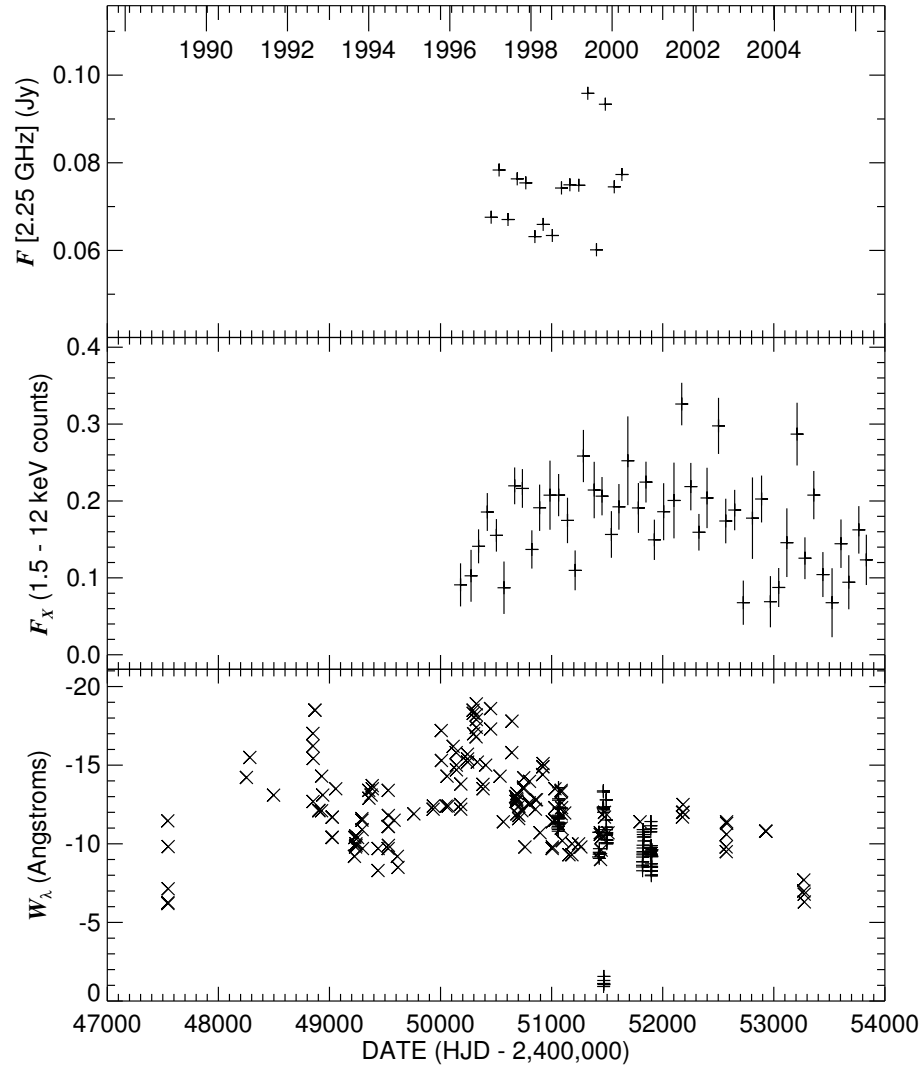

Figure 5.6: The time variations in radio flux (*top panel*), X-ray emission (*middle panel*), and Hα emission equivalent width (*lower panel*) over the period of active observation. The values in the upper two panels represent binned averages over time bins of three orbital periods. The X symbols in the lower plot represent other published equivalent width measurements.

their compact companions (Zamanov et al. 2001). Reig, Fabregat, & Coe (1997) show that the maximum Hα emission equivalent widths (a good measure of the maximum disk size) are correlated with orbital period for the BeXRBs. Okazaki & Negueruela (2001) found that these limiting radii are defined by the closest approach of the com-

panion in the high eccentricity systems and by resonances between the orbital period and the disk gas rotational periods in the low eccentricity systems. LS I +61 303 has an orbital eccentricity that falls between these two cases, where the important resonance radii are comparable in size to the periastron separation.

We can estimate the disk radius for LS I +61 303 from the Hα equivalent width data shown in Figure 5.6. We presented numerical models of the circumstellar disks of Be stars in Chapter 4, and we demonstrated that there are monotonic relationships between the emission line equivalent width and the ratio of the angular half-width at half maximum emission of the projected disk major axis to the radius of the star. The relationship depends upon the temperature of the star, the inclination of the disk normal to the line of sight, and the adopted outer boundary for the disk radius. We assumed a primary star effective temperature of $T_{\rm eff} = 29850$ K appropriate to a B0 V classification (Harmanec 1988), although we note that a lower temperature may be possible (Howarth 1983). Figure 5.7 illustrates the relations for the inclination limits of $i = 10^\circ$ and $i = 60^\circ$ suggested by Casares et al. (2005), and we use the mean of these cases in the radius estimations. Note that Hutchings & Crampton (1981) argue that the inclination may be larger, and if so, then our radius estimates will be somewhat low. We adopted an outer boundary for the disk as the Roche radius of the primary star at apastron. This assumption is not critical to the radius estimate as only weak, optically thin emission originates in the outer parts of the disk model.

The mean Hα equivalent width from the data presented in Figure 5.6 (less the very low points from 1999 October) is $W_\lambda = -11.7 \pm 2.5$ Å (standard deviation), and from the relations shown in Figure 5.7 the corresponding ratio of disk to stellar radius is $R_d/R_s = 4.6 \pm 0.4$. The expected disk truncation radius due to resonances

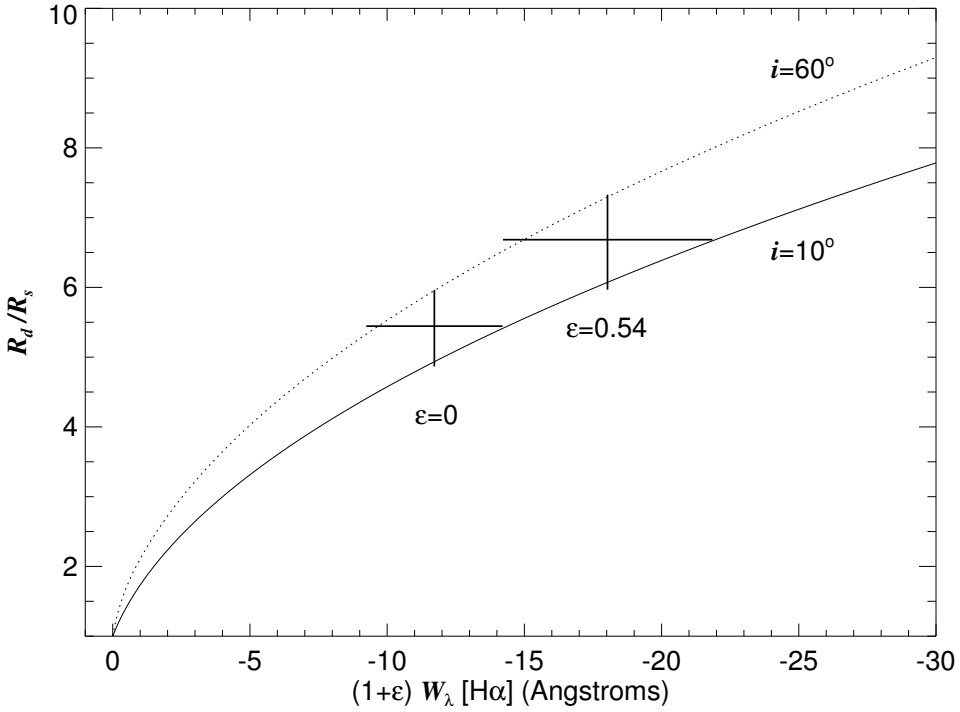

Figure 5.7: The predicted relationship between Hα equivalent width (referenced to the stellar continuum level) and disk radius for two values of disk inclination. The two crosses indicate the observed mean equivalent width with no adjustment for the disk continuum flux ($\epsilon = 0$) and with the optical disk flux contribution suggested by Casares et al. (2005) ($\epsilon = 0.54$).

with the orbital motion is given by

$$\frac{R_n}{R_s} = \left(\frac{GM_s}{4\pi^2}\right)^{1/3} \frac{1}{R_s} \left(\frac{P_{\rm orbit}}{n}\right)^{2/3} \quad (5.1)$$

$$= 37.4 \, \frac{(M_s/M_\odot)^{1/3}}{R_s/R_\odot} \frac{1}{n^{2/3}} \quad (5.2)$$

where n is the integer number of disk gas rotational periods per one orbital period. Okazaki & Negueruela (2001) predict that the $n = 4$ truncation radius will dominate in moderate eccentricity systems, and assuming a stellar mass of $M_s/M_\odot = 12.5 \pm 2.5$ (Casares et al. 2005) and a radius of $R_s/R_\odot = 6.7 \pm 0.9$ from the spectral classification (Harmanec 1988), then the predicted $n = 4$ truncation radius is $R_4/R_s = 5.1 \pm 0.8$.

This agrees within errors with the estimate from the mean equivalent width given above, so that the observations are consistent with the idea that the disk radius is regulated by the $n = 4$ resonance. Note that Casares et al. (2005) suggest that the disk contributes about 35% of the total continuum flux, so that the disk to stellar continuum flux ratio is $\epsilon = 0.54$ in the optical. If so, then we need to rescale the equivalent width by a factor of $1 + \epsilon$ in order to scale the Hα emission flux to the stellar flux alone. This leads to an estimated disk radius of $R_d/R_s = 5.5 \pm 0.5$ (see Fig. 5.7), which is slightly larger than the $n = 4$ truncation radius.

The record of Hα emission measurements indicates that the disk may occasionally grow to an even larger radius. The two equivalent width maxima shown in Figure 5.6 reach $W_\lambda = -18.5 \pm 0.5$ Å, and this value corresponds to a disk radius of $R_d/R_s = 5.6 \pm 0.1$ (for $\epsilon = 0$). The separation of the stars at periastron is given by

$$\frac{R_p}{R_s} = \frac{(1-e)a}{R_s} = 16.8 \, \frac{(M_{\rm total}/M_\odot)^{1/3}}{R_s/R_\odot} \tag{5.3}$$

and this is equal to 6.1 ± 1.2 for $M_{\rm total} = (14.5 \pm 4.0) M_\odot$ (Casares et al. 2005). Thus, it appears that the times of the largest observed Hα emission correspond to epochs when the disk almost reaches the limiting radius set by the close passage of the companion at periastron.

Okazaki et al. (2002) have made numerical hydrodynamical simulations of the Be star's disk response to the gravitational influence of a compact companion in an elliptical orbit. They show that the tidal pulls at periastron lead to the development of a large spiral wave in the disk that can extend far beyond the truncation radius and out to the vicinity of the companion (see their Fig. 11). Furthermore, Hayasaki & Okazaki (2005) show that a similar spiral pattern can be induced in the accretion disk surrounding the companion in the times shortly after periastron and that the presence of the pattern can promote mass accretion. We speculate that processes like

these are probably at work in LS I +61 303. The simulations show that the spiral wave starts at periastron as a density enhancement in the part of the disk facing the companion. The longitude of periastron is $\omega = 57°$, so the portion of the disk facing the companion at periastron will have a negative radial velocity for our line of sight, and the fact that we observe an increase in the strength of the approaching V peak of Hα at periastron (Fig. 5.4) is consistent with the formation of a spiral wave enhancement then. As the spiral feature develops after periastron, disk gas would be carried outwards past the truncation radius, and the mass accretion processes would then begin in earnest. The geometrical extension of the disk after periastron associated with the spiral feature would probably increase the projected area on the sky of high Hα optical depth causing the emission feature to increase in strength as observed (Fig. 5.5).

Our new determination of the time of periastron confirms that the X-ray and radio flux maxima occur some time after periastron (Massi 2004). Figure 5.5 shows that the X-ray flux attains a maximum near orbital phase $\phi(\mathrm{TG}) = 0.5$ while the radio maximum occurs later near $\phi(\mathrm{TG}) = 0.7$. If the mass transfer process were instantaneous, we might expect that both fluxes would peak at periastron where the companion encounters the densest part of the disk. However, Taylor et al. (1992) and Martí & Paredes (1995) argue that if the process can be described by Bondi-Hoyle accretion, then the mass accretion rate will also depend on the relative gas and accretor velocity and a second peak will occur later near apastron where the accretor's orbital velocity is slower. Massi (2004) suggests that the X-ray peak corresponds to the periastron accretion increase (with a phase lag caused by inverse Compton losses of relativistic electrons due to the large stellar flux field) and that the radio peak occurs near the slow motion apastron phase (where Compton losses are reduced because the stellar flux is weaker). If this radio flux peak arises from jets, then it is possible that

ionizing radiation from the jets will lower the neutral H population and Hα emission (leading to an Hα minimum near apastron; see Fig. 5.5). We speculate that the ionizing flux may sometimes become quite strong (perhaps from knots that develop in the jets) and cause sudden decreases in Hα emission strength such as we observed in 1999 October (Fig. 5.3).

Our study indicates that the extent and shape of the Be star's disk has a significant influence on the mass transfer rate in this microquasar system. We show in the next chapter that similar limiting disk radii and spiral wave extensions are also found in the BeXRB systems HDE 245770 and X Per.

5.5 Nature of the Visual Companion

LS I +61 303 has a nearby visual companion that we also recorded in the spectra made in 2000 December. This companion star has a separation of $11\farcs2$ and a position angle of 167° from LS I +61 303 according to coordinates listed in the Guide Star Catalog II[4] (where the companion is designated 0404701738). The companion is approximately 3.5 mag fainter in the optical than LS I +61 303. Our average spectrum shows a very broad Hα absorption line, no He I λ6678, a few weak metallic lines, and an interstellar line at 6613 Å that is identical in appearance to its counterpart in the spectrum of LS I +61 303. We compared the spectrum to several in the atlas by Valdes et al. (2004), and we tentatively classify the star as type A2 V. The radial velocity of the star from the Hα line is -40 ± 2 km s^{-1}.

It is possible that this companion is an outlying member of the Cas OB6 association as is LS I +61 303 (Mirabel, Rodrigues, & Liu 2004). The companion's radial velocity is comparable to that of other association members (Hillwig et al. 2006) including the nearby multiple star HD 16429 (McSwain 2003), and the similarity of the

[4]http://vizier.u-strasbg.fr/cgi-bin/VizieR?-source=I/271

interstellar line strengths suggests a distance comparable to that of LS I +61 303. However, the companion also appears in the 2MASS All-Sky Catalog of Point Sources (Cutri et al. 2003) (with a designation of 2MASS 02403208+6113340), and the near-IR magnitudes suggest that the star is closer than Cas OB6. Suppose the absolute K-band magnitude for a A2 V star is $M_K = 1.2 \pm 0.6$ (Cox 2000) and that the extinction is $A(K) = 0.36E(B-V) = 0.3$ (Howarth 1983; Fitzpatrick 1999). Then for the 2MASS magnitude of $K = 11.55 \pm 0.02$, the estimated distance is 1.0 ± 0.4 kpc, which would place the star in the foreground of the Cas OB6 stars at a distance of 1.9 kpc (Hillwig et al. 2006). Thus, unless the 2MASS magnitudes and/or the spectroscopic estimate of absolute magnitude are wrong, this companion is probably a chance optical alignment rather than a neighbor of LS I +61 303.

– 6 –

The Be X-ray Binaries HDE 245770 = A 0535+26 and X Persei

Abstract

We[1] present results from an Hα monitoring campaign of the Be X-ray binary systems HDE 245770 = A 0535+26 and X Per. We use the Hα equivalent widths together with adopted values of the Be star effective temperature, disk inclination, and disk outer boundary to determine the half-maximum emission radius of the disk as a function of time. The observations of HDE 245770 document the rapid spectral variability that apparently accompanied the regeneration of a new circumstellar disk. This disk grew rapidly during the years 1998 – 2000, and then slowed in growth in subsequent years. The outer disk radius is probably truncated by resonances between the disk gas and neutron star orbital periods. Two recent X-ray outbursts appear to coincide with the largest disk half-maximum emission radius attained over the last decade.

[1]Grundstrom, E. D.; Boyajian, T. S.; Finch, C.; Gies, D. R.; Huang, W.; McSwain, M. V.; O'Brien, D. P.; Riddle, R. L.; Trippe, M. L.; Williams, S. J.; Wingert, D. W.; Zaballa, R. A. - published as Grundstrom et al. (2007b)

Our observations of X Per indicate that its circumstellar disk has recently grown to near record proportions among observed time periods, and concurrently the system has dramatically increased in X-ray flux, presumably the result of enhanced mass accretion from the disk. We find that the Hα half-maximum emission radius of the disk surrounding X Per reached a size about six times larger than the stellar radius, a value, however, that is well below the minimum separation between the Be star and neutron star. We suggest that spiral arms excited by tidal interaction at periastron may help lift disk gas out to radii where accretion by the neutron star companion becomes more effective.

6.1 Introduction

Be X-ray binaries (BeXRBs) consist of rapidly rotating B-stars with neutron star companions (Coe 2000). The B-star primaries lose mass into an outflowing circumstellar disk, and if the disk reaches a radius comparable to the periastron separation, then disk gas accreted by the neutron star can power a significant (and often transient) X-ray source (Okazaki & Negueruela 2001; Okazaki et al. 2002). The disk gas is detected through observations of emission lines, an optical/infrared excess, and a net linear polarization caused by starlight scattered in the disk (Porter & Rivinius 2003). Be star disks are inherently time variable and can develop and disappear on timescales of years to decades (Underhill & Doazan 1982; Hubert & Floquet 1998). Thus, we expect that the X-ray accretion fluxes will vary on similar timescales. Here we present a joint study of the disk Hα emission flux and X-ray flux variations in two of the best studied BeXRBs, HDE 245770 = A 0535+26 and X Persei. We discuss similar co-variations of Hα emission and X-ray flux in Chapters 3 and 5 for the supergiant binary LS I +65 010 and the BeXRB microquasar LS I +61 303, respectively,

and in a companion paper on the black hole binary Cyg X-1 = HDE 226868 (Gies et al. 2003).

The remarkable Be star HDE 245770 (and X-ray counterpart A 0535+26) is one of the prototype objects of the BeXRB class. The primary star of HDE 245770 has a classification of O9.7 IIIe (Giovannelli & Graziati 1992) or B0 IIIe (Steele et al. 1998), but the luminosity class is still somewhat controversial as many of the luminosity criteria are based on spectral lines that are affected by disk emission (Wang & Gies 1998). The orbital period from peaks in the X-ray flux is approximately 110 d (Hutchings 1984; Coe et al. 2006), and a comparison of the times of maxima between the first and most recent epochs suggests a period of $P = 109.96 \pm 0.05$ d. The only reliable estimate of the other orbital elements comes from X-ray timing of the pulsar spin period during three outbursts in 1993 (Finger et al. 1994; Bildsten et al. 1997), and this solution indicates that the orbital eccentricity is $e = 0.47 \pm 0.02$. The radial velocity curve of the Be star has an amplitude that is smaller than or comparable to the velocity fluctuations introduced by emission contamination and other factors, so only upper limits are available for the Be star's semiamplitude and the system mass ratio, $M_2/M_1 < 0.12$ (Wang & Gies 1998). The star has a long and rich history of X-ray, optical, and infrared observations (Motch et al. 1991; Giovannelli & Graziati 1992; Clark et al. 1998; Negueruela et al. 1998; Haigh et al. 2004; Coe et al. 2006). Lyuty & Zaĭtseva (2000) present a remarkable record of the light curve variations back to the year 1898, and they show that after a quiescent stage in the first part of the century the star brightened by some 40% in the early 1970s. The circumstellar disk that appeared then provided the gas to power the X-ray source at the time coincident with the dawn of X-ray astronomy.

The emission from the disk of HDE 245770 in the form of optical and infrared continuum light and Balmer emission lines displays large temporal variations in the

record since the 1970s (Clark et al. 1998; Lyuty & Zaĭtseva 2000; Haigh et al. 2004). The dominant timescales of variability are $\sim$ 1500 d and 103 d, where the latter is the beat period of the long and orbital periods (Haigh et al. 2004). Haigh et al. (2004) argue that the disk IR flux tends to hover around three different brightness levels, and they suggest that these correspond to distinct disk radii that are defined by resonances between the disk gas and neutron star orbital periods. Okazaki & Negueruela (2001) developed a model to predict the resonant disk truncation radii in BeXRBs, and Haigh et al. (2004) found that the model predictions are consistent with the IR magnitude jumps. Coe et al. (2006) extended this analysis with additional JHK photometry and measurements of the Hα emission line. The Hα emission variations (Clark et al. 1998; Haigh et al. 1999; Lyuty & Zaĭtseva 2000; Haigh et al. 2004; Coe et al. 2006) indicate that the disk almost totally disappeared in 1998 but rebounded to its former strength over the next few years.

The binary system X Per (HD24534; B0 Ve, Lyubimkov et al. 1997) is the brightest and perhaps most famous member of the BeXRB class. X Per has displayed time variable optical emission lines since the earliest photographic spectrograms were made at the beginning of the last century (Cowley et al. 1972). The long term changes in the spectral appearance are reviewed by Roche et al. (1993) and Clark et al. (2001). In a seminal paper, Clark et al. (2001) describe the photometric and spectroscopic variations observed over the period 1987 through 2001, and during this time the star made a remarkable transformation from Be to B and back again to Be. Clark et al. (2001) discuss how these variations are related to the structural properties of the circumstellar disk. The orbital elements were determined by Delgado-Martí et al. (2001) by careful timing observations of the X-ray pulsar (pulse period $\approx$ 835 s) using the *Rossi X-Ray Timing Explorer (RXTE)* satellite. The orbital period is $P = 250.3$ d and the orbital eccentricity is $e = 0.11$.

Both HDE 245770 and X Per are among some hundred objects regularly observed with the *RXTE* All-Sky Monitor (ASM) instrument (Levine et al. 1996), and here we address the issue of how their disk size variations are related to the observed X-ray fluxes. We present our recent observations of their Hα emission lines in §6.2. We then show in §6.3 how the Hα emission strength is related to the disk radius, and we use these relations in §6.4 to document how the disk radius variations relate to the V-band and X-ray light curves. The disk radii appear to attain limits that are probably related to resonant truncation radii (Okazaki & Negueruela 2001), and we discuss in §6.5 how such limits affect the mass transfer process in these binaries. Finally §6.6 offers a reassessment of the orbital motion of X Per based upon radial velocity measurements of UV spectra from the *International Ultraviolet Explorer (IUE)* satellite, from which we derive limits on the binary's mass ratio and inclination.

6.2 Observations and Hα Variations

We observed both HDE 245770 and X Per between 1998 August and 2000 December with the Kitt Peak National Observatory 0.9 m coudé feed telescope. We used two spectrograph arrangements to record the red spectral region around Hα with resolving powers of $R = \lambda/\triangle\lambda = 4100$ and 9500. The details about the spectra and their reduction for these runs are given in Chapter 3. In addition to these primary runs, we obtained several more spectra during auxiliary runs in 2004 October and 2006 October (using grating B in second order for a resolving power $R = 9500$ over the range 6470 – 7140 Å and 6433 – 7143 Å, respectively). All the spectra record the Hα emission line and the He I λ6678 feature.

The general trends in the spectra are illustrated in Figures 6.1 – 6.3. We show in Figure 6.1 the set of spectra of HDE 245770 from the 1998 August – September run

that coincided with the time of disk loss. The spectra are arranged with their continua set at the time of observation and scaled so that 1 d along the y-axis corresponds to 10% of the continuum flux. We also show a model spectrum at the bottom of the figure that is derived from the grid of non-local thermodynamic equilibrium and line-blanketed model atmospheres calculated by Lanz & Hubeny (2003). This synthetic spectrum is based on the parameters of effective temperature $T_{\rm eff} = 28000$ K, gravity $\log g = 3.3$, and solar abundances (Giovannelli & Graziati 1992). The spectrum was broadened by a simple convolution with a rotational broadening function using a linear limb darkening coefficient of 0.24 (Wade & Rucinski 1985) and a projected rotational velocity of $V \sin i = 230$ km s^{-1} (Giovannelli & Graziati 1992; Wang & Gies 1998; Haigh et al. 2004). We see that there is evidence of residual emission components in both the Hα and He I λ6678 absorption lines at this time. The profiles also display significant night-to-night or faster variations. For example, there are well defined structures within the core of He I λ6678 that may result from photospheric nonradial pulsations (see the case of the similar star ζ Oph; Kambe et al. 1997), and there are variations in the relative strengths of the violet and red emission peaks in Hα. These suggest that mass loss processes leading to the development of the new disk were already underway at this time. Note that the model indicates that a line blend should be present for the C II λ6578, 6582 doublet, which appears to be absent from the HDE 245770 spectra. These lines weaken at higher temperature, but an increase in temperature would result in a model He I λ6678 profile weaker than observed. The absence of the C II features (and the weakness of the C IV profiles in the UV; Wang & Gies 1998) may point to a carbon deficiency caused by the presence of CNO-processed gas in the atmosphere of HDE 245770.

The disk emission strength of HDE 245770 had increased dramatically by the time of the next runs in 1999. We show in Figure 6.2 the average spectrum from each of

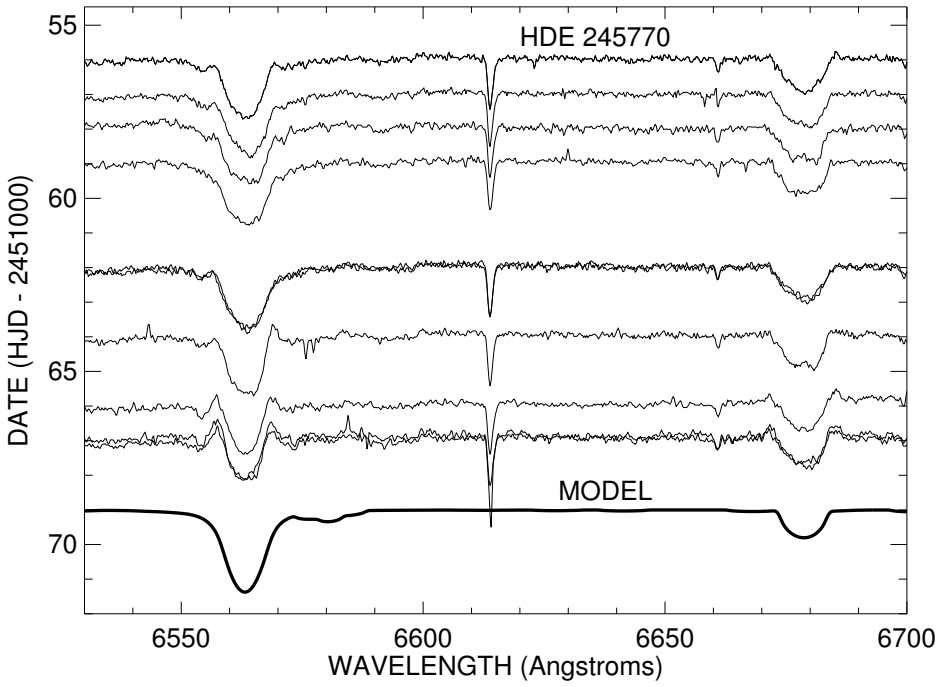

Figure 6.1: A sequence of red spectra of HDE 245770 from 1998 when the the disk had almost disappeared. Each spectrum has its continuum aligned with the heliocentric Julian date of observation, and each is scaled in flux so that 10% of the continuum equals 1 d of time. The bottom synthetic spectrum represents a model with $T_{\rm eff} = 28000$ K, $\log g = 3.3$, and $V \sin i = 230$ km s^{-1}. The features present include the stellar Hα λ6563 and He I λ6678 lines and the interstellar features at 6613 Å and 6660 Å.

the runs with the continuum levels offset for clarity. The growth in the Hα emission is accompanied by the appearance of emission in He I λ6678 that almost totally obscures the profile during the runs in 2000 and 2006. Note how the separation between the violet and red peaks of Hα decreases as the emission strengthens.

We show in Figure 6.3 the average spectrum of X Per from each of the runs, and we see that Hα and He I λ6678 were emission lines during this time. The overall morphology and strength of the lines agree well with the more extended time series presented by Clark et al. (2001). Inspection of Figure 7 in Clark et al. (2001) shows that our observations were made while the disk was active and generally increasing in strength.

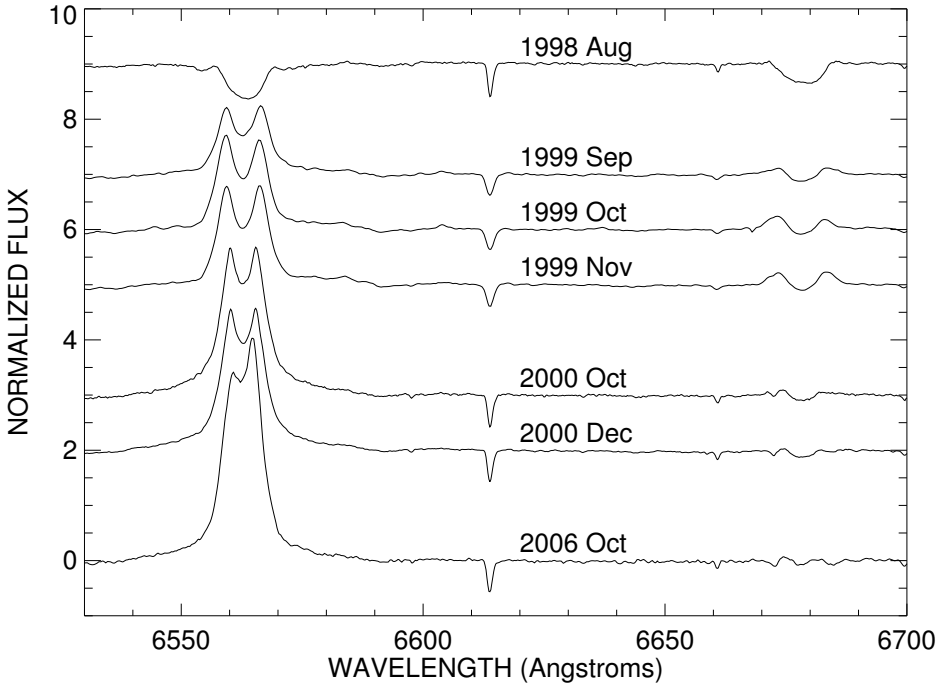

Figure 6.2: The average spectra of HDE 245770 from each of the runs plotted with their continua offset for clarity. Spectral intensity is scaled so that 100% of the continuum equals four units of normalized flux.

We made a number of measurements to characterize the profile variations of Hα for both stars, and these are summarized in Table 6.1. Column 1 lists the target name, column 2 gives the heliocentric Julian date of mid-exposure, and column 3 shows the corresponding orbital phase (from the ephemeris of Finger et al. 1994 for HDE 245770 and from Delgado-Martí et al. 2001 for X Per). Column 4 lists the equivalent width determined by a numerical integration of the line flux over the range 6536 – 6590 Å. We measured the radial velocity of the wings based upon a bisector position determined using the method of Shafter, Szkody, & Thorstensen (1986) as described in Appendix A. We used Gaussian functions with FWHM = 200 (100) km s^{-1} at sample positions in the wings of $\pm$320 ($\pm$190) km s^{-1} for HDE 245770 (X Per), and these radial velocities are given in column 5 of Table 6.1. Zamanov et al.

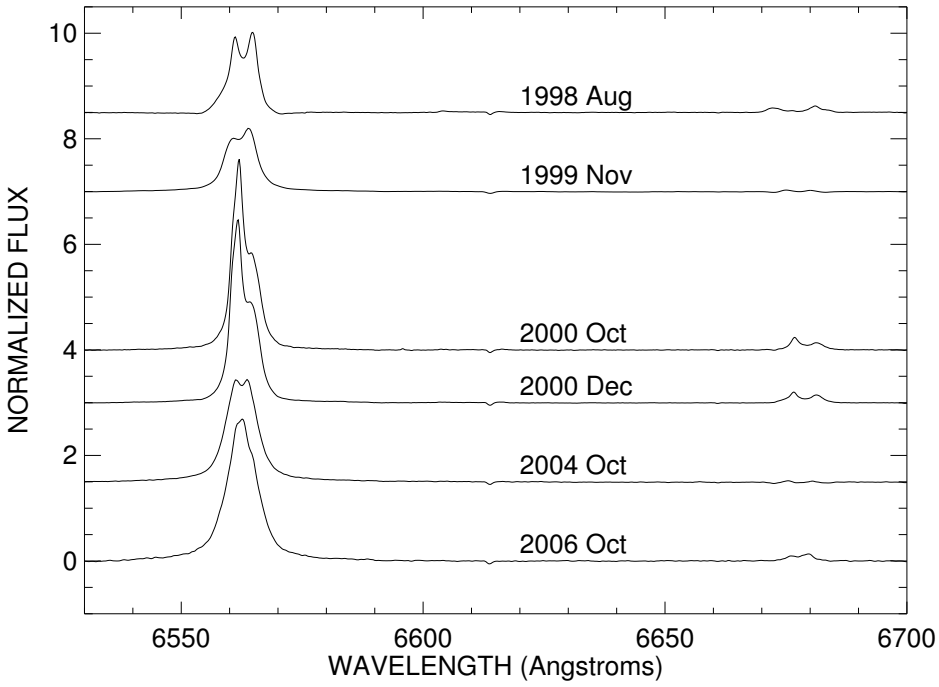

Figure 6.3: The mean spectra of X Per from each run (separated in rectified intensity for clarity). Spectral intensity is scaled so that 100% of the continuum equals one unit of normalized flux.

(1999) advocated making fits of double-peaked Hα profiles using Gaussian functions to match the violet V and red R peaks, and we have followed their approach here, although we caution that such a functional fit is poor in many instances. These double-Gaussian fits were restricted to the inner part of the profile ($|\triangle\lambda| < 6$ Å for HDE 245770 and $< 2 - 4$ Å for X Per) as the wings are much more extended that those of Gaussian functions. The remaining columns in Table 6.1 list the parameters for these fits: radial velocity of the V peak (col. 6), radial velocity of the R peak (col. 7), ratio of the equivalent widths of the V and R components (col. 8), V/R peak intensity ratio (col. 9), FWHM for the V peak (col. 10), and FWHM for the R peak (col. 11). Note that Hα has only one peak in the 2006 observations of X Per, so we fit a single Gaussian to the profiles of these three spectra.

Table 6.1: Hα Measurements

Star Name	Date (HJD−2,400,000)	Orbital Phase	W_λ (Å)	$V_r(W)$ (km s^{-1})	$V_r(V)$ (km s^{-1})	$V_r(R)$ (km s^{-1})	$W_\lambda(V)$ / $W_\lambda(R)$	V/R	FWHM(V) (Å)	FWHM(R) (Å)
HDE 245770	51055.969	0.103	1.76	18.4	···	···	···	···	···	···
HDE 245770	51056.989	0.112	1.96	42.4	···	···	···	···	···	···
HDE 245770	51057.960	0.121	1.41	32.4	···	···	···	···	···	···
HDE 245770	51058.950	0.130	2.16	30.5	···	···	···	···	···	···
HDE 245770	51061.954	0.157	1.96	38.0	···	···	···	···	···	···
HDE 245770	51061.993	0.158	2.07	31.7	···	···	···	···	···	···
HDE 245770	51063.962	0.176	1.62	21.1	···	···	···	···	···	···
HDE 245770	51065.981	0.194	1.05	16.5	···	···	···	···	···	···
HDE 245770	51066.902	0.202	0.52	18.0	···	···	···	···	···	···
HDE 245770	51066.976	0.203	0.88	20.3	···	···	···	···	···	···
HDE 245770	51419.972	0.403	−3.11	22.5	−147.7	165.5	0.80	0.96	4.41	5.34
HDE 245770	51419.995	0.403	−3.20	23.1	−144.9	165.6	0.80	0.95	4.68	5.52
HDE 245770	51425.987	0.458	−4.31	8.6	−158.3	161.6	0.95	0.97	5.12	5.26
HDE 245770	51428.950	0.485	−4.06	12.1	−151.8	165.0	0.96	0.98	4.97	5.10
HDE 245770	51464.958	0.811	−5.32	4.5	−157.6	156.7	0.98	1.06	4.84	5.24
HDE 245770	51464.980	0.811	−5.14	4.7	−155.8	158.8	1.00	1.05	4.89	5.14
HDE 245770	51465.936	0.820	−5.17	3.1	−156.5	154.2	0.99	1.05	4.75	5.04
HDE 245770	51465.957	0.820	−5.04	2.1	−156.6	153.9	0.99	1.03	4.81	5.01
HDE 245770	51466.906	0.829	−4.80	−3.6	−157.5	149.1	1.02	1.04	4.72	4.78
HDE 245770	51466.928	0.829	−4.79	−5.9	−158.5	149.3	1.06	1.03	4.81	4.69
HDE 245770	51467.988	0.839	−4.41	−3.6	−153.5	155.5	1.06	1.05	4.87	4.85
HDE 245770	51468.952	0.847	−4.54	−4.5	−152.6	159.5	1.22	1.06	5.28	4.61
HDE 245770	51468.974	0.847	−4.73	−1.5	−152.9	155.8	1.12	1.06	5.03	4.75
HDE 245770	51469.916	0.856	−4.87	−8.1	−155.9	152.1	1.12	1.06	5.05	4.76
HDE 245770	51491.904	0.055	−5.01	6.0	−148.6	154.3	1.01	0.97	4.96	4.78
HDE 245770	51492.833	0.064	−5.20	10.0	−148.0	153.6	0.93	1.00	4.74	5.09
HDE 245770	51493.827	0.073	−5.25	12.3	−150.5	156.9	0.92	0.98	4.82	5.10
HDE 245770	51494.869	0.082	−5.57	12.8	−147.5	163.4	0.95	1.01	4.76	5.08
HDE 245770	51494.890	0.082	−5.36	10.9	−148.5	156.6	0.96	1.01	4.74	4.98
HDE 245770	51495.944	0.092	−5.28	6.7	−148.6	157.8	1.01	0.99	4.92	4.84
HDE 245770	51496.919	0.101	−5.20	12.6	−147.7	161.0	0.94	1.00	4.69	4.98
HDE 245770	51497.852	0.109	−4.66	17.8	−144.8	161.8	0.92	0.96	4.76	4.98
HDE 245770	51817.905	0.011	−8.03	12.4	−126.1	133.5	0.92	0.96	4.77	5.00
HDE 245770	51818.908	0.020	−8.36	6.2	−120.7	136.8	1.04	0.98	5.11	4.78
HDE 245770	51819.899	0.029	−8.00	8.7	−120.8	136.4	1.04	1.00	4.96	4.77
HDE 245770	51821.884	0.047	−7.66	6.6	−121.6	132.3	0.99	0.98	4.83	4.77
HDE 245770	51822.888	0.056	−7.83	4.7	−123.3	133.3	0.99	0.98	4.89	4.84
HDE 245770	51823.830	0.065	−7.86	11.9	−119.7	134.9	0.98	1.00	4.84	4.90
HDE 245770	51823.934	0.066	−8.22	5.4	−122.1	134.8	1.01	1.01	4.93	4.92
HDE 245770	51824.855	0.074	−8.19	13.4	−121.5	134.8	0.94	0.96	4.90	5.01
HDE 245770	51824.962	0.075	−7.86	8.7	−121.9	131.6	0.94	0.99	4.76	5.02
HDE 245770	51830.913	0.129	−8.81	13.2	−115.1	140.6	1.09	1.03	5.15	4.88
HDE 245770	51890.840	0.672	−7.21	6.6	−119.4	130.1	1.03	1.01	4.84	4.76
HDE 245770	51890.861	0.672	−7.03	7.3	−120.6	129.6	1.00	0.99	4.79	4.72
HDE 245770	51892.806	0.690	−6.97	6.1	−119.8	127.1	0.98	0.99	4.79	4.83
HDE 245770	51892.827	0.690	−6.99	5.4	−117.8	130.3	1.01	0.99	4.88	4.76
HDE 245770	51893.812	0.699	−7.60	6.5	−117.2	131.6	1.04	0.99	4.96	4.71
HDE 245770	51893.833	0.699	−7.55	7.2	−114.8	134.4	1.10	0.99	5.03	4.56

Continued on Next Page...

Table 6.1 – Continued

Star Name	Date (HJD−2,400,000)	Orbital Phase	W_λ (Å)	$V_r(W)$ (km s^{-1})	$V_r(V)$ (km s^{-1})	$V_r(R)$ (km s^{-1})	$W_\lambda(V)$ / $W_\lambda(R)$	V/R	FWHM(V) (Å)	FWHM(R) (Å)
HDE 245770	51894.799	0.708	−7.61	5.7	−117.9	132.9	1.08	0.99	5.08	4.67
HDE 245770	51894.823	0.708	−7.65	5.4	−118.5	132.5	1.05	0.99	4.98	4.70
HDE 245770	51895.834	0.717	−7.63	7.5	−118.2	131.4	1.04	1.00	5.00	4.80
HDE 245770	51895.913	0.718	−7.53	7.4	−117.5	131.8	1.04	1.00	4.95	4.77
HDE 245770	51896.834	0.727	−7.37	7.5	−118.7	130.3	1.00	0.99	4.84	4.79
HDE 245770	51896.855	0.727	−7.46	5.7	−117.9	132.1	1.05	1.00	5.00	4.75
HDE 245770	51897.832	0.736	−7.47	9.2	−119.2	128.6	0.98	1.00	4.81	4.94
HDE 245770	51897.853	0.736	−7.57	8.9	−118.9	129.9	1.00	1.00	4.85	4.86
HDE 245770	51898.841	0.745	−7.77	8.0	−118.8	132.2	1.03	1.00	4.89	4.77
HDE 245770	51898.862	0.745	−7.78	8.2	−119.5	132.0	1.01	1.01	4.88	4.85
HDE 245770	51899.838	0.754	−7.90	8.3	−118.8	132.8	1.02	0.99	4.96	4.81
HDE 245770	51899.859	0.754	−7.86	8.5	−118.8	134.2	1.03	0.99	5.00	4.80
HDE 245770	51900.831	0.763	−7.95	6.1	−117.8	136.2	1.11	1.00	5.18	4.69
HDE 245770	51900.852	0.763	−8.00	6.3	−120.2	135.0	1.07	1.00	5.14	4.83
HDE 245770	51901.817	0.772	−7.87	8.3	−115.8	136.5	1.11	1.00	5.18	4.65
HDE 245770	51901.838	0.772	−7.79	9.4	−117.2	135.0	1.06	0.99	5.09	4.77
HDE 245770	54019.981	0.975	−10.08	0.5	−119.4	103.1	0.82	0.82	4.92	4.94
HDE 245770	54020.953	0.984	−10.21	2.8	−116.3	105.8	0.80	0.84	4.77	4.99
HDE 245770	54021.957	0.993	−10.16	3.1	−113.7	105.9	0.84	0.83	4.88	4.81
X Per	51055.896	0.811	−9.38	4.5	−73.1	93.0	0.79	0.92	2.71	3.16
X Per	51056.966	0.815	−9.09	4.6	−72.3	94.5	0.77	0.91	2.71	3.22
X Per	51057.948	0.819	−9.64	4.4	−71.2	93.5	0.82	0.92	2.74	3.09
X Per	51058.938	0.823	−9.50	4.0	−70.4	95.1	0.85	0.92	2.81	3.06
X Per	51061.986	0.835	−9.51	0.6	−67.6	92.5	0.99	0.93	2.92	2.74
X Per	51062.915	0.839	−9.49	0.8	−69.1	91.1	0.93	0.93	2.84	2.85
X Per	51063.954	0.843	−9.09	1.2	−68.9	92.5	0.90	0.90	2.85	2.85
X Per	51065.936	0.851	−9.25	0.7	−67.2	92.0	1.00	0.90	2.96	2.66
X Per	51066.937	0.855	−8.99	−1.1	−68.1	90.4	0.96	0.90	2.86	2.70
X Per	51491.878	0.553	−10.05	−15.1	−116.4	62.0	0.71	0.77	3.65	3.97
X Per	51492.818	0.557	−10.15	−11.8	−113.5	64.2	0.70	0.77	3.58	3.94
X Per	51493.813	0.561	−10.24	−10.6	−110.2	67.6	0.76	0.80	3.72	3.91
X Per	51494.845	0.565	−10.31	−12.5	−111.4	65.9	0.77	0.80	3.74	3.91
X Per	51494.853	0.565	−10.27	−12.4	−112.3	65.5	0.75	0.80	3.68	3.92
X Per	51495.873	0.569	−10.30	−11.7	−109.0	67.8	0.78	0.82	3.67	3.85
X Per	51496.859	0.573	−10.21	−13.5	−113.6	63.0	0.71	0.80	3.55	4.03
X Per	51497.830	0.577	−10.22	−12.9	−115.1	61.7	0.68	0.79	3.52	4.09
X Per	51817.899	0.855	−18.63	17.5	−42.7	118.6	2.29	2.05	3.17	2.83
X Per	51818.900	0.859	−18.69	16.0	−43.1	118.0	2.30	2.10	3.14	2.87
X Per	51819.887	0.863	−18.54	15.7	−43.0	115.8	2.34	2.09	3.13	2.79
X Per	51820.918	0.867	−18.59	15.7	−43.5	116.3	2.31	2.13	3.13	2.88
X Per	51821.873	0.871	−18.42	14.5	−43.5	116.4	2.41	2.15	3.12	2.79
X Per	51822.875	0.875	−18.49	14.7	−42.5	115.8	2.40	2.12	3.13	2.76
X Per	51823.823	0.879	−18.26	14.5	−42.3	116.1	2.47	2.15	3.15	2.74
X Per	51824.852	0.883	−18.53	15.8	−41.6	115.6	2.37	2.09	3.15	2.77
X Per	51824.959	0.884	−18.39	16.7	−40.9	116.3	2.37	2.08	3.15	2.76
X Per	51830.954	0.908	−19.59	11.9	−49.3	105.4	1.95	1.89	3.04	2.96
X Per	51888.787	0.139	−18.93	7.8	−59.0	104.3	1.75	1.85	3.09	3.26
X Per	51888.792	0.139	−18.95	8.9	−58.5	104.9	1.71	1.84	3.07	3.31
X Per	51889.738	0.142	−18.54	8.3	−59.1	99.9	1.66	1.86	3.01	3.38
X Per	51889.872	0.143	−19.32	7.5	−58.4	101.1	1.74	1.89	3.04	3.30

Continued on Next Page...

Table 6.1 – Continued

Star Name	Date (HJD−2,400,000)	Orbital Phase	W_λ (Å)	$V_r(W)$ (km s^{-1})	$V_r(V)$ (km s^{-1})	$V_r(R)$ (km s^{-1})	$W_\lambda(V)$ / $W_\lambda(R)$	V/R	FWHM(V) (Å)	FWHM(R) (Å)
X Per	51890.733	0.146	−19.21	7.7	−58.4	101.0	1.73	1.91	3.02	3.34
X Per	51892.756	0.154	−18.91	5.4	−59.6	100.0	1.83	1.91	2.99	3.12
X Per	51893.769	0.158	−19.00	7.6	−59.2	102.6	1.74	1.91	2.98	3.26
X Per	51894.767	0.162	−18.76	9.1	−57.7	102.8	1.76	1.80	2.99	3.07
X Per	51895.824	0.167	−18.64	9.0	−55.2	103.7	1.84	1.81	3.06	3.01
X Per	51896.797	0.171	−19.03	8.7	−55.0	103.7	1.92	1.83	3.08	2.94
X Per	51897.797	0.175	−18.85	8.2	−55.5	104.3	1.91	1.85	3.07	2.98
X Per	51898.806	0.179	−18.97	8.4	−55.0	105.2	1.93	1.85	3.10	2.97
X Per	51899.804	0.183	−18.93	8.7	−55.3	104.1	1.91	1.84	3.07	2.96
X Per	51900.797	0.187	−18.83	8.9	−54.0	105.5	1.95	1.89	3.09	2.99
X Per	51901.783	0.191	−19.26	9.0	−52.4	107.2	2.06	1.97	3.07	2.93
X Per	53290.922	0.740	−17.71	−9.7	−80.7	53.6	0.66	0.87	2.65	3.46
X Per	53290.926	0.740	−17.61	−9.4	−80.7	56.8	0.81	0.92	2.89	3.28
X Per	53292.922	0.748	−18.12	−9.3	−78.3	56.2	0.78	0.93	2.74	3.26
X Per	53292.928	0.748	−17.93	−9.1	−82.4	51.7	0.59	0.83	2.57	3.64
X Per	54019.950	0.653	−23.81	−6.4	−8.9	···	···	···	7.92	···
X Per	54020.939	0.657	−23.61	−4.4	−6.9	···	···	···	7.78	···
X Per	54021.930	0.661	−24.38	−4.5	−7.2	···	···	···	7.78	···

We find no compelling evidence that these fitting parameters vary with orbital phase, although we caution that our orbital phase coverage is incomplete. In particular, the radial velocity measurements for the Hα wings and emission peaks do not appear follow the orbital motion expected for the Be star (see Wang & Gies 1998 for HDE 245770 and Section 6.6 for X Per). We suspect that these velocity measurements are dominated by fluctuations related to the azimuthal distribution and non-Keplerian motion of the disk gas, and these variations confound attempts to measure the much smaller orbital motion in our data sets. The best strategy for measuring the orbital radial velocities of these Be stars may be to wait until an episode of disk loss occurs and then embark on a program of high dispersion, high S/N spectroscopy of emission-free lines in the blue part of the spectrum.

6.3 Disk Radius and Hα Strength

The Hα emission forms primarily in the disk surrounding the Be star, and the total flux of the feature (measured as the line equivalent width) is closely related to the size of the disk. In Chapter 4, we presented calculations of the disk size and emission strength for an extensive range of stellar and disk properties. The Be disk models are based upon a simple parameterization of disk properties outlined by Hummel & Vrancken (2000), from which we derive a synthetic Hα line profile and the angular distribution on the sky of the wavelength integrated Hα flux. The model predictions for the emission strength and angular size of the disks agree with observational results for bright Be stars whose disks have been resolved through optical long baseline interferometry.

The disk model assumes an axisymmetric gas structure with the gas density distribution set by a power law R^{-n} (where R is the distance from the rotational axis), an

exponential decline above and below the disk, and a base density at the star's surface. The disk surface brightness is set by its temperature, and we assume an isothermal disk with a gas temperature of $0.6T_{\rm eff}$ where $T_{\rm eff}$ is the effective temperature of the Be star. The spatial flux distribution is integrated along segments normal to the major axis of the projected disk to obtain a collapsed emission sum as a function of position along the major axis. We adopted a working definition of disk radius as the distance along the major axis from the star where the integrated Hα emission intensity of the disk declines to half of the peak value found at a position immediately adjacent to the photosphere (the half-width at half-maximum intensity radius, or HWHM radius for short).

The functional relationship between Hα equivalent width and disk HWHM radius for a specific Be star depends upon the star's $T_{\rm eff}$, the inclination of the disk normal to the line of sight, and the adopted outer boundary for the disk radius (Ch. 4). We list in Table 6.2 the values of these parameters that we adopt for HDE 245770 and X Per. The listed radii and masses are estimates from Okazaki & Negueruela (2001) and Lyubimkov et al. (1997) and the stellar effective temperatures are from Giovannelli & Graziati (1992) and Lyubimkov et al. (1997) for HDE 245770 and X Per, respectively. We assume that the disk is co-planar with the orbit, and we adopt the mid-range estimates of inclination from Wang & Gies (1998) and §6.6 for HDE 245770 and X Per, respectively. We set the outer boundary for the model disk equal to the Be star's Roche radius at apastron. The results are generally insensitive to this last assumption, as the Hα flux is small from the outer, optically thin portions of the disk. The predicted relationships between equivalent width W_λ[Hα] and the ratio of the disk HWHM radius to the stellar radius R_d/R_s are shown in Figure 6.4 for a large range in disk base density. The model equivalent width is referenced to the photospheric flux, and if the disk contributes a continuum flux fraction of $\epsilon = F^d_\lambda/F^s_\lambda$

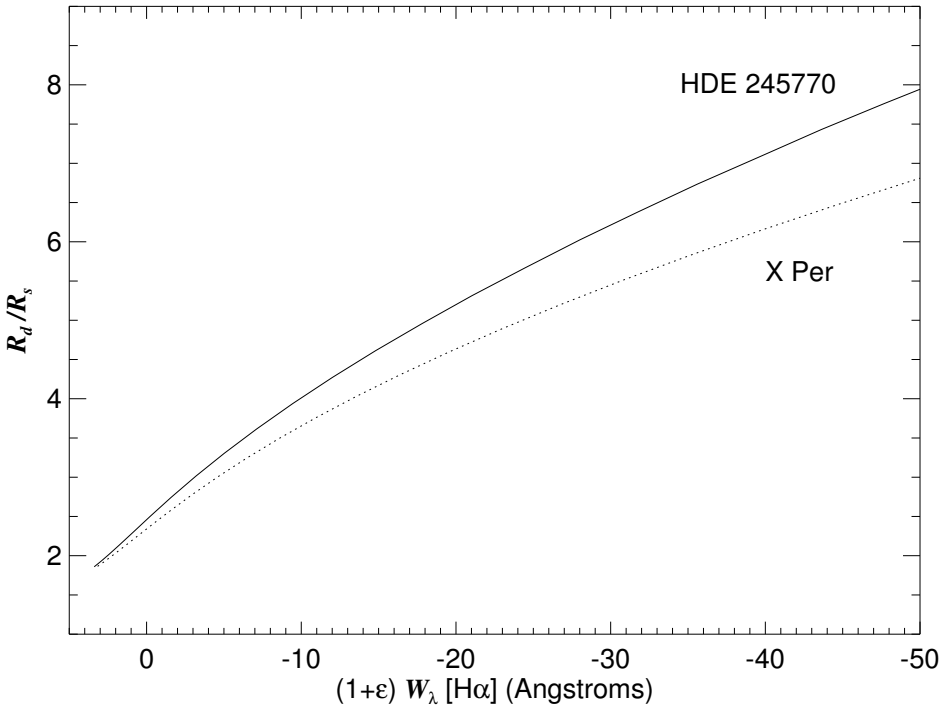

Figure 6.4: The model relation between rescaled Hα emission equivalent width and the ratio of disk radius (defined as the half maximum intensity radius of the integrated Hα flux) to the stellar radius.

then the observed equivalent width must be prorated by a factor of $(1 + \epsilon)$ in order to find the ratio of the disk to star radius R_d/R_s from Figure 6.4.

Table 6.2: Adopted Stellar and Disk Parameters

Parameter	HDE 245770	X Per
R_s ($R_\odot$) ..	15.	6.5
M_s ($M_\odot$) .	20.	15.5
T_s (K)	28000	29500
i (deg)	28.5	31.5
$R_{\rm outer}$ (R_s)	15.9	42.9
P_{orb} (d) ...	109.96	250.3
e	0.47	0.11

There are several features of these simple models that need to be considered in the derivation of a disk HWHM radius from the Hα equivalent width. First, if

the disk temperature differs from our assumed value of $0.6T_{\rm eff}$, then the predicted Hα equivalent width will change by a factor of approximately $T_{\rm disk}/(0.6T_{\rm eff})$ for a given disk radius. This is due to the fact the disk gas source function varies almost linearly with temperature for Hα in hot Be stars like these two targets. Second, the equatorial gas density is assumed to follow a power law R^{-n} with $n = 3.0$, the value often derived in studies of the IR flux excess of Be stars. The numerical relationship between W_λ[Hα] and R_d/R_s is relatively insensitive to the selected value of n (Ch. 4), although the base density for any position along the curve depends critically on n. We caution, however, that the actual disk density properties may vary significantly from a power law in these BeXRBs. For example, if the star experiences an episode of increased disk mass loss, a density enhancement may appear to propagate outwards over time and produce increased emission strength when the enhancement reaches the radius of the optically thick/thin boundary. Using the disk radius derived from the relation in Figure 6.4, we would correctly determine that the HWHM radius had increased but we would err if we assumed that the emission strengthening results from an increase in density at all radii.

Finally, it is possible the disk may be truncated by tidal or resonant effects at a radius smaller than our assumed outer boundary. If the disk density drops to zero in the outer optically thin zone, then only a small part of the total emission is lost and we would only slightly overestimate the emission flux for a given HWHM radius. Thus, the revised curves would appear slightly above those shown in Figure 6.4 (see an example of the variation with outer boundary in Fig. 4.1) and our derived HWHM radii will be slightly smaller than the actual values. On the other hand, if the disk density vanishes at a radius where the gas is optically thick, then the revised curves will reach an asymptotic limit slightly below the cut-off radius. The resulting functions would fall below the standard curves at the high emission end in Figure 6.4,

and we would then tend to overestimate the HWHM radii using the standard relations. The former case probably applies to the two targets we analyze here, as the HWHM radii we find are generally small compared to the suspected truncation radii (we discuss this further in §6.4). Thus, the HWHM radii measurements we derive may slightly underestimate the actual values. Our analysis is insufficient to detect the presence of a truncation radius, but if one exists, its radius will be larger than the HWHM radius.

6.4 Disk Growth and X-ray Accretion Flux

The mass transfer rate and subsequent accretion-driven X-ray flux will clearly depend on the changes in the radius of the Be star's disk that we can track through the variations in the Hα equivalent widths. Here we consider the long term variations in the Be star's disk as observed in the Hα emission flux and in the disk continuum flux (as seen in the observed V-band light curve). We then compare the derived disk radius variations with those observed in the X-ray light curves from the *RTXE*/ASM instrument (Levine et al. 1996).

6.4.1 HDE 245770

Lyuty & Zaĭtseva (2000) note that the V-band continuum of HDE 245770 may be much brighter than the stellar continuum alone (due to continuum light from the disk), and consequently the observed equivalent width referred to the combined continuum flux may underestimate the absolute Hα emission flux. In order to compare the Hα emission flux to a constant stellar continuum, we need to rescale the equivalent width by the factor $1+\epsilon$ where ϵ gives the ratio of the monochromatic disk-to-stellar continuum flux at wavelengths near Hα. Following Lyuty & Zaĭtseva (2000), we can estimate the rescaled flux by comparing the V magnitude at the time of the Hα

measurement with the magnitude of the star alone, $V = 9.50$, by

$$(1 + \epsilon)\ W_\lambda = 10^{-0.4(V-9.50)}\ W_\lambda. \tag{6.1}$$

Lyuty & Zaĭtseva (2000) present V magnitudes for dates contemporaneous with the Hα measurements through 1998, and we have used these to make the small corrections from equation (6.1). However, there are no published estimates of V for the succeeding years, so instead we relied on surrogate measurements of the J magnitude from Coe et al. (2006) in order to make these corrections. Haigh et al. (2004) (see their Fig. 1) show how the infrared magnitude variations track those observed in the V-band for HDE 245770, and we used a series of photometric V (Lyuty & Zaĭtseva 2000) and J observations (Coe et al. 2006) over a common time span to find a relation between these for HDE 245770,

$$(V - 9.50) = 0.32(J - 8.67), \tag{6.2}$$

which has an empirical scatter of ± 0.03 mag. We used the observed J magnitudes from Coe et al. (2006) with equation (6.2) to find V and transform the equivalent widths from 1999 onwards to an absolute scale. We then used Figure 6.4 to find estimates of the disk HWHM emission radius for the times of the Hα observations.

The observed light curve and derived disk HWHM radii are plotted in the middle and lower panels of Figure 6.5. The disk HWHM radii are derived from our W_λ data together with like measurements from Giovannelli et al. (1999), Lyuty & Zaĭtseva (2000), Piccioni et al. (2000a), Haigh et al. (2004), and Coe et al. (2006). We see that the disk almost disappeared in 1998 and then started to grow rapidly in radius over the next two years. The expansion rate slowed considerably by 2001 at a radius of $R_d/R_S \approx 4$. However, subsequent observations show that the disk continued to grow slowly and reached a maximum radius of $R_d/R_S \approx 5$ by 2005.

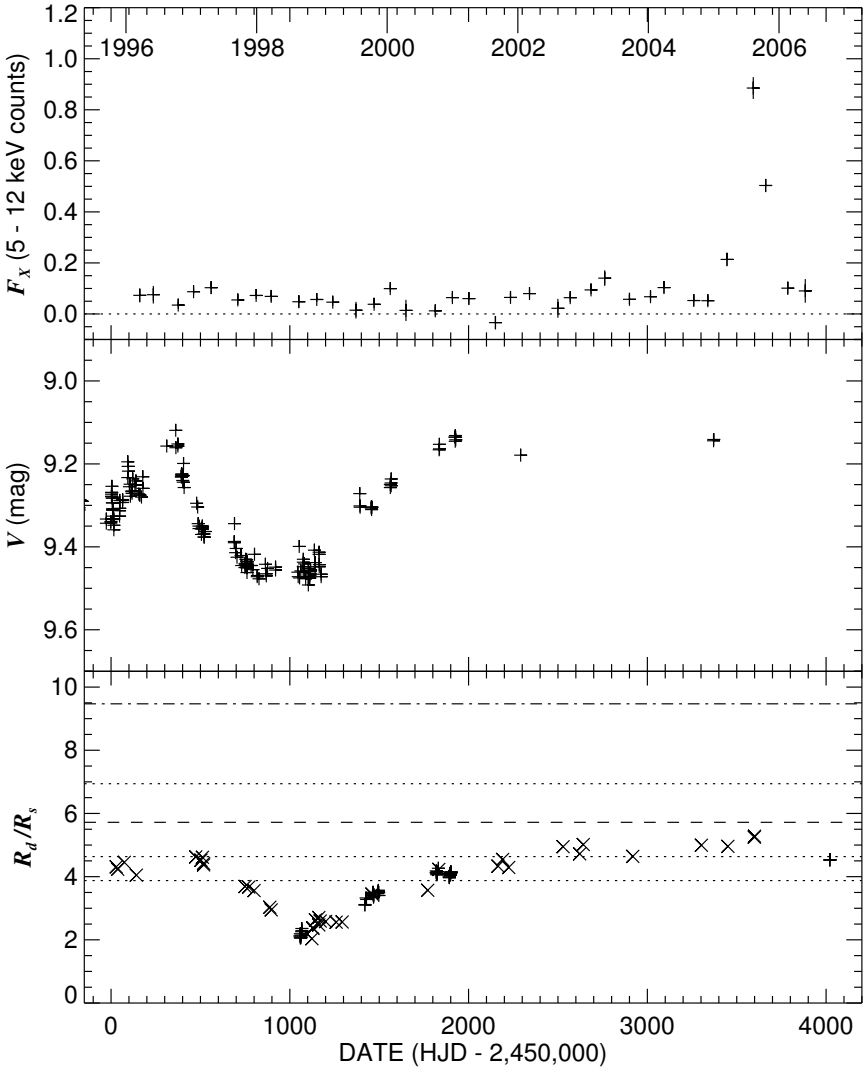

Figure 6.5: The time evolution of the X-ray flux (*top*), V (or J proxy) magnitude (*middle*), and disk radius (*bottom*) of HDE 245770. The two high points in the X-ray flux are two seperate outbursts (Coe et al. 2006). The disk radii are derived from the Hα equivalent widths and estimated V magnitudes (*plus signs* for data from Table 6.1 and *crosses* for values from other work). The dotted lines indicate three disk radii associated with the historic mean levels of emission identified by Lyuty & Zaĭtseva (2000). The dashed line indicates the disk truncation radius for $n = 5$, and the dot-dashed line at the top marks a radius equal to the periastron separation.

Coe et al. (2006) also present a time evolution diagram of disk radius (see their Fig. 7) that they derive from the velocity separation $\triangle V$ of the violet and red peaks

of the Hα profile (Huang 1972). Their method leads to somewhat smaller radii than our HWHM radii ($\approx 83\%$ as large using $\triangle V$ measurements derived from Table 6.1) because the radius derived from $\triangle V$ is based upon a velocity sampling weighted by the brighter parts of the disk while the HWHM radius corresponds to an outer boundary between the bright and faint parts of the disk. The two depictions of disk evolution are in general agreement except for estimates from 2005 August where Coe et al. determine a disk radius about twice as large as indicated in our Figure 6.5. We think this discrepancy is due to the fact Coe et al. relied on an extrapolation of a linear relationship between W_λ[Hα] and $\triangle V$ to estimate radius for the 2005 August data (for which no direct $\triangle V$ measurements were available). If one adopts a standard power law relation between these variables (Zamanov et al. 2001) rather than a linear fit (which tends to underestimate $\triangle V$ for strong emission), then the extrapolation leads to radii similar to those shown in Figure 6.5 for 2005 August.

We also show in the lower panel of Figure 6.5 dotted lines that indicate disk HWHM radii derived from mean levels of Hα strength in the past that were highlighted in the review by Lyuty & Zaĭtseva (2000) (and indicated in their Fig. 3). The lower two levels correspond to the two groupings of Hα strength observed between 1987 and 1998 while the upper level shows the much larger disk HWHM radius associated with data from 1975 through 1981 when the Hα emission was exceptionally strong ($W_\lambda \approx -26$ Å, de Loore et al. 1984; $V \approx 8.9$, Lyuty & Zaĭtseva 2000). Note that the deceleration in disk growth observed in 2001 occurred at the time when the disk HWHM radius had reached the lower cluster level.

Haigh et al. (2004) and Coe et al. (2006) argue that the tendency for the disk emission fluxes to cluster at specified levels is related to the presence of resonances between the disk gas and neutron star orbital periods that tend to truncate the disk at specific disk radii (Okazaki & Negueruela 2001). These truncation radii are given

by

$$\frac{R_n}{R_s} = \left(\frac{GM_s}{4\pi^2}\right)^{1/3} \frac{1}{R_s} \left(\frac{P_{\rm orbit}}{n}\right)^{2/3} = \frac{r(M_s/M_\odot)^{1/3}}{n^{2/3}R_s/R_\odot} \tag{6.3}$$

where n is the integer number of gas rotation periods per neutron star orbit and r is a constant equal to 97 if the resonance occurs with the orbital period or 92 if the resonance is with the shorter beat period (103 d; Larionov, Lyuty, & Zaitseva 2001) presumably caused by retrograde precession of the disk (Haigh et al. 2004). Okazaki & Negueruela (2001) predict that the important truncation radii for HDE 245770 will be those associated with the $n = 4$ and 5 resonances, and using their adopted parameters (Table 6.2) the resonance radii will occur at $R_d/R_s = 6.6$ and 5.7 for $n = 4$ and 5, respectively (for $r = 92$). The $n = 5$ truncation radius is indicated as a dashed line in the lower panel of Figure 6.5, and we see that the disk HWHM radius hovered slightly below this limit between 2001 and 2006. This suggests that the rapid disk growth phase ended when the outer parts of the disk reached the $n = 4$ or 5 resonance truncation radius.

The top panel of Figure 6.5 shows the mean X-ray fluxes[2] binned in time slots equal to one orbital period, and error bars indicate the standard deviation of the mean within the time bin. The slow expansion of the disk apparently led to the large X-ray outburst observed near JD 2,453,526 (Coe et al. 2006) and a second smaller outburst near JD 2,453,616. These outbursts occurred when the disk had reached its largest HWHM radius over the duration of the *RXTE*/ASM mission. The binary semimajor axis is approximately $17.9R_s$ (Table 6.2) and the periastron separation is $9.5R_s$ (shown as the *dot-dashed line* in lower panel of Fig. 6.5). The mean Roche radius of the Be star will be approximately $5.7R_s$ at periastron, about the size of disk HWHM radius at the time of the outbursts. This suggests that the disk had

[2]http://xte.mit.edu

grown to a size sufficient to permit active mass transfer at periastron around the epoch when the outbursts were observed. Furthermore, the huge emission strengths observed during 1976 – 1981 indicate that the disk may have attained a HWHM radius of $R_d/R_s = 9$ then (*top dotted line* in the lower panel of Fig. 6.5), exceeding the Roche limit at periastron.

We suspect that the mass transfer process is probably aided by the strong tidal forces that exist near periastron. Okazaki et al. (2002) present hydrodynamical simulations for BeXRBs that show how the periastron tides excite a two-arm spiral structure in the Be star disk, and the arm closest to the neutron star can lift material far beyond the nominal disk boundary to provide a source of gas accretion at phases beyond periastron. We show in Figure 6.6 the X-ray light curves binned in orbital phase according to the ephemeris of Finger et al. (1994) for the three energy bands observed by *RXTE*/ASM. The time sample is restricted to quiescent (non-outburst) dates. We see that the high energy flux attains a maximum near orbital phase 0.3, i.e., well past periastron at phase 0.0. A similar phase delay in the emission strength of Hβ was detected by Motch et al. (1991). These observations suggest that the disk does become more extended for a period following periastron, leading to a delayed peak in mass transfer and X-ray emission.

6.4.2 X Persei

The Hα emission equivalent widths of X Per observed in 2000 and 2004 and especially in 2006 are the largest measured over the last few decades (Roche et al. 1993; Piccioni et al. 2000b; Clark et al. 2001), and they indicate that the disk has grown significantly in size. Once again we need to rescale the equivalent widths to a constant stellar continuum flux level by considering the $(1 + \epsilon)$ factor. We estimated this flux excess

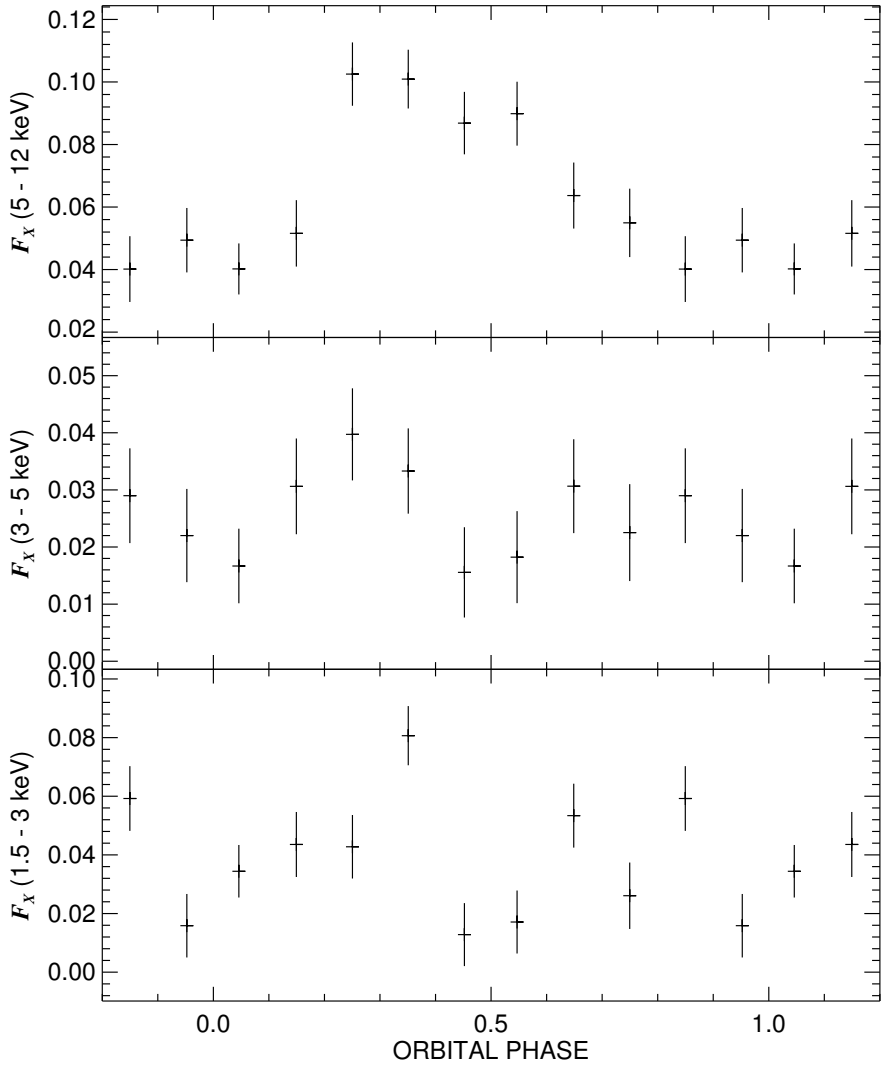

Figure 6.6: X-ray light curves of HDE 245770 from *RXTE*/ASM observations during quiescent dates formed by binning with the orbital ephemeris from Finger et al. (1994). The high energy band (*top panel*) appears to attain a maximum at a phase 0.3 past periastron.

using the V-band light curve and the relation

$$(1 + \epsilon)\ W_\lambda = 10^{-0.4(V-6.78)}\ W_\lambda \tag{6.4}$$

where the base level magnitude of the star alone, $V = 6.78$, is that observed during the last disk-free phase (Lyubimkov et al. 1997). The V-band light curve comes from

observations by the members of the American Association of Variable Star Observers (AAVSO) that we transformed to standard Johnson V magnitude using contemporaneous photometry from Zamanov & Zamanova (1995), Engin & Yuce (1997), and photoelectric measurements from the AAVSO (Percy & Bakos 2001). The transformed AAVSO measurements were binned into 25 d means to increase the S/N ratio.

Our results are plotted as function of time in Figure 6.7. The lower panel shows the time evolution of the disk HWHM radius derived from our Hα equivalent width measurements and other published values (Clark et al. 2001; Liu & Hang 2001; Zamanov et al. 2001). The middle panel shows the time binned V-band light curve from the AAVSO observations. We see that X Per reached a maximum of $V \approx 6.2$ in 2000 and then rose again to $V \approx 6.1$ where it has remained to the present. The circumstellar disk of X Per is now brighter than it has been for the past few decades (Roche et al. 1993). The top panel shows the binned X-ray fluxes observed with *RXTE*/ASM. We see that the first brightening episode corresponded to the onset of a slow increase in X-ray flux that eventually soared to a record high over the ASM observation period shortly after the second visual brightening. The X-ray flux continues to remain high during the current optically bright state.

The apparent increase in X-ray flux (and implied gas accretion rate) that accompanied the disk expansion confirms that the X-ray source is powered by gas from the Be star disk. However, the largest disk HWHM radius shown in Figure 6.7 is still much smaller than the separation between the Be star and neutron star. For example, the mean Roche radius at periastron is $34R_S$ (Table 6.2), which is a factor of five larger than the maximum disk HWHM radius ($R_d/R_s = 6.4$ in Fig. 6.7). The maximum predicted disk size due to the action of the tidally-driven eccentric instability occurs at the $3:1$ resonance radius between the disk gas and neutron star orbital

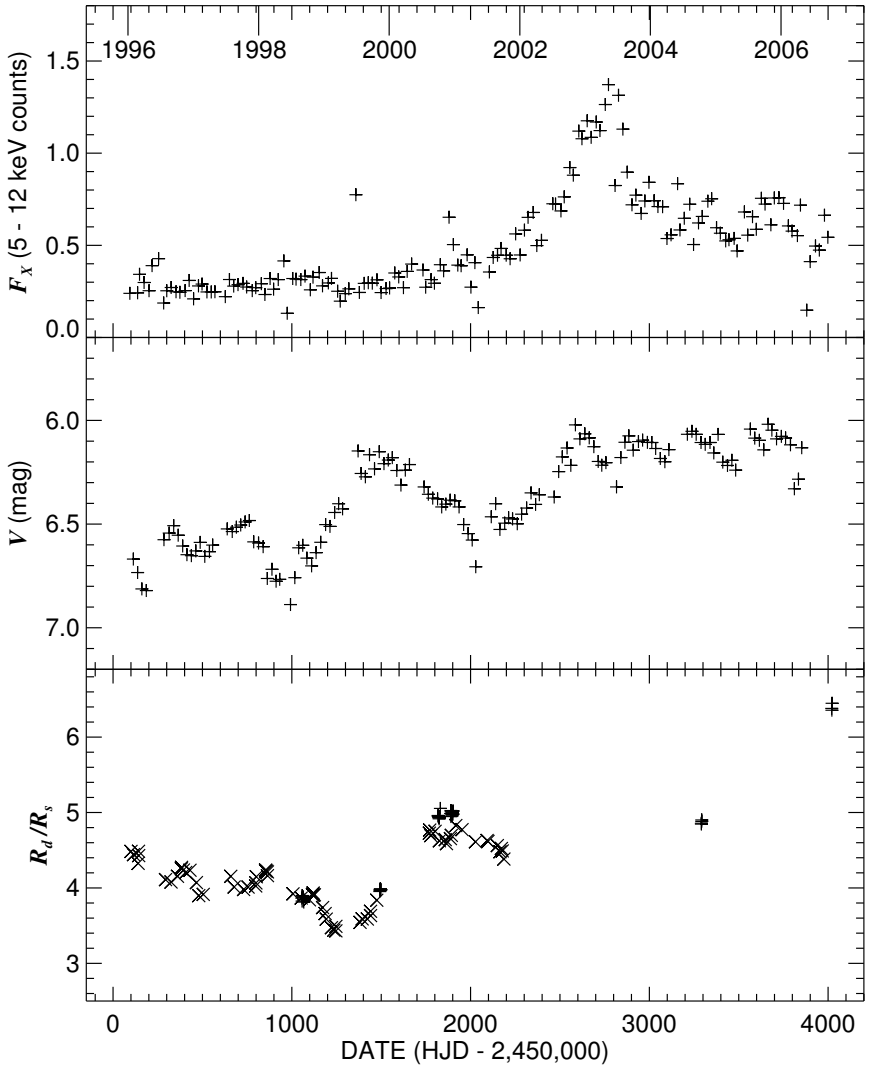

Figure 6.7: The time variations in X-ray flux (*top panel: RXTE*/ASM counts binned in 25 d increments), V magnitude (*middle panel:* AAVSO observations binned in 25 d increments), and the ratio of disk to stellar radius (*lower panel:* based upon the rescaled Hα equivalent width). for X Per. The plus symbols in the lower plot indicate radii derived from our equivalent width measurements, while the crosses are other published measurements.

periods (Okazaki & Negueruela 2001; Clark et al. 2001), and this radius occurs at $R_d/R_s = 31$ (Table 6.2). Once again the observed maximum HWHM radius is smaller than the predicted truncation limit.

However, tidal forces at periastron may excite a two-armed spiral in the disk, and the spiral arm facing the companion can lift disk gas out to close to the vicinity of the neutron star (Okazaki et al. 2002). If so, mass transfer will occur predominantly after periastron as the gas in the arm extension is accreted by the neutron star. We show in Figure 6.8 the X-ray light curves for X Per from fluxes recorded in the recent active state (HJD $>$ 2,452,200) that are binned according to the orbital ephemeris of Delgado-Martí et al. (2001). We see that there is an orbital modulation (particularly in the high energy band) that was not obvious in the earlier, low state data (Wen et al. 2006) and that the X-ray maximum occurs about one quarter of a period after periastron. This phase of maximum is consistent with post-periastron accretion from extended disk gas in a spiral arm.

6.5 Discussion

The Hα observations presented here and elsewhere document the remarkable and continuing changes that occur in the mass loss from the Be stars in these two BeXRB systems. The gas that enters their circumstellar disks becomes a reservoir of fuel for accretion by the neutron star companion, and the X-ray activity that accompanies the mass transfer increases dramatically as the disk radius increases in size. The disk growth is expected to be limited by gravitational interactions with the neutron star (Okazaki & Negueruela 2001; Okazaki et al. 2002). In low eccentricity binaries like X Per, the limiting radius occurs at the 3:1 resonance radius by the tidally-driven eccentric instability, while in high eccentricity systems like HDE 245770, the neutron star will approach closer to the Be star at periastron and higher integer resonances occurring at smaller radii will act to truncate the disk.

Our observations appear to confirm these expectations in the case of HDE 245770.

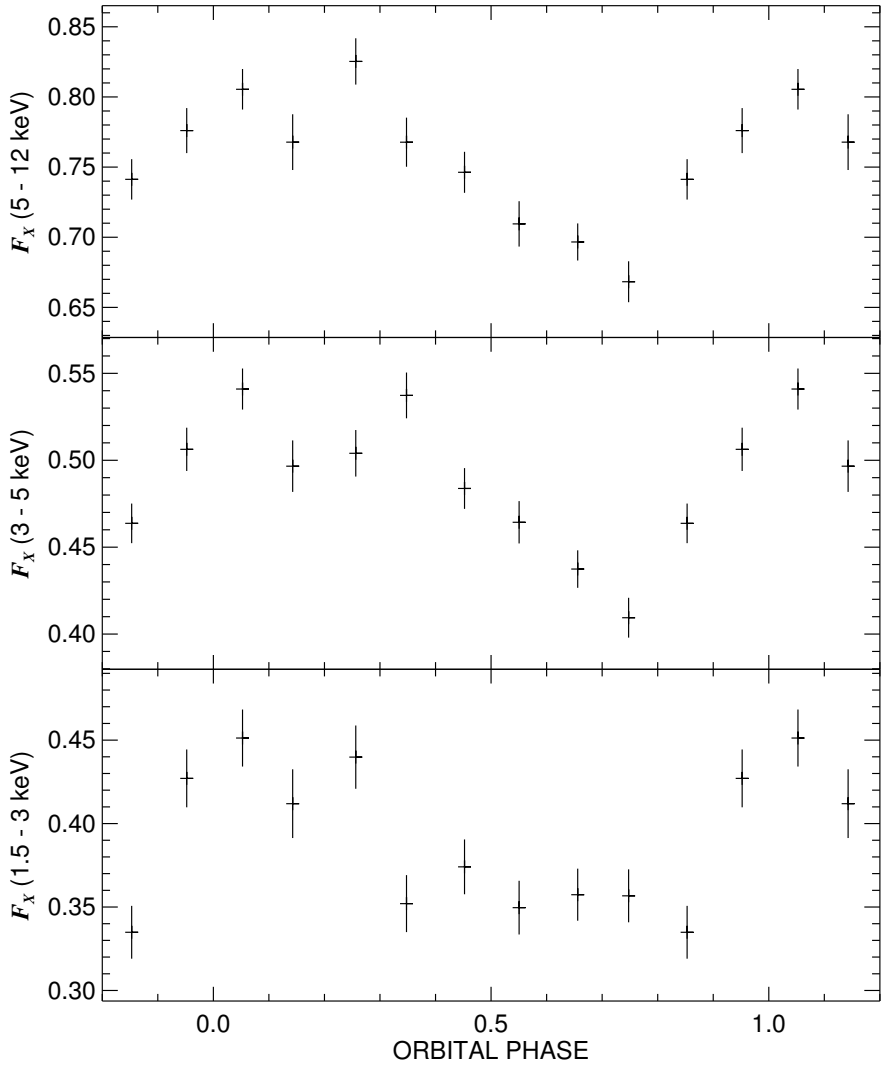

Figure 6.8: X-ray light curves of X Per from *RXTE*/ASM observations during active dates formed by binning with the orbital ephemeris from Delgado-Martí et al. (2001). The high energy band (*top panel*) appears to attain a maximum at a phase ≈ 0.25 past periastron. The vertical segments indicate the $\pm 1\sigma$ standard deviation of the mean within each bin.

The largest disk HWHM radius we find from the Hα equivalent width is comparable to both the $n = 5$ resonance radius and the mean Roche radius at the time of periastron. The historical maxima of Hα strength may imply that the disk HWHM radius can occasionally grow to even larger dimensions. We caution, however, that

it may be possible for Be disks of extreme density to attain very large Hα emission fluxes without radial growth. For example, pressure broadening in high density disks can lead to an increased flux in the wings of Hα and thus a larger emission equivalent width. Whether such high density and high pressure disks could remain confined by gravitational forces is an open question.

The case of X Per, on the other hand, shows that the mass transfer and X-ray accretion flux can increase even when the disk HWHM radius attains a size well below the critical value. We found that the recent X-ray flux increase occurred when the disk HWHM radius grew to about $R_d/R_s = 5$, much less than the resonant truncation radius of $R_3/R_s = 31$. There are two probable explanations for this difference. First, tidal forces at periastron promote the development of a two-arm spiral structure in the disk (Okazaki et al. 2002) and gas concentrated in the arm closest to the companion can be pushed outwards and accreted by the neutron star. Hydrodynamical models suggest that the gas accretion rate from the spiral arm will peak sometime after periastron, and we find that indeed the X-ray flux maximum lags periastron by $\approx 25\%$ of the orbital period in both the BeXRBs examined here and in the microquasar LS I +61 303 (Ch. 5). Second, the disk probably extends beyond the HWHM radius of the Hα emission that we use to define disk radius (Ch. 4). The disk density is described in our model in terms of a power law with radial distance from the star (Hummel & Vrancken 2000), and the lower gas density at larger radius may be entirely adequate to power the accretion-driven X-ray flux.

The observational record for both of these BeXRBs documents the growth of the disk from inside out. A comparison of the V-band light curves and Hα radii in both Figures 6.5 and 6.7 shows that the time evolution of the Hα emission lags behind that of the disk continuum flux. Clark et al. (2001) also noted this delay between the line and continuum fluxes, and they argue that the time lag is due to differences in

spatial origin. The continuum flux excess is probably formed in the inner part of the disk while the Hα emission is more optically thick and forms over a wider range of disk radius. Thus, an outwards propagating density enhancement would peak first in continuum light and later in the Hα flux. The fate of this outflow is unclear. Models by Okazaki et al. (2002) suggest that some of the mass falls back onto the Be star, some is accreted by the neutron star, and the remainder escapes from the system (presumably into a circumbinary region centered on the orbital plane). A search for such circumstellar structures might yield evidence of the ejected gas (for example, as a compact H II region surrounding X Per; Reynolds et al. 2005).

6.6 Mass Ratio Limit from *IUE* Radial Velocities of X Per

Several investigators have attempted to measure the orbital motion of X Per, but their results have generally been inconclusive because the lines are broad, shallow, and often marred by emission and because the semiamplitude is probably small (Hutchings 1977; Reynolds et al. 1992; Stickland 1992). The ideal spectral range to search for orbital motion is in the ultraviolet because the disk flux contribution is relatively small in the UV (Telting et al. 1998). Stickland (1992) used the spectra available at that time in the archive of the *IUE* to measure radial velocities, and he found that the velocity excursions were too small to measure orbital motion. Here we repeat the analysis of the now larger set of *IUE* spectra using the complementary orbital elements from the pulsar orbit (Delgado-Martí et al. 2001).

We obtained 43 high dispersion, short wavelength prime camera spectra of X Per from the *IUE* database maintained at the Multimission Archive at Space Telescope[3]. These spectra were transformed to a uniform $\log \lambda$, heliocentric wavelength grid, normalized to a pseudo-continuum, and excised of the main interstellar lines, and

[3]http://archive.stsci.edu/iue/

radial velocities were measured by cross-correlation (Penny, Gies, & Bagnuolo 1999). A mean formed from the average of all the spectra was used as a spectral template, and its absolute velocity was determined to be +0.8 km s^{-1} by cross-correlation with a similar spectrum of HD 34078 (Gies & Bolton 1986). We used the apparent shifts between each cross-correlation function and the ensemble mean of the functions to estimate the relative velocity shift for each spectrum, and then the final absolute velocities were set by adding the template velocity above. The results are listed in Table 6.3, which gives the heliocentric Julian date of mid-exposure, the orbital phase from the ephemeris of Delgado-Martí et al. (2001), and the measured radial velocity.

Table 6.3: *IUE* Radial Velocity Measurements for X Per

Date (HJD−2,400,000)	Orbital Phase	V_r (km s^{-1})
43602.749	0.034	−5.3
43705.644	0.445	3.3
43712.142	0.471	20.4
43784.061	0.758	6.2
43796.362	0.808	7.5
43850.204	0.023	4.3
43885.683	0.164	5.8
43885.749	0.165	−3.5
43885.806	0.165	−5.6
43947.719	0.412	1.6
44156.035	0.245	−0.7
44231.213	0.545	3.8
44319.029	0.896	−3.2
44319.087	0.896	−5.2
44319.138	0.896	−0.3
44319.187	0.896	−4.3
44319.238	0.897	−4.3
44319.279	0.897	−9.4
44323.732	0.915	2.3
44327.924	0.931	0.7
44582.952	0.950	−0.6
44582.991	0.950	4.2
44888.132	0.169	−3.9
48118.467	0.075	−4.4
49593.258	0.967	5.8
49593.325	0.968	2.1
49621.183	0.079	−0.2
49621.275	0.079	1.1

Continued on Next Page...

Table 6.3 – Continued

Date (HJD−2,400,000)	Orbital Phase	V_r (km s^{-1})
49643.343	0.168	−4.0
49647.365	0.184	−1.0
49715.074	0.454	2.5
49715.112	0.454	10.0
49715.159	0.454	6.3
49715.198	0.455	0.2
49748.731	0.589	0.2
49748.796	0.589	−0.9
49775.778	0.697	8.2
49775.824	0.697	7.0
49956.299	0.418	2.9
50000.094	0.593	−4.1
50104.187	0.009	−15.1
50124.212	0.089	1.2
50144.055	0.168	1.0

We then fit the *IUE* velocities using the non-linear, least-squares, orbital elements program of Morbey & Brosterhus (1974). This was a constrained solution in which all the elements were set from the pulsar results (Delgado-Martí et al. 2001) (with the longitude of periastron changed by 180°) with the exception of the systemic velocity γ and the semiamplitude K. The formal solution for these parameters is $\gamma = 1.0 \pm 0.9$ km s^{-1} and $K = 2.3 \pm 1.4$ km s^{-1}, and the observations and calculated radial velocity curve are illustrated in Figure 6.9. Clearly, the amplitude of motion is small enough that this result is of marginal significance, but the velocities do place a useful upper limit on the semiamplitude. The dotted line in Figure 6.9 shows the fit with a semiamplitude of $K + 2\sigma = 5.0$ km s^{-1}, and this appears to be a reasonable upper limit consistent with the spread in the *IUE* velocities.

The pulsar orbital elements (Delgado-Martí et al. 2001) give a neutron star orbital semiamplitude of $K = 39.8 \pm 0.4$ km s^{-1}, so the ratio of the upper limit of the Be star semiamplitude to that for the pulsar yields an upper limit on the mass ratio, $M_2/M_1 < 0.13$. We have plotted this constraint in the mass plane diagram in Figure 6.10 together with lines of constant orbital inclination derived from the pulsar

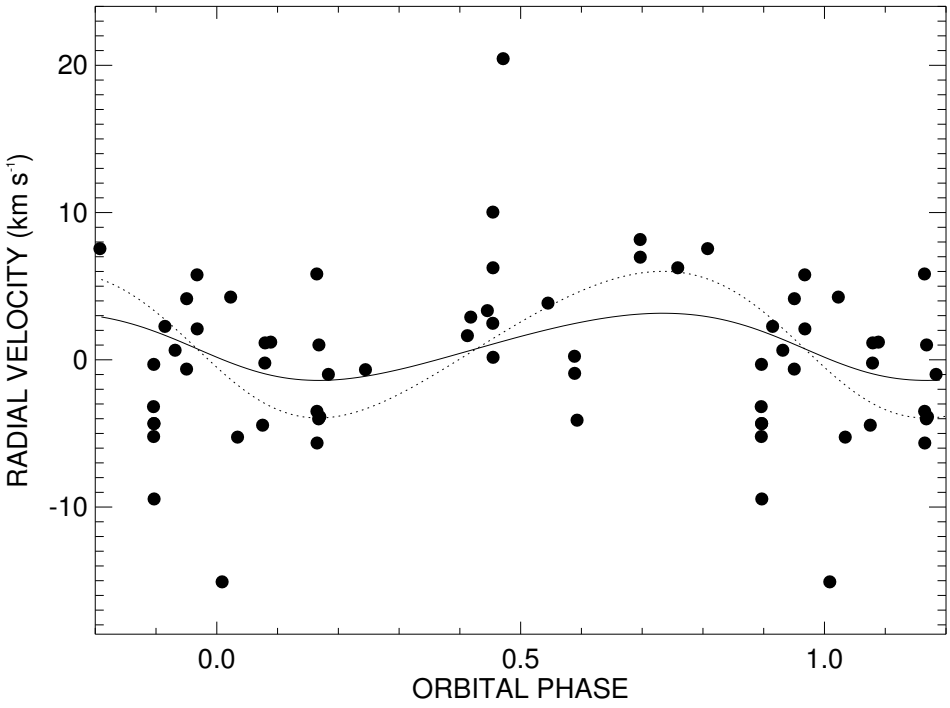

Figure 6.9: Radial velocities of X Per from *IUE* spectroscopy plotted against the orbital ephemeris of the X-ray pulsar. The solid line shows the nominal best fit of the Be star systemic velocity and semiamplitude (with all other parameters set by the pulsar orbit) while the dotted line shows a fit with the semiamplitude fixed at the 2σ upper limit.

mass function. A lower limit on the inclination of $i > 23°$ results from assuming that the star rotates slower than the critical rate (Clark et al. 2001). Harmanec (1988) presents a summary of mass and radii data from eclipsing binary stars, and the mass range for a B0 V star is probably between $\approx 11 M_\odot$ and $17 M_\odot$. The shaded region in Figure 6.10 shows this probable Be star range together with the observed range in neutron star mass (van Kerkwijk, van Paradijs, & Zuiderwijk 1995). This region in the mass plane corresponds to an inclination range of $i = 28°$ to $35°$.

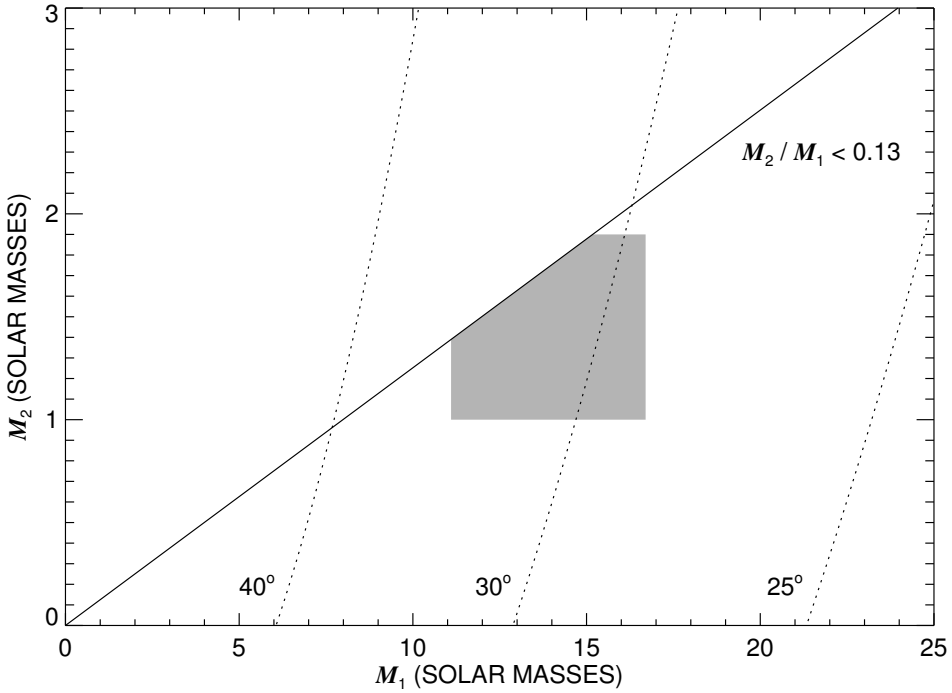

Figure 6.10: A mass plane diagram for X Per showing constraints on the Be star mass M_1 and the neutron star mass M_2. The solid line shows the upper limit on mass ratio determined from the *IUE* radial velocities, and the dotted lines show the mass relations for three values of orbital inclination. The shaded region shows the most probable range in masses for both components.

– 7 –

A Survey of Be Stars

7.1 Introduction

The current working definition of a Be star is "a non-supergiant B star whose spectrum has, or had at some time, one or more Balmer lines in emission" (Collins 1987). In order for a stellar spectral line to be in emission, there must be a hot emitting region around the star, such as a hot chromosphere or corona (these often flare and are usually cooler/late-type stars) or a region of circumstellar material. Be stars have circumstellar material and as one may suspect, the aforementioned definition of Be stars encompasses diverse phenomena such as newly forming stars (e.g., Herbig AeBe stars), stars in the process of active mass transfer (interacting binaries/Algol systems/accretion disk systems), and stars with equatorial "decretion" disks. The stars with equatorial decretion disks are called "classical" Be stars and they are the focus of my study.

The defining feature of a classical Be star is this equatorial disk. It is called a "decretion" disk to differentiate it from an accretion disk as the Be star disk is outflowing, not inflowing. For a time, there was debate about whether the shape of

the circumstellar material is a disk or is spherical (see Porter & Rivinius 2003), but interferometric measurements have confirmed their disk nature (e.g., Quirrenbach et al. 1997; Tycner et al. 2004, 2006; Gies et al. 2007). Other measurements that support the disk hypothesis are infrared excess (Waters 1986), polarization studies (see Bjorkman 2000, and references therein), and the actual shape of the emission lines. Figure 7.1 shows how observations of a rotating disk result in a double-peaked profile. One can see that the material with the largest radial velocity is near the star and moving roughly parallel to the line of sight. Slower-moving gas as well as gas moving perpendicular to the line of sight will populate the center of the profile.

In order to have an outflowing circumstellar disk, one must have a rapidly rotating object, and therefore another characteristic of classical Be stars is that they exhibit rapid rotation. Be stars (on average) more than any other class of stars rotate close to the critical limit where centrifugal force balances gravity at the equator. Generally, spectroscopic studies show the angular velocity of a Be star is about 70-80% of the critical limit (see §7.1.3). However, if the star is actually producing this decretion disk, one would expect the star to be rotating closer to the critical limit. One possible reason for the relatively low measured speed is that gravitational darkening has been largely ignored until a few years ago (see Townsend et al. 2004, for an excellent history and study of this phenomenon). Gravitational darkening occurs when a star spins fast and assumes the shape of an oblate spheroid with an equator wider than the poles. Because the equator is farther from the central fusion source, it is not as hot as the poles, so the equator appears darker and does not contribute the same amount of light to spectral lines as it would were the star not rotating. Also, due to the lower temperature, spectral lines look different, as they are temperature dependent. Because the extreme limbs at the equator are darkest yet produce the largest rotational Doppler shifts, the spectral line contributions for the extreme velocity po-

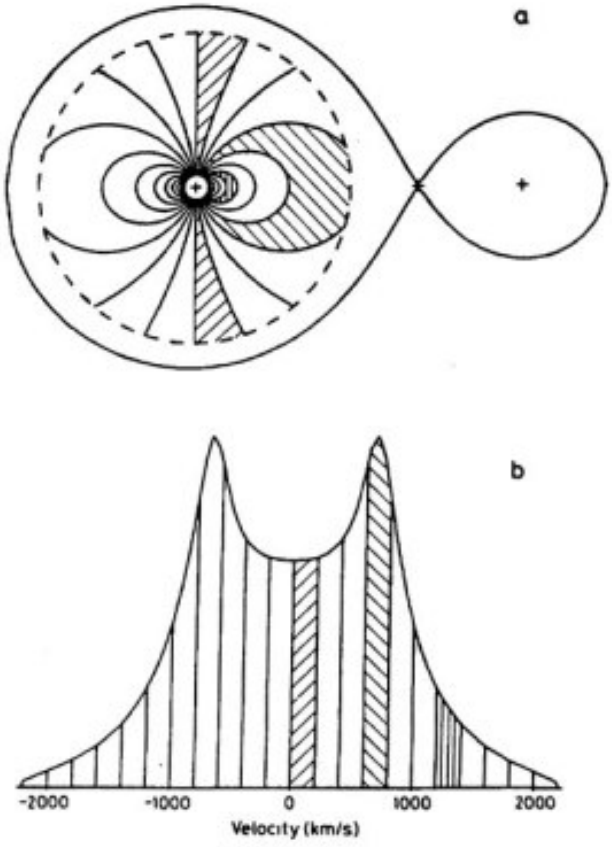

Figure 7.1: Diagram showing how a disk forms a double-peaked emission profile. *Top diagram* - schematic of a rotating disk. The dipole-like lines represent the tracing of loci of constant radial velocity in the disk as observed from the bottom of the page. There are four hatched regions (two have the same hatching) which correspond to regions in the bottom diagram. *Bottom diagram* - schematic of the emission profile of the above rotating disk. The profile is divided into velocity bins and the hatched regions correspond to velocity regions in the above diagram. Diagram from Horne & Marsh (1986).

sitions will appear quite weak and lead to measurements of rotation speeds that are too small. In another tactic, Cranmer (2005) uses Monte Carlo modeling to simulate distributions of $V \sin i$. These simulations take gravity darkening, limb darkening, and observational uncertainties into account. He finds the rotation speed of a Be star can be less than the anticipated critical speed, yet still produce a decretion disk.

An underlying problem in all of this is what actually causes the disk formation. No one knows. Porter & Rivinius (2003) state that whatever the mechanism is,

it must be able to create regions dense enough to account for both the continuum and line observations as well as provide angular momentum to the disk. Material could be ejected via stellar winds or non-radial pulsations. The disks could be wind-compressed, magnetically compressed, or viscous (see Porter & Rivinius 2003, for reviews of the models). None of the models sufficiently fulfill both of the above requirements. However, all assume a rotation speed of 70-80% of the critical velocity, so the higher rotation speeds derived when gravitational darkening is fully taken into account may take care of the problems (Townsend et al. 2004).

Another issue is that of why the Be stars spin so fast in the first place. Perhaps it is natal, perhaps not. Perhaps the star is part of a binary system where the companion has transferred mass (and angular momentum) to the Be star and spun it up (Gies 2000). This is one of the great questions in Be star research.

7.1.1 Disk Observations

In order to probe the properties of the classical Be star disk, I observed Balmer lines in emission and Fe II lines in both emission and absorption for those stars that exhibited them. Observations of Balmer Hα illuminate the general characteristics of the disk - this emission is strong as it is generated from a large surface area of optically thick gas. Observations of Balmer Hγ describe the inner parts of the disk as Hγ becomes optically thin a relatively short distance from the star (as opposed to Hα). Both Hα and Hγ will show evidence of density enhancements due to structure in the disk. Generally, this phenomenon will manifest itself in the strength of the emission peaks such that if one peak is higher than the other, then the density on the side of the star with the corresponding Doppler shift is enhanced. Sometimes, these peaks can show rapid variability, possibly indicative of one-armed spirals in the disk (Okazaki & Negueruela 2001). The presence of Fe II features may indicate the

starlight is observed directly through circumstellar material. Sometimes these lines are emission features which Arias et al. (2006) find arise from an optically thick (to Fe II) circumstellar envelope near the star (within $2.0 \pm 0.8\ R_*$). If one observes the starlight through more of the disk, the features become sharp absorption lines and these stars are called shell stars (Rivinius et al. 2006). As these shell stars are rapidly rotating Be stars observed close to edge-on, the underlying photospheric absorption will be very broad.

7.1.2 Timescales for Variability

Classical Be stars are inherently variable and do so on a variety of timescales in a variety of ways. In a study of photometric variations in HIPPARCOS data of 273 Be stars, Hubert & Floquet (1998) found that the degree of variability was highly dependent on temperature. For example, for short timescales (less than 3.5 days), 86% of the hot B stars (B0-3), 40% of the mid-range stars (B4-5), and 18% of the cool B stars (B6-9) showed variability. They also found that the long-term variability for the cooler stars (B6-9) was on a much longer timescale than that of the hotter stars (long term being at least the length of the four-year mission).

In general, the shortest timescale is that of non-radial pulsation (NRP). Rivinius et al. (2003) present a study of 27 Be stars and find NRP periods of 0.5 to 2.3 days. Another timescale is that for changing from shell to non-shell and back again. Why this happens no one knows for sure, but it is likely due to outflowing density enhancements in a flared circumstellar disk (or, much less likely, it could involve a change in inclination angle). For instance, the star Pleione (HD 23862) changes from shell to non-shell and back over the course of 20-30 years (e.g., Cramer et al. 1995) and I have spectra of both non-shell and shell phases (see Fig. C.38). These stars can also change from Be to B and back again. This happens over several years or decades

but it is not unusual for Be stars.

7.1.3 Previous Spectroscopic Surveys

There are several previous spectroscopic surveys of Be stars. Chauville et al. (2001) studied 116 Be stars over a period of 10 years. For each of their spectra, they measured quantities such as equivalent width, radial velocity shifts, and projected rotational velocity, and they found that Be stars rotate at 80% of critical angular velocity. Also, all of their spectra are available for download on SIMBAD. For 114 Be stars in the southern hemisphere, Levenhagen & Leister (2006) measured fundamental parameters such as effective temperature, projected rotational velocity and $\log g$. Another study of fundamental parameters was carried out by Frémat et al. (2006) for 64 stars using very careful and detailed modeling (gravity darkening was taken into account). The year before, they published a paper detailing the effects of gravity darkening on determination of fundamental parameters (Frémat et al. 2005) and found that the most probable average rate of angular velocity (Ω) was $\Omega/\Omega_{crit} \simeq 0.88$. In 2005, Zorec et al. studied 97 Be stars to determine the effects of fast rotation on fundamental parameters using both model atmospheres and evolutionary tracks for rotating stars. They found that massive ($M > 12\ M_{\odot}$) Be stars are Be relatively younger in their lifetimes than less massive Be stars. Using 58 Be stars, Steele et al. (1999) devised a constraint on the angular momentum evolution of Be stars - they found that any angular momentum lost to the decretion disk cannot be more than 15% of the angular momentum of the star. Finally, one of the more important studies was from Slettebak (1982). His *homogeneous* sample of the spectral type and projected rotational velocity of 182 stars over several years is very useful. He also has notes on prior observations of most of the stars in his sample. He found that one-fourth of the stars showed Fe II emission and that there were equal numbers of stars in the luminosity classes (III,

IV, and V).

7.1.4 Goals of This Survey

In undertaking this survey of Be stars, I wished to examine many characteristics and behaviors of Be stars. The timescales of variability in the disk may be examined through changes in the Balmer and Fe II shell lines. Using this homogeneous sample, I also wish to examine if there are any systematic differences in line broadening caused by gravitational darkening and temperature gradients in stars near critical rotation. Through collecting many spectra, one may discover prospective NRP candidates (as the lines profiles change). I also wish to comment on the incidence of binary companions (especially spectroscopic) as duplicity could be an explanation for why Be stars rotate so fast. The last specific goal of this survey is to determine which stars may be good candidates for observation with the CHARA Array to determine disk size. One advantage to having such a large body of data is that secondary goals may be addressed in the course of working on the primary goals.

7.2 Observations and Reductions

7.2.1 Observations

The targets for the survey sample were taken from the list of Yudin (2001). The restrictions on the sample are that the star be brighter than 8th magnitude, right ascension be between 16:30h and 8:00h (as befitted the observing season), and declination between -25 and $+70^\circ$ (the southern limit is dictated by both the horizon and the telescope configuration while the northern limit is dictated by the telescope configuration). The physical parameters for each of the 128 stars in the sample are listed in Table 7.1 which gives the HD number, HR number (if available), spectral

classification, effective temperature, log gravity, projected rotational velocity, a code for the source of these estimates, and other names used in the literature for particular targets. The main source is the work of Frémat et al. (2005) and the table lists their derived apparent values of the stellar parameters. For the remaining stars, the classifications and projected rotational velocities were taken mainly from the lists of Yudin (2001) and Abt et al. (2002). The temperatures and gravities for these remaining stars were adopted from other published works whenever possible (given by the reference code), but there were some 48 stars without any published estimates for these quantities. I estimated the temperatures for 44 of these last stars (marked by Q) by determining the reddening free Q parameter (Daflon et al. 1999) given by

$$Q = (U - B) - 0.72(B - V)$$

where $U-B$ and $B-V$ are the standard Johnson filter color indices. The temperatures were then determined by interpolation in the theoretical $(Q, T_{\rm eff})$ relation from Castelli & Kurucz (2003)[1] for solar metallicity models appropriate to main sequence stars ($\log g = 4.0$, microturbulent velocity $= 2$ km s^{-1}). The temperatures for the remaining four stars in the sample (marked by C) were set using their spectral classifications and the calibration from Underhill & Doazan (1982) (their Table 3-5). In all cases where no published information was available for gravity, this parameter was set to $\log g = 4.0$ for luminosity class IV and V stars and to $\log g = 3.5$ for luminosity class III stars (typical values among the B-stars; Underhill & Doazan 1982).

Table 7.1: Description of the Sample

HD Number	HR Number	Spectral Type	$T_{\rm eff}$ (kK)	$\log g$	$V \sin i$ (km s^{-1})	Source	Other Names
HD000144	7	B9 IIIe	12.0	3.4	125	1	10 Cas
HD004180	193	B2 Ve	14.4	3.3	195	1	22 Cas, o Cas
HD005394	264	B0 IVe+sh	26.4	3.8	432	1	γ Cas
HD006811	335	B6.5 IIIe	12.5	3.1	85	1	ϕ And

Continued on Next Page...

[1]http://kurucz.harvard.edu/grids/gridP00ODFNEW/ubvp00k2odfnew.dat

Table 7.1 – Continued

HD Number	HR Number	Spectral Type	$T_{\rm eff}$ (kK)	$\log g$	$V \sin i$ (km s^{-1})	Source	Other Names
HD007636		B2 IIIne	27.5	3.5	148	Q	V764 Cas
HD009709		B8 V	14.0	4.0	297	Q	
HD010516	496	B0.5 IVe+sh	25.6	3.9	440	1	ϕ Per
HD011415	542	B3 V	15.1	3.5	38	2	ϵ Cas
HD013661		B2 Ve	22.1	4.0	196	Q	V594 Per
HD013867		B5 Ve	13.7	4.0	93	Q	
HD018552	894	B8 Vne	12.7	3.5	286	1	
HD019243		B1 Ve	21.2	3.3	160	1	
HD020134		B2.5 Vep	19.9	4.0	87	Q	
HD020336	985	B2.5 Ven	18.7	3.9	328	1	BK Cam
HD020418	989	B5 V	15.6	3.7	262	3	31 Per
HD021362	1037	B6 Vn	14.2	3.8	313	3	
HD021455	1047	B7 V	13.3	4.0	138	Q	
HD021551	1051	B7 V	12.4	4.0	296	3	
HD021641		B8.5 Ve	12.0	4.2	170	3	
HD021650		B6 Ve	14.9	4.0	226	Q	
HD022192	1087	B4.5 Ve+sh	15.8	3.5	275	1	ψ Per, 37 Per
HD022780	1113	B7 Vne	13.3	3.4	285	1	
HD023016	1126	B8.5 Vne	12.2	3.9	235	1	13 Tau
HD023302	1142	B6 IIIe	12.8	3.4	170	1	17 Tau
HD023478		B3 IVe:	19.8	4.0	170	Q	
HD023480	1156	B6.5 IVe	13.7	3.6	240	1	23 Tau, V971 Tau
HD023552	1160	B8 Vne	12.7	3.8	220	1	
HD023630	1165	B7 IIIe	12.3	3.0	140	1	η Tau, 25 Tau
HD023800		B1.5 IVe	26.1	4.0	178	Q	
HD023862	1180	B8 Vpe+sh	12.1	3.9	286	1	28 Tau
HD024479	1204	B9.5Ve	10.5	4.0	110	Q	
HD024534	1209	O9.5 Vep	25.2	3.6	293	1	X Per
HD025799		B3 V	20.4	4.0	322	Q	V490 Per
HD025940	1273	B4 Ve	16.2	3.6	197	1	48 Per, MX Per
HD026670	1305	B6 V	14.5	4.0	263	Q	
HD029866	1500	B7.5 IVne	13.0	4.0	250	Q	
HD032343	1622	B3 Ve	16.1	3.8	95	1	11 Cam, BV Cam
HD036576	1858	B1.5 IVe	22.6	3.8	265	1	120 Tau
HD037202	1910	B1 IVe+sh	19.3	3.7	310	1	123 Tau, ζ Tau
HD041335	2142	B2 Vne	20.9	3.9	358	1	V696 Mon
HD058715	2845	B8 Ve	11.8	3.8	230	1	β CMi, 3 CMi
HD058978	2855	B0.5 IVne+sh	24.4	4.2	370	1	FY CMa
HD060855	2921	B2 Ve	20.0	4.0	239	Q	
HD149757	6175	O9 Ve	26.4	3.8	340	1	13 Oph, ζ Oph
HD162428		B7 IV/Ve	14.4	4.0	275	Q	
HD162732	6664	B6 IVe+sh	13.5	3.8	310	1	V744 Her, 88 Her
HD164284	6712	B2 IV/Ve+sh	21.6	3.9	280	1	66 Oph, V2048 Oph
HD164447	6720	B8 Vne	12.7	4.0	178	Q	V974 Her
HD166014	6779	B9.5 III	9.8	3.5	142	Q	o Her, 103 He
HD168797	6873	B3 Ve	21.0	4.0	251	4	NW Ser
HD168957		B4 Ve	16.6	4.0	88	Q	
HD171406	6971	B4 Ve	15.1	4.0	264	Q	V532 Lyr
HD171780	6984	B5 Vne	15.0	3.8	256	5	
HD173370	7040	B9 Ve	11.6	4.0	261	Q	4 Aql
HD174237	7084	B2.5 Ve	17.7	3.8	163	1	CX Dra
HD174638	7106	B7 Ve	12.8	2.6	131	6	β Lyr
HD175863		B5 Ve	14.5	4.0	170	Q	
HD175869	7158	B8 IIIep	12.2	3.3	175	1	64 Ser
HD177648		B2 Ve	20.2	4.0	265	Q	
HD178475	7262	B5 V	14.7	4.0	234	Q	ι Lyr, 18 Lyr
HD179343		B9 V+sh	12.2	4.0	261	Q	
HD181409	7335	B2 IVe	26.3	4.0	140	Q	
HD181615	7342	B2 Vpe	10.5	1.3	69	7	υ Sgr
HD183362	7403	B3 Ve+sh	21.0	4.0	220	4	V558 Lyr
HD183656	7415	B6 Ve+sh	12.6	3.3	270	1	V923 Aql
HD183914	7418	B8 Ve	13.2	3.8	220	1	6 Cyg
HD184279		B0.5 Ve+sh	30.4	3.9	212	8	V1294 Aql
HD185037	7457	B8 Vne	12.1	3.8	280	1	11 Cyg
HD187567	7554	B2.5 IVe	21.0	4.0	140	4	V1339 Aql
HD187811	7565	B2.5 Ve+sh	18.1	3.8	245	1	12 Vul
HD187851		B2 V	23.8	4.0	234	Q	V396 Vul
HD189687	7647	B3 IVe	18.1	3.5	200	1	25 Cyg, V1746 Cyg
HD191610	7708	B3 IVe	18.4	3.7	300	1	28 Cyg, V1624 Cyg
HD192044	7719	B7.5 Ve	12.6	3.4	245	1	20 Vul
HD192445		B2 Ve	22.6	4.0	242	Q	
HD192685	7739	B3 V	18.1	3.7	206	9	QR Vul
HD193009		B1.5 Ve	25.7	4.0	211	C,10	V2113 Cyg

Continued on Next Page...

Table 7.1 – Continued

HD Number	HR Number	Spectral Type	$T_{\rm eff}$ (kK)	$\log g$	$V \sin i$ (km s^{-1})	Source	Other Names
HD193182		B7 IV/Ve+sh	14.0	3.5	182	11	
HD193911	7789	B8 IIIne+sh	12.5	3.1	160	1	25 Vul
HD194244	7803	B9 Ve	10.7	4.0	221	Q	
HD194335	7807	B2 IIIne	22.1	4.1	360	1	V2119 Cyg
HD194883		B2 Ve	20.2	4.0	173	Q	V2120 Cyg
HD195325	7836	B9e+sh	10.4	4.0	250	Q	1 Del
HD195554	7843	B9 Vne	11.6	4.0	215	Q	
HD197419	7927	B2 IV-Ve	22.5	4.0	115	4	V568 Cyg
HD198183	7963	B5 Ve	13.9	3.2	125	1	54 Cyg, λ Cyg
HD198625	7983	B4 Ve	17.2	4.0	257	Q	V2136 Cyg
HD199218	8009	B8 Vnne	13.5	4.0	288	Q	
HD199356		B2 IVe	22.8	4.0	354	C	V2139 Cyg
HD200120	8047	B1.5 Ve+sh	21.8	3.8	379	1	59 Cyg, V832 Cyg
HD200310	8053	B1 Ve	27.0	4.0	320	12	60 Cyg, V1931 Cyg
HD201522		B7 IV	15.9	4.0	240	13	
HD201733	8103	B4 IVp	16.4	3.9	340	1	V2148 Cyg
HD202904	8146	B2.5 Vne	19.1	3.9	167	14	66 Cyg, υ Cyg
HD203025	8153	B2 IIIe	22.5	3.7	130	15	
HD203064	8154	O7.5 III((f))	34.5	3.5	300	16	68 Cyg
HD203374		B0 IVpe	24.6	3.5	333	1	
HD203467	8171	B2.5 Ve+sh	17.1	3.4	153	1	6 Cep, V382 Cep
HD203699		B3 IV	16.0	4.0	114	Q	
HD203731		B1 Vne	26.9	4.0	279	C	V2153 Cyg
HD204116		B1 Ve	23.8	4.0	170	Q	V2155 Cyg
HD204722		B2 Ve	28.6	4.0	210	Q	V2162 Cyg
HD204860		B4 Ve	16.8	4.0	226	Q	V2163 Cyg
HD205060		B6 Ve	14.1	4.0	214	Q	
HD205551	8259	B9 IIIe	12.2	4.0	166	Q	
HD206773		B0 Vpe	29.2	3.9	390	1	
HD207232		B7 V	13.5	4.0	281	Q	
HD208057	8356	B3 Ve	18.0	3.7	100	1	16 Peg, OQ Peg
HD208392		B1 IIIe	24.5	3.7	258	15	EM Cep
HD208682	8375	B2.5 Ve+sh	22.1	4.0	307	1	
HD210129	8438	B7 Vne	13.5	3.4	130	1	25 Peg
HD212044		B0 Ve	30.8	4.0	162	C	V357 Lac
HD212076	8520	B1.5 Vne	19.3	3.7	98	1	31 Peg, IN Peg
HD212571	8539	B1 Ve+sh	26.1	3.9	230	1	52 Aqr, π Aqr
HD212791		B6e	16.7	4.0	170	Q	V408 Lac
HD214167		B1 V	26.7	4.5	22	17	8 Lac A
HD214168	8603	B1 Ve	25.8	4.2	300	1	8 Lac B
HD216057	8682	B5 Vne	16.5	4.0	283	4	
HD216200	8690	B3 IV:e	14.8	2.6	199	18	14 Lac, V360 Lac
HD217050	8731	B3.5 IIIpe+sh	17.9	3.6	340	1	EW Lac
HD217543	8758	B3.5 Vpe	17.2	3.7	325	1	
HD217675	8762	B6 IIIpe+sh	14.1	3.2	274	1	o And, 1 And
HD217891	8773	B5 Ve	14.4	3.7	95	1	β Psc, 4 Psc
HD218393		B2 IIIne	20.7	3.3	0	Q,19	KX And
HD218674		B3 IV/Ve+sh	18.0	4.0	234	Q	KY And
HD224544	9068	B6 IVe+sh	14.8	3.4	260	1	
HD224559	9070	B3.5 Vne	15.9	3.6	300	1	LQ And
HD225095		B2 IVne	23.8	4.0	152	Q	

Temperatures and gravities from sources listed below except for those noted by: Q = temperature from Kurucz Q parameter, or C = temperature from spectral type (Underhill & Doazan 1982, Table 3-5). In these cases, gravity is $\log g = 4.0$ for class V and IV stars and $\log g = 3.5$ for class III stars. Spectral classifications and $V \sin i$ not listed in (1) are from Abt et al. (2002) and Yudin (2001). Other references: (1) Frémat et al. (2005), (2) Adelman et al. (2002), (3) Wolff (1990), (4) Theodossiou (1985), (5) Hummel & Vrancken (2000), (6) Linnell (2002), (7) Dudley & Jeffery (1990), (8) Levenhagen & Leister (2004), (9) Castelli (1991), (10) Steele et al. (1999), (11) Denizman

et al. (1993), (12) Koubský et al. (2000), (13) Gulati et al. (1989), (14) Neiner et al. (2005), (15) Leushin (1988), (16) Repolust et al. (2004), (17) Daflon et al. (2003), (18) Linnell et al. (2006), (19) Floquet et al. (1989)

I had several opportunities to obtain spectra of the sample at the KPNO 0.9 m coudé feed telescope, twice in 2004, once in 2005, and once in 2006. To sample the region around Hα (a.k.a. the "red" region), the spectrograph was configured to use camera 5 with the long collimator and diffraction grating B (in second order with order sorting filter OG 550). Grating B has 316 grooves mm^{-1} and is blazed at 12,000 Å. The detector was the T2KB CCD (a 2048 $\times$ 2048 device with 24μm square pixels). When sampling the Hγ region (a.k.a. the "blue" region), the telescope was again configured to use camera 5 with the long collimator and the T2KB CCD detector, but the grating was grating A (in second order with order sorting filter 4-96) which has 632 grooves mm^{-1} and is blazed at 12,000 Å. Dates of observation, wavelength coverage, and resolving power near the Hα and Hγ features are given in Table 7.2.

Table 7.2: Journal of Optical Spectroscopy

Dates	Dates (HJD-2,400,000)	Spectral Range (Å)	Resolving Power ($\lambda/\triangle\lambda$)
2004 Aug	53233 – 53238	4235 – 4587	12500
2004 Oct	53290 – 53295	6470 – 7140	9500
2005 Nov	53683 – 53638	4236 – 4588	12500
2006 Oct	54019 – 54024	6433 – 7143	9500
2006 Oct	54025 – 54031	4236 – 4588	12500

For my first run in 2004 August, my excellent trainer Dr. David Wingert and I obtained 319 spectra. On a solo run in 2004 October, I took 420 spectra. During 2005 October, I got 250 spectra on another solo run[2]. During the 2006 October

[2]An observing log and pictorial description of the telescopes and procedures may be found at http://www.chara.gsu.edu/∼erika/Observing/

run, I started solo, then trained Stephen Williams, who in turn (after I left) trained Tabetha Boyajian for a long run of both red and blue spectroscopy. We obtained 520 red spectra and 346 blue spectra. For all runs, exposure times were between 3 seconds and 30 minutes, depending on the stellar magnitude. Exposure times for the red spectra were generally less than those for blue spectra.

During the observations, we encountered one problem target, the close pair of HD 214167 and HD 214168. They are 23 arcsec apart (close enough to be in the same field, but far enough to take individual spectra of each), of comparable magnitude, and both are B type stars. One of them (HD 214168) is a Be star, but the other (HD 214167) is a good example of a sharp-lined, normal B star. They are often confused in the literature (and in fact, I confused them during my observations), so HD 214167 is sometimes mistakenly claimed to be a Be star.

7.2.2 Data Reduction

Each set of observations has numerous bias, flat field, and Th Ar comparison lamp calibration frames. Each spectrum was extracted and calibrated using standard routines in *IRAF*[3]. Line-free regions in the continuum of the blue spectra were fit with a sixth-order cubic spline and the red spectra were fit with a third-order cubic spline. Each spectrum was then divided by the appropriate fit to produce a rectified spectrum with a continuum level of 1. After extraction and calibration, I used the Interactive Data Language (IDL) for all other data reduction and analysis.

An additional step is required to make the red spectra ready for analysis as they contain numerous atmospheric water vapor and O_2 features that are very narrow (often called telluric lines). In order to identify and then remove these features, one

[3]IRAF is distributed by the National Optical Astronomical Observatory, which is operated by the Association of Universities for Research in Astronomy, Inc. (AURA), under cooperative agreement with the National Science Foundation.

must observe a rapidly rotating A-type star (I selected ζ Aquilae for my spectra) each night and at several different altitudes (to sample the differing column densities of atmosphere associated with the range in target observations). After removing the broad stellar features of ζ Aquilae, one is left with just the spectrum of these telluric lines. Each target spectrum is then compared to the library of telluric line spectra and the target spectrum is divided by the closest match. Occasionally, this removal resulted in artifacts which were excised by linear interpolation.

To facilitate analysis, all spectra for a particular star were gathered in two stacks, one for red spectra and one for blue spectra. Each stack consists of two parts, one file for wavelength and timing information and one file for the spectral intensity information of each individual spectrum. In the process of making the stacks, I removed telluric lines and any aforementioned artifacts from the red spectra and excised any other obvious glitches via linear interpolation. Such glitches are generally caused by cosmic rays hitting the CCD detector as evidenced by the fact that the number of glitches increased as exposure time increased. All stacking and removal was carried out using IDL programs written by Dr. Douglas R. Gies and Dr. Michelle Thaller.

The wavelength region for the first night of the blue run in 2006 October was not the same as for all other spectra, and therefore, the spectral intensity from 4235 to 4287 Å had to be set to 1 (the continuum level). The IDL program for carrying out this procedure (*fix2006.pro*) may be found in Appendix B.

In my examination of the red spectral stacks, I noticed there were certain spectra that did not look right when compared to other spectra in the stack. Emission in these spectra looked flattened and "washed out" in comparison. The offending spectrum always had quite strong Hα emission, and I discovered while looking through the observing logs that these particular exposures were almost always labeled as

"saturated," i.e., exposed beyond the linear limit for the CCD detector. Therefore, I removed these saturated spectra from the stacks.

7.2.3 Spectra

While there are a great number of features present in my spectra, there is a limited subset I show in the plots described below. Table 7.3 gives the wavelengths and ionic species of these important features. All "blue" features are from 4200 to 4600 Åand all "red" features are from 6500 to 6700 Å.

Table 7.3: Important spectral lines in the Be Star Survey

λ (Å)	Ion
4267.160	C II
4340.468	Hγ
4351.769	Fe II
4387.928	He I
4471.477	He I
4481.228	Mg II
4549.474	Fe II
4552.622	Si III
4567.872	Si III
4574.777	Si III
4583.837	Fe II
6516.081	Fe II
6562.682	Hα
6578.05	C II
6582.88	C II
6678.148	He I

As the complete blue spectra show many interesting features and are not marred by telluric lines, one may examine the entire wavelength range and group stars into categories based on overall appearance. Below is a description of the four major categories I found.

The first category I deemed "normal." These are stars that show many of the important lines and the continuum is flat (except for a very broad diffuse interstellar band around 4428 Å). Several examples of "normal" stars are shown in Figure 7.2.

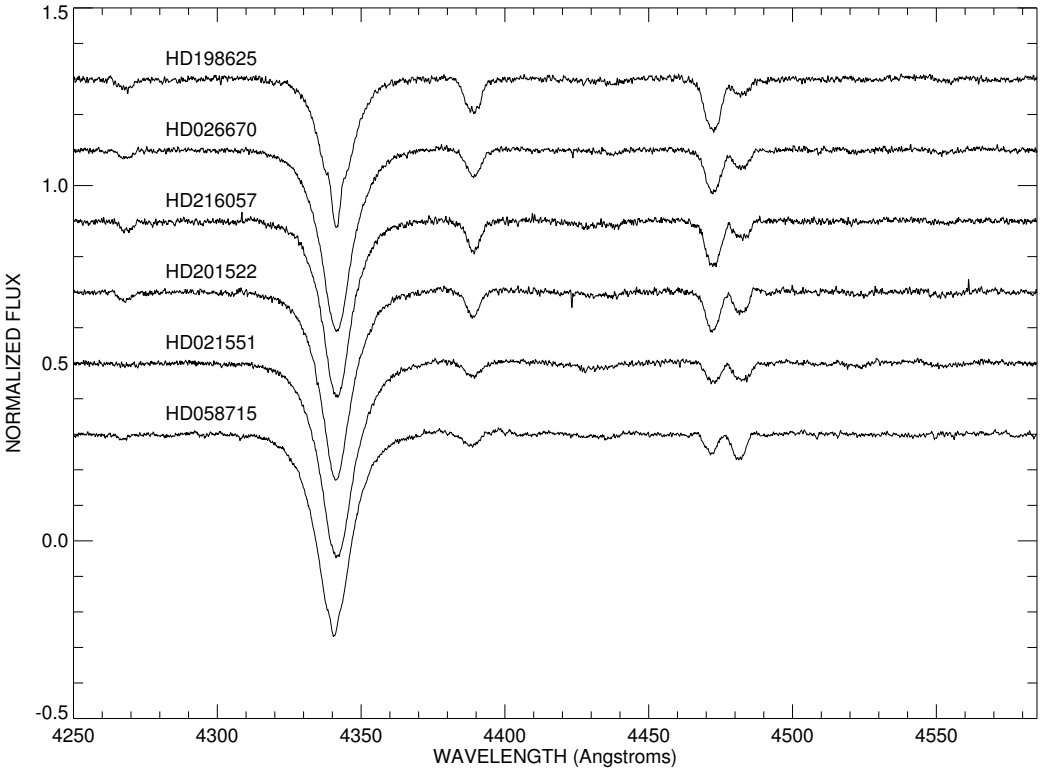

Figure 7.2: Individual spectra of some "normal" stars - offset for clarity.

I would like to point out that actually finding "normal" stars in my sample was surprisingly difficult.

The second category I deemed "squarish." Examples of this category are shown in Figure 7.3. Important absorption lines are present and look relatively normal (except for emission in Hγ in many cases). However, the continuum has many small absorption features (mainly of Fe II) that generally have a squarish appearance.

Stars in the third category I deemed "emission shell" and several examples are shown in Figure 7.4 These stars still show important spectral features, however, all examples show emission in the Hγ line and in the continuum, especially between 4490 and 4580 Å. The emission features of the "emission shell" stars line up with the absorption features of the "squarish" stars.

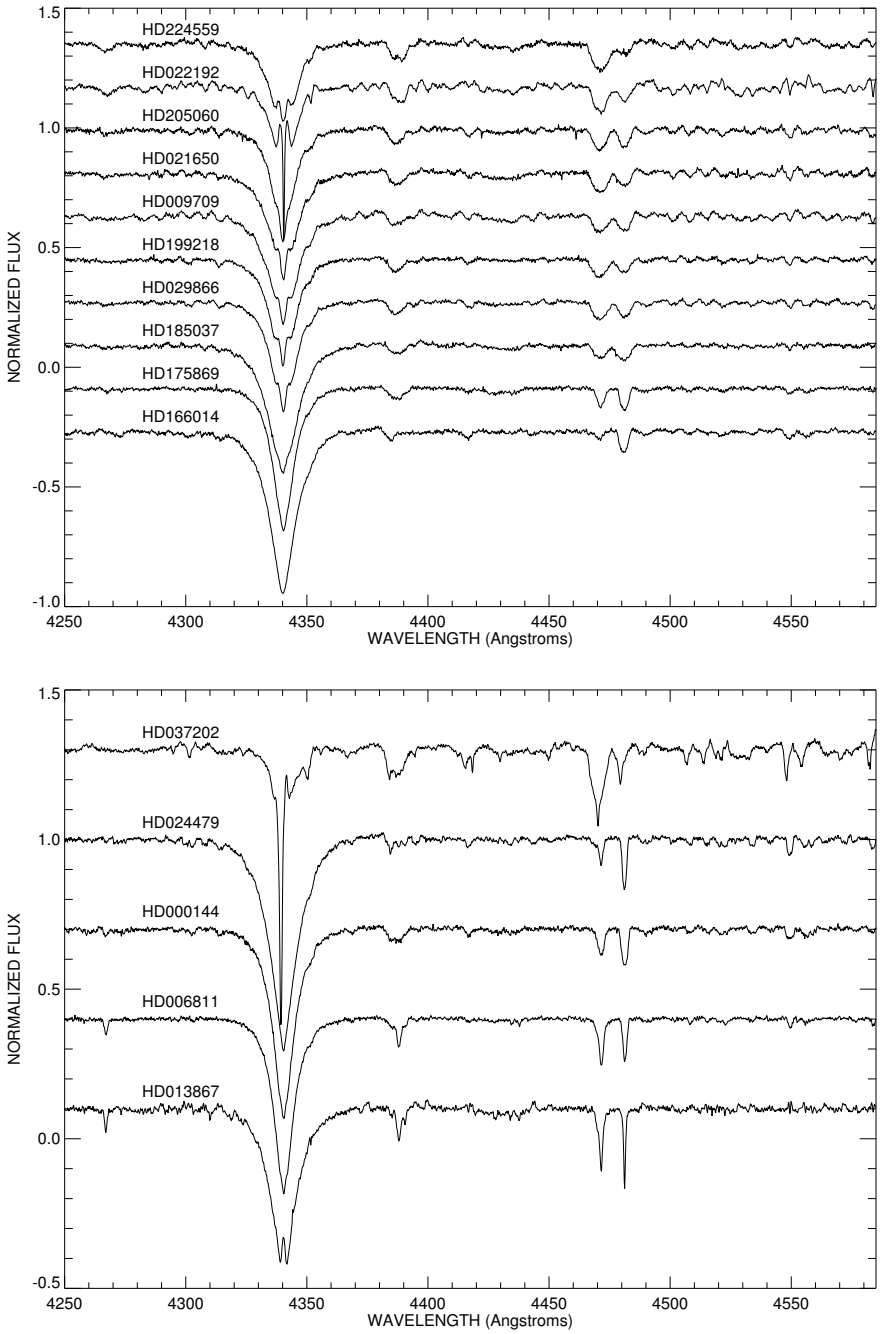

Figure 7.3: Individual spectra of some “squarish” stars - offset for clarity.

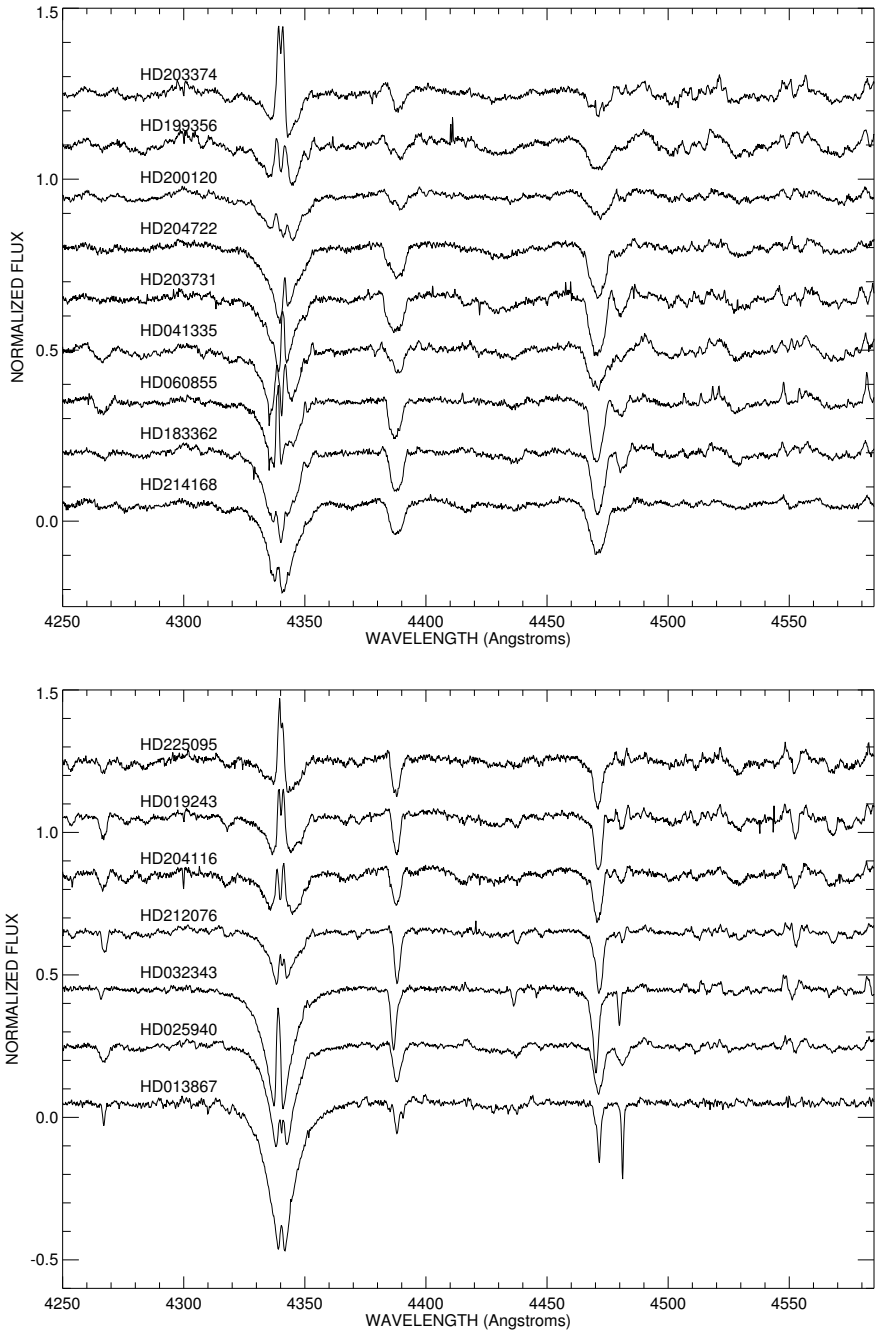

Figure 7.4: Individual spectra of some “emission shell” stars - offset for clarity.

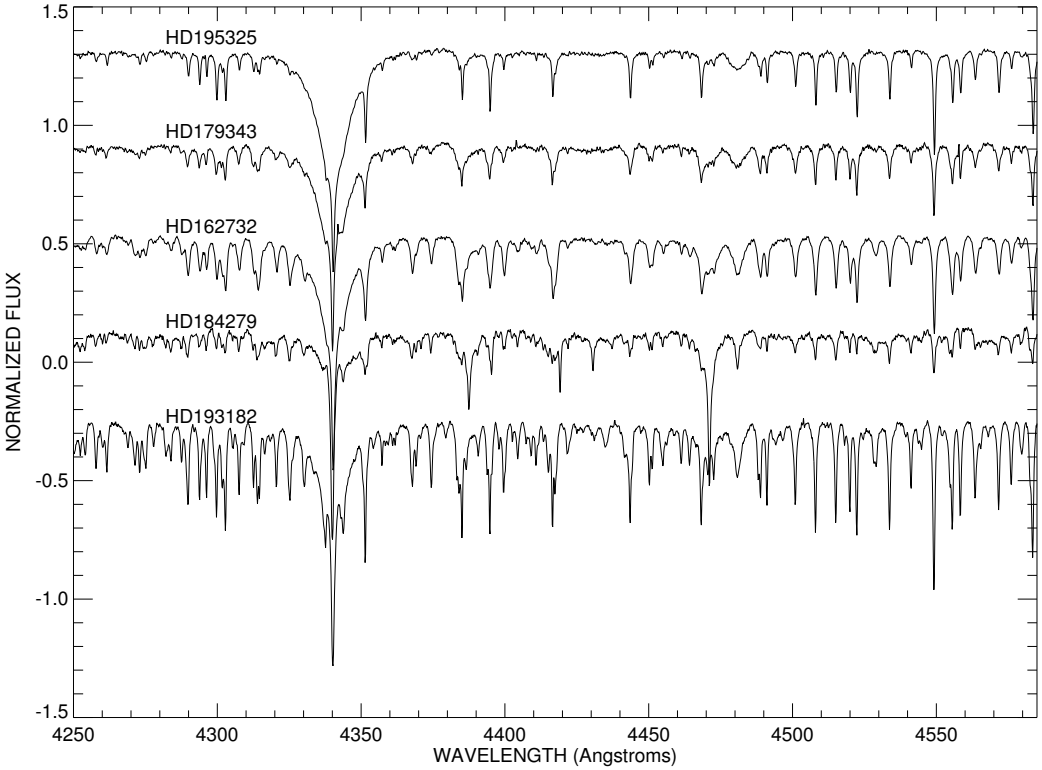

Figure 7.5: Individual spectra of some "shell" stars - offset for clarity.

The final category is "shell" stars. These stars have a distinctly different appearance from the other categories in that they exhibit "forests" of very sharp and deep absorption lines. "Shell" star examples are shown in Figure 7.5. While superficially these spectra look quite different, the "forest" of shell star lines matches perfectly with the features in the "squarish" and "emission shell" stars.

The common thread through all three not-"normal" categories is these lines are almost all produced by Fe II. The common explanation for such shell features is that we (the observers) are looking through some component of the circumstellar disk of the Be star - the more of the disk we look through, the more absorption there is. However, one must be cautious as stars at the cool end of the B-type and stars of the cooler A-type can produce this very same Fe II-dominated spectrum with very sharp

lines in their photospheres without having a circumstellar disk. The A supergiant Deneb is a good example of this phenomenon. Therefore, one must separate stars that exhibit shell features due to looking through a circumstellar disk and those that exhibit "shell" features produced in the photosphere. The emission shell features are likely produced by hot circumstellar material near the star (as it is moving fast as shown by the broadness of the features).

In Appendix C, I show a quadruple plot for every star in my 128-star sample. An example of such a plot is given in Figure 7.6. In the upper left is the Hα λ6563 line plotted in radial velocity space (the rest wavelength = 0 km s^{-1}). The upper line is the average spectrum from the 2004 observing run and is offset by 0.5 from the unit continuum for clarity. The lower line is the average from the 2006 observing run and is offset from the the continuum for clarity (the amount of the offset depends on the relative strength of emission/absorption between the 2004 and 2006 data). In the upper right, He I λ6678 is plotted against radial velocity. Again, the 2004 data are offset for clarity. In the lower left, the Hγ λ4340 is plotted. Again, the data for each run are averaged and then the plots offset for clarity. Finally, in the lower right, both He I λ4471 and Mg II λ4481 are plotted. The 0 km s^{-1} velocity is that of the rest wavelength of He I λ4471. Tick marks denote the rest wavelength of both ions (Mg II λ4481 is located at 654 km s^{-1} on this scale).

There are many versions of the IDL program to generate this plot. First, I had to determine if there were any stars that needed more attention than the program I originally wrote (*plot4all.pro* and *plot4.pro* in Appendix B). These stars were placed in a file with a comment on what needed to be "tweaked." After plotting the 104 "good" stars with a Post-Script-printing version of *plot4.pro*, I made a more interactive version of the program which allowed all four panels to be modified (*plot4tweakall.pro*).

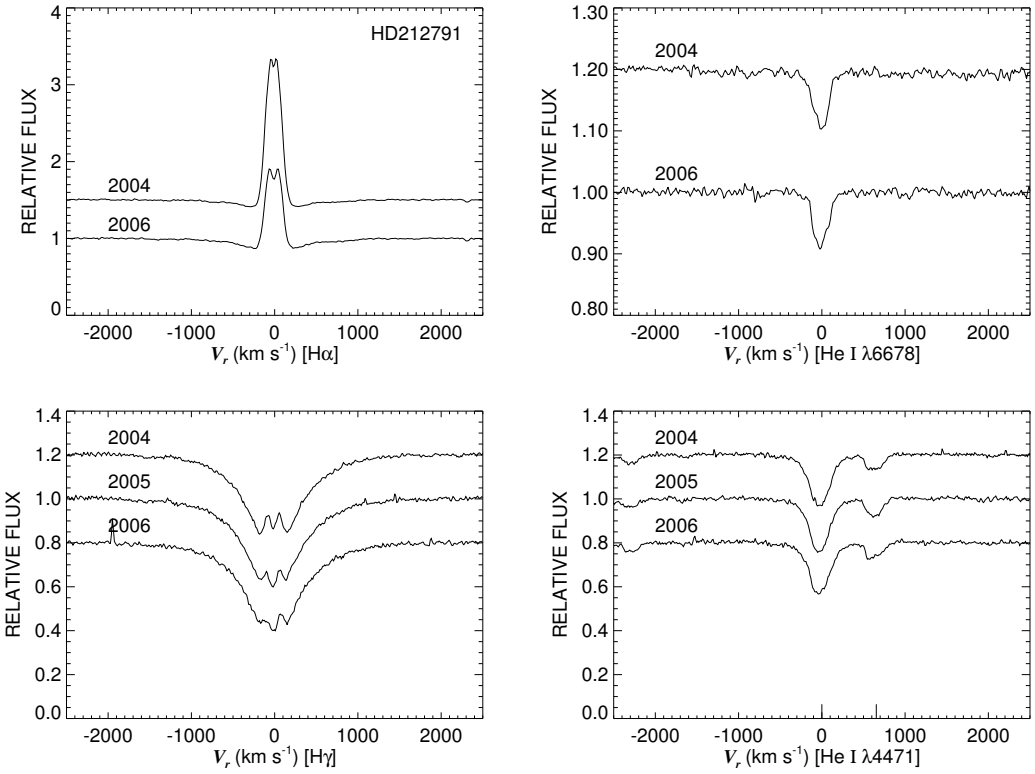

Figure 7.6: A quadruple plot as shown in Appendix C.

Certain stars described in Appendix C have more than just the quadruple plot. The spectra of these stars showed something interesting. For some stars, it was sufficient to show only the averages of each run to illustrate changes. But for other stars, it was very interesting to plot every spectrum I have. The various phenomena I found interesting were radial velocity shifts, line profile changes, and/or an increase/decrease in the strength of shell features. Such plots were generated using the programs *plotblue3eps.pro* and *plotblueps.pro*, which may be found in Appendix B

Each star also has a page of text associated with it. First, each star is given one or more labels. A "Classical Be Star" is defined in §7.1. Most of my sample has this label. Stars that do not show Hα emission at the times of my observation were put in the "NOT Be star" category after a literature search confirmed a lack of emission.

This label also can be "NOT Classical Be Star" for those stars that show emission but it is not from a decretion disk of a rapidly rotating B star. "Interacting Binary" stars are those that have references in the literature to active mass transfer. These stars often have a comparatively strange Hα emission profile. Stars I labeled "Non-Radial Pulsator" show the fast line profile variations indicative of non-radial pulsation. I added a question mark after this label for the stars I did not find references for in the literature but that I think exhibit NRP variations. "Shell Star" is used for those stars that show strong central absorption in Hα along with the Fe II shell features in absorption. These last two labels may be used in conjunction with other labels.

Of the 128 stars listed in Table 7.1, 110 are classical Be stars, nine do not seem to be Be stars at all, while two more are not classical Be stars. There are four definite and two likely interacting binaries and one star is a BeXRB. Three of the 110 currently show no emission but definitely have in the past. Twenty-one stars show evidence of non-radial pulsation (12 of those are ones I discovered). Eleven stars are labeled shell stars, however, many more stars have shell features but not the strong central absorption in Hα. Altogether, 85 of the 128 stars (66%) show Fe II shell features.

7.3 Measurements for B Star and Shell Features

For every spectrum, I measured various properties of selected lines. These measurements are found in Table C.1 for the red region and in Table C.2 for the blue region. In the red region, I measured Hα and He I λ6678. In the blue region, I measured Hγ, He I λ4471, and Mg II λ4481. As for the other important lines listed in Table 7.3, I did not measure them as they were unnecessary for my analysis (e.g., He I λ4387), they weren't recorded in all spectra (e.g., C II λ4267 in 2006), or were so temperature dependent that they appear only in a limited number of spectra (the Si III lines and

the red C II doublet).

7.3.1 Equivalent Width Measurements

For all five lines, I measured equivalent width (W_λ) and its associated error. Equivalent width is how much the flux of a spectral line deviates from the continuum over a certain range - it is like the "area under a curve." A positive value of equivalent width indicates the line is predominantly below the continuum (i.e., absorption) while a negative equivalent width value indicates an emission line. In the language of equations, equivalent width is

$$W_\lambda = \int_{\lambda_1}^{\lambda_2} \frac{F_c - F_\lambda}{F_c}\, \mathrm{d}\lambda = h_\lambda \sum_{j=1}^{M} \left[1 - \frac{F_j}{F_c}\right] \tag{7.1}$$

where F_c is the spectral flux of the continuum, F_λ is the spectral flux at the wavelengths measured, and λ_1 and λ_2 are the range of the spectral feature. Outside of λ_1 to λ_2, the spectral flux should be F_c. On the right, h_λ is the number of Ångstroms per pixel, M is the number of pixels over which equivalent width is measured, and (F_j/F_c) is the relative spectral flux at pixel j.

The total error (standard deviation) in equivalent width is (Chalabaev & Maillard 1983)

$$\sigma_T^2\left(W_\lambda\right) = \sum_{j=1}^{M} \left[\frac{\partial W_\lambda}{\partial F_j}\, \sigma\left(F_j\right)\right]^2 + \left[\frac{\partial W_\lambda}{\partial F_c}\, \sigma\left(F_c\right)\right]^2. \tag{7.2}$$

The partial derivative of equivalent width with respect to F_j is

$$\frac{\partial W_\lambda}{\partial F_j} = h_\lambda \left(0 - \frac{1}{F_c}\right) = -\frac{h_\lambda}{F_c}. \tag{7.3}$$

Because F_j appears in a single term of the sum (eq. 7.1), we do not need to take the derivative over the whole summation.

The partial derivative of equivalent width with respect to F_c

$$\frac{\partial W_\lambda}{\partial F_c} = h_\lambda \left(0 - \sum_{j=1}^{M} \frac{F_j}{F_c^2} \right) = \frac{1}{F_c} \left(\Delta\lambda - W_\lambda \right) \tag{7.4}$$

because we can re-work eq. 7.1 to find

$$h_\lambda \sum_{j=1}^{M} \frac{F_j}{F_c} = M h_\lambda - W_\lambda = \Delta\lambda - W_\lambda$$

where $\Delta\lambda$ is the range of wavelengths over which equivalent width is measured (equal to the step size h_λ times the number of points, M, in the range).

For the case where photon noise dominates (Chalabaev & Maillard 1983,eq. A9.5),

$$\sigma\left(F_j\right) = \left(\frac{F_j}{F_c} \right)^{1/2} \frac{F_c}{SNR} = \sigma_{cont} \left(\frac{F_j}{F_c} \right)^{1/2} F_c \tag{7.5}$$

where SNR is the signal-to-noise ratio which is the flux at the continuum divided by the standard deviation of the continuum (σ_{cont}). Therefore, since the continuum is rectified to 1.0, $SNR = 1/\sigma_{cont}$.

The uncertainty in the continuum flux is $\sigma(F_c) = \sigma_{cont}/\sqrt{N}$ where N is the number of effective points in the region used to make the rectification fit to the continuum. An upper limit on the number of points, N, is the number of pixels in the spectrum divided by the order of the fit used to rectify the continuum (in this case, the number of pixels is 2046 and we used a sixth-order fit). However, we cannot use this number as not all pixels in the spectrum were used in the fit (one does not include spectral features or points of high standard deviation). The number of points we used is a lower limit and is the wavelength range of the spectral feature divided by the number of Ångstroms per pixel all multiplied by 2 [$N = 2(\Delta\lambda/h_\lambda)$]. Points on both sides of the spectral feature are used to fit the region (which is the reason for the multiplicative factor of 2) and the fitted region relevant to the feature is akin to the size of the

feature.

The first term in eq. 7.2 using eq. 7.3 and 7.5 is

$$\begin{aligned}\sum_{j=1}^{M}\left[\frac{\partial W_\lambda}{\partial F_j}\,\sigma\left(F_j\right)\right]^2 &= \sum_{j=1}^{M}\left[-\left(\frac{h_\lambda}{F_c}\right)\sigma_{cont}\left(\frac{F_j}{F_c}\right)^{1/2}F_c\right]^2 \\ &= h_\lambda^2\,\sigma_{cont}^2\sum_{j=1}^{M}\frac{F_j}{F_c} = Mh_\lambda^2\,\sigma_{cont}^2\frac{\bar{F}_j}{\bar{F}_c} \\ &= h_\lambda\,\sigma_{cont}^2\left(\Delta\lambda - W_\lambda\right) \qquad (7.6)\end{aligned}$$

where

$$\frac{\bar{F}_c}{\bar{F}_j} = \frac{1}{M}\sum_{j=1}^{M}\frac{F_j}{F_c} = \frac{1}{Mh_\lambda}\left(\Delta\lambda - W_\lambda\right).$$

Therefore, substituting eq. 7.4, 7.6, and that for $\sigma(F_c)$ into eq. 7.2 and setting $F_c = 1$ (as it is in our spectra),

$$\begin{aligned}\sigma_T^2\left(W_\lambda\right) &= h_\lambda\,\sigma_{cont}^2\left(\Delta\lambda - W_\lambda\right) + \left[\frac{1}{F_c}\left(\Delta\lambda - W_\lambda\right)\frac{\sigma_{cont}}{\sqrt{N}}\right]^2 \\ &= \sigma_{cont}^2\left(\Delta\lambda - W_\lambda\right)\left(h_\lambda + \frac{\Delta\lambda - W_\lambda}{N}\right). \qquad (7.7)\end{aligned}$$

The equivalent width is sensitive to the range over which one determines it. Both Hα and Hγ are quite broad, therefore the ranges of these lines are quite large. The Hα range is from 6523 to 6607 Å (-1800 to $+2012$ km s^{-1} in velocity space). The range is asymmetric about the line due to the Fe II λ6516 feature, which is often seen in broad emission in my sample. The Hγ range is from 4311 to 4369 Å (-2006 to $+2006$ km s^{-1} in velocity space). One caveat to measuring equivalent width is that the measurement includes everything in the given range, including other absorption/emission lines and glitches. Therefore, one must examine both the equivalent width and the spectral

profile to know if the value has merit. This is especially important in stars with a very large number of shell lines.

7.3.2 Wing Bisector Measurements

As the majority of the hydrogen lines in my sample are "contaminated" by distinctly non-Gaussian shaped emission, calculating the radial velocity with the traditional method of fitting a Gaussian function to the feature would not work. As in previous chapters (2, 5, and 6), I determined the radial velocity shift of the wings of the hydrogen lines. The wings sample the fastest-moving gas (i.e., gas closest to the star) which should be moving with the star if it is a member of a binary system. The method of measuring the wing bisector position and its errors are described in Appendix A. The range of these measurements is very specific and I wrote a program to find ranges for both Hα and Hγ and output them to a file (using the IDL programs *checkhydrange.pro* and *checkhydrangeindiv.pro* in App. B). The wing velocity method assumes the feature is an emission line; therefore absorption lines had to be artificially inverted. In most Hα cases, there was no inversion as the emission lines were very strong, although there were a few requiring inversion (especially the stars I determined are not Be stars). In most Hγ cases, I inverted the line. In both lines, there were cases where there was some emission in the absorption line (see, for example, Figs. C.1, C.2, and C.5). I inverted those as well.

For the hydrogen lines, only measurements of equivalent width and wing velocity are required. Other effects such as pressure and Stark broadening render these lines useless for determining rotational broadening. To carry out the measurements, I used the IDL programs *measurehydchop.pro*, *measurehydindiv.pro*, *measurehyderr.pro*, and *hydchop.pro* (all found in App. B). Because there were many absorption lines that were partially filled in with emission and there were certain shell stars that had

very deep self-absorption in the middle of the emission, I occasionally had to excise such features via linear interpolation, as the wing velocity program would determine incorrect values. In the course of determining bisector error, one needs to know the error in the continuum. Therefore, I utilized the continuum just outside of the equivalent width range but had to check all regions for glitches or other lines.

7.3.3 First Moment Measurements

The three other lines (He I λ6678, He I λ4471, and Mg II λ4481) were almost always found in absorption and are useful for determining rotational broadening. Therefore, measurements for these three lines were made using different methods than for the hydrogen lines. The most common method for determining the radial velocity shift of a spectral line is to fit a Gaussian function to it and determine the shift of the center of the fit from the rest wavelength of the line. However, the Gaussian-fit method imposes a shape to the line and many of the lines found in this sample are not necessarily Gaussian. Therefore, I determined the statistical centroid, or first moment ($V1$), of the line. The first moment is found by taking the sum of the flux of the spectral feature at a velocity times that velocity. Because this results in both positive and negative numbers, the summation will give the central velocity of the feature. The equation for the first moment is

$$V1 = \frac{\int_{\lambda_1}^{\lambda_2} v \left(1 - \frac{F_\lambda}{F_c}\right) \, \mathrm{d}\lambda}{\int_{\lambda_1}^{\lambda_2} \left(1 - \frac{F_\lambda}{F_c}\right) \, \mathrm{d}\lambda} = \frac{h_\lambda}{W_\lambda} \sum_{j=1}^{M} v_j \left(1 - \frac{F_j}{F_c}\right) \tag{7.8}$$

where v is the velocity relative to the rest wavelength and v_j is that for pixel j.

As with the error in equivalent width (eq. 7.2), the error (standard deviation) in the first moment is

$$\sigma_T^2 \left(V1\right) = \sum_{j=1}^{M} \left[\frac{\partial V1}{\partial F_j} \, \sigma\left(F_j\right)\right]^2 + \left[\frac{\partial V1}{\partial F_c} \, \sigma\left(F_c\right)\right]^2 . \tag{7.9}$$

The partial derivative of the first moment with respect to F_j is

$$\frac{\partial V1}{\partial F_j} = \frac{h_\lambda}{W_\lambda}\left(0 - \frac{v_j}{F_c}\cdot 1\right) = -\frac{h_\lambda}{W_\lambda}\frac{v_j}{F_c}. \tag{7.10}$$

The partial derivative of the first moment with respect to F_c is

$$\frac{\partial W_\lambda}{\partial F_c} = \frac{h_\lambda}{W_\lambda}\left(0 + \sum_{j=1}^{M} v_j\ \frac{F_j}{F_c^2}\right) = -\frac{V1}{F_c} \tag{7.11}$$

because (as for equivalent width) we can re-work eq. 7.8 to find:

$$\sum_{j=1}^{M} v_j\ \frac{F_j}{F_c} = \sum_{j=1}^{M} v_j - \frac{W_\lambda}{h_\lambda}\ V1 = -\frac{W_\lambda}{h_\lambda}\ V1$$

because v_j is symmetric about $v = 0$ (therefore the sum over all v_j is 0).

The errors in F_j and F_c are both the same as for equivalent width.

The first term in eq. 7.9 using eq. 7.5 and 7.10 is:

$$\begin{aligned}
\sum_{j=1}^{M}\left[\frac{\partial V1}{\partial F_j}\ \sigma\left(F_j\right)\right]^2 &= \sum_{j=1}^{M}\left[-\frac{h_\lambda}{W_\lambda}\ \frac{v_j}{F_c}\ \sigma_{cont}\left(\frac{F_j}{F_c}\right)^{1/2} F_c\right]^2 \\
&= \left(\frac{h_\lambda}{W_\lambda}\right)^2 \sigma_{cont}^2 \sum_{j=1}^{M} v_j^2\ \frac{F_j}{F_c} \\
&= \left(\frac{h_\lambda}{W_\lambda}\right)^2 \sigma_{cont}^2\ \frac{2}{3}\ \frac{\left(v_{max} - V1\right)^3}{h_v}
\end{aligned} \tag{7.12}$$

because $v_j^2 F_j$ is really only important in the wings of the line where $F_j \approx 1$ and $|v_j|$ is large. Therefore,

$$\sum_{j=1}^{M} v_j^2\ \frac{F_j}{F_c} \approx h_v \sum_{j=1}^{M} v_j^2 = \int_{-v_{max}}^{v_{max}} \left(v_j - V1\right)^2\ \mathrm{d}v = \frac{2}{3}\ \left(v_{max} - V1\right)^3$$

where h_v is the Doppler velocity shift per pixel step and $V1$ must be included for symmetry.

Substituting everything into eq. 7.9 and setting F_c to 1,

$$\sigma_T^2\left(V1\right) = \left(\frac{h_\lambda}{W_\lambda}\right)^2 \sigma_{cont}^2 \ \frac{2}{3} \ \frac{\left(v_{max} - V1\right)^3}{h_v} + \frac{\sigma_{cont}^2}{N} \ V1^2. \tag{7.13}$$

7.3.4 Second Moment Measurements

Another useful measurement is the FWHM of the line. Such a measurement in velocity space is related to the projected rotational velocity of the star ($V \sin i$). However, FWHM is a measurement of the full-width at half- maximum of a Gaussian profile and I did not assume a Gaussian shape for the lines. The second moment ($V2$) of the line is a summation of the flux of the feature at a certain velocity times that velocity squared. The equation for the second moment is

$$V2 = \frac{\int_{\lambda_1}^{\lambda_2} (v - \bar{v})^2 \left(1 - \frac{F_\lambda}{F_c}\right) \ \mathrm{d}\lambda}{\int_{\lambda_1}^{\lambda_2} \left(1 - \frac{F_\lambda}{F_c}\right) \ \mathrm{d}\lambda} = \frac{h_\lambda}{W_\lambda} \sum_{j=1}^{M} (v_j - V1)^2 \left(1 - \frac{F_j}{F_c}\right). \tag{7.14}$$

We can liken $V2$ to the FWHM of a Gaussian by using

$$V2 = \frac{\int \left(x - \mu\right)^2 \frac{1}{\sigma\sqrt{2\pi}} \exp\left(-\frac{1}{2}\frac{x-\mu}{\sigma}^2\right) \ \mathrm{d}x}{\int \frac{1}{\sigma\sqrt{2\pi}} \exp\left(-\frac{1}{2}\frac{x-\mu}{\sigma}^2\right) \ \mathrm{d}x} = \sigma^2$$

where σ is related to the Gaussian FWHM by $FWHM = 2.354\sigma$. Therefore, the Gaussian equivalent full width of the second moment at half-maximum ($FWSM$) is $FWSM = 2.354\sqrt{V2}$.

As with the error in equivalent width (eq. 7.2) and V1 (eq. 7.9), the error (standard deviation) in the second moment is

$$\sigma_T^2\left(V2\right) = \sum_{j=1}^{M} \left[\frac{\partial V2}{\partial F_j} \ \sigma\left(F_j\right)\right]^2 + \left[\frac{\partial V2}{\partial F_c} \ \sigma\left(F_c\right)\right]^2. \tag{7.15}$$

The partial derivative of the second moment with respect to F_j is

$$\frac{\partial V2}{\partial F_j} = \frac{h_\lambda}{W_\lambda} \left(v_j - V1\right)^2 \left(0 - \frac{1}{F_c}\right) = -\frac{h_\lambda}{W_\lambda} \frac{\left(v_j - V1\right)^2}{F_c}. \tag{7.16}$$

The partial derivative of the second moment with respect to F_c is

$$\frac{\partial V2}{\partial F_c} = \frac{h_\lambda}{W_\lambda} \sum_{j=1}^{M} (v_j - V1)^2 \ \frac{F_j}{F_c} \frac{1}{F_c} = \frac{2}{3} \ \frac{h_\lambda}{W_\lambda} \ \frac{(v_{max} - V1)^3}{h_v} - V2 \tag{7.17}$$

because we can re-work eq. 7.14 to find

$$\begin{aligned} V2 &= \frac{h_\lambda}{W_\lambda} \left[\sum_{j=1}^{M} (v_j - V1)^2 - \sum_{j=1}^{M} (v_j - V1)^2 \ \frac{F_j}{F_c} \right] \\ \sum_{j=1}^{M} (v_j - V1)^2 \ \frac{F_j}{F_c} &= \frac{2}{3} \ \frac{(v_{max} - V1)^3}{h_v} - \frac{W_\lambda}{h_\lambda} \ V2 \end{aligned}$$

if we again assume the line wings are the most interesting and we set F_c equal to 1.

The first term in eq. 7.15 using eq. 7.5 and 7.16 is

$$\begin{aligned} \sum_{j=1}^{M} \left[\frac{\partial V2}{\partial F_j} \ \sigma(F_j) \right]^2 &= \sum_{j=1}^{M} \left[-\frac{h_\lambda}{W_\lambda} \ \frac{(v_j - V1)^2}{F_c} \ \sigma_{cont} \left(\frac{F_j}{F_c} \right)^{1/2} F_c \right]^2 \\ &= \left(\frac{h_\lambda}{W_\lambda} \right)^2 \sigma_{cont}^2 \sum_{j=1}^{M} (v_j - V1)^4 \ \frac{F_j}{F_c} \\ &= \left(\frac{h_\lambda}{W_\lambda} \right)^2 \sigma_{cont}^2 \ \frac{2}{5} \ \frac{(v_{max} - V1)^5}{h_v} \end{aligned} \tag{7.18}$$

because $(v_j - V1)^4 F_j$ is really only important in the wings of the line where $F_j \approx 1$ and where $V1$ is negligible compared to v_j. Therefore,

$$\sum_{j=1}^{M} (v_j - V1)^4 \ \frac{F_j}{F_c} \approx h_v \sum_{j=1}^{M} (v_j - V1)^4 = \int_{-v_{max}}^{v_{max}} (v_j - V1)^4 \ \mathrm{d}v = \frac{2}{5} \ (v_{max} - V1)^5 .$$

Substituting everything into eq. 7.15 and setting F_c to 1,

$$\sigma_T^2(V2) = \left(\frac{h_\lambda}{W_\lambda} \right)^2 \sigma_{cont}^2 \ \frac{2}{5} \ \frac{(v_{max} - V1)^5}{h_v} + \frac{\sigma_{cont}^2}{N} \left(\frac{2}{3} \frac{h_\lambda}{W_\lambda} \frac{(v_{max} - V1)^3}{h_v} - V2 \right)^2 . \tag{7.19}$$

The corresponding error in the $FWSM$ is found by taking the derivative of $FWSM = 2.354\sqrt{V2}$. Therefore

$$\sigma_T\,(FWSM) = \frac{2.354}{2}\ \frac{\sigma_T\,(V2)}{\sqrt{V2}}. \tag{7.20}$$

The first and second moments are very sensitive to the range one chooses. For instance, if there is a deviation from the continuum relatively far from the central wavelength, then even though the flux at that point may be small, the velocity is large and the statistical centroid is moved toward that discrepant point. Due to this consideration, I had to chose the measurement ranges very carefully and I developed the programs *checkabsrange.pro* and *checkabsrangeindiv.pro* (available in App. B) to loop through the spectra and output the ranges to files. Generally, the range for He I λ6678 was 6661 to 6687 Å (-404 to $+404$ km s^{-1} in velocity space). For He I λ4471 and Mg II λ4481, because they are so close, they often shared an upper and lower boundary (respectively). The respective default ranges were 4464 to 4477 Å and 4477 to 4485 Å (-469 to $+402$ km s^{-1} and -250 to $+267$ km s^{-1} in the appropriate velocity spaces). Once each spectrum had the appropriate range, I then used *measureallabs.pro* and *measureallabsindiv.pro* to determine the values (these programs and the companion programs *measureprofile.pro* and *measureproferr.pro* are in App. B).

7.3.5 The Line Measurements

All aforementioned measurements may be found in Table C.1 for the red spectra and in Table C.2 for the blue spectra, both in Appendix C. Table C.1 lists the star name and the date of observation in the first two columns. The next two columns (3 and 4) contain measurements and associated errors for Hα equivalent widths and wing velocities. The next three columns (5, 6, and 7) contain He I λ6678 information in the

form of equivalent widths, radial velocities (found via the first moment method), and $FWSM$ measurements. I did not include the actual values for the second moment ($V2$) as $FWSM$ provides the relevant information. Table C.2 also lists the star name and the date of observation in columns 1 and 2. Columns 3 and 4 again list data for the hydrogen line, this time Hγ equivalent widths and wing velocities. The next three columns (5, 6, and 7) show data for He I λ4471 (equivalent width, $V1$ radial velocities, and $FWSM$ respectively) and the last three columns (8, 9, and 10) show the same for Mg II λ4481. These tables were created using the IDL program *tablemake.pro* (found in App. B).

7.3.6 Shell Line Measurements

As mentioned in §7.2.3, the blue spectra of the survey sample may be grouped according to the amount and nature of shell features ("squarish," "emission shell," and "shell"). These shell features are mostly Fe II lines. The spectrum of the star Deneb (classification A2 Iae) is a good example of these photospheric iron features and it is plotted along with three representative stars ("emission shell," "squarish," and "shell") in Figure 7.7. This spectrum of Deneb was obtained from the on-line archive of high resolution spectra made with the ELODIE spectrograph and 1.93 m telescope at the Observatoire de Haute Provence, France[4]. It was smoothed to the resolution of the coudé feed spectra and resampled on my observed wavelength grid.

Each blue region stellar spectrum in the sample was cross-correlated with the spectrum of Deneb using the IDL program *fe2fits.pro*. For all but five stars, I used the region from 4490 to 4580 Å to cross-correlate the target and Deneb spectra. For the remaining five stars, I also included a region from 4400 to 4450 Å. Example cross-correlation functions (CCFs) for the three example stars are shown in Figure 7.8. One

[4]http://atlas.obs-hp.fr/elodie/

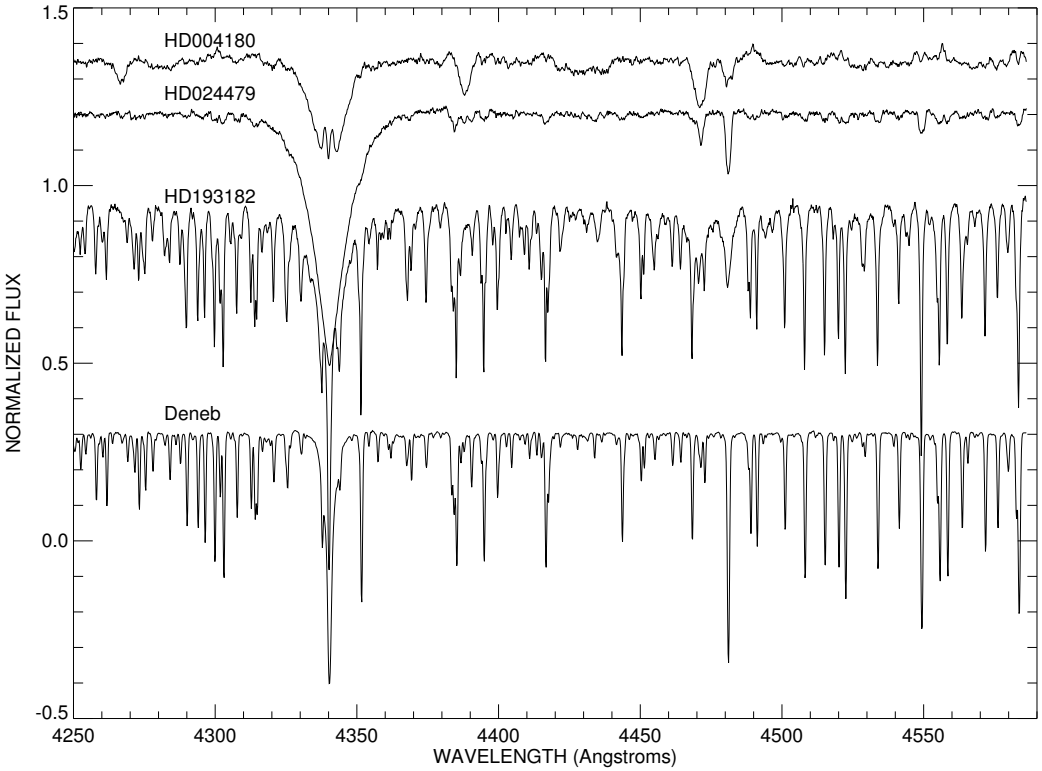

Figure 7.7: Comparison of three stars in each of the categories of "emission shell," "squarish," and "shell" with Deneb. Each spectrum is offset for clarity.

may observe that the ccf takes on the appearance of spectral lines in the corresponding category - HD004180 is "emission shell" and the CCF looks like a double-hump, HD024479 is "squarish" and the CCF looks like a small absorption line, and HD193182 is "shell" so the CCF looks like a very deep absorption line. For both the "squarish" and "shell" stars, oftentimes there were aliases around ± 500 km s^{-1} as there are so many lines closely spaced, shifting a little gives almost as good a fit as the correct fit.

In order to characterize the shell features, I measured the equivalent width in km s^{-1} (as there is no single central wavelength), the first moment ($V1$), and the $FWSM$ of the ccf. These measurements are given in Table C.3 in Appendix C. Columns 1 and 2 give the star name and the date of observation. Examining the equivalent width of the ccf (col. 3) gives clues to the category. For instance, a negative

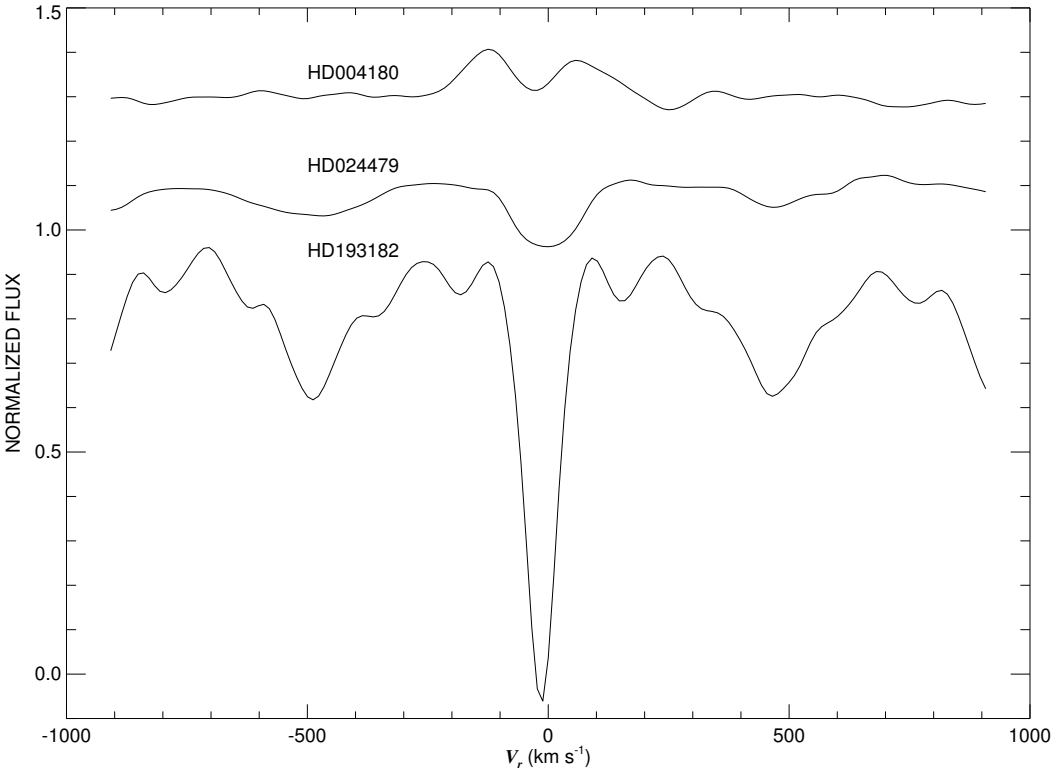

Figure 7.8: The cross-correlation function between Deneb and the same three stars as shown in Fig. 7.7. They are offset for clarity.

W_λ indicates the star is "emission shell" while a large W_λ (>35 km s^{-1}) may put it in the "shell" category as opposed to the smaller-featured "squarish" category. If there is no indication of shell features, there will be no measurement for W_λ. Surprisingly, only 43 stars in my 128 star sample showed no detectable shell features in the cross-correlation function. Three of those 43 are interacting binaries that do have shell features, but they are not all from Fe II and the cross-correlation result is ambiguous (it would be a flat line in Fig. 7.8). Examining the radial velocity of the ccf (col. 4), as with all other examinations of radial velocity, assists in determining duplicity. Should the shell features shift in the same manner as the other lines measured, then the shell is moving with the Be star. However, the spectrum could be a composite of two stars in a binary system, one Be and one A-type (or other type) star and the shell will move

differently from the Be star. Examining the $FWSM$ (col. 5) in tandem with the other measurements can provide insight into the narrowness of the features. Table C.3 was generated using the IDL program *tablemakefe.pro* found in Appendix B.

7.4 Correcting for Photospheric Absorption Components

Most of the targets have Balmer profiles that are a composite of disk emission and photospheric absorption. To fully understand the changes in Be stars, one must correct for the photospheric absorption underlying the emission. The cooler the star, the deeper the hydrogen lines. The theoretical relationship between equivalent width and effective temperature is shown in Figure 7.9.

The *dotted lines* are for Hα and the *solid lines* are for Hγ. The *top line* of each pair shows the relationship for $\log g = 4.0$ and the *lower line* represents $\log g = 3.5$. The theoretical equivalent widths were measured using the same range as the observations, and like the observations, they include any line blends present. For instance, the hump around $T_{\rm eff} \approx 25$ kK indicates the appearance of strong O II absorption lines near Hγ. The models for $\log g = 3.5$ and 4.0 and $T_{\rm eff} > 15$ kK are the synthetic spectra based on non-LTE, line blanketed models by Lanz & Hubeny (2007). For temperatures below 15 kK, I used synthetic spectra from the LTE, line blanketed models published by Martins et al. (2005b). In some cases, the predicted equivalent widths at 15 kK differ by as much as 10% between the models, and rather than introduce a discontinuity at this temperature, I multiplied each predicted equivalent width from the Martins et al. results by a factor to maintain equality at $T_{\rm eff} = 15$ kK.

Corrections for the underlying absorption should really include a term to account for the dilution of the spectral intensities by any continuum light from the disk. Let

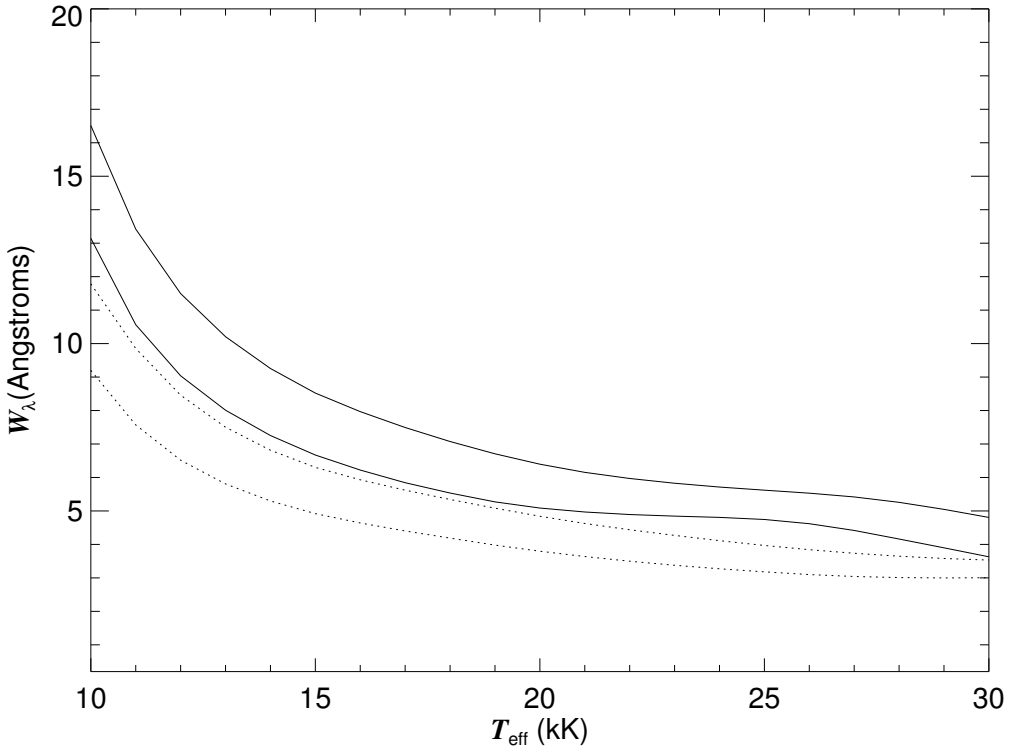

Figure 7.9: The correction for underlying photospheric absorption equivalent width of the hydrogen lines versus effective temperature of the star from Table 7.1. The two *solid lines* are relations for Hγ and the two *dotted lines* are relations for Hα. The *lower* of each of the pairs of curves represents corrections for stars with $\log g = 3.5$ while the *upper* is that for $\log g = 4.0$.

$\epsilon = F_d/F_s$, the ratio of disk to stellar flux. Then the corrected equivalent width is

$$W'_\lambda = (1+\epsilon)W_\lambda(\text{obs}) - W_\lambda(\text{model}).$$

Attempts to estimate ϵ from the equivalent widths of the absorption lines were inconclusive due to the uncertain emission filling conditions for these lines, and therefore I will assume $\epsilon = 0$ in what follows. However, by making this assumption, I will probably underestimate the actual emission equivalent width for those stars with the brightest disks and greatest Hα emission strength.

The error for the corrected equivalent width W'_λ includes the weighted error for the observations from each year plus an error based upon a 10% uncertainty in $T_{\rm eff}$

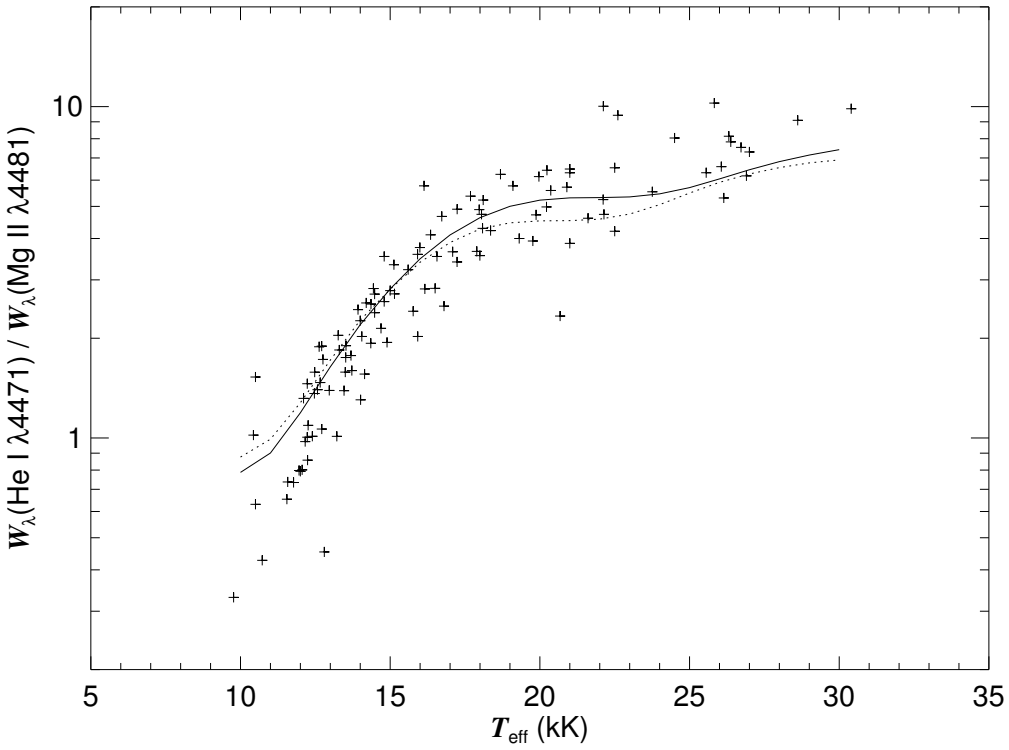

Figure 7.10: The ratio of the equivalent widths of the temperature dependent species He I λ4471 and Mg II λ4481 versus effective temperature of the star. The *solid line* is the theoretical relation for $\log g = 4.0$ and the *dotted line* is that for $\log g = 3.5$.

and a 0.25 dex uncertainty in $\log g$.

One may ask if this 10% uncertainty in $T_{\rm eff}$ is reasonable. Both He I λ4471 and Mg II λ4481 are sensitive to temperature; the magnesium line strength decreases as temperature increases and the helium line strength increases with increasing temperature up to about B2 then starts to decrease toward the O stars. Therefore, the ratio of the equivalent widths of the two lines may be used as a temperature gauge. Figure 7.10 shows this relationship for my sample. The model relationships for $\log g = 3.5$ and 4.0 are also plotted (the *dotted* and *solid* lines, respectively). The flatter region around 20 kK is where the helium line strength peaks and then begins to decrease. One must be aware of the uncertainties that appear in this diagram. In

Be stars, the helium line often gets filled in with emission (moreso for He I λ6678) and especially in stars with shell features, magnesium may develop emission. An example is HD 218393 = KX And, an interacting binary (the low point in the diagram). The magnesium line in its spectrum is too strong due to the influence of the cooler, mass-transferring binary companion. Despite these uncertainties, my sample stars show good agreement with the models and the 10% uncertainty in $T_{\rm eff}$ seems reasonable.

Table 7.4 gives the average measurements of W'_λ for each star for each of the observing runs. I chose to report averages as none of the sample stars show large equivalent width variations within a run. Column 1 gives the HD number of the star. The next two columns give information for Hα, first the corrected equivalent width and its error for 2004 and then the same for 2006. In the middle three columns, I give W'_λ and error for Hγ for the three runs (2004, 2005, 2006). The final three columns are for the equivalent width and error of the Fe II cross-correlation functions. These are not corrected as photospheric contributions will only be significant for the coolest B stars. In the case of the hydrogen lines, the value for W'_λ should never be positive as that would mean there is additional absorption the line. Therefore, any positive value indicates an incorrect temperature or gravity or perhaps a companion adding more equivalent width.

With corrected equivalent width in hand, one may ask several questions. First, how does Hγ emission vary with Hα emission? For stars with little to no shell features ($|W_\lambda$(Fe II)| less than 10 km s^{-1}), the relationship is shown in the upper panel of Figure 7.11. The different symbols denote different temperature groups (*diamonds* for greater than 18 kK, *plus signs* for less than 18 kK). In general, the trend is the more Hα emission, the more Hγ emission. The same relationship for stars with strong shell features ($|W_\lambda$(Fe II)| greater than 10 km s^{-1}) is shown in the lower panel of Figure 7.11. This plot shows no trend. The primary reason for this is that shell

features affect the equivalent width of Hγ more than that of Hα. One interesting thing to note is that none of the hotter shell stars have W'_λ(Hα) less than 12 Å.

A second question one may ask is how does the strength of the shell features change with W'_λ(Hα)? The equivalent width of the Fe II cross-correlation function is plotted against the corrected equivalent width of Hα in Figure 7.12. There are stars with no shell features at every Hα equivalent width. There are also some stars with some kind of shell features at nearly every Hα equivalent width. However, there are obvious regions with no data in this plot - shell absorption for large Hα equivalent width and shell emission at small Hα equivalent widths. The one large shell absorption with large W'_λ(Hα) is for the 2004 measurement for HD184279 (see Fig. C.87). Otherwise, if the star has copious shell absorption, it generally does not have large equivalent width. One reason for this may be that in order to have a very large equivalent width, one must see a great deal of surface area of the disk (it must be inclined so it is mostly face-on). As shell absorption is caused by looking through the disk at low inclination, the projected surface area of the disk must be relatively small. Therefore, one would not expect that very strong shell absorption would have very large Hα equivalent width. In order to have shell emission, one cannot be looking directly through the disk, therefore the observed surface area of the disk will naturally be larger and the equivalent width can be greater or the disk density needs to be large to create Fe II emission and if so, then the Hα emission will also be strong.

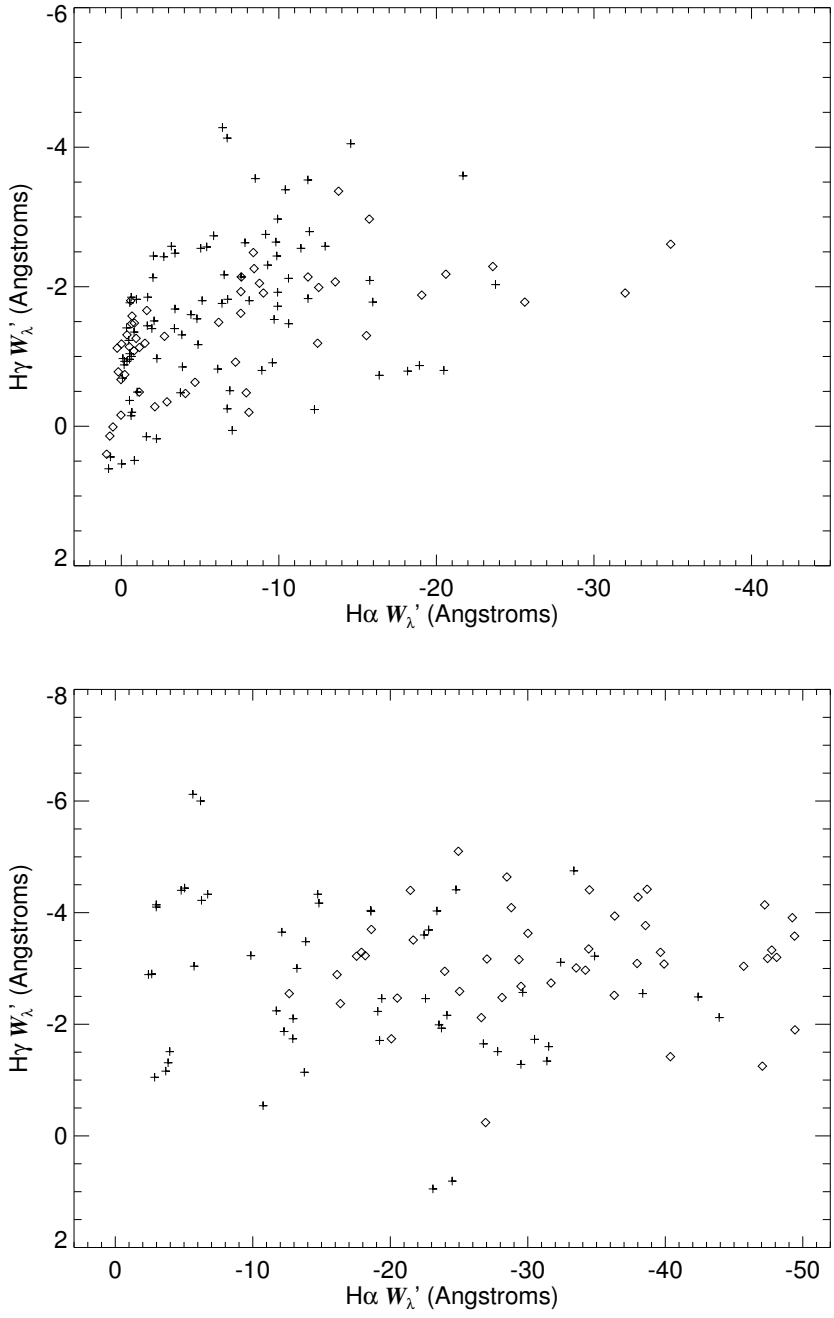

Figure 7.11: The relationship between the equivalent width of Hγ and the equivalent width of Hα. *Diamonds* denote hotter stars (greater than 18 kK) and *plus signs* signify cooler stars (less than 18 kK). The top panel is for stars that had an equivalent width of the Fe II lines cross-correlation function of less than $|10|$ km s^{-1} (i.e., non-shell stars). The bottom panel is for stars that had an equivalent width of the Fe II lines cross-correlation function of greater than $|10|$ km s^{-1} (i.e., shell stars).

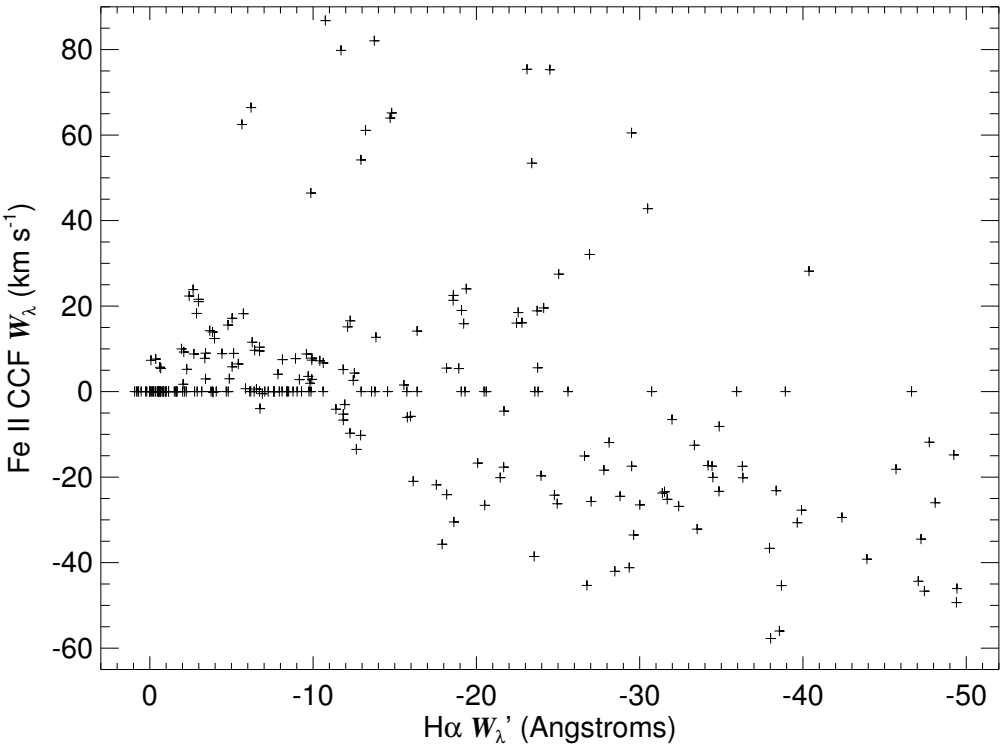

Figure 7.12: The equivalent width of the Fe II fitting cross-correlation function versus corrected Hα equivalent width.

Table 7.4: Average Corrected Equivalent Width Measurements For Each Run

	Hα W'_λ [Å]		Hγ W'_λ [Å]			Fe II CCF $W\lambda$ [km s^{-1}]		
Star	2004	2006	2004	2005	2006	2004	2005	2006
HD000144	-3.7 ± 1.1	-2.9 ± 1.1	-1.2 ± 1.5	-1.1 ± 1.6	-1.1 ± 1.5	14.2 ± 1.4	17.2 ± 0.2	18.3 ± 0.5
HD004180	-34.9 ± 0.6	-38.4 ± 0.7	-3.2 ± 0.8	-3.1 ± 0.8	-2.5 ± 0.8	-23.3 ± 3.0	-22.0 ± 0.9	-23.2 ± 0.9
HD005394	-34.5 ± 0.7	-36.3 ± 0.5	-4.4 ± 0.6	-4.4 ± 0.6	-3.9 ± 0.6	-20.1 ± 1.3	-18.9 ± 0.6	-20.1 ± 0.1
HD006811	-5.1 ± 0.9	-4.4 ± 0.9	-1.8 ± 1.3	-1.7 ± 1.3	-1.6 ± 1.3	8.9 ± 0.6	8.6 ± 0.7	8.9 ± 0.4
HD007636	-49.4 ± 0.4	-47.1 ± 0.2	-1.9 ± 0.6	-2.4 ± 0.6	-1.2 ± 0.6	-46.1 ± 0.3	-44.6 ± 0.3	-44.4 ± 1.2
HD009709	-19.1 ± 0.9	-23.7 ± 0.9	-2.2 ± 1.2	-2.3 ± 1.2	-1.9 ± 1.2	19.0 ± 0.7	20.1 ± 0.5	18.9 ± 0.7
HD010516	-45.7 ± 0.8	-34.9 ± 0.5	-3.0 ± 0.4	-3.0 ± 0.4	-2.6 ± 0.4	-18.2 ± 4.6	-9.8 ± 0.5	-8.2 ± 0.7
HD011415	-0.5 ± 0.6	-0.1 ± 0.7	-1.0 ± 0.9	-1.0 ± 0.9	-1.0 ± 0.9	···	···	···
HD013661	-32.0 ± 0.5	-25.6 ± 0.5	-1.9 ± 0.4	-1.8 ± 0.5	-1.8 ± 0.4	-6.5 ± 0.7	···	···
HD013867	-11.8 ± 1.0	-12.9 ± 1.0	-1.8 ± 1.3	-1.6 ± 1.3	-1.7 ± 1.3	-5.3 ± 1.5	-11.6 ± 1.1	-10.2 ± 0.7
HD018552	-18.9 ± 0.9	-18.2 ± 0.9	-0.9 ± 1.3	-0.9 ± 1.3	-0.8 ± 1.3	5.4 ± 0.6	5.9 ± 0.3	5.5 ± 1.2
HD019243	-49.4 ± 0.3	-47.4 ± 0.7	-3.6 ± 0.2	-3.6 ± 0.2	-3.2 ± 0.2	-49.3 ± 0.6	-48.5 ± 0.8	-46.7 ± 1.2
HD020134	-1.1 ± 0.5	-0.2 ± 0.5	-1.1 ± 0.7	-1.0 ± 0.6	-0.7 ± 0.6	···	···	···
HD020336	-12.5 ± 0.7	-16.4 ± 0.7	-2.0 ± 0.8	-2.5 ± 0.8	-2.4 ± 0.8	4.3 ± 0.5	13.5 ± 0.2	14.2 ± 1.1
HD020418	-0.6 ± 0.8	-0.2 ± 0.8	-1.0 ± 1.1	-1.0 ± 1.1	-0.9 ± 1.1	···	···	···
HD021362	-22.6 ± 1.0	-23.8 ± 1.0	-2.5 ± 1.3	-2.4 ± 1.3	-2.0 ± 1.3	18.5 ± 0.2	9.8 ± 0.2	5.6 ± 1.1
HD021455	-9.9 ± 1.0	-8.1 ± 1.0	-1.9 ± 1.4	-1.9 ± 1.4	-1.8 ± 1.4	7.4 ± 0.3	8.0 ± 0.7	7.5 ± 0.3
HD021551	-1.0 ± 1.3	-0.6 ± 1.3	-1.8 ± 1.8	-2.0 ± 1.8	-1.9 ± 1.8	···	···	···
HD021641	-9.6 ± 1.3	-8.9 ± 1.4	-0.9 ± 1.9	-0.9 ± 1.9	-0.8 ± 1.9	8.8 ± 0.4	7.4 ± 0.3	7.7 ± 0.7
HD021650	-19.4 ± 0.8	-24.1 ± 0.8	-2.5 ± 1.1	-2.4 ± 1.1	-2.2 ± 1.1	24.0 ± 0.5	23.2 ± 0.4	19.6 ± 0.7
HD022192	-42.4 ± 0.6	-43.9 ± 0.7	-2.5 ± 0.8	-2.5 ± 0.8	-2.1 ± 0.8	-29.4 ± 2.1	-39.3 ± 2.6	-39.2 ± 1.8
HD022780	-0.8 ± 0.7	-0.0 ± 0.7	0.5 ± 1.1	0.5 ± 1.1	0.5 ± 1.1	···	···	···
HD023016	-3.4 ± 1.4	-2.7 ± 1.4	-2.5 ± 1.8	-2.4 ± 1.8	-2.4 ± 1.8	9.0 ± 0.7	9.1 ± 0.4	8.8 ± 0.8
HD023302	-2.1 ± 0.9	-1.9 ± 0.9	-1.5 ± 1.2	-1.5 ± 1.2	-1.4 ± 1.2	9.2 ± 0.2	8.7 ± 0.6	···
HD023478	-4.1 ± 0.5	-2.9 ± 0.6	-0.5 ± 0.6	-0.4 ± 0.6	-0.3 ± 0.6	···	···	···
HD023480	-6.4 ± 0.9	-4.8 ± 0.9	-1.8 ± 1.3	-1.7 ± 1.3	-1.5 ± 1.3	···	···	···
HD023552	-9.9 ± 1.3	-9.3 ± 1.3	-2.4 ± 1.8	-2.4 ± 1.8	-2.3 ± 1.8	···	···	···
HD023630	-9.9 ± 0.9	-9.2 ± 0.9	-3.0 ± 1.4	-3.0 ± 1.4	-2.8 ± 1.4	2.9 ± 0.2	2.5 ± 0.3	2.8 ± 0.1
HD023800	-7.6 ± 0.3	-8.8 ± 0.4	-2.1 ± 0.4	-2.4 ± 0.4	-2.0 ± 0.4	···	···	···
HD023862	-33.4 ± 1.4	-23.4 ± 1.4	-4.8 ± 1.9	-5.0 ± 1.9	-4.0 ± 1.9	-12.6 ± 0.4	-1.9 ± 1.7	53.4 ± 1.5
HD024479	-3.0 ± 1.5	-3.0 ± 1.5	-4.1 ± 2.2	-4.2 ± 2.2	-4.1 ± 2.2	21.1 ± 0.2	20.4 ± 0.3	21.6 ± 0.7
HD024534	-21.5 ± 0.5	-24.9 ± 5.2	-4.4 ± 0.4	-4.8 ± 0.4	-5.1 ± 0.4	-20.1 ± 0.8	-20.6 ± 0.3	-26.2 ± 1.1
HD025799	0.0 ± 0.5	0.5 ± 0.5	-0.2 ± 0.6	-0.2 ± 0.6	0.0 ± 0.6	···	···	···
HD025940	-31.5 ± 0.6	-31.4 ± 0.8	-1.6 ± 0.8	-1.6 ± 0.9	-1.3 ± 0.9	-23.4 ± 1.0	-24.5 ± 1.2	-23.7 ± 0.4
HD026670	-0.5 ± 0.8	-0.2 ± 0.8	-1.0 ± 1.1	-1.0 ± 1.1	-0.9 ± 1.1	···	···	···
HD029866	-18.6 ± 1.1	-18.6 ± 1.1	-4.0 ± 1.5	-4.2 ± 1.5	-4.0 ± 1.5	22.5 ± 0.3	23.3 ± 0.6	21.4 ± 0.8
HD032343	-30.7 ± 0.8	-27.8 ± 0.8	···	-1.8 ± 1.1	-1.5 ± 1.1	···	-22.3 ± 0.5	-18.4 ± 0.6
HD036576	-35.9 ± 0.7	-47.7 ± 0.9	···	-3.5 ± 0.5	-3.3 ± 0.5	···	-19.7 ± 1.2	-11.8 ± 1.2
HD037202	-23.8 ± 0.7	-25.0 ± 0.9	···	-2.4 ± 0.8	-2.6 ± 0.8	···	22.5 ± 0.5	27.5 ± 0.7
HD041335	-38.9 ± 0.9	-39.9 ± 0.6	···	-3.7 ± 0.6	-3.1 ± 0.6	···	-27.2 ± 1.0	-27.7 ± 0.8
HD058715	-9.8 ± 1.6	-9.7 ± 1.6	···	-1.8 ± 2.2	-1.5 ± 2.2	···	3.8 ± 0.1	3.6 ± 0.3
HD058978	-19.3 ± 0.3	-17.9 ± 0.5	···	-3.6 ± 0.3	-3.3 ± 0.3	···	-42.2 ± 2.4	-35.7 ± 3.0
HD060855	-46.6 ± 0.5	-49.2 ± 0.7	···	-4.1 ± 0.6	-3.9 ± 0.6	···	-19.5 ± 0.6	-14.8 ± 0.3
HD162428	-12.3 ± 0.8	-19.2 ± 0.8	-1.9 ± 1.1	···	-1.7 ± 1.1	16.6 ± 0.3	···	15.9 ± 0.2
HD162732	-10.8 ± 1.1	-13.8 ± 1.1	-0.5 ± 1.5	-0.8 ± 1.5	-1.1 ± 1.5	86.8 ± 0.7	85.3 ± 2.1	82.0 ± 2.0
HD164284	-15.6 ± 0.6	-12.5 ± 0.6	-1.3 ± 0.5	-1.3 ± 0.5	-1.2 ± 0.5	1.6 ± 0.7	0.9 ± 0.2	2.6 ± 0.5
HD164447	-11.8 ± 1.2	-10.4 ± 1.2	-3.5 ± 1.7	-3.5 ± 1.7	-3.4 ± 1.7	5.2 ± 0.3	5.1 ± 0.5	7.2 ± 1.1
HD166014	-2.4 ± 0.9	-2.6 ± 0.9	-2.9 ± 1.3	-2.8 ± 1.3	-2.9 ± 1.3	22.4 ± 0.1	21.8 ± 0.4	23.9 ± 0.8

Continued on Next Page...

Table 7.4 – Continued

Star	Hα W'_λ [Å] 2004	2006	Hγ W'_λ [Å] 2004	2005	2006	Fe II CCF $W\lambda$ [km s^{-1}] 2004	2005	2006
HD168797	-0.0 ± 0.5	-0.8 ± 0.5	-1.2 ± 0.5	-1.4 ± 0.5	-1.1 ± 0.5	...	...	...
HD168957	-0.4 ± 0.6	-0.1 ± 0.6	-0.9 ± 0.9	-0.8 ± 0.9	-0.7 ± 0.9	7.6 ± 0.1	7.6 ± 0.3	7.3 ± 0.4
HD171406	-2.3 ± 0.7	-4.9 ± 0.7	-1.0 ± 1.0	-1.8 ± 1.0	-1.2 ± 1.0	5.2 ± 1.8	8.9 ± 0.8	3.0 ± 0.4
HD171780	-6.1 ± 0.8	-3.8 ± 0.8	-0.8 ± 1.2	-0.5 ± 1.2	-0.5 ± 1.2	...	...	...
HD173370	-6.4 ± 1.6	-6.3 ± 1.6	-4.3 ± 2.3	-4.2 ± 2.3	-4.2 ± 2.3	9.7 ± 1.2	13.8 ± 0.5	11.5 ± 0.4
HD174237	-6.8 ± 0.7	-3.9 ± 0.7	-1.8 ± 1.0	-1.6 ± 1.0	-0.8 ± 1.0	-4.0 ± 4.7	-5.7 ± 0.8	-0.2 ± 3.3
HD175863	-14.6 ± 0.8	-8.5 ± 0.8	-4.0 ± 1.1	-3.8 ± 1.1	-3.5 ± 1.1	...	...	...
HD175869	-4.0 ± 0.9	-3.8 ± 0.9	-1.5 ± 1.4	-1.3 ± 1.4	-1.3 ± 1.4	12.4 ± 0.2	12.3 ± 0.1	13.9 ± 0.2
HD177648	-8.4 ± 0.5	-9.0 ± 0.5	-2.3 ± 0.6	-2.4 ± 0.6	-1.9 ± 0.6	...	...	...
HD178475	-5.7 ± 0.8	-2.0 ± 0.8	-3.0 ± 1.1	-2.6 ± 1.1	-2.4 ± 1.1	18.2 ± 4.5	1.4 ± 0.2	1.7 ± 0.4
HD179343	-14.8 ± 1.3	-14.7 ± 1.3	-4.2 ± 1.8	-4.1 ± 1.8	-4.3 ± 1.8	65.2 ± 2.1	67.0 ± 2.1	64.0 ± 2.1
HD181409	0.3 ± 0.3	0.2 ± 0.4	-1.1 ± 0.4	-1.0 ± 0.4	-0.8 ± 0.4	...	...	...
HD183362	-27.0 ± 0.5	-31.7 ± 1.1	-3.2 ± 0.5	-2.8 ± 0.5	-2.7 ± 0.5	-25.7 ± 1.4	-23.0 ± 1.2	-25.2 ± 1.3
HD183656	-12.9 ± 0.9	-11.7 ± 0.9	-2.1 ± 1.3	-2.4 ± 1.2	-2.2 ± 1.2	54.2 ± 1.4	48.7 ± 2.0	79.8 ± 2.7
HD183914	-6.7 ± 1.1	-7.0 ± 1.1	-0.2 ± 1.5	-0.0 ± 1.5	0.1 ± 1.5	...	...	...
HD184279	-40.4 ± 0.3	-26.9 ± 0.4	-1.4 ± 0.5	-0.6 ± 0.5	-0.2 ± 0.5	28.2 ± 1.1	30.6 ± 0.8	32.1 ± 0.7
HD185037	-9.9 ± 1.5	-10.6 ± 1.5	-1.7 ± 2.0	-1.7 ± 2.0	-1.5 ± 2.0	7.8 ± 0.3	8.4 ± 0.1	6.7 ± 1.4
HD187567	-21.7 ± 0.5	-24.0 ± 0.5	-3.5 ± 0.5	-3.4 ± 0.5	-3.0 ± 0.5	-17.7 ± 0.5	-19.0 ± 1.1	-19.7 ± 0.9
HD187811	-7.6 ± 0.7	-2.1 ± 0.7	-1.6 ± 0.9	-0.8 ± 0.9	-0.3 ± 0.9	...	...	...
HD187851	-0.6 ± 0.4	-0.7 ± 0.4	-1.8 ± 0.3	-1.5 ± 0.3	-1.6 ± 0.3	...	...	...
HD189687	-7.2 ± 0.4	-4.7 ± 0.4	-0.9 ± 0.6	-0.7 ± 0.6	-0.6 ± 0.6	...	...	...
HD191610	-13.6 ± 0.7	-6.2 ± 0.7	-2.1 ± 0.9	-2.1 ± 0.9	-1.5 ± 0.9	...	...	...
HD192044	-15.8 ± 0.9	-16.0 ± 0.9	-2.1 ± 1.3	-2.0 ± 1.3	-1.8 ± 1.3	-6.0 ± 0.3	-5.7 ± 0.3	-5.8 ± 0.1
HD192445	-34.2 ± 0.4	-36.3 ± 2.2	-3.0 ± 0.4	-3.0 ± 0.4	-2.5 ± 0.4	-17.3 ± 0.0	-18.4 ± 1.3	-17.5 ± 1.5
HD192685	0.0 ± 0.7	-1.1 ± 0.7	-0.7 ± 0.9	-1.2 ± 0.9	-0.5 ± 0.9	...	...	...
HD193009	-28.8 ± 0.4	-30.0 ± 0.3	-4.1 ± 0.4	-4.0 ± 0.4	-3.6 ± 0.4	-24.5 ± 4.3	-23.1 ± 1.0	-26.5 ± 0.8
HD193182	-23.1 ± 0.7	-24.5 ± 0.8	0.9 ± 1.0	1.1 ± 1.0	0.8 ± 1.0	75.4 ± 0.7	74.8 ± 1.7	75.3 ± 1.8
HD193911	-11.9 ± 0.9	-11.4 ± 0.9	-2.8 ± 1.3	-2.8 ± 1.3	-2.5 ± 1.3	-3.0 ± 0.1	-5.3 ± 0.3	-4.1 ± 0.8
HD194244	-5.0 ± 1.6	-4.8 ± 1.6	-4.4 ± 2.4	-4.4 ± 2.4	-4.4 ± 2.4	17.1 ± 1.2	16.2 ± 0.7	15.6 ± 1.0
HD194335	-12.7 ± 0.4	-11.8 ± 0.4	-2.5 ± 0.4	-2.2 ± 0.4	-2.1 ± 0.4	-13.5 ± 2.7	-3.7 ± 0.3	-6.7 ± 0.0
HD194883	-28.1 ± 0.5	-26.6 ± 0.5	-2.5 ± 0.6	-2.4 ± 0.6	-2.1 ± 0.6	-11.9 ± 0.8	-12.8 ± 0.8	-15.1 ± 0.8
HD195325	-6.2 ± 1.4	-5.6 ± 1.4	-6.0 ± 2.1	-6.2 ± 2.1	-6.1 ± 2.1	66.4 ± 0.7	65.0 ± 1.9	62.5 ± 0.5
HD195554	-5.4 ± 1.6	-5.0 ± 1.6	-2.6 ± 2.3	-2.5 ± 2.3	-2.5 ± 2.3	6.5 ± 0.5	5.2 ± 0.5	5.8 ± 0.4
HD197419	-7.9 ± 0.4	-8.1 ± 0.6	-0.5 ± 0.4	-0.5 ± 0.4	-0.2 ± 0.4	...	...	...
HD198183	-0.6 ± 0.6	-0.7 ± 0.6	-0.1 ± 0.9	-0.1 ± 0.9	-0.2 ± 0.9	5.7 ± 0.3	5.9 ± 0.4	5.4 ± 0.6
HD198625	-10.6 ± 0.6	-1.6 ± 0.6	-2.1 ± 0.8	-1.7 ± 0.8	-1.4 ± 0.8	...	...	...
HD199218	-22.8 ± 1.0	-22.5 ± 1.0	-3.7 ± 1.4	-3.6 ± 1.4	-3.6 ± 1.4	16.1 ± 0.7	15.6 ± 0.9	16.0 ± 0.9
HD199356	-38.0 ± 0.4	-38.6 ± 2.1	-4.3 ± 0.4	-4.3 ± 0.4	-3.8 ± 0.4	-57.7 ± 1.2	-57.7 ± 1.0	-56.0 ± 1.3
HD200120	-16.1 ± 0.6	-17.6 ± 0.6	-2.9 ± 0.6	-3.4 ± 0.6	-3.2 ± 0.6	-21.0 ± 1.1	-20.6 ± 0.6	-21.8 ± 6.7
HD200310	-1.6 ± 0.3	-0.9 ± 0.3	-1.7 ± 0.5	-1.6 ± 0.5	-1.3 ± 0.5	...	...	...
HD201522	-2.2 ± 0.6	-1.6 ± 0.7	0.2 ± 0.9	0.1 ± 0.9	0.1 ± 0.9	...	...	...
HD201733	-3.2 ± 0.6	-2.0 ± 0.7	-2.6 ± 0.9	-2.2 ± 0.9	-2.1 ± 0.9	...	...	...
HD202904	-39.6 ± 0.6	-29.5 ± 0.6	-3.3 ± 0.7	-3.5 ± 0.7	-2.7 ± 0.7	-30.7 ± 0.5	-23.1 ± 1.0	-17.4 ± 0.8
HD203025	-2.7 ± 0.5	-1.5 ± 0.5	-1.3 ± 0.5	-1.1 ± 0.5	-1.2 ± 0.5	...	...	...
HD203374	-47.2 ± 0.3	-48.1 ± 0.3	-4.1 ± 0.3	-4.0 ± 0.3	-3.2 ± 0.4	-34.5 ± 0.9	-26.8 ± 2.3	-26.0 ± 1.1
HD203467	-32.4 ± 0.4	-29.6 ± 0.4	-3.1 ± 0.6	-3.4 ± 0.6	-2.6 ± 0.6	-26.8 ± 2.3	-32.8 ± 1.2	-33.5 ± 5.5
HD203699	-24.8 ± 0.6	-21.7 ± 0.7	-4.4 ± 0.9	-3.8 ± 0.9	-3.6 ± 0.9	-24.2 ± 1.1	-12.9 ± 0.5	-4.6 ± 0.6
HD203731	-33.5 ± 0.3	-38.0 ± 0.6	-3.0 ± 0.5	-2.9 ± 0.5	-3.1 ± 0.5	-32.2 ± 0.6	-43.7 ± 0.9	-36.7 ± 0.9
HD204116	...	-34.4 ± 1.1	-3.7 ± 0.3	-3.8 ± 0.3	-3.4 ± 0.3	-23.7 ± 1.6	-22.3 ± 1.3	-17.4 ± 1.0
HD204722	-20.5 ± 0.2	-20.1 ± 0.2	-2.5 ± 0.5	-2.3 ± 0.5	-1.7 ± 0.5	-26.6 ± 0.8	-30.5 ± 0.8	-16.7 ± 0.7

Continued on Next Page...

Table 7.4 – Continued

Star	Hα W'_λ [Å] 2004	2006	Hγ W'_λ [Å] 2004	2005	2006	Fe II CCF $W\lambda$ [km s^{-1}] 2004	2005	2006
HD204860	-5.9 ± 0.6	-9.8 ± 0.6	-2.7 ± 0.8	-2.9 ± 0.8	-2.6 ± 0.8	0.7 ± 0.6	34.4 ± 0.7	1.9 ± 0.2
HD205060	-12.1 ± 0.9	-13.8 ± 0.9	-3.6 ± 1.2	-3.7 ± 1.2	-3.5 ± 1.2	15.2 ± 1.1	22.0 ± 1.5	12.7 ± 1.9
HD205551	-6.7 ± 1.4	-6.7 ± 1.4	-4.3 ± 1.8	-4.1 ± 1.8	-4.1 ± 1.8	10.4 ± 0.8	9.0 ± 0.3	9.5 ± 0.4
HD206773	-13.8 ± 0.2	-15.7 ± 0.8	-3.4 ± 0.6	-3.5 ± 0.6	-3.0 ± 0.6	···	···	···
HD207232	-9.9 ± 1.0	-13.2 ± 1.0	-3.2 ± 1.4	-3.2 ± 1.4	-3.0 ± 1.4	46.4 ± 5.5	63.6 ± 0.4	61.1 ± 0.9
HD208057	0.7 ± 0.6	0.8 ± 0.6	0.4 ± 0.9	0.5 ± 0.8	0.6 ± 0.8	···	···	···
HD208392	-0.8 ± 0.5	-0.5 ± 0.7	-1.5 ± 0.5	-1.2 ± 0.5	-1.1 ± 0.5	···	···	···
HD208682	-0.7 ± 0.5	-0.4 ± 0.5	-1.5 ± 0.5	-1.3 ± 0.4	-1.3 ± 0.5	···	···	···
HD210129	-6.9 ± 0.7	-12.3 ± 0.7	-0.5 ± 1.1	-0.1 ± 1.1	-0.2 ± 1.1	-0.5 ± 0.1	-3.8 ± 0.6	-9.7 ± 0.4
HD212044	-18.2 ± 0.1	-23.6 ± 1.1	-3.2 ± 0.4	-2.8 ± 0.4	-2.3 ± 0.4	-24.1 ± 0.0	-18.4 ± 1.3	···
HD212076	-18.6 ± 0.7	-29.4 ± 0.7	-3.7 ± 0.8	-3.7 ± 0.8	-3.2 ± 0.8	-30.5 ± 1.0	-44.7 ± 0.4	-41.2 ± 0.6
HD212571	-8.4 ± 0.4	-7.6 ± 0.4	-2.5 ± 0.5	-2.6 ± 0.5	-1.9 ± 0.5	···	···	···
HD212791	-12.9 ± 0.6	-7.6 ± 0.6	-2.6 ± 0.8	-2.2 ± 0.8	-2.1 ± 0.8	···	···	···
HD214167	0.7 ± 0.3	0.9 ± 0.3	0.1 ± 0.4	0.4 ± 0.4	0.4 ± 0.4	···	···	···
HD214168	-20.6 ± 0.3	-19.1 ± 0.4	-2.2 ± 0.3	-2.1 ± 0.3	-1.9 ± 0.3	···	···	···
HD216057	-1.0 ± 0.6	-0.5 ± 0.6	-0.5 ± 0.9	-0.5 ± 0.9	-0.4 ± 0.9	···	···	···
HD216200	-3.4 ± 0.6	-3.4 ± 0.7	-1.7 ± 0.8	-1.3 ± 0.8	-1.4 ± 0.8	3.0 ± 1.2	7.3 ± 0.3	7.8 ± 1.7
HD217050	-30.5 ± 0.6	-29.5 ± 0.5	-1.7 ± 0.7	-1.3 ± 0.7	-1.3 ± 0.7	42.8 ± 1.4	52.3 ± 0.7	60.5 ± 3.4
HD217543	-0.3 ± 0.7	-3.8 ± 0.8	-1.4 ± 0.9	-1.0 ± 0.9	-1.3 ± 0.9	···	···	···
HD217675	-1.7 ± 0.6	-0.5 ± 0.6	-1.9 ± 0.9	-1.7 ± 0.9	-1.8 ± 0.9	···	···	···
HD217891	-20.5 ± 0.9	-16.4 ± 0.9	-0.8 ± 1.2	-0.7 ± 1.2	-0.7 ± 1.2	···	···	···
HD218674	-7.8 ± 0.6	-6.5 ± 0.6	-2.6 ± 0.8	-2.5 ± 0.8	-2.2 ± 0.8	4.1 ± 0.6	3.5 ± 0.1	0.6 ± 0.1
HD224544	-0.8 ± 0.5	-0.5 ± 0.5	-1.4 ± 0.8	-1.3 ± 0.8	-1.2 ± 0.8	···	···	···
HD224559	-23.5 ± 0.7	-26.8 ± 0.7	-2.0 ± 0.9	-1.9 ± 0.9	-1.6 ± 0.9	-38.6 ± 2.6	-43.1 ± 3.3	-45.3 ± 1.8
HD225095	-28.5 ± 0.5	-38.7 ± 0.4	-4.6 ± 0.4	-4.9 ± 0.4	-4.4 ± 0.3	-42.0 ± 0.5	-42.0 ± 2.5	-45.4 ± 0.4

7.5 Projected Rotational Velocity

In order to fully describe the sample, I must compare the FWSM measurements to the published projected rotational velocity, $V \sin i$, to find a relation between them. From the start, I eliminated five stars from this and all following analyses, three interacting binaries and two O stars. The eliminated interacting binaries are HD 174638 (β Lyr), HD 181615 (υ Sgr), and HD 218393 (KX And). While there are other interacting binaries in the sample, these three are involved in active mass transfer and have such unusual spectral features that they are not characteristic in any way of classical Be stars. The stars HD 149757 and HD 203064, while they have no emission, are both O type and therefore also are not characteristic of classical Be stars.

The He I λ6678 line is often filled with emission, and therefore any measurements of its FWSM are unreliable. More reliable measurements are generated from He I λ4471 and Mg II λ4481 and plots of $V \sin i$ (from Table 7.1) with both lines are shown in Figures 7.13 and 7.14. The *solid lines* in each plot are empirical fits to the data. The fit for He I λ4471 is $V \sin i = 1.051\sqrt{FWSM^2 - 257^2}$ and that for Mg II λ4481 is $V \sin i = 0.883\sqrt{FWSM^2 - 83^2}$. Stars that fell below a threshold equivalent width (0.15 Å) are not found on the plots (one star eliminated based on a weak helium line, 23 based on weak magnesium line equivalent width).

While the blue helium and magnesium lines are more reliable than the red helium line, they are not without their problems. Helium can show signs of being filled with emission and its strength varies with temperature. The magnesium line also varies with temperature but it is generally smaller. Therefore when it is broadened by fast rotation, it blends with He I and becomes unusable. Three stars were omitted from the fit for He I λ4471: HD 5394 (γ Cas), HD 10516 (ϕ Per), and HD 23478. The first two have very narrow non-photospheric central components and the third has

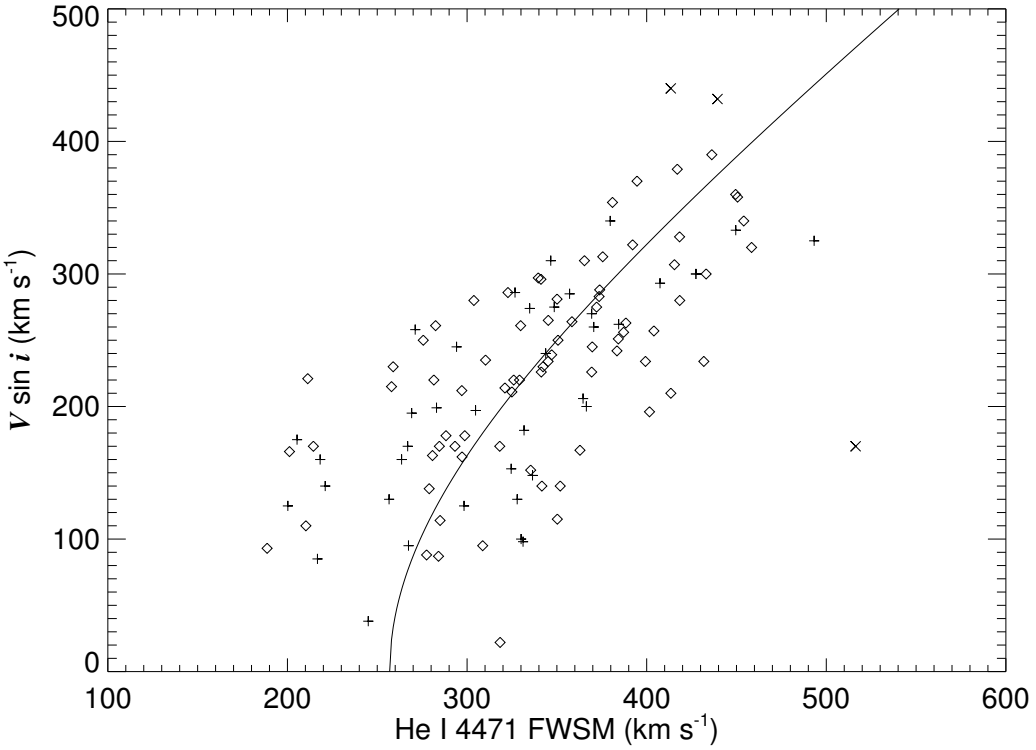

Figure 7.13: The relationship between published $V \sin i$ and the average FWSM of He I λ4471. The *solid line* is a fit to the data. The *diamonds* are stars with $\log g > 3.75$, the *plus signs* are stars with $\log g < 3.75$, and the *crosses* are stars omitted from the fit as discussed in the text. Errors in $V \sin i$ are unknown and the errors in FWSM are given in Table C.2 (all smaller than the symbol).

very broad wings that are likely related to strong pressure broadening or magnetic broadening. The weaker Mg II line sample has 18 stars omitted from the fit. Many of the omitted stars have a strong shell component (HD 9709, 10516, 20336, 21362, 22192, 37202, 41335, 162732, 193182, 207232, 217050, and 224559) while the rest are weak due to emission filling or blending with He I λ4471 (HD 25799, 183362, 200310, 201733, 208682, 217543). All points eliminated from the fit are shown in the plots by $\times$.

The spread of the plot is indicative of the spread in $\log g$ and the fact that emission will fill in the spectral lines. One can see that pressure broadening plays a bigger role

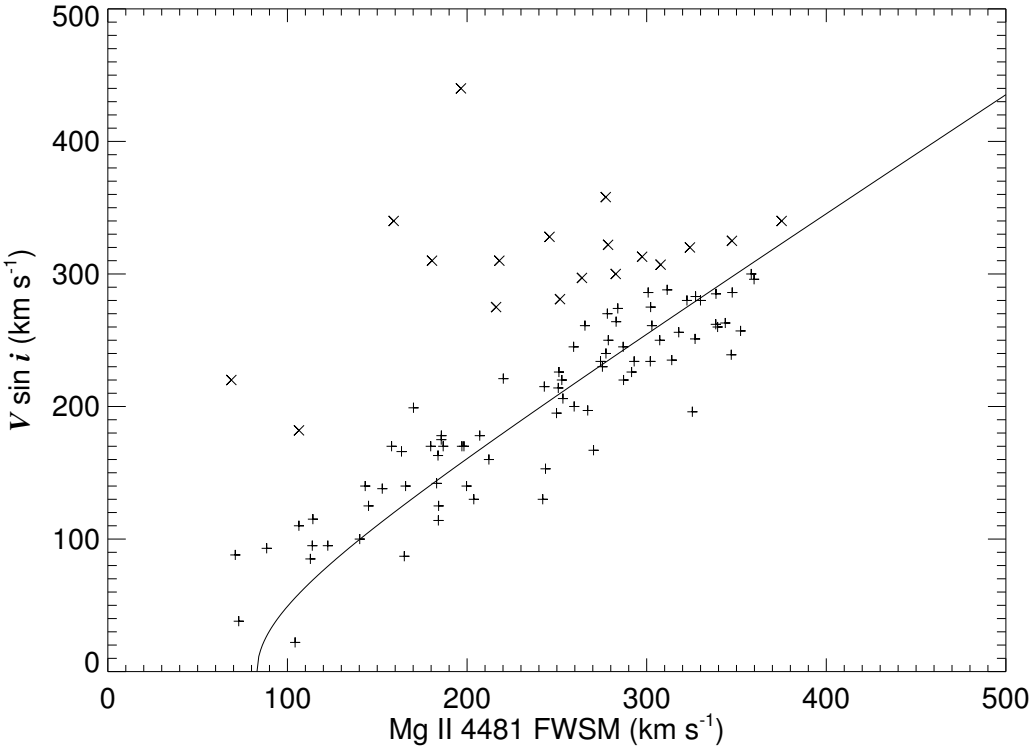

Figure 7.14: The relationship between published $V \sin i$ and the average FWSM of Mg II λ4481. The *solid line* is a fit to the data. *Crosses* are stars omitted from the fit as discussed in the text. Errors in $v \sin i$ are unknown and the errors in FWSM are given in Table C.2 (all smaller than the symbol).

in the spread of the He I λ4471 line FWSM than in the case of the Mg II λ4481 FWSM.

From the fits found in these plots, we may determine $V \sin i$ for the four stars in Table 7.1 that had no published value for $V \sin i$, HD 177648, HD 194883, HD 201522, and HD 203731. While I can use FWSM of both lines and get two values for $V \sin i$, the results may not agree. For HD 177648, $V \sin i(\mathrm{He}) = 265 \pm 30$ km s^{-1} and $V \sin i(\mathrm{Mg}) = 227 \pm 44$ km s^{-1} but the Mg II line is filled with emission. This is also the case for HD 194883 ($V \sin i(\mathrm{He}) = 173 \pm 19$ km s^{-1} and Mg II filled in) and HD 203731 ($V \sin i(\mathrm{He}) = 279 \pm 24$ km s^{-1} and $V \sin i(\mathrm{Mg}) = 110 \pm 70$ km s^{-1}) so I just used the value for the He I line in these cases. The final star, HD 201522,

had values of $V \sin i(\mathrm{He}) = 235 \pm 8$ km s^{-1} and $V \sin i(\mathrm{Mg}) = 244 \pm 6$ km s^{-1} and its mean is $V \sin i = 240 \pm 6$. The errors were found from the standard deviation of each FWSM measurement.

As described in §7.1, gravity darkening affects the spectral lines by making them narrower than they would be if all parts of the star contributed equal amounts of light (as a slowly rotating star would do). Also, the temperatures at the equator and at the poles are different, so any spectral lines with temperature dependence will also be affected. For instance, the strength of He I λ4471 in B stars increases with temperature up to about $T_{\mathrm{eff}} = 18$ kK then decreases again. The strength of Mg II λ4481 decreases with increasing temperature. Therefore, at the cooler equator, Mg II should be relatively stronger than He I. Also, the wings of a spectral line are formed in equatorial zones at the stellar limbs so the wings are more sensitive to temperature. The core of a spectral line is dominated by zero velocity parts of the star (the poles), so the He I λ4471 line will be core-dominated. Thus, due to the effects of gravity darkening, we should expect broader Mg II and narrower He I features than in a slowly rotating star. In order to determine if these gravity darkening effects are seen, I have taken the ratio of the FWSMs of these lines. At low $V \sin i$, the ratio will be large as He I λ4471 is more affected by pressure broadening than Mg II λ4481 (as it is lighter) plus this helium line is a multiplet so the superposition of multiple components will artificially broaden the line. At high $V \sin i$, the ratio should be declining.

This effect will be seen most clearly for stars with effective temperatures of 18 kK or less as that is where the equivalent width of He I λ4471 starts to level off and then decrease again (see Fig. 7.9). I also omitted the same stars I omitted before (interacting binaries, O stars, stars that had very weak lines). Thus the sample was reduced to 61 stars. The relationship between the ratio of the FWSM for helium and

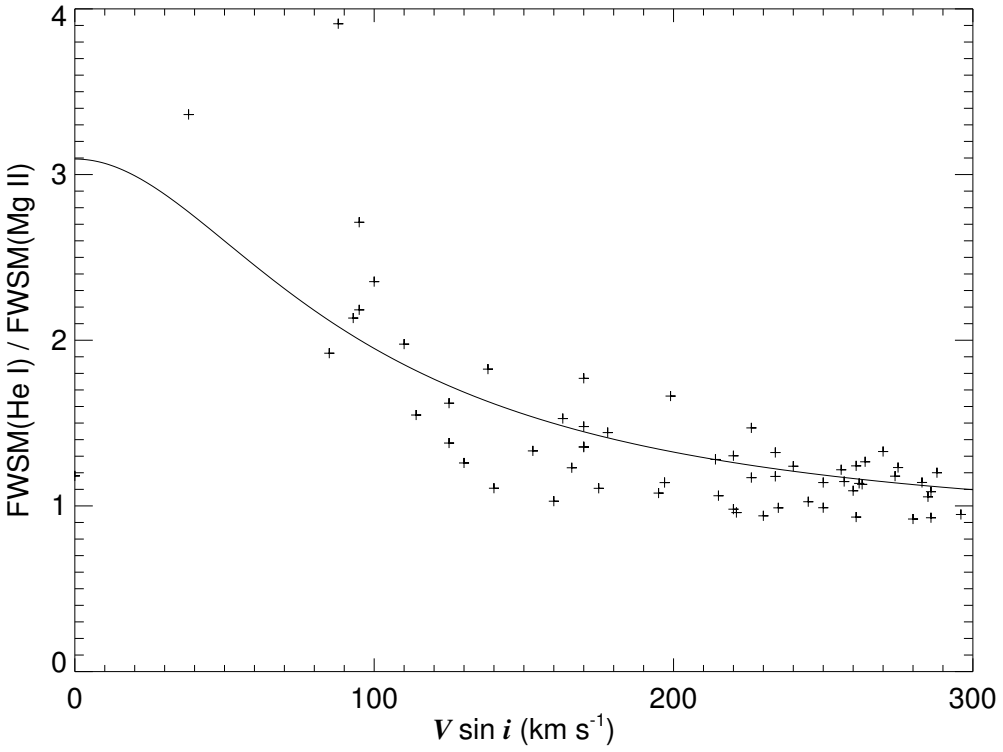

Figure 7.15: The relationship between the ratio of FWSM(He I λ4471) and FWSM(Mg II λ4481) and published $V \sin i$ (from Table 7.1) for stars less than 18 kK. The *solid line* is the result of the ratio of the empirical fits found in Figures 7.13 and 7.14. Errors in $V \sin i$ are unknown and the errors in FWSM are given in Table C.2 (all smaller than the symbol).

that for magnesium versus published $V \sin i$ is presented in Figure 7.15. The *solid line* is the ratio of the fits from Figures 7.13 and 7.14. The highest point (at ratio $\approx$ 4) is the narrow-lined star HD 168957 (there are other smaller values for $V sini$ in the literature and He I λ4471 is a multiplet - see Fig. C.65). The fit is consistent with the hypothesis that the ratio will decrease with increasing $V \sin i$. However, more detailed modeling is required. I will also note that if the Mg II λ4481 has any emission in it (such as the horns often observed), the gravity darkening effect will be removed.

7.6 Disk Variability

Visual inspection of the plots in Appendix C show that the rule amongst these stars is they change on the timescales of my observations. The emission profile often changes shape (peaks get higher on one side than the other and then switch) and equivalent width. So, how do the variabilities of the equivalent widths of Hα, Hγ, and the Fe II cross-correlation functions compare? I decided to find the fractional variation in equivalent width for each of the three features for each star. Using the values in Table 7.4 for the average W' for each run, I found the range of W'_λ and divided it by the mean W'_λ to get the fractional variation. Some of the stars observed show no emission (at least over the period of my observations) so I did not include them in the statistics that follow. In order to automate the process, I compared the error in W' to the measurement of W'_λ – if W'_λ was smaller than the error, it was omitted. I also omitted the three interacting binaries, the two O stars, and the often mistaken non-Be star HD 214167 as before, plus two stars that only had data from one run. Table 7.5 shows the average and median fractional variation in corrected equivalent width for each of these three features. Column 1 gives the values for Hα, Hγ values are in column 2, and the Fe II CCF values are in column 3.

Table 7.5: Fractional variations in equivalent width

	Hα W'_λ	Hγ W'_λ	Fe II CCF W_λ
Mean variation	25.4%	18.8%	44.8%
Median variation	12.8%	15.0%	19.4%
Sample size	108	98	81

One notices that the medians are about the same, so small fractional variation is not uncommon. It is also helpful to consider the cumulative distribution of the fractional variation that is shown in Figure 7.16. The distribution curves look roughly

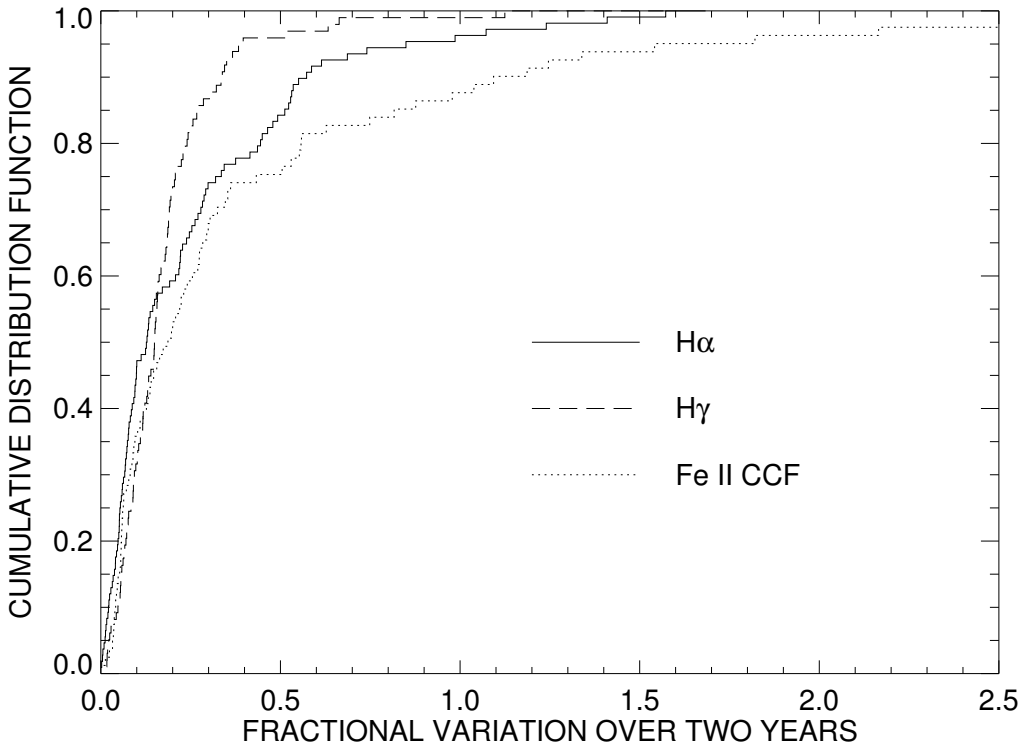

Figure 7.16: Cumulative distributions for the fractional variation of equivalent widths. The distribution in Hα is denoted by the *solid line*, Hγ by the *dashed line*, and the Fe II shell line cross-correlation function by the *dotted line*.

the same up until about 35% change and then they diverge. The largest fractional variations are in shell features while the smallest are in Hα. This distribution function should be useful benchmark for comparison with the variablility properties of other Be star surveys.

As evident from the above statistics, if one wants to see large changes in Be stars, one should look at the shell features. A spectacular example of changes in shell features is the star Pleione (HD 23862) (shown in Fig. 7.17). This star has long been known to switch between a shell and a non-shell phase, and I happened to catch the change. It started as an emission shell star in 2004 and then became an absorption shell star. Many other stars in this survey also exhibit interesting shell changes and

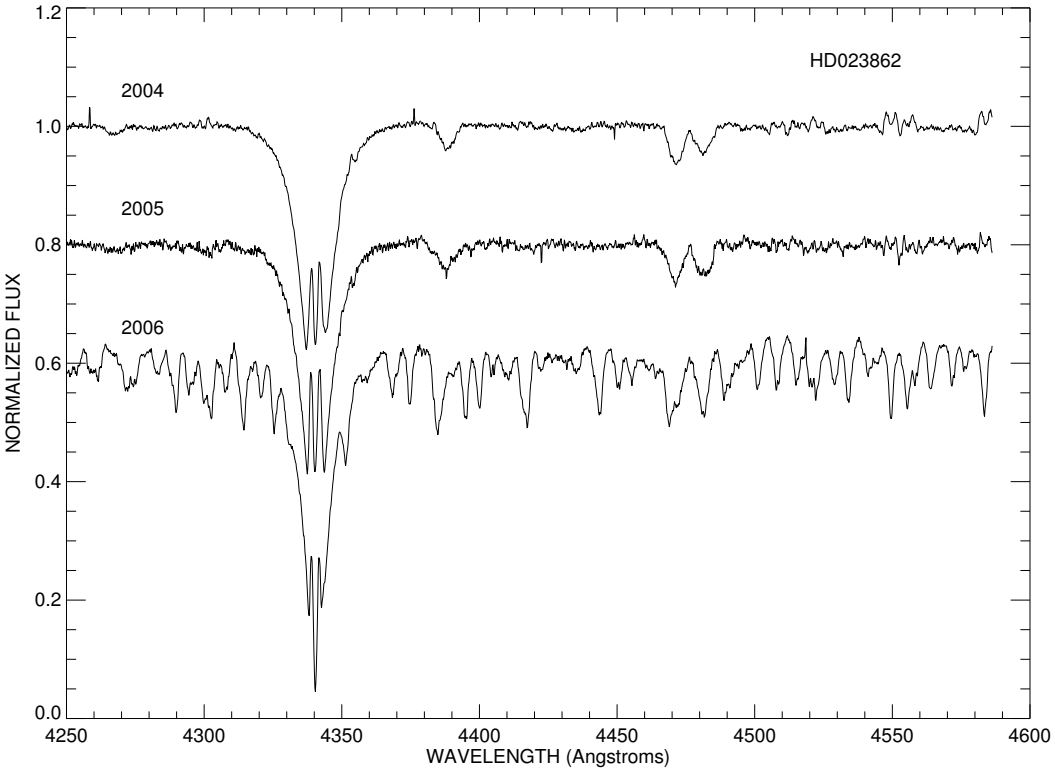

Figure 7.17: A plot of the normalized flux versus wavelength for the extremely variable blue spectrum of Pleione (HD23862). The *top line* is the average blue spectrum of the 2004 run, the *middle line* is the same for 2005, and the *bottom line* is for the 2006 run. They are offset from each other for clarity.

their spectra are plotted in Appendix C.

Using the corrected equivalent width of Hα emission, I found that 91% of the 121 star sample showed emission in 2004. In 2006, 88% of the 122 star sample showed Hα emission. This is not unexpected as the observing list was taken from a sample of Be stars. However, there are some things to note in these statistics. First, the sample size differs as one star was not observed in 2004 but was in 2006 (plus the six stars I always omit are omitted again). Second, in looking at the actual spectra of the stars that apparently showed no emission, I found that three of them in 2006 actually did have emission (it was very small), so that means the absorption line correction was incorrect (poor temperature estimate). With these added in, the percentages

become 91% and 90%. Of the 12 stars that showed no emission in 2004 and 2006, 7 of them are actually not even Be stars at all (I did a literature search on them as described App. C). With these stars taken out of the sample, the activity percentages (i.e., stars with Hα emission in my sample) become 96% and 96% for 2004 and 2006, respectively. Note that the lists of stars with emission were not exactly the same between 2004 and 2006 – there were 3 stars that turned off/on during the course of my observations. This shows that while my sample was drawn from a list of Be stars that have shown activity (i.e., Hα emission) in the past, not all of them show activity now.

But perhaps an even more interesting result is that a significant fraction of the sample shows Fe II shell features. Table 7.6 gives the fractional percentages of the stars in my sample that exhibit Fe II features. I have included sample size as I omitted the six stars I previously mentioned again plus the sample was expanded from 2004 to 2006.

Table 7.6: Statistics regarding Fe II features

	2004	2005	2006
Percentage with Fe II in absorption	35.5	34.7	36.1
Percentage with Fe II in emission	28.7	31.4	28.7
Percentage with no Fe II features	35.6	33.9	35.2
Sample size	115	121	122

There is no mention in the literature of a two-thirds of a Be star sample having Fe II emission/absorption features. This shows that the circumstellar material around the Be star may not be confined to just an equatorial disk, the disks may be "puffier" than previously thought, or that the whole star is enshrouded by at least a thin layer of circumstellar material. Slettebak (1982) did note that one-fourth of his sample

showed Fe II in emission. I think that the relatively high resolution of my spectra makes the small "squarish" absorption easy to see as it is not blended into the noise.

All of this seems reasonable when looking at the spectra in Appendix C as well.

7.7 Photospheric Variability

Several of the stars in my sample showed rapidly changing line profiles. Rivinius et al. (2003) states that such variability is nearly ubiquitous in hotter B stars. These rapid variations are likely related to non-radial pulsation of the star. Radial pulsation is when the whole surface of the star increases in size and then decreases in size. Non-radial pulsation involves more complex patterns of pulsation involving multiple zones of the star. This phenomenon manifests itself as regions of varying velocity and temperature that move across the surface of the star with a period that is not the period of rotation.

One of the best examples of non-radial pulsation is π Aqr. Bjorkman et al. (2002) discuss the physical properties of this Be star spectroscopic binary. Rivinius et al. (2003) first discussed the fast moving bumps observed in their high resolution spectra and found a period of approximately 2 hours. Examples of He I λ6678 and Si III λ4552 are shown in Figures 7.18 and 7.19, respectively. The 2000 data were obtained by Peters (private communication). As one can see, the resolution of my 2004 and 2006 data is lower than that of the 2000 data, and that by 2004, this line developed emission wings. However, this does not prevent observation of NRP. One must be aware of the signatures of NRP in a star, and therefore, any stars that showed line profile changes but not radial velocity shifts I flagged as suspected non-radial pulsators in Appendix C. I found nine stars that were already listed in the literature but found 15 more candidates.

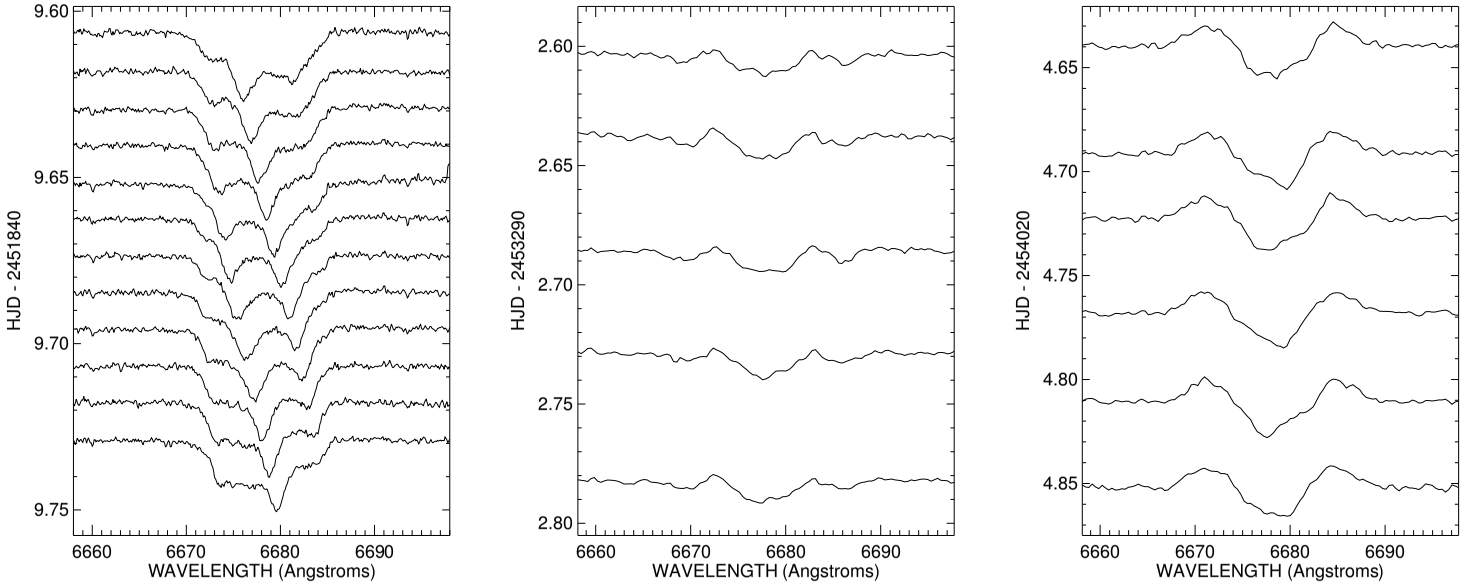

Figure 7.18: π Aqr plots showing non-radial pulsation centered on He I λ6678 for the nights of 2000 Nov. 1, 2004 Oct. 12, and 2006 Oct. 12 (from *left* to *right*). Notice the left to right (blue to red) progression of the bumps in the 2000 data especially. The period is approximately 2 hours (i.e., it takes 2 hours for the bumps to cycle through to the next position).

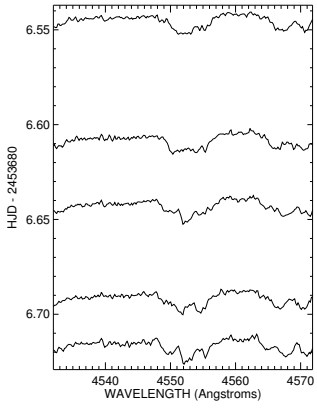

Figure 7.19: π Aqr plot showing non-radial pulsation centered on Si III $\lambda 4552$ for the night of 2005 Nov 12.

7.8 Binaries and Multiple Stars

Many stars are in binary systems and B stars are no exception. There are 27 known spectroscopic binaries in my sample with periods ranging from a few days to a few years. After searching the Washington Double Star Catalog[5], I found that 42 stars have an entry with 100 companions all told. Twenty-two of these companions are less than one arcsec away from their respective stars. Any of these visual companions that may actually be binary companions are relatively wide and likely do not affect the circumstellar disk of the Be star.

There are 101 stars that are not known in the literature as spectroscopic binaries, but I suspect at least 20 of these show radial velocity variations related to orbital motion around a companion. Each of these stars is noted in Appendix C. I will caution that single-spectrum "snapshots" of non-radial pulsations may mimic motions caused by a companion, so these stars do need more data. Another major difficulty in studying the radial velocity shifts of Be stars is that there is emission that fills in spectral features and introduces spurious shifts. One way to get around this is to observe in ultraviolet wavelengths as emission does not play as big of a role there. However, observing at ultraviolet wavelengths is logistically very difficult at this time. Therefore, more data and careful study of each suspected binary system is warranted, yet this is why there are not many known Be star binaries with periods longer than about 200 days.

7.9 Conclusions

My multiyear spectroscopic survey of the emission and shell line variations in 128 Be (and other) stars offers an important sample for our understanding of Be disks and

[5]http://ad.usno.navy.mil/wds/ maintainted by B. Mason and W. Hartkopf

their temporal evolution. First, nearly all (96%) of the actual Be stars in my sample showed emission during each of the runs. However, the 4% showing no emission did not always include the same stars, so some stars turned on or off. The sample shows the median fractional variation in the spectral features associated with emission is about 15%, so again, these stars vary significantly on a yearly timescale. I found that two-thirds of my sample show Fe II shell features of some sort, a much larger fraction than recognized in prior studies in the literature. This suggests that circumstellar disks around Be stars are more extensive than previously realized. I also found a number of stars that may be non-radial pulsators that deserve further observational work. Another set of stars that should be observed more are the 20 or more spectroscopic binary candidates.

– 8 –

Conclusions

8.1 Summary of Results

In this dissertation, I have presented studies of different kinds of hot stars with disks. I studied several binary star systems with active mass transfer, one in a rapid mass transfer phase and four with less rapid transfer onto a neutron star. I also performed a survey of 128 Be (and other) stars. These studies have led to better understanding of the characteristics of such systems and the mass loss processes involved therein.

RY Scuti is actively involved in copious mass transfer and is changing before our very eyes. Following a thorough spectroscopic study of this massive and complex system, we determined reliable masses and orbital elements. We also used tomographic separation of the components to find a pseudo-photosphere of an accretion torus surrounding the massive companion. To explain the many complex features indicative of mass flows seen in the spectra, we devised a cartoon model of the system.

The spectroscopic study of four massive X-ray binaries has revealed the nature of the mass-transferring wind and outflow disks, and has provided improved orbital elements when possible. For the B supergiant LS I +65 010, we found a maximum

in X-ray emission at periastron and a minimum when the neutron star companion was behind the star (the X-rays were attenuated by the wind). We were able to use a newly devised model that relates the equivalent width of Hα to the size of the circumstellar disk to study the other three systems. The model shows that the maxiumum disk radii are truncated by gravitational interactions with the neutron star companion. In the microquasar (LS I +61 303) system, we found that the X-ray flux and Hα emission reach maxima after periastron, which we find is indicative of the development of a density wave in the circumstellar disk that will promote mass transfer to the neutron star. In the HDE 245770 system, we record the growth of a new circumstellar disk and the truncation of that disk at a radius with orbital resonances commensurate with the motion of the companion. For the X Per system, we find a near-record sized disk and copious X-ray emission. Although the disk size is smaller than the periastron separation, we hypothesize that spiral arms excited by tidal interaction with the companion at periastron provide the means of mass transfer to the companion. Each of these systems provides a useful laboratory for studying the effects of companions on the circumstellar disks of Be stars.

Utilizing data from a survey of 128 Be (and other) stars, I was able to characterize some aspects of disk variability in Be stars. In 2004, 96% of the actual Be star sample was active (showed Hα emission) and 96% was also active in 2006 (however not all the same stars were active). Two thirds of the sample showed Fe II features of various strengths. Non-radial pulsation was present or suspected in 19% of the sample. One third of the sample has at least one visual companion with 17% having a visual companion closer than 1 arcsec. There are many spectroscopic binaries in the sample, and 22% of these have already-known periods. I suspect there are 20-40 (another 15-30%) other spectroscopic binaries in the sample. These suspected binaries have small velocity variations, which may result from non-radial pulsations

instead. The study of gravitational darkening effects was somewhat inconclusive but a comparison of the rotationally broadened profiles of He I λ4471 and Mg II λ4481 is consistent with expectations for rotationally distorted and gravity darkened stars. Further analysis is needed. In general, the circumstellar disks of Be stars are not constant or static (for a variety of reasons) and manifest that variability in many ways.

8.2 Future Work

In the future, I plan to continue to monitor the 128 Be survey stars (perhaps removing some of the non-Be stars). I may also be able to perform a similar survey in the southern hemisphere. More detailed modeling is required for the relationship between $V \sin i$ and the width of the temperature dependent He I λ4471 and Mg II λ4481 lines. As I found many candidates for non-radial pulsation, I plan to conduct intensive time series campaigns on those stars. Utilizing the data I have right now, together with measurements from the literature, I plan to further investigate disk variability and duplicity (especially for lesser-studied stars). A literature search for these measurements is already underway. Continuing observations will also help define interesting targets for speckle studies and interferometric observations.

In the end, I hope that my survey and its continuance will be able to help answer many of the big questions about Be stars, either by me and my future collaborators/minions, or by others (as I will make these data available to the community). First, what is the actual circumstellar environment of a Be star and how does it change? How enshrouded in circumstellar material are these stars? This harkens to the discovery of so much "shelliness" in my sample. Second, how many Be stars show signs of duplicity? Duplicity (and thus mass transfer) may be a good explanation

for the rapid rotation of these stars. Third, what role does gravity darkening play in the determination of the rotation speed of a Be star and how close are these stars to critical rotation? Fourth, what role does non-radial pulsation play in Be stars, what percentage of Be stars show evidence of it, and what sorts of periods of pulsation are common?

References

Abt, H. A., & Hunter, Jr., J. H. 1962, ApJ, 136, 381

Abt, H. A., Levato, H., & Grosso, M. 2002, ApJ, 573, 359

Adelman, S. J., Pintado, O. I., Nieva, F., Rayle, K. E., & Sanders, Jr., S. E. 2002, A&A, 392, 1031

Ak, H., et al. 2007, A&A, 463, 233

Albert, J., et al. 2006, Science, 312, 1771

Andrillat, Y. 1983, A&AS, 53, 319

Antokhina, E. A., & Cherepashchuk, A. M. 1988, Soviet Astronomy Letters, 14, 105

Antokhina, E. A., & Kumsiashvili, M. I. 1999, Astronomy Letters, 25, 662

Apparao, K. M. V., Tarafdar, S. P., Verma, R. P., Iyengar, K. V. K., & Ghosh, K. K. 1993, Astrophys. Astr., 14, 131

Appenzeller, I. 1967, PASP, 79, 102

Arias, M. L., Zorec, J., Cidale, L., Ringuelet, A. E., Morrell, N. I., & Ballereau, D. 2006, A&A, 460, 821

Bagnuolo, Jr., W. G., Gies, D. R., Hahula, M. E., Wiemker, R., & Wiggs, M. S. 1994, ApJ, 423, 446

Bidelman, W. P. 1988, PASP, 100, 1084

Bildsten, L., et al. 1997, ApJS, 113, 367

Bjorkman, K. S. 2000, in ASP Conference Series, Vol. 214, IAU Colloq. 175: The Be Phenomenon in Early-Type Stars, ed. M. A. Smith, H. F. Henrichs, & J. Fabregat (San Francisco: ASP), 384

Bjorkman, K. S., Miroshnichenko, A. S., McDavid, D., & Pogrosheva, T. M. 2002, ApJ, 573, 812

Bonning, E. W., & Falanga, M. 2005, A&A, 436, L31

Bowers, R. L., & Deeming, T. 1984, Astrophysics. Volume 1 - Stars (Boston: Jones and Bartlett Publishers, Inc.)

Bozic, H., Harmanec, P., Horn, J., Koubsky, P., Scholz, G., McDavid, D., Hubert, A.-M., & Hubert, H. 1995, A&A, 304, 235

Brandt, N., & Podsiadlowski, P. 1995, MNRAS, 274, 461

Brunini, A. 1998, Planet. Space Sci., 47, 175

Carciofi, A. C., & Bjorkman, J. E. 2006, ApJ, 639, 1081

Casares, J., Ribas, I., Paredes, J. M., Martí, J., & Allende Prieto, C. 2005, MNRAS, 360, 1105

Castelli, F. 1991, A&A, 251, 106

Castelli, F., & Kurucz, R. L. 2003, in IAU Symposium, Vol. 210, Modelling of Stellar Atmospheres, ed. N. Piskunov, W. W. Weiss, & D. F. Gray (San Francisco: ASP), 20

Chalabaev, A., & Maillard, J. P. 1983, A&A, 127, 279

Chauville, J., Zorec, J., Ballereau, D., Morrell, N., Cidale, L., & Garcia, A. 2001, A&A, 378, 861

Chesneau, O., et al. 2005, A&A, 435, 275

Clark, J. S., Tarasov, A. E., Okazaki, A. T., Roche, P., & Lyuty, V. M. 2001, A&A,

380, 615

Clark, J. S., et al. 1998, MNRAS, 294, 165

Coe, M. J. 2000, in The Be Phenomenon in Early-Type Stars, IAU Coll. 175 (ASP Conf. Vol. 214), ed. M. A. Smith, H. F. Henrichs, & J. Fabregat (San Francisco: ASP), 656

Coe, M. J., Reig, P., McBride, V. A., Galache, J. L., & Fabregat, J. 2006, MNRAS, 368, 447

Collins, II, G. W. 1987, in IAU Colloq. 92: Physics of Be Stars, ed. A. Slettebak & T. P. Snow (Cambridge: Cambridge Univ. Press), 3

Cowley, A. P., & Hutchings, J. B. 1976, PASP, 88, 456

Cowley, A. P., McLaughlin, D. B., Toney, J., & MacConnell, D. J. 1972, PASP, 84, 834

Cox, A. N. 2000, Allen's Astrophysical Quantities (4th Ed.) (New York: AIP)

Cramer, N., Doazan, V., Nicolet, B., de La Fuente, A., & Barylak, M. 1995, A&A, 301, 811

Crampton, D., Hutchings, J. B., & Cowley, A. P. 1985, ApJ, 299, 839

Cranmer, S. R. 2005, ApJ, 634, 585

Cutri, R. M., et al. 2003, 2MASS All Sky Catalog of Point Sources (Pasadena: Univ. Massachusetts/IPAC)

Dachs, J., Kiehling, R., & Engels, D. 1988, A&A, 194, 167

Daflon, S., Cunha, K., & Becker, S. R. 1999, ApJ, 522, 950

Daflon, S., Cunha, K., Smith, V. V., & Butler, K. 2003, A&A, 399, 525

de Loore, C., et al. 1984, A&A, 141, 279

Delgado-Martí, H., Levine, A. M., Pfahl, E., & Rappaport, S. A. 2001, ApJ, 546, 455

Denizman, L., Koktay, T., Hack, M., & Eker, T. 1993, Ap&SS, 208, 135

Djurašević, G., Zakirov, M., Eshankulova, M., & Erkapić, S. 2001, A&A, 374, 638

Dudley, R. E., & Jeffery, C. S. 1990, MNRAS, 247, 400

Eggen, O. J. 1963, AJ, 68, 483

Eggleton, P. P. 1983, ApJ, 268, 368

Engin, S., & Yuce, K. 1997, IBVS, 4454, 1

Farrell, S. A., Sood, R. K., & O'Neill, P. M. 2006, MNRAS, 367, 1457

Finger, M. H., Cominsky, L. R., Wilson, R. B., Harmon, B. A., & Fishman, G. J. 1994, in The Evolution of X-ray Binaries, ed. S. Holt & C. S. Day (New York: AIP), 459

Finley, J. P., Belloni, T., & Cassinelli, J. P. 1992, A&A, 262, L25

Fitzpatrick, E. L. 1999, PASP, 111, 63

Floquet, M., Hubert, A. M., Chauville, J., Chatzichristou, H., & Maillard, J. P. 1989, A&A, 214, 295

Floquet, M., Hubert, A. M., Hubert, H., Ballereau, D., & Chauville, J. 1995, A&A, 294, 227

Fontaine, G., Villeneuve, B., Landstreet, J. D., & Taylor, R. H. 1982, ApJS, 49, 259

Frémat, Y., Neiner, C., Hubert, A.-M., Floquet, M., Zorec, J., Janot-Pacheco, E., & Renan de Medeiros, J. 2006, A&A, 451, 1053

Frémat, Y., Zorec, J., Hubert, A.-M., & Floquet, M. 2005, A&A, 440, 305

Friend, D. B., & Castor, J. I. 1982, ApJ, 261, 293

Fullerton, A. W., Massa, D. L., Prinja, R. K., Owocki, S. P., & Cranmer, S. R. 1997, A&A, 327, 699

Gaposchkin, S., & Shapley, H. 1937, Annals of Harvard College Observatory, 105, 509

Gehrz, R. D., et al. 1995, ApJ, 439, 417

Gehrz, R. D., Smith, N., Jones, B., Puetter, R., & Yahil, A. 2001, ApJ, 559, 395

Gies, D. R. 2000, in IAU Colloq. 175: The Be Phenomenon in Early-Type Stars

Gies, D. R., et al. 2007, ApJ, 654, 527

Gies, D. R., Bagnuolo, Jr., W. G., Ferrara, E. C., Kaye, A. B., Thaller, M. L., Penny, L. R., & Peters, G. J. 1998, ApJ, 493, 440

Gies, D. R., & Bolton, C. T. 1986, ApJS, 61, 419

Gies, D. R., et al. 2003, ApJ, 583, 424

Giovannelli, F., & Graziati, L. S. 1992, Space Sci. Rev., 59, 1

Giovannelli, F., Sabau-Graziati, L., Bernabei, S., & Galleti, S. 1999, IAU Circ., 7293, 1

Giuricin, G., & Mardirossian, F. 1981, A&A, 101, 138

Golovatyi, V. V., & Skulskii, M. Y. 1992, Soviet Astronomy, 36, 550

Gray, D. F. 1992, The Observation and Analysis of Stellar Photospheres (2nd ed.; Cambridge, UK : Cambridge University Press)

Gregory, P. C. 2002, ApJ, 575, 427

Grundstrom, E. D., et al. 2007a, ApJ, 656, 431

——. 2007b, ApJ, 660, 1398

——. 2007c, ApJ, 656, 437

Grundstrom, E. D., & Gies, D. R. 2006, ApJ, 651, L53

Grundstrom, E. D., Gies, D. R., Hillwig, T. C., McSwain, M. V., Smith, N., Gehrz, R. D., Stahl, O., & Kaufer, A. 2007d, ArXiv e-prints, 706

Gulati, R. K., Malagnini, M. L., & Morossi, C. 1989, A&AS, 80, 73

Hahula, M. E., & Gies, D. R. 1994, in IAU Symposium, Vol. 162, Pulsation, Rotation, and Mass Loss in Early-Type Stars, ed. L. A. Balona, H. F. Henrichs, & J. M. Le Contel, 100–+

Haigh, N. J., Coe, M. J., & Fabregat, J. 2004, MNRAS, 350, 1457

Haigh, N. J., Coe, M. J., Steele, I. A., & Fabregat, J. 1999, MNRAS, 310, L21

Hall, T. A., Finley, J. P., Corbet, R. H. D., & Thomas, R. C. 2000, ApJ, 536, 450

Harmanec, P. 1984, Bull. Astr. Inst. Cz., 35, 193

Harmanec, P. 1987, in IAU Colloq. 92: Physics of Be Stars, ed. A. Slettebak & T. P. Snow (Cambridge: Cambridge Univ. Press), 339

——. 1988, Bull. Astr. Inst. Cz., 39, 329

——. 2001, PAICz, 89, 9

——. 2002, Astronomische Nachrichten, 323, 87

Harmanec, P., et al. 1996, A&A, 312, 879

Harries, T. J. 2000, MNRAS, 315, 722

Hayasaki, K., & Okazaki, A. T. 2005, MNRAS, 360, L15

Herrero, A., Kudritzki, R. P., Gabler, R., Vilchez, J. M., & Gabler, A. 1995, A&A, 297, 556

Hilditch, R. W. 2001, An Introduction to Close Binary Stars (Cambridge, UK : Cambridge University Press)

Hilditch, R. W., McLean, B. J., & Reid, I. N. 1982, MNRAS, 200, 1153

Hill, G., Harmanec, P., Pavlovski, K., Bozic, H., Hadrava, P., Koubsky, P., & Ziznovsky, J. 1997, A&A, 324, 965

Hillwig, T. C., Gies, D. R., Bagnuolo, Jr., W. G., Huang, W., McSwain, M. V., & Wingert, D. W. 2006, ApJ, 639, 1069

Horn, J., Hubert, A. M., Hubert, H., Koubsky, P., & Bailloux, N. 1992, A&A, 259, L5

Horne, K. 1995, A&A, 297, 273

Horne, K., & Marsh, T. R. 1986, MNRAS, 218, 761

Howarth, I. D. 1983, MNRAS, 203, 801

Huang, S.-S. 1972, ApJ, 171, 549

Hubert, A. M., & Floquet, M. 1998, A&A, 335, 565

Hubert, A. M., et al. 1997, A&A, 324, 929

Hummel, W., & Vrancken, M. 1995, A&A, 302, 751

——. 2000, A&A, 359, 1075

Hutchings, J. B. 1977, MNRAS, 181, 619

——. 1984, PASP, 96, 312

Hutchings, J. B., & Crampton, D. 1981, PASP, 93, 486

Kalas, P., & Jewitt, D. 1997, Nature, 386, 52

Kambe, E., et al. 1997, ApJ, 481, 406

Kaper, L. 1998, in Boulder-Munich II: Properties of Hot Luminous Stars (ASP Conf. Vol. 131), ed. I. Howarth (San Francisco: ASP), 427

King, A. R., & Jameson, R. F. 1979, A&A, 71, 326

Koenigsberger, G., Canalizo, G., Arrieta, A., Richer, M. G., & Georgiev, L. 2003, Rev. Mexicana Astron. Astrofis., 39, 17

Koubsky, P. 1978, Bull. Astr. Inst. Cz., 29, 288

Koubský, P., Ak, H., Harmanec, P., Yang, S., & Božić, H. 2004, in ASP Conference Series, Vol. 310, IAU Colloq. 193: Variable Stars in the Local Group, ed. D. W. Kurtz & K. R. Pollard, 387

Koubsky, P., Harmanec, P., Gulliver, A. F., Ballereau, D., & Chauville, J. 1989, Bull. Astr. Inst. Cz., 40, 31

Koubský, P., et al. 2000, A&A, 356, 913

Koubský, P., Harmanec, P., Yang, S., Netolický, M., Škoda, P., Šlechta, M., & Korčáková, D. 2006, A&A, 459, 849

Kreiner, J. M. 2004, Acta Astron., 54, 207

Lamers, H. J. G. L. M., van den Heuvel, E. P. J., & Petterson, J. A. 1976, A&A, 49, 327

Lanz, T., & Hubeny, I. 2003, ApJS, 146, 417

——. 2007, ApJS, 169, 83

Larionov, V., Lyuty, V. M., & Zaitseva, G. V. 2001, A&A, 378, 837

Leahy, D. A. 2001, A&A, 380, 516

Leushin, V. V. 1988, Soviet Astronomy, 32, 430

Levenhagen, R. S., & Leister, N. V. 2004, AJ, 127, 1176

——. 2006, MNRAS, 371, 252

Levine, A. M., Bradt, H., Cui, W., Jernigan, J. G., Morgan, E. H., Remillard, R., Shirey, R. E., & Smith, D. A. 1996, ApJ, 469, L33

Li, X.-D., & van den Heuvel, E. P. J. 1999, ApJ, 513, L45

Linnell, A. P. 2002, MNRAS, 334, 963

Linnell, A. P., et al. 2006, A&A, 455, 1037

Liu, Q.-Z., & Hang, H.-R. 1999, A&A, 350, 855

——. 2001, Ap&SS, 275, 401

Liu, Q. Z., Hang, H. R., Wu, G. J., Chang, J., & Zhu, Z. X. 2000, A&A, 359, 646

Liu, Q. Z., & Yan, J. Z. 2005, New Astr., 11, 130

Lubow, S. H., & Shu, F. H. 1975, ApJ, 198, 383

Lucy, L. B. 2005, A&A, 439, 663

Lucy, L. B., & Sweeney, M. A. 1971, AJ, 76, 544

Lyubimkov, L. S., Rostopchin, S. I., Roche, P., & Tarasov, A. E. 1997, MNRAS, 286, 549

Lyuty, V. M., & Zaĭtseva, G. V. 2000, Astr. Lett., 26, 9

Maintz, M., Rivinius, T., Stahl, O., Stefl, S., & Appenzeller, I. 2005, PAICz, 93, 21

Markova, N., & Valchev, T. 2000, A&A, 363, 995

Marlborough, J. M., & Peters, G. J. 1986, ApJS, 62, 875

Martí, J., & Paredes, J. M. 1995, A&A, 298, 151

Martins, F., Schaerer, D., & Hillier, D. J. 2005a, A&A, 436, 1049

Martins, L. P., Delgado, R. M. G., Leitherer, C., Cerviño, M., & Hauschildt, P. 2005b, MNRAS, 358, 49

Massi, M. 2004, A&A, 422, 267

Massi, M., Ribó, M., Paredes, J. M., Garrington, S. T., Peracaula, M., & Martí, J. 2004, A&A, 414, L1

McErlean, N. D., Lennon, D. J., & Dufton, P. L. 1999, A&A, 349, 553

McSwain, M. V. 2003, ApJ, 595, 1124

McSwain, M. V., & Gies, D. R. 2005, ApJ, 622, 1052

McSwain, M. V., Gies, D. R., Huang, W., Wiita, P. J., Wingert, D. W., & Kaper, L. 2004, ApJ, 600, 927

Merrill, P. W., & Burwell, C. G. 1943, Contributions from the Mount Wilson Observatory / Carnegie Institution of Washington, 682, 1

Milano, L., Vittone, A., Ciatti, F., Mammano, A., Margoni, R., & Strazzulla, G. 1981, A&A, 100, 59

Mirabel, I. F., Rodrigues, I., & Liu, Q. Z. 2004, A&A, 422, L29

Morbey, C. L., & Brosterhus, E. B. 1974, PASP, 86, 455

Morel, T., Marchenko, S. V., Pati, A. K., Kuppuswamy, K., Carini, M. T., Wood, E., & Zimmerman, R. 2004, MNRAS, 351, 552

Morgan, W. W., Code, A. D., & Whitford, A. E. 1955, ApJS, 2, 41

Morris, S. L., Bolton, C. T., Fernie, J. D., & Percy, J. R. 1988, PASP, 100, 954

Motch, C., Stella, L., Janot-Pacheco, E., & Mouchet, M. 1991, ApJ, 369, 490

Nazarenko, V. V., & Glazunova, L. V. 2003, Astr. Rep., 47, 1027

——. 2006a, Astr. Rep., 50, 369

——. 2006b, Astr. Rep., 50, 380

Negueruela, I., Reig, P., Coe, M. J., & Fabregat, J. 1998, A&A, 336, 251

Negueruela, I., Steele, I. A., & Bernabeu, G. 2004, Astronomische Nachrichten, 325, 749

Neiner, C., et al. 2005, A&A, 437, 257

North, J. R., Tuthill, P. G., Tango, W. J., & Davis, J. 2007, MNRAS, 377, 415

Ochsenbein, F., & Halbwachs, J. L. 1982, A&AS, 47, 523

Okazaki, A. T., Bate, M. R., Ogilvie, G. I., & Pringle, J. E. 2002, MNRAS, 337, 967

Okazaki, A. T., & Negueruela, I. 2001, A&A, 377, 161

Paredes, J. M., Martí, J., Peracaula, M., & Ribó, M. 1997, A&A, 320, L25

Paredes, J. M., et al. 1994, A&A, 288, 519

Pavlovski, K., & Ruzic, Z. 1988, A&AS, 76, 137

Penny, L. R., Gies, D. R., & Bagnuolo, Jr., W. G. 1999, ApJ, 518, 450

Percy, J. R., & Bakos, A. G. 2001, PASP, 113, 748

Percy, J. R., Hosick, J., Kincaide, H., & Pang, C. 2002, PASP, 114, 551

Peters, G. J. 1976, in IAU Symposium, Vol. 70, Be and Shell Stars, ed. A. Slettebak (Dordrecht: D. Reidel Publishing), 417

Peters, G. J. 1983, PASP, 95, 311

Petrovic, J., Langer, N., & van der Hucht, K. A. 2005, A&A, 435, 1013

Piccioni, A., et al. 2000a, in The Be Phenomenon in Early-Type Stars, IAU Colloq. 175 (ASP Conf. Vol. 214), ed. M. A. Smith, H. F. Henrichs, & J. Fabregat (San Francisco: ASP), 569

Piccioni, A., Bartolini, C., Bernabei, S., Galleti, S., Guarnieri, A., & Valentini, G. 2000b, in The Be Phenomenon in Early-Type Stars, IAU Colloq. 175 (ASP Conf. Vol. 214), ed. M. A. Smith, H. F. Henrichs, & J. Fabregat (San Francisco: ASP), 585

Popper, D. M. 1943, ApJ, 97, 394

Porter, J. M., & Rivinius, T. 2003, PASP, 115, 1153

Punsly, B. 1999, ApJ, 519, 336

Quirrenbach, A., et al. 1997, ApJ, 479, 477

Rappaport, S., & van den Heuvel, E. P. J. 1982, in IAU Symposium, Vol. 98, Be Stars, ed. M. Jaschek & H.-G. Groth (Dordrecht: D. Reidel Publishing Co.), 327–344

Ray, P. S., Foster, R. S., Waltman, E. B., Tavani, M., & Ghigo, F. D. 1997, ApJ, 491, 381

Reig, P., Chakrabarty, D., Coe, M. J., Fabregat, J., Negueruela, I., Prince, T. A., Roche, P., & Steele, I. A. 1996, A&A, 311, 879

Reig, P., Fabregat, J., & Coe, M. J. 1997, A&A, 322, 193

Reig, P., Ribó, M., Paredes, J. M., & Martí, J. 2003, A&A, 405, 285

Repolust, T., Puls, J., & Herrero, A. 2004, A&A, 415, 349

Reynolds, A. P., Hilditch, R. W., Bell, S. A., Pollacco, D. L., & Edwin, R. P. 1992, MNRAS, 258, 439

Reynolds, R. J., Chaudhary, V., Madsen, G. J., & Haffner, L. M. 2005, AJ, 129, 927

Rivinius, T., Baade, D., & Štefl, S. 2003, A&A, 411, 229

Rivinius, T., & Štefl, S. 2000, in ASP Conference Series, Vol. 214, IAU Colloq. 175: The Be Phenomenon in Early-Type Stars, ed. M. A. Smith, H. F. Henrichs, & J. Fabregat, 581

Rivinius, T., Štefl, S., & Baade, D. 2006, A&A, 459, 137

Rivinius, T., Štefl, S., Maintz, M., Stahl, O., & Baade, D. 2004, A&A, 427, 307

Roberts, D. H., Lehar, J., & Dreher, J. W. 1987, AJ, 93, 968

Roche, P., et al. 1993, A&A, 270, 122

Ryans, R. S. I., Dufton, P. L., Rolleston, W. R. J., Lennon, D. J., Keenan, F. P., Smoker, J. V., & Lambert, D. L. 2002, MNRAS, 336, 577

Sahade, J., West, R. M., & Skul'Skii, M. Y. 2002, Rev. Mexicana Astron. Astrofis., 38, 259

Scargle, J. D. 1982, ApJ, 263, 835

Shafter, A. W., Szkody, P., & Thorstensen, J. R. 1986, ApJ, 308, 765

Skul'Skii, M. Y. 1992, Soviet Ast., 36, 411

Skul'Skii, M. Y., & West, R. M. 1993, Astr. Rep., 37, 594

Slettebak, A. 1982, ApJS, 50, 55

Smith, N., Gehrz, R. D., & Goss, W. M. 2001, AJ, 122, 2700

Smith, N., Gehrz, R. D., Humphreys, R. M., Davidson, K., Jones, T. J., & Krautter, J. 1999, AJ, 118, 960

Smith, N., Gehrz, R. D., Stahl, O., Balick, B., & Kaufer, A. 2002, ApJ, 578, 464

Stee, P., de Araujo, F. X., Vakili, F., Mourard, D., Arnold, L., Bonneau, D., Morand, F., & Tallon-Bosc, I. 1995, A&A, 300, 219

Steele, I. A., Negueruela, I., & Clark, J. S. 1999, A&AS, 137, 147

Steele, I. A., Negueruela, I., Coe, M. J., & Roche, P. 1998, MNRAS, 297, L5

Stickland, D. J. 1992, MNRAS, 257, 21P

Tarasov, A. E. 2000, in ASP Conf. Ser. 214: The Be Phenomenon in Early-Type Stars, ed. M. A. Smith, H. F. Henrichs, & J. Fabregat (San Francisco: ASP), 644

Taylor, A. R., & Gregory, P. C. 1982, ApJ, 255, 210

Taylor, A. R., Kenny, H. T., Spencer, R. E., & Tzioumis, A. 1992, ApJ, 395, 268

Telting, J. H., Waters, L. B. F. M., Roche, P., Boogert, A. C. A., Clark, J. S., de Martino, D., & Persi, P. 1998, MNRAS, 296, 785

Theodossiou, E. 1985, MNRAS, 214, 327

Townsend, R. H. D., Owocki, S. P., & Howarth, I. D. 2004, MNRAS, 350, 189

Tycner, C., et al. 2006, AJ, 131, 2710

——. 2004, AJ, 127, 1194

——. 2005, ApJ, 624, 359

Umana, G., Maxted, P. F. L., Trigilio, C., Fender, R. P., Leone, F., & Yerli, S. K. 2000, A&A, 358, 229

Underhill, A., & Doazan, V. 1982, B Stars With and Without Emission Lines, NASA SP-456 (Washington, DC: NASA)

Underhill, A. B., Divan, L., Prevot-Burnichon, M.-L., & Doazan, V. 1979, MNRAS, 189, 601

Šimon, V. 1999, A&AS, 134, 1

Štefl, S., Harmanec, P., Horn, J., Koubsky, P., Kriz, S., Hadrava, P., Bozic, H., & Pavlovski, K. 1990, Bull. Astr. Inst. Cz., 41, 29

Valdes, F., Gupta, R., Rose, J. A., Singh, H. P., & Bell, D. J. 2004, ApJS, 152, 251

van Kerkwijk, M. H., van Paradijs, J., & Zuiderwijk, E. J. 1995, A&A, 303, 497

Wade, R. A., & Rucinski, S. M. 1985, A&AS, 60, 471

Walborn, N. R. 1976, ApJ, 205, 419

——. 1982, AJ, 87, 1300

Walborn, N. R., & Fitzpatrick, E. L. 1990, PASP, 102, 379

Wang, Z. X., & Gies, D. R. 1998, PASP, 110, 1310

Waters, L. B. F. M. 1986, A&A, 162, 121

Waters, L. B. F. M., Cote, J., & Pols, O. R. 1991, A&A, 250, 437

Wen, L., Cui, W., Levine, A. M., & Bradt, H. V. 1999, ApJ, 525, 968

Wen, L., Levine, A. M., Corbet, R. H. D., & Bradt, H. V. 2006, ApJS, 163, 372

Wilson, R. 1958, MNRAS, 118, 92

Wolff, S. C. 1990, AJ, 100, 1994

Yudin, R. V. 2001, A&A, 368, 912

Zamanov, R., & Martí, J. 2000, A&A, 358, L55

Zamanov, R. K., Martí, J., Paredes, J. M., Fabregat, J., Ribó, M., & Tarasov, A. E. 1999, A&A, 351, 543

Zamanov, R. K., Reig, P., Martí, J., Coe, M. J., Fabregat, J., Tomov, N. A., & Valchev, T. 2001, A&A, 367, 884

Zamanov, R. K., & Zamanova, V. I. 1995, IBVS, 4189, 1

Zorec, J., Frémat, Y., & Cidale, L. 2005, A&A, 441, 235

Appendices

– A –

Wing Velocities by Cross Correlation

A.1 The Method

We want to sample the wings of the hydrogen lines because the cores are affected by emission and the wings sample the most rapidly moving gas. We arbitrarily chose to sample at the 25%-of-maximum or -minimum level. The following method was first used by Shafter et al. (1986).

In a sentence, this method uses two oppositely signed Gaussian functions and determines the mid-point position between the wings by cross-correlating these Gaussians with the spectral line profile.

These two Gaussians are separated by a length (Δx) which is the distance between the midpoints of the two Gaussians divided by two. Each Gaussian has a FWHM of $\approx \Delta x$ divided by 3.5 (see Fig. A.1).

This template is cross-correlated with the spectral feature and when the cross-correlation function crosses zero, one finds the radial velocity of the wings as the sampled line bisector (as shown in Figure A.2).

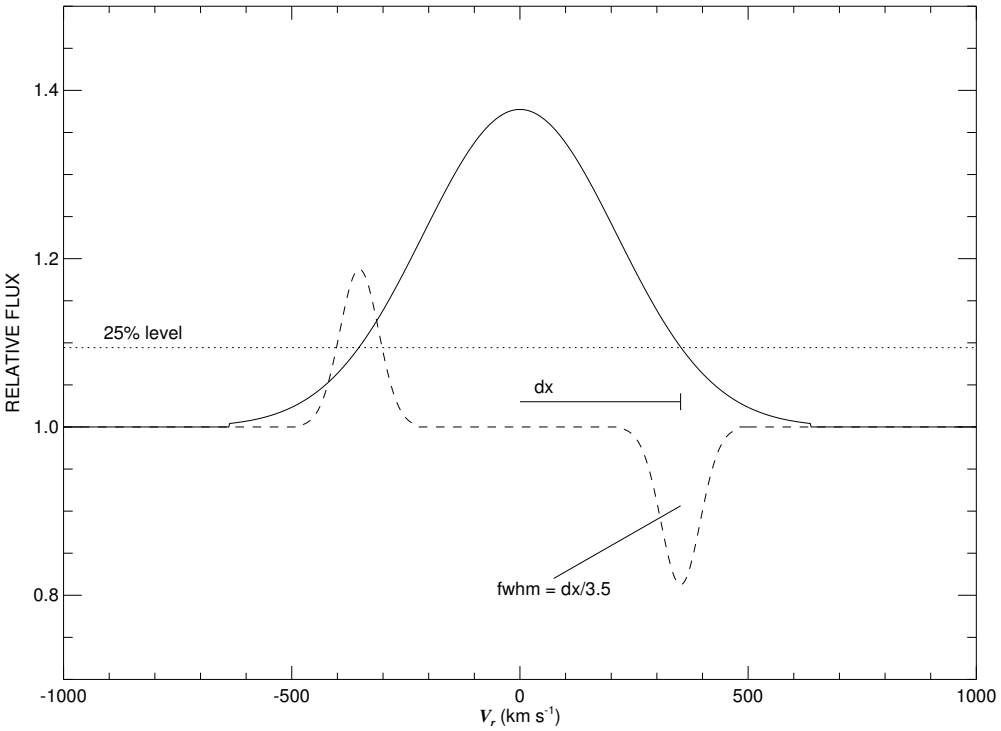

Figure A.1: Wing velocity measurement diagram

A.2 The Errors

We assume the shape of the spectral line profile is Gaussian (it is not, but it approximates well enough). Therefore, the function is

$$f = \exp\left[-\frac{1}{2}\left(\frac{\Delta x}{\sigma}\right)^2\right] \tag{A.1}$$

The error in the wing velocity is related to the slope of the curve at the point we measure on the x-axis (either λ or v) by $\sigma\,(vel) = \sigma\,(f_j)\,/\,(df/dv)$. The steeper the slope of the curve, the fewer points on the x-axis will be covered by a range on the y-axis (the y-axis range is determined by the signal-to-noise ratio).

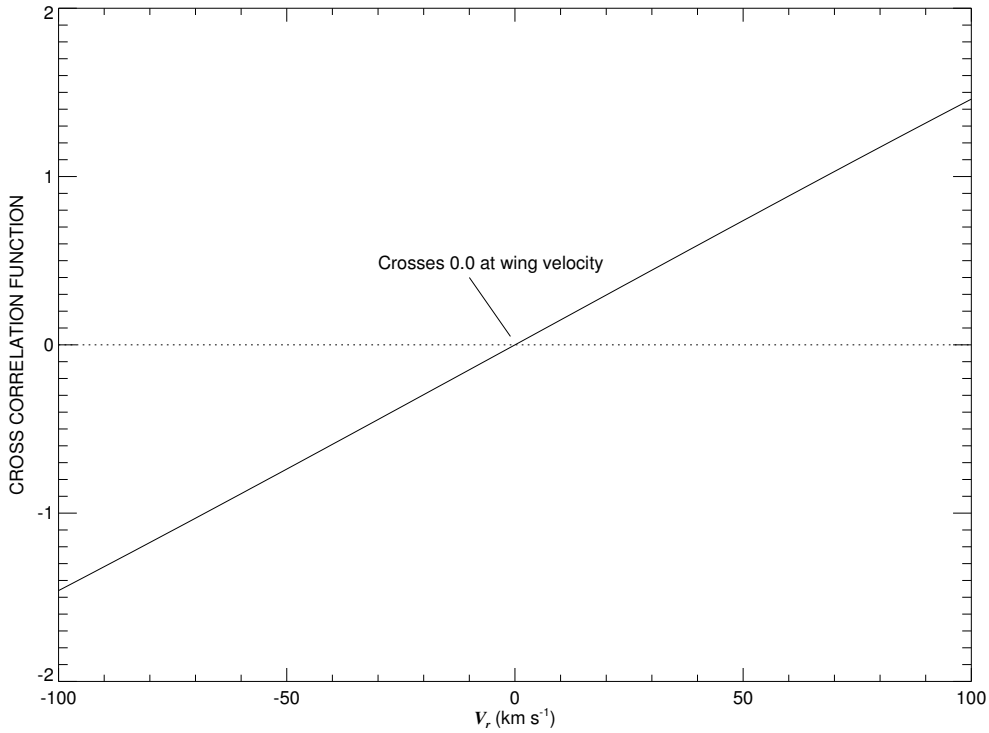

Figure A.2: Wing velocity cross-correlation diagram

Since the slope of the line is the change in x over the change in y, using the Gaussian above,

$$\frac{df}{dx} = -\frac{\Delta x}{\sigma^2} \exp\left[-\frac{1}{2}\left(\frac{\Delta x}{\sigma}\right)^2\right]. \tag{A.2}$$

Since we evaluated the wing velocity at the 25% level, we may evaluate both the function (eq. A.1) and the slope (eq. A.2) at 0.25:

$$\begin{aligned} 0.25 &= \exp\left[-\frac{1}{2}\left(\frac{\Delta x}{\sigma}\right)^2\right] \\ \ln 4 &= \frac{1}{2}\left(\frac{\Delta x}{\sigma}\right)^2 \\ \Delta x &= \sigma\sqrt{2\ln 4} \qquad \text{(A.3)} \\ \frac{df}{dx} &= -0.25\ \frac{\Delta x}{\sigma^2} = -\frac{1}{2}\frac{\ln 4}{\mathrm{d}x} \qquad \text{(A.4)} \end{aligned}$$

where $\mathrm{d}x$ may be either $\mathrm{d}\lambda$ or $\mathrm{d}v$ (depending if one works in wavelength or velocity space).

One may also consider the slope to relate the error in x $[\sigma(vel)]$ to the error in y $[\sigma(F_x)]$ where F_x is the value of the spectral feature at the point x. Therefore, the error in the wing velocity at the 25% level is

$$\sigma(vel) = \frac{2}{\ln 4}\ \sigma(F_x)\ \mathrm{d}x.$$

However, we must also take into account the fact that we are estimating the bisector position from two regions and we must also consider the second error. Thus,

$$\Delta wingvel = \frac{1}{2}\sqrt{\Delta v_{lo}^2 + \Delta v_{hi}^2} = \frac{1}{2}\sqrt{2\ \Delta v^2} = \frac{\sigma\,(vel)}{\sqrt{2N}}$$

since the change in velocity is symmetric about the midpoint and the error in the position of the 25% level goes as $1/\sqrt{N}$. The number of points the Gaussians cover, N, is the FWHM of the Gaussians divided by the step size (h_x). We chose a Gaussian FWHM of $\Delta x/3.5$. We also know $\sigma(F_x) = (F_x/F_c)^{1/2}\ F_c\ \sigma_{cont}$ (see eq. 7.5) and we

have set the continuum to 1 so $F_c = 1$. Therefore,

$$\begin{aligned} \sigma(wingvel) &= \frac{2}{\ln 4}\sqrt{F_x}\ \sigma_{cont}\ \mathrm{d}x\ \frac{1}{\sqrt{2}}\ \sqrt{\frac{3.5}{\mathrm{d}x}h_x} \\ &= \frac{\sqrt{7}}{\ln 4}\ \sigma_{cont}\ \sqrt{F_x\ \mathrm{d}x\ h_x} \end{aligned} \tag{A.5}$$

where x can be either λ or v.

– B –

Useful Programs

This appendix gives descriptions of many of the programs I used during this research. All listed programs may be found in the accompanying CD or at `http://www.chara.gsu.edu/~erika/Research/programs.html` .

B.1 RY Scuti Programs

- *subcs-v3* – interactive program to remove the sharp nebular features from the Coudé Feed data by shifting the [N II λ6583] feature, scaling it, and subtracting it from the other [N II] line, Hα, and He I λ6678.
- *subcsFEint* – remove the sharp nebular features from the FEROS data by excising them via linear interpolation (removed the same lines as *subcs-v3*)
- *fixrectha* – fix the rectification in the vicinity of Hα (used in *subcs-v3* and *subcsFEint*)
- *plotorbo* – generate the phase-ordered plots seen in Ch. 2 (written by Gies, slightly modified by me)
- *exciseneb* – excise the sharp nebular features and telluric regions from the FEROS spectra via linear interpolation, make a new stack of excised spectra
- *rescaleflux* – rescale the emission flux to a constant quadrature flux
- *readphot* – read the Djurasevic photometry file for use in other programs

- *getvreqwerr* – find errors in $W_\lambda(\mathrm{H}\alpha)$ and $V_r(\mathrm{H}\alpha)$
- *pbryscuti* – make Fig. 2.17 (modifed from an earlier Gies program)
- *ploteqw* – make Fig. 2.18
- *lhvsfwo* – compare line widths with Lanz & Hubeny models and determine $V \sin i$ using *lhvsfw* (written previously by Gies, modified by Boyajian and I)
- *lhvsfw* – determine FWHM vs. $V \sin i$ using Lanz & Hubeny models with simple linear limb darkening (in lhtrans) (written previously by Gies)

B.2 X-Ray Binaries

- *runtwogauss* – interactive program to make a double Gaussian fit of a double-peaked spectral line (for the V/R stuff in Table 6.1)
- *XPer/makelatex-XPer* – make the X Per part of Table 6.1
- *HDE245770/makelatex-245770* – make the HDE 245770 part of Table 6.1
- *XPer/profavg-06.pro* – plot the average profile for each run (specific to X Per) (Fig. 6.3)
- *HDE245770/profavg-06.pro* – plot the average profile for each run (specific to HDE 245770) (Fig. 6.2)
- *rxhorbvar* – for the microquasar - make a triple plot of radio, X-ray, and Hα vs orbital phase (Fig. 5.5)

B.3 Be Star Disks

- *eqwfwhm* – get Hα equivalent width and image FWHM from *hvlines* output
- *hvlines* – numerical version of simple shell line model from Hummel & Vrancken (2000). This version does only Hα and returns equivalent width and optical depth unity disk radius.
- *hvlinesg* – run *hvlines* for a grid of densities

- *beradius* – find the half maximum intensity radius of a Be star disk from the Hα equivalent width using adopted stellar/disk parameters
- *readhv* – read in results from *hvlinesg*
- *haeqw* – Estimate H-alpha equivalent width of Be star disks, (has subprograms *inclination*, *raddisk*, *harmanec*)
- *plothr* – make Fig. 4.1
- *bediskplot* – make Fig. 4.2

B.4 Be Star Survey Programs

- *readfile* – read a data file as an array of strings for later use/parsing (currently one of my very favorites)
- *fix2006* – set a bad region in one night of 2006 blue data to 1.0

B.4.1 Plotting Programs

- *plotblue1s* – plot single spectra from a file (makes Figs. 7.2, 7.3, 7.4, 7.5)
- *plotdeneb* – make Figures 7.7 and 7.8
- *plot4* – make the quadruple plot in the appendix - appears on screen
- *plot4all* – run the *plot4* program for a list of stars, make a file of plots that need no modification and a file of plots that need further modification to look good
- *plot4eps* – the same as *plot4*, except print to a Post-Script file
- *plot4goodeps* – run *plot4eps* on all stars that need no futher modification
- *plot4tweakall* – interactive program to make the quadruple plot and has the ability to modify all panels, then prints the final version to a Post-Script file
- *plotblue3eps* – interactive program to plot the average spectrum of each blue run for one star, first to the screen, then to a Post-Script file (after appropriate modification) (the resultant plots are seen in Appendix C)

- *plotblueps* – interactive program to plot all blue spectra for a star, first to the screen, then to a Post-Script file (after appropriate modification) (the resultant plots are seen in Appendix C)

- *plotredps* – the same as *plotblueps* except for the red data

B.4.2 Measurement Programs

- *checkhydrange* – interactive program to find the range for the *velas* program for the hydrogen lines for an entire stack of spectra of one star, output ranges to a file and also make a file of stars that need more modification

- *checkhydrangeindiv* – the same as *checkhydrange* except one finds the range for each individual spectrum of the star

- *checkabsrange* – interactive program to find the range for equivalent width, first moment, and second moment for the three absorption lines (He I λ6678, He I λ4471, and Mg II λ4481) for an entire stack of spectra of one star, output ranges to a file and also makes a file of stars that need more modification

- *checkabsrangeindiv* – the same as *checkabsrange* except one finds ranges for each individual spectrum of the star

- *measurehydchop* – interactive program to measure the equivalent width and wing velocity of the hydrogen lines (Hα and Hγ) and their errors using the ranges from *checkhydrange*; utilizes *hydchop*; put results into files for each line.

- *measurehydindiv* – the same as *measurehydchop* except for individual ranges from *checkhydrangeindiv*

- *measurehyderr* – interactive program to find the error for the hydrogen measurements (called in *measurehydchop* and *measurehydindiv*)

- *hydchop* – interactive program to "chop" out emission features in the hydrogen lines via linear interpolation (called in *measurehydchop* and *measurehydindiv*)

- *measureallabs* – measure the equivalent width and first and second moments of the three absorption lines and their errors (using *measureprofile* and *measureproferr*); output results to a file for each line

- *measureallabsindiv* – same as *measureallabs* except for individual spectrum ranges from *checkabsrangeindiv*
- *measureprofile* – measure the equivalent width and first and second moments of an absorption profile using a given range
- *measureproferr* – interactive program to measure the error in equivalent width and first and second moments of an absorption profile (error range found interactively)
- *fe2fits* – interactive program to fit an Fe II spectrum (a.k.a. Deneb) via cross-correlation and measure the equivalent width and first and second moments and their errors of the resultant cross-correlation function; results output to a file

B.4.3 Table-Making Programs

- *tablemake* – LaTeX format red and blue measurements for two tables
- *readhyd* – read a hydrogen line measurement file (called in *tablemake*)
- *readabs* – read an absorption line measurement file (called in *tablemake*)
- *tablemakefe* – LaTeX format Fe II fitting data for a table
- *tablemakewprime* – LaTeX format W'_λ data for a table
- *readwprime* – read the W'_λ data file (called in *tablemakewprime*)

B.4.4 Survey Results Programs

- *readkurucz* – read Kurucz models for various T_{eff} and $\log g$, picks out a particular $\log g$, calculate the Q parameter
- *daflonq* – estimate T_{eff} from Kurucz Q-parameter and a calibration (works in concert with *readkurucz*, but does not call it directly)
- *lheqw* – estimate equivalent widths for stellar models from the Lanz& Hubeny grids for input T_{eff} and $\log g$
- *starpar* – look up stellar parameters in stars.txt

- *eqwav* – find the corrected average equivalent widths for Hα and Hγ for each run (calls *obsrunav*, *getmeashg/ha/fe*, *lheqw*)
- *obsrunav* – find averages and standard deviations of the input quantity
- *getmeasfe, getmeasha, getmeashe, getmeashg, getmeasmg* – read the measurements files for Fe II CCFs, Hα, He I λ4471, Hγ, and Mg II λ4481, respectively
- *hplots* – make Figure 7.9 (calls *lheqw*)
- *teffcheck* – make Figure 7.10 (calls *lheqw*)
- *eqwavplots* – make the individual parts of Figure 7.11 (calls *lheqw* and *starpar*)
- *eqwhafeplots* – make Figure 7.12
- *vsinimeas* – compare $V \sin i$ with FWSM measurements (calls *starpar* and *obsrunav*), plot on-screen
- *vsiniplots* – make Figures 7.13 and 7.14 from *vsinimeas* results
- *eqwstatsplots* – deterimine statistical information on variability in corrected equivalent width for Hα, Hγ, and normal equivalent width for Fe II CCFs for each star then make Figure 7.16 (calls *starpar*)
- *eqwsummary* – determine variablity of the whole sample (in hydrogen and Fe II lines) (calls *starpar*)

B.4.5 Appendix-Related Programs

- *wingvelex* – make Figs A.1 and A.2
- *makenote* – make a template appendix note file for each survey star with various parameters inserted
- *makenotevel* – make a velocity table file for each star's appendix note
- *makeapp* – make the appendix chapter inserting the appropriate note and figures for each star (this is a great program :))

– C –

Information on Individual Be Survey Stars

C.1 Red Spectral Measurements Table

Table C.1: Spectral line data for the Hα region

Star Name	HJD (−2400000)	W_λ (Hα) (Å)	V_r (Hα) (km s^{-1})	W_λ (He I) (Å)	V_r (He I) (km s^{-1})	FWSM (He I) (km s^{-1})
HD000144	53290.752	2.854 ± 0.028	−3.0 ± 0.6	0.103 ± 0.008	−14.4 ± 12.0	171 ± 53
HD000144	53292.785	2.945 ± 0.024	−1.8 ± 0.5	0.105 ± 0.007	14.4 ± 10.7	240 ± 24
HD000144	53294.754	2.845 ± 0.039	−9.1 ± 0.8	0.071 ± 0.017	···	···
HD000144	54019.801	3.728 ± 0.030	0.8 ± 0.6	0.073 ± 0.012	···	···
HD000144	54020.804	3.650 ± 0.027	−3.0 ± 0.6	0.052 ± 0.010	···	···
HD000144	54021.799	3.692 ± 0.034	6.5 ± 0.7	0.082 ± 0.016	···	···
HD000144	54023.779	3.722 ± 0.024	−1.0 ± 0.5	0.077 ± 0.010	···	···
HD004180	53290.756	−29.803 ± 0.038	−28.7 ± 0.7	0.323 ± 0.011	−37.5 ± 4.0	222 ± 10
HD004180	53292.790	−29.665 ± 0.019	−29.5 ± 0.4	0.312 ± 0.007	−28.5 ± 2.8	254 ± 6
HD004180	53292.791	−29.733 ± 0.037	−29.9 ± 0.7	0.285 ± 0.008	−44.8 ± 3.5	227 ± 9
HD004180	53294.760	−30.065 ± 0.055	−28.4 ± 1.0	0.301 ± 0.015	−26.1 ± 6.2	231 ± 16
HD004180	53294.763	−30.135 ± 0.042	−28.6 ± 0.8	0.314 ± 0.011	−37.4 ± 4.2	248 ± 10
HD004180	54019.806	−32.892 ± 0.066	−0.8 ± 1.3	0.255 ± 0.020	−9.0 ± 9.7	230 ± 25
HD004180	54020.808	−33.645 ± 0.055	−1.1 ± 1.1	0.218 ± 0.014	−23.8 ± 7.9	213 ± 22
HD004180	54022.782	−32.478 ± 0.098	0.2 ± 1.9	0.293 ± 0.028	−36.3 ± 11.5	151 ± 46
HD004180	54022.788	−32.811 ± 0.072	0.7 ± 1.4	0.242 ± 0.021	−23.7 ± 10.8	101 ± 65
HD004180	54022.794	−33.553 ± 0.050	0.4 ± 1.0	0.251 ± 0.014	−22.8 ± 7.0	187 ± 22
HD004180	54023.784	−33.305 ± 0.057	−0.1 ± 1.1	0.284 ± 0.016	−6.0 ± 6.8	213 ± 19
HD005394	53290.757	−30.450 ± 0.028	−8.9 ± 0.6	0.376 ± 0.006	−13.9 ± 3.3	558 ± 5
HD005394	53290.758	−30.900 ± 0.042	−9.2 ± 0.8	0.386 ± 0.011	0.8 ± 5.3	563 ± 9
HD005394	53290.759	−30.788 ± 0.043	−8.3 ± 0.9	0.396 ± 0.014	2.5 ± 6.8	546 ± 12
HD005394	53292.792	−30.474 ± 0.041	−9.6 ± 0.8	0.311 ± 0.008	16.0 ± 5.1	568 ± 8
HD005394	53292.793	−31.007 ± 0.037	−9.8 ± 0.7	0.304 ± 0.012	−18.7 ± 7.4	568 ± 12
HD005394	53292.794	−31.201 ± 0.034	−8.9 ± 0.7	0.310 ± 0.013	21.5 ± 7.9	539 ± 14
HD005394	53294.767	−31.868 ± 0.047	−9.1 ± 0.9	0.363 ± 0.020	−4.6 ± 10.8	561 ± 18
HD005394	53294.768	−31.829 ± 0.042	−9.3 ± 0.8	0.420 ± 0.015	−9.9 ± 6.8	551 ± 12
HD005394	54019.808	−32.966 ± 0.051	−1.6 ± 1.0	0.166 ± 0.016	41.3 ± 19.0	509 ± 36
HD005394	54020.809	−32.517 ± 0.043	−0.7 ± 0.9	0.153 ± 0.010	−7.4 ± 12.8	654 ± 19
HD005394	54020.810	−33.047 ± 0.043	−1.6 ± 0.9	0.190 ± 0.017	−55.7 ± 17.2	580 ± 29
HD005394	54021.802	−32.341 ± 0.065	−1.2 ± 1.3	0.199 ± 0.024	17.9 ± 22.8	561 ± 39
HD005394	54022.795	−32.651 ± 0.050	−1.6 ± 1.0	0.204 ± 0.018	−23.2 ± 16.8	589 ± 27
HD005394	54023.785	−33.118 ± 0.045	−1.1 ± 0.9	0.183 ± 0.016	−55.7 ± 16.5	602 ± 26
HD006811	53290.763	1.079 ± 0.014	0.1 ± 0.3	0.134 ± 0.006	6.5 ± 4.8	116 ± 23
HD006811	53292.797	0.950 ± 0.028	1.9 ± 0.6	0.158 ± 0.007	0.0 ± 5.2	82 ± 35
HD006811	53294.772	0.748 ± 0.065	−11.0 ± 1.4	0.157 ± 0.022	7.5 ± 15.9	146 ± 60
HD006811	54019.810	1.712 ± 0.032	2.4 ± 0.7	0.125 ± 0.009	27.8 ± 8.7	···
HD006811	54020.813	1.796 ± 0.023	4.6 ± 0.5	0.113 ± 0.006	21.3 ± 6.0	40 ± 83
HD006811	54021.805	1.773 ± 0.029	2.5 ± 0.6	0.140 ± 0.010	14.3 ± 7.9	128 ± 34
HD006811	54023.788	1.739 ± 0.026	6.5 ± 0.6	0.138 ± 0.009	4.6 ± 7.5	86 ± 48
HD007636	53290.790	−46.390 ± 0.046	−14.3 ± 0.9	0.307 ± 0.013	−6.0 ± 6.1	267 ± 18
HD007636	53290.794	−46.803 ± 0.051	−14.3 ± 1.0	0.324 ± 0.015	−9.2 ± 7.0	289 ± 19
HD007636	53291.773	−46.367 ± 0.055	−14.6 ± 1.1	0.287 ± 0.010	9.1 ± 5.0	235 ± 17
HD007636	53291.777	−46.661 ± 0.061	−14.0 ± 1.2	0.306 ± 0.020	1.5 ± 9.7	254 ± 31
HD007636	53292.803	−45.899 ± 0.046	−14.8 ± 0.9	0.252 ± 0.010	−2.8 ± 5.8	234 ± 20
HD007636	53292.810	−46.522 ± 0.053	−15.1 ± 1.0	0.238 ± 0.015	3.2 ± 9.5	211 ± 36
HD007636	54019.816	−43.984 ± 0.061	−11.4 ± 1.2	0.269 ± 0.014	−1.9 ± 7.7	130 ± 48
HD007636	54019.819	−44.132 ± 0.076	−11.5 ± 1.5	0.252 ± 0.018	11.5 ± 10.7	···
HD007636	54020.815	−44.191 ± 0.058	−11.6 ± 1.1	0.234 ± 0.015	−17.0 ± 9.7	67 ± 109

Continued on Next Page...

Table C.1 – Continued

Star Name	HJD (−2400000)	W_λ (Hα) (Å)	V_r (Hα) (km s^{-1})	W_λ (He I) (Å)	V_r (He I) (km s^{-1})	FWSM (He I) (km s^{-1})
HD007636	54021.806	-43.789 ± 0.073	-11.8 ± 1.4	0.279 ± 0.022	-36.0 ± 11.6	···
HD007636	54023.790	-44.011 ± 0.076	-11.1 ± 1.5	0.328 ± 0.028	-20.4 ± 12.7	161 ± 59
HD009709	53290.800	-12.268 ± 0.029	-2.1 ± 0.6	0.114 ± 0.012	-17.9 ± 20.1	297 ± 66
HD009709	53291.803	-12.400 ± 0.034	-3.0 ± 0.7	0.177 ± 0.012	-9.0 ± 12.5	419 ± 29
HD009709	53291.808	-12.160 ± 0.040	-3.1 ± 0.8	0.164 ± 0.013	-6.3 ± 15.5	378 ± 40
HD009709	54019.822	-16.841 ± 0.035	-4.8 ± 0.7	0.074 ± 0.015	···	···
HD009709	54020.819	-16.895 ± 0.035	-3.5 ± 0.7	0.074 ± 0.013	···	···
HD009709	54021.810	-17.016 ± 0.051	-4.6 ± 1.0	0.096 ± 0.018	···	···
HD009709	54023.801	-16.949 ± 0.039	-4.0 ± 0.8	0.146 ± 0.015	-29.4 ± 19.1	304 ± 61
HD010516	53290.807	-41.888 ± 0.059	12.9 ± 1.3	0.905 ± 0.013	0.1 ± 2.7	485 ± 7
HD010516	53290.808	-42.062 ± 0.065	12.9 ± 1.4	0.890 ± 0.019	6.8 ± 4.0	473 ± 11
HD010516	53290.809	-41.878 ± 0.075	13.3 ± 1.6	0.880 ± 0.016	5.6 ± 3.3	479 ± 9
HD010516	53291.794	-41.818 ± 0.051	12.3 ± 1.1	0.815 ± 0.010	5.5 ± 2.3	478 ± 6
HD010516	53291.795	-42.760 ± 0.062	13.3 ± 1.3	0.805 ± 0.017	13.4 ± 3.8	474 ± 10
HD010516	53292.813	-40.865 ± 0.049	11.0 ± 1.1	0.800 ± 0.009	8.9 ± 2.1	471 ± 5
HD010516	53292.814	-41.974 ± 0.053	11.6 ± 1.1	0.774 ± 0.013	13.1 ± 3.1	463 ± 8
HD010516	53294.781	-43.117 ± 0.106	14.2 ± 2.3	0.777 ± 0.030	-44.0 ± 8.4	492 ± 18
HD010516	53294.785	-43.282 ± 0.081	14.9 ± 1.7	0.778 ± 0.015	-59.4 ± 4.6	496 ± 10
HD010516	54019.826	-31.598 ± 0.056	-1.5 ± 1.2	0.342 ± 0.020	-38.6 ± 12.5	···
HD010516	54020.827	-31.034 ± 0.040	-3.7 ± 0.9	0.377 ± 0.016	-43.7 ± 9.5	···
HD010516	54021.812	-31.018 ± 0.057	-4.9 ± 1.3	0.438 ± 0.016	34.0 ± 5.9	163 ± 46
HD010516	54022.798	-30.657 ± 0.062	-4.2 ± 1.4	0.478 ± 0.028	14.1 ± 10.5	154 ± 90
HD010516	54023.811	-31.245 ± 0.042	-4.5 ± 0.9	0.417 ± 0.019	-7.4 ± 8.8	···
HD011415	53290.809	4.526 ± 0.020	-17.0 ± 0.4	0.370 ± 0.008	-8.7 ± 1.5	92 ± 6
HD011415	53292.815	4.430 ± 0.021	-14.2 ± 0.4	0.389 ± 0.007	-8.0 ± 1.3	98 ± 5
HD011415	53294.789	4.539 ± 0.030	-7.5 ± 0.5	0.404 ± 0.009	-13.1 ± 1.5	98 ± 5
HD011415	54019.827	5.071 ± 0.032	-13.3 ± 0.6	0.337 ± 0.012	-5.5 ± 2.4	63 ± 14
HD011415	54020.896	4.913 ± 0.036	-13.5 ± 0.6	0.382 ± 0.015	-6.0 ± 2.7	87 ± 12
HD011415	54021.813	4.762 ± 0.044	-18.7 ± 0.8	0.359 ± 0.010	-7.4 ± 2.0	76 ± 10
HD011415	54023.812	4.870 ± 0.035	-16.9 ± 0.6	0.332 ± 0.008	-10.5 ± 1.7	94 ± 6
HD013661	53290.817	-27.483 ± 0.034	-23.7 ± 0.7	0.557 ± 0.015	-48.5 ± 5.8	334 ± 19
HD013661	53290.824	-27.709 ± 0.046	-24.2 ± 0.9	0.519 ± 0.017	-36.7 ± 7.4	319 ± 25
HD013661	54019.836	-21.308 ± 0.047	-29.3 ± 0.9	0.491 ± 0.016	-12.0 ± 7.3	166 ± 48
HD013661	54020.903	-21.317 ± 0.048	-27.6 ± 0.9	0.440 ± 0.020	-46.7 ± 10.1	163 ± 69
HD013661	54021.820	-20.767 ± 0.055	-28.9 ± 1.1	0.527 ± 0.018	-8.3 ± 7.8	282 ± 30
HD013661	54023.822	-21.303 ± 0.054	-28.0 ± 1.0	0.471 ± 0.020	-62.3 ± 9.2	199 ± 51
HD013867	53291.783	-5.042 ± 0.029	-1.7 ± 0.4	0.145 ± 0.007	2.0 ± 3.5	87 ± 13
HD013867	53291.790	-4.709 ± 0.024	-1.5 ± 0.3	0.124 ± 0.009	-7.1 ± 5.1	74 ± 23
HD013867	54019.850	-5.909 ± 0.046	-3.0 ± 0.6	0.107 ± 0.008	-1.0 ± 5.4	52 ± 35
HD013867	54019.856	-5.748 ± 0.044	-2.5 ± 0.6	0.123 ± 0.009	6.4 ± 5.2	31 ± 57
HD013867	54020.912	-6.036 ± 0.029	-2.5 ± 0.4	0.114 ± 0.008	-11.3 ± 5.1	62 ± 28
HD013867	54021.827	-6.040 ± 0.041	-3.1 ± 0.6	0.139 ± 0.016	-7.6 ± 8.2	87 ± 32
HD013867	54023.833	-5.669 ± 0.037	-2.5 ± 0.5	0.128 ± 0.011	-1.5 ± 5.7	66 ± 29
HD018552	53290.857	-12.931 ± 0.030	-6.7 ± 0.6	0.144 ± 0.012	-6.8 ± 13.4	266 ± 38
HD018552	53290.861	-12.788 ± 0.042	-7.6 ± 0.8	0.154 ± 0.013	6.6 ± 13.5	295 ± 34
HD018552	53292.835	-13.111 ± 0.031	-7.2 ± 0.6	0.146 ± 0.009	20.1 ± 9.6	271 ± 26
HD018552	53292.840	-12.807 ± 0.024	-7.2 ± 0.5	0.123 ± 0.011	-0.4 ± 13.8	281 ± 37
HD018552	54019.860	-12.315 ± 0.039	-11.0 ± 0.7	0.105 ± 0.014	26.0 ± 21.5	273 ± 60
HD018552	54020.917	-11.944 ± 0.042	-10.9 ± 0.8	0.107 ± 0.011	-18.8 ± 15.6	287 ± 41
HD018552	54021.831	-12.086 ± 0.052	-11.6 ± 1.0	0.083 ± 0.015	···	···

Continued on Next Page...

Table C.1 – Continued

Star Name	HJD (−2400000)	W_λ (Hα) (Å)	V_r (Hα) (km s^{-1})	W_λ (He I) (Å)	V_r (He I) (km s^{-1})	FWSM (He I) (km s^{-1})
HD018552	54023.838	-12.215 ± 0.036	-10.7 ± 0.7	0.125 ± 0.012	-16.3 ± 14.6	300 ± 37
HD019243	53291.832	-45.869 ± 0.065	-6.2 ± 1.3	0.355 ± 0.015	21.9 ± 6.8	239 ± 20
HD019243	53291.835	-45.736 ± 0.064	-6.7 ± 1.3	0.358 ± 0.025	13.5 ± 11.1	252 ± 32
HD019243	54019.869	-43.433 ± 0.074	-26.8 ± 1.4	0.286 ± 0.021	-25.7 ± 11.6	...
HD019243	54019.871	-43.985 ± 0.078	-26.7 ± 1.5	0.283 ± 0.027	-26.4 ± 15.1	88 ± 136
HD019243	54021.834	-43.072 ± 0.083	-25.8 ± 1.6	0.296 ± 0.023	-31.2 ± 12.4	...
HD019243	54023.842	-44.447 ± 0.061	-25.4 ± 1.2	0.324 ± 0.022	-33.0 ± 10.8	75 ± 114
HD020134	53291.840	3.720 ± 0.033	-16.6 ± 0.7	0.504 ± 0.009	-14.2 ± 2.0	177 ± 6
HD020134	54019.877	4.662 ± 0.040	-15.8 ± 0.9	0.495 ± 0.014	-18.4 ± 3.1	175 ± 9
HD020134	54020.919	4.719 ± 0.039	-20.9 ± 0.8	0.514 ± 0.010	-20.3 ± 2.1	180 ± 6
HD020134	54021.838	4.840 ± 0.045	-10.5 ± 1.0	0.500 ± 0.011	-16.9 ± 2.5	173 ± 7
HD020134	54023.855	4.413 ± 0.040	-16.7 ± 0.9	0.488 ± 0.012	-26.9 ± 2.7	157 ± 9
HD020336	53290.866	-7.675 ± 0.035	6.1 ± 0.7	0.551 ± 0.012	-29.7 ± 4.1	304 ± 13
HD020336	53292.848	-7.329 ± 0.033	3.9 ± 0.7	0.524 ± 0.009	26.1 ± 3.5	244 ± 14
HD020336	53294.860	-7.850 ± 0.025	-0.7 ± 0.5	0.648 ± 0.011	15.2 ± 3.4	336 ± 9
HD020336	54019.885	-11.085 ± 0.050	14.0 ± 1.0	0.520 ± 0.015	35.3 ± 5.7	377 ± 14
HD020336	54021.850	-11.542 ± 0.030	19.4 ± 0.6	0.534 ± 0.012	-10.0 ± 4.3	381 ± 11
HD020336	54023.865	-11.630 ± 0.030	16.0 ± 0.6	0.567 ± 0.009	17.7 ± 3.3	411 ± 7
HD020418	53290.865	4.674 ± 0.027	-1.5 ± 0.6	0.409 ± 0.014	-9.0 ± 6.4	347 ± 18
HD020418	53292.845	4.624 ± 0.028	-0.3 ± 0.6	0.413 ± 0.011	-2.8 ± 5.0	355 ± 13
HD020418	54019.883	5.145 ± 0.030	-3.4 ± 0.6	0.346 ± 0.015	2.9 ± 8.1	294 ± 27
HD020418	54021.849	5.131 ± 0.032	-3.0 ± 0.7	0.377 ± 0.016	-17.8 ± 8.2	346 ± 23
HD020418	54023.863	5.031 ± 0.022	-0.7 ± 0.5	0.370 ± 0.010	-29.7 ± 5.4	303 ± 17
HD021362	53291.847	-16.309 ± 0.024	3.4 ± 0.5	0.359 ± 0.009	5.5 ± 4.9	432 ± 11
HD021362	53291.849	-16.354 ± 0.034	3.3 ± 0.7	0.354 ± 0.013	-7.8 ± 6.9	419 ± 16
HD021362	53294.868	-16.749 ± 0.031	2.6 ± 0.6	0.353 ± 0.010	-17.2 ± 5.5	410 ± 13
HD021362	53294.873	-16.433 ± 0.039	2.7 ± 0.8	0.360 ± 0.015	-30.4 ± 8.1	400 ± 19
HD021362	54019.889	-17.509 ± 0.039	1.5 ± 0.8	0.178 ± 0.015	36.7 ± 16.3	...
HD021362	54019.891	-17.161 ± 0.048	1.4 ± 1.0	0.210 ± 0.015	29.3 ± 13.3	237 ± 54
HD021362	54021.853	-17.566 ± 0.044	0.4 ± 0.9	0.251 ± 0.018	-16.9 ± 14.1	358 ± 38
HD021362	54023.870	-17.706 ± 0.030	1.2 ± 0.6	0.268 ± 0.010	-18.7 ± 7.4	310 ± 23
HD021362	54023.872	-17.966 ± 0.036	1.7 ± 0.7	0.224 ± 0.014	-32.3 ± 12.3	297 ± 40
HD021455	53290.871	-2.635 ± 0.027	3.3 ± 0.4	0.198 ± 0.007	3.2 ± 4.1	140 ± 16
HD021455	53290.874	-2.446 ± 0.032	3.4 ± 0.5	0.188 ± 0.010	7.9 ± 6.3	114 ± 30
HD021455	53292.854	-2.581 ± 0.019	4.4 ± 0.3	0.180 ± 0.008	3.5 ± 5.2	124 ± 23
HD021455	53292.858	-2.698 ± 0.027	4.1 ± 0.4	0.205 ± 0.008	15.8 ± 4.6	154 ± 16
HD021455	54019.894	-0.856 ± 0.034	2.1 ± 0.5	0.179 ± 0.009	11.6 ± 6.0	148 ± 22
HD021455	54021.855	-0.921 ± 0.036	1.4 ± 0.5	0.181 ± 0.010	5.0 ± 6.7	144 ± 26
HD021455	54023.876	-0.732 ± 0.022	2.7 ± 0.3	0.197 ± 0.008	7.4 ± 4.6	148 ± 17
HD021551	53290.877	7.158 ± 0.020	-8.4 ± 0.5	0.137 ± 0.009	-4.4 ± 12.3	391 ± 30
HD021551	53292.863	7.079 ± 0.018	-5.2 ± 0.5	0.133 ± 0.010	2.5 ± 13.8	413 ± 32
HD021551	54019.897	7.408 ± 0.034	0.6 ± 0.9	0.084 ± 0.017	...	...
HD021551	54021.864	7.046 ± 0.024	-2.5 ± 0.6	0.112 ± 0.009	-17.7 ± 14.8	336 ± 42
HD021551	54023.882	7.605 ± 0.015	9.0 ± 0.4	0.084 ± 0.009	...	...
HD021641	53291.863	-1.115 ± 0.024	6.3 ± 0.6	0.085 ± 0.007	...	...
HD021641	53291.868	-1.182 ± 0.036	0.4 ± 0.9	0.083 ± 0.011	...	...
HD021641	54019.905	-0.597 ± 0.036	-2.8 ± 0.9	0.040 ± 0.013	...	...
HD021641	54021.876	-0.675 ± 0.031	0.6 ± 0.7	0.043 ± 0.008	...	...
HD021641	54023.895	-0.165 ± 0.030	11.1 ± 0.7	0.057 ± 0.009	...	...
HD021650	53291.855	-13.030 ± 0.027	3.9 ± 0.6	0.318 ± 0.011	-1.8 ± 6.7	428 ± 15

Continued on Next Page...

Table C.1 – Continued

Star Name	HJD (−2400000)	W_λ (Hα) (Å)	V_r (Hα) (km s^{-1})	W_λ (He I) (Å)	V_r (He I) (km s^{-1})	FWSM (He I) (km s^{-1})
HD021650	54019.901	-17.663 ± 0.047	1.6 ± 1.0	0.141 ± 0.018	65.2 ± 24.4	196 ± 121
HD021650	54021.870	-17.797 ± 0.044	2.5 ± 0.9	0.210 ± 0.016	-17.4 ± 14.7	368 ± 39
HD021650	54023.888	-17.805 ± 0.037	2.4 ± 0.8	0.180 ± 0.020	-29.7 ± 21.6	301 ± 70
HD022192	53291.871	-37.245 ± 0.035	3.8 ± 0.7	0.481 ± 0.009	-2.8 ± 3.8	448 ± 8
HD022192	53291.872	-37.924 ± 0.050	5.0 ± 1.0	0.441 ± 0.021	-5.4 ± 9.0	430 ± 20
HD022192	53294.805	-37.786 ± 0.036	3.5 ± 0.7	0.436 ± 0.012	-21.4 ± 5.3	424 ± 12
HD022192	53294.811	-37.733 ± 0.033	3.4 ± 0.7	0.471 ± 0.010	-24.1 ± 4.1	411 ± 9
HD022192	53294.814	-38.091 ± 0.056	3.6 ± 1.2	0.378 ± 0.014	-36.1 ± 7.2	386 ± 18
HD022192	54019.909	-38.826 ± 0.055	2.9 ± 1.2	0.236 ± 0.021	23.2 ± 17.5	257 ± 66
HD022192	54019.910	-38.921 ± 0.076	2.5 ± 1.6	0.215 ± 0.032	60.0 ± 28.5	192 ± 145
HD022192	54020.925	-39.567 ± 0.061	3.9 ± 1.3	0.261 ± 0.020	-28.6 ± 14.5	292 ± 48
HD022192	54021.895	-38.805 ± 0.058	2.1 ± 1.2	0.269 ± 0.018	-53.0 ± 12.6	240 ± 51
HD022192	54023.900	-39.810 ± 0.053	3.6 ± 1.1	0.340 ± 0.022	-56.6 ± 12.6	316 ± 38
HD022780	53290.881	4.939 ± 0.017	-5.8 ± 0.4	0.236 ± 0.009	-13.4 ± 7.7	361 ± 20
HD022780	53292.868	4.795 ± 0.023	5.5 ± 0.6	0.208 ± 0.009	-10.7 ± 8.6	365 ± 22
HD022780	53294.882	4.735 ± 0.017	-5.8 ± 0.4	0.205 ± 0.011	-5.8 ± 10.2	371 ± 26
HD022780	54019.912	5.841 ± 0.031	-4.5 ± 0.8	0.169 ± 0.014	48.6 ± 16.2	136 ± 116
HD022780	54021.898	5.513 ± 0.031	5.2 ± 0.8	0.237 ± 0.017	-28.0 ± 13.9	383 ± 35
HD022780	54023.904	5.587 ± 0.023	6.5 ± 0.6	0.220 ± 0.013	-49.2 ± 11.0	270 ± 39
HD023016	53291.875	4.546 ± 0.025	9.9 ± 0.6	0.192 ± 0.013	-2.7 ± 12.9	457 ± 27
HD023016	53294.854	4.526 ± 0.028	15.1 ± 0.7	0.196 ± 0.012	-51.2 ± 11.3	429 ± 25
HD023016	54019.916	5.605 ± 0.043	4.2 ± 1.1	0.049 ± 0.018	...	...
HD023016	54021.902	4.963 ± 0.030	9.5 ± 0.8	0.085 ± 0.012	...	...
HD023016	54023.908	5.345 ± 0.030	14.4 ± 0.8	0.131 ± 0.015	-32.1 ± 22.4	367 ± 59
HD023302	53290.887	4.038 ± 0.037	7.3 ± 0.9	0.222 ± 0.011	-0.9 ± 6.7	200 ± 23
HD023302	53292.872	3.918 ± 0.023	8.6 ± 0.5	0.199 ± 0.007	0.2 ± 4.8	204 ± 16
HD023302	53294.817	3.819 ± 0.026	8.4 ± 0.6	0.205 ± 0.006	6.4 ± 3.9	230 ± 10
HD023302	54019.918	4.004 ± 0.035	7.6 ± 0.8	0.141 ± 0.016	-9.9 ± 15.5	159 ± 67
HD023302	54021.904	3.965 ± 0.022	6.9 ± 0.5	0.157 ± 0.009	-6.0 ± 7.8	154 ± 35
HD023302	54023.943	4.145 ± 0.025	12.6 ± 0.6	0.186 ± 0.009	-0.5 ± 7.0	200 ± 24
HD023478	53290.892	0.835 ± 0.034	31.6 ± 0.6	0.639 ± 0.015	8.9 ± 5.0	350 ± 15
HD023478	53292.881	0.820 ± 0.022	12.6 ± 0.4	0.576 ± 0.010	10.2 ± 3.6	330 ± 11
HD023478	54019.927	2.608 ± 0.053	32.6 ± 0.9	0.559 ± 0.017	52.4 ± 6.5	237 ± 24
HD023478	54021.908	1.838 ± 0.028	16.8 ± 0.5	0.616 ± 0.014	21.6 ± 4.8	305 ± 14
HD023478	54023.950	1.970 ± 0.036	39.0 ± 0.6	0.644 ± 0.014	17.3 ± 4.6	320 ± 12
HD023480	53290.889	-0.442 ± 0.020	8.5 ± 0.3	0.232 ± 0.007	-8.4 ± 4.7	287 ± 12
HD023480	53292.874	-0.422 ± 0.021	8.6 ± 0.3	0.211 ± 0.010	-4.9 ± 6.6	286 ± 17
HD023480	53294.821	-0.531 ± 0.021	9.6 ± 0.3	0.290 ± 0.010	-0.1 ± 5.0	307 ± 12
HD023480	53294.824	-0.780 ± 0.024	9.8 ± 0.4	0.197 ± 0.008	-1.8 ± 5.9	240 ± 18
HD023480	54019.920	1.031 ± 0.040	6.7 ± 0.7	0.174 ± 0.016	5.3 ± 13.5	253 ± 39
HD023480	54020.927	1.256 ± 0.032	9.2 ± 0.5	0.175 ± 0.011	7.1 ± 9.0	260 ± 23
HD023480	54021.905	0.967 ± 0.022	8.9 ± 0.4	0.197 ± 0.008	-15.6 ± 5.9	253 ± 17
HD023480	54023.945	1.060 ± 0.029	7.5 ± 0.5	0.239 ± 0.012	-14.1 ± 7.6	296 ± 19
HD023552	53291.878	-2.852 ± 0.022	-19.1 ± 0.4	0.192 ± 0.007	-14.7 ± 5.0	247 ± 13
HD023552	53291.883	-2.824 ± 0.028	-19.1 ± 0.5	0.198 ± 0.008	-12.1 ± 5.2	237 ± 14
HD023552	53294.889	-3.022 ± 0.018	-17.8 ± 0.3	0.172 ± 0.008	-30.1 ± 6.2	219 ± 18
HD023552	54019.930	-2.083 ± 0.046	-11.8 ± 0.8	0.151 ± 0.017	-13.1 ± 14.9	225 ± 43
HD023552	54020.935	-2.203 ± 0.032	-14.4 ± 0.5	0.137 ± 0.009	-27.4 ± 8.8	207 ± 28
HD023552	54021.912	-2.567 ± 0.031	-12.7 ± 0.5	0.179 ± 0.009	-22.4 ± 6.6	223 ± 19
HD023552	54023.956	-2.373 ± 0.027	-14.0 ± 0.4	0.168 ± 0.010	-16.0 ± 8.1	251 ± 21

Continued on Next Page...

Table C.1 – Continued

Star Name	HJD (−2400000)	W_λ (Hα) (Å)	V_r (Hα) (km s^{-1})	W_λ (He I) (Å)	V_r (He I) (km s^{-1})	FWSM (He I) (km s^{-1})
HD023630	53290.896	-3.568 ± 0.018	7.9 ± 0.3	0.167 ± 0.006	0.4 ± 3.7	229 ± 10
HD023630	53290.897	-3.423 ± 0.020	7.9 ± 0.3	0.165 ± 0.009	-15.7 ± 6.2	224 ± 15
HD023630	53292.888	-3.652 ± 0.020	8.4 ± 0.3	0.185 ± 0.006	-6.6 ± 3.5	237 ± 9
HD023630	53292.889	-3.722 ± 0.027	8.1 ± 0.4	0.174 ± 0.007	-10.3 ± 4.4	219 ± 11
HD023630	53294.826	-3.650 ± 0.026	8.5 ± 0.4	0.230 ± 0.010	-7.2 ± 4.7	239 ± 12
HD023630	54019.934	-2.647 ± 0.044	6.1 ± 0.7	0.123 ± 0.015	31.5 ± 13.3	131 ± 65
HD023630	54019.935	-2.915 ± 0.031	6.7 ± 0.5	0.098 ± 0.010	...	...
HD023630	54020.929	-2.628 ± 0.030	8.1 ± 0.5	0.112 ± 0.009	-19.6 ± 9.1	138 ± 36
HD023630	54021.917	-2.897 ± 0.031	6.9 ± 0.5	0.132 ± 0.010	-19.6 ± 8.0	222 ± 20
HD023630	54023.962	-2.940 ± 0.028	8.0 ± 0.4	0.158 ± 0.010	-7.3 ± 6.8	224 ± 19
HD023800	53290.906	-3.835 ± 0.030	12.4 ± 0.6	0.912 ± 0.011	-23.1 ± 1.7	275 ± 4
HD023800	53292.905	-3.768 ± 0.025	12.0 ± 0.5	0.834 ± 0.016	-27.1 ± 2.7	264 ± 7
HD023800	54019.941	-4.770 ± 0.036	-28.3 ± 0.7	0.813 ± 0.015	-0.6 ± 2.6	235 ± 10
HD023800	54021.924	-4.894 ± 0.034	-26.4 ± 0.6	0.828 ± 0.014	-8.1 ± 2.4	241 ± 9
HD023800	54024.869	-5.103 ± 0.030	-32.9 ± 0.6	0.840 ± 0.016	-4.2 ± 2.7	240 ± 11
HD023862	53290.899	-25.324 ± 0.029	12.6 ± 0.6	0.177 ± 0.009	7.6 ± 7.9	348 ± 18
HD023862	53290.901	-25.170 ± 0.033	12.7 ± 0.6	0.179 ± 0.010	0.6 ± 8.7	334 ± 20
HD023862	53292.894	-24.947 ± 0.036	12.7 ± 0.7	0.144 ± 0.010	-6.6 ± 11.0	297 ± 29
HD023862	53292.896	-24.795 ± 0.035	13.1 ± 0.7	0.144 ± 0.011	2.4 ± 11.7	341 ± 27
HD023862	53294.832	-25.556 ± 0.034	12.9 ± 0.7	0.210 ± 0.014	10.9 ± 10.4	334 ± 24
HD023862	53294.835	-25.769 ± 0.045	13.2 ± 0.9	0.139 ± 0.015	43.1 ± 17.1	338 ± 28
HD023862	54019.937	-15.250 ± 0.053	3.3 ± 0.9	0.126 ± 0.016	6.4 ± 20.6	189 ± 86
HD023862	54020.933	-15.387 ± 0.037	2.0 ± 0.6	0.136 ± 0.014	-26.8 ± 16.0	114 ± 110
HD023862	54021.921	-15.393 ± 0.047	3.2 ± 0.8	0.144 ± 0.010	-5.4 ± 11.0	162 ± 53
HD023862	54023.964	-14.714 ± 0.068	1.9 ± 1.2	0.166 ± 0.024	-29.9 ± 23.1	166 ± 110
HD024479	53290.913	7.845 ± 0.026	-4.5 ± 0.7	0.055 ± 0.008	...	...
HD024479	53290.915	7.798 ± 0.027	1.7 ± 0.7	0.057 ± 0.006	...	...
HD024479	53292.930	7.905 ± 0.026	1.6 ± 0.7	0.031 ± 0.007	...	...
HD024479	53294.838	7.776 ± 0.029	-2.9 ± 0.7	0.001 ± 0.012	...	...
HD024479	53294.840	7.862 ± 0.028	-0.9 ± 0.7	-0.009 ± 0.010	...	...
HD024479	54019.952	8.191 ± 0.033	-0.1 ± 0.8	0.035 ± 0.009	...	...
HD024479	54021.931	7.644 ± 0.027	-2.3 ± 0.7	0.043 ± 0.006	...	...
HD024479	54024.873	7.813 ± 0.026	1.7 ± 0.7	0.041 ± 0.008	...	...
HD024534	53290.922	-17.926 ± 0.028	-9.4 ± 0.5	0.229 ± 0.011	-22.8 ± 9.7	605 ± 16
HD024534	53290.926	-17.750 ± 0.034	-9.1 ± 0.7	0.224 ± 0.015	-22.7 ± 14.1	605 ± 24
HD024534	53292.922	-18.567 ± 0.034	-9.1 ± 0.7	0.160 ± 0.012	-14.4 ± 14.9	646 ± 23
HD024534	53292.928	-18.358 ± 0.040	-9.4 ± 0.8	0.184 ± 0.011	13.0 ± 10.9	623 ± 16
HD024534	54019.948	-15.452 ± 0.041	-6.3 ± 0.8	-0.681 ± 0.011	...	...
HD024534	54019.950	-24.606 ± 0.050	-7.8 ± 1.0	-0.674 ± 0.019	...	...
HD024534	54020.939	-25.771 ± 0.060	-7.3 ± 1.2	-0.705 ± 0.018	...	...
HD024534	54021.930	-24.604 ± 0.048	-6.9 ± 1.0	-0.651 ± 0.017	...	...
HD025799	53291.888	4.749 ± 0.021	46.7 ± 0.5	0.664 ± 0.010	56.7 ± 3.1	334 ± 4
HD025799	53292.938	4.851 ± 0.029	44.7 ± 0.7	0.613 ± 0.014	55.6 ± 5.0	327 ± 7
HD025799	54019.960	5.474 ± 0.037	36.7 ± 0.9	0.537 ± 0.015	37.1 ± 5.9	257 ± 23
HD025799	54021.938	5.325 ± 0.029	26.7 ± 0.7	0.583 ± 0.016	15.9 ± 5.9	293 ± 20
HD025799	54024.885	5.174 ± 0.027	7.0 ± 0.6	0.555 ± 0.018	11.6 ± 6.8	292 ± 23
HD025940	53291.893	-26.927 ± 0.037	4.6 ± 0.7	0.373 ± 0.009	21.4 ± 4.3	268 ± 12
HD025940	53291.894	-26.847 ± 0.041	5.3 ± 0.8	0.372 ± 0.015	11.9 ± 6.7	269 ± 19
HD025940	53292.945	-26.427 ± 0.041	3.7 ± 0.7	0.340 ± 0.015	6.8 ± 7.3	257 ± 22
HD025940	53292.946	-26.765 ± 0.065	4.5 ± 1.2	0.337 ± 0.016	7.8 ± 7.8	255 ± 24

Continued on Next Page...

Table C.1 – Continued

Star Name	HJD (−2400000)	W_λ (Hα) (Å)	V_r (Hα) (km s^{-1})	W_λ (He I) (Å)	V_r (He I) (km s^{-1})	FWSM (He I) (km s^{-1})
HD025940	53294.847	-26.695 ± 0.035	5.1 ± 0.6	0.312 ± 0.013	-0.1 ± 7.3	235 ± 24
HD025940	54019.966	-26.313 ± 0.056	2.4 ± 1.0	0.270 ± 0.019	0.9 ± 11.7	234 ± 40
HD025940	54020.943	-26.337 ± 0.060	3.6 ± 1.1	0.239 ± 0.017	-5.0 ± 11.9	182 ± 52
HD025940	54021.941	-26.519 ± 0.048	3.3 ± 0.9	0.262 ± 0.015	-3.8 ± 9.9	215 ± 36
HD025940	54024.889	-27.415 ± 0.063	2.1 ± 1.2	0.281 ± 0.023	-3.0 ± 13.6	200 ± 54
HD026670	53290.928	6.187 ± 0.026	-0.2 ± 0.7	0.291 ± 0.018	30.5 ± 12.1	357 ± 33
HD026670	53291.896	6.047 ± 0.020	7.8 ± 0.5	0.309 ± 0.011	3.7 ± 6.8	377 ± 17
HD026670	53291.899	6.068 ± 0.017	1.5 ± 0.4	0.288 ± 0.009	1.4 ± 6.3	368 ± 16
HD026670	53292.948	6.106 ± 0.025	1.7 ± 0.6	0.242 ± 0.010	-12.6 ± 8.0	345 ± 22
HD026670	53294.896	5.873 ± 0.023	-1.8 ± 0.6	0.257 ± 0.010	-2.3 ± 7.8	370 ± 20
HD026670	54019.968	6.400 ± 0.030	-2.3 ± 0.8	0.237 ± 0.014	56.5 ± 11.4	306 ± 36
HD026670	54020.946	6.657 ± 0.025	1.8 ± 0.6	0.239 ± 0.012	-25.9 ± 9.9	360 ± 26
HD026670	54021.945	6.277 ± 0.016	2.7 ± 0.4	0.233 ± 0.010	-5.2 ± 8.2	324 ± 24
HD029866	53291.904	-11.123 ± 0.025	11.9 ± 0.5	0.253 ± 0.007	6.6 ± 4.8	354 ± 11
HD029866	53291.908	-10.989 ± 0.029	11.7 ± 0.6	0.291 ± 0.009	14.5 ± 4.9	361 ± 11
HD029866	53292.954	-11.087 ± 0.031	11.0 ± 0.6	0.199 ± 0.008	0.1 ± 6.7	335 ± 16
HD029866	53292.959	-11.008 ± 0.027	10.5 ± 0.5	0.188 ± 0.013	2.7 ± 11.4	347 ± 27
HD029866	53294.903	-11.200 ± 0.021	12.3 ± 0.4	0.212 ± 0.007	1.6 ± 5.7	348 ± 13
HD029866	53294.909	-10.858 ± 0.025	12.1 ± 0.5	0.248 ± 0.011	1.8 ± 7.4	378 ± 16
HD029866	54019.971	-10.900 ± 0.041	12.2 ± 0.8	0.140 ± 0.013	49.1 ± 15.6	276 ± 38
HD029866	54021.947	-10.897 ± 0.038	13.2 ± 0.7	0.172 ± 0.014	4.9 ± 13.1	360 ± 29
HD029866	54024.892	-11.249 ± 0.032	12.8 ± 0.6	0.146 ± 0.012	-0.4 ± 13.1	319 ± 33
HD032343	53291.912	-25.063 ± 0.050	-7.3 ± 0.9	0.355 ± 0.010	-9.2 ± 1.8	119 ± 4
HD032343	53292.962	-25.283 ± 0.038	-8.0 ± 0.7	0.336 ± 0.008	-13.5 ± 1.6	106 ± 4
HD032343	53292.964	-25.264 ± 0.065	-8.0 ± 1.2	0.339 ± 0.010	-16.1 ± 1.8	117 ± 4
HD032343	53294.919	-25.764 ± 0.046	-7.2 ± 0.8	0.332 ± 0.009	-9.2 ± 1.7	111 ± 4
HD032343	54019.976	-22.159 ± 0.064	-8.8 ± 1.1	0.319 ± 0.013	-9.8 ± 2.6	113 ± 7
HD032343	54021.950	-22.327 ± 0.048	-8.7 ± 0.8	0.330 ± 0.013	-14.2 ± 2.4	104 ± 7
HD032343	54021.951	-22.732 ± 0.045	-9.1 ± 0.8	0.327 ± 0.009	-13.3 ± 1.7	108 ± 5
HD032343	54024.897	-22.339 ± 0.053	-8.2 ± 0.9	0.324 ± 0.015	-16.1 ± 2.9	101 ± 9
HD036576	53291.918	-32.488 ± 0.038	45.3 ± 0.8	0.391 ± 0.011	29.6 ± 7.5	296 ± 31
HD036576	53291.919	-32.263 ± 0.038	45.2 ± 0.8	0.369 ± 0.016	2.7 ± 11.3	261 ± 53
HD036576	53292.972	-31.431 ± 0.045	44.3 ± 0.9	0.370 ± 0.011	-12.7 ± 7.5	269 ± 34
HD036576	53292.974	-31.309 ± 0.042	44.5 ± 0.9	0.373 ± 0.018	-7.9 ± 12.2	232 ± 65
HD036576	53294.926	-32.118 ± 0.051	44.2 ± 1.0	0.330 ± 0.017	-14.1 ± 12.9	167 ± 95
HD036576	54019.991	-44.753 ± 0.080	47.9 ± 1.6	0.232 ± 0.023	45.9 ± 25.4	...
HD036576	54021.962	-43.570 ± 0.064	47.5 ± 1.3	0.240 ± 0.025	62.1 ± 26.9	247 ± 68
HD036576	54024.901	-43.350 ± 0.062	47.6 ± 1.2	0.200 ± 0.023	160.9 ± 29.5	...
HD037202	53291.922	-19.249 ± 0.052	36.4 ± 1.2	1.627 ± 0.012	26.8 ± 1.4	324 ± 3
HD037202	53291.923	-19.420 ± 0.046	36.1 ± 1.0	1.592 ± 0.012	31.5 ± 1.4	312 ± 3
HD037202	53292.975	-19.005 ± 0.046	33.5 ± 1.0	1.522 ± 0.008	26.1 ± 1.0	293 ± 3
HD037202	53292.976	-19.509 ± 0.055	33.4 ± 1.2	1.555 ± 0.015	22.8 ± 1.8	301 ± 5
HD037202	53294.943	-19.476 ± 0.066	36.9 ± 1.5	1.673 ± 0.024	17.8 ± 2.7	318 ± 7
HD037202	53294.953	-19.730 ± 0.064	36.8 ± 1.4	1.615 ± 0.019	21.9 ± 2.2	297 ± 6
HD037202	54019.995	-20.520 ± 0.039	16.3 ± 0.8	1.216 ± 0.011	7.8 ± 1.8	274 ± 6
HD037202	54020.967	-20.077 ± 0.044	20.6 ± 1.0	1.289 ± 0.014	-7.9 ± 2.2	293 ± 7
HD037202	54024.921	-21.378 ± 0.047	19.9 ± 1.0	1.365 ± 0.013	7.2 ± 1.9	257 ± 7
HD041335	53291.935	-35.179 ± 0.058	45.8 ± 1.2	0.494 ± 0.016	37.1 ± 7.8	469 ± 19
HD041335	53292.994	-34.632 ± 0.052	45.8 ± 1.1	0.575 ± 0.014	49.7 ± 5.6	507 ± 7
HD041335	53294.964	-33.605 ± 0.049	46.0 ± 1.0	0.657 ± 0.013	31.4 ± 4.6	486 ± 11

Continued on Next Page...

Table C.1 – Continued

Star Name	HJD (−2400000)	W_λ (Hα) (Å)	V_r (Hα) (km s^{-1})	W_λ (He I) (Å)	V_r (He I) (km s^{-1})	FWSM (He I) (km s^{-1})
HD041335	53294.970	-34.824 ± 0.052	45.9 ± 1.1	0.617 ± 0.013	32.5 ± 4.9	485 ± 11
HD041335	54020.979	-35.368 ± 0.071	50.1 ± 1.5	0.382 ± 0.017	7.0 ± 10.4	430 ± 27
HD041335	54024.934	-35.614 ± 0.070	46.4 ± 1.5	0.432 ± 0.018	29.5 ± 9.9	437 ± 26
HD058715	53291.991	-1.895 ± 0.019	13.2 ± 0.3	0.083 ± 0.005	...	...
HD058715	53291.992	-1.362 ± 0.027	14.5 ± 0.5	0.056 ± 0.009	...	...
HD058715	53293.017	-1.857 ± 0.029	12.3 ± 0.5	0.065 ± 0.007	...	...
HD058715	53293.018	-1.559 ± 0.026	12.8 ± 0.4	0.068 ± 0.007	...	...
HD058715	53294.990	-1.873 ± 0.029	13.0 ± 0.5	0.100 ± 0.011	...	...
HD058715	53294.990	-1.833 ± 0.035	13.2 ± 0.6	0.100 ± 0.011	...	...
HD058715	54020.985	-1.515 ± 0.035	11.7 ± 0.6	0.058 ± 0.010	...	...
HD058715	54024.971	-1.678 ± 0.027	11.9 ± 0.5	0.044 ± 0.008	...	...
HD058715	54024.973	-1.755 ± 0.021	10.9 ± 0.4	0.044 ± 0.006	...	...
HD058978	53291.988	-15.359 ± 0.029	52.3 ± 0.7	0.551 ± 0.008	163.7 ± 1.3	350 ± 2
HD058978	53293.014	-15.239 ± 0.044	45.7 ± 1.0	0.529 ± 0.019	163.8 ± 3.2	342 ± 5
HD058978	53294.994	-15.209 ± 0.033	42.2 ± 0.8	0.301 ± 0.009	211.8 ± 1.9	395 ± 2
HD058978	53294.996	-15.123 ± 0.037	40.8 ± 0.9	0.335 ± 0.011	194.5 ± 2.3	443 ± 2
HD058978	54020.984	-13.641 ± 0.050	35.6 ± 1.2	0.514 ± 0.017	-39.6 ± 7.4	459 ± 17
HD058978	54024.967	-14.069 ± 0.050	42.6 ± 1.2	0.409 ± 0.011	56.2 ± 4.2	488 ± 7
HD060855	53291.996	-41.762 ± 0.048	40.7 ± 1.0	0.648 ± 0.012	52.2 ± 4.7	305 ± 13
HD060855	53291.997	-41.789 ± 0.042	39.6 ± 0.9	0.633 ± 0.019	27.0 ± 7.5	296 ± 31
HD060855	53295.008	-41.883 ± 0.064	41.0 ± 1.3	0.501 ± 0.016	32.7 ± 7.9	126 ± 76
HD060855	54020.987	-44.054 ± 0.064	50.0 ± 1.3	0.529 ± 0.019	-5.0 ± 8.7	154 ± 69
HD060855	54024.975	-44.717 ± 0.062	46.4 ± 1.3	0.540 ± 0.016	17.1 ± 7.5	100 ± 91
HD149757	54020.583	2.869 ± 0.072	-6.7 ± 1.5	0.928 ± 0.035	15.4 ± 8.6	467 ± 16
HD149757	54023.565	2.692 ± 0.040	-16.6 ± 0.9	0.961 ± 0.018	12.4 ± 4.3	455 ± 10
HD162428	53292.570	-5.634 ± 0.023	-21.5 ± 0.4	0.183 ± 0.010	-26.3 ± 10.4	295 ± 34
HD162428	54023.572	-12.585 ± 0.029	-18.5 ± 0.6	0.144 ± 0.018	-90.3 ± 23.3	311 ± 73
HD162732	53292.578	-4.397 ± 0.021	-10.9 ± 0.5	0.366 ± 0.008	-21.4 ± 3.4	311 ± 12
HD162732	54021.632	-7.198 ± 0.047	-5.9 ± 1.0	0.335 ± 0.016	-20.2 ± 7.6	321 ± 26
HD162732	54023.578	-7.509 ± 0.035	-7.4 ± 0.7	0.333 ± 0.013	-31.3 ± 6.2	314 ± 16
HD164284	53290.597	-11.030 ± 0.020	-1.0 ± 0.4	0.469 ± 0.008	-6.2 ± 2.8	228 ± 9
HD164284	53290.604	-10.774 ± 0.021	-0.3 ± 0.4	0.467 ± 0.008	4.4 ± 2.8	236 ± 10
HD164284	53294.577	-11.636 ± 0.024	-0.4 ± 0.4	0.361 ± 0.012	-9.2 ± 5.0	168 ± 23
HD164284	53294.579	-11.563 ± 0.032	-0.3 ± 0.6	0.392 ± 0.011	-6.2 ± 4.4	199 ± 17
HD164284	54019.590	-8.058 ± 0.020	-2.4 ± 0.4	0.416 ± 0.008	-0.8 ± 2.9	272 ± 9
HD164284	54019.592	-8.291 ± 0.026	-2.1 ± 0.5	0.387 ± 0.011	-9.5 ± 4.5	250 ± 14
HD164284	54023.597	-7.537 ± 0.038	-1.9 ± 0.7	0.485 ± 0.019	-1.2 ± 5.9	306 ± 16
HD164447	53291.584	-4.012 ± 0.015	-42.4 ± 0.3	0.183 ± 0.006	-37.9 ± 3.1	224 ± 6
HD164447	54021.637	-2.702 ± 0.040	-36.3 ± 0.6	0.183 ± 0.015	-42.3 ± 7.6	236 ± 15
HD164447	54023.601	-2.530 ± 0.028	-36.7 ± 0.5	0.154 ± 0.011	-40.0 ± 6.8	191 ± 17
HD166014	53290.593	6.679 ± 0.030	-26.8 ± 0.8	0.036 ± 0.009	...	...
HD166014	53292.567	6.846 ± 0.022	-25.3 ± 0.6	0.003 ± 0.007	...	...
HD166014	54019.596	6.379 ± 0.029	-29.0 ± 0.7	0.017 ± 0.012	...	...
HD166014	54023.604	6.725 ± 0.029	-21.1 ± 0.7	0.011 ± 0.010	...	...
HD168797	53292.584	4.620 ± 0.016	-9.3 ± 0.4	0.675 ± 0.009	-13.5 ± 2.3	337 ± 5
HD168797	54020.615	3.555 ± 0.043	-6.7 ± 1.0	0.541 ± 0.015	-30.1 ± 4.8	287 ± 13
HD168797	54023.613	3.926 ± 0.026	-24.5 ± 0.6	0.583 ± 0.014	-29.2 ± 3.9	310 ± 10
HD168957	53295.649	5.394 ± 0.018	-39.8 ± 0.5	0.376 ± 0.008	-31.0 ± 1.1	71 ± 13
HD168957	54022.560	5.575 ± 0.033	-26.6 ± 0.7	0.372 ± 0.009	-29.8 ± 1.3	72 ± 15
HD168957	54023.607	5.770 ± 0.030	-18.6 ± 0.7	0.386 ± 0.008	-31.3 ± 1.1	76 ± 12

Continued on Next Page...

Table C.1 – Continued

Star Name	HJD (−2400000)	W_λ (Hα) (Å)	V_r (Hα) (km s^{-1})	W_λ (He I) (Å)	V_r (He I) (km s^{-1})	FWSM (He I) (km s^{-1})
HD171406	53294.584	3.992 ± 0.018	-22.4 ± 0.5	0.273 ± 0.010	-28.5 ± 6.7	231 ± 25
HD171406	54021.645	1.168 ± 0.045	-2.8 ± 1.1	0.347 ± 0.014	-21.5 ± 6.8	341 ± 16
HD171406	54023.618	1.443 ± 0.024	1.2 ± 0.6	0.300 ± 0.013	-24.4 ± 7.5	281 ± 22
HD171780	53294.590	-0.373 ± 0.028	-19.7 ± 0.5	0.303 ± 0.012	-27.2 ± 6.4	280 ± 18
HD171780	54021.649	1.972 ± 0.092	-17.1 ± 1.6	0.289 ± 0.041	-36.4 ± 23.0	309 ± 59
HD171780	54023.623	2.005 ± 0.021	-19.9 ± 0.4	0.296 ± 0.010	-20.1 ± 5.3	269 ± 15
HD173370	53291.589	2.625 ± 0.018	-14.0 ± 0.4	0.100 ± 0.005	···	···
HD173370	54020.613	2.812 ± 0.045	-14.6 ± 1.0	0.085 ± 0.020	···	···
HD173370	54023.626	2.778 ± 0.017	-3.3 ± 0.4	0.070 ± 0.008	···	···
HD174237	53290.603	-1.871 ± 0.023	4.4 ± 0.5	0.598 ± 0.009	94.4 ± 2.1	158 ± 9
HD174237	54019.600	1.085 ± 0.031	-0.4 ± 0.7	0.467 ± 0.014	20.4 ± 6.1	···
HD174237	54023.630	0.923 ± 0.029	-10.4 ± 0.6	0.383 ± 0.019	-4.2 ± 11.2	···
HD174638	53290.596	-12.357 ± 0.034	21.9 ± 0.7	-2.972 ± 0.023	···	···
HD174638	53290.600	-12.819 ± 0.038	21.1 ± 0.8	-2.967 ± 0.028	···	···
HD174638	54019.602	-13.593 ± 0.045	-36.5 ± 1.0	-3.326 ± 0.020	···	···
HD174638	54019.603	-14.294 ± 0.066	-36.8 ± 1.5	-3.325 ± 0.023	···	···
HD174638	54023.633	-26.581 ± 0.043	-40.2 ± 0.9	-2.440 ± 0.031	···	···
HD174638	54023.634	-27.654 ± 0.067	-40.1 ± 1.4	-2.451 ± 0.036	···	···
HD175863	53294.600	-7.993 ± 0.028	-12.6 ± 0.5	0.374 ± 0.009	-27.0 ± 2.1	200 ± 4
HD175863	54022.572	-1.930 ± 0.028	-16.4 ± 0.5	0.298 ± 0.011	-28.0 ± 3.2	188 ± 7
HD175863	54023.638	-1.943 ± 0.031	-18.2 ± 0.5	0.325 ± 0.010	-26.2 ± 2.5	194 ± 5
HD175869	53291.592	2.381 ± 0.026	-11.7 ± 0.6	0.116 ± 0.007	7.0 ± 7.4	180 ± 23
HD175869	54023.648	2.509 ± 0.025	-6.5 ± 0.5	0.091 ± 0.008	···	···
HD177648	53292.592	-3.634 ± 0.022	-9.9 ± 0.4	0.510 ± 0.009	0.3 ± 2.3	283 ± 5
HD177648	54022.577	-4.286 ± 0.027	-6.7 ± 0.5	0.451 ± 0.014	-26.0 ± 4.2	262 ± 10
HD177648	54023.654	-4.041 ± 0.046	-9.9 ± 0.9	0.497 ± 0.011	-14.8 ± 2.9	250 ± 7
HD178475	53291.595	0.729 ± 0.023	-21.6 ± 0.4	0.406 ± 0.011	-22.6 ± 5.7	391 ± 15
HD178475	54020.625	4.417 ± 0.036	-19.7 ± 0.7	0.266 ± 0.014	-37.2 ± 11.4	288 ± 42
HD178475	54024.621	4.367 ± 0.029	-18.2 ± 0.6	0.281 ± 0.015	-23.7 ± 11.4	295 ± 40
HD178475	54024.622	4.465 ± 0.025	-22.8 ± 0.5	0.282 ± 0.012	-40.5 ± 9.1	283 ± 34
HD179343	53292.603	-6.569 ± 0.022	-8.2 ± 0.4	0.188 ± 0.008	-4.6 ± 6.8	268 ± 19
HD179343	54021.655	-6.479 ± 0.043	-8.8 ± 0.9	0.144 ± 0.013	-58.4 ± 18.3	99 ± 167
HD179343	54024.626	-6.488 ± 0.029	-9.7 ± 0.6	0.153 ± 0.013	-18.2 ± 14.4	255 ± 44
HD181409	53290.612	4.009 ± 0.028	22.9 ± 0.6	0.750 ± 0.008	38.9 ± 1.7	194 ± 6
HD181409	53290.617	4.108 ± 0.023	27.3 ± 0.5	0.743 ± 0.008	37.2 ± 1.7	196 ± 6
HD181409	54019.608	3.830 ± 0.036	26.0 ± 0.8	0.684 ± 0.009	34.1 ± 2.2	173 ± 9
HD181409	54024.631	4.120 ± 0.030	32.7 ± 0.6	0.732 ± 0.009	32.5 ± 2.0	196 ± 7
HD181615	54019.617	2.661 ± 0.131	···	0.721 ± 0.040	3.0 ± 3.5	100 ± 10
HD181615	54019.619	-0.400 ± 0.394	···	0.706 ± 0.042	3.4 ± 3.8	98 ± 11
HD181615	54019.620	-0.577 ± 0.138	···	0.705 ± 0.044	3.4 ± 3.9	98 ± 11
HD181615	54022.583	0.860 ± 0.146	···	0.659 ± 0.050	-6.6 ± 5.3	92 ± 18
HD181615	54022.584	0.180 ± 0.153	···	0.666 ± 0.048	-6.6 ± 5.1	93 ± 17
HD181615	54024.638	-1.247 ± 0.157	···	0.659 ± 0.047	-9.0 ± 5.2	92 ± 18
HD183362	53290.623	-22.549 ± 0.024	-23.8 ± 0.5	0.582 ± 0.010	-8.9 ± 3.4	384 ± 8
HD183362	53290.627	-22.193 ± 0.029	-23.5 ± 0.6	0.578 ± 0.009	-10.0 ± 3.1	385 ± 7
HD183362	54019.615	-26.397 ± 0.051	-18.1 ± 1.1	0.417 ± 0.017	-53.8 ± 8.1	150 ± 52
HD183362	54024.641	-27.750 ± 0.052	-16.2 ± 1.1	0.397 ± 0.017	-5.1 ± 8.3	188 ± 42
HD183656	53290.631	-6.954 ± 0.027	-7.4 ± 0.5	0.496 ± 0.010	-31.5 ± 3.8	362 ± 9
HD183656	53290.635	-6.791 ± 0.023	-7.3 ± 0.5	0.464 ± 0.011	-35.7 ± 4.4	340 ± 12
HD183656	54019.624	-5.644 ± 0.029	-26.7 ± 0.6	0.458 ± 0.011	-10.7 ± 4.3	316 ± 14

Continued on Next Page...

Table C.1 – Continued

Star Name	HJD (−2400000)	W_λ (Hα) (Å)	V_r (Hα) (km s^{-1})	W_λ (He I) (Å)	V_r (He I) (km s^{-1})	FWSM (He I) (km s^{-1})
HD183656	54019.626	-5.540 ± 0.037	-27.0 ± 0.7	0.435 ± 0.018	-6.8 ± 7.1	326 ± 22
HD183656	54024.644	-5.719 ± 0.034	-29.2 ± 0.7	0.435 ± 0.015	-16.4 ± 6.1	330 ± 19
HD183914	53291.599	0.072 ± 0.021	-19.8 ± 0.4	0.108 ± 0.008	1.8 ± 10.6	281 ± 27
HD183914	54020.631	-0.182 ± 0.057	-16.5 ± 0.9	0.063 ± 0.018	...	...
HD183914	54024.651	-0.258 ± 0.023	-20.2 ± 0.4	0.074 ± 0.008	...	...
HD184279	53294.608	-37.110 ± 0.052	-9.6 ± 1.1	1.366 ± 0.008	-19.5 ± 1.3	304 ± 4
HD184279	53294.615	-36.815 ± 0.045	-9.1 ± 1.0	1.396 ± 0.012	-21.6 ± 1.9	299 ± 6
HD184279	54022.588	-23.548 ± 0.047	-4.8 ± 1.1	1.414 ± 0.015	-18.9 ± 2.2	199 ± 11
HD184279	54023.660	-23.185 ± 0.046	-6.3 ± 1.1	1.426 ± 0.017	-18.8 ± 2.6	215 ± 12
HD184279	54024.655	-23.878 ± 0.053	-6.8 ± 1.2	1.437 ± 0.015	-14.0 ± 2.2	225 ± 9
HD185037	53291.603	-2.408 ± 0.020	-19.3 ± 0.4	0.100 ± 0.006	9.4 ± 7.0	220 ± 18
HD185037	53291.606	-2.415 ± 0.023	-19.8 ± 0.4	0.096 ± 0.008	...	...
HD185037	54021.663	-3.052 ± 0.027	-19.4 ± 0.5	0.064 ± 0.012	...	...
HD185037	54024.662	-3.158 ± 0.025	-20.6 ± 0.4	0.082 ± 0.007	...	...
HD187567	53294.622	-17.064 ± 0.015	-10.3 ± 0.3	0.486 ± 0.007	-55.4 ± 2.6	249 ± 10
HD187567	53294.626	-16.958 ± 0.029	-10.1 ± 0.5	0.493 ± 0.009	-47.8 ± 3.7	283 ± 12
HD187567	54024.670	-19.330 ± 0.037	-21.0 ± 0.7	0.500 ± 0.016	-6.9 ± 6.0	328 ± 17
HD187811	53291.609	-2.699 ± 0.023	-16.8 ± 0.5	0.488 ± 0.009	-19.4 ± 2.9	255 ± 8
HD187811	54020.672	2.564 ± 0.024	-13.0 ± 0.5	0.457 ± 0.011	-22.8 ± 3.8	250 ± 11
HD187811	54024.673	2.889 ± 0.020	-29.8 ± 0.4	0.442 ± 0.007	-24.9 ± 2.5	265 ± 7
HD187851	53294.633	3.548 ± 0.031	-37.5 ± 0.5	0.843 ± 0.014	-47.2 ± 3.4	374 ± 9
HD187851	54022.595	3.466 ± 0.032	-24.3 ± 0.5	0.827 ± 0.016	-12.2 ± 3.8	379 ± 12
HD187851	54023.668	3.358 ± 0.034	-10.3 ± 0.6	0.859 ± 0.017	-15.1 ± 3.8	381 ± 11
HD187851	54024.682	3.541 ± 0.026	-0.4 ± 0.4	0.790 ± 0.014	-4.6 ± 3.5	379 ± 11
HD189687	53291.611	-3.083 ± 0.032	56.3 ± 0.6	0.635 ± 0.010	-19.4 ± 2.4	301 ± 6
HD189687	54021.672	-0.486 ± 0.022	-29.9 ± 0.4	0.564 ± 0.010	1.3 ± 2.6	279 ± 7
HD191610	53290.639	-8.969 ± 0.026	-9.1 ± 0.5	0.641 ± 0.012	-47.9 ± 3.5	318 ± 10
HD191610	54019.630	-1.601 ± 0.027	-12.1 ± 0.5	0.552 ± 0.013	-18.5 ± 4.4	345 ± 12
HD191610	54019.631	-1.470 ± 0.031	-11.5 ± 0.6	0.568 ± 0.012	-13.4 ± 4.2	347 ± 11
HD191610	54022.601	-1.610 ± 0.023	-9.8 ± 0.4	0.562 ± 0.010	-21.0 ± 3.5	361 ± 9
HD192044	53291.624	-9.623 ± 0.026	-21.5 ± 0.5	0.187 ± 0.007	-18.0 ± 5.7	263 ± 16
HD192044	53291.627	-9.709 ± 0.031	-21.3 ± 0.6	0.174 ± 0.009	9.5 ± 7.8	236 ± 25
HD192044	54020.604	-9.661 ± 0.036	-22.0 ± 0.6	0.107 ± 0.010	-55.6 ± 15.0	126 ± 89
HD192044	54024.694	-9.920 ± 0.022	-21.8 ± 0.4	0.154 ± 0.010	-24.2 ± 10.0	250 ± 30
HD192445	53292.613	-29.856 ± 0.031	-8.9 ± 0.6	0.622 ± 0.010	-22.1 ± 3.2	394 ± 7
HD192445	53292.619	-29.849 ± 0.042	-9.1 ± 0.8	0.632 ± 0.013	-25.7 ± 4.2	395 ± 10
HD192445	54019.649	-30.543 ± 0.058	-26.6 ± 1.1	0.525 ± 0.019	-22.3 ± 7.1	344 ± 20
HD192445	54024.697	-33.625 ± 0.063	-26.6 ± 1.2	0.498 ± 0.018	-8.5 ± 7.0	345 ± 19
HD192685	53291.631	4.767 ± 0.020	-10.3 ± 0.5	0.619 ± 0.007	-4.4 ± 1.8	292 ± 5
HD192685	53295.643	4.676 ± 0.022	-10.8 ± 0.5	0.567 ± 0.008	-12.6 ± 2.5	275 ± 7
HD192685	54020.601	3.603 ± 0.033	-6.6 ± 0.8	0.540 ± 0.013	-14.2 ± 4.2	255 ± 14
HD192685	54024.702	3.553 ± 0.023	-5.1 ± 0.5	0.544 ± 0.007	-7.1 ± 2.1	262 ± 6
HD193009	53292.625	-25.154 ± 0.046	-15.6 ± 0.9	0.460 ± 0.011	4.8 ± 3.6	267 ± 10
HD193009	53292.631	-24.765 ± 0.038	-16.1 ± 0.8	0.440 ± 0.012	-0.7 ± 4.1	258 ± 12
HD193009	54021.680	-26.185 ± 0.054	0.5 ± 1.1	0.359 ± 0.012	27.7 ± 5.1	192 ± 19
HD193009	54024.706	-26.082 ± 0.053	-3.7 ± 1.1	0.339 ± 0.019	43.1 ± 8.4	242 ± 25
HD193182	53292.638	-17.887 ± 0.037	-15.8 ± 0.8	0.466 ± 0.010	-24.8 ± 3.1	279 ± 11
HD193182	53292.643	-17.745 ± 0.031	-15.4 ± 0.7	0.493 ± 0.012	-26.8 ± 3.6	282 ± 9
HD193182	54022.605	-18.750 ± 0.038	-15.8 ± 0.8	0.385 ± 0.011	-25.5 ± 4.3	269 ± 11
HD193182	54023.596	-19.276 ± 0.029	-17.7 ± 0.6	0.375 ± 0.014	-40.2 ± 5.9	236 ± 19

Continued on Next Page...

Table C.1 – Continued

Star Name	HJD (−2400000)	W_λ (Hα) (Å)	V_r (Hα) (km s^{-1})	W_λ (He I) (Å)	V_r (He I) (km s^{-1})	FWSM (He I) (km s^{-1})
HD193182	54024.711	-19.498 ± 0.037	-18.8 ± 0.8	0.344 ± 0.014	-25.1 ± 5.9	225 ± 27
HD193911	53292.646	-5.752 ± 0.028	-2.8 ± 0.4	0.164 ± 0.008	-5.3 ± 4.5	170 ± 17
HD193911	54021.683	-5.249 ± 0.032	-3.1 ± 0.5	0.163 ± 0.010	-4.6 ± 5.2	200 ± 17
HD193911	54024.717	-5.174 ± 0.037	-4.1 ± 0.6	0.160 ± 0.009	8.3 ± 5.1	190 ± 17
HD194244	53292.653	5.343 ± 0.024	-20.3 ± 0.6	0.045 ± 0.008	...	...
HD194244	54020.662	5.854 ± 0.040	-13.7 ± 1.0	0.037 ± 0.014	...	...
HD194244	54024.727	5.497 ± 0.025	-23.9 ± 0.6	0.022 ± 0.011	...	...
HD194335	53292.650	-8.234 ± 0.030	-24.9 ± 0.7	0.454 ± 0.010	-31.9 ± 3.3	328 ± 8
HD194335	54021.687	-7.390 ± 0.024	-9.1 ± 0.5	0.416 ± 0.009	-2.1 ± 3.3	328 ± 10
HD194335	54024.723	-7.520 ± 0.032	-6.8 ± 0.7	0.402 ± 0.016	-32.1 ± 6.1	331 ± 14
HD194883	53294.646	-23.339 ± 0.027	-18.6 ± 0.5	0.342 ± 0.011	-26.7 ± 3.8	208 ± 11
HD194883	54023.587	-21.847 ± 0.030	-19.8 ± 0.5	0.350 ± 0.008	-24.1 ± 2.9	217 ± 8
HD194883	54024.731	-21.778 ± 0.052	-19.3 ± 0.9	0.325 ± 0.015	-30.4 ± 5.7	207 ± 17
HD195325	53294.676	4.755 ± 0.016	-19.5 ± 0.5	0.071 ± 0.006	...	...
HD195325	54021.690	5.152 ± 0.038	-22.3 ± 1.1	0.077 ± 0.008	...	...
HD195325	54023.677	5.381 ± 0.024	-4.0 ± 0.7	0.080 ± 0.007	...	...
HD195554	53292.657	3.666 ± 0.028	-23.5 ± 0.4	0.029 ± 0.008	...	...
HD195554	54020.676	3.971 ± 0.025	-16.9 ± 0.4	0.055 ± 0.008	...	...
HD195554	54024.734	4.146 ± 0.028	-16.9 ± 0.4	0.045 ± 0.008	...	...
HD197419	53294.684	-3.578 ± 0.035	-6.2 ± 0.5	0.446 ± 0.010	-6.4 ± 1.6	118 ± 4
HD197419	54023.593	-4.053 ± 0.035	-6.6 ± 0.5	0.436 ± 0.009	-5.5 ± 1.5	120 ± 4
HD197419	54024.738	-3.492 ± 0.032	-7.3 ± 0.4	0.452 ± 0.010	-3.6 ± 1.6	116 ± 4
HD198183	53290.674	4.715 ± 0.028	-31.6 ± 0.6	0.247 ± 0.007	-27.3 ± 2.9	135 ± 10
HD198183	54019.658	4.604 ± 0.035	-18.4 ± 0.8	0.259 ± 0.009	-15.9 ± 3.6	158 ± 11
HD198183	54021.693	4.748 ± 0.042	-13.5 ± 1.0	0.245 ± 0.011	-23.3 ± 4.8	108 ± 22
HD198183	54023.681	4.675 ± 0.025	-14.5 ± 0.6	0.284 ± 0.008	-18.7 ± 3.1	172 ± 9
HD198625	53292.662	-5.059 ± 0.018	-14.1 ± 0.4	0.534 ± 0.009	-18.3 ± 3.1	326 ± 8
HD198625	54021.698	3.837 ± 0.022	-7.9 ± 0.4	0.457 ± 0.010	6.5 ± 3.9	351 ± 9
HD198625	54023.687	4.031 ± 0.030	-16.6 ± 0.6	0.423 ± 0.011	1.7 ± 4.7	334 ± 12
HD199218	53295.686	-15.637 ± 0.021	-16.8 ± 0.4	0.176 ± 0.008	-47.2 ± 7.7	337 ± 19
HD199218	54020.683	-15.474 ± 0.032	-15.7 ± 0.6	0.154 ± 0.010	10.4 ± 10.3	280 ± 43
HD199218	54023.695	-15.101 ± 0.035	-17.4 ± 0.7	0.168 ± 0.014	-69.9 ± 13.8	283 ± 42
HD199356	53295.695	-33.717 ± 0.046	-12.3 ± 1.0	0.512 ± 0.019	-11.9 ± 7.0	528 ± 13
HD199356	54021.712	-32.827 ± 0.060	-16.3 ± 1.4	0.296 ± 0.018	15.8 ± 11.6	492 ± 22
HD199356	54023.699	-35.789 ± 0.062	-14.8 ± 1.4	0.375 ± 0.024	-21.4 ± 12.3	482 ± 25
HD200120	53291.634	-12.020 ± 0.022	-9.3 ± 0.5	0.124 ± 0.010	125.5 ± 12.0	500 ± 22
HD200120	53291.635	-12.162 ± 0.039	-8.6 ± 0.8	0.144 ± 0.013	150.7 ± 13.6	411 ± 31
HD200120	54019.660	-13.468 ± 0.035	-7.6 ± 0.7	-0.003 ± 0.013	...	...
HD200120	54019.662	-13.529 ± 0.046	-9.3 ± 1.0	-0.008 ± 0.016	...	...
HD200120	54023.707	-13.437 ± 0.039	5.1 ± 0.8	0.055 ± 0.012	...	...
HD200310	53291.637	2.117 ± 0.021	-17.5 ± 0.3	0.845 ± 0.013	-24.5 ± 2.7	418 ± 8
HD200310	54020.692	2.844 ± 0.028	-18.9 ± 0.4	0.730 ± 0.013	-7.0 ± 3.2	356 ± 11
HD200310	54023.710	2.743 ± 0.027	-25.9 ± 0.4	0.749 ± 0.013	-25.9 ± 3.0	363 ± 11
HD201522	53294.694	3.729 ± 0.043	-3.3 ± 1.0	0.231 ± 0.019	-60.7 ± 15.3	358 ± 39
HD201522	54021.703	4.143 ± 0.030	-9.4 ± 0.7	0.206 ± 0.013	-11.8 ± 11.3	339 ± 31
HD201522	54023.719	4.680 ± 0.039	0.7 ± 0.9	0.212 ± 0.019	-12.8 ± 16.7	319 ± 49
HD201522	54024.747	4.416 ± 0.030	-6.4 ± 0.7	0.215 ± 0.017	-6.4 ± 14.1	361 ± 38
HD201733	53292.671	2.494 ± 0.017	21.4 ± 0.3	0.896 ± 0.009	-7.2 ± 2.1	374 ± 5
HD201733	54020.707	3.526 ± 0.023	21.8 ± 0.3	0.863 ± 0.012	36.1 ± 2.7	393 ± 6
HD201733	54024.753	3.834 ± 0.025	14.4 ± 0.3	0.969 ± 0.012	39.2 ± 2.5	407 ± 6

Continued on Next Page...

Table C.1 – Continued

Star Name	HJD (−2400000)	W_λ (Hα) (Å)	V_r (Hα) (km s^{-1})	W_λ (He I) (Å)	V_r (He I) (km s^{-1})	FWSM (He I) (km s^{-1})
HD202904	53290.678	-34.787 ± 0.045	-3.9 ± 0.9	0.463 ± 0.015	0.4 ± 5.7	300 ± 16
HD202904	54019.665	-24.740 ± 0.041	-0.1 ± 0.8	0.578 ± 0.012	6.4 ± 3.8	323 ± 10
HD202904	54024.762	-24.544 ± 0.042	1.7 ± 0.8	0.515 ± 0.017	-1.5 ± 5.8	286 ± 18
HD203025	53292.678	1.062 ± 0.025	-25.6 ± 0.3	0.772 ± 0.009	-31.4 ± 1.8	237 ± 5
HD203025	54021.718	2.407 ± 0.032	-4.6 ± 0.4	0.737 ± 0.015	-4.9 ± 3.0	230 ± 9
HD203025	54024.758	2.196 ± 0.032	-17.6 ± 0.4	0.694 ± 0.013	-30.7 ± 2.9	211 ± 10
HD203064	53291.639	1.325 ± 0.018	-8.1 ± 0.3	0.995 ± 0.013	123.5 ± 4.5	499 ± 4
HD203064	54020.694	1.439 ± 0.036	-1.0 ± 0.6	0.859 ± 0.018	143.3 ± 7.1	452 ± 7
HD203064	54024.764	1.303 ± 0.029	6.1 ± 0.5	0.907 ± 0.015	129.6 ± 5.6	471 ± 5
HD203374	53292.693	-44.022 ± 0.046	-31.5 ± 0.9	0.022 ± 0.014	...	...
HD203374	54019.722	-44.726 ± 0.080	-16.4 ± 1.5	-0.122 ± 0.023	...	...
HD203374	54024.846	-45.029 ± 0.073	-16.2 ± 1.4	-0.081 ± 0.018	...	...
HD203467	53291.641	-28.050 ± 0.028	-10.1 ± 0.5	0.537 ± 0.009	-27.9 ± 2.4	343 ± 10
HD203467	53291.643	-27.886 ± 0.047	-9.9 ± 0.9	0.569 ± 0.016	-28.3 ± 4.0	354 ± 16
HD203467	54019.727	-25.105 ± 0.044	-14.3 ± 0.8	0.390 ± 0.012	-35.7 ± 4.2	293 ± 21
HD203467	54024.771	-25.351 ± 0.039	-13.5 ± 0.7	0.433 ± 0.013	-33.1 ± 4.1	256 ± 23
HD203699	53291.650	-18.889 ± 0.032	1.2 ± 0.5	0.411 ± 0.008	0.5 ± 2.9	228 ± 9
HD203699	53291.655	-18.791 ± 0.034	1.2 ± 0.6	0.401 ± 0.011	5.4 ± 4.1	214 ± 13
HD203699	54021.737	-15.568 ± 0.037	-0.7 ± 0.6	0.388 ± 0.011	-8.0 ± 4.3	170 ± 18
HD203699	54024.780	-15.919 ± 0.035	0.2 ± 0.6	0.402 ± 0.011	-0.4 ± 4.2	191 ± 16
HD203731	53292.701	-29.778 ± 0.040	-12.1 ± 0.8	0.855 ± 0.018	-60.7 ± 4.4	355 ± 13
HD203731	54021.729	-33.838 ± 0.051	-28.9 ± 1.0	0.684 ± 0.024	15.4 ± 7.0	344 ± 34
HD203731	54024.776	-34.542 ± 0.049	-32.0 ± 1.0	0.744 ± 0.021	11.8 ± 5.7	281 ± 34
HD204116	54019.683	-29.424 ± 0.046	-11.3 ± 0.9	0.417 ± 0.023	-37.9 ± 10.8	304 ± 34
HD204116	54024.785	-30.837 ± 0.037	-12.5 ± 0.7	0.378 ± 0.020	-49.0 ± 10.2	355 ± 28
HD204722	53295.708	-16.905 ± 0.036	-0.2 ± 0.8	0.399 ± 0.012	-36.4 ± 5.1	368 ± 24
HD204722	54020.728	-16.561 ± 0.039	-33.5 ± 0.8	0.294 ± 0.019	126.6 ± 11.0	...
HD204722	54024.791	-16.393 ± 0.040	-29.8 ± 0.9	0.305 ± 0.012	83.3 ± 6.7	...
HD204860	53292.712	-0.196 ± 0.031	2.9 ± 0.6	0.554 ± 0.010	-13.0 ± 2.9	343 ± 7
HD204860	53292.721	-0.163 ± 0.030	4.6 ± 0.6	0.531 ± 0.010	-12.7 ± 3.1	345 ± 7
HD204860	54020.699	-4.073 ± 0.032	-7.2 ± 0.6	0.413 ± 0.011	-16.0 ± 4.6	290 ± 13
HD204860	54024.800	-4.189 ± 0.032	-10.2 ± 0.6	0.416 ± 0.014	-28.5 ± 5.5	283 ± 16
HD205060	53294.711	-5.372 ± 0.028	-10.7 ± 0.5	0.208 ± 0.013	-36.0 ± 12.4	292 ± 41
HD205060	54021.741	-7.115 ± 0.028	7.6 ± 0.5	0.187 ± 0.008	-48.9 ± 8.3	314 ± 25
HD205060	54024.805	-7.103 ± 0.037	8.3 ± 0.7	0.208 ± 0.020	-9.7 ± 18.4	274 ± 65
HD205551	53291.662	1.590 ± 0.020	-23.8 ± 0.4	0.129 ± 0.005	-12.4 ± 3.8	163 ± 10
HD205551	54020.703	1.844 ± 0.030	-24.9 ± 0.6	0.087 ± 0.008	...	...
HD205551	54024.812	1.373 ± 0.027	-20.6 ± 0.6	0.061 ± 0.007	...	...
HD206773	53291.667	-10.349 ± 0.022	-8.0 ± 0.5	-0.111 ± 0.013	...	...
HD206773	54020.712	-11.850 ± 0.030	1.2 ± 0.7	-0.359 ± 0.020	...	...
HD206773	54024.817	-12.912 ± 0.035	0.4 ± 0.8	-0.398 ± 0.016	...	...
HD207232	53291.675	-2.672 ± 0.020	-18.5 ± 0.4	0.225 ± 0.008	-2.5 ± 5.0	315 ± 10
HD207232	54021.749	-5.851 ± 0.037	-13.0 ± 0.7	0.160 ± 0.012	-31.9 ± 10.0	210 ± 33
HD207232	54024.823	-6.136 ± 0.029	-14.9 ± 0.6	0.161 ± 0.011	-24.3 ± 9.5	244 ± 27
HD208057	53290.696	5.268 ± 0.025	-23.8 ± 0.6	0.470 ± 0.007	-19.4 ± 1.5	162 ± 4
HD208057	53292.732	5.296 ± 0.021	-21.6 ± 0.5	0.437 ± 0.009	-16.8 ± 1.9	157 ± 5
HD208057	54019.694	5.472 ± 0.032	-19.7 ± 0.7	0.430 ± 0.009	-17.3 ± 1.9	157 ± 5
HD208057	54022.766	5.331 ± 0.033	-32.7 ± 0.7	0.419 ± 0.009	-30.2 ± 2.0	136 ± 7
HD208392	53290.701	2.721 ± 0.024	-15.6 ± 0.5	0.900 ± 0.010	-13.0 ± 2.2	407 ± 5
HD208392	54019.698	3.350 ± 0.029	-10.8 ± 0.6	0.851 ± 0.015	-35.0 ± 3.5	413 ± 8

Continued on Next Page...

Table C.1 – Continued

Star Name	HJD (−2400000)	W_λ (Hα) (Å)	V_r (Hα) (km s^{-1})	W_λ (He I) (Å)	V_r (He I) (km s^{-1})	FWSM (He I) (km s^{-1})
HD208392	54024.829	2.677 ± 0.032	-20.2 ± 0.6	0.948 ± 0.019	-12.5 ± 3.9	331 ± 11
HD208682	53290.707	3.579 ± 0.024	1.8 ± 0.5	0.764 ± 0.012	3.1 ± 3.1	394 ± 7
HD208682	53292.737	3.835 ± 0.023	11.7 ± 0.5	0.775 ± 0.014	-15.1 ± 3.5	381 ± 9
HD208682	54019.702	4.121 ± 0.037	-17.9 ± 0.7	0.724 ± 0.012	-12.3 ± 3.3	374 ± 8
HD208682	54024.835	3.904 ± 0.038	-12.0 ± 0.8	0.662 ± 0.017	-19.9 ± 4.9	371 ± 13
HD210129	53291.681	-1.422 ± 0.024	-56.4 ± 0.4	0.189 ± 0.007	-48.0 ± 3.8	198 ± 10
HD210129	53291.684	-1.445 ± 0.029	-56.8 ± 0.4	0.194 ± 0.010	-48.2 ± 5.2	200 ± 13
HD210129	53295.721	-1.326 ± 0.019	-56.4 ± 0.3	0.137 ± 0.005	-76.5 ± 3.7	71 ± 26
HD210129	53295.725	-1.234 ± 0.026	-56.6 ± 0.4	0.130 ± 0.009	-81.3 ± 6.8	43 ± 82
HD210129	54019.731	-6.729 ± 0.032	-57.0 ± 0.5	0.134 ± 0.011	-51.6 ± 8.4	171 ± 25
HD210129	54021.756	-6.675 ± 0.045	-57.8 ± 0.7	0.124 ± 0.013	-55.6 ± 10.5	204 ± 26
HD212044	53291.691	-14.666 ± 0.036	-15.6 ± 0.7	0.398 ± 0.011	-32.4 ± 5.3	359 ± 14
HD212044	53291.697	-14.619 ± 0.037	-16.2 ± 0.7	0.397 ± 0.011	-34.6 ± 5.1	355 ± 14
HD212044	54020.721	-18.579 ± 0.069	-10.2 ± 1.3	0.100 ± 0.025	...	...
HD212044	54024.842	-20.493 ± 0.038	-11.3 ± 0.7	0.010 ± 0.016	...	...
HD212076	53290.713	-14.144 ± 0.027	9.2 ± 0.4	0.396 ± 0.007	24.7 ± 2.6	210 ± 5
HD212076	53290.714	-13.897 ± 0.036	9.0 ± 0.6	0.403 ± 0.012	30.6 ± 4.3	193 ± 9
HD212076	53292.744	-14.341 ± 0.029	12.2 ± 0.5	0.335 ± 0.006	3.9 ± 2.4	139 ± 12
HD212076	53292.746	-14.317 ± 0.031	12.5 ± 0.5	0.359 ± 0.008	4.3 ± 3.4	159 ± 14
HD212076	54019.708	-24.996 ± 0.074	9.2 ± 1.3	0.247 ± 0.020	15.5 ± 11.4	126 ± 63
HD212076	54020.763	-24.752 ± 0.045	10.7 ± 0.8	0.217 ± 0.010	27.1 ± 6.5	81 ± 34
HD212076	54022.774	-25.128 ± 0.047	11.7 ± 0.9	0.233 ± 0.011	-10.1 ± 6.6	75 ± 61
HD212571	53290.692	-4.383 ± 0.027	-6.8 ± 0.6	0.514 ± 0.012	-15.6 ± 6.5	600 ± 15
HD212571	53290.781	-4.230 ± 0.022	-7.6 ± 0.5	0.492 ± 0.012	-21.6 ± 6.8	585 ± 16
HD212571	53290.805	-4.245 ± 0.026	-7.2 ± 0.6	0.474 ± 0.013	-1.0 ± 7.7	572 ± 19
HD212571	53291.632	-4.959 ± 0.025	-10.5 ± 0.5	0.522 ± 0.012	-6.8 ± 6.3	621 ± 14
HD212571	53291.686	-4.790 ± 0.030	-12.5 ± 0.6	0.511 ± 0.013	-9.8 ± 6.9	626 ± 15
HD212571	53291.769	-4.712 ± 0.023	-10.7 ± 0.5	0.480 ± 0.012	-5.3 ± 7.3	637 ± 16
HD212571	53291.812	-4.554 ± 0.025	-9.3 ± 0.5	0.470 ± 0.015	-16.5 ± 8.9	599 ± 21
HD212571	53292.602	-4.806 ± 0.019	-10.0 ± 0.4	0.514 ± 0.010	-4.1 ± 5.7	627 ± 12
HD212571	53292.637	-4.873 ± 0.028	-10.3 ± 0.6	0.500 ± 0.013	-12.2 ± 7.0	607 ± 16
HD212571	53292.685	-4.644 ± 0.024	-8.2 ± 0.5	0.498 ± 0.011	-34.7 ± 6.1	588 ± 14
HD212571	53292.728	-4.639 ± 0.029	-10.7 ± 0.6	0.456 ± 0.014	-9.0 ± 8.7	560 ± 22
HD212571	53292.782	-4.533 ± 0.021	-9.6 ± 0.5	0.424 ± 0.009	-17.5 ± 6.0	570 ± 14
HD212571	53294.598	-4.786 ± 0.016	-8.2 ± 0.3	0.429 ± 0.012	-4.8 ± 7.9	587 ± 19
HD212571	53294.643	-4.868 ± 0.018	-5.9 ± 0.4	0.482 ± 0.010	-19.9 ± 5.7	592 ± 13
HD212571	53294.681	-4.615 ± 0.030	-7.5 ± 0.6	0.454 ± 0.012	-23.0 ± 7.5	555 ± 19
HD212571	53294.719	-4.620 ± 0.038	-6.9 ± 0.8	0.409 ± 0.025	-8.1 ± 17.3	545 ± 45
HD212571	53295.642	-4.869 ± 0.021	-12.5 ± 0.4	0.463 ± 0.010	-21.3 ± 6.3	597 ± 14
HD212571	53295.683	-4.710 ± 0.019	-12.1 ± 0.4	0.435 ± 0.011	-14.4 ± 7.1	570 ± 17
HD212571	53295.717	-4.566 ± 0.018	-12.0 ± 0.4	0.372 ± 0.012	-19.8 ± 8.8	551 ± 22
HD212571	54019.670	-4.092 ± 0.034	5.1 ± 0.7	0.022 ± 0.015	...	...
HD212571	54019.672	-4.318 ± 0.040	3.5 ± 0.9	0.041 ± 0.019	...	...
HD212571	54019.733	-4.136 ± 0.039	1.4 ± 0.8	0.025 ± 0.018	...	...
HD212571	54019.845	-4.358 ± 0.040	0.0 ± 0.9	0.036 ± 0.022	...	...
HD212571	54020.668	-3.824 ± 0.079	4.8 ± 1.7	0.086 ± 0.041	...	...
HD212571	54020.671	-3.839 ± 0.038	0.6 ± 0.8	-0.008 ± 0.012	...	...
HD212571	54020.766	-3.980 ± 0.035	3.4 ± 0.8	0.000 ± 0.019	...	...
HD212571	54020.824	-4.000 ± 0.032	4.4 ± 0.7	-0.011 ± 0.014	...	...
HD212571	54021.646	-3.843 ± 0.026	4.9 ± 0.6	-0.022 ± 0.013	...	...

Continued on Next Page...

Table C.1 – Continued

Star Name	HJD (−2400000)	W_λ (Hα) (Å)	V_r (Hα) (km s^{-1})	W_λ (He I) (Å)	V_r (He I) (km s^{-1})	FWSM (He I) (km s^{-1})
HD212571	54021.697	-3.772 ± 0.044	6.9 ± 0.9	0.028 ± 0.020	···	···
HD212571	54021.747	-3.843 ± 0.025	3.9 ± 0.5	0.015 ± 0.013	···	···
HD212571	54021.786	-3.869 ± 0.038	6.6 ± 0.8	-0.013 ± 0.015	···	···
HD212571	54021.847	-3.860 ± 0.036	6.5 ± 0.8	0.022 ± 0.018	···	···
HD212571	54022.619	-4.102 ± 0.056	4.7 ± 1.2	0.088 ± 0.023	···	···
HD212571	54022.760	-3.928 ± 0.041	3.9 ± 0.9	0.056 ± 0.019	···	···
HD212571	54023.676	-3.766 ± 0.029	0.8 ± 0.6	0.012 ± 0.021	···	···
HD212571	54023.715	-3.639 ± 0.039	0.4 ± 0.8	-0.009 ± 0.022	···	···
HD212571	54023.754	-3.780 ± 0.039	2.6 ± 0.9	-0.016 ± 0.018	···	···
HD212571	54023.797	-3.685 ± 0.044	-2.3 ± 0.9	0.013 ± 0.024	···	···
HD212571	54024.639	-3.759 ± 0.027	2.3 ± 0.6	0.054 ± 0.017	···	···
HD212571	54024.691	-3.858 ± 0.029	0.8 ± 0.6	0.013 ± 0.018	···	···
HD212571	54024.722	-3.786 ± 0.026	0.3 ± 0.6	0.026 ± 0.015	···	···
HD212571	54024.768	-3.689 ± 0.027	0.3 ± 0.6	0.008 ± 0.017	···	···
HD212571	54024.810	-3.877 ± 0.032	0.9 ± 0.7	0.048 ± 0.014	···	···
HD212571	54024.851	-4.001 ± 0.036	5.5 ± 0.8	0.023 ± 0.018	···	···
HD212791	53291.708	-7.230 ± 0.024	-11.9 ± 0.4	0.513 ± 0.011	-13.6 ± 2.7	229 ± 7
HD212791	54020.754	-1.923 ± 0.030	-11.7 ± 0.4	0.423 ± 0.012	-10.9 ± 3.6	197 ± 11
HD212791	54021.759	-1.830 ± 0.049	-11.3 ± 0.7	0.449 ± 0.014	-16.5 ± 3.7	209 ± 10
HD214167	53291.717	4.453 ± 0.025	-16.5 ± 0.5	0.679 ± 0.008	-10.4 ± 1.0	109 ± 3
HD214167	53295.731	4.556 ± 0.029	-17.5 ± 0.6	0.650 ± 0.007	-14.0 ± 1.0	102 ± 3
HD214167	54020.735	4.749 ± 0.029	-24.1 ± 0.6	0.651 ± 0.010	-6.5 ± 1.2	107 ± 4
HD214167	54021.771	4.742 ± 0.023	-11.8 ± 0.5	0.657 ± 0.008	-11.0 ± 0.9	106 ± 3
HD214167	54023.733	4.569 ± 0.030	-2.2 ± 0.6	0.668 ± 0.008	-10.5 ± 1.0	107 ± 3
HD214168	53291.721	-16.799 ± 0.023	-17.8 ± 0.5	0.665 ± 0.009	12.0 ± 2.7	401 ± 6
HD214168	53291.723	-16.794 ± 0.025	-18.8 ± 0.5	0.657 ± 0.012	9.9 ± 3.6	405 ± 8
HD214168	53295.738	-16.547 ± 0.031	-18.2 ± 0.6	0.611 ± 0.013	-5.8 ± 4.2	362 ± 11
HD214168	54020.743	-14.942 ± 0.036	20.8 ± 0.7	0.514 ± 0.016	-15.1 ± 6.1	361 ± 16
HD214168	54021.768	-14.927 ± 0.044	19.9 ± 0.9	0.600 ± 0.018	-11.8 ± 5.9	404 ± 14
HD214168	54023.738	-15.409 ± 0.024	18.3 ± 0.5	0.585 ± 0.012	-24.2 ± 4.0	397 ± 9
HD216200	53291.733	1.746 ± 0.029	16.6 ± 0.4	0.587 ± 0.016	39.3 ± 5.5	170 ± 32
HD216200	53294.725	1.356 ± 0.035	-14.8 ± 0.5	0.636 ± 0.015	-24.4 ± 4.7	229 ± 21
HD216200	54020.746	2.191 ± 0.042	-31.1 ± 0.6	0.525 ± 0.016	-42.4 ± 6.2	92 ± 68
HD216200	54023.750	1.438 ± 0.024	-52.3 ± 0.3	0.559 ± 0.011	-69.6 ± 3.9	168 ± 23
HD217050	53290.783	-26.120 ± 0.019	-14.1 ± 0.4	1.124 ± 0.010	-25.9 ± 1.5	330 ± 7
HD217050	53290.786	-25.668 ± 0.028	-14.0 ± 0.6	1.134 ± 0.011	-25.6 ± 1.6	326 ± 7
HD217050	53292.749	-26.309 ± 0.021	-14.8 ± 0.5	1.071 ± 0.009	-20.0 ± 1.4	344 ± 6
HD217050	53292.751	-26.460 ± 0.055	-14.7 ± 1.2	1.070 ± 0.010	-18.2 ± 1.8	358 ± 4
HD217050	54019.711	-25.124 ± 0.057	-7.3 ± 1.3	1.196 ± 0.020	-1.8 ± 2.7	317 ± 11
HD217050	54020.769	-25.132 ± 0.047	-8.7 ± 1.0	0.999 ± 0.012	25.0 ± 1.8	291 ± 7
HD217543	53291.738	4.463 ± 0.019	-10.2 ± 0.4	0.971 ± 0.012	-20.9 ± 2.7	449 ± 6
HD217543	54019.740	1.388 ± 0.036	3.0 ± 0.7	1.098 ± 0.016	-28.3 ± 3.1	412 ± 8
HD217543	54020.773	0.710 ± 0.027	-6.4 ± 0.6	1.154 ± 0.017	-29.8 ± 3.1	413 ± 8
HD217675	53290.715	3.571 ± 0.021	-9.2 ± 0.6	0.416 ± 0.007	-20.0 ± 2.4	304 ± 6
HD217675	53292.754	3.632 ± 0.019	-11.6 ± 0.5	0.405 ± 0.007	-20.0 ± 2.7	294 ± 7
HD217675	54019.742	4.633 ± 0.028	3.8 ± 0.7	0.353 ± 0.009	-19.6 ± 3.7	291 ± 9
HD217675	54020.775	4.812 ± 0.023	7.2 ± 0.6	0.395 ± 0.009	-9.2 ± 3.3	313 ± 7
HD217675	54022.779	4.733 ± 0.045	-8.0 ± 1.2	0.353 ± 0.024	-32.3 ± 10.3	255 ± 30
HD217891	53290.720	-14.902 ± 0.035	4.8 ± 0.5	0.244 ± 0.008	4.8 ± 2.9	115 ± 10
HD217891	53292.759	-14.714 ± 0.030	5.6 ± 0.5	0.219 ± 0.007	8.4 ± 2.9	106 ± 11

Continued on Next Page...

Table C.1 – Continued

Star Name	HJD (−2400000)	W_λ (Hα) (Å)	V_r (Hα) (km s^{-1})	W_λ (He I) (Å)	V_r (He I) (km s^{-1})	FWSM (He I) (km s^{-1})
HD217891	53292.761	-14.822 ± 0.036	5.6 ± 0.5	0.227 ± 0.008	-0.2 ± 3.2	113 ± 11
HD217891	54019.746	-10.824 ± 0.051	5.6 ± 0.7	0.180 ± 0.008	13.7 ± 3.8	83 ± 18
HD217891	54019.747	-10.742 ± 0.053	5.8 ± 0.8	0.225 ± 0.015	11.0 ± 5.8	130 ± 18
HD217891	54020.778	-10.778 ± 0.043	6.1 ± 0.6	0.194 ± 0.010	2.9 ± 4.2	112 ± 15
HD217891	54022.778	-10.600 ± 0.033	6.2 ± 0.5	0.196 ± 0.008	-4.6 ± 3.5	116 ± 12
HD218393	53290.731	-20.525 ± 0.081	18.1 ± 1.6	0.998 ± 0.016	-177.8 ± 2.3	345 ± 45
HD218393	53291.750	-21.382 ± 0.073	20.6 ± 1.5	1.034 ± 0.016	-191.6 ± 2.4	349 ± 46
HD218393	53291.753	-21.476 ± 0.075	19.8 ± 1.5	1.055 ± 0.017	-191.0 ± 2.6	348 ± 49
HD218393	54019.759	-18.538 ± 0.078	22.8 ± 1.5	0.667 ± 0.020	-115.5 ± 3.1	300 ± 77
HD218393	54020.784	-18.631 ± 0.075	13.6 ± 1.4	0.761 ± 0.022	-114.4 ± 2.9	270 ± 80
HD218393	54021.775	-18.205 ± 0.083	8.7 ± 1.6	0.741 ± 0.019	-141.1 ± 3.1	308 ± 73
HD218674	53290.737	-2.510 ± 0.020	-7.5 ± 0.4	0.786 ± 0.011	-7.0 ± 2.6	352 ± 7
HD218674	54019.763	-1.482 ± 0.033	-18.3 ± 0.7	0.809 ± 0.014	-31.8 ± 3.3	329 ± 9
HD218674	54020.788	-0.989 ± 0.033	-18.2 ± 0.7	0.742 ± 0.021	-22.6 ± 5.5	291 ± 18
HD218674	54023.758	-1.086 ± 0.035	-16.6 ± 0.7	0.702 ± 0.016	-59.3 ± 4.3	257 ± 16
HD224544	53290.749	4.130 ± 0.019	-7.0 ± 0.4	0.427 ± 0.011	-2.4 ± 4.9	325 ± 13
HD224544	53292.777	4.256 ± 0.019	-7.9 ± 0.4	0.422 ± 0.009	-10.0 ± 4.1	308 ± 12
HD224544	53294.737	4.108 ± 0.034	-7.2 ± 0.7	0.465 ± 0.014	-2.1 ± 5.9	348 ± 15
HD224544	54019.768	4.625 ± 0.034	-10.3 ± 0.7	0.384 ± 0.013	-7.7 ± 6.6	328 ± 18
HD224544	54020.797	4.552 ± 0.034	-10.1 ± 0.7	0.374 ± 0.012	-20.8 ± 5.9	300 ± 18
HD224544	54021.783	4.468 ± 0.026	-7.6 ± 0.5	0.381 ± 0.013	-27.9 ± 6.6	294 ± 20
HD224544	54023.770	4.491 ± 0.036	-8.1 ± 0.7	0.364 ± 0.015	-32.2 ± 7.6	284 ± 24
HD224559	53290.743	-18.694 ± 0.030	-0.8 ± 0.6	0.445 ± 0.012	-4.3 ± 5.1	417 ± 12
HD224559	53292.766	-18.408 ± 0.028	-2.7 ± 0.6	0.465 ± 0.008	-2.8 ± 3.5	431 ± 8
HD224559	53294.746	-18.828 ± 0.032	-1.4 ± 0.7	0.404 ± 0.014	1.4 ± 6.8	414 ± 16
HD224559	54019.771	-21.778 ± 0.040	-3.3 ± 0.8	0.246 ± 0.016	-9.7 ± 12.4	270 ± 45
HD224559	54020.792	-21.789 ± 0.052	-1.7 ± 1.1	0.307 ± 0.017	-3.8 ± 10.7	353 ± 29
HD224559	54021.779	-21.550 ± 0.046	-0.9 ± 0.9	0.308 ± 0.019	9.5 ± 11.7	353 ± 32
HD224559	54023.765	-22.164 ± 0.038	-3.4 ± 0.8	0.359 ± 0.014	-13.3 ± 7.8	384 ± 19
HD225095	53290.770	-24.690 ± 0.050	-32.1 ± 0.9	0.394 ± 0.018	-50.8 ± 8.6	407 ± 20
HD225095	53290.777	-24.648 ± 0.054	-32.2 ± 1.0	0.388 ± 0.014	-66.1 ± 6.9	353 ± 19
HD225095	53291.760	-24.167 ± 0.039	-34.7 ± 0.7	0.430 ± 0.008	-35.6 ± 3.7	343 ± 10
HD225095	53291.766	-24.095 ± 0.043	-33.9 ± 0.8	0.420 ± 0.016	-44.5 ± 7.3	360 ± 19
HD225095	54019.797	-34.415 ± 0.069	-27.5 ± 1.3	0.171 ± 0.017	-48.3 ± 19.0	···
HD225095	54020.800	-34.473 ± 0.049	-26.3 ± 1.0	0.157 ± 0.016	-118.9 ± 20.0	···
HD225095	54021.794	-34.827 ± 0.059	-25.9 ± 1.2	0.156 ± 0.018	-132.4 ± 22.7	···
HD225095	54023.775	-34.459 ± 0.059	-26.0 ± 1.2	0.138 ± 0.017	11.1 ± 24.1	···

C.2 Blue Spectral Measurements Table

Table C.2: Spectral line data for the Hγ region

Star Name	HJD (−2400000)	W_λ (Hγ) (Å)	V_r (Hγ) (km s^{-1})	W_λ (He I) (Å)	V_r (He I) (km s^{-1})	FWSM (He I) (km s^{-1})	W_λ (Mg II) (Å)	V_r (Mg II) (km s^{-1})	FWSM (Mg II) (km s^{-1})
HD000144	53233.911	7.868 ± 0.020	−2.0 ± 0.8	0.236 ± 0.010	−9.8 ± 5.2	145 ± 30	0.312 ± 0.008	−1.6 ± 2.8	133 ± 11
HD000144	53236.946	7.920 ± 0.029	−2.5 ± 1.1	0.262 ± 0.011	−13.6 ± 5.5	206 ± 22	0.337 ± 0.010	−6.1 ± 3.1	150 ± 10
HD000144	53238.946	8.033 ± 0.020	−4.8 ± 0.8	0.269 ± 0.011	−5.7 ± 5.1	210 ± 20	0.345 ± 0.009	−4.0 ± 2.9	159 ± 9
HD000144	53684.742	7.947 ± 0.017	−6.4 ± 0.7	0.277 ± 0.011	−6.7 ± 5.1	213 ± 20	0.340 ± 0.009	−2.1 ± 3.0	151 ± 10
HD000144	53688.787	8.168 ± 0.018	−6.8 ± 0.7	0.264 ± 0.010	−13.0 ± 4.9	193 ± 21	0.327 ± 0.009	−6.5 ± 2.8	139 ± 10
HD000144	54025.822	7.975 ± 0.019	−9.5 ± 0.7	0.258 ± 0.011	−15.3 ± 5.2	186 ± 23	0.319 ± 0.009	−3.0 ± 3.0	139 ± 11
HD000144	54030.784	8.107 ± 0.021	−5.7 ± 0.8	0.276 ± 0.011	−9.9 ± 4.9	201 ± 20	0.341 ± 0.009	−7.0 ± 2.8	141 ± 10
HD000144	54031.805	8.084 ± 0.021	−2.1 ± 0.8	0.278 ± 0.011	−12.1 ± 5.2	212 ± 20	0.332 ± 0.010	−6.1 ± 3.1	138 ± 11
HD004180	53233.917	3.804 ± 0.030	−36.4 ± 1.2	0.584 ± 0.016	−27.2 ± 3.5	255 ± 18	0.186 ± 0.009	−22.2 ± 6.4	165 ± 28
HD004180	53236.950	3.753 ± 0.033	−39.8 ± 1.4	0.585 ± 0.006	−21.9 ± 1.3	256 ± 6	0.200 ± 0.006	−35.5 ± 4.5	190 ± 17
HD004180	53238.950	3.781 ± 0.034	−40.7 ± 1.4	0.592 ± 0.008	−30.9 ± 1.8	262 ± 9	0.210 ± 0.009	−28.5 ± 5.8	186 ± 22
HD004180	53684.625	3.882 ± 0.030	−8.1 ± 1.2	0.645 ± 0.007	5.9 ± 1.4	274 ± 6	0.233 ± 0.007	−8.3 ± 4.4	281 ± 14
HD004180	53684.754	3.915 ± 0.030	−8.5 ± 1.2	0.650 ± 0.007	6.9 ± 1.3	274 ± 6	0.237 ± 0.007	−4.0 ± 4.0	281 ± 13
HD004180	53686.697	3.949 ± 0.029	−17.8 ± 1.2	0.630 ± 0.009	−3.4 ± 1.7	270 ± 8	0.230 ± 0.009	−20.9 ± 5.3	253 ± 15
HD004180	53686.870	3.880 ± 0.028	−12.0 ± 1.1	0.637 ± 0.009	−4.1 ± 1.7	266 ± 8	0.239 ± 0.008	−20.8 ± 4.7	260 ± 12
HD004180	54025.731	4.588 ± 0.033	−36.3 ± 1.3	0.660 ± 0.008	−9.3 ± 1.5	278 ± 7	0.215 ± 0.008	−15.7 ± 5.2	247 ± 15
HD004180	54030.792	4.436 ± 0.030	−20.5 ± 1.2	0.632 ± 0.009	0.9 ± 1.8	268 ± 9	0.215 ± 0.009	−12.1 ± 5.7	271 ± 20
HD004180	54031.810	4.348 ± 0.028	−20.6 ± 1.2	0.632 ± 0.007	−1.3 ± 1.5	267 ± 7	0.226 ± 0.007	−24.1 ± 4.5	249 ± 12
HD005394	53233.913	0.635 ± 0.025	−10.0 ± 0.5	0.448 ± 0.015	−37.0 ± 6.4	398 ± 15	−0.072 ± 0.012	···	···
HD005394	53236.950	0.738 ± 0.029	−11.1 ± 0.6	0.482 ± 0.013	−31.7 ± 5.2	443 ± 16	−0.050 ± 0.011	···	···
HD005394	53238.950	0.717 ± 0.026	−12.8 ± 0.6	0.463 ± 0.014	−21.1 ± 5.7	419 ± 19	−0.060 ± 0.011	···	···
HD005394	53684.739	0.685 ± 0.023	−19.0 ± 0.5	0.519 ± 0.013	−29.5 ± 4.6	459 ± 14	−0.039 ± 0.010	···	···
HD005394	53685.737	0.730 ± 0.024	−18.7 ± 0.5	0.504 ± 0.013	−36.0 ± 4.7	439 ± 10	−0.027 ± 0.010	···	···
HD005394	53688.749	0.632 ± 0.026	−19.2 ± 0.6	0.515 ± 0.013	−33.9 ± 4.6	456 ± 9	−0.028 ± 0.010	···	···
HD005394	54025.756	1.294 ± 0.029	−12.8 ± 0.6	0.495 ± 0.013	−33.1 ± 4.9	434 ± 16	−0.054 ± 0.010	···	···
HD005394	54030.794	1.152 ± 0.027	−8.7 ± 0.6	0.488 ± 0.014	−29.7 ± 5.5	437 ± 18	−0.040 ± 0.011	···	···
HD005394	54031.812	1.065 ± 0.027	−10.2 ± 0.6	0.470 ± 0.014	−24.0 ± 5.7	423 ± 19	−0.046 ± 0.011	···	···
HD006811	53233.919	6.749 ± 0.018	3.6 ± 0.7	0.414 ± 0.008	−11.0 ± 2.3	199 ± 11	0.258 ± 0.006	0.9 ± 1.9	104 ± 7
HD006811	53236.954	6.700 ± 0.019	3.5 ± 0.7	0.418 ± 0.006	−11.6 ± 1.8	216 ± 8	0.271 ± 0.005	3.3 ± 1.4	115 ± 5
HD006811	53238.953	6.788 ± 0.018	2.0 ± 0.7	0.408 ± 0.007	−7.7 ± 2.2	203 ± 10	0.263 ± 0.005	1.3 ± 1.7	110 ± 6
HD006811	53684.669	6.764 ± 0.015	2.2 ± 0.6	0.431 ± 0.006	−4.8 ± 1.8	222 ± 7	0.270 ± 0.005	1.9 ± 1.5	115 ± 5
HD006811	53684.830	6.824 ± 0.015	0.7 ± 0.6	0.426 ± 0.007	−5.9 ± 2.1	225 ± 8	0.265 ± 0.005	4.4 ± 1.7	113 ± 6
HD006811	53686.716	6.818 ± 0.017	−0.8 ± 0.7	0.433 ± 0.007	−11.5 ± 2.1	222 ± 8	0.279 ± 0.005	−1.0 ± 1.6	115 ± 5
HD006811	53688.658	6.899 ± 0.015	−0.3 ± 0.6	0.425 ± 0.007	−11.5 ± 2.1	213 ± 9	0.272 ± 0.006	0.3 ± 1.7	115 ± 6
HD006811	53688.836	7.068 ± 0.016	−0.5 ± 0.6	0.427 ± 0.006	−8.3 ± 1.8	219 ± 7	0.275 ± 0.005	3.7 ± 1.4	120 ± 4
HD006811	54025.759	6.956 ± 0.018	−3.1 ± 0.7	0.437 ± 0.007	−12.2 ± 2.0	221 ± 8	0.266 ± 0.005	0.9 ± 1.6	105 ± 6
HD006811	54027.801	6.921 ± 0.018	−0.7 ± 0.7	0.441 ± 0.007	−8.1 ± 1.8	224 ± 7	0.272 ± 0.005	−0.6 ± 1.5	110 ± 5
HD006811	54029.853	7.055 ± 0.018	−0.1 ± 0.7	0.390 ± 0.008	−9.2 ± 2.4	190 ± 11	0.251 ± 0.006	2.8 ± 1.9	98 ± 7
HD006811	54031.816	6.793 ± 0.021	1.2 ± 0.8	0.430 ± 0.008	−7.3 ± 2.1	214 ± 9	0.271 ± 0.006	1.7 ± 1.7	112 ± 6
HD007636	53235.913	2.339 ± 0.034	12.3 ± 1.2	0.960 ± 0.017	−18.4 ± 3.4	318 ± 15	0.042 ± 0.014	···	···
HD007636	53237.894	2.452 ± 0.033	12.9 ± 1.2	0.913 ± 0.019	−11.2 ± 4.0	321 ± 18	0.053 ± 0.016	···	···
HD007636	53684.765	1.880 ± 0.033	17.9 ± 1.2	0.884 ± 0.016	−8.5 ± 3.4	358 ± 13	0.061 ± 0.013	···	···
HD007636	53687.758	1.902 ± 0.032	5.8 ± 1.1	0.864 ± 0.017	−24.8 ± 3.7	331 ± 16	0.037 ± 0.013	···	···
HD007636	54025.767	3.042 ± 0.039	−19.0 ± 1.4	0.986 ± 0.017	−24.6 ± 3.2	343 ± 13	0.041 ± 0.013	···	···
HD007636	54029.839	3.055 ± 0.031	−8.9 ± 1.1	0.978 ± 0.018	−25.9 ± 3.6	332 ± 15	0.040 ± 0.015	···	···
HD009709	53234.917	6.968 ± 0.030	−7.8 ± 1.4	0.400 ± 0.012	−8.2 ± 4.2	333 ± 18	0.284 ± 0.012	−37.2 ± 6.6	262 ± 20
HD009709	53237.908	7.067 ± 0.032	−9.2 ± 1.5	0.402 ± 0.011	−12.2 ± 3.9	354 ± 15	0.314 ± 0.011	−39.6 ± 5.5	292 ± 15
HD009709	53684.783	6.913 ± 0.034	−20.0 ± 1.6	0.413 ± 0.010	−10.0 ± 3.5	344 ± 14	0.323 ± 0.010	−32.7 ± 5.0	284 ± 14

Continued on Next Page...

Table C.2 – Continued

Star Name	HJD (−2400000)	W_λ (Hγ) (Å)	V_r (Hγ) (km s^{-1})	W_λ (He I) (Å)	V_r (He I) (km s^{-1})	FWSM (He I) (km s^{-1})	W_λ (Mg II) (Å)	V_r (Mg II) (km s^{-1})	FWSM (Mg II) (km s^{-1})
HD009709	53687.781	6.926 ± 0.032	−15.6 ± 1.5	0.405 ± 0.009	−13.0 ± 3.2	342 ± 13	0.304 ± 0.009	−51.1 ± 4.7	237 ± 16
HD009709	54025.786	7.301 ± 0.030	−30.1 ± 1.4	0.426 ± 0.009	−14.3 ± 3.0	338 ± 12	0.331 ± 0.009	−36.4 ± 4.3	271 ± 12
HD009709	54029.856	7.327 ± 0.032	−26.0 ± 1.5	0.372 ± 0.008	−8.7 ± 3.1	326 ± 13	0.288 ± 0.008	−56.9 ± 4.5	219 ± 16
HD010516	53233.921	2.393 ± 0.026	42.6 ± 1.0	1.001 ± 0.014	−24.4 ± 3.0	417 ± 10	0.157 ± 0.012	−19.7 ± 10.6	206 ± 36
HD010516	53236.955	2.329 ± 0.028	38.4 ± 1.1	1.018 ± 0.014	−22.3 ± 2.9	457 ± 14	0.171 ± 0.010	−28.4 ± 9.4	210 ± 32
HD010516	53238.953	2.310 ± 0.029	12.6 ± 1.1	1.002 ± 0.015	−23.1 ± 3.1	436 ± 15	0.154 ± 0.011	−21.5 ± 10.5	206 ± 36
HD010516	53684.771	2.478 ± 0.022	56.6 ± 0.9	1.098 ± 0.011	−51.9 ± 2.4	408 ± 13	0.147 ± 0.008	−64.2 ± 7.0	170 ± 26
HD010516	53686.707	2.342 ± 0.023	67.3 ± 0.9	1.055 ± 0.010	−46.4 ± 2.1	403 ± 11	0.162 ± 0.007	−70.9 ± 5.8	173 ± 21
HD010516	54025.794	2.820 ± 0.022	64.8 ± 0.9	1.018 ± 0.008	−29.8 ± 1.7	416 ± 9	0.157 ± 0.005	−53.7 ± 4.4	191 ± 13
HD010516	54030.796	2.749 ± 0.022	66.0 ± 0.9	0.983 ± 0.009	−45.1 ± 2.0	388 ± 11	0.170 ± 0.006	−52.6 ± 4.5	205 ± 13
HD010516	54031.818	2.754 ± 0.022	86.3 ± 0.9	0.971 ± 0.011	−20.3 ± 2.4	392 ± 13	0.151 ± 0.008	−58.1 ± 6.6	196 ± 20
HD011415	53233.925	5.792 ± 0.017	−7.9 ± 0.6	0.855 ± 0.008	−26.5 ± 1.2	230 ± 6	0.256 ± 0.005	−12.3 ± 1.0	71 ± 3
HD011415	53236.956	5.739 ± 0.020	−9.4 ± 0.7	0.862 ± 0.007	−26.5 ± 1.0	242 ± 5	0.267 ± 0.004	−11.1 ± 0.8	76 ± 2
HD011415	53238.954	5.737 ± 0.019	−12.7 ± 0.7	0.875 ± 0.006	−25.7 ± 0.9	244 ± 4	0.267 ± 0.004	−10.5 ± 0.8	71 ± 2
HD011415	53684.772	5.771 ± 0.019	−11.0 ± 0.6	0.889 ± 0.007	−28.8 ± 1.0	250 ± 5	0.266 ± 0.004	−12.3 ± 0.8	73 ± 2
HD011415	53688.784	5.754 ± 0.020	−15.6 ± 0.7	0.899 ± 0.007	−26.4 ± 1.1	247 ± 5	0.279 ± 0.004	−10.9 ± 0.8	74 ± 3
HD011415	54025.796	5.760 ± 0.019	−9.6 ± 0.7	0.892 ± 0.006	−23.6 ± 0.8	245 ± 4	0.253 ± 0.003	−6.2 ± 0.7	59 ± 3
HD011415	54027.803	5.838 ± 0.020	−11.4 ± 0.7	0.893 ± 0.007	−27.4 ± 1.1	250 ± 5	0.268 ± 0.004	−13.1 ± 0.9	72 ± 3
HD011415	54029.869	5.815 ± 0.016	−12.6 ± 0.6	0.887 ± 0.007	−23.4 ± 1.0	243 ± 5	0.267 ± 0.004	−10.1 ± 0.8	76 ± 2
HD011415	54030.799	5.874 ± 0.017	−11.5 ± 0.6	0.882 ± 0.007	−25.5 ± 1.0	243 ± 5	0.262 ± 0.004	−11.1 ± 0.8	75 ± 2
HD011415	54031.819	5.824 ± 0.020	−8.6 ± 0.7	0.882 ± 0.008	−23.0 ± 1.2	244 ± 6	0.264 ± 0.005	−10.2 ± 0.9	74 ± 3
HD013661	53235.926	3.995 ± 0.026	−37.3 ± 1.2	1.152 ± 0.009	−60.7 ± 1.1	393 ± 9	0.191 ± 0.009	−90.1 ± 7.4	219 ± 27
HD013661	53237.923	4.056 ± 0.019	−37.3 ± 0.9	1.142 ± 0.010	−56.1 ± 1.2	396 ± 10	0.183 ± 0.010	−102.2 ± 8.6	218 ± 32
HD013661	53684.794	4.241 ± 0.027	−31.4 ± 1.2	1.184 ± 0.010	−60.3 ± 1.2	406 ± 9	0.267 ± 0.009	−69.5 ± 5.8	347 ± 13
HD013661	53687.805	4.081 ± 0.017	−32.6 ± 0.8	1.197 ± 0.009	−70.0 ± 1.0	416 ± 8	0.253 ± 0.008	−72.2 ± 5.3	347 ± 12
HD013661	54025.810	4.163 ± 0.022	−31.3 ± 1.0	1.202 ± 0.010	−65.7 ± 1.1	396 ± 9	0.250 ± 0.009	−84.2 ± 6.1	310 ± 16
HD013661	54026.830	4.170 ± 0.023	−29.2 ± 1.0	1.197 ± 0.010	−70.2 ± 1.2	391 ± 10	0.280 ± 0.010	−59.4 ± 5.6	332 ± 14
HD013867	53235.944	7.707 ± 0.036	1.1 ± 1.6	0.460 ± 0.009	−3.1 ± 2.6	196 ± 10	0.283 ± 0.006	−1.6 ± 1.8	82 ± 8
HD013867	53237.940	7.674 ± 0.035	1.5 ± 1.6	0.434 ± 0.011	−4.4 ± 3.1	185 ± 13	0.287 ± 0.007	−2.9 ± 2.0	81 ± 9
HD013867	53685.761	7.863 ± 0.035	−2.9 ± 1.6	0.466 ± 0.008	−4.4 ± 2.3	194 ± 9	0.297 ± 0.006	0.4 ± 1.5	97 ± 5
HD013867	53687.852	7.875 ± 0.029	−8.9 ± 1.3	0.445 ± 0.011	3.0 ± 3.1	180 ± 13	0.272 ± 0.007	−2.1 ± 2.2	79 ± 10
HD013867	54026.814	7.770 ± 0.032	−9.2 ± 1.5	0.458 ± 0.009	1.9 ± 2.6	185 ± 11	0.278 ± 0.006	−2.4 ± 1.8	87 ± 7
HD013867	54030.802	7.785 ± 0.027	−8.1 ± 1.2	0.459 ± 0.010	0.4 ± 2.6	182 ± 12	0.287 ± 0.007	−2.7 ± 1.8	89 ± 7
HD018552	53233.933	7.558 ± 0.015	−15.8 ± 0.7	0.355 ± 0.006	−21.1 ± 2.5	297 ± 9	0.327 ± 0.006	−17.9 ± 3.0	284 ± 8
HD018552	53236.960	7.273 ± 0.017	−17.1 ± 0.8	0.364 ± 0.006	−22.1 ± 2.5	323 ± 8	0.353 ± 0.006	−19.8 ± 2.8	304 ± 7
HD018552	53239.012	7.442 ± 0.014	−17.2 ± 0.7	0.363 ± 0.007	−20.9 ± 2.7	322 ± 9	0.321 ± 0.007	−27.9 ± 3.4	288 ± 9
HD018552	53684.803	7.328 ± 0.018	−19.4 ± 0.8	0.397 ± 0.008	−18.0 ± 2.9	340 ± 9	0.370 ± 0.008	−15.6 ± 3.4	311 ± 8
HD018552	53686.704	7.350 ± 0.017	−20.3 ± 0.8	0.372 ± 0.007	−16.8 ± 2.7	331 ± 9	0.372 ± 0.007	−20.7 ± 3.0	305 ± 7
HD018552	53686.876	7.502 ± 0.016	−25.7 ± 0.7	0.359 ± 0.007	−21.1 ± 2.6	330 ± 8	0.349 ± 0.007	−23.3 ± 3.0	300 ± 7
HD018552	54026.802	7.584 ± 0.015	−23.1 ± 0.7	0.401 ± 0.008	−18.3 ± 2.6	329 ± 8	0.367 ± 0.008	−25.4 ± 3.2	314 ± 7
HD018552	54029.884	7.567 ± 0.019	−21.0 ± 0.9	0.377 ± 0.008	−19.4 ± 3.1	328 ± 10	0.347 ± 0.008	−29.8 ± 3.7	305 ± 9
HD018552	54031.829	7.364 ± 0.018	−20.1 ± 0.8	0.373 ± 0.008	−16.6 ± 2.8	337 ± 9	0.333 ± 0.008	−26.4 ± 3.5	284 ± 9
HD019243	53235.956	1.321 ± 0.020	82.5 ± 0.7	0.660 ± 0.016	−29.1 ± 2.2	255 ± 29	0.008 ± 0.009	···	···
HD019243	53237.952	1.415 ± 0.021	81.4 ± 0.8	0.624 ± 0.010	−28.5 ± 1.5	234 ± 21	−0.030 ± 0.008	···	···
HD019243	53686.766	1.391 ± 0.017	71.7 ± 0.6	0.679 ± 0.009	−52.6 ± 1.2	256 ± 15	0.005 ± 0.011	···	···
HD019243	54026.845	1.771 ± 0.019	49.1 ± 0.7	0.686 ± 0.011	−57.8 ± 1.4	267 ± 17	0.037 ± 0.010	···	···
HD019243	54027.812	1.806 ± 0.020	49.4 ± 0.8	0.690 ± 0.011	−61.9 ± 1.5	283 ± 18	0.020 ± 0.011	···	···
HD019243	54029.901	1.737 ± 0.018	40.3 ± 0.7	0.675 ± 0.008	−55.8 ± 1.1	268 ± 14	0.025 ± 0.011	···	···
HD020134	53235.969	5.106 ± 0.024	−9.1 ± 0.9	1.092 ± 0.008	−35.1 ± 1.1	276 ± 3	0.203 ± 0.006	−20.4 ± 2.8	151 ± 8
HD020134	53237.964	5.490 ± 0.023	−10.9 ± 0.8	1.089 ± 0.007	−36.3 ± 1.0	282 ± 2	0.227 ± 0.005	−22.6 ± 2.2	162 ± 6

Continued on Next Page...

Table C.2 – Continued

Star Name	HJD (−2400000)	W_λ (Hγ) (Å)	V_r (Hγ) (km s^{-1})	W_λ (He I) (Å)	V_r (He I) (km s^{-1})	FWSM (He I) (km s^{-1})	W_λ (Mg II) (Å)	V_r (Mg II) (km s^{-1})	FWSM (Mg II) (km s^{-1})
HD020134	53686.782	5.438 ± 0.028	−16.8 ± 1.0	1.152 ± 0.009	−32.2 ± 1.2	296 ± 3	0.247 ± 0.007	−20.0 ± 2.7	173 ± 7
HD020134	54027.827	5.654 ± 0.025	−22.6 ± 0.9	1.104 ± 0.008	−35.2 ± 1.1	281 ± 3	0.241 ± 0.006	−26.5 ± 2.3	171 ± 6
HD020134	54029.916	5.730 ± 0.024	−20.2 ± 0.9	1.127 ± 0.009	−32.1 ± 1.2	284 ± 3	0.256 ± 0.007	−24.7 ± 2.5	162 ± 7
HD020336	53234.925	4.494 ± 0.018	31.8 ± 0.8	1.229 ± 0.009	−8.8 ± 1.5	411 ± 5	0.168 ± 0.007	−19.8 ± 5.8	242 ± 15
HD020336	53237.973	4.366 ± 0.022	37.6 ± 1.0	1.256 ± 0.008	−12.5 ± 1.2	419 ± 4	0.186 ± 0.006	−19.5 ± 4.3	255 ± 11
HD020336	53239.014	4.421 ± 0.022	40.7 ± 1.0	1.231 ± 0.011	−14.7 ± 1.7	419 ± 5	0.201 ± 0.009	−33.7 ± 5.7	274 ± 13
HD020336	53684.812	3.998 ± 0.017	15.3 ± 0.7	1.163 ± 0.006	−17.5 ± 1.0	417 ± 3	0.189 ± 0.005	−30.0 ± 3.3	233 ± 9
HD020336	53685.740	3.924 ± 0.020	13.0 ± 0.9	1.199 ± 0.007	−13.2 ± 1.1	416 ± 3	0.188 ± 0.006	−20.7 ± 3.9	226 ± 11
HD020336	54026.864	4.109 ± 0.019	8.7 ± 0.8	1.157 ± 0.009	−3.1 ± 1.4	426 ± 4	0.208 ± 0.007	−26.8 ± 4.3	262 ± 10
HD020336	54029.939	4.059 ± 0.026	5.0 ± 1.2	1.148 ± 0.010	−12.8 ± 1.6	422 ± 5	0.190 ± 0.008	−33.8 ± 5.4	246 ± 14
HD020336	54031.843	3.960 ± 0.026	13.5 ± 1.1	1.148 ± 0.009	−8.5 ± 1.5	414 ± 5	0.180 ± 0.007	−34.7 ± 5.3	226 ± 15
HD020418	53234.930	6.026 ± 0.018	3.3 ± 0.8	0.915 ± 0.008	−17.4 ± 1.5	373 ± 6	0.271 ± 0.007	−14.8 ± 4.1	334 ± 9
HD020418	53238.956	6.163 ± 0.013	3.4 ± 0.6	0.920 ± 0.007	−19.1 ± 1.2	381 ± 5	0.286 ± 0.006	−21.1 ± 3.1	332 ± 7
HD020418	53684.810	6.098 ± 0.015	2.4 ± 0.6	0.945 ± 0.007	−20.3 ± 1.3	394 ± 5	0.306 ± 0.006	−16.6 ± 3.2	345 ± 6
HD020418	54026.859	6.194 ± 0.012	−2.1 ± 0.5	0.931 ± 0.007	−22.5 ± 1.2	386 ± 5	0.297 ± 0.006	−16.4 ± 3.1	343 ± 6
HD020418	54029.935	6.245 ± 0.018	1.4 ± 0.7	0.910 ± 0.007	−20.0 ± 1.3	384 ± 5	0.267 ± 0.006	−22.6 ± 3.5	334 ± 7
HD020418	54031.840	6.110 ± 0.017	−0.6 ± 0.7	0.912 ± 0.007	−21.1 ± 1.2	381 ± 5	0.281 ± 0.006	−20.4 ± 3.2	337 ± 7
HD021362	53234.936	5.822 ± 0.022	−29.6 ± 0.9	0.615 ± 0.012	−8.7 ± 3.0	342 ± 13	0.222 ± 0.011	−36.1 ± 8.1	187 ± 36
HD021362	53238.960	5.890 ± 0.019	−26.3 ± 0.8	0.643 ± 0.008	−6.3 ± 2.0	358 ± 8	0.256 ± 0.007	−39.5 ± 4.9	210 ± 19
HD021362	53684.817	5.922 ± 0.017	−23.6 ± 0.7	0.680 ± 0.007	−6.0 ± 1.6	385 ± 6	0.270 ± 0.006	−14.3 ± 3.9	291 ± 11
HD021362	54026.869	6.248 ± 0.016	−21.4 ± 0.7	0.685 ± 0.008	−11.0 ± 1.8	377 ± 7	0.281 ± 0.007	−13.4 ± 4.3	329 ± 10
HD021362	54029.943	6.521 ± 0.022	−21.4 ± 0.9	0.665 ± 0.008	−11.6 ± 1.9	375 ± 7	0.244 ± 0.007	−31.2 ± 5.0	302 ± 13
HD021362	54031.848	6.168 ± 0.019	−25.9 ± 0.8	0.690 ± 0.008	−13.0 ± 1.8	382 ± 7	0.264 ± 0.007	−31.8 ± 4.7	308 ± 12
HD021455	53236.964	7.996 ± 0.019	−0.6 ± 0.8	0.652 ± 0.009	−16.6 ± 1.7	278 ± 11	0.333 ± 0.006	0.6 ± 1.6	159 ± 4
HD021455	53238.983	8.095 ± 0.022	10.9 ± 1.0	0.661 ± 0.009	−17.6 ± 1.7	277 ± 10	0.323 ± 0.006	−0.9 ± 1.6	154 ± 4
HD021455	53684.823	8.072 ± 0.019	5.1 ± 0.8	0.669 ± 0.009	−11.7 ± 1.8	280 ± 11	0.330 ± 0.007	0.1 ± 1.7	151 ± 4
HD021455	54026.879	8.053 ± 0.021	2.8 ± 1.0	0.673 ± 0.007	−13.5 ± 1.4	281 ± 8	0.325 ± 0.005	−0.7 ± 1.4	149 ± 3
HD021455	54029.950	8.352 ± 0.024	8.9 ± 1.1	0.638 ± 0.009	−20.2 ± 1.8	277 ± 11	0.304 ± 0.006	1.6 ± 1.8	148 ± 5
HD021455	54031.856	8.112 ± 0.023	6.7 ± 1.0	0.654 ± 0.009	−13.0 ± 1.8	274 ± 11	0.320 ± 0.006	0.2 ± 1.7	152 ± 4
HD021551	53234.944	9.180 ± 0.014	8.5 ± 0.6	0.306 ± 0.007	−14.8 ± 3.5	320 ± 11	0.309 ± 0.008	1.9 ± 4.3	351 ± 10
HD021551	53238.964	9.142 ± 0.016	6.4 ± 0.7	0.340 ± 0.007	−17.3 ± 2.8	343 ± 8	0.342 ± 0.007	−3.9 ± 3.5	363 ± 8
HD021551	53684.828	8.984 ± 0.022	7.3 ± 1.0	0.338 ± 0.010	−11.5 ± 4.2	362 ± 12	0.321 ± 0.010	0.5 ± 5.5	375 ± 12
HD021551	53687.818	8.967 ± 0.012	4.3 ± 0.6	0.321 ± 0.007	−10.9 ± 3.0	342 ± 9	0.295 ± 0.007	−11.0 ± 4.0	336 ± 10
HD021551	54026.888	9.108 ± 0.014	7.4 ± 0.6	0.346 ± 0.007	−3.3 ± 2.8	344 ± 8	0.347 ± 0.007	−6.1 ± 3.5	375 ± 8
HD021551	54029.957	9.211 ± 0.017	7.7 ± 0.8	0.292 ± 0.007	−7.1 ± 3.4	334 ± 11	0.289 ± 0.007	−17.5 ± 4.3	336 ± 11
HD021551	54031.852	9.046 ± 0.021	10.4 ± 0.9	0.324 ± 0.007	−4.4 ± 3.2	338 ± 9	0.327 ± 0.007	−5.4 ± 3.9	366 ± 9
HD021641	53236.970	10.590 ± 0.021	−2.6 ± 0.9	0.269 ± 0.007	−5.3 ± 3.6	207 ± 11	0.349 ± 0.006	0.6 ± 1.8	158 ± 5
HD021641	53238.999	10.575 ± 0.017	5.6 ± 0.7	0.270 ± 0.006	−7.3 ± 3.1	215 ± 9	0.352 ± 0.005	−3.0 ± 1.5	160 ± 4
HD021641	53686.812	10.626 ± 0.014	−6.5 ± 0.6	0.273 ± 0.007	−8.1 ± 3.4	218 ± 10	0.346 ± 0.006	−1.0 ± 1.7	155 ± 5
HD021641	54026.911	10.536 ± 0.017	−0.7 ± 0.7	0.283 ± 0.007	2.2 ± 3.4	219 ± 10	0.349 ± 0.006	−0.7 ± 1.8	162 ± 5
HD021641	54029.980	10.897 ± 0.022	4.0 ± 1.0	0.269 ± 0.008	3.3 ± 3.9	203 ± 12	0.344 ± 0.007	0.2 ± 1.9	159 ± 5
HD021641	54031.924	10.738 ± 0.019	2.0 ± 0.8	0.281 ± 0.007	−1.9 ± 3.4	217 ± 10	0.327 ± 0.006	−1.6 ± 1.8	148 ± 6
HD021650	53236.982	6.138 ± 0.036	−12.9 ± 1.6	0.543 ± 0.008	−20.8 ± 2.4	381 ± 8	0.251 ± 0.008	−35.2 ± 5.1	247 ± 17
HD021650	53686.798	6.230 ± 0.027	−18.0 ± 1.2	0.563 ± 0.009	−17.9 ± 2.7	369 ± 9	0.295 ± 0.009	−28.2 ± 5.0	249 ± 16
HD021650	54026.897	6.327 ± 0.025	−17.0 ± 1.1	0.543 ± 0.009	−4.1 ± 2.6	363 ± 9	0.296 ± 0.008	−18.5 ± 4.8	267 ± 14
HD021650	54029.965	6.531 ± 0.022	−24.1 ± 1.0	0.501 ± 0.011	−14.7 ± 3.4	348 ± 12	0.256 ± 0.010	−39.8 ± 6.6	218 ± 25
HD022192	53234.951	3.823 ± 0.027	−9.7 ± 1.0	0.647 ± 0.020	−10.0 ± 5.5	355 ± 15	0.283 ± 0.020	−19.4 ± 12.5	261 ± 41
HD022192	53238.967	3.842 ± 0.029	−3.6 ± 1.0	0.656 ± 0.020	−6.0 ± 5.3	356 ± 14	0.288 ± 0.019	−27.4 ± 11.8	265 ± 39
HD022192	53684.757	3.801 ± 0.031	−7.6 ± 1.1	0.679 ± 0.019	−3.4 ± 4.8	352 ± 13	0.294 ± 0.018	−33.1 ± 10.9	215 ± 44
HD022192	53684.963	3.910 ± 0.027	−8.7 ± 1.0	0.672 ± 0.019	−4.8 ± 5.0	351 ± 14	0.277 ± 0.019	−28.9 ± 12.1	201 ± 52

Continued on Next Page...

Table C.2 – Continued

Star Name	HJD (−2400000)	W_λ (Hγ) (Å)	V_r (Hγ) (km s^{-1})	W_λ (He I) (Å)	V_r (He I) (km s^{-1})	FWSM (He I) (km s^{-1})	W_λ (Mg II) (Å)	V_r (Mg II) (km s^{-1})	FWSM (Mg II) (km s^{-1})
HD022192	53687.752	3.800 ± 0.030	-11.3 ± 1.1	0.670 ± 0.020	-10.3 ± 5.2	348 ± 15	0.276 ± 0.019	-31.4 ± 12.6	166 ± 66
HD022192	53687.922	3.896 ± 0.029	-11.1 ± 1.1	0.639 ± 0.020	-3.3 ± 5.5	337 ± 16	0.247 ± 0.019	-43.8 ± 14.0	109 ± 112
HD022192	54026.924	4.172 ± 0.031	-12.5 ± 1.1	0.678 ± 0.018	-9.3 ± 4.7	342 ± 13	0.275 ± 0.017	-32.8 ± 11.5	152 ± 66
HD022192	54030.824	4.291 ± 0.033	-14.4 ± 1.2	0.698 ± 0.019	-6.2 ± 4.8	352 ± 13	0.279 ± 0.018	-37.6 ± 11.9	161 ± 64
HD022192	54031.863	4.154 ± 0.036	-8.5 ± 1.3	0.649 ± 0.021	-5.1 ± 5.6	335 ± 16	0.250 ± 0.020	-51.1 ± 14.4	76 ± 164
HD022780	53233.949	8.246 ± 0.014	2.5 ± 0.6	0.568 ± 0.007	-29.6 ± 1.8	334 ± 4	0.296 ± 0.007	-15.0 ± 3.6	330 ± 8
HD022780	53237.977	8.298 ± 0.013	6.6 ± 0.6	0.602 ± 0.006	-25.8 ± 1.5	367 ± 4	0.329 ± 0.006	-10.8 ± 2.8	337 ± 6
HD022780	53684.834	8.305 ± 0.013	6.6 ± 0.6	0.606 ± 0.007	-15.4 ± 1.7	366 ± 5	0.336 ± 0.007	-14.7 ± 3.1	346 ± 7
HD022780	54027.844	8.299 ± 0.016	7.0 ± 0.7	0.607 ± 0.008	-20.7 ± 1.9	365 ± 6	0.326 ± 0.008	-16.4 ± 3.6	338 ± 8
HD022780	54030.002	8.383 ± 0.017	10.8 ± 0.8	0.573 ± 0.009	-14.2 ± 2.2	358 ± 7	0.315 ± 0.008	-19.9 ± 4.2	332 ± 9
HD022780	54031.865	8.265 ± 0.019	4.7 ± 0.9	0.594 ± 0.007	-16.9 ± 1.7	362 ± 5	0.321 ± 0.007	-17.8 ± 3.2	341 ± 7
HD023016	53234.959	8.395 ± 0.015	23.3 ± 0.7	0.305 ± 0.008	0.1 ± 4.1	291 ± 12	0.311 ± 0.008	9.3 ± 4.0	316 ± 9
HD023016	53238.971	8.294 ± 0.016	17.1 ± 0.7	0.328 ± 0.007	0.4 ± 3.2	312 ± 9	0.322 ± 0.007	2.2 ± 3.2	305 ± 8
HD023016	53684.839	8.460 ± 0.018	13.7 ± 0.8	0.332 ± 0.007	-1.3 ± 3.3	319 ± 9	0.325 ± 0.007	10.6 ± 3.3	323 ± 8
HD023016	54027.850	8.380 ± 0.020	18.2 ± 0.9	0.312 ± 0.007	6.2 ± 3.8	307 ± 10	0.313 ± 0.007	5.2 ± 3.7	308 ± 9
HD023016	54029.996	8.408 ± 0.018	21.4 ± 0.8	0.303 ± 0.009	9.8 ± 4.7	299 ± 13	0.302 ± 0.009	5.4 ± 4.7	307 ± 11
HD023016	54031.870	8.379 ± 0.025	21.0 ± 1.1	0.332 ± 0.009	0.0 ± 4.0	318 ± 11	0.331 ± 0.008	3.5 ± 4.0	319 ± 9
HD023302	53236.991	6.770 ± 0.016	8.6 ± 0.7	0.505 ± 0.008	-5.5 ± 2.2	261 ± 7	0.298 ± 0.006	10.4 ± 2.6	196 ± 7
HD023302	53238.979	6.732 ± 0.017	9.4 ± 0.7	0.515 ± 0.007	-7.6 ± 2.0	267 ± 6	0.317 ± 0.006	3.5 ± 2.3	208 ± 6
HD023302	53684.842	6.725 ± 0.014	7.6 ± 0.6	0.529 ± 0.008	-5.3 ± 2.2	275 ± 6	0.301 ± 0.007	7.3 ± 2.7	203 ± 8
HD023302	54027.856	6.788 ± 0.016	4.1 ± 0.6	0.523 ± 0.007	-6.0 ± 2.0	267 ± 6	0.298 ± 0.006	-0.5 ± 2.6	193 ± 7
HD023302	54028.927	6.892 ± 0.017	7.6 ± 0.7	0.511 ± 0.008	-9.0 ± 2.3	263 ± 6	0.286 ± 0.007	0.2 ± 2.9	181 ± 9
HD023302	54030.827	6.890 ± 0.017	6.1 ± 0.7	0.528 ± 0.007	-4.8 ± 2.0	265 ± 6	0.295 ± 0.006	-0.6 ± 2.5	191 ± 7
HD023302	54031.874	6.903 ± 0.018	4.4 ± 0.7	0.527 ± 0.008	-6.0 ± 2.3	268 ± 7	0.304 ± 0.007	2.7 ± 2.9	196 ± 8
HD023478	53236.995	6.001 ± 0.025	14.9 ± 1.0	1.203 ± 0.010	-15.3 ± 1.7	504 ± 8	0.313 ± 0.006	3.6 ± 1.9	181 ± 5
HD023478	53684.848	6.035 ± 0.026	21.9 ± 1.1	1.565 ± 0.012	-25.0 ± 1.7	531 ± 7	0.355 ± 0.007	4.4 ± 2.1	192 ± 5
HD023478	54027.861	6.062 ± 0.026	20.7 ± 1.1	1.241 ± 0.010	-28.6 ± 1.7	524 ± 8	0.316 ± 0.006	7.2 ± 2.0	190 ± 5
HD023478	54030.832	6.202 ± 0.025	23.8 ± 1.0	1.143 ± 0.008	-21.9 ± 1.6	516 ± 7	0.297 ± 0.005	2.4 ± 1.7	184 ± 4
HD023478	54031.933	6.078 ± 0.030	31.2 ± 1.2	1.089 ± 0.010	-20.3 ± 2.0	496 ± 10	0.290 ± 0.006	7.8 ± 2.1	185 ± 5
HD023480	53233.940	6.271 ± 0.011	17.6 ± 0.5	0.523 ± 0.007	-8.0 ± 2.4	318 ± 10	0.302 ± 0.005	6.7 ± 2.2	276 ± 5
HD023480	53237.008	6.231 ± 0.016	21.3 ± 0.7	0.532 ± 0.008	-9.1 ± 2.8	343 ± 11	0.312 ± 0.006	7.3 ± 2.6	280 ± 5
HD023480	53238.980	6.269 ± 0.015	16.5 ± 0.7	0.537 ± 0.008	-14.5 ± 2.8	345 ± 11	0.314 ± 0.006	-4.3 ± 2.6	278 ± 6
HD023480	53684.761	6.305 ± 0.012	21.8 ± 0.5	0.559 ± 0.007	-9.8 ± 2.3	356 ± 9	0.302 ± 0.005	3.1 ± 2.4	280 ± 5
HD023480	53684.967	6.406 ± 0.014	18.1 ± 0.6	0.539 ± 0.007	-5.8 ± 2.4	341 ± 10	0.313 ± 0.005	8.0 ± 2.2	282 ± 5
HD023480	54027.858	6.496 ± 0.016	20.7 ± 0.7	0.555 ± 0.008	-8.0 ± 2.8	352 ± 11	0.314 ± 0.006	4.4 ± 2.7	281 ± 6
HD023480	54028.925	6.476 ± 0.018	17.2 ± 0.8	0.542 ± 0.008	-12.1 ± 2.8	343 ± 11	0.289 ± 0.006	4.0 ± 2.8	265 ± 6
HD023480	54030.829	6.515 ± 0.015	19.3 ± 0.7	0.556 ± 0.008	-12.9 ± 2.8	352 ± 11	0.302 ± 0.006	3.5 ± 2.8	273 ± 6
HD023480	54031.875	6.386 ± 0.019	21.6 ± 0.9	0.551 ± 0.009	-11.5 ± 3.0	338 ± 12	0.302 ± 0.007	-3.0 ± 2.9	269 ± 7
HD023552	53237.981	7.071 ± 0.018	-24.5 ± 0.8	0.511 ± 0.008	-20.4 ± 2.9	320 ± 13	0.276 ± 0.006	-20.4 ± 2.9	247 ± 7
HD023552	53684.855	7.104 ± 0.018	-15.3 ± 0.8	0.558 ± 0.007	-14.1 ± 2.4	342 ± 10	0.301 ± 0.006	-10.7 ± 2.5	257 ± 6
HD023552	54027.872	7.183 ± 0.018	-22.1 ± 0.8	0.508 ± 0.009	-18.2 ± 3.2	298 ± 15	0.270 ± 0.007	-19.8 ± 3.2	258 ± 8
HD023552	54030.845	7.234 ± 0.017	-25.6 ± 0.8	0.546 ± 0.009	-19.5 ± 3.1	333 ± 13	0.277 ± 0.007	-26.0 ± 3.3	248 ± 8
HD023552	54031.876	7.171 ± 0.020	-16.9 ± 0.9	0.540 ± 0.008	-14.0 ± 2.7	332 ± 11	0.278 ± 0.006	-18.9 ± 2.9	249 ± 7
HD023630	53234.969	5.891 ± 0.016	6.8 ± 0.6	0.343 ± 0.007	6.6 ± 2.6	220 ± 10	0.323 ± 0.006	6.9 ± 2.4	202 ± 7
HD023630	53234.971	5.815 ± 0.014	5.2 ± 0.5	0.337 ± 0.008	6.2 ± 2.8	214 ± 11	0.311 ± 0.007	8.2 ± 2.7	199 ± 8
HD023630	53238.974	5.746 ± 0.012	5.4 ± 0.5	0.342 ± 0.006	8.2 ± 2.0	213 ± 8	0.325 ± 0.005	3.7 ± 1.9	203 ± 5
HD023630	53686.843	5.818 ± 0.016	2.6 ± 0.6	0.343 ± 0.007	8.5 ± 2.5	230 ± 9	0.311 ± 0.006	10.2 ± 2.4	190 ± 7
HD023630	54027.882	6.027 ± 0.016	1.2 ± 0.6	0.356 ± 0.007	8.4 ± 2.3	232 ± 8	0.326 ± 0.006	3.4 ± 2.2	204 ± 6
HD023630	54030.871	6.012 ± 0.017	2.2 ± 0.7	0.353 ± 0.006	11.6 ± 2.2	216 ± 8	0.309 ± 0.006	0.9 ± 2.2	197 ± 6
HD023630	54031.886	6.015 ± 0.017	3.2 ± 0.6	0.354 ± 0.006	9.0 ± 2.2	217 ± 9	0.316 ± 0.006	2.0 ± 2.2	195 ± 6

Continued on Next Page...

Table C.2 – Continued

Star Name	HJD (−2400000)	W_λ (Hγ) (Å)	V_r (Hγ) (km s^{-1})	W_λ (He I) (Å)	V_r (He I) (km s^{-1})	FWSM (He I) (km s^{-1})	W_λ (Mg II) (Å)	V_r (Mg II) (km s^{-1})	FWSM (Mg II) (km s^{-1})
HD023800	53237.991	3.374 ± 0.022	74.3 ± 0.9	0.869 ± 0.010	−38.0 ± 1.6	265 ± 16	0.155 ± 0.009	−67.3 ± 6.7	···
HD023800	53684.863	3.133 ± 0.021	40.0 ± 0.8	0.902 ± 0.011	−45.0 ± 1.7	302 ± 15	0.189 ± 0.010	−57.5 ± 6.1	197 ± 19
HD023800	54027.888	3.356 ± 0.019	68.3 ± 0.8	0.863 ± 0.012	−22.5 ± 2.0	262 ± 21	0.153 ± 0.011	−29.8 ± 8.5	94 ± 103
HD023800	54030.853	3.496 ± 0.017	62.4 ± 0.7	0.919 ± 0.011	−28.9 ± 1.6	306 ± 15	0.174 ± 0.009	−46.6 ± 6.5	195 ± 21
HD023800	54031.940	3.554 ± 0.023	72.9 ± 0.9	0.905 ± 0.011	−22.8 ± 1.6	287 ± 16	0.160 ± 0.009	−45.4 ± 7.0	100 ± 44
HD023862	53234.967	6.375 ± 0.017	7.8 ± 0.6	0.351 ± 0.008	9.5 ± 3.5	309 ± 10	0.275 ± 0.008	3.7 ± 4.8	360 ± 11
HD023862	53238.976	6.227 ± 0.017	6.2 ± 0.7	0.372 ± 0.007	5.5 ± 2.7	332 ± 7	0.299 ± 0.007	−0.7 ± 3.6	362 ± 8
HD023862	53686.845	6.094 ± 0.025	6.7 ± 1.0	0.361 ± 0.009	−15.9 ± 4.1	340 ± 9	0.318 ± 0.009	8.4 ± 4.9	327 ± 11
HD023862	54027.884	6.931 ± 0.029	−13.9 ± 1.2	0.521 ± 0.011	−69.6 ± 3.2	320 ± 8	0.318 ± 0.012	−22.4 ± 6.5	109 ± 49
HD023862	54031.887	7.083 ± 0.023	−14.1 ± 0.9	0.525 ± 0.008	−71.4 ± 2.5	315 ± 6	0.301 ± 0.010	−27.5 ± 5.6	69 ± 67
HD024479	53237.000	10.801 ± 0.028	3.2 ± 1.3	0.201 ± 0.011	−34.3 ± 4.7	203 ± 40	0.334 ± 0.008	1.3 ± 2.0	110 ± 6
HD024479	53238.987	10.851 ± 0.023	6.8 ± 1.0	0.200 ± 0.010	−31.0 ± 4.4	198 ± 38	0.324 ± 0.008	−1.9 ± 1.9	104 ± 6
HD024479	53686.847	10.804 ± 0.024	1.0 ± 1.1	0.224 ± 0.010	−32.8 ± 3.7	229 ± 28	0.353 ± 0.007	0.0 ± 1.6	112 ± 5
HD024479	54027.904	10.770 ± 0.027	0.5 ± 1.2	0.200 ± 0.011	−35.1 ± 4.7	212 ± 38	0.333 ± 0.008	−2.4 ± 1.9	105 ± 7
HD024479	54028.916	10.918 ± 0.022	5.6 ± 1.0	0.230 ± 0.010	−34.2 ± 3.8	220 ± 30	0.338 ± 0.008	−1.2 ± 1.8	107 ± 6
HD024479	54030.893	10.893 ± 0.029	4.6 ± 1.3	0.211 ± 0.010	−24.7 ± 3.9	198 ± 34	0.329 ± 0.007	−2.2 ± 1.7	102 ± 6
HD024479	54031.896	10.895 ± 0.027	4.9 ± 1.2	0.202 ± 0.010	−18.8 ± 4.4	185 ± 40	0.321 ± 0.008	−2.5 ± 1.9	95 ± 7
HD024534	53238.002	0.533 ± 0.018	−17.0 ± 0.4	0.439 ± 0.013	−48.4 ± 6.0	362 ± 31	−0.091 ± 0.010	···	···
HD024534	53684.872	0.133 ± 0.023	−31.4 ± 0.5	0.397 ± 0.012	−48.0 ± 6.0	436 ± 26	−0.114 ± 0.009	···	···
HD024534	53687.867	0.215 ± 0.028	−31.2 ± 0.6	0.359 ± 0.013	−64.3 ± 8.0	408 ± 21	−0.125 ± 0.011	···	···
HD024534	54031.890	−0.171 ± 0.025	−24.3 ± 0.6	0.119 ± 0.012	−120.6 ± 25.2	247 ± 127	−0.296 ± 0.010	···	···
HD025799	53238.011	6.146 ± 0.014	44.6 ± 0.6	1.363 ± 0.006	6.4 ± 0.8	388 ± 3	0.231 ± 0.005	13.5 ± 2.7	279 ± 5
HD025799	53684.880	6.128 ± 0.020	31.0 ± 0.9	1.389 ± 0.007	3.7 ± 1.0	389 ± 3	0.249 ± 0.006	0.2 ± 3.0	280 ± 6
HD025799	53688.859	6.156 ± 0.020	38.0 ± 0.9	1.420 ± 0.007	3.7 ± 1.0	399 ± 3	0.243 ± 0.006	7.3 ± 3.2	280 ± 7
HD025799	54026.931	6.280 ± 0.021	32.2 ± 0.9	1.412 ± 0.009	−0.4 ± 1.3	394 ± 4	0.259 ± 0.007	0.3 ± 3.8	272 ± 9
HD025799	54030.902	6.303 ± 0.019	40.0 ± 0.9	1.394 ± 0.007	7.6 ± 1.0	391 ± 3	0.262 ± 0.006	4.1 ± 2.8	282 ± 6
HD025799	54031.914	6.385 ± 0.025	27.1 ± 1.1	1.402 ± 0.008	−2.2 ± 1.1	392 ± 4	0.257 ± 0.006	−11.6 ± 3.3	271 ± 7
HD025940	53237.002	4.816 ± 0.028	2.0 ± 1.1	0.779 ± 0.012	5.9 ± 3.2	305 ± 9	0.272 ± 0.011	−0.7 ± 5.2	269 ± 12
HD025940	53238.989	4.802 ± 0.026	1.8 ± 1.1	0.776 ± 0.012	5.2 ± 3.2	302 ± 10	0.286 ± 0.011	−8.1 ± 5.0	259 ± 12
HD025940	53686.850	4.690 ± 0.028	0.5 ± 1.1	0.785 ± 0.011	7.6 ± 2.8	306 ± 8	0.282 ± 0.010	−1.2 ± 4.5	268 ± 10
HD025940	53687.905	4.852 ± 0.027	−3.5 ± 1.1	0.787 ± 0.013	6.2 ± 3.4	301 ± 10	0.275 ± 0.012	−3.8 ± 5.6	261 ± 13
HD025940	54026.942	5.094 ± 0.026	−2.8 ± 1.1	0.800 ± 0.013	10.8 ± 3.3	307 ± 10	0.286 ± 0.012	−7.7 ± 5.3	278 ± 12
HD025940	54027.913	5.019 ± 0.028	−4.6 ± 1.1	0.779 ± 0.012	6.6 ± 3.2	304 ± 9	0.271 ± 0.011	−5.3 ± 5.3	268 ± 12
HD025940	54031.902	5.083 ± 0.027	−6.5 ± 1.1	0.776 ± 0.014	4.1 ± 3.6	303 ± 11	0.270 ± 0.012	−7.7 ± 5.9	260 ± 14
HD026670	53237.005	7.871 ± 0.021	9.6 ± 0.9	0.761 ± 0.008	−18.1 ± 1.5	394 ± 7	0.322 ± 0.007	−11.4 ± 3.5	354 ± 7
HD026670	53238.992	7.981 ± 0.016	4.8 ± 0.7	0.752 ± 0.007	−20.0 ± 1.5	382 ± 7	0.318 ± 0.007	−15.0 ± 3.5	337 ± 8
HD026670	53686.853	7.966 ± 0.015	4.1 ± 0.7	0.782 ± 0.007	−17.9 ± 1.3	388 ± 6	0.324 ± 0.006	−13.7 ± 3.0	342 ± 7
HD026670	53688.865	7.868 ± 0.017	0.5 ± 0.8	0.742 ± 0.007	−21.7 ± 1.5	392 ± 6	0.288 ± 0.007	−12.1 ± 3.7	347 ± 8
HD026670	54026.945	7.916 ± 0.016	7.7 ± 0.7	0.763 ± 0.007	−20.2 ± 1.4	387 ± 6	0.334 ± 0.006	−21.1 ± 3.1	338 ± 7
HD026670	54027.915	7.945 ± 0.019	5.0 ± 0.8	0.759 ± 0.007	−20.4 ± 1.5	390 ± 6	0.326 ± 0.007	−10.4 ± 3.4	346 ± 7
HD026670	54030.006	8.206 ± 0.017	7.3 ± 0.8	0.744 ± 0.008	−18.2 ± 1.8	385 ± 8	0.297 ± 0.008	−21.7 ± 4.2	335 ± 10
HD026670	54031.902	8.017 ± 0.019	8.1 ± 0.8	0.748 ± 0.007	−20.7 ± 1.5	383 ± 7	0.309 ± 0.007	−15.7 ± 3.5	345 ± 8
HD029866	53239.004	6.233 ± 0.024	10.6 ± 1.1	0.424 ± 0.012	−14.1 ± 4.3	342 ± 17	0.305 ± 0.012	−14.8 ± 6.1	288 ± 17
HD029866	53684.888	6.106 ± 0.026	11.3 ± 1.2	0.448 ± 0.012	−8.3 ± 4.1	347 ± 16	0.326 ± 0.012	6.4 ± 5.8	318 ± 13
HD029866	53687.874	6.098 ± 0.021	5.3 ± 1.0	0.448 ± 0.011	−14.3 ± 3.8	356 ± 14	0.319 ± 0.011	0.1 ± 5.5	296 ± 15
HD029866	54026.953	6.304 ± 0.025	16.1 ± 1.2	0.473 ± 0.010	−9.6 ± 3.2	356 ± 12	0.336 ± 0.010	−3.4 ± 4.7	319 ± 11
HD029866	54030.014	6.215 ± 0.023	12.0 ± 1.1	0.409 ± 0.013	−10.1 ± 4.9	344 ± 19	0.290 ± 0.013	−2.7 ± 7.0	297 ± 19
HD029866	54031.907	6.102 ± 0.026	6.1 ± 1.2	0.435 ± 0.011	−8.6 ± 3.9	348 ± 15	0.319 ± 0.011	−1.7 ± 5.4	305 ± 14
HD032343	53686.862	5.408 ± 0.023	−21.4 ± 1.0	1.056 ± 0.011	−26.0 ± 1.9	307 ± 5	0.179 ± 0.007	−14.2 ± 2.5	113 ± 7
HD032343	53687.907	5.343 ± 0.024	−20.4 ± 1.0	1.064 ± 0.011	−21.9 ± 1.9	306 ± 5	0.169 ± 0.007	−12.3 ± 2.6	111 ± 7

Continued on Next Page...

Table C.2 – Continued

Star Name	HJD (−2400000)	W_λ (Hγ) (Å)	V_r (Hγ) (km s^{-1})	W_λ (He I) (Å)	V_r (He I) (km s^{-1})	FWSM (He I) (km s^{-1})	W_λ (Mg II) (Å)	V_r (Mg II) (km s^{-1})	FWSM (Mg II) (km s^{-1})
HD032343	54026.964	5.685 ± 0.020	−15.9 ± 0.9	1.080 ± 0.010	−22.4 ± 1.6	310 ± 4	0.193 ± 0.006	−7.6 ± 2.1	112 ± 5
HD032343	54027.921	5.661 ± 0.024	−17.4 ± 1.0	1.045 ± 0.010	−21.2 ± 1.7	304 ± 4	0.180 ± 0.006	−8.1 ± 2.2	107 ± 6
HD032343	54030.915	5.759 ± 0.019	−19.2 ± 0.8	1.087 ± 0.010	−19.6 ± 1.7	313 ± 4	0.191 ± 0.007	−9.4 ± 2.2	116 ± 6
HD032343	54031.949	5.647 ± 0.024	−14.0 ± 1.0	1.068 ± 0.010	−20.0 ± 1.7	310 ± 4	0.191 ± 0.007	−6.0 ± 2.2	119 ± 5
HD036576	53686.866	1.956 ± 0.031	49.0 ± 1.3	0.878 ± 0.011	26.5 ± 2.5	342 ± 12	0.019 ± 0.010	···	···
HD036576	53687.913	1.907 ± 0.026	50.2 ± 1.1	0.832 ± 0.012	24.3 ± 2.9	348 ± 13	−0.021 ± 0.011	···	···
HD036576	54026.971	2.058 ± 0.023	57.3 ± 0.9	0.869 ± 0.009	2.1 ± 2.0	329 ± 10	0.052 ± 0.008	···	···
HD036576	54028.928	2.298 ± 0.027	60.5 ± 1.1	0.890 ± 0.009	16.6 ± 1.9	341 ± 9	0.041 ± 0.008	···	···
HD036576	54031.953	2.131 ± 0.024	68.5 ± 1.0	0.901 ± 0.010	7.6 ± 2.1	362 ± 9	0.067 ± 0.008	···	···
HD037202	53684.896	3.449 ± 0.028	79.8 ± 1.0	1.215 ± 0.007	4.3 ± 1.2	361 ± 4	0.268 ± 0.006	−42.1 ± 3.5	158 ± 16
HD037202	53687.884	3.472 ± 0.030	99.1 ± 1.1	1.171 ± 0.010	−2.1 ± 1.7	334 ± 7	0.284 ± 0.008	−40.4 ± 4.8	183 ± 20
HD037202	54027.010	3.427 ± 0.038	80.9 ± 1.4	1.204 ± 0.010	5.9 ± 1.6	330 ± 7	0.332 ± 0.012	−7.2 ± 4.9	198 ± 16
HD037202	54027.953	3.292 ± 0.041	61.7 ± 1.5	1.262 ± 0.009	3.1 ± 1.4	360 ± 7	0.359 ± 0.011	−12.4 ± 5.4	216 ± 20
HD037202	54030.951	3.317 ± 0.039	63.7 ± 1.4	1.303 ± 0.012	−2.4 ± 1.7	350 ± 9	0.316 ± 0.011	−12.7 ± 6.0	156 ± 31
HD037202	54031.973	3.103 ± 0.033	91.5 ± 1.2	1.196 ± 0.008	−0.2 ± 1.3	321 ± 7	0.301 ± 0.008	−19.3 ± 4.6	120 ± 31
HD041335	53686.910	2.276 ± 0.033	39.3 ± 1.3	0.864 ± 0.010	37.2 ± 2.4	453 ± 6	0.147 ± 0.008	−33.5 ± 6.8	267 ± 16
HD041335	53687.917	2.165 ± 0.030	45.1 ± 1.2	0.804 ± 0.010	44.9 ± 2.7	441 ± 7	0.143 ± 0.008	−36.9 ± 7.3	247 ± 19
HD041335	54027.956	2.738 ± 0.033	38.6 ± 1.3	0.837 ± 0.010	39.9 ± 2.6	457 ± 6	0.158 ± 0.008	−26.2 ± 6.4	278 ± 15
HD041335	54028.943	2.785 ± 0.031	30.7 ± 1.2	0.879 ± 0.009	39.1 ± 2.3	457 ± 5	0.151 ± 0.007	−27.2 ± 6.5	275 ± 15
HD041335	54030.942	2.797 ± 0.030	54.4 ± 1.1	0.854 ± 0.011	41.5 ± 2.6	446 ± 7	0.144 ± 0.008	−35.3 ± 7.8	264 ± 19
HD041335	54031.975	2.979 ± 0.033	32.0 ± 1.3	0.832 ± 0.011	44.2 ± 2.9	440 ± 7	0.141 ± 0.008	−34.4 ± 8.0	266 ± 19
HD058715	53684.971	9.157 ± 0.017	2.3 ± 0.8	0.261 ± 0.005	17.7 ± 2.7	275 ± 8	0.362 ± 0.005	10.6 ± 2.0	280 ± 5
HD058715	53688.024	9.294 ± 0.017	1.3 ± 0.8	0.242 ± 0.006	23.2 ± 3.8	244 ± 13	0.334 ± 0.006	9.1 ± 2.8	270 ± 7
HD058715	53688.992	9.157 ± 0.016	−2.7 ± 0.7	0.247 ± 0.006	22.1 ± 3.3	264 ± 10	0.345 ± 0.005	8.4 ± 2.4	269 ± 6
HD058715	54027.035	9.283 ± 0.015	1.8 ± 0.7	0.267 ± 0.005	19.8 ± 2.9	265 ± 9	0.350 ± 0.005	9.6 ± 2.3	276 ± 6
HD058715	54028.981	9.526 ± 0.016	1.5 ± 0.7	0.247 ± 0.007	23.3 ± 4.3	249 ± 14	0.325 ± 0.007	8.9 ± 3.3	262 ± 9
HD058715	54030.976	9.489 ± 0.016	2.1 ± 0.7	0.256 ± 0.005	23.1 ± 2.7	246 ± 9	0.345 ± 0.004	5.6 ± 2.0	277 ± 5
HD058715	54031.990	9.469 ± 0.017	5.6 ± 0.8	0.249 ± 0.006	27.0 ± 3.2	247 ± 11	0.348 ± 0.005	6.7 ± 2.3	278 ± 6
HD058978	53684.967	2.171 ± 0.032	128.9 ± 1.2	0.707 ± 0.016	−31.6 ± 4.8	392 ± 21	0.070 ± 0.012	···	···
HD058978	53687.924	2.088 ± 0.030	130.2 ± 1.1	0.710 ± 0.014	−17.3 ± 3.8	400 ± 16	0.049 ± 0.010	···	···
HD058978	53688.988	2.074 ± 0.031	120.7 ± 1.2	0.695 ± 0.015	−9.4 ± 4.2	389 ± 18	0.046 ± 0.011	···	···
HD058978	54027.968	2.450 ± 0.034	99.9 ± 1.3	0.742 ± 0.013	21.7 ± 4.4	398 ± 13	0.019 ± 0.009	···	···
HD058978	54028.973	2.523 ± 0.033	105.1 ± 1.2	0.719 ± 0.013	21.5 ± 4.7	395 ± 14	0.016 ± 0.009	···	···
HD058978	54030.969	2.301 ± 0.034	92.3 ± 1.3	0.716 ± 0.016	26.7 ± 5.5	390 ± 13	−0.004 ± 0.011	···	···
HD058978	54031.986	2.267 ± 0.033	92.4 ± 1.2	0.656 ± 0.015	25.9 ± 5.7	393 ± 14	−0.013 ± 0.011	···	···
HD060855	53684.973	2.252 ± 0.028	46.0 ± 1.1	1.043 ± 0.011	21.9 ± 1.9	361 ± 8	0.171 ± 0.009	30.6 ± 7.4	286 ± 15
HD060855	53688.994	2.280 ± 0.025	33.1 ± 1.0	1.008 ± 0.011	14.4 ± 2.1	349 ± 9	0.152 ± 0.010	18.5 ± 8.9	271 ± 19
HD060855	54028.983	2.535 ± 0.031	42.3 ± 1.2	1.036 ± 0.012	5.3 ± 2.1	334 ± 9	0.168 ± 0.010	−1.7 ± 8.2	213 ± 26
HD060855	54030.978	2.471 ± 0.022	37.9 ± 0.9	1.025 ± 0.011	4.7 ± 1.9	341 ± 8	0.180 ± 0.009	−7.4 ± 6.8	238 ± 19
HD060855	54031.991	2.502 ± 0.028	40.3 ± 1.1	1.026 ± 0.012	0.1 ± 2.1	344 ± 9	0.150 ± 0.010	−9.2 ± 8.9	221 ± 27
HD149757	54031.544	2.882 ± 0.040	32.4 ± 1.4	0.925 ± 0.018	−19.9 ± 3.6	458 ± 11	0.134 ± 0.014	−42.8 ± 13.5	231 ± 38
HD149757	54031.545	2.992 ± 0.030	23.4 ± 1.0	0.908 ± 0.011	−19.2 ± 2.4	451 ± 7	0.102 ± 0.009	−43.6 ± 11.5	253 ± 29
HD162428	53234.651	7.157 ± 0.018	−13.3 ± 0.8	0.610 ± 0.010	−45.6 ± 2.4	373 ± 13	0.307 ± 0.010	−32.3 ± 4.5	319 ± 10
HD162428	53237.629	7.091 ± 0.018	−13.9 ± 0.8	0.607 ± 0.007	−42.4 ± 1.6	387 ± 8	0.298 ± 0.006	−42.1 ± 3.1	311 ± 7
HD162428	54028.572	7.286 ± 0.020	−41.2 ± 0.9	0.515 ± 0.007	−21.0 ± 2.0	340 ± 12	0.288 ± 0.007	−47.9 ± 3.3	275 ± 9
HD162732	53234.704	8.133 ± 0.052	−11.8 ± 1.8	0.964 ± 0.011	−72.4 ± 2.4	354 ± 6	0.458 ± 0.013	−24.0 ± 5.7	197 ± 26
HD162732	53237.640	8.139 ± 0.067	−10.6 ± 2.3	0.983 ± 0.010	−70.6 ± 2.1	365 ± 5	0.476 ± 0.014	−25.1 ± 5.9	201 ± 26
HD162732	53688.548	7.842 ± 0.055	−4.2 ± 1.9	0.947 ± 0.008	−61.0 ± 1.6	370 ± 4	0.513 ± 0.008	−11.1 ± 2.8	234 ± 10
HD162732	54027.570	7.534 ± 0.061	−9.1 ± 2.1	0.848 ± 0.006	−59.5 ± 1.5	364 ± 3	0.454 ± 0.006	−22.2 ± 2.6	206 ± 11
HD164284	53234.641	4.620 ± 0.018	20.9 ± 0.8	1.204 ± 0.010	−33.8 ± 1.3	422 ± 8	0.250 ± 0.008	−44.6 ± 6.4	328 ± 18

Continued on Next Page...

Table C.2 – Continued

Star Name	HJD (−2400000)	W_λ (Hγ) (Å)	V_r (Hγ) (km s^{-1})	W_λ (He I) (Å)	V_r (He I) (km s^{-1})	FWSM (He I) (km s^{-1})	W_λ (Mg II) (Å)	V_r (Mg II) (km s^{-1})	FWSM (Mg II) (km s^{-1})
HD164284	53237.620	4.598 ± 0.018	24.8 ± 0.8	1.190 ± 0.007	−28.5 ± 1.0	426 ± 6	0.265 ± 0.006	−39.5 ± 4.6	329 ± 12
HD164284	53684.544	4.598 ± 0.019	12.7 ± 0.8	1.182 ± 0.008	−34.3 ± 1.1	427 ± 7	0.263 ± 0.007	−43.8 ± 5.4	335 ± 14
HD164284	54027.582	4.648 ± 0.019	22.2 ± 0.9	1.132 ± 0.008	−31.2 ± 1.2	394 ± 8	0.238 ± 0.007	−40.1 ± 5.9	291 ± 18
HD164284	54030.570	4.793 ± 0.018	13.7 ± 0.8	1.139 ± 0.009	−36.7 ± 1.2	413 ± 8	0.245 ± 0.008	−53.9 ± 6.1	313 ± 17
HD164447	53234.716	7.084 ± 0.016	−42.6 ± 0.7	0.497 ± 0.010	−59.7 ± 3.7	300 ± 11	0.325 ± 0.007	−47.1 ± 1.9	208 ± 4
HD164447	53237.649	7.125 ± 0.014	−41.2 ± 0.6	0.457 ± 0.008	−60.7 ± 3.1	285 ± 10	0.318 ± 0.005	−48.0 ± 1.5	206 ± 3
HD164447	53686.545	7.109 ± 0.018	−36.9 ± 0.8	0.503 ± 0.009	−59.7 ± 3.4	327 ± 9	0.332 ± 0.007	−49.5 ± 1.7	213 ± 3
HD164447	54028.586	7.205 ± 0.016	−42.2 ± 0.7	0.457 ± 0.009	−59.3 ± 3.7	282 ± 12	0.315 ± 0.007	−49.1 ± 1.8	202 ± 4
HD164447	54030.574	7.328 ± 0.019	−34.6 ± 0.9	0.478 ± 0.009	−61.7 ± 3.6	287 ± 11	0.331 ± 0.007	−47.6 ± 1.7	204 ± 3
HD166014	53234.698	10.220 ± 0.023	−14.3 ± 1.1	0.097 ± 0.010	···	···	0.311 ± 0.007	−27.2 ± 2.4	186 ± 6
HD166014	53237.653	10.307 ± 0.023	−11.0 ± 1.1	0.098 ± 0.012	···	···	0.307 ± 0.009	−27.0 ± 3.1	180 ± 9
HD166014	53238.616	10.227 ± 0.021	−13.7 ± 1.0	0.098 ± 0.015	···	···	0.319 ± 0.011	−33.0 ± 3.6	194 ± 10
HD166014	53683.573	10.378 ± 0.029	−14.1 ± 1.3	0.156 ± 0.017	···	···	0.342 ± 0.013	−23.1 ± 3.9	185 ± 11
HD166014	54027.587	10.300 ± 0.014	−14.2 ± 0.6	0.092 ± 0.012	···	···	0.312 ± 0.009	−27.3 ± 3.0	187 ± 8
HD166014	54030.583	10.252 ± 0.014	−10.6 ± 0.6	0.108 ± 0.013	···	···	0.307 ± 0.010	−30.6 ± 3.3	179 ± 10
HD166014	54031.552	10.186 ± 0.014	−13.4 ± 0.6	0.068 ± 0.012	···	···	0.282 ± 0.009	−29.9 ± 3.3	157 ± 11
HD168797	53234.725	4.999 ± 0.016	−7.6 ± 0.6	1.091 ± 0.009	−49.0 ± 1.1	382 ± 10	0.269 ± 0.008	−49.8 ± 3.9	324 ± 8
HD168797	53237.658	4.955 ± 0.015	0.5 ± 0.6	1.136 ± 0.008	−38.2 ± 0.9	395 ± 8	0.311 ± 0.007	−40.3 ± 3.0	337 ± 6
HD168797	53686.549	4.785 ± 0.020	−7.9 ± 0.8	1.123 ± 0.009	−46.2 ± 1.0	370 ± 10	0.301 ± 0.008	−53.9 ± 3.5	306 ± 8
HD168797	54027.590	5.095 ± 0.016	−12.0 ± 0.6	1.105 ± 0.007	−39.9 ± 0.8	384 ± 7	0.290 ± 0.006	−48.4 ± 2.8	337 ± 6
HD168797	54031.558	5.030 ± 0.020	−15.0 ± 0.8	1.090 ± 0.007	−40.2 ± 0.9	383 ± 8	0.255 ± 0.006	−46.3 ± 3.4	313 ± 7
HD168957	53235.715	6.789 ± 0.019	−26.2 ± 0.8	1.072 ± 0.008	−37.9 ± 1.4	271 ± 4	0.307 ± 0.005	−26.9 ± 0.9	73 ± 3
HD168957	53238.624	6.763 ± 0.016	−21.7 ± 0.6	1.083 ± 0.009	−40.5 ± 1.5	280 ± 4	0.308 ± 0.005	−31.5 ± 1.1	68 ± 4
HD168957	53687.546	6.896 ± 0.016	−26.4 ± 0.6	1.073 ± 0.006	−38.3 ± 1.1	276 ± 3	0.305 ± 0.004	−29.0 ± 0.8	71 ± 3
HD168957	54029.600	7.005 ± 0.019	−27.0 ± 0.8	1.084 ± 0.009	−38.5 ± 1.5	283 ± 4	0.300 ± 0.005	−29.1 ± 1.1	69 ± 4
HD171406	53235.727	7.533 ± 0.023	−4.6 ± 1.0	0.862 ± 0.009	−27.7 ± 1.9	359 ± 4	0.333 ± 0.008	−25.7 ± 3.5	291 ± 8
HD171406	53238.635	7.417 ± 0.022	−7.4 ± 1.0	0.819 ± 0.008	−31.6 ± 1.7	366 ± 4	0.310 ± 0.007	−30.4 ± 3.2	303 ± 7
HD171406	53687.561	6.621 ± 0.025	−22.2 ± 1.1	0.800 ± 0.009	−23.5 ± 2.1	349 ± 5	0.265 ± 0.008	−23.4 ± 4.5	200 ± 15
HD171406	54028.596	7.276 ± 0.015	−9.0 ± 0.7	0.801 ± 0.007	−28.4 ± 1.7	354 ± 4	0.285 ± 0.007	−20.5 ± 3.3	273 ± 8
HD171780	53234.732	6.947 ± 0.017	−1.2 ± 0.8	0.882 ± 0.011	−38.1 ± 1.8	377 ± 11	0.322 ± 0.010	−23.3 ± 5.0	329 ± 11
HD171780	53237.663	6.962 ± 0.013	−0.5 ± 0.6	0.881 ± 0.008	−39.5 ± 1.3	389 ± 7	0.324 ± 0.007	−34.5 ± 3.5	326 ± 8
HD171780	53686.555	7.252 ± 0.014	−11.3 ± 0.6	0.890 ± 0.007	−44.8 ± 1.2	386 ± 7	0.316 ± 0.007	−41.2 ± 3.3	310 ± 8
HD171780	54028.605	7.299 ± 0.017	−11.0 ± 0.8	0.887 ± 0.007	−44.1 ± 1.1	389 ± 6	0.313 ± 0.006	−39.3 ± 3.1	311 ± 7
HD173370	53234.739	8.099 ± 0.016	7.7 ± 0.7	0.224 ± 0.010	−24.4 ± 6.0	250 ± 37	0.293 ± 0.009	−2.6 ± 5.3	293 ± 15
HD173370	53237.670	7.970 ± 0.015	10.1 ± 0.7	0.247 ± 0.008	−15.4 ± 4.2	297 ± 22	0.334 ± 0.007	−10.5 ± 3.7	309 ± 10
HD173370	53683.579	8.098 ± 0.038	6.2 ± 1.7	0.234 ± 0.017	−29.3 ± 10.2	322 ± 49	0.315 ± 0.017	−0.2 ± 9.1	304 ± 25
HD173370	54027.599	8.107 ± 0.014	5.8 ± 0.6	0.217 ± 0.009	−19.5 ± 5.8	261 ± 35	0.315 ± 0.009	−11.1 ± 4.8	299 ± 13
HD173370	54030.585	8.049 ± 0.022	7.2 ± 1.0	0.239 ± 0.009	−26.5 ± 5.4	275 ± 31	0.314 ± 0.009	−13.8 ± 4.9	301 ± 13
HD174237	53235.734	4.519 ± 0.025	66.6 ± 1.0	1.060 ± 0.009	12.8 ± 1.6	238 ± 5	0.178 ± 0.009	32.9 ± 5.0	···
HD174237	53238.640	4.734 ± 0.022	−9.6 ± 0.9	1.079 ± 0.010	−37.3 ± 2.0	210 ± 9	0.165 ± 0.009	−9.2 ± 7.2	···
HD174237	53684.552	4.875 ± 0.024	64.6 ± 1.0	1.052 ± 0.010	6.1 ± 1.4	260 ± 5	0.176 ± 0.010	4.7 ± 6.5	···
HD174237	54028.613	5.766 ± 0.021	−6.2 ± 0.9	1.180 ± 0.008	−26.1 ± 1.2	301 ± 3	0.234 ± 0.007	−6.4 ± 4.1	195 ± 13
HD174237	54031.568	5.469 ± 0.020	6.9 ± 0.8	1.139 ± 0.008	−6.3 ± 1.1	297 ± 3	0.220 ± 0.007	−4.8 ± 4.2	166 ± 16
HD174638	53234.695	1.618 ± 0.034	−143.4 ± 0.8	0.303 ± 0.023	−187.0 ± 16.7	···	0.698 ± 0.019	14.8 ± 3.2	···
HD174638	53234.696	1.712 ± 0.024	−143.8 ± 0.6	0.337 ± 0.018	−187.2 ± 11.9	···	0.725 ± 0.019	10.9 ± 3.0	···
HD174638	53237.671	2.143 ± 0.021	−247.2 ± 0.6	−0.054 ± 0.012	···	···	0.260 ± 0.011	−209.5 ± 12.5	···
HD174638	53238.662	1.778 ± 0.024	−257.0 ± 0.7	−0.426 ± 0.014	···	···	0.169 ± 0.012	−267.2 ± 24.8	···
HD174638	53683.577	1.314 ± 0.030	209.1 ± 0.9	−0.758 ± 0.016	···	···	0.382 ± 0.009	141.1 ± 1.5	81 ± 8
HD174638	54027.605	1.922 ± 0.021	−242.1 ± 0.6	−0.271 ± 0.013	···	···	0.338 ± 0.007	−188.4 ± 2.0	96 ± 8
HD174638	54028.620	1.736 ± 0.025	−236.0 ± 0.7	−0.730 ± 0.016	···	···	0.256 ± 0.009	−161.8 ± 2.4	···

Continued on Next Page...

Table C.2 – Continued

Star Name	HJD (−2400000)	W_λ (Hγ) (Å)	V_r (Hγ) (km s^{-1})	W_λ (He I) (Å)	V_r (He I) (km s^{-1})	FWSM (He I) (km s^{-1})	W_λ (Mg II) (Å)	V_r (Mg II) (km s^{-1})	FWSM (Mg II) (km s^{-1})
HD174638	54030.590	2.118 ± 0.035	−82.7 ± 0.7	−1.539 ± 0.009	···	···	0.501 ± 0.010	−32.0 ± 2.1	···
HD174638	54031.555	1.533 ± 0.035	−2.0 ± 0.6	−1.448 ± 0.021	···	···	0.503 ± 0.011	50.5 ± 1.0	39 ± 8
HD175863	53235.744	4.923 ± 0.022	−11.2 ± 0.9	0.791 ± 0.009	−35.0 ± 1.8	282 ± 8	0.278 ± 0.007	−17.2 ± 2.8	192 ± 7
HD175863	53238.667	4.819 ± 0.016	−16.1 ± 0.7	0.780 ± 0.008	−35.8 ± 1.7	296 ± 7	0.283 ± 0.007	−22.8 ± 2.4	202 ± 6
HD175863	53688.562	5.130 ± 0.017	−9.1 ± 0.7	0.781 ± 0.008	−31.9 ± 1.6	296 ± 7	0.286 ± 0.006	−15.2 ± 2.4	189 ± 6
HD175863	54028.623	5.349 ± 0.019	−23.0 ± 0.8	0.781 ± 0.007	−32.7 ± 1.3	294 ± 6	0.296 ± 0.005	−22.0 ± 1.9	202 ± 4
HD175869	53234.744	7.349 ± 0.016	−4.4 ± 0.7	0.277 ± 0.009	−13.2 ± 4.0	184 ± 29	0.306 ± 0.007	−9.3 ± 2.7	182 ± 8
HD175869	53237.675	7.223 ± 0.015	−6.0 ± 0.6	0.277 ± 0.009	−6.6 ± 4.0	227 ± 23	0.323 ± 0.007	−8.5 ± 2.6	191 ± 7
HD175869	53684.554	7.489 ± 0.017	−12.5 ± 0.7	0.280 ± 0.011	−1.2 ± 4.8	202 ± 31	0.341 ± 0.009	−6.8 ± 3.0	193 ± 8
HD175869	54029.613	7.503 ± 0.016	−7.4 ± 0.6	0.265 ± 0.010	−6.6 ± 4.6	212 ± 29	0.299 ± 0.008	−10.4 ± 3.1	177 ± 10
HD175869	54031.574	7.448 ± 0.016	−7.9 ± 0.7	0.249 ± 0.010	2.7 ± 5.1	91 ± 75	0.307 ± 0.008	−15.9 ± 3.2	178 ± 10
HD177648	53237.683	4.079 ± 0.022	6.2 ± 1.0	1.089 ± 0.010	−46.0 ± 1.6	348 ± 4	0.187 ± 0.008	−47.5 ± 5.2	182 ± 17
HD177648	53687.573	3.905 ± 0.021	10.8 ± 0.9	1.055 ± 0.009	−20.9 ± 1.5	355 ± 6	0.207 ± 0.007	−19.2 ± 4.2	249 ± 10
HD177648	54028.636	4.431 ± 0.025	13.0 ± 1.1	1.095 ± 0.009	−21.6 ± 1.5	386 ± 6	0.236 ± 0.007	−20.0 ± 3.8	299 ± 7
HD178475	53234.746	5.716 ± 0.016	17.7 ± 0.7	0.637 ± 0.015	−44.7 ± 4.2	339 ± 20	0.349 ± 0.013	−35.4 ± 5.6	270 ± 15
HD178475	53237.706	5.699 ± 0.022	5.4 ± 1.0	0.649 ± 0.009	−52.8 ± 2.5	351 ± 6	0.341 ± 0.008	−27.6 ± 3.3	281 ± 13
HD178475	53686.560	6.101 ± 0.016	−16.5 ± 0.7	0.696 ± 0.006	−37.6 ± 1.5	341 ± 7	0.315 ± 0.005	−34.0 ± 2.4	289 ± 6
HD178475	54027.608	6.342 ± 0.015	−10.9 ± 0.7	0.671 ± 0.007	−42.1 ± 1.9	342 ± 8	0.298 ± 0.006	−33.3 ± 3.1	301 ± 7
HD178475	54031.580	6.261 ± 0.017	−12.2 ± 0.8	0.682 ± 0.006	−39.2 ± 1.7	344 ± 7	0.300 ± 0.006	−36.3 ± 2.8	298 ± 6
HD179343	53237.699	7.028 ± 0.033	−7.0 ± 1.1	0.518 ± 0.012	−85.2 ± 4.6	339 ± 13	0.363 ± 0.011	−10.9 ± 5.5	274 ± 17
HD179343	53684.560	7.100 ± 0.035	−7.5 ± 1.2	0.529 ± 0.010	−80.9 ± 3.9	334 ± 11	0.361 ± 0.011	−9.1 ± 5.4	274 ± 17
HD179343	54029.619	6.872 ± 0.031	−6.0 ± 1.1	0.455 ± 0.011	−99.2 ± 5.4	297 ± 19	0.306 ± 0.010	−23.5 ± 6.1	231 ± 23
HD181409	53235.756	4.369 ± 0.014	77.8 ± 0.6	1.348 ± 0.010	1.8 ± 1.4	334 ± 7	0.170 ± 0.007	7.6 ± 4.7	150 ± 17
HD181409	53238.679	4.388 ± 0.017	77.1 ± 0.7	1.354 ± 0.010	−1.4 ± 1.4	345 ± 7	0.164 ± 0.007	4.0 ± 5.1	145 ± 19
HD181409	53238.685	4.376 ± 0.017	78.7 ± 0.7	1.363 ± 0.012	−2.6 ± 1.6	345 ± 8	0.161 ± 0.008	0.7 ± 6.0	136 ± 24
HD181409	53687.585	4.491 ± 0.015	64.9 ± 0.6	1.362 ± 0.013	−8.2 ± 1.7	343 ± 9	0.173 ± 0.008	−1.3 ± 5.9	140 ± 23
HD181409	54028.655	4.720 ± 0.016	77.9 ± 0.6	1.352 ± 0.011	−1.7 ± 1.5	340 ± 7	0.163 ± 0.007	1.2 ± 5.2	138 ± 21
HD181615	54031.584	3.988 ± 0.218	···	1.147 ± 0.062	−20.5 ± 11.6	276 ± 40	0.751 ± 0.040	−25.7 ± 2.5	76 ± 113
HD183362	53235.762	2.982 ± 0.016	−46.2 ± 0.6	0.965 ± 0.012	−37.8 ± 2.3	329 ± 11	0.163 ± 0.011	−52.8 ± 11.4	72 ± 124
HD183362	53687.594	3.344 ± 0.016	−38.4 ± 0.6	1.023 ± 0.012	−30.5 ± 1.8	327 ± 8	0.170 ± 0.010	−36.3 ± 9.9	60 ± 123
HD183362	54029.634	3.416 ± 0.020	−35.1 ± 0.8	0.932 ± 0.011	−32.9 ± 2.0	321 ± 8	0.126 ± 0.010	−33.9 ± 11.1	80 ± 95
HD183656	53234.753	6.384 ± 0.019	−21.9 ± 0.7	0.718 ± 0.007	−47.9 ± 1.9	362 ± 10	0.356 ± 0.007	−27.9 ± 3.1	267 ± 9
HD183656	53237.712	6.167 ± 0.022	−19.6 ± 0.8	0.757 ± 0.008	−54.3 ± 2.0	383 ± 10	0.435 ± 0.008	−27.3 ± 3.0	301 ± 8
HD183656	53686.564	5.950 ± 0.026	−20.1 ± 0.9	0.755 ± 0.007	−45.0 ± 1.7	378 ± 9	0.398 ± 0.007	−29.5 ± 2.8	285 ± 8
HD183656	54029.641	6.150 ± 0.032	−3.3 ± 1.1	0.760 ± 0.009	−62.5 ± 2.4	332 ± 14	0.387 ± 0.009	−14.1 ± 3.6	210 ± 13
HD183914	53234.759	9.028 ± 0.015	−21.8 ± 0.7	0.342 ± 0.008	−16.5 ± 3.4	275 ± 14	0.327 ± 0.008	−20.7 ± 2.7	281 ± 12
HD183914	53237.715	9.007 ± 0.016	−23.9 ± 0.7	0.332 ± 0.007	−9.4 ± 2.9	291 ± 11	0.323 ± 0.006	−29.8 ± 2.3	282 ± 10
HD183914	53684.568	9.235 ± 0.015	−24.5 ± 0.7	0.337 ± 0.007	−5.6 ± 3.1	290 ± 12	0.353 ± 0.007	−22.1 ± 2.2	301 ± 9
HD183914	54027.621	9.364 ± 0.017	−25.3 ± 0.8	0.324 ± 0.005	−10.0 ± 2.2	277 ± 8	0.329 ± 0.005	−27.9 ± 1.6	287 ± 7
HD183914	54031.591	9.296 ± 0.015	−24.1 ± 0.7	0.338 ± 0.005	−9.0 ± 2.1	277 ± 8	0.320 ± 0.005	−33.6 ± 1.6	282 ± 7
HD184279	53237.724	3.150 ± 0.060	79.0 ± 2.0	1.362 ± 0.016	−34.3 ± 2.7	301 ± 9	0.147 ± 0.012	−36.3 ± 14.0	···
HD184279	53688.570	3.969 ± 0.068	57.0 ± 2.3	1.467 ± 0.019	−36.0 ± 3.1	295 ± 11	0.150 ± 0.014	−55.2 ± 18.0	···
HD184279	54029.648	4.329 ± 0.061	61.4 ± 2.1	1.413 ± 0.019	−40.0 ± 3.3	291 ± 12	0.102 ± 0.014	−90.9 ± 31.5	···
HD185037	53234.763	8.579 ± 0.017	−25.9 ± 0.8	0.281 ± 0.008	−8.4 ± 3.3	275 ± 19	0.353 ± 0.008	−28.5 ± 3.0	324 ± 11
HD185037	53237.731	8.552 ± 0.015	−27.4 ± 0.7	0.274 ± 0.006	−9.6 ± 2.7	305 ± 14	0.360 ± 0.006	−23.9 ± 2.4	332 ± 8
HD185037	53684.575	8.546 ± 0.020	−28.3 ± 0.9	0.293 ± 0.007	−8.3 ± 2.9	320 ± 14	0.363 ± 0.007	−31.1 ± 2.7	336 ± 9
HD185037	54029.662	8.854 ± 0.018	−28.9 ± 0.8	0.294 ± 0.007	−6.9 ± 2.8	300 ± 15	0.367 ± 0.007	−39.9 ± 2.7	340 ± 5
HD185037	54031.596	8.700 ± 0.030	−30.6 ± 1.4	0.288 ± 0.005	−6.4 ± 2.2	303 ± 11	0.346 ± 0.005	−33.1 ± 2.2	321 ± 5
HD187567	53235.771	2.702 ± 0.026	4.9 ± 1.0	1.014 ± 0.011	−21.2 ± 2.1	343 ± 8	0.127 ± 0.009	−34.2 ± 9.1	···
HD187567	53238.693	2.600 ± 0.023	1.8 ± 0.9	0.993 ± 0.013	−26.5 ± 2.5	350 ± 10	0.172 ± 0.010	−51.4 ± 7.8	102 ± 49

Continued on Next Page...

Table C.2 – Continued

Star Name	HJD (−2400000)	W_λ (Hγ) (Å)	V_r (Hγ) (km s^{-1})	W_λ (He I) (Å)	V_r (He I) (km s^{-1})	FWSM (He I) (km s^{-1})	W_λ (Mg II) (Å)	V_r (Mg II) (km s^{-1})	FWSM (Mg II) (km s^{-1})
HD187567	53686.569	2.737 ± 0.026	−1.9 ± 1.0	1.026 ± 0.013	−15.5 ± 2.4	354 ± 9	0.159 ± 0.010	−10.8 ± 8.3	187 ± 28
HD187567	54029.671	3.200 ± 0.024	−20.9 ± 0.9	0.964 ± 0.014	−32.0 ± 2.7	356 ± 7	0.138 ± 0.011	−65.7 ± 10.2	138 ± 47
HD187811	53234.768	4.597 ± 0.015	−8.0 ± 0.7	1.023 ± 0.008	−37.3 ± 1.3	350 ± 6	0.222 ± 0.007	−63.6 ± 4.1	180 ± 15
HD187811	53237.736	5.057 ± 0.014	−19.3 ± 0.6	1.067 ± 0.007	−39.6 ± 1.1	370 ± 5	0.227 ± 0.006	−47.2 ± 3.6	202 ± 12
HD187811	53684.578	5.626 ± 0.018	−14.9 ± 0.8	1.157 ± 0.008	−35.5 ± 1.2	379 ± 5	0.263 ± 0.007	−28.7 ± 3.5	264 ± 9
HD187811	54027.626	6.210 ± 0.015	−12.5 ± 0.7	1.120 ± 0.006	−40.1 ± 0.9	369 ± 4	0.277 ± 0.005	−34.4 ± 2.4	273 ± 6
HD187811	54031.603	6.144 ± 0.019	−14.8 ± 0.8	1.142 ± 0.007	−37.9 ± 1.0	372 ± 4	0.268 ± 0.006	−36.3 ± 3.0	272 ± 7
HD187851	53236.774	3.939 ± 0.026	31.1 ± 1.0	1.078 ± 0.011	−18.3 ± 1.7	428 ± 11	0.200 ± 0.009	−30.1 ± 9.6	227 ± 42
HD187851	53688.586	4.209 ± 0.023	33.9 ± 0.9	1.085 ± 0.010	−22.3 ± 1.6	437 ± 10	0.185 ± 0.008	−57.1 ± 9.6	194 ± 50
HD187851	54028.665	4.163 ± 0.027	36.5 ± 1.0	1.056 ± 0.012	−9.1 ± 2.0	426 ± 13	0.198 ± 0.010	−7.0 ± 11.1	337 ± 33
HD189687	53234.771	4.542 ± 0.020	−3.3 ± 0.7	1.147 ± 0.009	−31.8 ± 1.5	348 ± 6	0.210 ± 0.007	−25.5 ± 4.6	232 ± 12
HD189687	53237.737	4.622 ± 0.016	0.1 ± 0.6	1.164 ± 0.007	−31.5 ± 1.2	368 ± 4	0.216 ± 0.006	−27.0 ± 3.7	245 ± 9
HD189687	53684.581	4.776 ± 0.020	9.6 ± 0.8	1.193 ± 0.008	−15.9 ± 1.3	376 ± 4	0.248 ± 0.006	−7.5 ± 3.3	264 ± 8
HD189687	54027.631	4.894 ± 0.018	6.9 ± 0.7	1.148 ± 0.005	−22.7 ± 0.9	363 ± 3	0.217 ± 0.004	−11.1 ± 2.5	267 ± 6
HD189687	54031.608	4.869 ± 0.016	4.5 ± 0.6	1.151 ± 0.007	−20.1 ± 1.2	369 ± 4	0.212 ± 0.006	−17.9 ± 3.5	260 ± 8
HD191610	53233.802	3.982 ± 0.018	3.4 ± 0.8	1.158 ± 0.007	−35.6 ± 1.0	407 ± 6	0.262 ± 0.007	−29.9 ± 4.2	356 ± 9
HD191610	53237.740	4.063 ± 0.017	3.2 ± 0.7	1.150 ± 0.007	−46.4 ± 1.0	427 ± 6	0.263 ± 0.006	−35.4 ± 4.1	356 ± 9
HD191610	53684.584	3.981 ± 0.019	5.8 ± 0.8	1.180 ± 0.008	−31.7 ± 1.1	420 ± 7	0.276 ± 0.007	−37.8 ± 4.5	328 ± 11
HD191610	54031.613	4.605 ± 0.015	−5.0 ± 0.6	1.174 ± 0.005	−44.9 ± 0.7	438 ± 4	0.289 ± 0.005	−45.9 ± 2.7	368 ± 6
HD192044	53234.776	6.338 ± 0.018	−33.7 ± 0.8	0.416 ± 0.008	−13.7 ± 2.7	277 ± 11	0.296 ± 0.007	−24.9 ± 2.9	287 ± 11
HD192044	53237.759	6.374 ± 0.011	−35.4 ± 0.5	0.421 ± 0.008	−7.3 ± 2.7	295 ± 10	0.313 ± 0.007	−25.7 ± 2.7	288 ± 10
HD192044	53686.576	6.449 ± 0.020	−38.4 ± 0.9	0.430 ± 0.007	−9.3 ± 2.3	298 ± 9	0.316 ± 0.006	−28.8 ± 2.4	289 ± 9
HD192044	54027.635	6.668 ± 0.015	−36.8 ± 0.7	0.410 ± 0.007	−11.6 ± 2.4	294 ± 9	0.295 ± 0.006	−25.8 ± 2.5	293 ± 9
HD192044	54031.617	6.681 ± 0.021	−39.8 ± 1.0	0.430 ± 0.007	−11.9 ± 2.3	300 ± 9	0.284 ± 0.006	−33.6 ± 2.7	282 ± 6
HD192445	53233.818	2.904 ± 0.024	−1.0 ± 1.0	1.186 ± 0.012	−23.8 ± 2.0	387 ± 7	0.115 ± 0.010	−93.6 ± 11.3	···
HD192445	53238.703	2.916 ± 0.021	−3.9 ± 0.8	1.192 ± 0.013	−25.7 ± 2.1	386 ± 7	0.125 ± 0.011	−69.6 ± 10.9	149 ± 47
HD192445	53687.615	2.922 ± 0.015	−11.9 ± 0.6	1.157 ± 0.012	−22.6 ± 2.0	386 ± 7	0.137 ± 0.010	−64.8 ± 9.0	224 ± 26
HD192445	54029.683	3.368 ± 0.020	−27.7 ± 0.8	1.084 ± 0.013	−20.0 ± 2.3	370 ± 8	0.099 ± 0.010	···	···
HD192685	53234.780	5.523 ± 0.018	9.9 ± 0.7	1.205 ± 0.009	−20.8 ± 1.5	349 ± 6	0.261 ± 0.008	−20.4 ± 3.8	242 ± 10
HD192685	53237.762	5.603 ± 0.019	9.2 ± 0.8	1.182 ± 0.008	−19.9 ± 1.2	366 ± 4	0.255 ± 0.006	−15.2 ± 3.1	241 ± 8
HD192685	53684.586	5.058 ± 0.020	−4.1 ± 0.8	1.180 ± 0.008	−27.2 ± 1.3	368 ± 5	0.208 ± 0.007	−24.8 ± 4.1	201 ± 13
HD192685	54027.642	5.755 ± 0.014	11.8 ± 0.6	1.186 ± 0.006	−16.5 ± 0.9	360 ± 3	0.251 ± 0.005	−12.6 ± 2.4	264 ± 5
HD192685	54030.594	5.725 ± 0.012	9.9 ± 0.5	1.238 ± 0.007	−13.5 ± 1.1	372 ± 4	0.267 ± 0.005	−15.5 ± 2.7	264 ± 6
HD193009	53234.793	1.475 ± 0.028	2.0 ± 1.2	0.822 ± 0.017	−39.5 ± 4.0	332 ± 11	0.028 ± 0.014	···	···
HD193009	53238.717	1.461 ± 0.035	54.7 ± 1.5	0.844 ± 0.018	−17.2 ± 4.1	324 ± 18	0.055 ± 0.015	···	···
HD193009	53687.630	1.531 ± 0.038	28.9 ± 1.6	0.823 ± 0.014	−21.9 ± 3.2	321 ± 14	0.079 ± 0.011	···	···
HD193009	54027.646	1.929 ± 0.041	−14.5 ± 1.7	0.767 ± 0.018	−26.0 ± 4.6	307 ± 21	−0.009 ± 0.015	···	···
HD193182	53234.805	8.194 ± 0.100	−10.5 ± 3.3	1.034 ± 0.025	−99.4 ± 6.1	327 ± 20	0.434 ± 0.019	−43.3 ± 7.9	···
HD193182	53238.727	8.215 ± 0.077	−9.8 ± 2.5	1.092 ± 0.028	−98.8 ± 6.3	347 ± 20	0.481 ± 0.022	−47.1 ± 8.4	95 ± 75
HD193182	53687.646	8.362 ± 0.100	−13.2 ± 3.3	1.098 ± 0.018	−97.5 ± 4.1	335 ± 13	0.489 ± 0.017	−47.8 ± 6.4	104 ± 52
HD193182	54029.697	8.062 ± 0.101	−7.5 ± 3.3	1.031 ± 0.018	−101.6 ± 4.4	319 ± 15	0.469 ± 0.017	−45.5 ± 6.4	112 ± 48
HD193911	53234.783	5.682 ± 0.018	−8.6 ± 0.7	0.387 ± 0.007	−7.9 ± 1.9	202 ± 13	0.282 ± 0.006	−4.8 ± 2.1	206 ± 6
HD193911	53238.733	5.857 ± 0.018	−11.4 ± 0.7	0.402 ± 0.006	−7.8 ± 1.6	222 ± 9	0.305 ± 0.005	−14.6 ± 1.6	216 ± 5
HD193911	53684.589	5.805 ± 0.017	−7.6 ± 0.7	0.412 ± 0.007	1.3 ± 1.9	224 ± 11	0.297 ± 0.006	−7.9 ± 2.1	213 ± 6
HD193911	54026.622	6.033 ± 0.020	−8.3 ± 0.8	0.397 ± 0.006	0.0 ± 1.7	221 ± 10	0.280 ± 0.006	−8.2 ± 1.9	214 ± 6
HD193911	54027.661	5.932 ± 0.015	−8.6 ± 0.6	0.391 ± 0.006	−1.7 ± 1.6	222 ± 10	0.289 ± 0.005	−6.3 ± 1.7	214 ± 5
HD193911	54031.634	6.077 ± 0.016	−8.1 ± 0.7	0.384 ± 0.005	2.3 ± 1.5	211 ± 9	0.283 ± 0.005	−10.6 ± 1.6	206 ± 5
HD194244	53235.778	9.857 ± 0.019	−9.1 ± 0.9	0.161 ± 0.014	−56.8 ± 15.6	···	0.346 ± 0.010	−24.0 ± 3.9	215 ± 11
HD194244	53238.738	9.788 ± 0.022	−10.1 ± 1.0	0.165 ± 0.013	−44.0 ± 14.9	211 ± 68	0.368 ± 0.010	−25.0 ± 3.6	231 ± 10
HD194244	53686.587	9.906 ± 0.020	−12.7 ± 0.9	0.141 ± 0.014	−53.4 ± 18.1	···	0.361 ± 0.010	−29.1 ± 3.8	230 ± 10

Continued on Next Page...

Table C.2 – Continued

Star Name	HJD (−2400000)	W_λ (Hγ) (Å)	V_r (Hγ) (km s^{-1})	W_λ (He I) (Å)	V_r (He I) (km s^{-1})	FWSM (He I) (km s^{-1})	W_λ (Mg II) (Å)	V_r (Mg II) (km s^{-1})	FWSM (Mg II) (km s^{-1})
HD194244	54027.673	9.894 ± 0.019	−11.9 ± 0.8	0.140 ± 0.012	−16.4 ± 15.9	···	0.337 ± 0.009	−25.1 ± 3.6	209 ± 11
HD194244	54031.646	9.839 ± 0.021	−8.9 ± 0.9	0.130 ± 0.013	−51.0 ± 18.6	···	0.311 ± 0.010	−25.6 ± 4.2	208 ± 13
HD194335	53234.813	3.316 ± 0.022	−3.3 ± 1.0	1.149 ± 0.011	−59.9 ± 1.5	426 ± 12	0.082 ± 0.008	···	···
HD194335	53238.741	3.489 ± 0.021	−6.7 ± 0.9	1.193 ± 0.010	−59.8 ± 1.4	442 ± 10	0.095 ± 0.008	···	···
HD194335	53686.582	3.736 ± 0.019	23.0 ± 0.9	1.253 ± 0.007	−39.3 ± 0.9	454 ± 7	0.141 ± 0.006	−87.5 ± 5.1	262 ± 12
HD194335	54027.667	3.709 ± 0.021	12.3 ± 0.9	1.198 ± 0.009	−48.0 ± 1.2	451 ± 9	0.113 ± 0.007	−102.1 ± 7.7	192 ± 25
HD194335	54031.640	3.872 ± 0.017	8.5 ± 0.7	1.223 ± 0.009	−56.2 ± 1.1	456 ± 8	0.110 ± 0.007	−120.4 ± 7.6	173 ± 28
HD194883	53235.785	3.863 ± 0.023	−23.1 ± 0.9	0.862 ± 0.011	−24.9 ± 2.1	297 ± 5	0.144 ± 0.010	−20.9 ± 8.0	117 ± 67
HD194883	53688.606	3.927 ± 0.026	−28.9 ± 1.1	0.854 ± 0.011	−28.3 ± 2.2	315 ± 5	0.115 ± 0.010	−92.8 ± 10.5	···
HD194883	54028.685	4.218 ± 0.023	−34.1 ± 1.0	0.847 ± 0.012	−24.9 ± 2.4	302 ± 6	0.131 ± 0.011	−22.8 ± 9.9	118 ± 82
HD195325	53234.821	9.162 ± 0.025	−6.0 ± 0.9	0.334 ± 0.011	−130.8 ± 7.3	251 ± 29	0.306 ± 0.012	−9.0 ± 7.0	257 ± 24
HD195325	53238.747	9.194 ± 0.024	−10.3 ± 0.9	0.362 ± 0.009	−119.5 ± 5.5	296 ± 18	0.353 ± 0.009	−18.5 ± 4.7	301 ± 14
HD195325	53687.652	9.035 ± 0.023	−9.6 ± 0.8	0.322 ± 0.010	−124.0 ± 6.4	270 ± 23	0.320 ± 0.011	−21.0 ± 6.5	277 ± 22
HD195325	54027.689	9.000 ± 0.025	−10.1 ± 0.9	0.286 ± 0.010	−126.2 ± 7.3	270 ± 27	0.297 ± 0.010	−8.9 ± 6.2	265 ± 21
HD195325	54031.661	9.112 ± 0.023	−8.6 ± 0.9	0.291 ± 0.009	−124.5 ± 6.6	265 ± 25	0.281 ± 0.011	−24.6 ± 7.6	243 ± 29
HD195554	53235.797	9.694 ± 0.019	−19.0 ± 0.8	0.240 ± 0.009	−36.7 ± 4.9	262 ± 13	0.355 ± 0.008	−23.9 ± 2.4	252 ± 9
HD195554	53238.749	9.899 ± 0.020	−20.5 ± 0.9	0.230 ± 0.009	−48.0 ± 5.3	273 ± 13	0.348 ± 0.008	−31.2 ± 2.6	244 ± 6
HD195554	53684.613	9.839 ± 0.018	−25.0 ± 0.8	0.222 ± 0.010	−31.4 ± 5.9	248 ± 16	0.319 ± 0.009	−27.9 ± 3.1	236 ± 13
HD195554	54027.681	9.756 ± 0.019	−18.5 ± 0.9	0.205 ± 0.009	−31.6 ± 6.1	256 ± 16	0.332 ± 0.008	−31.7 ± 2.8	243 ± 6
HD195554	54031.655	9.865 ± 0.020	−19.3 ± 0.9	0.200 ± 0.008	−41.6 ± 5.5	239 ± 16	0.317 ± 0.007	−25.7 ± 2.6	225 ± 11
HD197419	53235.804	5.390 ± 0.025	0.2 ± 1.0	1.312 ± 0.011	−29.5 ± 1.5	342 ± 8	0.187 ± 0.006	−9.6 ± 2.0	111 ± 5
HD197419	53238.756	5.449 ± 0.023	−1.5 ± 0.9	1.334 ± 0.009	−32.7 ± 1.3	354 ± 7	0.193 ± 0.005	−10.2 ± 1.7	109 ± 5
HD197419	53686.595	5.412 ± 0.023	−9.3 ± 0.9	1.290 ± 0.009	−36.4 ± 1.3	354 ± 7	0.162 ± 0.005	−11.8 ± 1.9	88 ± 7
HD197419	54028.701	5.701 ± 0.018	−8.8 ± 0.7	1.325 ± 0.007	−36.7 ± 1.0	348 ± 5	0.221 ± 0.004	−9.1 ± 1.2	121 ± 3
HD198183	53234.825	7.191 ± 0.017	−16.5 ± 0.8	0.756 ± 0.009	−39.1 ± 2.4	294 ± 7	0.315 ± 0.007	−25.6 ± 1.9	186 ± 9
HD198183	53237.763	7.140 ± 0.015	−14.6 ± 0.7	0.734 ± 0.008	−37.0 ± 2.2	294 ± 7	0.294 ± 0.006	−27.4 ± 1.8	174 ± 9
HD198183	53684.616	7.161 ± 0.015	−19.5 ± 0.7	0.746 ± 0.007	−34.4 ± 1.9	304 ± 6	0.306 ± 0.005	−25.6 ± 1.5	187 ± 7
HD198183	54026.612	6.971 ± 0.016	−16.6 ± 0.7	0.755 ± 0.007	−36.2 ± 1.9	306 ± 6	0.302 ± 0.005	−28.9 ± 1.5	188 ± 7
HD198183	54030.598	7.115 ± 0.018	−10.8 ± 0.8	0.761 ± 0.006	−31.3 ± 1.6	297 ± 5	0.314 ± 0.005	−26.2 ± 1.2	179 ± 6
HD198183	54031.669	7.224 ± 0.015	−12.3 ± 0.7	0.724 ± 0.008	−37.2 ± 2.1	287 ± 6	0.305 ± 0.006	−27.2 ± 1.6	188 ± 7
HD198625	53235.810	5.275 ± 0.020	−8.1 ± 0.7	1.000 ± 0.009	−30.8 ± 1.4	403 ± 6	0.299 ± 0.008	−11.0 ± 4.7	368 ± 11
HD198625	53238.761	5.270 ± 0.018	−11.3 ± 0.7	0.979 ± 0.009	−41.7 ± 1.5	403 ± 7	0.274 ± 0.009	−37.7 ± 5.6	322 ± 15
HD198625	53686.603	5.653 ± 0.020	−6.4 ± 0.8	0.987 ± 0.007	−33.4 ± 1.1	404 ± 5	0.275 ± 0.006	−23.6 ± 4.1	351 ± 10
HD198625	54027.698	5.950 ± 0.021	1.1 ± 0.8	0.968 ± 0.007	−22.8 ± 1.2	404 ± 5	0.299 ± 0.006	−24.3 ± 3.9	353 ± 9
HD199218	53234.832	6.001 ± 0.019	−21.0 ± 0.9	0.480 ± 0.013	−38.8 ± 4.0	358 ± 21	0.292 ± 0.012	−27.3 ± 6.9	301 ± 19
HD199218	53237.813	6.099 ± 0.022	−12.2 ± 1.0	0.472 ± 0.010	−36.4 ± 3.2	375 ± 16	0.318 ± 0.009	−22.2 ± 5.0	332 ± 12
HD199218	53688.634	6.112 ± 0.021	−21.2 ± 0.9	0.473 ± 0.011	−36.9 ± 3.4	377 ± 17	0.287 ± 0.010	−34.7 ± 5.9	274 ± 17
HD199218	54030.601	6.135 ± 0.021	−19.8 ± 0.9	0.492 ± 0.010	−37.2 ± 3.1	378 ± 15	0.303 ± 0.010	−31.5 ± 5.3	312 ± 14
HD199356	53236.798	1.575 ± 0.023	5.1 ± 0.9	0.587 ± 0.025	21.4 ± 8.3	381 ± 65	−0.002 ± 0.018	···	···
HD199356	53688.647	1.535 ± 0.026	−2.0 ± 1.0	0.590 ± 0.028	24.2 ± 9.2	348 ± 80	−0.037 ± 0.020	···	···
HD199356	54030.612	2.086 ± 0.021	−20.6 ± 0.8	0.578 ± 0.025	−12.7 ± 8.5	401 ± 63	−0.025 ± 0.018	···	···
HD200120	53234.836	2.643 ± 0.027	30.1 ± 1.0	0.500 ± 0.016	−9.6 ± 6.8	393 ± 38	0.016 ± 0.011	···	···
HD200120	53237.765	2.657 ± 0.027	26.7 ± 1.0	0.487 ± 0.014	−4.8 ± 6.0	378 ± 35	0.013 ± 0.010	···	···
HD200120	53684.619	2.178 ± 0.024	36.1 ± 0.9	0.475 ± 0.014	6.3 ± 6.2	437 ± 31	−0.015 ± 0.010	···	···
HD200120	54026.607	2.375 ± 0.026	21.9 ± 1.0	0.442 ± 0.014	19.5 ± 6.6	453 ± 32	−0.048 ± 0.010	···	···
HD200120	54031.680	2.252 ± 0.027	16.9 ± 1.0	0.373 ± 0.017	32.4 ± 9.5	388 ± 54	−0.078 ± 0.012	···	···
HD200310	53234.839	3.759 ± 0.019	64.2 ± 0.8	1.059 ± 0.014	−22.6 ± 2.7	447 ± 10	0.176 ± 0.011	14.0 ± 11.7	324 ± 32
HD200310	53237.767	3.751 ± 0.022	32.0 ± 0.9	1.052 ± 0.011	−36.9 ± 2.2	439 ± 8	0.147 ± 0.009	−33.0 ± 11.1	147 ± 67
HD200310	53684.625	3.809 ± 0.022	59.2 ± 0.9	1.057 ± 0.011	−23.1 ± 2.2	443 ± 8	0.142 ± 0.009	−26.8 ± 11.9	224 ± 47
HD200310	54026.600	4.148 ± 0.020	32.3 ± 0.8	1.147 ± 0.010	−28.6 ± 1.8	468 ± 6	0.143 ± 0.008	−16.6 ± 10.6	272 ± 34

Continued on Next Page...

Table C.2 – Continued

Star Name	HJD (−2400000)	W_λ (Hγ) (Å)	V_r (Hγ) (km s^{-1})	W_λ (He I) (Å)	V_r (He I) (km s^{-1})	FWSM (He I) (km s^{-1})	W_λ (Mg II) (Å)	V_r (Mg II) (km s^{-1})	FWSM (Mg II) (km s^{-1})
HD200310	54031.684	4.180 ± 0.021	20.9 ± 0.8	1.132 ± 0.010	−40.9 ± 1.9	475 ± 7	0.108 ± 0.008	−71.4 ± 14.7	115 ± 113
HD201522	53237.777	8.194 ± 0.016	7.1 ± 0.7	0.610 ± 0.008	−13.4 ± 2.4	335 ± 6	0.296 ± 0.007	−10.5 ± 3.1	284 ± 9
HD201522	53688.666	8.152 ± 0.019	4.1 ± 0.9	0.634 ± 0.009	−18.1 ± 2.7	344 ± 7	0.317 ± 0.008	−17.9 ± 3.5	284 ± 8
HD201522	54030.637	8.162 ± 0.017	1.1 ± 0.8	0.637 ± 0.009	−16.5 ± 2.7	343 ± 7	0.317 ± 0.008	−18.6 ± 3.5	295 ± 8
HD201733	53235.817	4.863 ± 0.017	13.5 ± 0.7	1.235 ± 0.008	−0.8 ± 1.2	449 ± 5	0.351 ± 0.007	33.7 ± 4.5	392 ± 11
HD201733	53238.767	5.163 ± 0.016	17.1 ± 0.6	1.277 ± 0.009	−6.4 ± 1.3	443 ± 5	0.276 ± 0.008	4.6 ± 6.1	359 ± 17
HD201733	53686.613	5.357 ± 0.015	12.6 ± 0.6	1.221 ± 0.006	−6.7 ± 1.0	451 ± 3	0.255 ± 0.006	6.6 ± 4.8	352 ± 13
HD201733	54030.659	5.473 ± 0.016	12.8 ± 0.6	1.191 ± 0.008	−7.1 ± 1.3	470 ± 4	0.262 ± 0.007	10.7 ± 5.8	385 ± 15
HD202904	53234.843	3.125 ± 0.027	−8.4 ± 1.1	1.066 ± 0.007	−11.4 ± 1.4	349 ± 5	0.087 ± 0.006	···	···
HD202904	53237.788	3.129 ± 0.020	−6.2 ± 0.8	1.060 ± 0.010	−14.9 ± 1.7	357 ± 7	0.077 ± 0.008	···	···
HD202904	53684.628	2.972 ± 0.028	−12.1 ± 1.1	1.025 ± 0.015	−12.5 ± 2.8	367 ± 11	0.141 ± 0.006	−44.6 ± 5.4	201 ± 17
HD202904	54025.622	3.787 ± 0.031	−6.8 ± 1.3	1.059 ± 0.012	−7.3 ± 2.3	385 ± 8	0.198 ± 0.010	8.8 ± 6.6	270 ± 13
HD202904	54025.626	3.822 ± 0.026	−16.0 ± 1.1	1.045 ± 0.013	−4.8 ± 2.5	378 ± 9	0.200 ± 0.011	4.7 ± 7.0	261 ± 17
HD202904	54031.689	3.644 ± 0.023	4.8 ± 0.9	0.995 ± 0.012	1.5 ± 2.4	362 ± 9	0.199 ± 0.010	3.9 ± 6.5	277 ± 15
HD203025	53236.808	3.913 ± 0.026	9.4 ± 0.9	1.089 ± 0.008	−23.9 ± 1.3	325 ± 7	0.258 ± 0.007	−24.2 ± 4.4	248 ± 13
HD203025	53238.778	4.109 ± 0.031	−19.5 ± 1.1	1.091 ± 0.011	−56.2 ± 1.6	336 ± 8	0.243 ± 0.009	−71.4 ± 6.0	219 ± 21
HD203025	53687.662	4.213 ± 0.025	−17.8 ± 0.9	1.083 ± 0.009	−53.7 ± 1.4	330 ± 7	0.230 ± 0.008	−78.0 ± 5.3	181 ± 22
HD203025	54030.668	4.090 ± 0.024	−1.4 ± 0.8	1.097 ± 0.009	−34.2 ± 1.3	322 ± 7	0.285 ± 0.008	−29.3 ± 4.1	262 ± 12
HD203064	53234.845	2.259 ± 0.024	21.4 ± 0.7	0.748 ± 0.008	21.0 ± 2.0	380 ± 7	0.057 ± 0.007	···	···
HD203064	53237.819	2.411 ± 0.025	19.1 ± 0.8	0.772 ± 0.009	13.9 ± 2.3	391 ± 7	0.059 ± 0.008	···	···
HD203064	53684.631	2.395 ± 0.023	10.9 ± 0.7	0.764 ± 0.008	19.0 ± 2.0	401 ± 6	0.043 ± 0.007	···	···
HD203064	54025.631	2.712 ± 0.020	21.3 ± 0.6	0.752 ± 0.007	23.5 ± 1.9	393 ± 6	0.013 ± 0.007	···	···
HD203064	54031.692	2.393 ± 0.023	19.5 ± 0.7	0.695 ± 0.008	25.4 ± 2.1	379 ± 7	0.020 ± 0.007	···	···
HD203374	53236.817	0.631 ± 0.036	53.5 ± 1.1	0.397 ± 0.010	−44.7 ± 4.3	408 ± 24	−0.110 ± 0.007	···	···
HD203374	53687.673	0.742 ± 0.037	80.1 ± 1.1	0.400 ± 0.009	−10.7 ± 4.1	442 ± 21	−0.076 ± 0.007	···	···
HD203374	54025.640	1.757 ± 0.020	31.1 ± 0.6	0.464 ± 0.011	−24.5 ± 4.2	466 ± 20	−0.071 ± 0.007	···	···
HD203374	54025.649	1.304 ± 0.023	62.2 ± 0.7	0.428 ± 0.009	−29.7 ± 3.6	464 ± 18	−0.076 ± 0.007	···	···
HD203467	53236.824	2.744 ± 0.027	−1.9 ± 1.0	0.787 ± 0.015	−8.1 ± 3.5	342 ± 14	0.218 ± 0.012	−1.3 ± 6.9	236 ± 18
HD203467	53238.771	2.670 ± 0.027	0.7 ± 1.0	0.731 ± 0.017	−5.9 ± 4.4	317 ± 19	0.212 ± 0.013	1.6 ± 8.2	241 ± 22
HD203467	53684.657	2.402 ± 0.033	−5.8 ± 1.2	0.746 ± 0.017	−10.5 ± 4.3	312 ± 19	0.164 ± 0.013	−5.9 ± 10.6	162 ± 42
HD203467	54027.707	3.230 ± 0.029	−14.0 ± 1.1	0.717 ± 0.015	−17.0 ± 4.0	314 ± 18	0.205 ± 0.012	−5.2 ± 7.6	247 ± 19
HD203467	54031.698	3.258 ± 0.025	−19.3 ± 0.9	0.755 ± 0.016	−12.6 ± 4.1	324 ± 18	0.202 ± 0.013	−18.2 ± 8.4	268 ± 20
HD203699	53234.852	3.504 ± 0.023	4.8 ± 0.9	0.811 ± 0.012	−8.8 ± 3.0	284 ± 10	0.150 ± 0.010	−4.9 ± 8.6	45 ± 123
HD203699	53237.826	3.623 ± 0.024	4.8 ± 0.9	0.823 ± 0.011	−3.8 ± 2.8	287 ± 9	0.184 ± 0.009	−6.0 ± 6.7	135 ± 32
HD203699	53686.621	4.156 ± 0.024	2.1 ± 0.9	0.880 ± 0.005	−10.2 ± 1.3	288 ± 4	0.236 ± 0.005	2.0 ± 2.5	194 ± 8
HD203699	54028.712	4.386 ± 0.020	1.4 ± 0.7	0.880 ± 0.008	−9.8 ± 1.9	276 ± 6	0.250 ± 0.007	−11.8 ± 3.7	166 ± 14
HD203731	53236.836	2.417 ± 0.020	19.8 ± 0.8	1.116 ± 0.008	−52.9 ± 1.2	371 ± 6	0.170 ± 0.008	−109.5 ± 5.5	54 ± 65
HD203731	53688.687	2.509 ± 0.025	−14.2 ± 1.0	1.077 ± 0.011	−53.0 ± 1.7	348 ± 9	0.139 ± 0.012	−72.7 ± 10.4	···
HD203731	54027.712	2.339 ± 0.046	−7.3 ± 1.8	1.004 ± 0.012	−41.0 ± 1.9	386 ± 9	0.183 ± 0.010	17.2 ± 6.8	175 ± 34
HD204116	53237.798	2.010 ± 0.021	48.6 ± 0.8	0.705 ± 0.009	−55.1 ± 1.3	274 ± 10	0.043 ± 0.007	···	···
HD204116	53688.707	1.932 ± 0.039	54.7 ± 1.5	0.667 ± 0.010	−53.8 ± 1.5	263 ± 13	0.023 ± 0.008	···	···
HD204116	54028.724	2.385 ± 0.031	41.8 ± 1.2	0.671 ± 0.012	−55.0 ± 1.8	318 ± 13	0.063 ± 0.010	···	···
HD204722	53236.853	2.654 ± 0.018	6.5 ± 0.7	1.013 ± 0.009	−55.0 ± 1.1	414 ± 10	0.021 ± 0.007	···	···
HD204722	53687.686	2.832 ± 0.020	33.5 ± 0.8	1.039 ± 0.011	−41.7 ± 1.3	406 ± 12	0.057 ± 0.009	···	···
HD204722	54030.679	3.386 ± 0.018	7.5 ± 0.7	1.082 ± 0.011	−35.8 ± 1.3	417 ± 12	0.119 ± 0.008	−51.1 ± 10.7	286 ± 28
HD204860	53235.835	4.807 ± 0.015	5.7 ± 0.6	0.780 ± 0.008	−16.1 ± 1.7	341 ± 5	0.321 ± 0.007	−9.2 ± 3.2	309 ± 7
HD204860	53238.792	4.934 ± 0.017	1.3 ± 0.6	0.767 ± 0.007	−18.3 ± 1.5	345 ± 4	0.290 ± 0.006	−2.0 ± 2.9	307 ± 7
HD204860	53686.630	4.697 ± 0.031	−11.3 ± 1.2	0.755 ± 0.015	−30.5 ± 3.3	312 ± 8	0.286 ± 0.013	−15.6 ± 6.5	127 ± 36
HD204860	54030.697	4.945 ± 0.019	−9.7 ± 0.7	0.794 ± 0.006	−18.5 ± 1.2	344 ± 4	0.324 ± 0.005	−22.9 ± 2.2	274 ± 5
HD205060	53236.869	5.521 ± 0.019	−4.4 ± 0.7	0.455 ± 0.010	−22.2 ± 4.0	336 ± 17	0.284 ± 0.007	−2.6 ± 3.4	246 ± 9

Continued on Next Page...

Table C.2 – Continued

Star Name	HJD (−2400000)	W_λ (Hγ) (Å)	V_r (Hγ) (km s^{-1})	W_λ (He I) (Å)	V_r (He I) (km s^{-1})	FWSM (He I) (km s^{-1})	W_λ (Mg II) (Å)	V_r (Mg II) (km s^{-1})	FWSM (Mg II) (km s^{-1})
HD205060	53238.871	5.484 ± 0.018	−9.7 ± 0.7	0.461 ± 0.011	−15.3 ± 4.5	321 ± 20	0.298 ± 0.008	−12.7 ± 3.7	252 ± 9
HD205060	53688.728	5.475 ± 0.027	−14.7 ± 1.0	0.484 ± 0.014	−22.6 ± 5.5	326 ± 24	0.325 ± 0.011	−3.8 ± 4.5	249 ± 11
HD205060	54030.712	5.672 ± 0.021	−5.3 ± 0.8	0.464 ± 0.012	−9.1 ± 4.8	284 ± 24	0.294 ± 0.009	1.8 ± 4.1	255 ± 10
HD205551	53235.824	6.883 ± 0.020	−20.6 ± 0.8	0.295 ± 0.010	−30.6 ± 3.1	194 ± 22	0.295 ± 0.009	−26.7 ± 2.9	165 ± 8
HD205551	53237.831	7.022 ± 0.018	−21.9 ± 0.7	0.305 ± 0.007	−31.1 ± 2.2	220 ± 14	0.309 ± 0.006	−27.3 ± 2.0	165 ± 5
HD205551	53686.638	7.212 ± 0.015	−27.0 ± 0.6	0.283 ± 0.007	−28.0 ± 2.4	199 ± 17	0.290 ± 0.006	−27.4 ± 2.2	160 ± 6
HD205551	54029.763	7.173 ± 0.019	−26.7 ± 0.7	0.283 ± 0.008	−28.0 ± 2.6	188 ± 19	0.309 ± 0.007	−25.2 ± 2.3	170 ± 6
HD205551	54031.704	7.154 ± 0.014	−22.9 ± 0.6	0.288 ± 0.008	−24.4 ± 2.5	185 ± 19	0.284 ± 0.007	−26.1 ± 2.3	154 ± 7
HD206773	53236.882	1.355 ± 0.019	89.3 ± 0.7	0.351 ± 0.009	−74.2 ± 4.6	339 ± 13	0.017 ± 0.007	···	···
HD206773	53238.883	1.403 ± 0.022	70.1 ± 0.9	0.326 ± 0.008	−78.9 ± 4.5	339 ± 12	−0.009 ± 0.006	···	···
HD206773	53688.740	1.261 ± 0.018	49.1 ± 0.7	0.375 ± 0.007	−49.2 ± 3.4	499 ± 6	0.043 ± 0.005	···	···
HD206773	54030.726	1.772 ± 0.018	129.5 ± 0.8	0.312 ± 0.009	−77.1 ± 5.3	371 ± 13	−0.027 ± 0.007	···	···
HD207232	53235.870	6.495 ± 0.019	−11.5 ± 0.8	0.488 ± 0.021	−58.6 ± 6.1	341 ± 41	0.365 ± 0.017	−24.9 ± 5.8	268 ± 13
HD207232	53238.804	6.585 ± 0.017	−13.5 ± 0.7	0.469 ± 0.019	−58.4 ± 5.9	331 ± 41	0.352 ± 0.016	−27.3 ± 5.6	266 ± 13
HD207232	53687.702	6.567 ± 0.033	−34.9 ± 1.4	0.473 ± 0.016	−51.8 ± 4.9	343 ± 33	0.337 ± 0.013	−35.7 ± 4.9	236 ± 13
HD207232	54030.739	6.770 ± 0.025	−41.8 ± 1.0	0.504 ± 0.017	−47.8 ± 4.8	369 ± 30	0.343 ± 0.014	−30.8 ± 5.0	237 ± 13
HD208057	53234.857	6.433 ± 0.016	−12.5 ± 0.6	1.236 ± 0.007	−31.4 ± 1.1	324 ± 3	0.256 ± 0.004	−18.4 ± 1.0	138 ± 4
HD208057	53237.837	6.585 ± 0.014	−12.1 ± 0.6	1.239 ± 0.007	−26.3 ± 1.0	334 ± 4	0.257 ± 0.004	−16.7 ± 1.0	135 ± 4
HD208057	53684.669	6.622 ± 0.014	−18.0 ± 0.6	1.242 ± 0.009	−34.3 ± 1.4	335 ± 3	0.254 ± 0.005	−22.0 ± 1.3	142 ± 2
HD208057	54027.729	6.701 ± 0.017	−16.5 ± 0.7	1.211 ± 0.006	−34.1 ± 0.9	329 ± 2	0.245 ± 0.003	−22.1 ± 0.9	142 ± 1
HD208057	54030.753	6.721 ± 0.016	−11.8 ± 0.6	1.214 ± 0.008	−29.4 ± 1.2	324 ± 3	0.260 ± 0.005	−14.8 ± 1.1	134 ± 4
HD208057	54031.712	6.658 ± 0.017	−14.4 ± 0.7	1.244 ± 0.005	−30.0 ± 0.8	332 ± 2	0.248 ± 0.003	−13.1 ± 0.8	136 ± 3
HD208392	53235.883	3.665 ± 0.023	115.6 ± 0.9	0.948 ± 0.014	−23.5 ± 2.2	275 ± 41	0.127 ± 0.011	−73.9 ± 13.8	310 ± 36
HD208392	53238.833	3.633 ± 0.027	113.6 ± 1.1	0.922 ± 0.014	−25.4 ± 2.2	166 ± 70	0.075 ± 0.011	···	···
HD208392	53686.650	3.958 ± 0.034	119.9 ± 1.4	0.965 ± 0.014	−22.8 ± 2.2	295 ± 39	0.102 ± 0.011	−50.1 ± 17.9	324 ± 45
HD208392	54027.734	3.993 ± 0.033	98.9 ± 1.3	0.873 ± 0.015	−21.5 ± 2.6	278 ± 48	0.051 ± 0.012	···	···
HD208682	53235.842	4.352 ± 0.024	33.0 ± 1.0	1.116 ± 0.013	−22.9 ± 1.9	407 ± 11	0.216 ± 0.011	−25.5 ± 8.2	315 ± 21
HD208682	53238.859	4.548 ± 0.027	20.5 ± 1.1	1.155 ± 0.009	−34.3 ± 1.4	406 ± 8	0.222 ± 0.008	−43.5 ± 5.9	297 ± 16
HD208682	53684.673	4.574 ± 0.026	16.6 ± 1.0	1.183 ± 0.008	−33.9 ± 1.2	422 ± 6	0.228 ± 0.007	−40.3 ± 5.1	308 ± 13
HD208682	54027.748	4.640 ± 0.027	9.7 ± 1.1	1.089 ± 0.009	−35.5 ± 1.4	412 ± 8	0.182 ± 0.008	−33.6 ± 6.9	316 ± 17
HD208682	54031.715	4.567 ± 0.021	17.5 ± 0.8	1.121 ± 0.009	−32.7 ± 1.4	421 ± 8	0.223 ± 0.008	−36.3 ± 5.9	305 ± 15
HD210129	53235.851	7.049 ± 0.016	−56.3 ± 0.7	0.546 ± 0.006	−62.0 ± 1.0	249 ± 8	0.289 ± 0.005	−49.7 ± 1.6	188 ± 4
HD210129	53238.846	7.164 ± 0.014	−58.0 ± 0.6	0.555 ± 0.007	−64.9 ± 1.1	262 ± 8	0.299 ± 0.006	−52.6 ± 1.8	192 ± 4
HD210129	53684.678	7.507 ± 0.023	−63.5 ± 1.0	0.505 ± 0.006	−57.7 ± 1.0	260 ± 8	0.313 ± 0.005	−56.9 ± 1.4	217 ± 3
HD210129	54025.662	7.287 ± 0.022	−69.4 ± 1.0	0.518 ± 0.007	−55.5 ± 1.3	262 ± 10	0.296 ± 0.007	−58.3 ± 2.0	207 ± 4
HD210129	54031.734	7.494 ± 0.024	−63.3 ± 1.1	0.489 ± 0.008	−53.5 ± 1.6	245 ± 13	0.287 ± 0.007	−59.0 ± 2.3	204 ± 5
HD212044	53235.857	1.548 ± 0.035	55.2 ± 1.3	0.736 ± 0.013	−54.9 ± 2.3	299 ± 24	−0.064 ± 0.013	···	···
HD212044	53238.852	1.601 ± 0.037	75.0 ± 1.4	0.727 ± 0.012	−22.9 ± 2.1	287 ± 23	−0.098 ± 0.011	···	···
HD212044	53686.664	2.038 ± 0.031	25.2 ± 1.2	0.772 ± 0.008	−93.3 ± 1.3	309 ± 13	−0.078 ± 0.008	···	···
HD212044	54025.675	2.436 ± 0.034	52.8 ± 1.3	0.773 ± 0.012	−57.2 ± 1.9	294 ± 20	−0.053 ± 0.011	···	···
HD212044	54025.689	2.611 ± 0.039	50.2 ± 1.5	0.759 ± 0.009	−56.3 ± 1.5	283 ± 17	−0.059 ± 0.009	···	···
HD212076	53233.833	2.173 ± 0.019	44.2 ± 0.7	0.913 ± 0.011	−12.5 ± 2.2	305 ± 10	0.073 ± 0.005	···	···
HD212076	53236.894	2.214 ± 0.026	51.1 ± 1.0	0.904 ± 0.013	−6.4 ± 2.8	326 ± 12	0.071 ± 0.006	···	···
HD212076	53238.894	2.094 ± 0.022	37.3 ± 0.8	0.893 ± 0.010	−12.4 ± 2.2	330 ± 9	0.049 ± 0.005	···	···
HD212076	53684.682	2.121 ± 0.016	45.0 ± 0.6	0.973 ± 0.014	−10.6 ± 2.8	343 ± 11	−0.019 ± 0.006	···	···
HD212076	53687.731	2.168 ± 0.022	47.9 ± 0.8	0.968 ± 0.013	−12.2 ± 2.7	344 ± 11	−0.012 ± 0.006	···	···
HD212076	54027.760	2.695 ± 0.014	23.9 ± 0.5	1.009 ± 0.007	−20.8 ± 1.4	333 ± 5	−0.013 ± 0.005	···	···
HD212076	54031.740	2.699 ± 0.034	23.3 ± 1.3	0.999 ± 0.007	−22.6 ± 1.4	331 ± 6	−0.014 ± 0.006	···	···
HD212571	53233.838	2.852 ± 0.025	132.5 ± 1.0	0.827 ± 0.010	−47.0 ± 1.8	338 ± 15	0.106 ± 0.008	−64.4 ± 12.9	183 ± 57
HD212571	53236.896	2.875 ± 0.027	136.0 ± 1.1	0.782 ± 0.012	−51.7 ± 2.3	325 ± 20	0.081 ± 0.010	···	···

Continued on Next Page...

Table C.2 – Continued

Star Name	HJD (−2400000)	W_λ (Hγ) (Å)	V_r (Hγ) (km s^{-1})	W_λ (He I) (Å)	V_r (He I) (km s^{-1})	FWSM (He I) (km s^{-1})	W_λ (Mg II) (Å)	V_r (Mg II) (km s^{-1})	FWSM (Mg II) (km s^{-1})
HD212571	53238.896	2.898 ± 0.027	147.0 ± 1.1	0.781 ± 0.011	-43.1 ± 2.1	290 ± 21	0.095 ± 0.009	...	...
HD212571	53684.610	2.725 ± 0.025	105.9 ± 1.0	0.737 ± 0.012	-40.8 ± 2.5	351 ± 21	0.110 ± 0.010	-79.1 ± 15.5	238 ± 52
HD212571	53684.694	2.701 ± 0.025	108.7 ± 1.0	0.763 ± 0.012	-43.4 ± 2.4	350 ± 19	0.104 ± 0.010	-98.1 ± 15.9	142 ± 90
HD212571	53684.733	2.685 ± 0.027	103.0 ± 1.1	0.772 ± 0.011	-41.7 ± 2.2	369 ± 17	0.129 ± 0.010	-70.8 ± 12.2	258 ± 38
HD212571	53685.707	2.666 ± 0.029	99.2 ± 1.1	0.752 ± 0.012	-40.6 ± 2.5	343 ± 21	0.105 ± 0.011	-78.4 ± 16.3	168 ± 78
HD212571	53685.749	2.825 ± 0.026	100.7 ± 1.0	0.761 ± 0.012	-49.9 ± 2.3	359 ± 18	0.128 ± 0.010	-78.0 ± 12.5	251 ± 40
HD212571	53686.545	2.634 ± 0.026	106.9 ± 1.0	0.760 ± 0.014	-48.1 ± 2.8	355 ± 23	0.113 ± 0.012	-81.4 ± 17.3	166 ± 84
HD212571	53686.609	2.741 ± 0.026	113.8 ± 1.0	0.753 ± 0.012	-45.5 ± 2.4	344 ± 20	0.109 ± 0.010	-83.0 ± 15.1	164 ± 74
HD212571	53686.643	2.676 ± 0.025	113.3 ± 1.0	0.738 ± 0.012	-39.9 ± 2.5	346 ± 21	0.116 ± 0.011	-92.4 ± 14.9	125 ± 96
HD212571	53686.692	2.817 ± 0.028	101.6 ± 1.1	0.749 ± 0.012	-44.2 ± 2.5	345 ± 21	0.113 ± 0.010	-106.4 ± 14.9	...
HD212571	53686.717	2.758 ± 0.031	114.9 ± 1.2	0.742 ± 0.011	-47.7 ± 2.3	336 ± 19	0.133 ± 0.009	-77.2 ± 11.6	217 ± 43
HD212571	53687.559	2.789 ± 0.026	96.0 ± 1.0	0.751 ± 0.012	-38.4 ± 2.4	354 ± 20	0.128 ± 0.010	-82.9 ± 13.0	240 ± 44
HD212571	53687.641	2.916 ± 0.025	100.5 ± 1.0	0.757 ± 0.013	-44.8 ± 2.6	363 ± 21	0.113 ± 0.011	-85.8 ± 16.1	211 ± 62
HD212571	53687.695	2.880 ± 0.025	100.6 ± 1.0	0.760 ± 0.011	-45.2 ± 2.3	350 ± 19	0.113 ± 0.010	-100.1 ± 14.0	104 ± 109
HD212571	53687.729	2.664 ± 0.028	105.9 ± 1.1	0.716 ± 0.013	-40.3 ± 2.7	320 ± 24	0.089 ± 0.011	...	...
HD212571	53688.558	2.681 ± 0.024	98.4 ± 0.9	0.727 ± 0.012	-46.9 ± 2.5	352 ± 21	0.121 ± 0.010	-99.5 ± 13.9	166 ± 68
HD212571	53688.599	2.724 ± 0.026	107.5 ± 1.0	0.750 ± 0.011	-48.3 ± 2.2	365 ± 17	0.103 ± 0.009	-107.8 ± 14.5	...
HD212571	53688.641	2.758 ± 0.026	91.5 ± 1.0	0.723 ± 0.011	-45.2 ± 2.3	341 ± 19	0.103 ± 0.009	-121.3 ± 14.8	...
HD212571	53688.678	2.811 ± 0.025	111.9 ± 1.0	0.723 ± 0.013	-39.9 ± 2.8	332 ± 24	0.114 ± 0.011	-105.0 ± 16.2	74 ± 178
HD212571	53688.720	2.730 ± 0.027	102.0 ± 1.1	0.757 ± 0.013	-44.7 ± 2.6	366 ± 20	0.120 ± 0.011	-103.9 ± 15.1	133 ± 91
HD212571	54025.703	3.438 ± 0.026	120.7 ± 1.0	0.865 ± 0.010	-31.6 ± 1.8	307 ± 17	0.109 ± 0.009	-65.6 ± 12.9	94 ± 111
HD212571	54031.746	3.445 ± 0.026	114.6 ± 1.0	0.852 ± 0.011	-34.8 ± 1.9	301 ± 18	0.080 ± 0.009	...	...
HD212791	53234.865	5.014 ± 0.024	-4.9 ± 1.0	1.097 ± 0.013	-31.6 ± 1.7	311 ± 10	0.241 ± 0.009	-15.8 ± 4.2	190 ± 11
HD212791	53237.846	5.077 ± 0.023	-9.8 ± 0.9	1.115 ± 0.011	-37.6 ± 1.5	319 ± 8	0.224 ± 0.008	-23.9 ± 3.9	174 ± 11
HD212791	53687.718	5.388 ± 0.022	-10.6 ± 0.9	1.134 ± 0.008	-36.8 ± 1.0	316 ± 6	0.250 ± 0.006	-24.2 ± 2.6	164 ± 8
HD212791	54028.755	5.485 ± 0.019	-6.5 ± 0.8	1.121 ± 0.009	-32.5 ± 1.2	322 ± 7	0.236 ± 0.007	-18.3 ± 3.1	192 ± 8
HD214167	53234.888	5.536 ± 0.028	-8.1 ± 1.0	1.487 ± 0.010	-39.8 ± 1.2	314 ± 7	0.193 ± 0.009	-26.6 ± 3.4	100 ± 12
HD214167	53236.902	5.602 ± 0.026	-0.3 ± 0.9	1.522 ± 0.014	-39.9 ± 1.7	330 ± 10	0.194 ± 0.010	-23.6 ± 3.5	110 ± 11
HD214167	53238.902	5.682 ± 0.038	-2.8 ± 1.3	1.492 ± 0.013	-39.4 ± 1.5	319 ± 9	0.207 ± 0.008	-27.1 ± 3.0	106 ± 10
HD214167	53684.691	5.875 ± 0.030	-6.3 ± 1.0	1.517 ± 0.012	-40.0 ± 1.5	323 ± 9	0.200 ± 0.008	-32.1 ± 3.2	101 ± 12
HD214167	54028.779	5.914 ± 0.029	-7.6 ± 1.0	1.464 ± 0.011	-39.6 ± 1.3	311 ± 8	0.196 ± 0.007	-25.0 ± 2.6	103 ± 9
HD214167	54031.757	5.786 ± 0.029	-6.1 ± 1.0	1.471 ± 0.012	-38.6 ± 1.4	316 ± 9	0.192 ± 0.008	-24.2 ± 2.9	102 ± 10
HD214168	53233.849	3.392 ± 0.022	26.6 ± 0.9	1.059 ± 0.011	-31.0 ± 1.7	408 ± 14	0.089 ± 0.008	...	...
HD214168	53236.898	3.321 ± 0.025	24.0 ± 1.0	1.102 ± 0.010	-33.6 ± 1.5	431 ± 12	0.115 ± 0.008	-63.9 ± 12.8	80 ± 143
HD214168	53238.897	3.365 ± 0.023	21.1 ± 0.9	1.126 ± 0.010	-35.1 ± 1.5	427 ± 12	0.120 ± 0.008	-72.4 ± 12.3	...
HD214168	53684.686	3.485 ± 0.024	24.6 ± 0.9	1.073 ± 0.011	-30.8 ± 1.7	444 ± 13	0.100 ± 0.008	-82.1 ± 16.1	95 ± 152
HD214168	53687.736	3.376 ± 0.020	21.1 ± 0.8	1.062 ± 0.008	-36.4 ± 1.4	450 ± 10	0.080 ± 0.007	...	...
HD214168	54028.788	3.741 ± 0.022	7.3 ± 0.8	1.097 ± 0.010	-33.0 ± 1.6	429 ± 13	0.091 ± 0.008	...	...
HD214168	54029.774	3.633 ± 0.022	9.9 ± 0.8	1.055 ± 0.011	-37.3 ± 1.8	424 ± 14	0.077 ± 0.009	...	...
HD214168	54031.752	3.632 ± 0.020	10.3 ± 0.8	1.079 ± 0.010	-36.6 ± 1.6	435 ± 12	0.078 ± 0.008	...	...
HD216057	53233.878	7.056 ± 0.022	4.6 ± 1.0	0.767 ± 0.008	-28.0 ± 1.7	359 ± 8	0.249 ± 0.008	-17.4 ± 5.3	308 ± 14
HD216057	53236.904	7.198 ± 0.022	1.2 ± 1.0	0.814 ± 0.007	-25.0 ± 1.4	381 ± 6	0.290 ± 0.007	-10.9 ± 4.1	328 ± 10
HD216057	53238.905	7.344 ± 0.015	-1.7 ± 0.7	0.789 ± 0.007	-19.8 ± 1.4	365 ± 6	0.285 ± 0.006	-19.2 ± 3.9	318 ± 10
HD216057	53684.699	7.262 ± 0.016	2.4 ± 0.7	0.832 ± 0.007	-20.9 ± 1.3	383 ± 5	0.299 ± 0.006	-16.2 ± 3.6	342 ± 9
HD216057	54025.708	7.233 ± 0.015	-4.6 ± 0.7	0.799 ± 0.007	-25.8 ± 1.4	373 ± 6	0.281 ± 0.007	-20.5 ± 4.2	326 ± 10
HD216057	54029.782	7.477 ± 0.015	-2.2 ± 0.7	0.780 ± 0.007	-16.6 ± 1.5	368 ± 7	0.272 ± 0.007	-19.6 ± 4.3	325 ± 11
HD216200	53233.872	5.238 ± 0.036	-16.6 ± 1.3	1.028 ± 0.013	-52.9 ± 2.1	258 ± 6	0.262 ± 0.012	-13.0 ± 5.6	120 ± 43
HD216200	53236.912	5.050 ± 0.026	-5.3 ± 1.0	0.993 ± 0.010	-37.9 ± 1.6	284 ± 4	0.292 ± 0.009	-3.0 ± 3.7	163 ± 21
HD216200	53238.911	5.097 ± 0.035	27.3 ± 1.3	0.988 ± 0.012	-3.7 ± 2.0	293 ± 8	0.270 ± 0.011	15.0 ± 4.9	131 ± 34
HD216200	53685.711	5.451 ± 0.036	15.8 ± 1.4	0.996 ± 0.013	-31.0 ± 2.1	294 ± 5	0.277 ± 0.012	-1.9 ± 5.1	87 ± 55

Continued on Next Page...

Table C.2 – Continued

Star Name	HJD (−2400000)	W_λ (Hγ) (Å)	V_r (Hγ) (km s^{-1})	W_λ (He I) (Å)	V_r (He I) (km s^{-1})	FWSM (He I) (km s^{-1})	W_λ (Mg II) (Å)	V_r (Mg II) (km s^{-1})	FWSM (Mg II) (km s^{-1})
HD216200	54028.795	5.554 ± 0.041	-3.1 ± 1.6	1.002 ± 0.011	-34.5 ± 1.9	290 ± 5	0.290 ± 0.010	2.0 ± 4.4	95 ± 43
HD216200	54029.790	5.426 ± 0.035	-10.2 ± 1.3	1.035 ± 0.012	-51.7 ± 1.9	289 ± 5	0.306 ± 0.011	-19.9 ± 4.3	159 ± 17
HD216200	54031.766	5.212 ± 0.036	-18.3 ± 1.4	1.005 ± 0.012	-58.2 ± 2.0	263 ± 6	0.275 ± 0.011	-31.7 ± 5.0	211 ± 15
HD217050	53233.857	4.078 ± 0.030	3.1 ± 1.1	1.099 ± 0.013	-37.8 ± 2.7	368 ± 7	0.260 ± 0.011	-42.2 ± 6.6	66 ± 75
HD217050	53236.914	4.070 ± 0.035	0.2 ± 1.3	1.125 ± 0.014	-39.5 ± 2.8	383 ± 7	0.278 ± 0.011	-41.1 ± 6.7	124 ± 41
HD217050	53238.915	4.026 ± 0.028	0.0 ± 1.0	1.118 ± 0.014	-36.1 ± 2.8	381 ± 7	0.278 ± 0.011	-34.9 ± 6.3	120 ± 38
HD217050	53684.704	4.451 ± 0.029	-8.2 ± 1.0	1.288 ± 0.019	-38.6 ± 3.2	392 ± 8	0.417 ± 0.015	-23.9 ± 5.4	186 ± 20
HD217050	54028.802	4.488 ± 0.024	-10.7 ± 0.9	1.222 ± 0.015	-16.8 ± 3.1	382 ± 9	0.336 ± 0.011	24.0 ± 5.9	...
HD217050	54029.798	4.536 ± 0.026	-9.6 ± 0.9	1.195 ± 0.016	-30.0 ± 3.5	356 ± 12	0.340 ± 0.013	19.7 ± 6.6	...
HD217050	54031.772	4.494 ± 0.026	-8.3 ± 0.9	1.230 ± 0.013	-18.4 ± 2.7	383 ± 8	0.330 ± 0.011	29.7 ± 5.7	...
HD217543	53233.886	4.896 ± 0.018	-11.3 ± 0.7	1.237 ± 0.007	-30.8 ± 1.2	501 ± 4	0.235 ± 0.007	23.9 ± 6.4	395 ± 17
HD217543	53236.919	4.973 ± 0.017	-5.1 ± 0.7	1.317 ± 0.009	-21.5 ± 1.3	500 ± 5	0.259 ± 0.008	24.2 ± 6.9	361 ± 20
HD217543	53238.920	4.992 ± 0.016	-5.0 ± 0.6	1.273 ± 0.008	-25.1 ± 1.2	494 ± 4	0.254 ± 0.007	5.9 ± 6.1	382 ± 17
HD217543	53684.708	5.395 ± 0.021	-8.7 ± 0.8	1.305 ± 0.008	-24.8 ± 1.1	494 ± 4	0.223 ± 0.007	0.9 ± 6.8	350 ± 20
HD217543	54028.808	5.028 ± 0.017	-15.5 ± 0.7	1.406 ± 0.006	-7.4 ± 0.8	489 ± 3	0.293 ± 0.005	-10.7 ± 4.2	301 ± 14
HD217543	54029.804	5.093 ± 0.015	-13.8 ± 0.6	1.362 ± 0.007	-20.4 ± 1.0	486 ± 4	0.299 ± 0.006	5.1 ± 4.9	317 ± 16
HD217675	53233.864	5.394 ± 0.019	-7.8 ± 0.7	0.668 ± 0.008	-23.3 ± 1.9	326 ± 7	0.345 ± 0.007	-6.7 ± 3.3	276 ± 9
HD217675	53236.925	5.416 ± 0.017	-12.7 ± 0.6	0.680 ± 0.007	-26.4 ± 1.7	335 ± 6	0.392 ± 0.007	-10.2 ± 2.6	282 ± 7
HD217675	53238.923	5.329 ± 0.016	-10.9 ± 0.6	0.694 ± 0.007	-28.7 ± 1.6	339 ± 3	0.364 ± 0.006	-22.5 ± 2.7	275 ± 7
HD217675	53684.712	5.534 ± 0.013	-13.3 ± 0.5	0.663 ± 0.007	-20.3 ± 1.7	340 ± 6	0.297 ± 0.006	-19.7 ± 3.3	294 ± 8
HD217675	54028.819	5.563 ± 0.014	-15.1 ± 0.5	0.687 ± 0.006	-22.9 ± 1.3	330 ± 4	0.300 ± 0.005	-18.1 ± 2.7	287 ± 7
HD217675	54029.772	5.395 ± 0.017	-13.0 ± 0.6	0.666 ± 0.009	-22.8 ± 2.1	335 ± 7	0.312 ± 0.008	-19.0 ± 4.0	294 ± 10
HD217675	54031.777	5.360 ± 0.015	-13.1 ± 0.5	0.686 ± 0.006	-28.0 ± 1.5	333 ± 3	0.300 ± 0.006	-17.6 ± 3.0	282 ± 8
HD217891	53233.843	6.887 ± 0.014	2.8 ± 0.6	0.711 ± 0.005	-5.1 ± 1.4	258 ± 4	0.274 ± 0.004	2.5 ± 1.0	119 ± 3
HD217891	53236.929	6.947 ± 0.015	3.4 ± 0.7	0.728 ± 0.006	0.0 ± 1.6	270 ± 5	0.275 ± 0.004	5.5 ± 1.2	119 ± 3
HD217891	53238.927	6.916 ± 0.013	3.2 ± 0.6	0.730 ± 0.007	-3.2 ± 1.7	270 ± 5	0.265 ± 0.005	3.5 ± 1.4	115 ± 4
HD217891	53684.575	6.955 ± 0.013	1.2 ± 0.6	0.738 ± 0.006	-0.1 ± 1.4	274 ± 4	0.284 ± 0.004	4.0 ± 1.1	119 ± 3
HD217891	53684.724	6.975 ± 0.025	-1.9 ± 1.1	0.738 ± 0.009	0.3 ± 2.3	273 ± 7	0.276 ± 0.006	-0.8 ± 1.8	110 ± 6
HD217891	53684.726	7.026 ± 0.011	0.0 ± 0.5	0.725 ± 0.006	0.7 ± 1.5	273 ± 4	0.278 ± 0.004	4.4 ± 1.1	117 ± 3
HD217891	54027.765	6.985 ± 0.016	-2.2 ± 0.7	0.648 ± 0.006	1.8 ± 1.7	260 ± 5	0.273 ± 0.004	3.0 ± 1.2	133 ± 3
HD217891	54031.780	6.987 ± 0.016	2.0 ± 0.7	0.643 ± 0.006	4.0 ± 1.8	253 ± 6	0.281 ± 0.004	7.9 ± 1.2	132 ± 3
HD218393	53234.899	2.813 ± 0.048	-130.1 ± 1.0	0.989 ± 0.019	-94.4 ± 3.4	322 ± 31	0.390 ± 0.016	-51.0 ± 5.4	184 ± 18
HD218393	53237.865	3.037 ± 0.100	-107.2 ± 2.1	0.959 ± 0.025	-103.2 ± 4.8	323 ± 43	0.421 ± 0.020	-36.5 ± 6.0	106 ± 33
HD218393	53684.718	2.773 ± 0.055	-112.6 ± 1.0	0.922 ± 0.028	-140.4 ± 6.4	377 ± 16	0.302 ± 0.023	-69.6 ± 11.3	134 ± 57
HD218393	54025.720	3.214 ± 0.062	-184.9 ± 1.4	0.984 ± 0.026	-103.7 ± 4.8	376 ± 11	0.411 ± 0.021	-10.3 ± 5.3	184 ± 23
HD218393	54031.784	2.525 ± 0.061	-105.2 ± 1.1	0.815 ± 0.029	-96.7 ± 6.3	300 ± 61	0.424 ± 0.023	-32.5 ± 6.6	134 ± 29
HD218674	53233.906	4.455 ± 0.020	7.0 ± 0.8	1.106 ± 0.009	-8.7 ± 1.2	396 ± 5	0.310 ± 0.008	-17.8 ± 4.2	291 ± 11
HD218674	53236.931	4.350 ± 0.021	0.9 ± 0.8	1.111 ± 0.009	-25.4 ± 1.3	399 ± 5	0.321 ± 0.008	-19.7 ± 4.1	289 ± 11
HD218674	53238.929	4.509 ± 0.020	-0.2 ± 0.8	1.082 ± 0.007	-25.8 ± 1.0	397 ± 4	0.330 ± 0.006	-30.7 ± 3.1	275 ± 9
HD218674	53685.717	4.602 ± 0.019	-18.3 ± 0.7	1.098 ± 0.007	-36.0 ± 1.1	398 ± 4	0.297 ± 0.007	-36.8 ± 3.9	293 ± 10
HD218674	54027.768	4.832 ± 0.023	-14.1 ± 0.9	1.078 ± 0.009	-37.0 ± 1.4	401 ± 5	0.257 ± 0.009	-43.9 ± 5.5	334 ± 13
HD218674	54031.797	4.962 ± 0.019	-12.7 ± 0.7	1.096 ± 0.007	-34.6 ± 1.1	403 ± 4	0.285 ± 0.007	-45.7 ± 3.9	336 ± 9
HD224544	53233.892	5.452 ± 0.016	-1.5 ± 0.6	0.840 ± 0.008	-33.9 ± 1.2	359 ± 9	0.312 ± 0.007	-26.5 ± 3.4	329 ± 7
HD224544	53236.940	5.449 ± 0.020	-0.5 ± 0.8	0.842 ± 0.008	-31.0 ± 1.2	379 ± 9	0.333 ± 0.007	-22.2 ± 3.3	347 ± 7
HD224544	53238.938	5.400 ± 0.017	-3.4 ± 0.6	0.856 ± 0.008	-30.9 ± 1.2	370 ± 9	0.348 ± 0.007	-21.5 ± 3.1	347 ± 6
HD224544	53684.731	5.471 ± 0.016	-5.5 ± 0.6	0.833 ± 0.009	-31.0 ± 1.3	368 ± 10	0.323 ± 0.008	-25.8 ± 3.7	337 ± 8
HD224544	53686.712	5.488 ± 0.015	-11.3 ± 0.6	0.821 ± 0.007	-38.6 ± 1.1	374 ± 8	0.320 ± 0.007	-31.0 ± 3.1	341 ± 6
HD224544	54027.792	5.461 ± 0.017	-10.9 ± 0.7	0.807 ± 0.006	-38.3 ± 1.0	368 ± 7	0.295 ± 0.006	-32.5 ± 2.8	327 ± 6
HD224544	54029.827	5.651 ± 0.017	-8.7 ± 0.6	0.839 ± 0.008	-34.4 ± 1.2	374 ± 9	0.330 ± 0.007	-34.6 ± 3.2	344 ± 7
HD224559	53233.898	4.671 ± 0.022	-17.0 ± 0.8	0.871 ± 0.010	-6.1 ± 2.2	426 ± 7	0.233 ± 0.008	-12.6 ± 4.4	282 ± 10

Continued on Next Page...

Table C.2 – Continued

Star Name	HJD (−2400000)	W_λ (Hγ) (Å)	V_r (Hγ) (km s^{-1})	W_λ (He I) (Å)	V_r (He I) (km s^{-1})	FWSM (He I) (km s^{-1})	W_λ (Mg II) (Å)	V_r (Mg II) (km s^{-1})	FWSM (Mg II) (km s^{-1})
HD224559	53236.944	4.574 ± 0.031	-15.6 ± 1.2	0.895 ± 0.011	-3.7 ± 2.2	437 ± 7	0.255 ± 0.008	-12.4 ± 4.3	286 ± 9
HD224559	53238.943	4.569 ± 0.025	-21.8 ± 1.0	0.885 ± 0.010	-1.8 ± 2.2	439 ± 7	0.259 ± 0.008	-10.0 ± 4.1	296 ± 9
HD224559	53684.749	4.670 ± 0.032	-23.3 ± 1.2	0.852 ± 0.012	0.7 ± 2.7	432 ± 9	0.227 ± 0.010	-24.2 ± 5.5	286 ± 12
HD224559	53687.745	4.633 ± 0.028	-26.4 ± 1.1	0.826 ± 0.012	0.3 ± 2.7	407 ± 9	0.227 ± 0.009	-15.9 ± 5.4	269 ± 13
HD224559	54027.782	4.830 ± 0.036	-27.0 ± 1.4	0.811 ± 0.011	-7.2 ± 2.6	420 ± 8	0.226 ± 0.009	-22.4 ± 5.0	266 ± 12
HD224559	54029.816	5.034 ± 0.031	-27.6 ± 1.2	0.773 ± 0.012	-1.6 ± 3.1	409 ± 10	0.213 ± 0.010	-20.3 ± 6.0	275 ± 14
HD225095	53235.899	1.033 ± 0.020	46.6 ± 0.7	0.716 ± 0.015	-56.5 ± 4.0	322 ± 12	-0.109 ± 0.012	···	···
HD225095	53237.881	1.176 ± 0.024	58.4 ± 0.9	0.727 ± 0.008	-40.2 ± 2.2	328 ± 6	-0.081 ± 0.007	···	···
HD225095	53685.727	0.748 ± 0.024	62.1 ± 0.9	0.744 ± 0.015	-45.1 ± 3.8	343 ± 10	-0.073 ± 0.012	···	···
HD225095	53688.772	0.942 ± 0.034	53.7 ± 1.3	0.718 ± 0.016	-58.8 ± 4.2	334 ± 12	-0.059 ± 0.013	···	···
HD225095	54025.744	1.315 ± 0.015	25.5 ± 0.5	0.808 ± 0.015	-52.5 ± 3.4	356 ± 9	-0.105 ± 0.012	···	···
HD225095	54030.762	1.286 ± 0.033	19.6 ± 1.2	0.770 ± 0.016	-66.2 ± 4.0	328 ± 11	-0.111 ± 0.013	···	···

C.3 Blue Shell Fitting Spectral Measurements Table

Table C.3: Be Star Survey Equivalent Width, Radial Velocity and FWSM Measurements from Shell Line Fitting

Star Name	HJD (−2,400,000)	W_λ (km s^{-1})	V_r (km s^{-1})	FWSM (km s^{-1})
HD000144	53233.911	13.84 ± 0.24	-7.1 ± 1.2	149 ± 3
HD000144	53236.946	14.15 ± 0.50	5.6 ± 2.1	137 ± 5
HD000144	53238.946	18.01 ± 0.72	-8.7 ± 2.8	170 ± 6
HD000144	53684.742	17.28 ± 0.27	2.4 ± 1.0	161 ± 2
HD000144	53688.787	17.01 ± 0.44	0.5 ± 1.6	164 ± 3
HD000144	54025.822	18.51 ± 0.35	-2.9 ± 1.3	162 ± 3
HD000144	54030.784	18.60 ± 0.25	-0.9 ± 0.9	162 ± 2
HD000144	54031.805	17.62 ± 0.31	2.4 ± 1.1	161 ± 2
HD004180	53233.917	-19.81 ± 1.23	-34.5 ± 7.5	159 ± 38
HD004180	53236.950	-23.12 ± 1.19	-48.8 ± 6.4	238 ± 21
HD004180	53238.950	-25.80 ± 1.00	-42.3 ± 4.1	262 ± 11
HD004180	53684.625	-22.94 ± 1.42	-14.4 ± 7.5	192 ± 30
HD004180	53684.754	-22.61 ± 1.36	-7.8 ± 6.7	208 ± 23
HD004180	53686.697	-21.10 ± 1.27	-3.0 ± 6.6	210 ± 22
HD004180	53686.870	-21.48 ± 1.34	-4.7 ± 6.8	204 ± 24
HD004180	54025.731	-23.33 ± 1.59	-17.0 ± 7.5	207 ± 26
HD004180	54030.792	-24.09 ± 1.72	-12.4 ± 7.6	195 ± 28
HD004180	54031.810	-22.18 ± 1.66	-20.1 ± 8.3	146 ± 41
HD005394	53233.913	-21.35 ± 0.82	4.1 ± 4.0	327 ± 8
HD005394	53236.950	-19.34 ± 0.89	3.6 ± 4.8	315 ± 10
HD005394	53238.950	-19.10 ± 0.97	-3.9 ± 5.5	309 ± 12
HD005394	53684.739	-19.32 ± 0.86	-4.7 ± 4.8	310 ± 11
HD005394	53685.737	-19.27 ± 0.80	-8.8 ± 4.6	316 ± 10
HD005394	53688.749	-18.20 ± 0.78	-7.5 ± 4.7	301 ± 11
HD005394	54025.756	-20.14 ± 0.48	6.2 ± 2.4	309 ± 5
HD005394	54030.794	-20.04 ± 0.77	-5.1 ± 4.2	305 ± 9
HD005394	54031.812	-20.32 ± 0.83	-2.5 ± 4.4	297 ± 10
HD006811	53233.919	9.37 ± 0.21	5.1 ± 1.3	124 ± 3
HD006811	53236.954	8.37 ± 0.40	8.8 ± 2.6	113 ± 8
HD006811	53238.953	8.50 ± 0.26	10.5 ± 1.7	115 ± 5
HD006811	53684.669	8.47 ± 0.44	10.3 ± 2.8	109 ± 8
HD006811	53684.830	9.45 ± 0.34	8.1 ± 2.0	117 ± 6
HD006811	53686.716	8.40 ± 0.43	4.8 ± 3.0	108 ± 10
HD006811	53688.658	8.52 ± 0.55	5.0 ± 3.8	114 ± 11
HD006811	53688.836	7.64 ± 0.45	3.9 ± 3.4	97 ± 12
HD006811	54025.759	8.79 ± 0.34	5.9 ± 2.2	113 ± 6
HD006811	54027.801	8.37 ± 0.34	11.8 ± 2.1	105 ± 6
HD006811	54029.853	9.30 ± 0.29	14.1 ± 1.6	122 ± 4
HD006811	54031.816	8.90 ± 0.33	12.6 ± 2.0	119 ± 5
HD007636	53235.913	-46.18 ± 0.49	-12.8 ± 0.8	196 ± 2
HD007636	53237.894	-45.60 ± 1.03	-17.1 ± 1.8	193 ± 5
HD007636	53684.765	-44.34 ± 0.93	-2.4 ± 1.5	219 ± 3
HD007636	53687.758	-44.71 ± 0.77	-18.2 ± 1.4	210 ± 3
HD007636	54025.767	-44.86 ± 0.61	-10.7 ± 1.0	194 ± 2
HD007636	54029.839	-42.86 ± 1.06	-19.2 ± 1.9	189 ± 5
HD009709	53234.917	19.36 ± 0.29	-3.1 ± 1.0	158 ± 2
HD009709	53237.908	18.42 ± 0.35	-2.9 ± 1.3	156 ± 3
HD009709	53684.783	20.53 ± 0.38	-2.1 ± 1.2	156 ± 3
HD009709	53687.781	19.87 ± 0.31	2.9 ± 1.0	153 ± 2
HD009709	54025.786	19.30 ± 0.24	-0.8 ± 0.8	145 ± 2
HD009709	54029.856	18.38 ± 0.27	-0.3 ± 1.0	151 ± 2
HD010516	53233.921	-14.82 ± 0.89	-198.0 ± 4.6	217 ± 10
HD010516	53236.955	-22.27 ± 0.83	-226.8 ± 3.1	238 ± 7
HD010516	53238.954	-14.50 ± 1.46	-212.3 ± 8.8	198 ± 24
HD010516	53684.771	-9.50 ± 0.58	-228.0 ± 5.1	183 ± 15
HD010516	53686.707	-10.15 ± 0.62	-228.1 ± 5.0	188 ± 14
HD010516	54025.794	-8.53 ± 0.30	-239.2 ± 2.1	171 ± 4
HD010516	54030.796	-7.76 ± 0.19	-250.8 ± 1.4	176 ± 3
HD010516	54031.818	-9.67 ± 0.48	-232.8 ± 2.4	159 ± 5
HD011415	53233.925	...	...	...
HD011415	53236.956	...	...	...
HD011415	53238.954	...	...	...
HD011415	53684.772	...	...	...
HD011415	53688.784	...	...	...

Continued on Next Page...

Table C.3 – Continued

Star Name	HJD (−2,400,000)	W_λ (Å)	V_r (km s^{-1})	FWSM (km s^{-1})
HD011415	54025.796	···	···	···
HD011415	54027.803	···	···	···
HD011415	54029.869	···	···	···
HD011415	54030.799	···	···	···
HD011415	54031.819	···	···	···
HD013661	53235.926	-6.80 ± 0.47	-128.7 ± 6.5	169 ± 22
HD013661	53237.923	-5.73 ± 0.81	-119.8 ± 9.3	128 ± 31
HD013661	53684.794	···	···	···
HD013661	53687.806	···	···	···
HD013661	54025.810	···	···	···
HD013661	54026.830	···	···	···
HD013867	53235.944	-4.67 ± 0.25	-0.4 ± 2.1	121 ± 4
HD013867	53237.940	-7.22 ± 0.45	-24.2 ± 5.1	125 ± 20
HD013867	53685.761	-11.72 ± 0.18	-3.4 ± 0.9	143 ± 2
HD013867	53687.852	-8.30 ± 0.78	-7.2 ± 7.3	115 ± 30
HD013867	54026.814	-9.57 ± 0.46	-15.7 ± 2.3	130 ± 5
HD013867	54030.802	-10.57 ± 0.33	-14.1 ± 1.9	125 ± 6
HD018552	53233.933	5.96 ± 0.45	-15.9 ± 5.3	81 ± 26
HD018552	53236.960	4.84 ± 0.54	-27.3 ± 7.5	62 ± 48
HD018552	53239.012	5.04 ± 0.62	-29.4 ± 10.8	···
HD018552	53684.803	6.01 ± 0.61	-25.6 ± 8.6	···
HD018552	53686.704	5.53 ± 0.37	-14.8 ± 3.6	89 ± 13
HD018552	53686.876	6.08 ± 0.27	-18.8 ± 2.7	85 ± 11
HD018552	54026.802	6.11 ± 0.34	-25.6 ± 2.4	106 ± 6
HD018552	54029.884	6.06 ± 0.26	-12.4 ± 2.2	107 ± 6
HD018552	54031.829	3.84 ± 0.35	-12.9 ± 4.7	88 ± 17
HD019243	53235.956	-49.09 ± 0.90	-7.5 ± 1.4	185 ± 4
HD019243	53237.952	-49.97 ± 1.42	-8.2 ± 2.2	188 ± 6
HD019243	53686.766	-48.48 ± 0.78	-15.9 ± 1.1	194 ± 3
HD019243	54026.845	-48.16 ± 1.92	-45.0 ± 3.2	187 ± 9
HD019243	54027.812	-46.79 ± 1.16	-39.9 ± 2.4	183 ± 8
HD019243	54029.901	-45.27 ± 1.69	-47.6 ± 3.8	174 ± 14
HD020134	53235.969	···	···	···
HD020134	53237.964	···	···	···
HD020134	53686.782	···	···	···
HD020134	54027.827	···	···	···
HD020134	54029.916	···	···	···
HD020336	53234.925	3.81 ± 0.30	28.3 ± 3.3	108 ± 8
HD020336	53237.973	4.14 ± 0.21	16.8 ± 1.9	77 ± 5
HD020336	53239.014	4.82 ± 0.22	28.8 ± 1.7	99 ± 3
HD020336	53684.812	13.73 ± 0.50	25.8 ± 2.8	174 ± 7
HD020336	53685.740	13.40 ± 0.35	20.1 ± 1.9	180 ± 5
HD020336	54026.864	15.57 ± 0.57	5.8 ± 2.9	183 ± 7
HD020336	54029.939	13.85 ± 0.62	20.7 ± 2.8	171 ± 6
HD020336	54031.844	13.42 ± 0.45	31.8 ± 2.2	179 ± 5
HD020418	53234.930	···	···	···
HD020418	53238.956	···	···	···
HD020418	53684.810	···	···	···
HD020418	54026.859	···	···	···
HD020418	54029.935	···	···	···
HD020418	54031.840	···	···	···
HD021362	53234.935	18.20 ± 0.56	6.8 ± 1.9	165 ± 4
HD021362	53238.960	18.58 ± 0.32	2.3 ± 1.1	161 ± 2
HD021362	53684.817	9.79 ± 0.24	15.5 ± 1.4	130 ± 3
HD021362	54026.869	6.14 ± 0.29	8.2 ± 2.8	117 ± 9
HD021362	54029.943	5.87 ± 0.26	18.4 ± 1.9	122 ± 4
HD021362	54031.848	3.66 ± 0.41	9.6 ± 6.9	78 ± 33
HD021455	53236.964	7.60 ± 0.52	7.8 ± 4.4	127 ± 14
HD021455	53238.983	7.17 ± 0.48	3.5 ± 4.4	138 ± 13
HD021455	53684.823	8.02 ± 0.70	16.4 ± 5.1	140 ± 14
HD021455	54026.879	7.24 ± 0.48	-1.6 ± 4.6	156 ± 13
HD021455	54029.950	7.62 ± 0.64	10.6 ± 5.2	129 ± 16
HD021455	54031.856	7.69 ± 0.53	-5.1 ± 5.0	148 ± 15
HD021551	53234.944	···	···	···
HD021551	53238.964	···	···	···
HD021551	53684.828	···	···	···
HD021551	53687.818	···	···	···
HD021551	54026.888	···	···	···
HD021551	54029.957	···	···	···
HD021551	54031.852	···	···	···
HD021641	53236.970	8.86 ± 0.21	2.3 ± 1.5	153 ± 3
HD021641	53238.999	7.53 ± 0.94	-3.4 ± 7.7	···
HD021641	53686.812	7.37 ± 0.35	0.1 ± 2.6	136 ± 7

Continued on Next Page...

Table C.3 – Continued

Star Name	HJD (−2,400,000)	W_λ (Å)	V_r (km s^{-1})	FWSM (km s^{-1})
HD021641	54026.910	8.39 ± 0.40	−6.2 ± 3.0	148 ± 7
HD021641	54029.980	7.28 ± 0.47	12.2 ± 3.6	126 ± 10
HD021641	54031.924	7.26 ± 0.45	2.4 ± 3.8	131 ± 11
HD021650	53236.982	24.04 ± 0.45	2.3 ± 1.4	179 ± 3
HD021650	53686.798	23.21 ± 0.41	−3.6 ± 1.3	174 ± 3
HD021650	54026.897	19.13 ± 0.29	−3.1 ± 1.3	170 ± 3
HD021650	54029.965	20.08 ± 0.31	4.1 ± 1.3	163 ± 4
HD022192	53234.951	−31.07 ± 1.91	1.4 ± 11.1	381 ± 35
HD022192	53238.967	−28.13 ± 1.70	−7.6 ± 11.6	348 ± 42
HD022192	53684.757	−40.41 ± 1.82	−0.4 ± 8.2	458 ± 21
HD022192	53684.963	−41.80 ± 2.24	12.2 ± 9.2	455 ± 24
HD022192	53687.752	−39.20 ± 1.96	−3.5 ± 9.2	450 ± 25
HD022192	53687.922	−34.96 ± 2.38	9.8 ± 12.3	400 ± 37
HD022192	54026.924	−39.38 ± 2.28	−9.5 ± 10.8	450 ± 29
HD022192	54030.824	−37.30 ± 2.43	−1.9 ± 12.2	434 ± 35
HD022192	54031.863	−40.89 ± 2.46	−5.8 ± 11.4	454 ± 32
HD022780	53233.949	...	...	...
HD022780	53237.977	...	...	...
HD022780	53684.834	...	...	...
HD022780	54027.844	...	...	...
HD022780	54030.002	...	...	...
HD022780	54031.865	...	...	...
HD023016	53234.959	9.41 ± 0.40	37.3 ± 5.7	287 ± 17
HD023016	53238.971	8.44 ± 0.46	22.4 ± 8.3	287 ± 27
HD023016	53684.839	9.13 ± 0.37	41.9 ± 3.9	307 ± 8
HD023016	54027.850	9.34 ± 0.26	51.8 ± 3.0	339 ± 6
HD023016	54029.996	8.10 ± 0.47	39.0 ± 6.4	265 ± 17
HD023016	54031.870	8.12 ± 0.38	15.5 ± 8.0	272 ± 30
HD023302	53236.991	9.41 ± 0.64	21.3 ± 5.5	193 ± 14
HD023302	53238.979	9.06 ± 0.70	6.2 ± 7.3	167 ± 26
HD023302	53684.842	8.72 ± 0.60	14.7 ± 4.6	183 ± 11
HD023302	54027.856	9.64 ± 0.43	6.1 ± 3.3	197 ± 7
HD023302	54028.927	10.53 ± 0.36	4.7 ± 2.7	195 ± 7
HD023302	54030.827	10.00 ± 0.52	18.2 ± 3.4	189 ± 7
HD023302	54031.874	8.61 ± 0.75	28.6 ± 4.2	155 ± 9
HD023478	53236.995	...	...	...
HD023478	53684.848	...	...	...
HD023478	54027.861	...	...	...
HD023478	54030.832	...	...	...
HD023478	54031.933	...	...	...
HD023480	53233.940	...	...	...
HD023480	53237.008	...	...	...
HD023480	53238.980	...	...	...
HD023480	53684.761	...	...	...
HD023480	53684.967	...	...	...
HD023480	54027.858	...	...	...
HD023480	54028.925	...	...	...
HD023480	54030.829	...	...	...
HD023480	54031.875	...	...	...
HD023552	53237.981	...	...	...
HD023552	53684.855	...	...	...
HD023552	54027.872	...	...	...
HD023552	54030.845	...	...	...
HD023552	54031.876	...	...	...
HD023630	53234.969	3.07 ± 0.15	9.6 ± 2.0	77 ± 6
HD023630	53234.971	2.57 ± 0.14	10.7 ± 2.6	81 ± 9
HD023630	53238.974	2.93 ± 0.11	−0.3 ± 1.6	83 ± 4
HD023630	53686.843	2.45 ± 0.28	3.6 ± 4.0	46 ± 18
HD023630	54027.882	2.83 ± 0.18	9.2 ± 1.9	82 ± 4
HD023630	54030.871	2.71 ± 0.23	16.2 ± 3.5	87 ± 10
HD023630	54031.886	2.85 ± 0.25	17.2 ± 2.2	81 ± 4
HD023800	53237.991	...	...	...
HD023800	53684.863	...	...	...
HD023800	54027.888	...	...	...
HD023800	54030.853	...	...	...
HD023800	54031.940	...	...	...
HD023862	53234.967	−12.22 ± 1.51	8.2 ± 11.3	202 ± 33
HD023862	53238.976	−12.81 ± 1.34	−0.2 ± 10.1	207 ± 30
HD023862	53686.845	−1.89 ± 1.71	−42.3 ± 94.7	...
HD023862	54027.884	51.98 ± 0.62	−2.9 ± 1.0	146 ± 3
HD023862	54031.887	54.21 ± 0.46	0.3 ± 0.7	148 ± 2
HD024479	53237.000	21.17 ± 0.34	−5.5 ± 1.1	119 ± 3
HD024479	53238.987	20.87 ± 0.43	−10.3 ± 1.4	120 ± 4

Continued on Next Page...

Table C.3 – Continued

Star Name	HJD (−2,400,000)	W_λ (Å)	V_r (km s^{-1})	FWSM (km s^{-1})
HD024479	53686.847	20.38 ± 0.28	−8.3 ± 0.9	112 ± 3
HD024479	54027.904	21.78 ± 0.19	−7.1 ± 0.6	123 ± 1
HD024479	54028.916	22.86 ± 0.29	−6.1 ± 0.8	123 ± 2
HD024479	54030.893	21.32 ± 0.18	−6.1 ± 0.6	125 ± 1
HD024479	54031.896	20.84 ± 0.25	−5.7 ± 0.8	122 ± 2
HD024534	53238.002	−20.12 ± 0.83	−48.0 ± 4.9	284 ± 13
HD024534	53684.872	−20.81 ± 0.91	−53.5 ± 4.8	255 ± 13
HD024534	53687.867	−20.40 ± 0.88	−42.2 ± 4.7	248 ± 13
HD024534	54031.890	−26.23 ± 1.13	−22.2 ± 3.3	216 ± 8
HD025799	53238.011	...	...	...
HD025799	53684.880	...	...	...
HD025799	53688.859	...	...	...
HD025799	54026.931	...	...	...
HD025799	54030.902	...	...	...
HD025799	54031.914	...	...	...
HD025940	53237.002	−24.12 ± 1.36	−8.8 ± 4.4	172 ± 13
HD025940	53238.989	−22.71 ± 1.41	−7.2 ± 4.8	166 ± 15
HD025940	53686.850	−23.36 ± 1.52	−7.5 ± 5.0	165 ± 15
HD025940	53687.905	−25.16 ± 1.15	−9.8 ± 3.6	175 ± 10
HD025940	54026.942	−24.04 ± 1.19	−13.0 ± 4.0	167 ± 12
HD025940	54027.912	−23.83 ± 1.29	−14.6 ± 4.4	166 ± 14
HD025940	54031.902	−23.28 ± 1.28	−12.8 ± 4.4	166 ± 14
HD026670	53237.005	...	...	...
HD026670	53238.992	...	...	...
HD026670	53686.853	...	...	...
HD026670	53688.865	...	...	...
HD026670	54026.945	...	...	...
HD026670	54027.915	...	...	...
HD026670	54030.006	...	...	...
HD026670	54031.902	...	...	...
HD029866	53239.004	22.50 ± 0.32	11.8 ± 1.3	169 ± 3
HD029866	53684.888	23.02 ± 0.27	25.2 ± 1.0	182 ± 2
HD029866	53687.874	23.94 ± 0.39	25.9 ± 1.7	197 ± 5
HD029866	54026.953	20.59 ± 0.38	25.0 ± 1.4	182 ± 3
HD029866	54030.014	21.44 ± 0.32	28.0 ± 1.1	177 ± 2
HD029866	54031.907	22.46 ± 0.50	25.3 ± 1.6	182 ± 4
HD032343	53686.861	−22.57 ± 0.27	2.1 ± 1.0	148 ± 3
HD032343	53687.907	−21.76 ± 0.42	−5.3 ± 1.8	138 ± 7
HD032343	54026.964	−18.21 ± 0.36	−12.0 ± 1.8	124 ± 8
HD032343	54027.921	−17.66 ± 0.54	−11.8 ± 2.5	122 ± 10
HD032343	54030.915	−18.89 ± 0.32	−11.9 ± 1.4	138 ± 5
HD032343	54031.949	−17.48 ± 0.84	−19.4 ± 5.0	102 ± 31
HD036576	53686.866	−19.02 ± 0.78	−43.8 ± 3.0	233 ± 6
HD036576	53687.913	−20.81 ± 1.02	−43.1 ± 3.6	256 ± 7
HD036576	54026.971	−12.44 ± 0.61	−67.3 ± 4.3	168 ± 15
HD036576	54028.928	−13.18 ± 0.90	−56.2 ± 5.6	165 ± 18
HD036576	54031.953	−10.68 ± 0.59	−68.9 ± 5.0	183 ± 16
HD037202	53684.897	22.89 ± 0.94	−26.3 ± 3.5	98 ± 17
HD037202	53687.884	22.23 ± 0.79	−25.4 ± 3.3	81 ± 21
HD037202	54027.010	28.23 ± 1.18	−3.5 ± 2.2	107 ± 6
HD037202	54027.953	27.78 ± 1.08	−3.7 ± 2.2	104 ± 6
HD037202	54030.951	26.63 ± 1.00	−5.3 ± 1.7	95 ± 4
HD037202	54031.973	27.53 ± 1.02	−0.2 ± 1.6	97 ± 4
HD041335	53686.910	−26.48 ± 1.00	−17.7 ± 2.9	270 ± 5
HD041335	53687.917	−27.89 ± 0.91	−1.4 ± 2.8	284 ± 5
HD041335	54027.956	−26.79 ± 1.34	−5.7 ± 4.3	298 ± 8
HD041335	54028.943	−27.21 ± 1.07	−17.3 ± 3.2	294 ± 6
HD041335	54030.942	−28.28 ± 1.09	−17.8 ± 3.6	310 ± 7
HD041335	54031.975	−28.36 ± 1.09	1.0 ± 3.2	289 ± 6
HD058715	53684.971	3.53 ± 0.26	16.2 ± 2.8	67 ± 9
HD058715	53688.024	3.64 ± 0.27	15.4 ± 3.3	87 ± 10
HD058715	53688.992	3.84 ± 0.11	13.2 ± 1.0	83 ± 2
HD058715	54027.035	3.61 ± 0.07	16.2 ± 0.7	92 ± 1
HD058715	54028.981	3.86 ± 0.11	11.2 ± 1.3	102 ± 3
HD058715	54030.976	3.70 ± 0.12	13.5 ± 1.2	100 ± 3
HD058715	54031.990	3.20 ± 0.09	7.3 ± 1.4	93 ± 4
HD058978	53684.967	−39.97 ± 1.51	−53.4 ± 4.3	539 ± 6
HD058978	53687.923	−43.39 ± 2.10	−46.5 ± 7.2	539 ± 14
HD058978	53688.988	−44.25 ± 1.66	−47.4 ± 5.7	543 ± 11
HD058978	54027.968	−37.13 ± 0.91	−7.0 ± 3.9	518 ± 8
HD058978	54028.973	−36.16 ± 1.29	−9.0 ± 5.4	525 ± 10
HD058978	54030.969	−28.42 ± 2.32	−18.0 ± 18.3	455 ± 58
HD058978	54031.986	−31.87 ± 2.41	21.4 ± 12.3	458 ± 30

Continued on Next Page...

Table C.3 – Continued

Star Name	HJD (−2,400,000)	W_λ (Å)	V_r (km s^{-1})	FWSM (km s^{-1})
HD060855	53684.973	-19.11 ± 0.88	-72.6 ± 4.6	215 ± 13
HD060855	53688.994	-19.89 ± 0.87	-74.1 ± 3.7	208 ± 9
HD060855	54028.983	-14.50 ± 1.00	-92.7 ± 6.4	149 ± 25
HD060855	54030.978	-14.81 ± 1.01	-79.7 ± 6.6	169 ± 24
HD060855	54031.991	-15.21 ± 1.20	-73.3 ± 6.9	174 ± 22
HD149757	54031.543	3.41 ± 0.27	-139.2 ± 1.4	···
HD149757	54031.545	2.83 ± 0.17	-145.3 ± 1.7	64 ± 4
HD162428	53234.651	16.43 ± 0.42	-34.6 ± 2.2	245 ± 5
HD162428	53237.629	16.90 ± 0.63	-12.0 ± 3.6	278 ± 8
HD162428	54028.573	15.88 ± 0.22	-12.3 ± 1.1	167 ± 2
HD162732	53234.704	87.22 ± 2.06	-9.0 ± 1.6	105 ± 4
HD162732	53237.640	86.20 ± 2.30	-8.1 ± 1.9	104 ± 5
HD162732	53688.548	85.31 ± 2.14	-0.8 ± 1.6	101 ± 4
HD162732	54027.570	82.05 ± 2.01	-6.0 ± 1.5	97 ± 4
HD164284	53234.641	1.90 ± 0.18	-17.6 ± 3.3	38 ± 18
HD164284	53237.620	0.93 ± 0.24	16.8 ± 12.5	···
HD164284	53684.544	0.87 ± 0.21	-44.9 ± 4.4	···
HD164284	54027.582	3.23 ± 0.29	0.5 ± 3.7	92 ± 10
HD164284	54030.570	2.39 ± 0.18	0.5 ± 4.4	127 ± 12
HD164447	53234.716	4.93 ± 0.58	-51.8 ± 4.6	108 ± 10
HD164447	53237.649	5.34 ± 0.51	-45.1 ± 4.5	119 ± 10
HD164447	53686.545	5.13 ± 0.48	-37.9 ± 3.9	119 ± 8
HD164447	54028.586	6.35 ± 0.59	-37.7 ± 3.9	123 ± 8
HD164447	54030.574	7.88 ± 0.53	-29.3 ± 3.6	151 ± 7
HD166014	53234.698	22.40 ± 0.58	-21.8 ± 2.5	203 ± 7
HD166014	53237.653	22.46 ± 0.40	-14.4 ± 1.6	206 ± 4
HD166014	53238.616	22.23 ± 0.38	-21.1 ± 1.7	201 ± 5
HD166014	53683.573	21.76 ± 0.44	-18.3 ± 2.1	194 ± 6
HD166014	54027.587	22.75 ± 0.48	-16.8 ± 1.8	212 ± 4
HD166014	54030.583	24.44 ± 0.34	-15.2 ± 1.3	208 ± 3
HD166014	54031.552	23.82 ± 0.49	-16.8 ± 1.9	215 ± 5
HD168797	53234.725	···	···	···
HD168797	53237.658	···	···	···
HD168797	53686.549	···	···	···
HD168797	54027.590	···	···	···
HD168797	54031.558	···	···	···
HD168957	53235.715	7.72 ± 0.28	-24.7 ± 1.4	67 ± 4
HD168957	53238.624	7.51 ± 0.30	-27.0 ± 1.3	60 ± 4
HD168957	53687.546	7.60 ± 0.33	-27.0 ± 1.4	66 ± 4
HD168957	54029.599	7.32 ± 0.39	-29.3 ± 2.2	55 ± 9
HD171406	53235.727	5.92 ± 0.20	-18.5 ± 1.4	70 ± 5
HD171406	53238.635	3.03 ± 0.35	-81.4 ± 3.2	49 ± 11
HD171406	53687.561	8.93 ± 0.77	-15.6 ± 2.6	70 ± 6
HD171406	54028.596	3.01 ± 0.42	-66.0 ± 3.6	46 ± 12
HD171780	53234.732	···	···	···
HD171780	53237.664	···	···	···
HD171780	53686.555	···	···	···
HD171780	54028.605	···	···	···
HD173370	53234.739	10.48 ± 0.56	-1.1 ± 4.3	220 ± 10
HD173370	53237.670	8.71 ± 0.61	-17.4 ± 4.5	224 ± 8
HD173370	53683.579	13.77 ± 0.47	-27.9 ± 3.3	266 ± 7
HD173370	54027.599	12.25 ± 0.72	-12.6 ± 4.7	252 ± 9
HD173370	54030.585	11.43 ± 0.28	23.3 ± 2.4	244 ± 6
HD174237	53235.734	-6.57 ± 0.70	25.1 ± 8.4	171 ± 24
HD174237	53238.640	0.33 ± 0.90	···	···
HD174237	53684.552	-5.68 ± 0.79	-10.4 ± 13.1	82 ± 91
HD174237	54028.613	1.36 ± 0.24	79.0 ± 7.2	97 ± 18
HD174237	54031.568	-3.72 ± 0.36	19.7 ± 6.6	67 ± 39
HD174638	53234.695	87.56 ± 1.52	-4.3 ± 1.8	196 ± 5
HD174638	53234.696	89.25 ± 1.15	-5.5 ± 1.4	203 ± 4
HD174638	53237.671	28.37 ± 0.35	-193.4 ± 0.6	79 ± 1
HD174638	53238.662	31.32 ± 0.62	-194.1 ± 1.1	73 ± 3
HD174638	53683.577	31.83 ± 0.68	156.9 ± 1.1	73 ± 3
HD174638	54027.605	28.22 ± 0.63	-195.7 ± 1.1	75 ± 2
HD174638	54028.620	32.21 ± 0.57	-173.6 ± 0.9	75 ± 2
HD174638	54030.590	51.63 ± 0.48	-27.8 ± 0.4	75 ± 1
HD174638	54031.555	49.05 ± 0.37	55.4 ± 0.3	78 ± 0
HD175863	53235.744	···	···	···
HD175863	53238.668	···	···	···
HD175863	53688.562	···	···	···
HD175863	54028.623	···	···	···
HD175869	53234.744	12.28 ± 0.31	5.2 ± 2.0	177 ± 5
HD175869	53237.675	12.51 ± 0.26	2.1 ± 1.6	180 ± 4

Continued on Next Page...

Table C.3 – Continued

Star Name	HJD (−2,400,000)	W_λ (Å)	V_r (km s^{-1})	FWSM (km s^{-1})
HD175869	53684.554	12.33 ± 0.12	5.5 ± 0.9	200 ± 2
HD175869	54029.613	13.98 ± 0.07	−6.1 ± 0.4	188 ± 1
HD175869	54031.574	13.62 ± 0.20	0.5 ± 1.3	196 ± 3
HD177648	53237.683	...	...	...
HD177648	53687.573	...	...	...
HD177648	54028.636	...	...	...
HD178475	53234.746	24.73 ± 0.96	−22.7 ± 4.4	199 ± 15
HD178475	53237.705	16.67 ± 0.47	−36.1 ± 3.0	194 ± 10
HD178475	53686.560	1.43 ± 0.18	−10.9 ± 3.9	...
HD178475	54027.608	1.09 ± 0.54	24.8 ± 14.2	...
HD178475	54031.580	1.85 ± 0.24	−26.3 ± 8.7	71 ± 48
HD179343	53237.699	65.19 ± 2.06	−17.2 ± 2.0	106 ± 6
HD179343	53684.560	67.04 ± 2.08	−14.3 ± 2.1	112 ± 6
HD179343	54029.619	63.98 ± 2.07	−20.3 ± 1.9	105 ± 5
HD181409	53235.756	...	...	...
HD181409	53238.679	...	...	...
HD181409	53238.685	...	...	...
HD181409	53687.585	...	...	...
HD181409	54028.655	...	...	...
HD181615	54031.584	61.39 ± 0.29	−138.9 ± 0.3	66 ± 0
HD183362	53235.762	−25.70 ± 1.43	−30.0 ± 6.6	394 ± 13
HD183362	53687.594	−22.97 ± 1.25	−21.8 ± 5.8	349 ± 11
HD183362	54029.634	−25.19 ± 1.28	−20.1 ± 6.2	360 ± 14
HD183656	53234.753	53.28 ± 2.10	−56.4 ± 2.1	85 ± 6
HD183656	53237.712	55.25 ± 2.27	−56.1 ± 2.2	89 ± 6
HD183656	53686.564	48.69 ± 1.97	−16.4 ± 2.0	83 ± 6
HD183656	54029.641	79.80 ± 2.71	18.0 ± 2.1	105 ± 5
HD183914	53234.759	...	...	...
HD183914	53237.715	...	...	...
HD183914	53684.568	...	...	...
HD183914	54027.621	...	...	...
HD183914	54031.591	...	...	...
HD184279	53237.724	28.17 ± 1.08	−16.6 ± 2.2	32 ± 22
HD184279	53688.570	30.61 ± 0.75	−23.1 ± 1.3	61 ± 6
HD184279	54029.648	32.07 ± 0.68	−19.9 ± 1.1	72 ± 4
HD185037	53234.762	7.98 ± 0.13	−14.2 ± 1.0	145 ± 2
HD185037	53237.731	7.50 ± 0.20	−11.0 ± 1.4	133 ± 3
HD185037	53684.575	8.41 ± 0.12	−5.9 ± 1.0	143 ± 2
HD185037	54029.662	8.65 ± 0.22	−11.0 ± 1.4	139 ± 3
HD185037	54031.596	6.21 ± 0.11	−3.3 ± 0.9	125 ± 2
HD187567	53235.771	−17.28 ± 0.97	−17.9 ± 6.3	251 ± 18
HD187567	53238.693	−17.95 ± 0.82	−30.1 ± 5.8	278 ± 16
HD187567	53686.569	−19.04 ± 1.07	−3.5 ± 5.1	240 ± 13
HD187567	54029.671	−19.70 ± 0.95	−40.5 ± 5.8	219 ± 20
HD187811	53234.768	...	...	...
HD187811	53237.736	...	...	...
HD187811	53684.578	...	...	...
HD187811	54027.626	...	...	...
HD187811	54031.603	...	...	...
HD187851	53236.774	...	...	...
HD187851	53688.586	...	...	...
HD187851	54028.665	...	...	...
HD189687	53234.771	...	...	...
HD189687	53237.737	...	...	...
HD189687	53684.581	...	...	...
HD189687	54027.631	...	...	...
HD189687	54031.608	...	...	...
HD191610	53233.802	...	...	...
HD191610	53237.740	...	...	...
HD191610	53684.584	...	...	...
HD191610	54031.613	...	...	...
HD192044	53234.776	−6.20 ± 0.47	−13.9 ± 8.1	362 ± 15
HD192044	53237.759	−5.67 ± 0.67	−72.8 ± 15.1	320 ± 38
HD192044	53686.576	−5.74 ± 0.35	−40.7 ± 7.3	328 ± 16
HD192044	54027.635	−5.90 ± 0.46	−12.9 ± 8.2	352 ± 16
HD192044	54031.617	−5.72 ± 0.37	−22.9 ± 7.4	349 ± 15
HD192445	53233.818	−17.26 ± 1.26	49.7 ± 8.5	217 ± 29
HD192445	53238.703	−17.30 ± 0.78	54.2 ± 3.8	227 ± 9
HD192445	53687.615	−18.35 ± 1.29	26.2 ± 8.9	240 ± 30
HD192445	54029.683	−17.47 ± 1.46	63.0 ± 9.4	233 ± 29
HD192685	53234.779	...	...	...
HD192685	53237.762	...	...	...
HD192685	53684.586	...	...	...

Continued on Next Page...

Table C.3 – Continued

Star Name	HJD (−2,400,000)	W_λ (Å)	V_r (km s^{-1})	FWSM (km s^{-1})
HD192685	54027.642	...	...	...
HD192685	54030.594	...	...	...
HD193009	53234.793	-19.31 ± 0.99	41.6 ± 4.4	237 ± 10
HD193009	53238.717	-26.27 ± 0.58	2.4 ± 2.5	276 ± 6
HD193009	53687.630	-23.08 ± 0.97	-1.6 ± 3.1	275 ± 5
HD193009	54027.646	-26.49 ± 0.84	-22.9 ± 3.3	271 ± 8
HD193182	53234.805	74.86 ± 1.69	-20.1 ± 1.4	68 ± 5
HD193182	53238.727	75.84 ± 1.60	-21.5 ± 1.3	67 ± 5
HD193182	53687.646	74.80 ± 1.68	-20.7 ± 1.3	66 ± 5
HD193182	54029.697	75.29 ± 1.78	-20.9 ± 1.4	67 ± 5
HD193911	53234.783	-2.98 ± 0.15	-19.1 ± 3.9	258 ± 7
HD193911	53238.733	-3.23 ± 0.32	-23.3 ± 9.1	247 ± 21
HD193911	53684.589	-5.31 ± 0.34	-12.2 ± 5.2	250 ± 11
HD193911	54026.622	-5.23 ± 0.29	-17.0 ± 4.8	244 ± 10
HD193911	54027.661	-3.36 ± 0.33	-24.9 ± 9.5	266 ± 21
HD193911	54031.634	-3.94 ± 0.17	-28.9 ± 3.5	241 ± 7
HD194244	53235.778	16.27 ± 0.72	-5.9 ± 4.1	199 ± 12
HD194244	53238.738	17.97 ± 0.70	-1.8 ± 3.5	234 ± 8
HD194244	53686.587	16.20 ± 0.68	-7.8 ± 4.0	221 ± 10
HD194244	54027.673	15.04 ± 0.53	11.1 ± 2.9	187 ± 8
HD194244	54031.646	16.47 ± 0.70	2.2 ± 3.7	217 ± 9
HD194335	53234.813	-11.85 ± 0.54	33.3 ± 5.4	519 ± 8
HD194335	53238.741	-15.64 ± 0.61	10.8 ± 5.1	510 ± 9
HD194335	53686.582	-3.73 ± 0.30	134.6 ± 5.6	411 ± 7
HD194335	54027.667	-6.70 ± 0.40	59.6 ± 7.9	532 ± 13
HD194335	54031.640	-6.64 ± 0.30	21.2 ± 6.2	533 ± 10
HD194883	53235.785	-11.91 ± 0.80	-62.4 ± 8.9	206 ± 36
HD194883	53688.606	-12.81 ± 0.76	-20.4 ± 6.1	221 ± 18
HD194883	54028.685	-15.06 ± 0.84	-49.9 ± 6.5	233 ± 20
HD195325	53234.821	65.98 ± 1.95	-6.3 ± 1.6	82 ± 5
HD195325	53238.747	66.90 ± 1.97	-7.3 ± 1.6	84 ± 5
HD195325	53687.652	64.98 ± 1.92	-7.4 ± 1.6	80 ± 5
HD195325	54027.689	62.77 ± 1.85	-7.8 ± 1.6	80 ± 5
HD195325	54031.661	62.13 ± 2.00	-6.5 ± 1.7	79 ± 5
HD195554	53235.797	6.98 ± 0.70	3.7 ± 8.9	150 ± 31
HD195554	53238.749	6.21 ± 0.49	-23.2 ± 4.0	136 ± 9
HD195554	53684.613	5.16 ± 0.52	-20.1 ± 4.9	139 ± 10
HD195554	54027.681	6.03 ± 0.57	-23.2 ± 7.9	157 ± 25
HD195554	54031.655	5.49 ± 0.69	6.8 ± 7.0	...
HD197419	53235.804	...	...	...
HD197419	53238.756	...	...	...
HD197419	53686.595	...	...	...
HD197419	54028.701	...	...	...
HD198183	53234.825	5.40 ± 0.44	-1.1 ± 14.8	141 ± 110
HD198183	53237.764	5.84 ± 0.30	16.2 ± 6.3	205 ± 23
HD198183	53684.616	5.86 ± 0.42	36.9 ± 8.9	234 ± 29
HD198183	54026.613	5.35 ± 0.27	25.5 ± 5.5	178 ± 21
HD198183	54030.598	6.13 ± 0.40	31.3 ± 6.8	239 ± 19
HD198183	54031.669	4.77 ± 0.44	40.2 ± 10.0	182 ± 38
HD198625	53235.810	...	...	...
HD198625	53238.761	...	...	...
HD198625	53686.603	...	...	...
HD198625	54027.698	...	...	...
HD199218	53234.832	15.57 ± 1.17	-15.1 ± 4.9	160 ± 12
HD199218	53237.813	16.55 ± 1.06	-12.2 ± 5.0	162 ± 14
HD199218	53688.634	15.56 ± 0.90	-13.5 ± 3.7	162 ± 9
HD199218	54030.601	16.03 ± 0.95	-8.9 ± 3.5	157 ± 8
HD199356	53236.798	-57.74 ± 1.16	-1.4 ± 3.3	477 ± 7
HD199356	53688.647	-57.68 ± 1.02	-4.5 ± 3.1	482 ± 7
HD199356	54030.612	-55.99 ± 1.29	-21.7 ± 3.6	480 ± 8
HD200120	53234.836	-22.00 ± 0.90	-41.4 ± 8.7	504 ± 23
HD200120	53237.765	-20.39 ± 0.69	-41.7 ± 6.9	477 ± 18
HD200120	53684.619	-20.64 ± 0.60	-2.3 ± 5.6	500 ± 13
HD200120	54026.607	-17.56 ± 0.50	-16.5 ± 5.9	427 ± 17
HD200120	54031.681	-27.15 ± 0.56	4.7 ± 3.5	471 ± 8
HD200310	53234.839	...	...	...
HD200310	53237.767	...	...	...
HD200310	53684.625	...	...	...
HD200310	54026.600	...	...	...
HD200310	54031.684	...	...	...
HD201522	53237.777	...	...	...
HD201522	53688.666	...	...	...
HD201522	54030.637	...	...	...

Continued on Next Page...

Table C.3 – Continued

Star Name	HJD (−2,400,000)	W_λ (Å)	V_r (km s^{-1})	FWSM (km s^{-1})
HD201733	53235.817	···	···	···
HD201733	53238.767	···	···	···
HD201733	53686.613	···	···	···
HD201733	54030.659	···	···	···
HD202904	53234.843	-30.34 ± 1.28	1.5 ± 3.9	220 ± 11
HD202904	53237.788	-31.05 ± 1.42	-10.2 ± 4.6	217 ± 14
HD202904	53684.628	-23.15 ± 1.00	-9.1 ± 5.0	205 ± 18
HD202904	54025.622	-16.72 ± 0.95	-5.2 ± 5.4	223 ± 15
HD202904	54025.626	-17.30 ± 0.72	-8.7 ± 3.8	237 ± 10
HD202904	54031.689	-18.51 ± 0.98	-20.2 ± 5.9	203 ± 21
HD203025	53236.808	···	···	···
HD203025	53238.778	···	···	···
HD203025	53687.662	···	···	···
HD203025	54030.668	···	···	···
HD203064	53234.845	···	···	···
HD203064	53237.819	···	···	···
HD203064	53684.631	···	···	···
HD203064	54025.631	···	···	···
HD203064	54031.692	···	···	···
HD203374	53236.817	-34.50 ± 0.92	-47.0 ± 1.8	215 ± 14
HD203374	53687.673	-26.79 ± 2.28	-33.7 ± 6.9	156 ± 25
HD203374	54025.640	-26.75 ± 1.52	-34.1 ± 4.7	197 ± 13
HD203374	54025.649	-25.18 ± 1.58	-32.5 ± 4.4	186 ± 12
HD203467	53236.824	-28.76 ± 1.41	-7.2 ± 4.4	226 ± 11
HD203467	53238.771	-25.42 ± 1.21	-20.0 ± 4.8	229 ± 14
HD203467	53684.657	-32.82 ± 1.17	-23.3 ± 3.4	232 ± 9
HD203467	54027.707	-26.53 ± 1.02	-44.5 ± 4.2	219 ± 14
HD203467	54031.698	-35.73 ± 0.57	-15.6 ± 1.2	232 ± 2
HD203699	53234.852	-24.68 ± 0.69	10.2 ± 2.4	249 ± 5
HD203699	53237.827	-22.98 ± 1.14	3.6 ± 4.2	230 ± 10
HD203699	53686.621	-12.90 ± 0.50	-0.6 ± 2.9	187 ± 7
HD203699	54028.712	-4.57 ± 0.55	-22.6 ± 11.9	123 ± 56
HD203731	53236.836	-32.16 ± 0.58	-44.5 ± 2.8	510 ± 6
HD203731	53688.687	-43.70 ± 0.95	-58.8 ± 3.2	522 ± 6
HD203731	54027.713	-36.66 ± 0.89	-17.9 ± 4.5	550 ± 10
HD204116	53237.798	-23.74 ± 1.62	-42.5 ± 6.7	166 ± 26
HD204116	53688.707	-22.26 ± 1.30	-32.6 ± 5.7	170 ± 21
HD204116	54028.724	-17.45 ± 1.00	-36.1 ± 7.0	230 ± 24
HD204722	53236.853	-26.60 ± 0.81	-12.1 ± 4.2	526 ± 7
HD204722	53687.686	-30.47 ± 0.82	-46.6 ± 4.5	513 ± 9
HD204722	54030.679	-16.73 ± 0.67	-3.0 ± 6.1	457 ± 13
HD204860	53235.835	1.09 ± 0.14	-9.1 ± 5.7	99 ± 16
HD204860	53238.792	0.28 ± 0.14	···	···
HD204860	53686.630	34.40 ± 0.72	-8.0 ± 2.2	174 ± 7
HD204860	54030.697	1.95 ± 0.18	26.3 ± 3.6	86 ± 10
HD205060	53236.869	13.73 ± 1.14	-32.0 ± 7.6	114 ± 36
HD205060	53238.871	15.58 ± 0.63	-23.4 ± 3.5	159 ± 11
HD205060	53688.728	21.96 ± 1.53	-19.1 ± 8.3	111 ± 52
HD205060	54030.711	12.69 ± 1.87	32.0 ± 9.7	···
HD205551	53235.824	11.13 ± 0.33	-28.3 ± 1.8	153 ± 4
HD205551	53237.831	9.97 ± 0.25	-28.1 ± 1.7	154 ± 4
HD205551	53686.638	9.02 ± 0.35	-22.9 ± 2.2	128 ± 6
HD205551	54029.763	9.15 ± 0.46	-26.1 ± 2.8	137 ± 7
HD205551	54031.704	9.77 ± 0.39	-16.4 ± 2.6	163 ± 6
HD206773	53236.882	···	···	···
HD206773	53238.883	···	···	···
HD206773	53688.740	···	···	···
HD206773	54030.726	···	···	···
HD207232	53235.870	41.78 ± 1.46	-35.5 ± 5.8	103 ± 54
HD207232	53238.804	49.64 ± 1.21	-7.4 ± 2.6	216 ± 8
HD207232	53687.702	63.58 ± 0.43	-34.0 ± 0.6	189 ± 1
HD207232	54030.739	61.10 ± 0.88	-35.7 ± 1.1	165 ± 3
HD208057	53234.857	···	···	···
HD208057	53237.837	···	···	···
HD208057	53684.669	···	···	···
HD208057	54027.728	···	···	···
HD208057	54030.753	···	···	···
HD208057	54031.712	···	···	···
HD208392	53235.883	···	···	···
HD208392	53238.833	···	···	···
HD208392	53686.651	···	···	···
HD208392	54027.734	···	···	···
HD208682	53235.842	···	···	···

Continued on Next Page...

Table C.3 – Continued

Star Name	HJD (−2,400,000)	W_λ (Å)	V_r (km s^{-1})	FWSM (km s^{-1})
HD208682	53238.859	···	···	···
HD208682	53684.673	···	···	···
HD208682	54027.748	···	···	···
HD208682	54031.715	···	···	···
HD210129	53235.851	-0.54 ± 0.47	···	···
HD210129	53238.846	-0.44 ± 0.48	···	···
HD210129	53684.678	-3.83 ± 0.63	6.1 ± 5.2	66 ± 19
HD210129	54025.662	-9.97 ± 0.56	-68.2 ± 4.6	188 ± 12
HD210129	54031.734	-9.40 ± 0.65	-74.7 ± 6.3	184 ± 20
HD212044	53235.857	-24.10 ± 1.25	-34.9 ± 6.0	195 ± 23
HD212044	53238.852	-24.10 ± 1.97	-11.4 ± 7.9	198 ± 26
HD212044	53686.664	-18.44 ± 1.28	-51.5 ± 7.8	175 ± 31
HD212044	54025.675	···	···	···
HD212044	54025.689	···	···	···
HD212076	53233.833	-29.52 ± 0.61	4.0 ± 1.5	181 ± 4
HD212076	53236.894	-31.26 ± 0.77	6.7 ± 1.7	188 ± 4
HD212076	53238.894	-31.08 ± 0.69	16.8 ± 1.4	181 ± 3
HD212076	53684.682	-44.49 ± 0.87	18.5 ± 1.2	175 ± 3
HD212076	53687.731	-45.02 ± 0.97	11.3 ± 1.4	175 ± 3
HD212076	54027.760	-41.40 ± 0.41	8.5 ± 0.7	171 ± 1
HD212076	54031.740	-40.50 ± 0.72	4.9 ± 1.2	164 ± 3
HD212571	53233.838	···	···	···
HD212571	53236.896	···	···	···
HD212571	53238.896	···	···	···
HD212571	53684.611	···	···	···
HD212571	53684.694	···	···	···
HD212571	53684.733	···	···	···
HD212571	53685.707	···	···	···
HD212571	53685.749	···	···	···
HD212571	53686.545	···	···	···
HD212571	53686.609	···	···	···
HD212571	53686.643	···	···	···
HD212571	53686.692	···	···	···
HD212571	53686.717	···	···	···
HD212571	53687.559	···	···	···
HD212571	53687.641	···	···	···
HD212571	53687.695	···	···	···
HD212571	53687.729	···	···	···
HD212571	53688.558	···	···	···
HD212571	53688.599	···	···	···
HD212571	53688.641	···	···	···
HD212571	53688.677	···	···	···
HD212571	53688.720	···	···	···
HD212571	54025.703	···	···	···
HD212571	54031.746	···	···	···
HD212791	53234.865	···	···	···
HD212791	53237.846	···	···	···
HD212791	53687.718	···	···	···
HD212791	54028.755	···	···	···
HD214167	53233.849	···	···	···
HD214167	53236.898	···	···	···
HD214167	53238.897	···	···	···
HD214167	53684.686	···	···	···
HD214167	53687.736	···	···	···
HD214167	54028.788	···	···	···
HD214167	54029.774	···	···	···
HD214167	54031.752	···	···	···
HD214168	53234.888	···	···	···
HD214168	53236.902	···	···	···
HD214168	53238.902	···	···	···
HD214168	53684.691	···	···	···
HD214168	54028.779	···	···	···
HD214168	54031.757	···	···	···
HD216057	53233.878	···	···	···
HD216057	53236.904	···	···	···
HD216057	53238.905	···	···	···
HD216057	53684.699	···	···	···
HD216057	54025.708	···	···	···
HD216057	54029.781	···	···	···
HD216200	53233.872	6.04 ± 0.46	115.1 ± 3.2	48 ± 16
HD216200	53236.912	2.31 ± 0.12	87.6 ± 2.1	55 ± 9
HD216200	53238.911	3.86 ± 0.17	-143.1 ± 1.3	61 ± 3
HD216200	53685.711	7.30 ± 0.35	-63.5 ± 1.6	54 ± 6

Continued on Next Page...

Table C.3 – Continued

Star Name	HJD (−2,400,000)	W_λ (Å)	V_r (km s^{-1})	FWSM (km s^{-1})
HD216200	54028.795	7.17 ± 0.44	−55.2 ± 2.1	50 ± 9
HD216200	54029.790	8.67 ± 0.19	37.1 ± 0.7	73 ± 2
HD216200	54031.766	5.22 ± 0.35	155.5 ± 1.9	51 ± 6
HD217050	53233.857	42.90 ± 0.62	−22.4 ± 1.1	118 ± 3
HD217050	53236.914	44.25 ± 0.56	−24.8 ± 0.9	120 ± 3
HD217050	53238.915	41.51 ± 0.51	−21.9 ± 1.0	118 ± 3
HD217050	53684.704	52.33 ± 0.65	−15.3 ± 0.8	100 ± 2
HD217050	54028.802	61.43 ± 0.40	45.3 ± 0.7	152 ± 2
HD217050	54029.798	64.05 ± 0.52	45.3 ± 0.9	154 ± 3
HD217050	54031.772	57.02 ± 0.43	44.1 ± 0.8	146 ± 3
HD217543	53233.886	···	···	···
HD217543	53236.919	···	···	···
HD217543	53238.920	···	···	···
HD217543	53684.708	···	···	···
HD217543	54028.808	···	···	···
HD217543	54029.804	···	···	···
HD217675	53233.864	···	···	···
HD217675	53236.925	···	···	···
HD217675	53238.923	···	···	···
HD217675	53684.712	···	···	···
HD217675	54028.819	···	···	···
HD217675	54029.772	···	···	···
HD217675	54031.777	···	···	···
HD217891	53233.843	···	···	···
HD217891	53236.929	···	···	···
HD217891	53238.927	···	···	···
HD217891	53684.575	···	···	···
HD217891	53684.724	···	···	···
HD217891	53684.726	···	···	···
HD217891	54027.765	···	···	···
HD217891	54031.780	···	···	···
HD218393	53234.899	39.03 ± 0.58	1.9 ± 1.2	164 ± 3
HD218393	53237.865	65.85 ± 0.79	4.9 ± 0.8	117 ± 2
HD218393	53684.718	32.45 ± 0.67	0.5 ± 0.9	88 ± 2
HD218393	54025.720	29.57 ± 0.35	−12.9 ± 0.7	108 ± 1
HD218393	54031.784	50.06 ± 0.38	−14.3 ± 0.5	124 ± 1
HD218674	53233.906	4.43 ± 0.10	−17.8 ± 1.5	152 ± 4
HD218674	53236.931	3.45 ± 0.13	−18.6 ± 2.0	122 ± 5
HD218674	53238.929	4.04 ± 0.23	−7.6 ± 3.7	108 ± 13
HD218674	53685.717	3.52 ± 0.15	−4.0 ± 2.8	118 ± 9
HD218674	54027.768	0.48 ± 0.35	···	···
HD218674	54031.797	0.70 ± 0.30	···	···
HD224544	53233.892	···	···	···
HD224544	53236.940	···	···	···
HD224544	53238.938	···	···	···
HD224544	53684.731	···	···	···
HD224544	53686.712	···	···	···
HD224544	54027.792	···	···	···
HD224544	54029.827	···	···	···
HD224559	53233.898	−32.71 ± 1.32	−17.0 ± 7.7	507 ± 19
HD224559	53236.944	−39.33 ± 0.30	0.2 ± 1.2	520 ± 2
HD224559	53238.943	−32.53 ± 1.09	−11.1 ± 6.2	510 ± 14
HD224559	53684.749	−45.50 ± 0.72	20.6 ± 2.8	525 ± 6
HD224559	53687.745	−40.78 ± 0.70	5.8 ± 2.8	507 ± 6
HD224559	54027.781	−46.67 ± 0.87	−3.9 ± 3.2	515 ± 7
HD224559	54029.816	−44.09 ± 0.84	2.5 ± 2.8	510 ± 5
HD225095	53235.899	−41.77 ± 0.89	−32.9 ± 1.7	199 ± 4
HD225095	53237.881	−42.49 ± 1.19	−38.6 ± 2.5	187 ± 8
HD225095	53685.727	−43.79 ± 1.17	−28.9 ± 2.2	212 ± 6
HD225095	53688.772	−40.32 ± 1.14	−31.4 ± 2.5	205 ± 7
HD225095	54025.744	−45.14 ± 0.91	−33.1 ± 1.6	206 ± 4
HD225095	54030.762	−45.71 ± 1.10	−34.7 ± 1.8	199 ± 4

C.4 Spectra and Notes for Individual Stars

HD000144

Classical Be Star

- Other Names: HR 7, 10 Cas
- Spectral Type: B9 IIIe
- V magnitude: 5.54
- In WDS?: no
- Known spectroscopic binary?: no
- Velocity variations seen in these data?: very small if there

	Hα	He I λ6678	Hγ	He I λ4471	Mg II λ4481	Fe II ccfs
Mean RV (km s^{-1})	-1.5	0.0	-5.0	-10.8	-4.5	-1.1
RV range (km s^{-1})	-9.1 to 6.5	-14.4 to 14.4	-9.5 to -2.0	-15.3 to -5.7	-7.0 to -1.6	-8.7 to 5.6
RV change (km s^{-1})	15.6	28.8	7.5	9.6	5.4	14.3

- Shell classification: squarish
- Do shell features move with the star?: N/A
- Notes on emission and absorption features: seems to be emission "horns" in He I λ6678 so velocity variations are likely spurious
- Other notes: This star is also plotted in Figure 7.3.

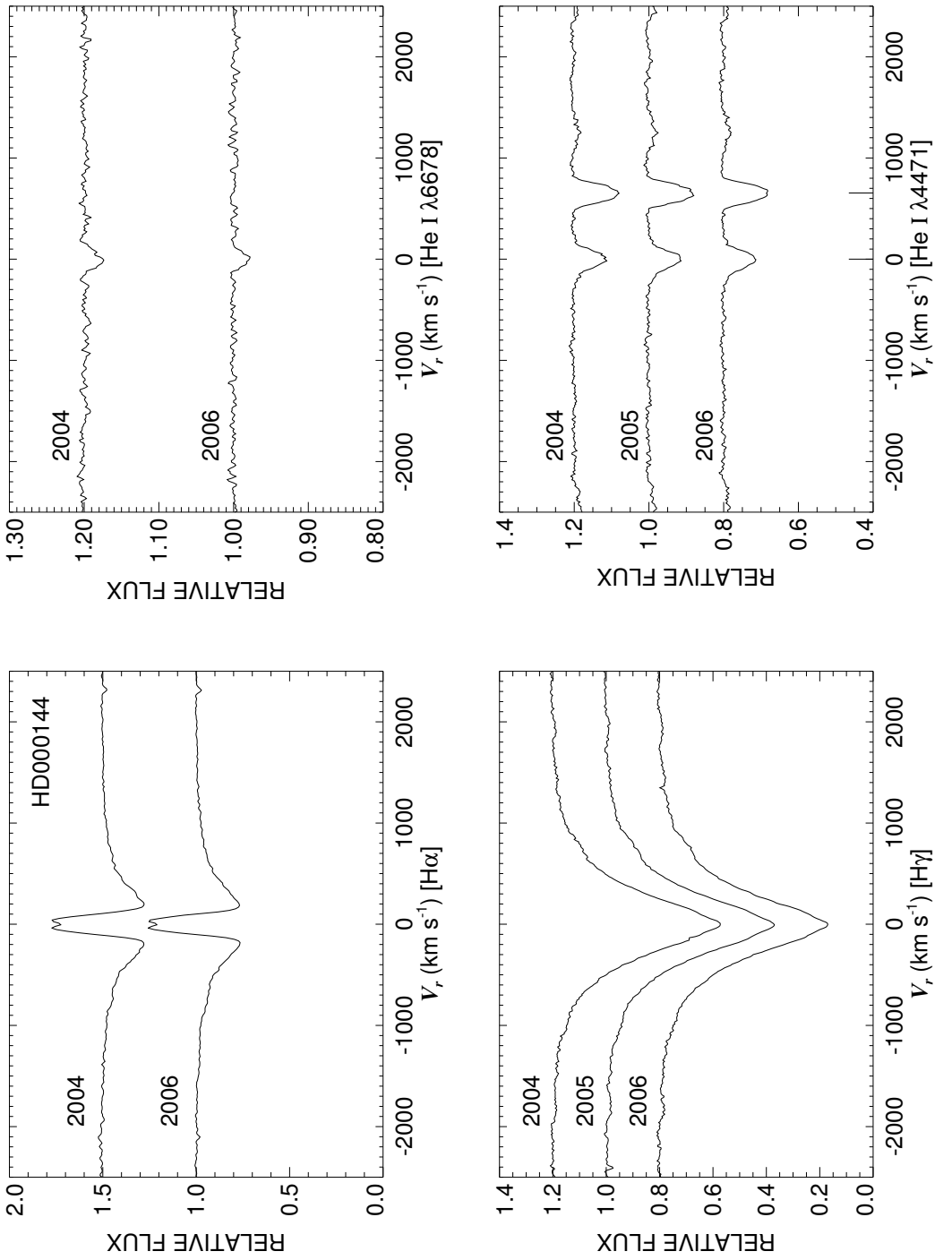

Figure C.1: A quadruple plot of HD000144 as described in §7.2.3 and Figure 7.6.

HD004180

Classical Be Star

- Other Names: HR 193, 22 Cas, *o* Cas
- Spectral Type: B2 Ve
- V magnitude: 4.43
- In WDS?: no
- Known spectroscopic binary?: maybe - Koubský et al. (2004) revive the binary theory with a period of 1031.3 d, others have argued the variations are likely due to long-term variations in the circumstellar Be disk.
- Velocity variations seen in these data?: yes (see Fig. C.3 esp. Mg II λ4481)

	Hα	He I λ6678	Hγ	He I λ4471	Mg II λ4481	Fe II ccfs
Mean RV (km s^{-1})	-13.5	-25.7	-24.1	-8.4	-19.2	-20.5
RV range (km s^{-1})	-29.9 to 0.7	-44.8 to -6.0	-40.7 to -8.1	-30.9 to 6.9	-35.5 to -4.0	-48.8 to -3.0
RV change (km s^{-1})	30.6	38.8	32.6	37.8	31.5	45.8

- Shell classification: shell emission
- Do shell features move with the star?: yes
- Notes on emission and absorption features: He I λ6678 may be slightly filled in (see right wing of 2004 spectra) therefore radial velocity data for that line is useless. The more interesting things to note are the unusual features seen best in Mg II λ4481 in Figure C.3 - it seems there may be a very close binary (period $\approx$4 d?) orbiting the Be star with a period of perhaps the aforementioned 1033 d period.
- Other notes:

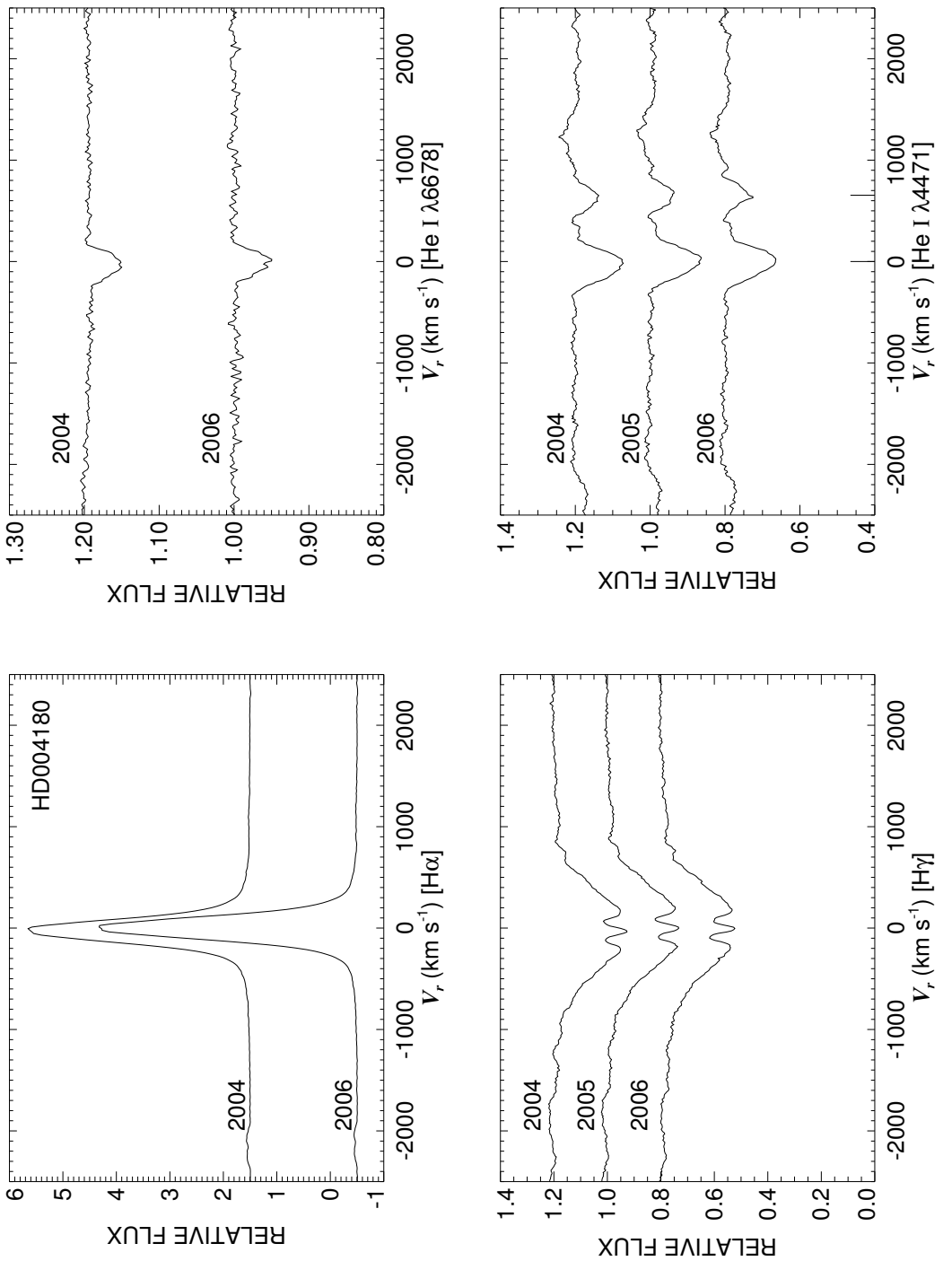

Figure C.2: A quadruple plot of HD004180 as described in §7.2.3 and Figure 7.6.

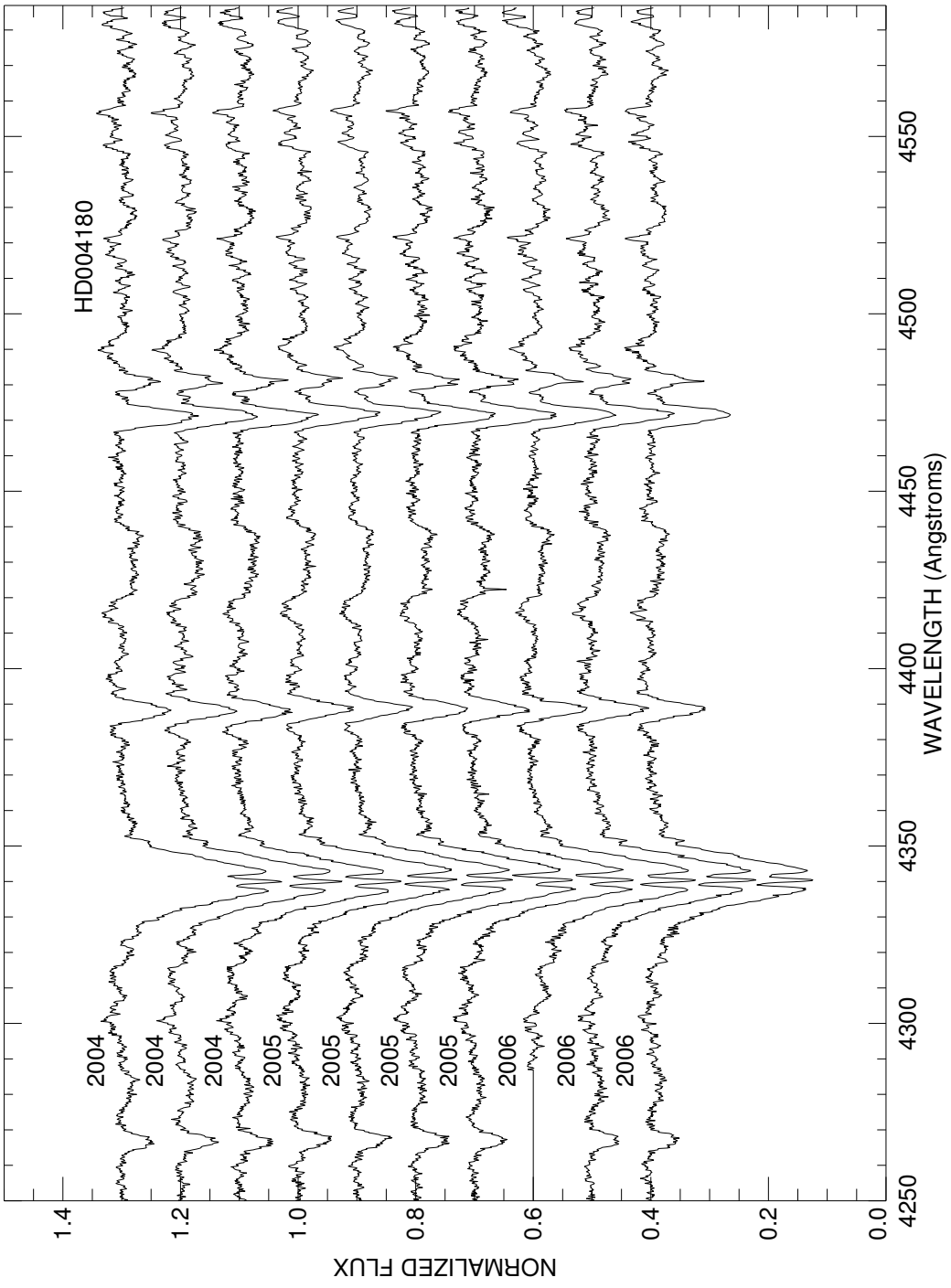

Figure C.3: A plot of all spectra of HD004180 in the blue region. Each is labeled with the year of observation and they are offset for clarity.

HD005394

Classical Be Star

- Other Names: HR 264, γ Cas
- Spectral Type: B0 IVe+sh
- V magnitude: 2.29
- In WDS?: yes - 10.9 mag companion 2.2 arcsec away (discovered in 1888) and 12.9 mag companion 53 arcsec away (discovered in 1879)
- Known spectroscopic binary?: yes - Harmanec (2001) reports a period of 203.59 d
- Velocity variations seen in these data?: yes

	Hα	He I λ6678	Hγ	He I λ4471	Mg II λ4481	Fe II ccfs
Mean RV (km s^{-1})	-5.8	-6.4	-13.6	-30.7	···	-2.1
RV range (km s^{-1})	-9.8 to -0.7	-55.7 to 41.3	-19.2 to -8.7	-37.0 to -21.1	···	-8.8 to 6.2
RV change (km s^{-1})	9.1	97.0	10.5	15.9	···	15.0

- Shell classification: emission shell
- Do shell features move with the star?: yes
- Additional plot because: variations in the blue spectra
- Notes on emission and absorption features: filled-in He I λ6678 useless for RV studies
- Other notes: Has interferometric measurements, both CHARA K$'$ (Gies et al. 2007) and Hα (Quirrenbach et al. 1997; Tycner et al. 2005, 2006).

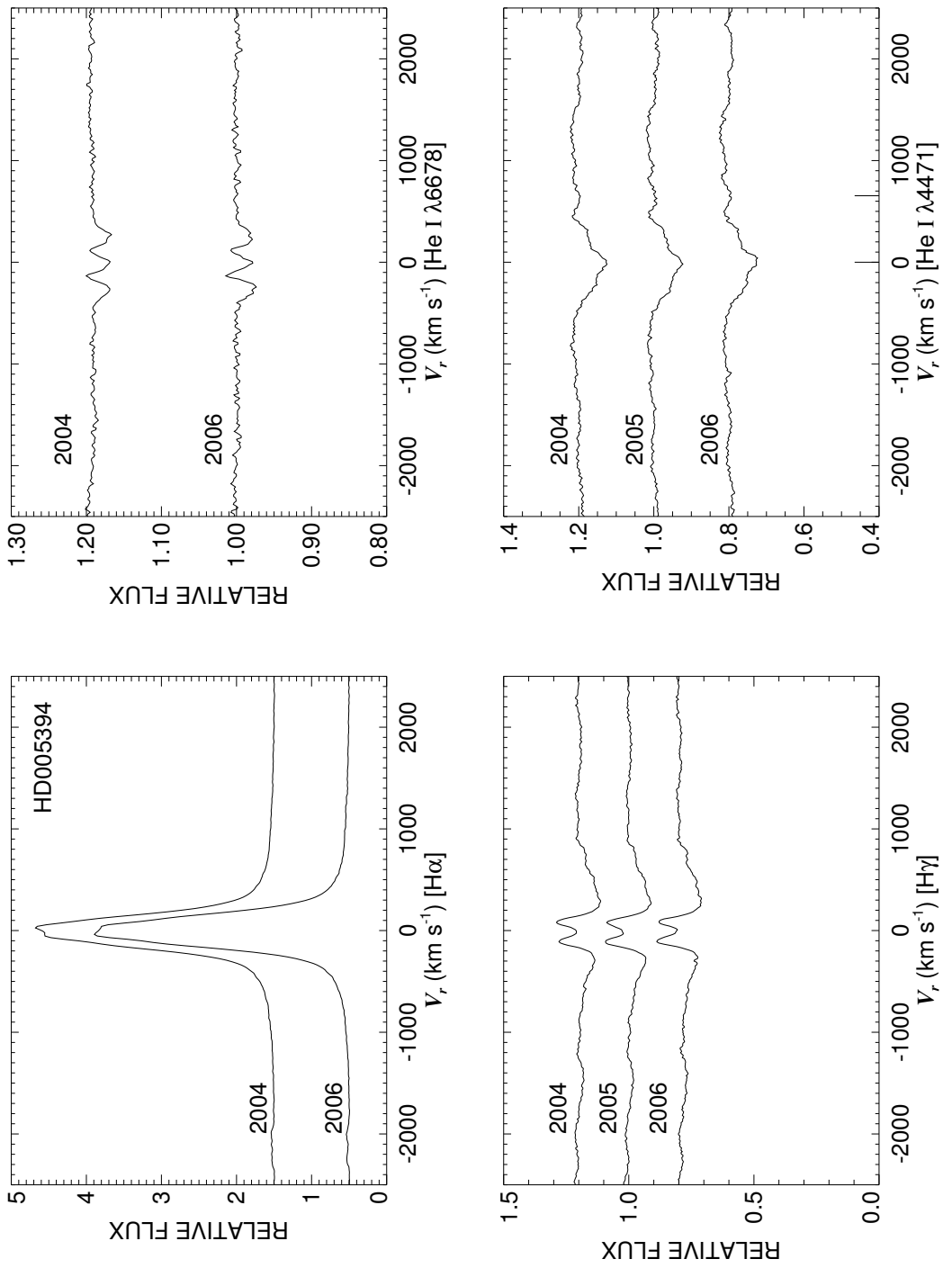

Figure C.4: A quadruple plot of HD005394 as described in §7.2.3 and Figure 7.6.

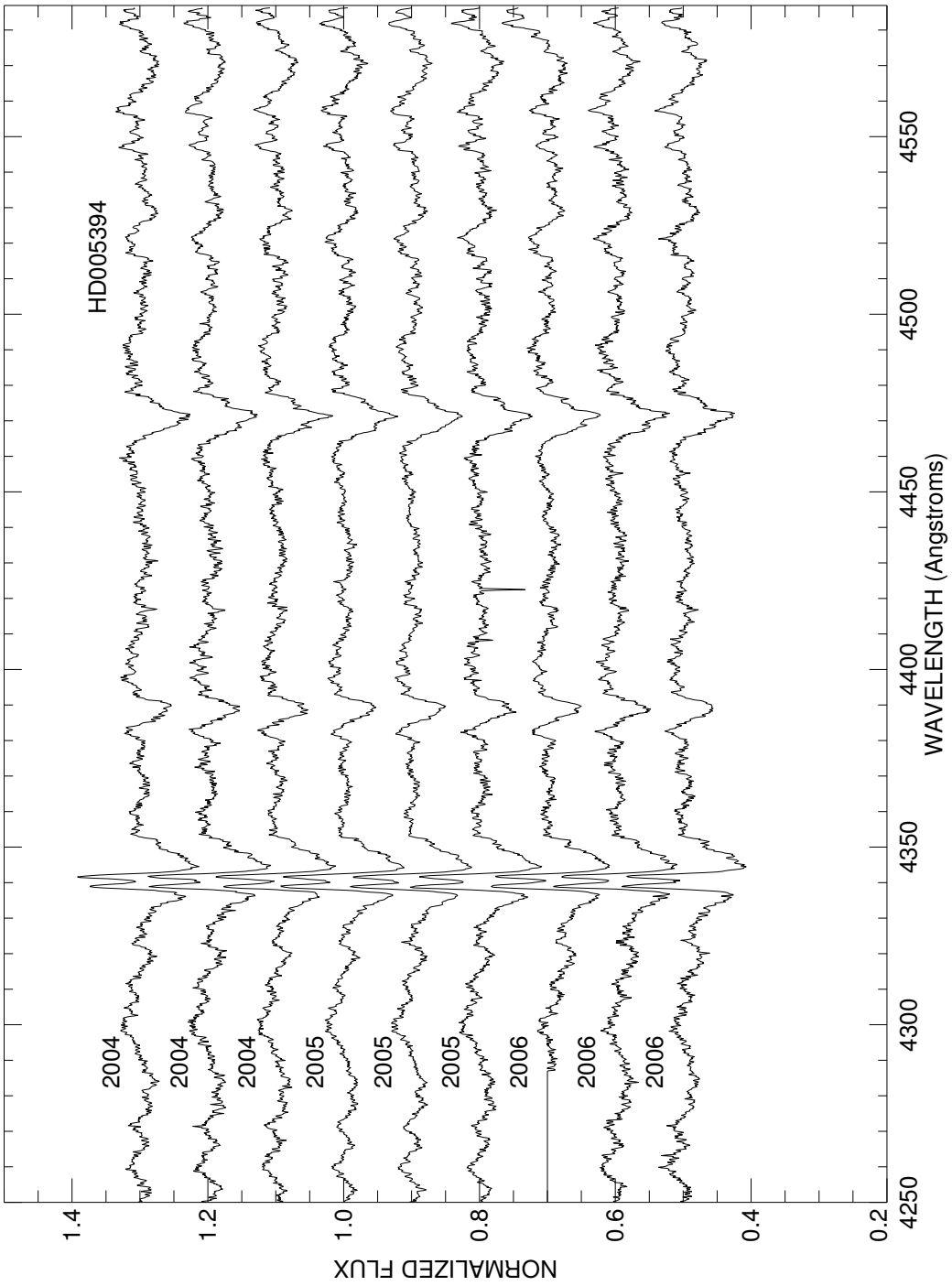

Figure C.5: A plot of all spectra of HD005394 in the blue region. Each is labeled with the year of observation and they are offset for clarity.

HD006811

Classical Be Star

- Other Names: HR 335, ϕ And
- Spectral Type: B6.5 IIIe
- V magnitude: 4.19
- In WDS?: yes - 5.61 mag companion 0.4 arcsec away (discovered in 1851)
- Known spectroscopic binary?: no
- Velocity variations seen in these data?: possibly very small

	Hα	He I λ6678	Hγ	He I λ4471	Mg II λ4481	Fe II ccfs
Mean RV (km s^{-1})	1.0	11.7	0.6	-9.1	1.6	8.4
RV range (km s^{-1})	-11.0 to 6.5	0.0 to 27.8	-3.1 to 3.6	-12.2 to -4.8	-1.0 to 4.4	3.9 to 14.1
RV change (km s^{-1})	17.5	27.8	6.7	7.4	5.4	10.2

- Shell classification: squarish
- Do shell features move with the star?: yes (if the star varies)
- Notes on emission and absorption features: He I λ6678 looks filled in (esp. in 2006)
- Other notes: Possibly a pole-on Be star (the narrow lines and non-horned emission) This star is also plotted in Figure 7.3.

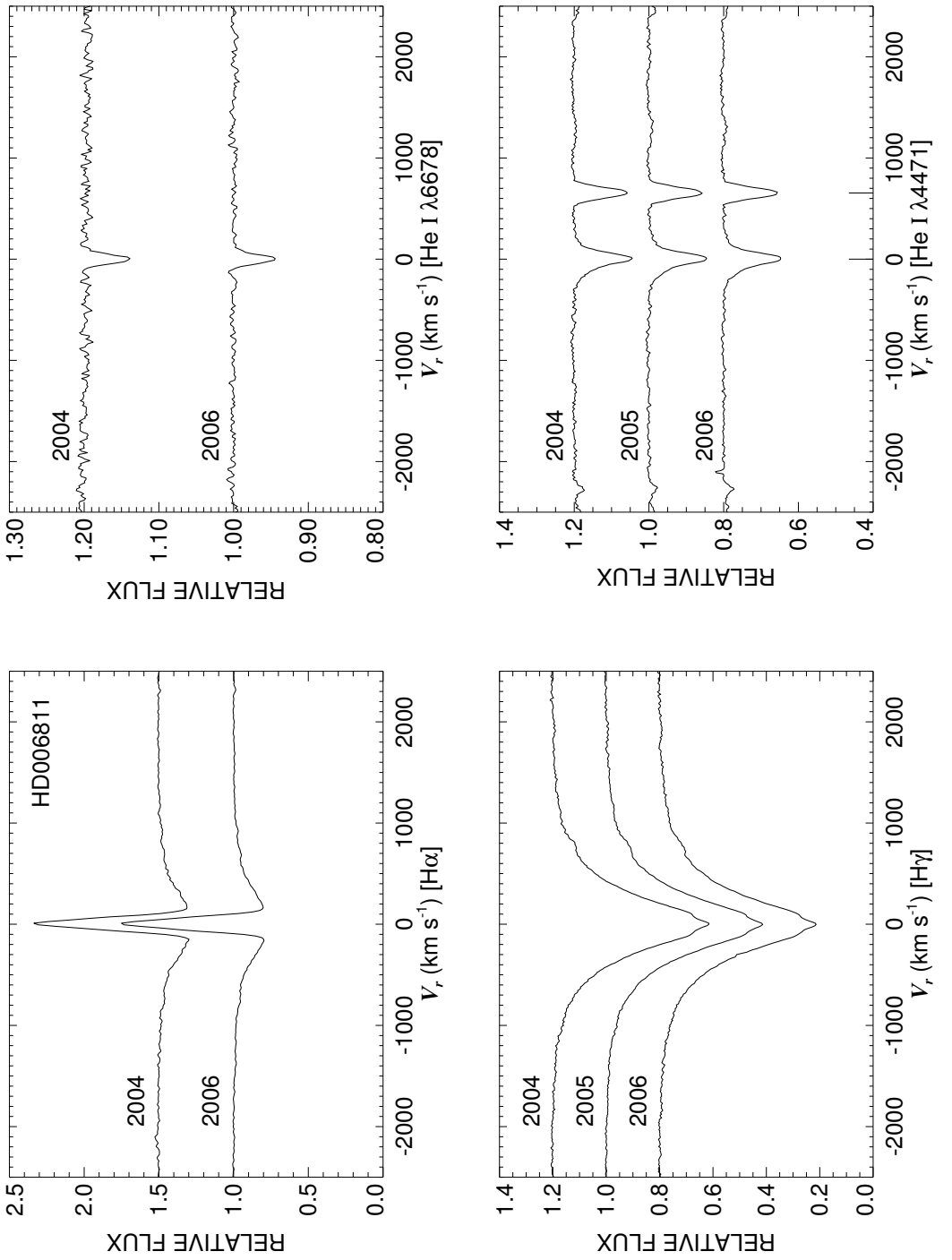

Figure C.6: A quadruple plot of HD006811 as described in §7.2.3 and Figure 7.6.

HD007636

Classical Be Star; Shell Star

- Other Names: V764 Cas
- Spectral Type: B2 IIIne
- V magnitude: 6.93
- In WDS?: no
- Known spectroscopic binary?: no
- Velocity variations seen in these data?: unlikely

	Hα	He I λ6678	Hγ	He I λ4471	Mg II λ4481	Fe II ccfs
Mean RV (km s^{-1})	-13.1	-6.2	3.5	-18.9	···	-13.4
RV range (km s^{-1})	-15.1 to -11.1	-36.0 to 11.5	-19.0 to 17.9	-25.9 to -8.5	···	-19.2 to -2.4
RV change (km s^{-1})	4.0	47.5	36.9	17.4	···	16.8

- Shell classification: emission shell
- Do shell features move with the star?: N/A
- Notes on emission and absorption features: Huge Hα emission. He I λ6678 and Mg II λ4481 both filled in and unreliable for RV studies. Line profile variations in the helium lines very obvious but likely caused by variations in emission symmetry (as seen in Hγ, see Fig. C.8).
- Other notes:

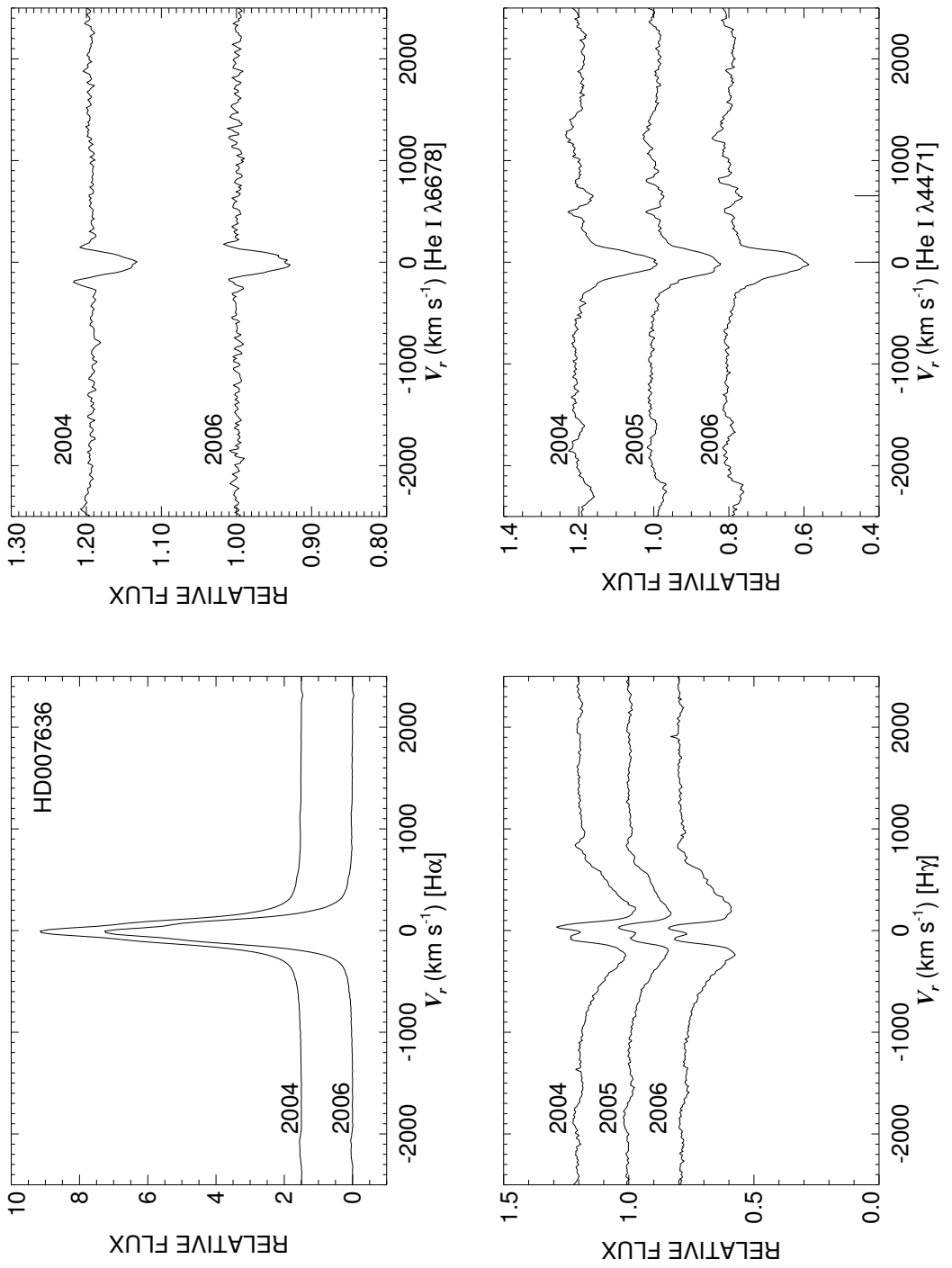

Figure C.7: A quadruple plot of HD007636 as described in §7.2.3 and Figure 7.6.

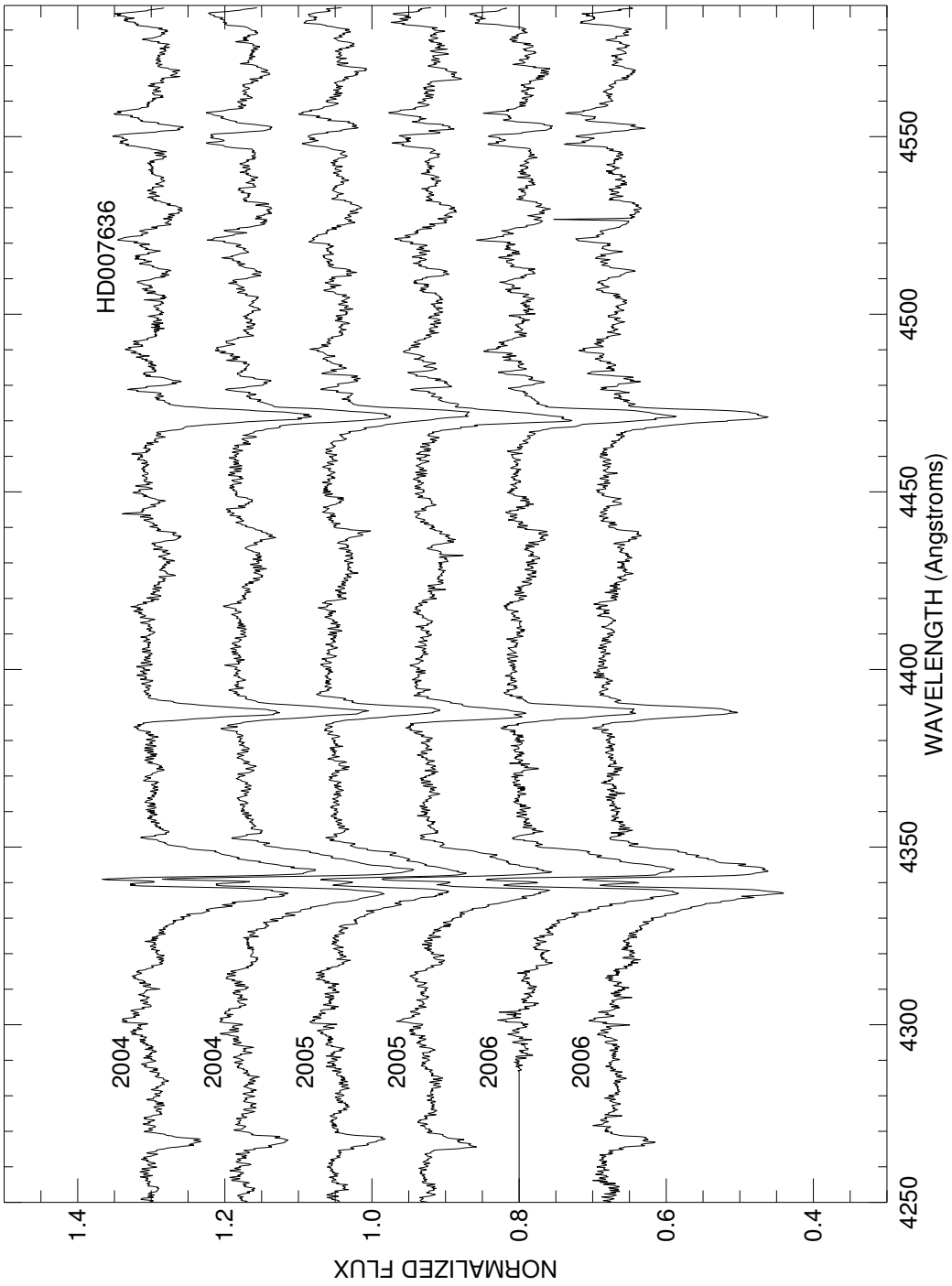

Figure C.8: A plot of all spectra of HD007636 in the blue region. Each is labeled with the year of observation and they are offset for clarity.

HD009709

Classical Be Star

- Other Names:
- Spectral Type: B8 V
- V magnitude: 7.00
- In WDS?: no
- Known spectroscopic binary?: no
- Velocity variations seen in these data?: no (unknown causes for Mg II λ4481 variations)

	Hα	He I λ6678	Hγ	He I λ4471	Mg II λ4481	Fe II ccfs
Mean RV (km s^{-1})	-3.6	-15.6	-18.1	-11.1	-42.3	-1.0
RV range (km s^{-1})	-4.8 to -2.1	-29.4 to -6.3	-30.1 to -7.8	-14.3 to -8.2	-56.9 to -32.7	-3.1 to 2.9
RV change (km s^{-1})	2.7	23.1	22.3	6.1	24.2	6.0

- Shell classification: squarish
- Do shell features move with the star?: N/A
- Notes on emission and absorption features: He I λ6678 is completely filled in with emission
- Other notes: This star is also plotted in Figure 7.3.

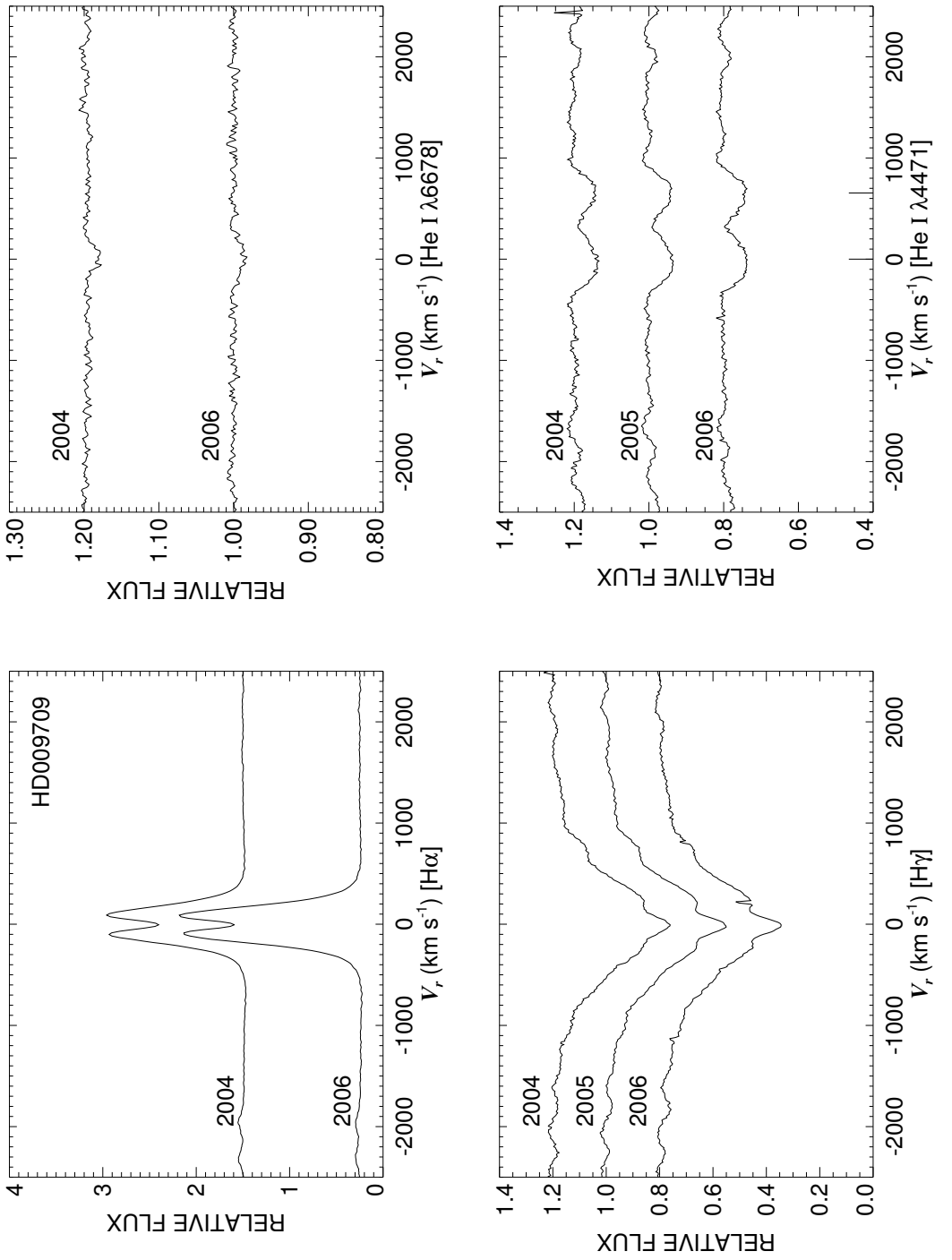

Figure C.9: A quadruple plot of HD009709 as described in §7.2.3 and Figure 7.6.

HD010516

Classical Be Star

- Other Names: HR 496, ϕ Per
- Spectral Type: B0.5 IVe+sh
- V magnitude: 4.00
- In WDS?: no
- Known spectroscopic binary?: yes - Bozic et al. (1995) give 126.6731 d; the secondary is a hot, stripped subdwarf (Gies et al. 1998)
- Velocity variations seen in these data?: yes (see Fig. C.11)

	Hα	He I λ6678	Hγ	He I λ4471	Mg II λ4481	Fe II ccfs
Mean RV (km s^{-1})	7.0	-6.5	54.3	-32.9	-46.1	-227.0
RV range (km s^{-1})	-4.9 to 14.9	-59.4 to 34.0	12.6 to 86.3	-51.9 to -20.3	-70.9 to -19.7	-250.8 to -198.0
RV change (km s^{-1})	19.8	93.4	73.7	31.6	51.2	52.7

- Shell classification: emission shell (gets smaller from 2004 to 2006)
- Do shell features move with the star?: possibly
- Notes on emission and absorption features: All radial velocities (except perhaps Hα) are a bit unusual due to the nature of the system.
- Other notes: Has both Hα (Quirrenbach et al. 1997; Tycner et al. 2006) and CHARA K$'$ (Gies et al. 2007) interferometric measurements of the disk. This is the star system in the painting on Doug's wall ;) and it is available at http://imgsrc.hubblesite.org/hu/db/1997/39/images/a/formats/full_jpg.jpg

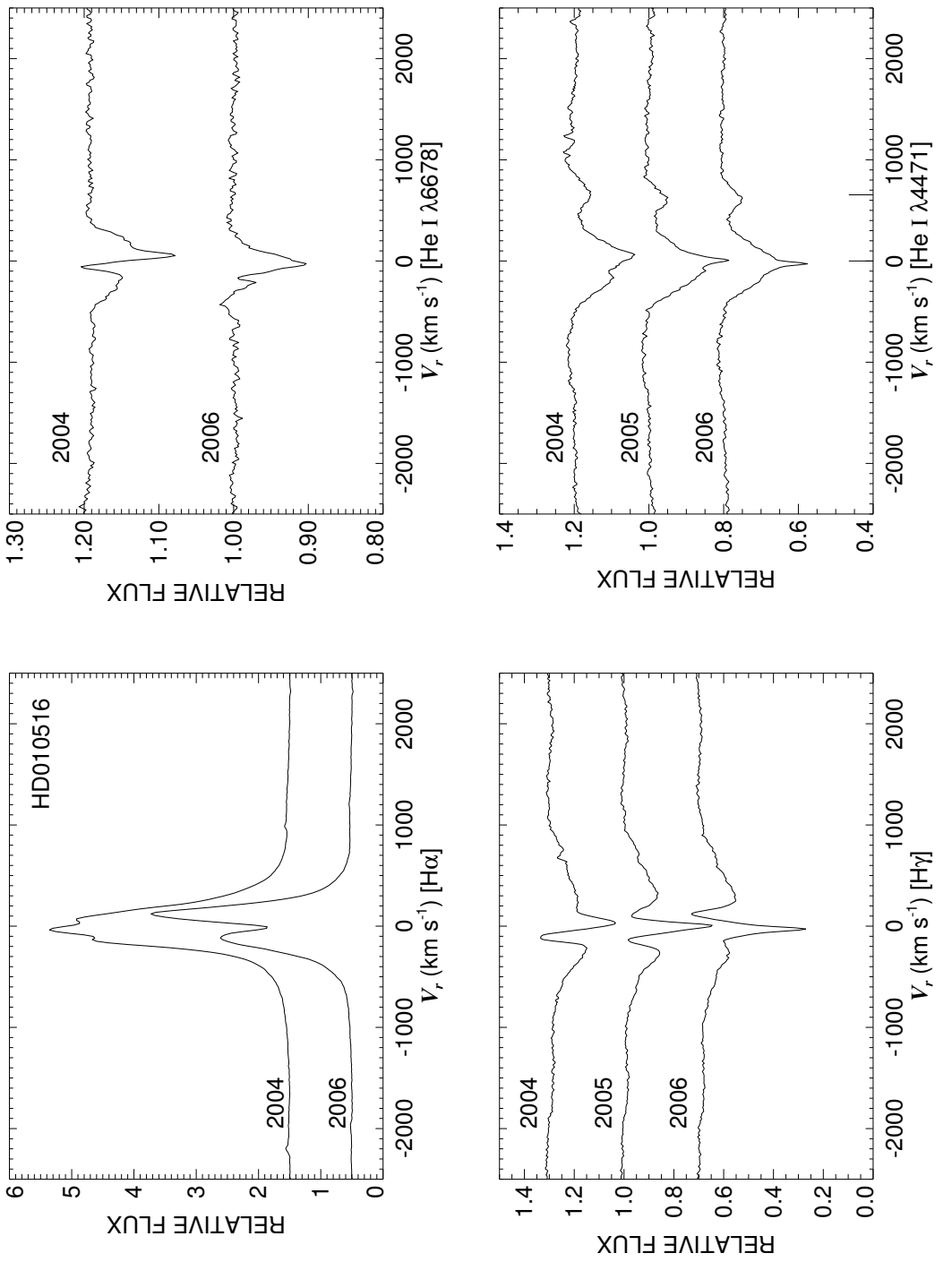

Figure C.10: A quadruple plot of HD010516 as described in §7.2.3 and Figure 7.6.

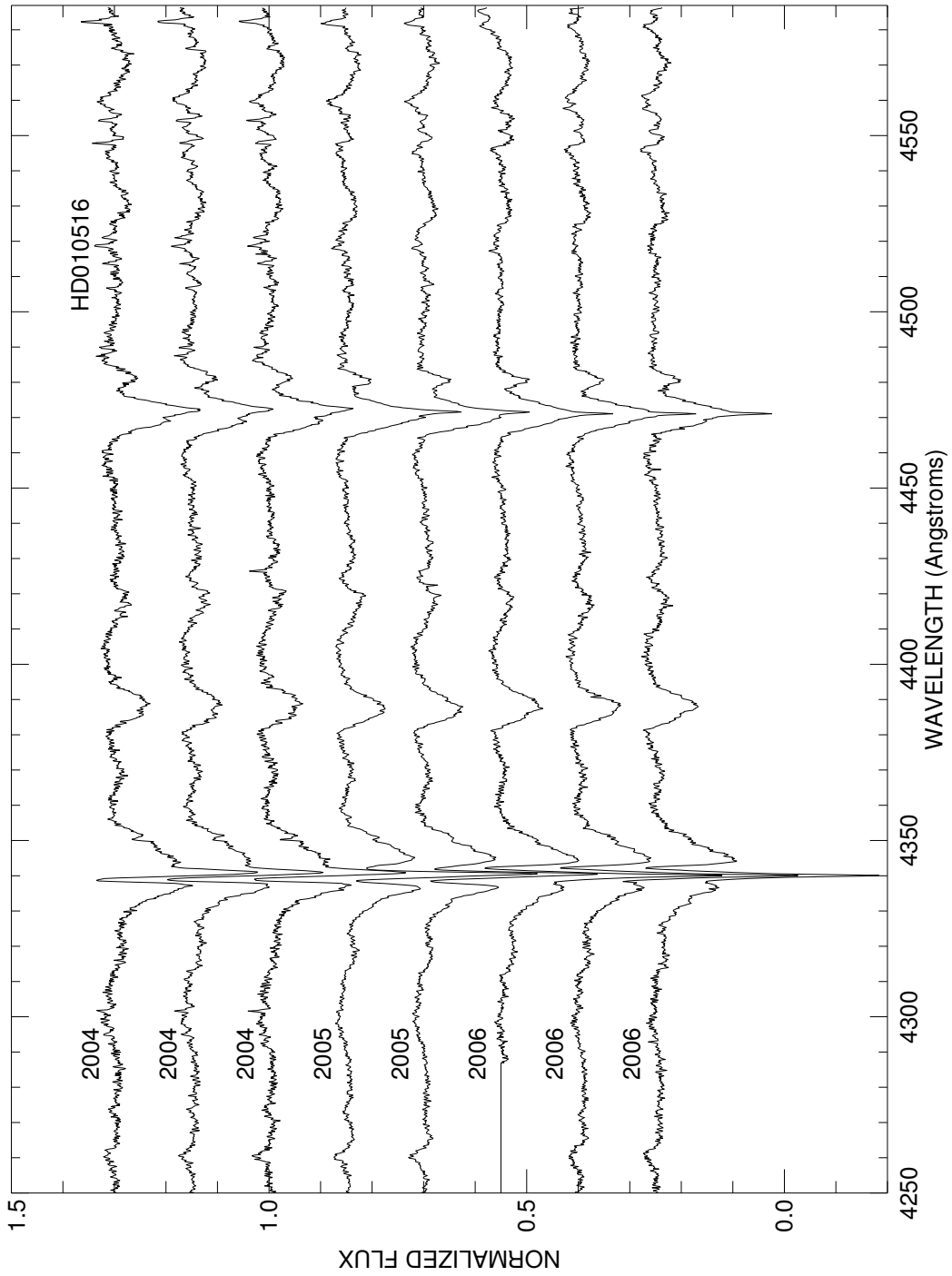

Figure C.11: A plot of all spectra of HD010516 in the blue region. Each is labeled with the year of observation and they are offset for clarity.

HD011415

NOT Be Star

- Other Names: HR 542, ϵ Cas
- Spectral Type: B3 V
- V magnitude: 3.21
- In WDS?: no
- Known spectroscopic binary?: no
- Velocity variations seen in these data?: no

	Hα	He I λ6678	Hγ	He I λ4471	Mg II λ4481	Fe II ccfs
Mean RV (km s^{-1})	-14.4	-8.5	-11.0	-25.7	-10.8	···
RV range (km s^{-1})	-18.7 to -7.5	-13.1 to -5.5	-15.6 to -7.9	-28.8 to -23.0	-13.1 to -6.2	···
RV change (km s^{-1})	11.2	7.6	7.7	5.8	6.9	···

- Shell classification: N/A
- Notes on emission and absorption features: no emission, just a narrow-lined B star
- Other notes: had a "shell" classification in the Bright Star Catalog but it is not a Be star (no one has seen Balmer-line emission).

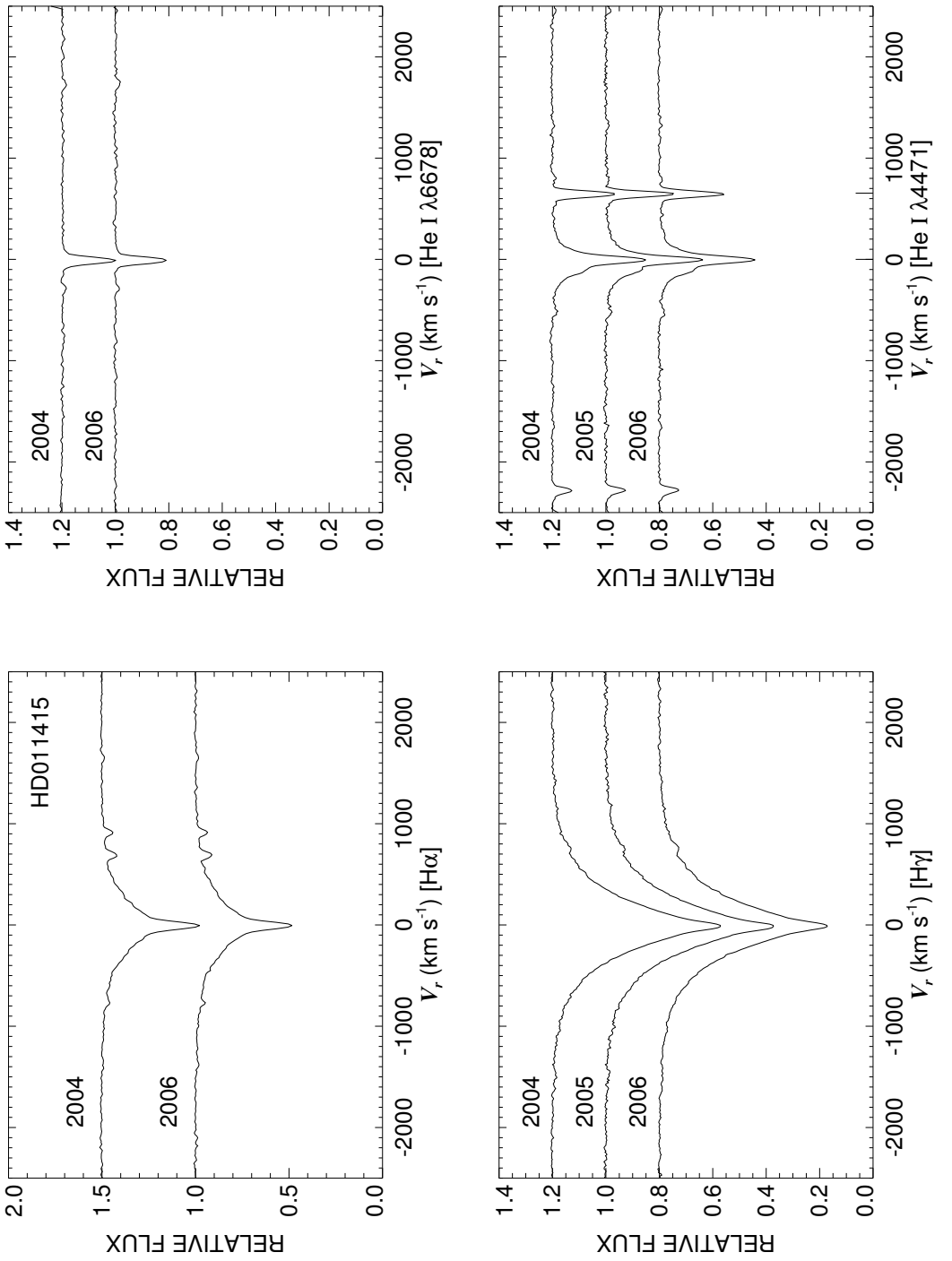

Figure C.12: A quadruple plot of HD011415 as described in §7.2.3 and Figure 7.6.

HD013661

Classical Be Star

- Other Names: V594 Per
- Spectral Type: B2 Ve
- V magnitude: 7.83
- In WDS?: no
- Known spectroscopic binary?: no
- Velocity variations seen in these data?: no

	Hα	He I λ6678	Hγ	He I λ4471	Mg II λ4481	Fe II ccfs
Mean RV (km s^{-1})	-27.0	-35.8	-33.2	-63.8	-79.6	-124.2
RV range (km s^{-1})	-29.3 to -23.7	-62.3 to -8.3	-37.3 to -29.2	-70.2 to -56.1	-102.2 to -59.4	-128.7 to -119.8
RV change (km s^{-1})	5.6	54.0	8.1	14.1	42.8	9.0

- Shell classification: emission shell in 2004 but goes away in 2005
- Do shell features move with the star?: N/A
- Notes on emission and absorption features: Hγ peaks change (see Fig. C.14), Mg II λ4481 has a bit of an emission horn on the right, possible NRP in blue helium lines?
- Other notes:

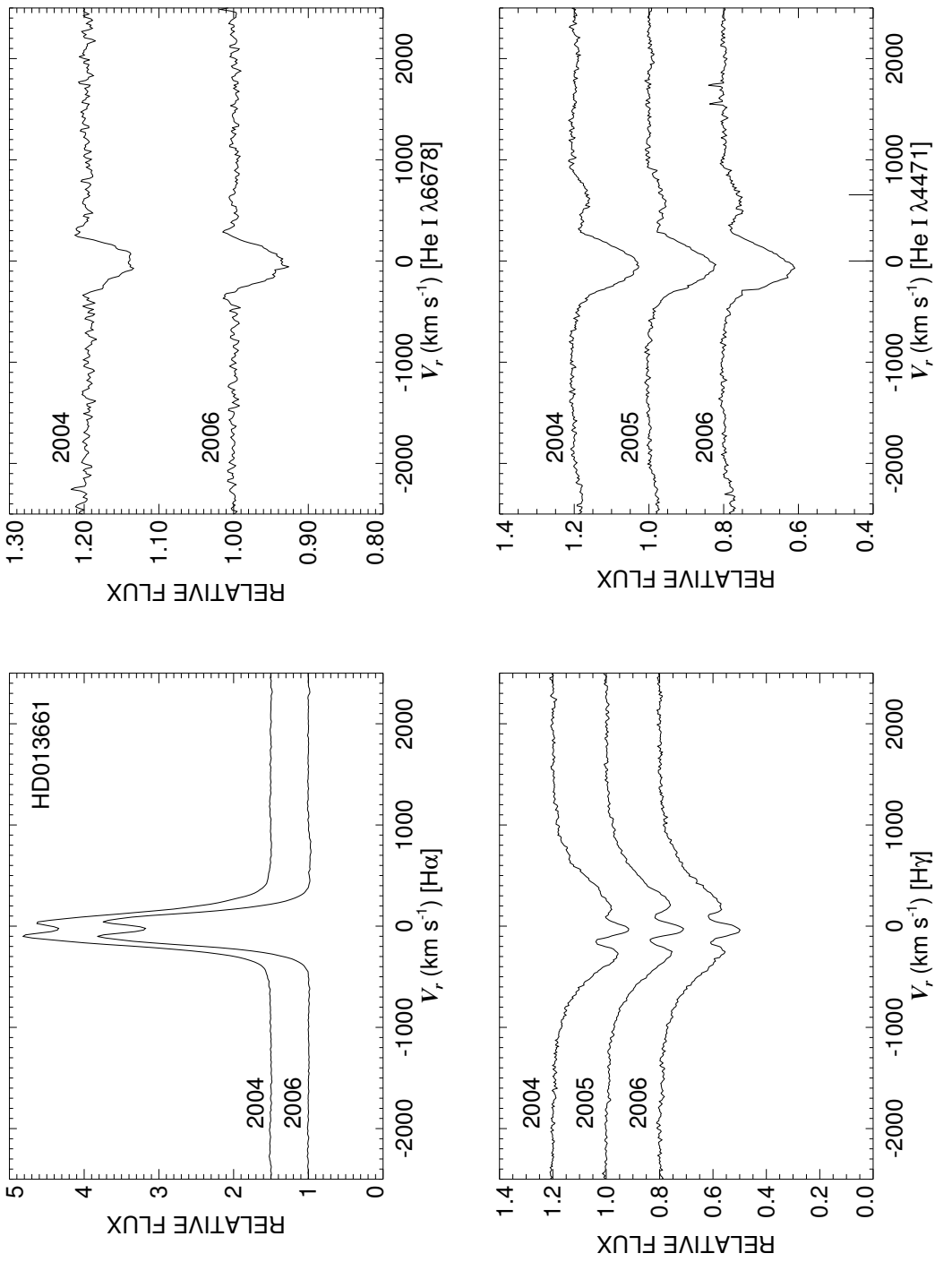

Figure C.13: A quadruple plot of HD013661 as described in §7.2.3 and Figure 7.6.

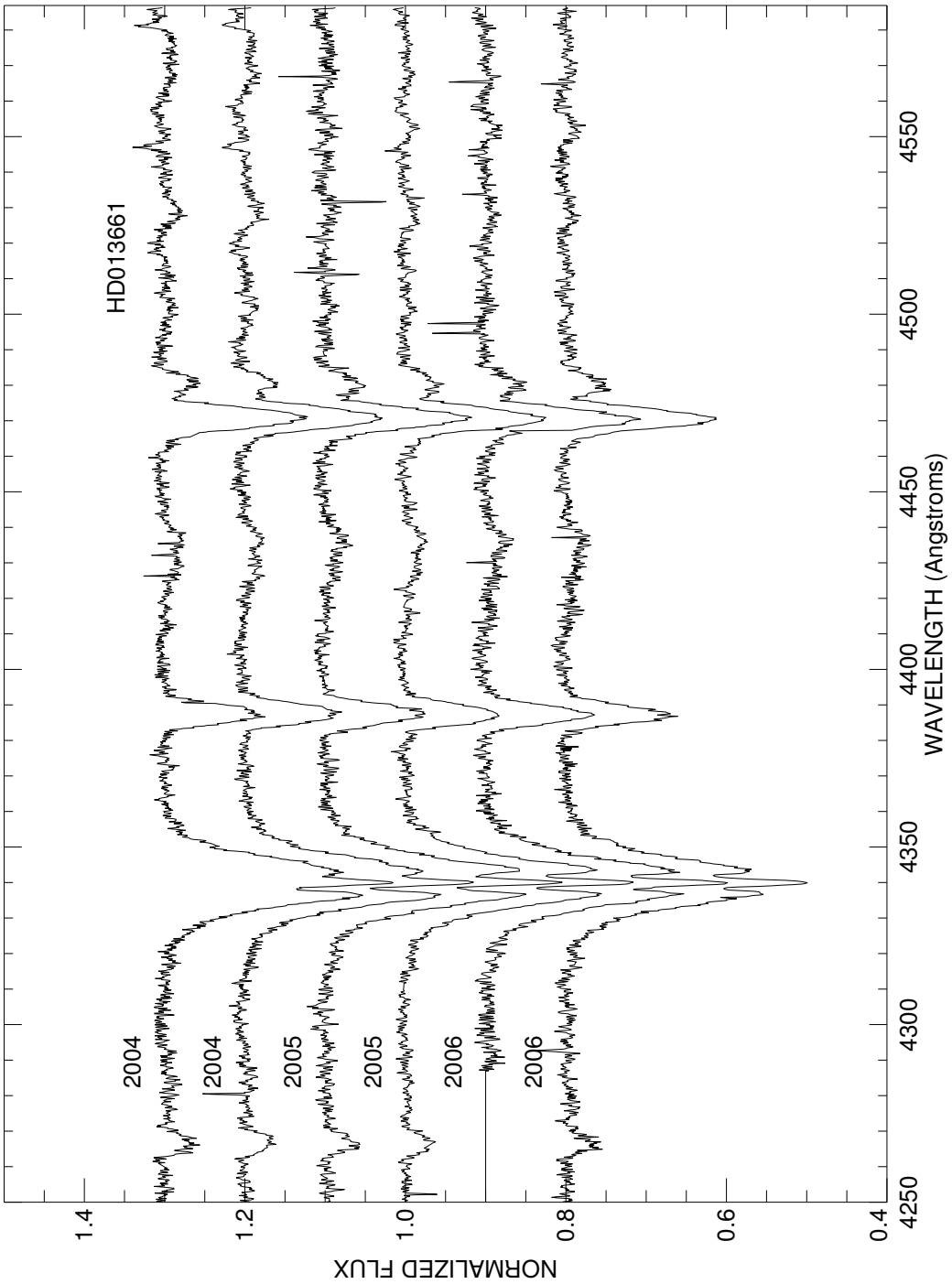

Figure C.14: A plot of all spectra of HD013661 in the blue region. Each is labeled with the year of observation and they are offset for clarity.

HD013867

Classical Be Star

- Other Names:
- Spectral Type: B5 Ve
- V magnitude: 7.72
- In WDS?: no
- Known spectroscopic binary?: no
- Velocity variations seen in these data?: no

	Hα	He I λ6678	Hγ	He I λ4471	Mg II λ4481	Fe II ccfs
Mean RV (km s^{-1})	-2.4	-2.9	-4.4	-1.1	-1.9	-10.8
RV range (km s^{-1})	-3.1 to -1.5	-11.3 to 6.4	-9.2 to 1.5	-4.4 to 3.0	-2.9 to 0.4	-24.2 to -0.4
RV change (km s^{-1})	1.6	17.7	10.7	7.4	3.3	23.8

- Shell classification: emission shell
- Do shell features move with the star?: N/A
- Notes on emission and absorption features: Hα grows in 2006 (yet Hγ does not). Narrow lines and lack of double-peaked Hα suggests a pole-on orientation. The blue "extension" in He I λ4471 is the result of the multiple components of helium in this region.
- Other notes: This star is also plotted in Figure 7.4.

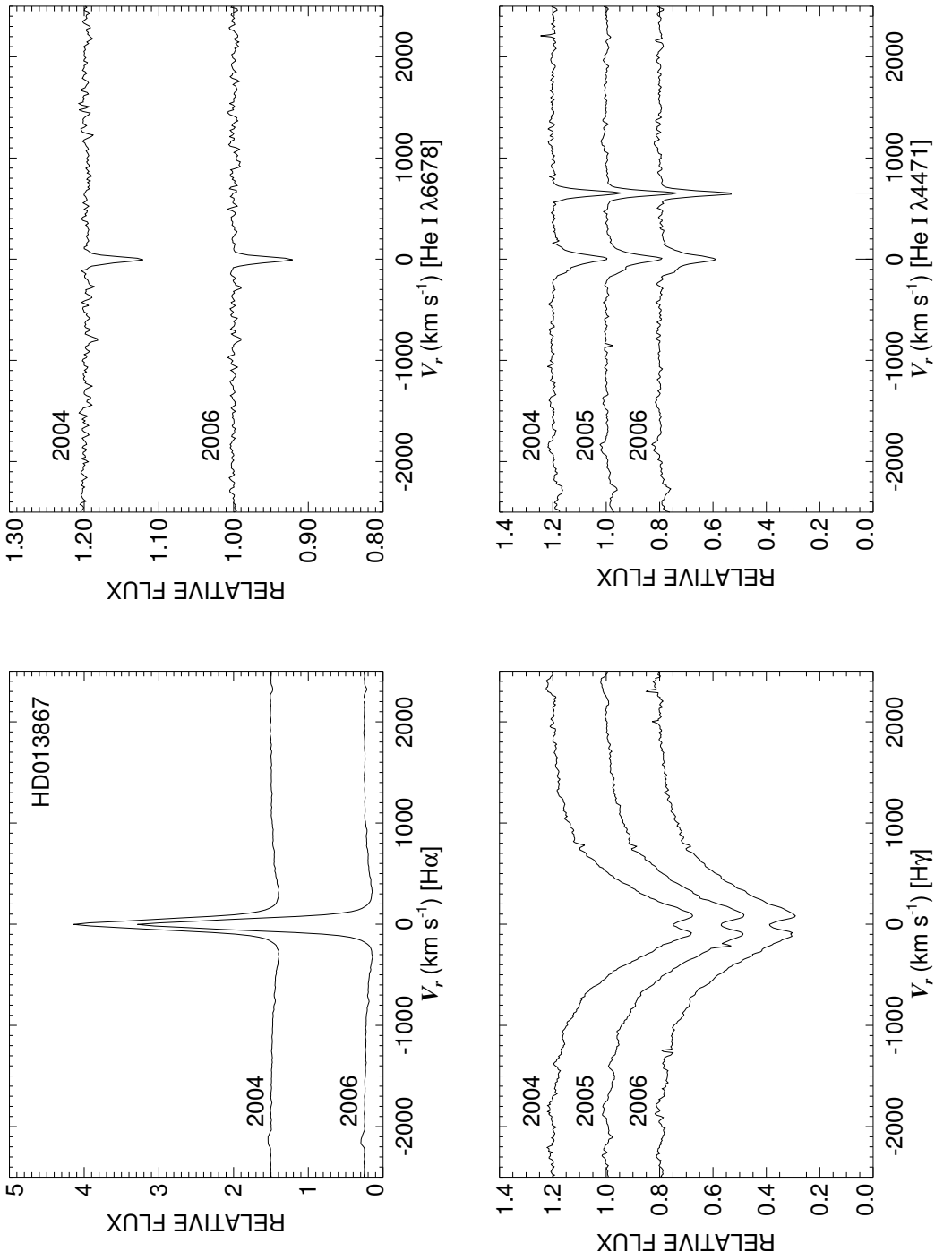

Figure C.15: A quadruple plot of HD013867 as described in §7.2.3 and Figure 7.6.

HD018552

Classical Be Star

- Other Names: HR 894
- Spectral Type: B8 Vne
- V magnitude: 6.06
- In WDS?: no
- Known spectroscopic binary?: no
- Velocity variations seen in these data?: perhaps very small

	Hα	He I λ6678	Hγ	He I λ4471	Mg II λ4481	Fe II ccfs
Mean RV (km s^{-1})	-9.1	1.5	-20.0	-19.4	-23.0	-20.3
RV range (km s^{-1})	-11.6 to -6.7	-18.8 to 26.0	-25.7 to -15.8	-22.1 to -16.6	-29.8 to -15.6	-29.4 to -12.4
RV change (km s^{-1})	4.9	44.8	9.9	5.5	14.2	16.9

- Shell classification: squarish
- Do shell features move with the star?: yes (if it moves at all)
- Notes on emission and absorption features: He I λ6678 nearly completely filled in (useless for RV studies).
- Other notes:

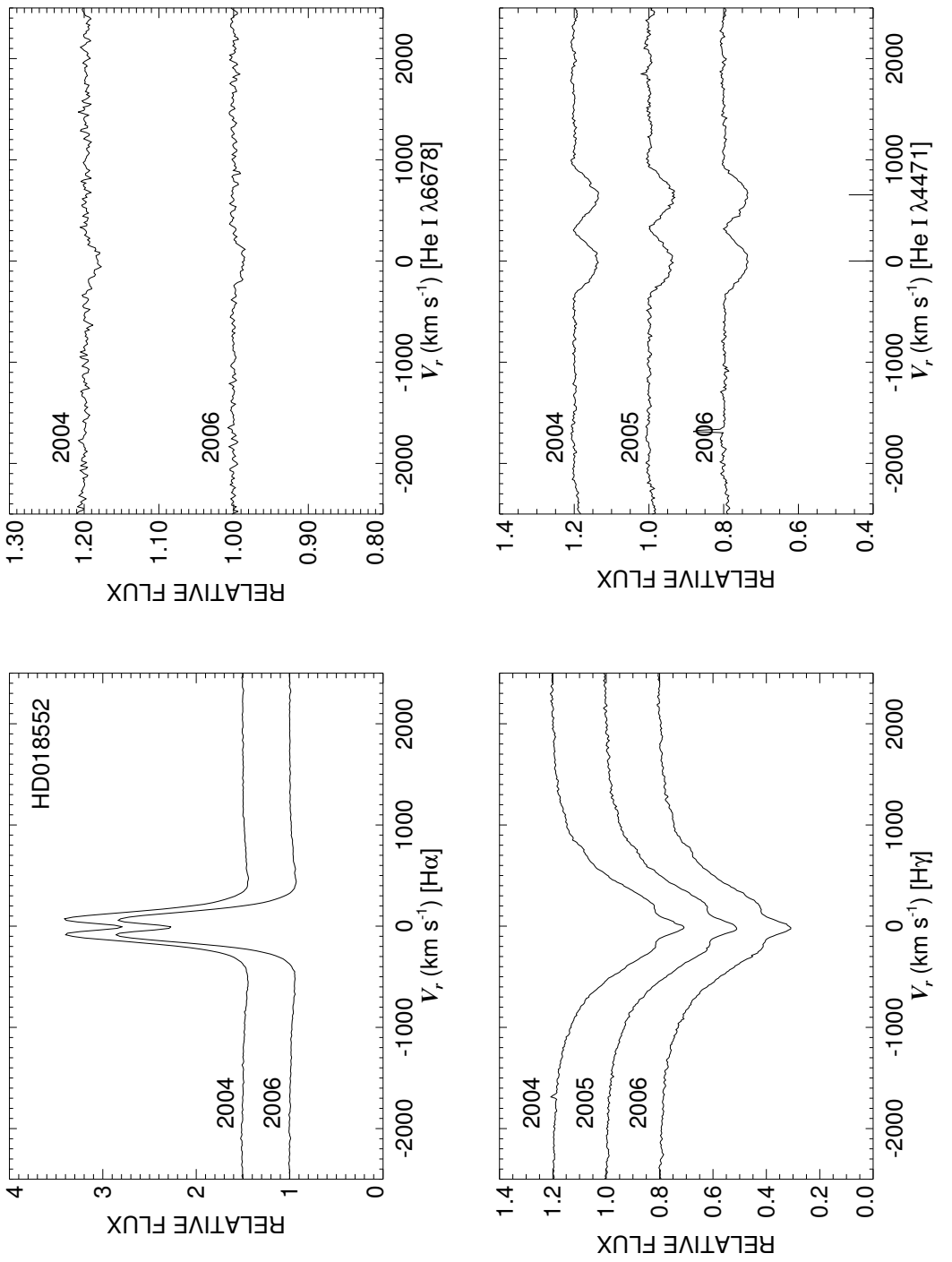

Figure C.16: A quadruple plot of HD018552 as described in §7.2.3 and Figure 7.6.

HD019243

Classical Be Star

- Other Names:
- Spectral Type: B1 Ve
- V magnitude: 6.71
- In WDS?: yes - 9.72 mag companion 0.2 arecsec away (discovered in 1991)
- Known spectroscopic binary?: no
- Velocity variations seen in these data?: yes

	Hα	He I λ6678	Hγ	He I λ4471	Mg II λ4481	Fe II ccfs
Mean RV (km s^{-1})	-19.6	-13.5	62.4	-47.6	···	-27.4
RV range (km s^{-1})	-26.8 to -6.2	-33.0 to 21.9	40.3 to 82.5	-61.9 to -28.5	···	-47.6 to -7.5
RV change (km s^{-1})	20.6	54.9	42.2	33.4	···	40.1

- Shell classification: emission shell
- Do shell features move with the star?: yes
- Notes on emission and absorption features: Huge Hα emission. He I λ6678 and Mg II λ4481 have emission horns and are useless for RV studies. Hγ peaks change. Long term velocity variations seen in all lines.
- Other notes: This star is also plotted in Figure 7.4.

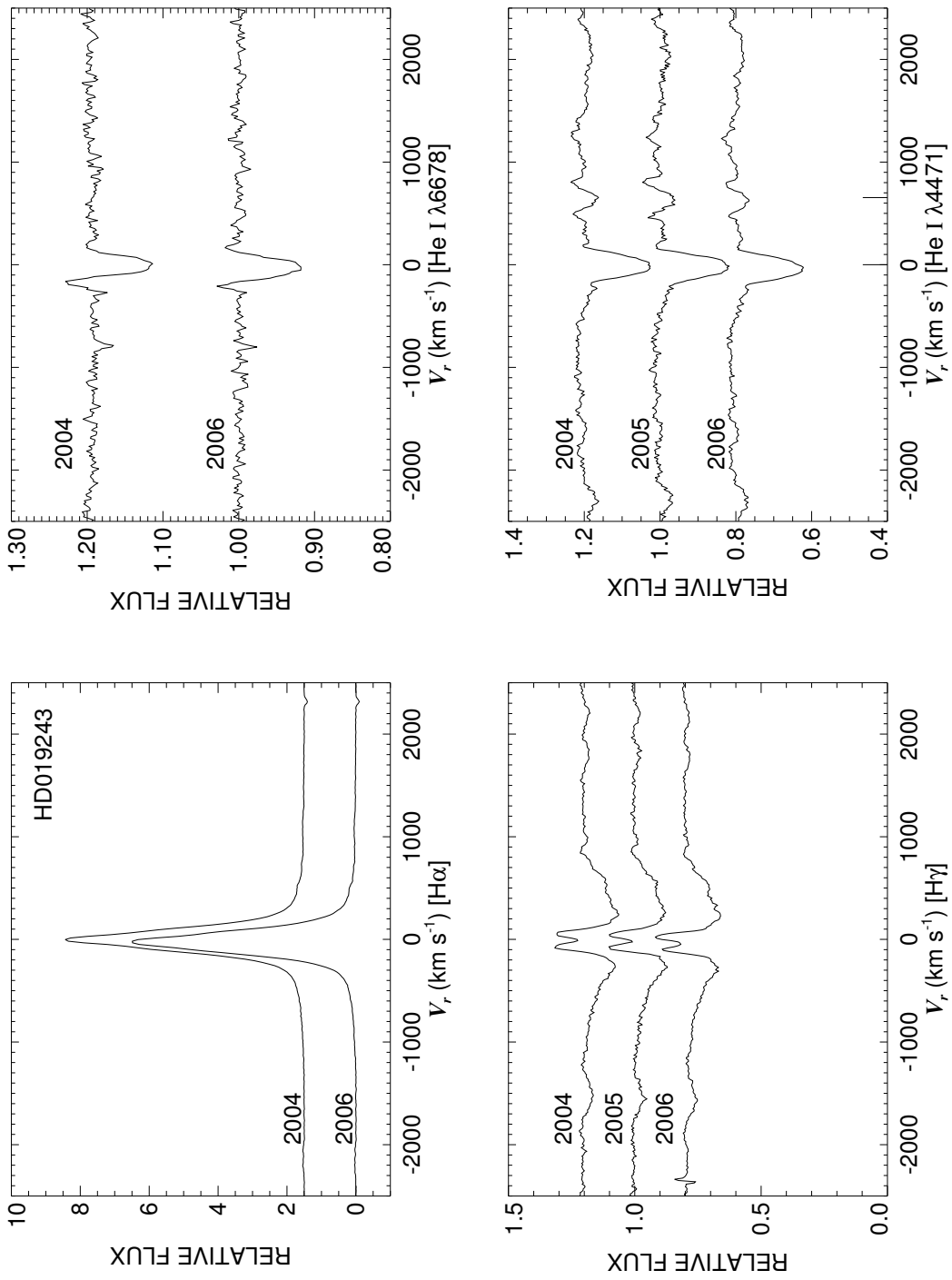

Figure C.17: A quadruple plot of HD019243 as described in §7.2.3 and Figure 7.6.

HD020134

Classical Be Star

- Other Names:
- Spectral Type: B2.5 Vep
- V magnitude: 7.54
- In WDS?: no
- Known spectroscopic binary?: no
- Velocity variations seen in these data?: no

	Hα	He I λ6678	Hγ	He I λ4471	Mg II λ4481	Fe II ccfs
Mean RV (km s^{-1})	-16.1	-19.3	-15.9	-34.2	-22.8	···
RV range (km s^{-1})	-20.9 to -10.5	-26.9 to -14.2	-22.6 to -9.1	-36.3 to -32.1	-26.5 to -20.0	···
RV change (km s^{-1})	10.4	12.7	13.5	4.2	6.5	···

- Shell classification: normal
- Notes on emission and absorption features: Hα is slightly filled in with emission in 2004 but it goes away in 2006. Hγ gets slightly filled in with emission in 2005 but it is not there in either 2004 or 2006. The other three absorption lines show line profile variations of unknown origin.
- Other notes:

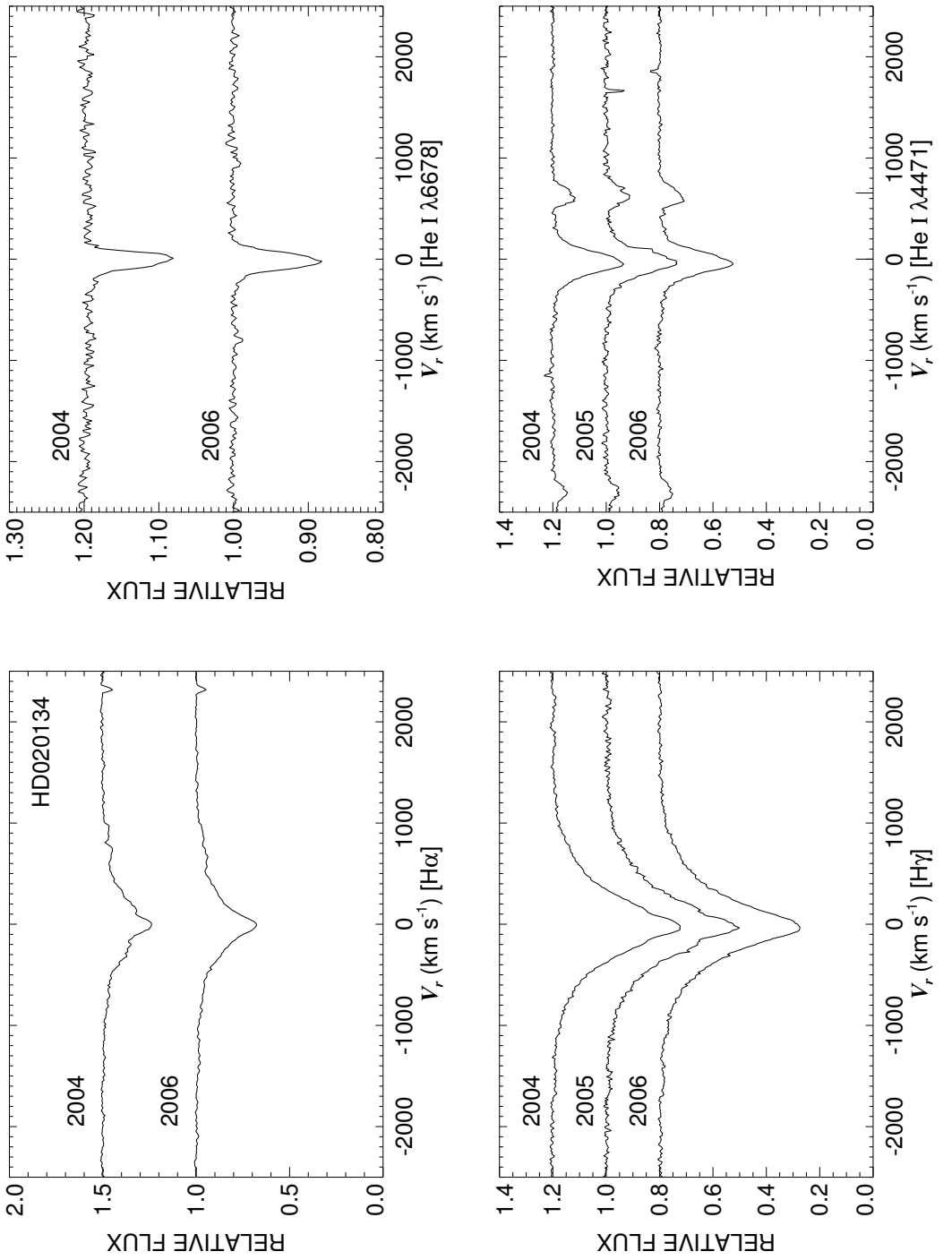

Figure C.18: A quadruple plot of HD020134 as described in §7.2.3 and Figure 7.6.

HD020336

Classical Be Star; Non-Radial Pulsator?

- Other Names: HR 985, BK Cam
- Spectral Type: B2.5 Ven
- V magnitude: 4.62
- In WDS?: yes - 12.5 mag companion 121 arcsec away (discovered in 1911)
- Known spectroscopic binary?: no
- Velocity variations seen in these data?: yes, fast - either a close companion causing a composite spectrum or NRP (see Fig. C.20)

	Hα	He I λ6678	Hγ	He I λ4471	Mg II λ4481	Fe II ccfs
Mean RV (km s^{-1})	9.8	9.1	20.7	-11.4	-27.4	22.3
RV range (km s^{-1})	-0.7 to 19.4	-29.7 to 35.3	5.0 to 40.7	-17.5 to -3.1	-34.7 to -19.5	5.8 to 31.8
RV change (km s^{-1})	20.1	65.0	35.7	14.4	15.2	26.0

- Shell classification: squarish (increases in 2005)
- Do shell features move with the star?: yes
- Notes on emission and absorption features: Hα gets bigger and so do the shell features. Mg II λ4481 is suspiciously narrow compared to He I λ4471 and seems to have an emission horn on the right side.
- Other notes:

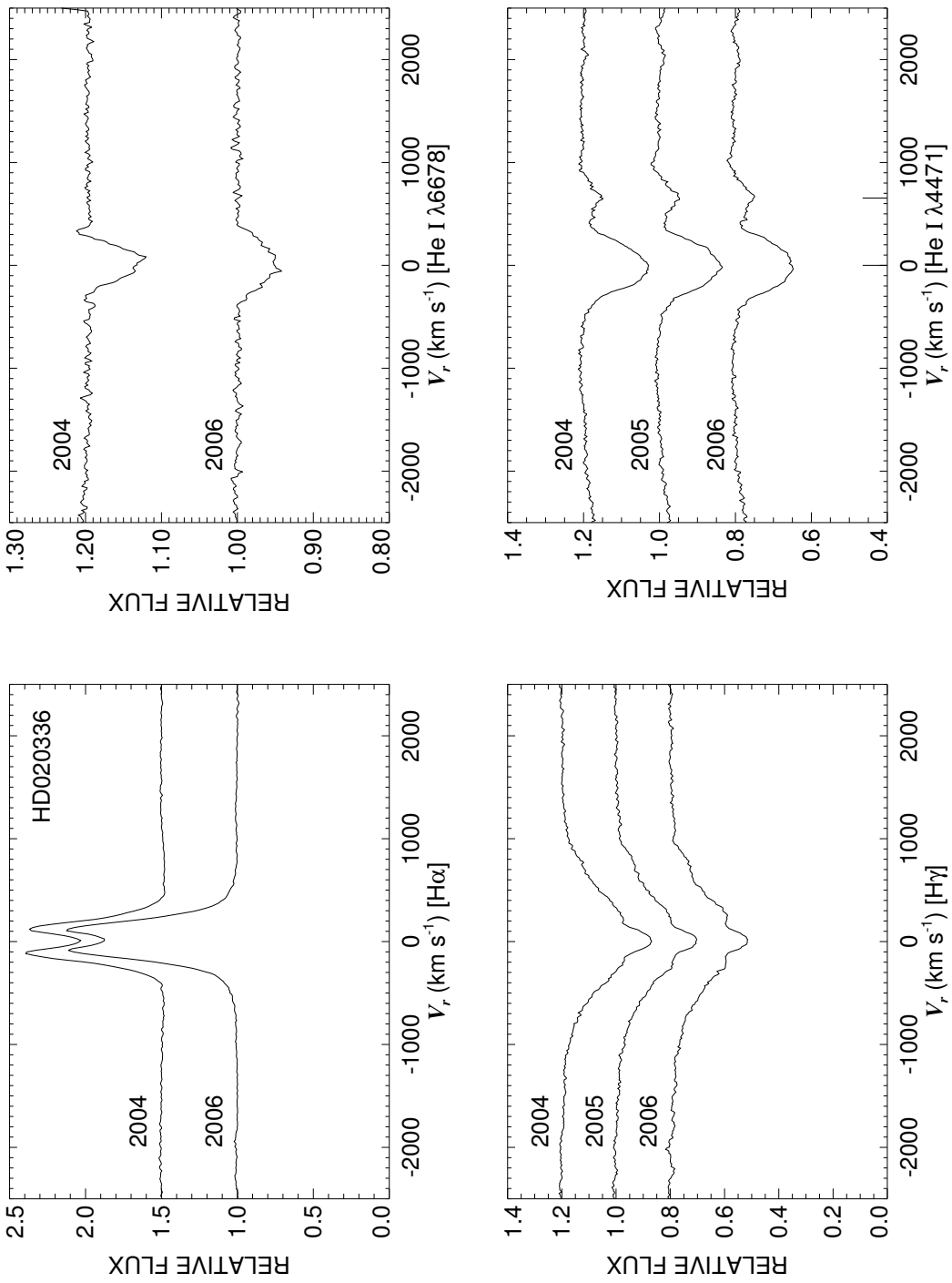

Figure C.19: A quadruple plot of HD020336 as described in §7.2.3 and Figure 7.6.

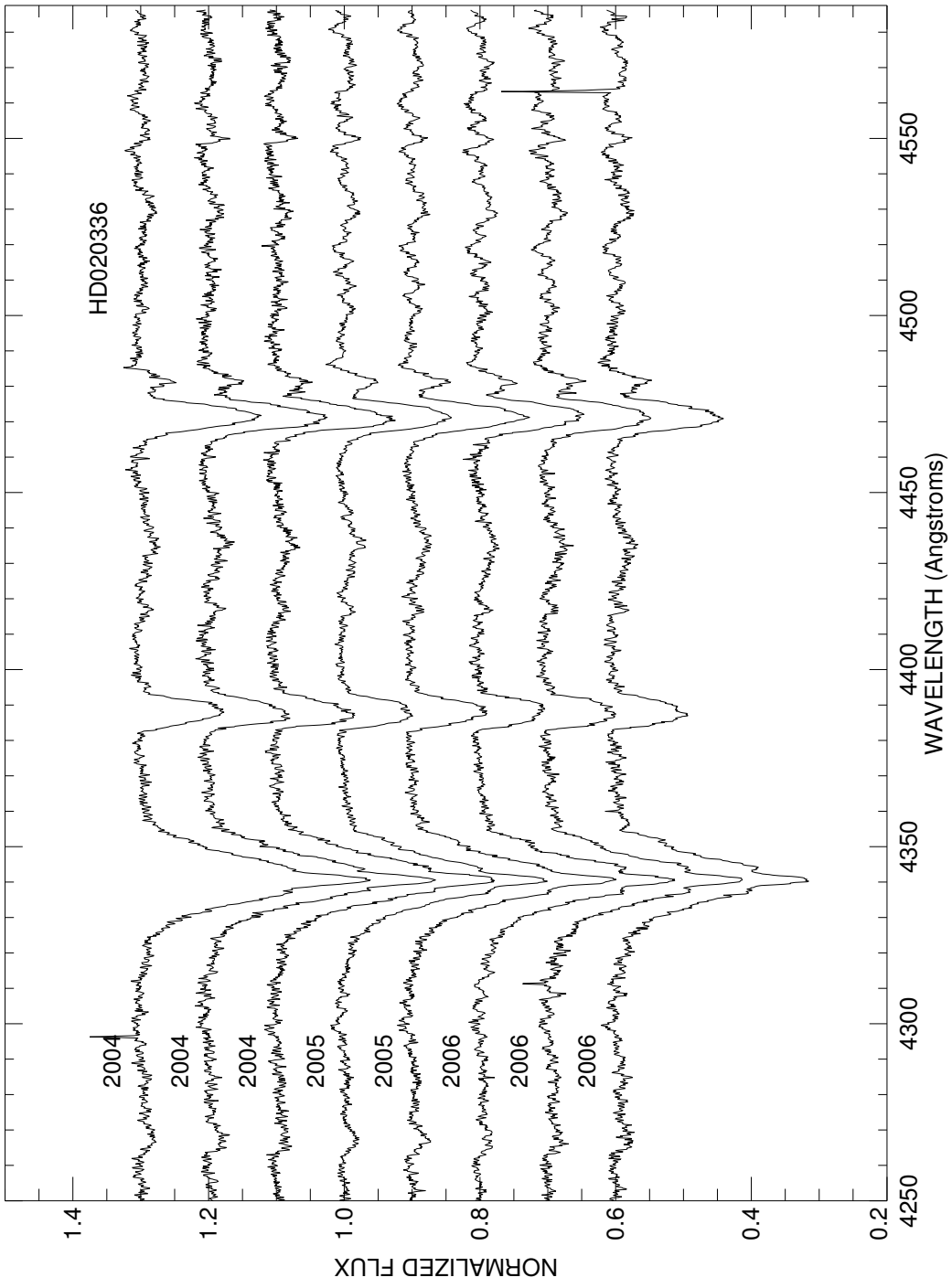

Figure C.20: A plot of all spectra of HD020336 in the blue region. Each is labeled with the year of observation and they are offset for clarity.

HD020418

NOT Be Star

- Other Names: HR 989, 31 Per
- Spectral Type: B5 V
- V magnitude: 4.96
- In WDS?: no
- Known spectroscopic binary?: no
- Velocity variations seen in these data?: no

	Hα	He I λ6678	Hγ	He I λ4471	Mg II λ4481	Fe II ccfs
Mean RV (km s^{-1})	-1.8	-11.3	1.3	-20.1	-18.7	···
RV range (km s^{-1})	-3.4 to -0.3	-29.7 to 2.9	-2.1 to 3.4	-22.5 to -17.4	-22.6 to -14.8	···
RV change (km s^{-1})	3.1	32.6	5.5	5.1	7.8	···

- Other notes: This is NOT a Be star (no record of emission).

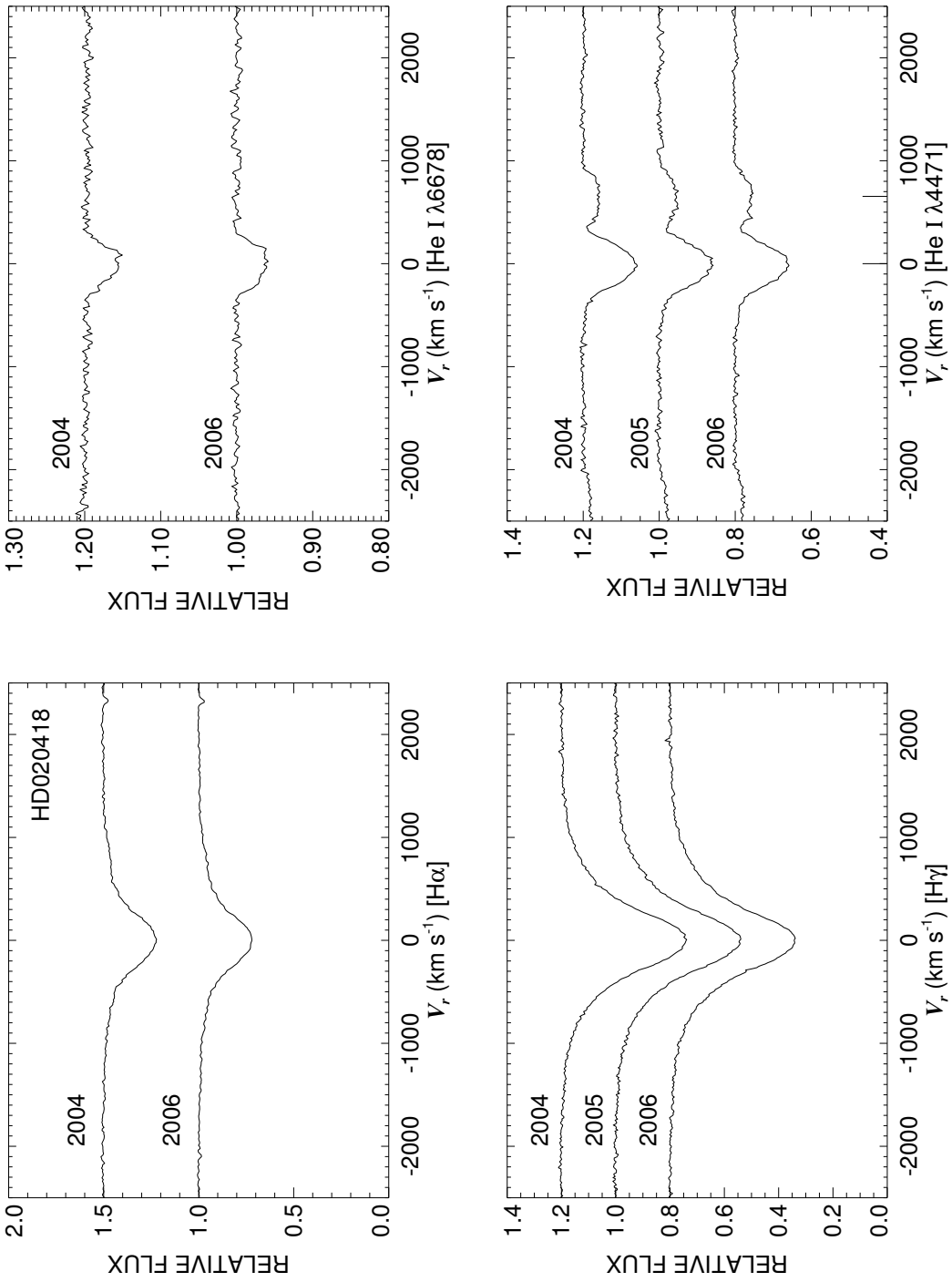

Figure C.21: A quadruple plot of HD020418 as described in §7.2.3 and Figure 7.6.

HD021362

Classical Be Star

- Other Names: HR 1037
- Spectral Type: B6 Vn
- V magnitude: 5.52
- In WDS?: no
- Known spectroscopic binary?: no
- Velocity variations seen in these data?: no

	Hα	He I λ6678	Hγ	He I λ4471	Mg II λ4481	Fe II ccfs
Mean RV (km s^{-1})	2.0	-5.8	-24.7	-9.4	-27.7	10.1
RV range (km s^{-1})	0.4 to 3.4	-32.3 to 36.7	-29.6 to -21.4	-13.0 to -6.0	-39.5 to -13.4	2.3 to 18.4
RV change (km s^{-1})	3.0	69.0	8.2	7.0	26.1	16.1

- Shell classification: squarish (changes can be seen in Fig C.23)
- Do shell features move with the star?: N/A
- Notes on emission and absorption features: Hα strength increases while the shell strength decreases. Both He I λ6678 and Mg II λ4481 have emission on the right and are therefore unusable for RV studies.
- Other notes:

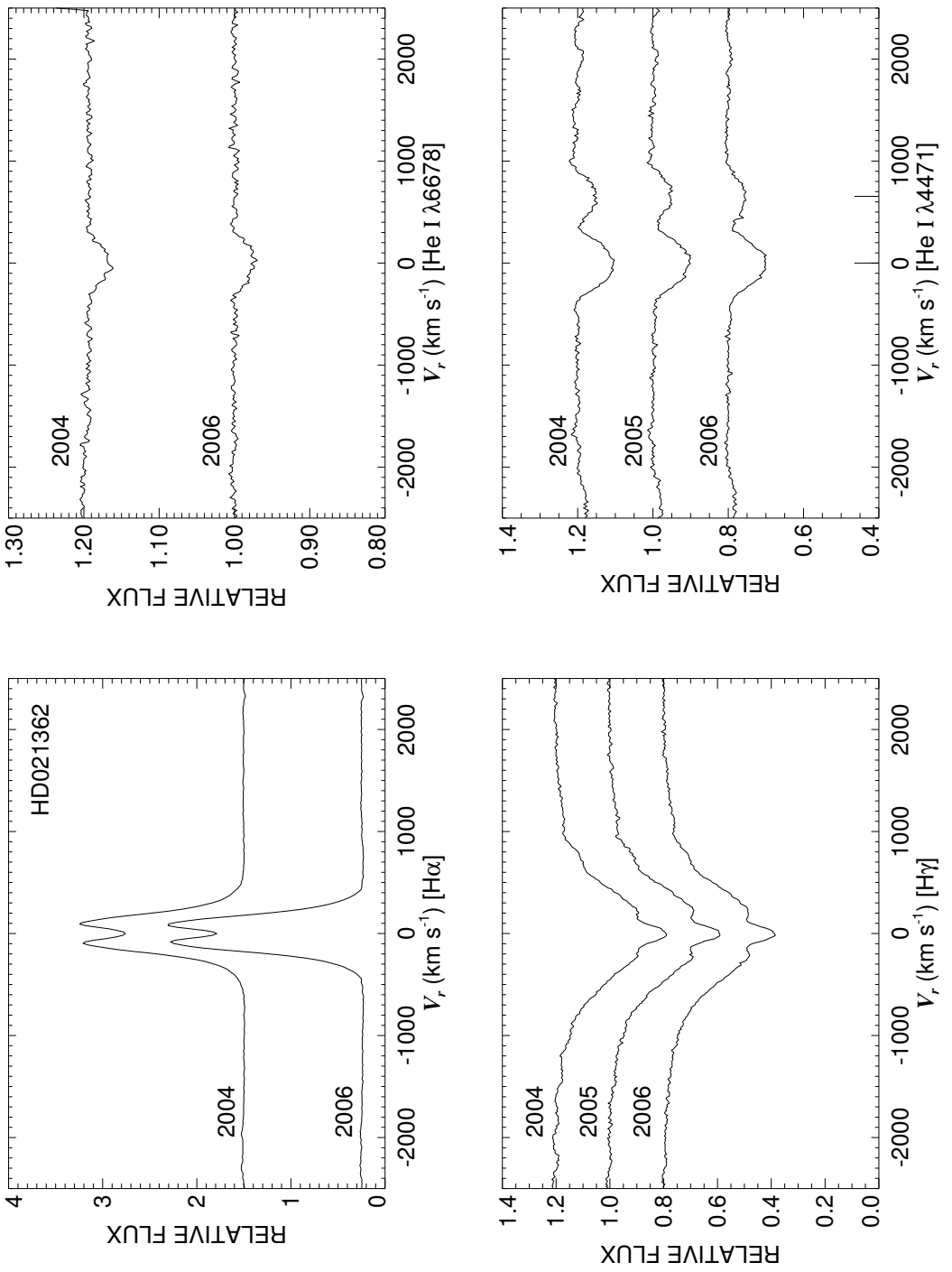

Figure C.22: A quadruple plot of HD021362 as described in §7.2.3 and Figure 7.6.

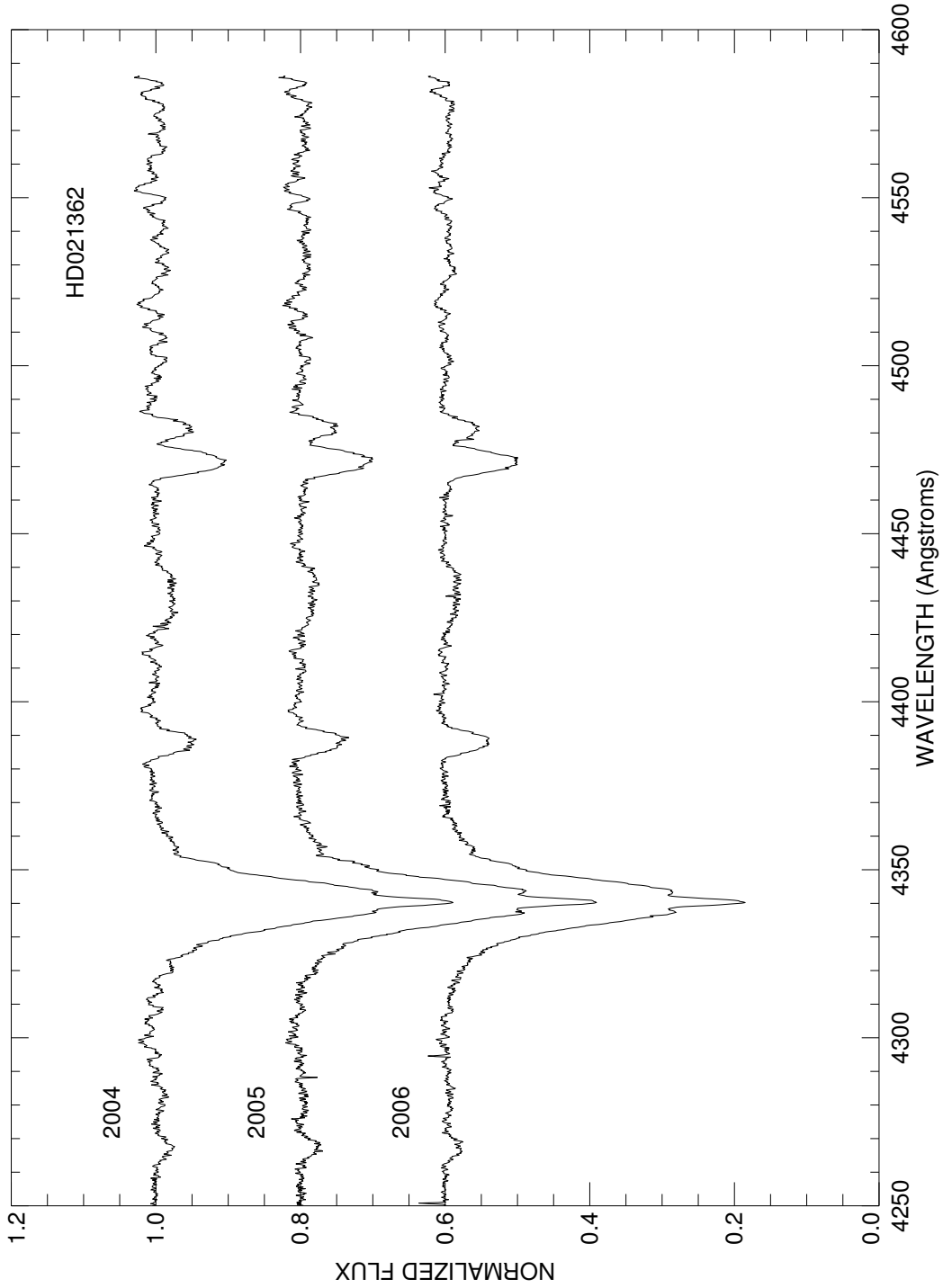

Figure C.23: A plot of the averages for each run in the blue region of HD021362. Each is labeled with the year of observation and they are offset from each other for clarity.

HD021455

Classical Be Star

- Other Names: HR 1047
- Spectral Type: B7 V
- V magnitude: 6.31
- In WDS?: yes - 10.8 mag companion 30 arcsec away (discovered in 1843)
- Known spectroscopic binary?: no
- Velocity variations seen in these data?: no

	Hα	He I λ6678	Hγ	He I λ4471	Mg II λ4481	Fe II ccfs
Mean RV (km s^{-1})	3.1	7.8	5.6	-15.4	0.2	5.3
RV range (km s^{-1})	1.4 to 4.4	3.2 to 15.8	-0.6 to 10.9	-20.2 to -11.7	-0.9 to 1.6	-5.1 to 16.4
RV change (km s^{-1})	3.0	12.6	11.5	8.5	2.5	21.5

- Shell classification: squarish
- Do shell features move with the star?: N/A
- Notes on emission and absorption features: Hα strength decreases slightly from 2004 to 2006.
- Other notes:

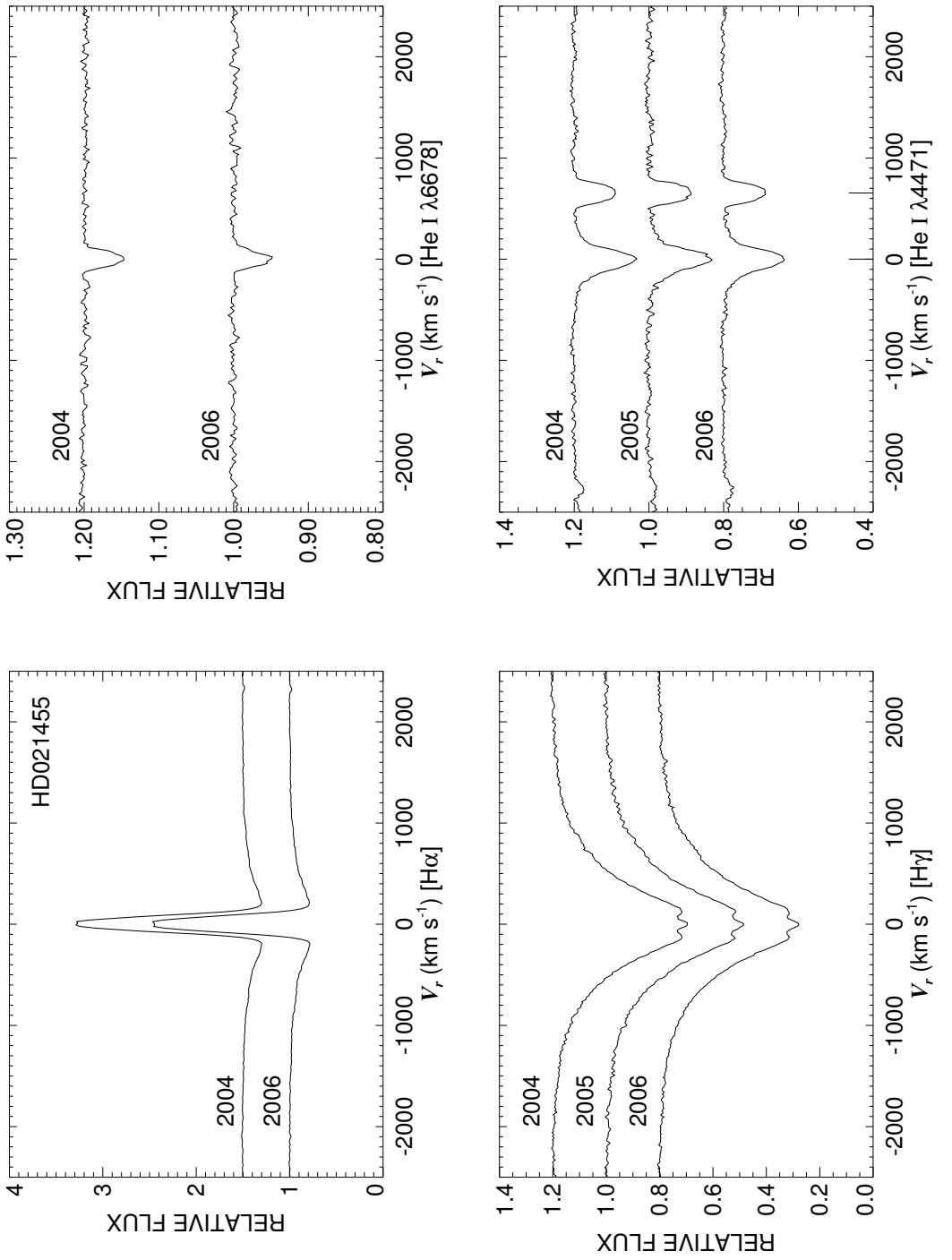

Figure C.24: A quadruple plot of HD021455 as described in §7.2.3 and Figure 7.6.

HD021551

NOT Be Star

- Other Names: HR 1051
- Spectral Type: B7 V
- V magnitude: 5.77
- In WDS?: no
- Known spectroscopic binary?: no
- Velocity variations seen in these data?: yes

	Hα	He I λ6678	Hγ	He I λ4471	Mg II λ4481	Fe II ccfs
Mean RV (km s^{-1})	-1.3	-6.5	7.4	-9.9	-5.9	···
RV range (km s^{-1})	-8.4 to 9.0	-17.7 to 2.5	4.3 to 10.4	-17.3 to -3.3	-17.5 to 1.9	···
RV change (km s^{-1})	17.4	20.2	6.1	14.0	19.4	···

- Notes on emission and absorption features: no emission
- Other notes: This shell was denoted as a "shell" star by Abt & Hunter (1962) but no one has seen in since (see Slettebak (1982)) - Abt & Hunter had just one spectrum but seemed to be careful in general. I use this star in Figure 7.2 to show what a "normal" spectrum looks like.

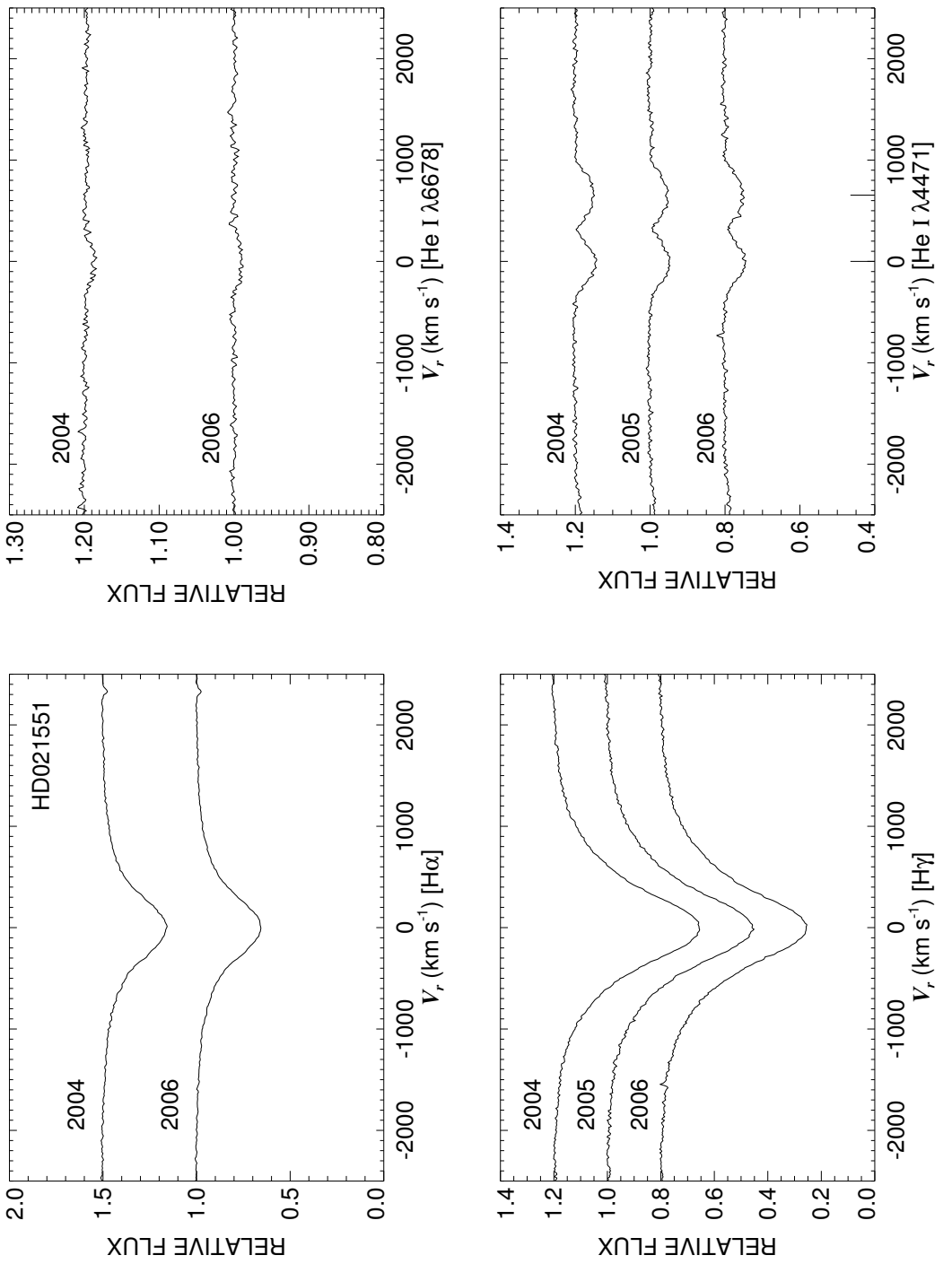

Figure C.25: A quadruple plot of HD021551 as described in §7.2.3 and Figure 7.6.

HD021641

Classical Be Star

- Other Names:
- Spectral Type: B8.5 Ve
- V magnitude: 6.74
- In WDS?: yes - 10.7 mag companion 32 arcsec away (discovered in 1843) and 12.5 mag companion 50 arcsec away (discovered in 1944)
- Known spectroscopic binary?: no
- Velocity variations seen in these data?: no

	Hα	He I λ6678	Hγ	He I λ4471	Mg II λ4481	Fe II ccfs
Mean RV (km s^{-1})	3.1	···	0.3	-2.8	-0.9	1.3
RV range (km s^{-1})	-2.8 to 11.1	···	-6.5 to 5.6	-8.1 to 3.3	-3.0 to 0.6	-6.2 to 12.2
RV change (km s^{-1})	13.9	···	12.1	11.4	3.6	18.4

- Shell classification: squarish
- Do shell features move with the star?: N/A
- Notes on emission and absorption features: He I λ6678 nearly completely filled in.
- Other notes:

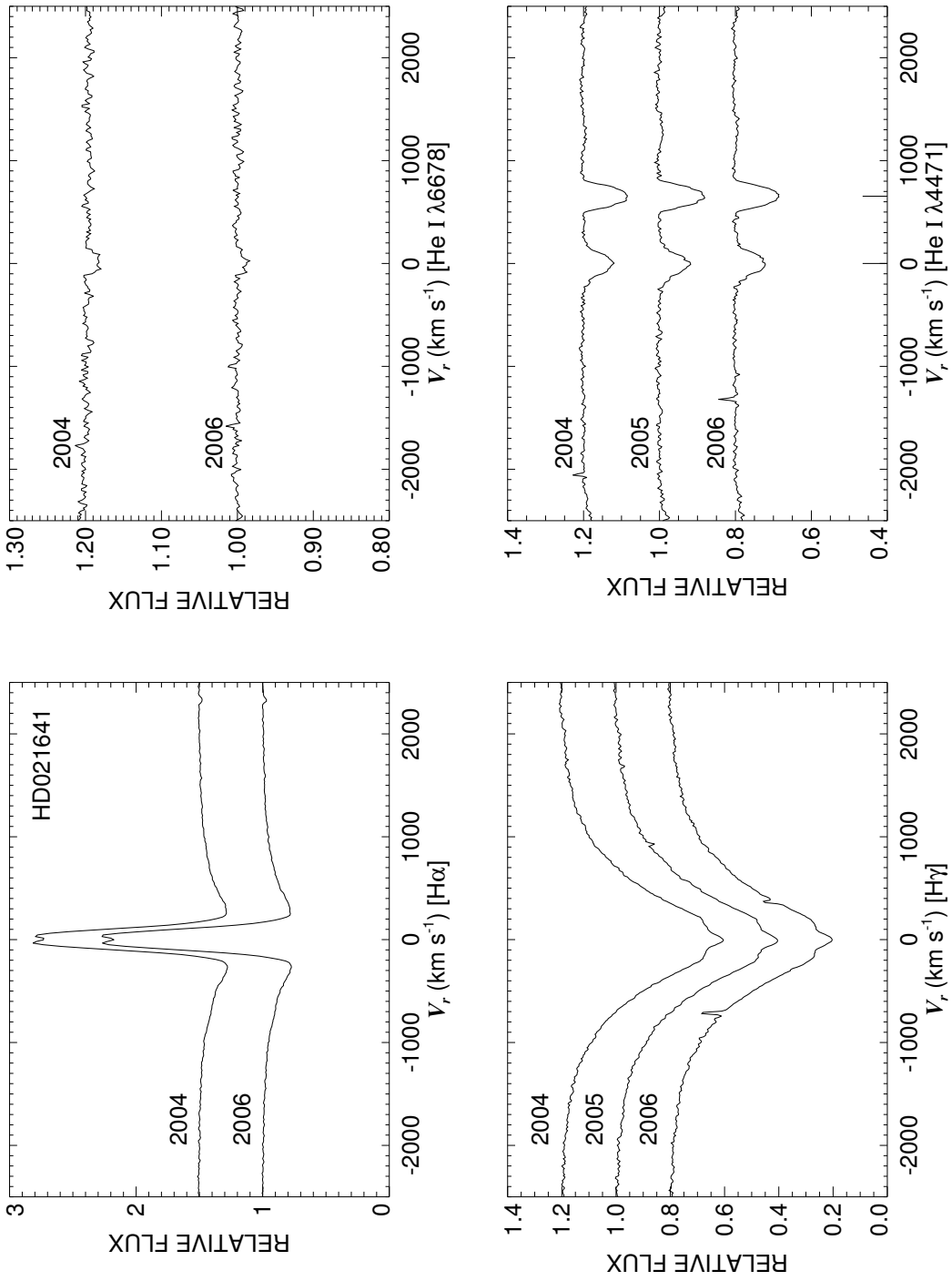

Figure C.26: A quadruple plot of HD021641 as described in §7.2.3 and Figure 7.6.

HD021650

Classical Be Star

- Other Names:
- Spectral Type: B6 Ve
- V magnitude: 7.36
- In WDS?: no
- Known spectroscopic binary?: no
- Velocity variations seen in these data?: if there, very small

	Hα	He I λ6678	Hγ	He I λ4471	Mg II λ4481	Fe II ccfs
Mean RV (km s^{-1})	2.6	4.1	-18.0	-14.4	-30.4	-0.1
RV range (km s^{-1})	1.6 to 3.9	-29.7 to 65.2	-24.1 to -12.9	-20.8 to -4.1	-39.8 to -18.5	-3.6 to 4.1
RV change (km s^{-1})	2.3	94.9	11.2	16.7	21.3	7.8

- Shell classification: squarish
- Do shell features move with the star?: if there, yes
- Notes on emission and absorption features: Hα emission grows from 2004 to 2006 (so does Hγ emission). He I λ6678 is almost totally filled in.
- Other notes: This star is also plotted in Figure 7.3.

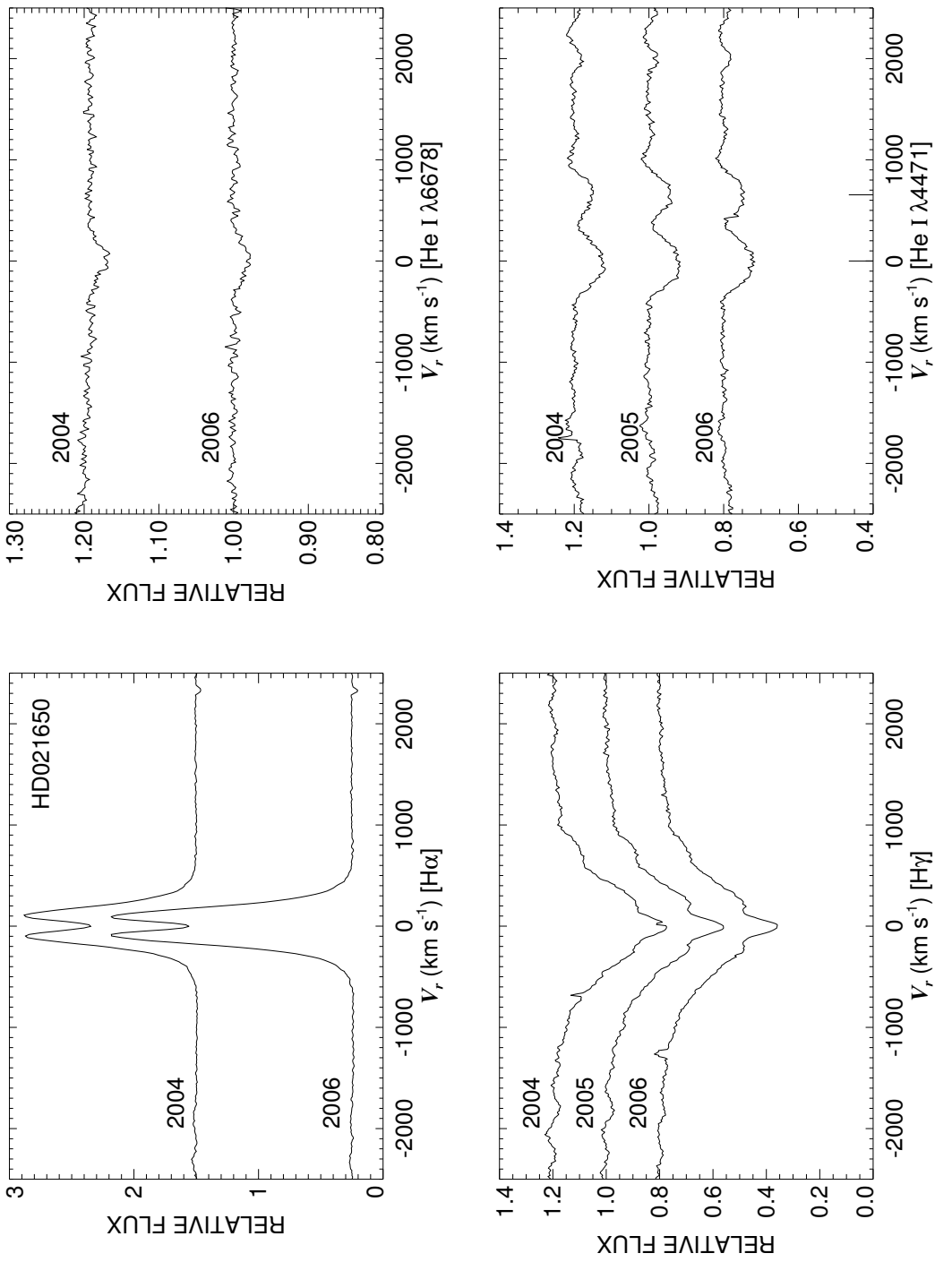

Figure C.27: A quadruple plot of HD021650 as described in §7.2.3 and Figure 7.6.

HD022192

Classical Be Star; Shell Star

- Other Names: HR 1087, ψ Per, 37 Per
- Spectral Type: B4.5 Ve+sh
- V magnitude: 4.25
- In WDS?: no
- Known spectroscopic binary?: no
- Velocity variations seen in these data?: no

	Hα	He I λ6678	Hγ	He I λ4471	Mg II λ4481	Fe II ccfs
Mean RV (km s^{-1})	3.4	-14.5	-9.7	-6.5	-33.9	-0.6
RV range (km s^{-1})	2.1 to 5.0	-56.6 to 60.0	-14.4 to -3.6	-10.3 to -3.3	-51.1 to -19.4	-9.5 to 12.2
RV change (km s^{-1})	2.9	116.6	10.8	7.0	31.7	21.7

- Shell classification: squarish (they increase esp. from 2004 to 2005)
- Do shell features move with the star?: N/A
- Notes on emission and absorption features: Strong hydrogen self-absorption signifies nearly edge-on orientation.
- Other notes: This star has Hα interferometric measurements (Quirrenbach et al. 1997). It is also plotted in Figure 7.3.

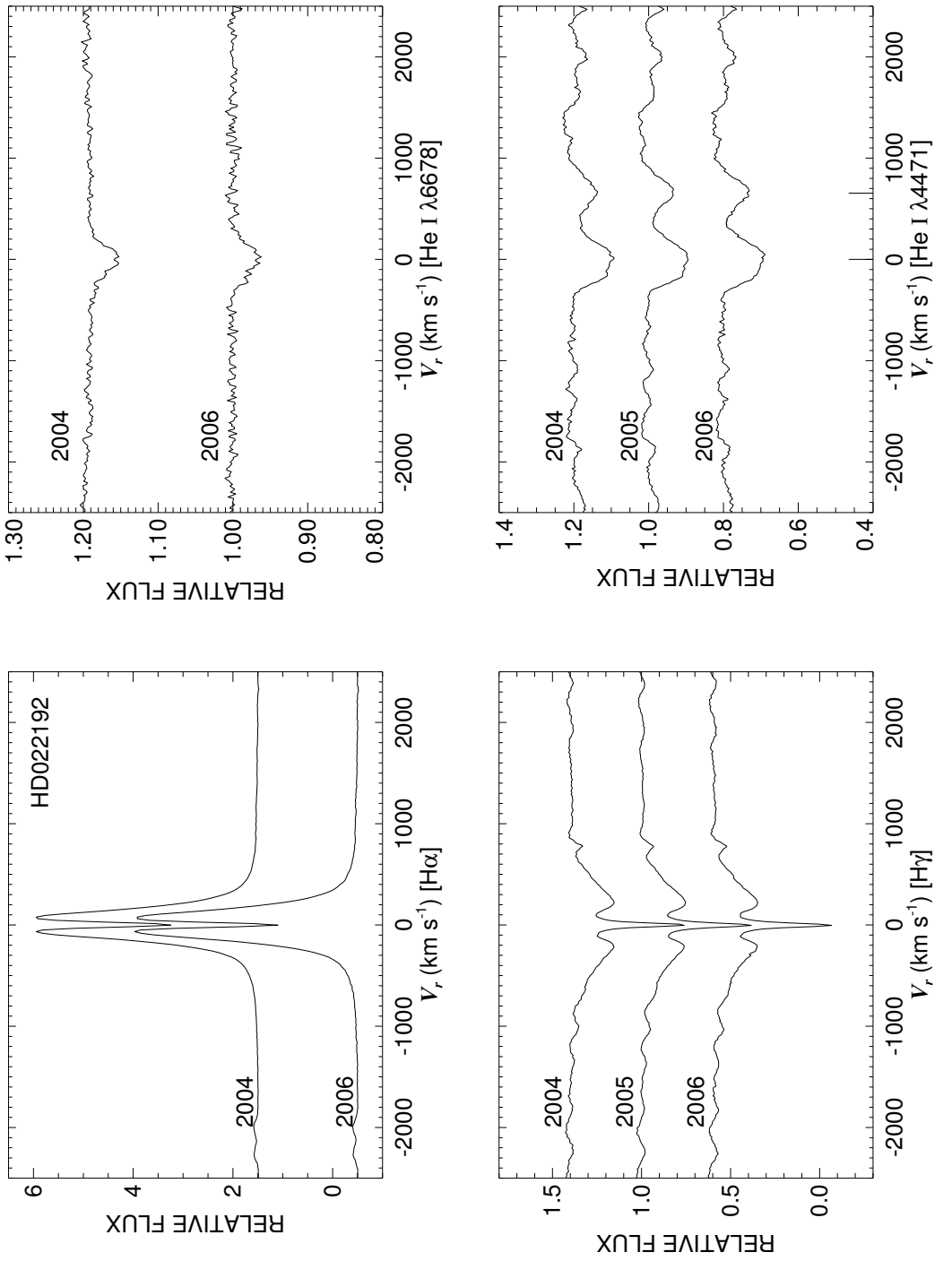

Figure C.28: A quadruple plot of HD022192 as described in §7.2.3 and Figure 7.6.

HD022780

Classical Be Star

- Other Names: HR 1113
- Spectral Type: B7 Vne
- V magnitude: 5.47
- In WDS?: no
- Known spectroscopic binary?: no
- Velocity variations seen in these data?: no (small if there)

	Hα	He I λ6678	Hγ	He I λ4471	Mg II λ4481	Fe II ccfs
Mean RV (km s^{-1})	0.2	-9.8	6.4	-20.4	-15.8	···
RV range (km s^{-1})	-5.8 to 6.5	-49.2 to 48.6	2.5 to 10.8	-29.6 to -14.2	-19.9 to -10.8	···
RV change (km s^{-1})	12.3	97.8	8.3	15.4	9.1	···

- Shell classification: normal
- Notes on emission and absorption features: Emission in Hα decreasing. He I λ6678 measurements unreliable as it is rotationally broadened plus may be filled in with some emission.
- Other notes:

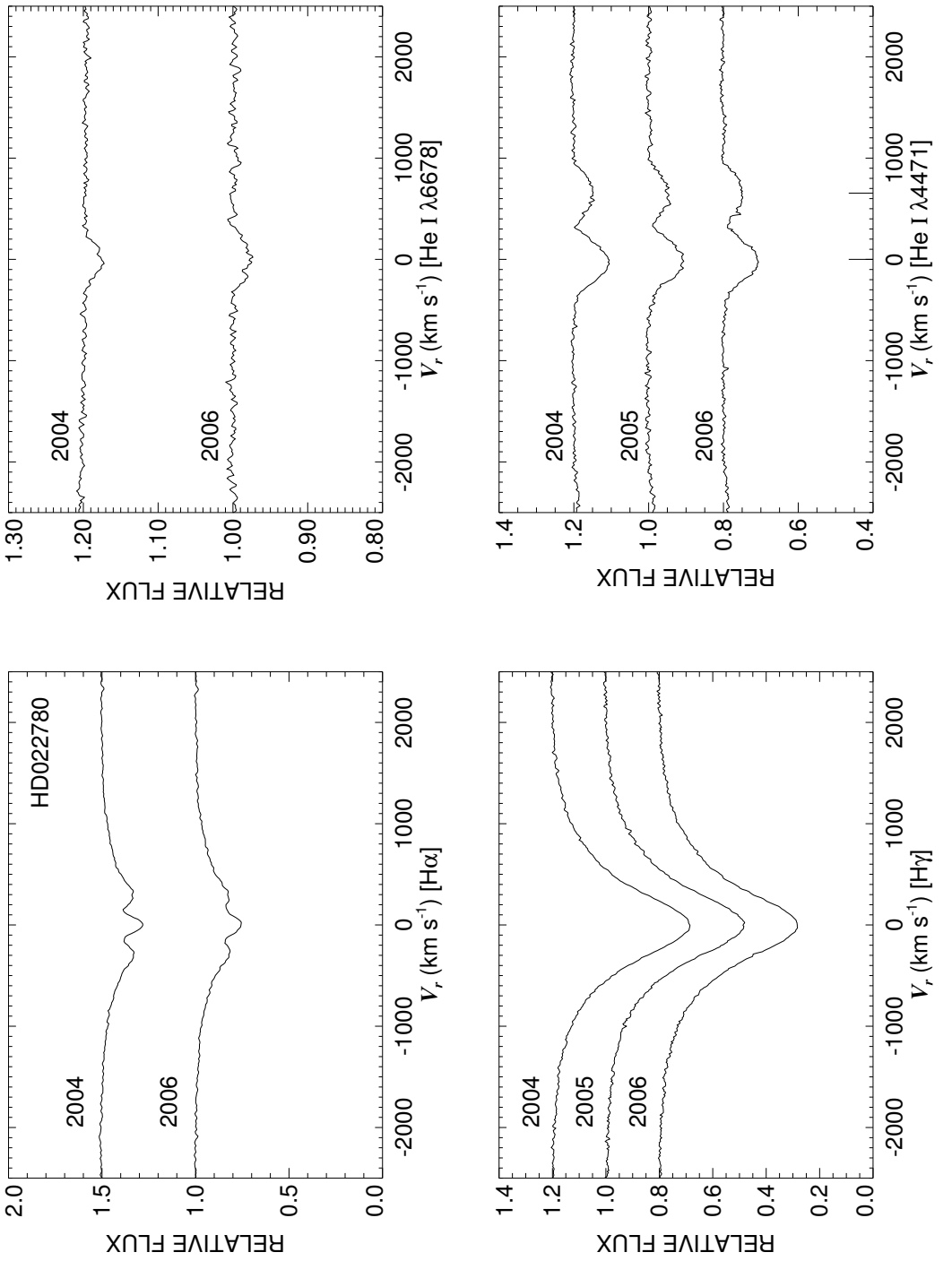

Figure C.29: A quadruple plot of HD022780 as described in §7.2.3 and Figure 7.6.

HD023016

Classical Be Star

- Other Names: HR 1126, 13 Tau
- Spectral Type: B8.5 Vne
- V magnitude: 5.66
- In WDS?: no
- Known spectroscopic binary?: no
- Velocity variations seen in these data?: no

	Hα	He I λ6678	Hγ	He I λ4471	Mg II λ4481	Fe II ccfs
Mean RV (km s^{-1})	10.6	-28.7	19.1	2.5	6.0	34.6
RV range (km s^{-1})	4.2 to 15.1	-51.2 to -2.7	13.7 to 23.3	-1.3 to 9.8	2.2 to 10.6	15.5 to 51.8
RV change (km s^{-1})	10.9	48.5	9.6	11.1	8.4	36.3

- Shell classification: squarish
- Do shell features move with the star?: N/A
- Notes on emission and absorption features: He I λ6678 practically non-existent (emission filling).
- Other notes:

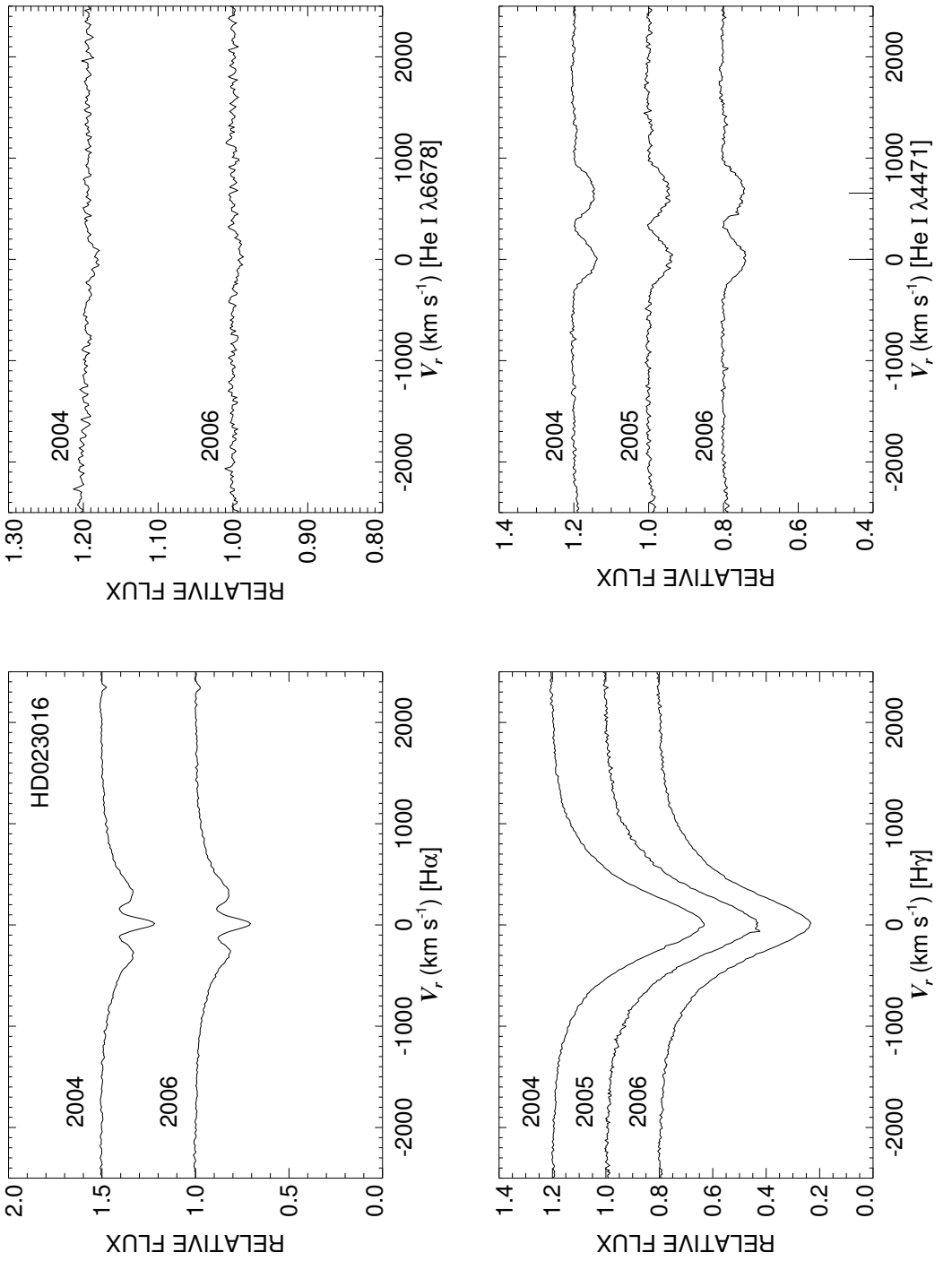

Figure C.30: A quadruple plot of HD023016 as described in §7.2.3 and Figure 7.6.

HD023302

Classical Be Star

- Other Names: HR 1142, 17 Tau, Electra
- Spectral Type: B6 IIIe
- V magnitude: 3.61
- In WDS?: yes - 4 fainter companions (mag 13, 13, 11, 10) at 105, 150, 231, and 181 arcsec away (discovered in 1886)
- Known spectroscopic binary?: possibly - Harmanec (2001) gives a possible period of 100.5 d from other people (and refers to the fact the orbital motion has never been confirmed)
- Velocity variations seen in these data?: no

	Hα	He I λ6678	Hγ	He I λ4471	Mg II λ4481	Fe II ccfs
Mean RV (km s^{-1})	8.6	-1.8	6.8	-6.3	3.3	14.3
RV range (km s^{-1})	6.9 to 12.6	-9.9 to 6.4	4.1 to 9.4	-9.0 to -4.8	-0.6 to 10.4	4.7 to 28.6
RV change (km s^{-1})	5.7	16.3	5.3	4.2	11.0	23.9

- Shell classification: squarish
- Do shell features move with the star?: N/A
- Notes on emission and absorption features: Hα emission grows from 2004 to 2006. He I λ6678 appears to have some small emission horns (esp. in 2004).
- Other notes:

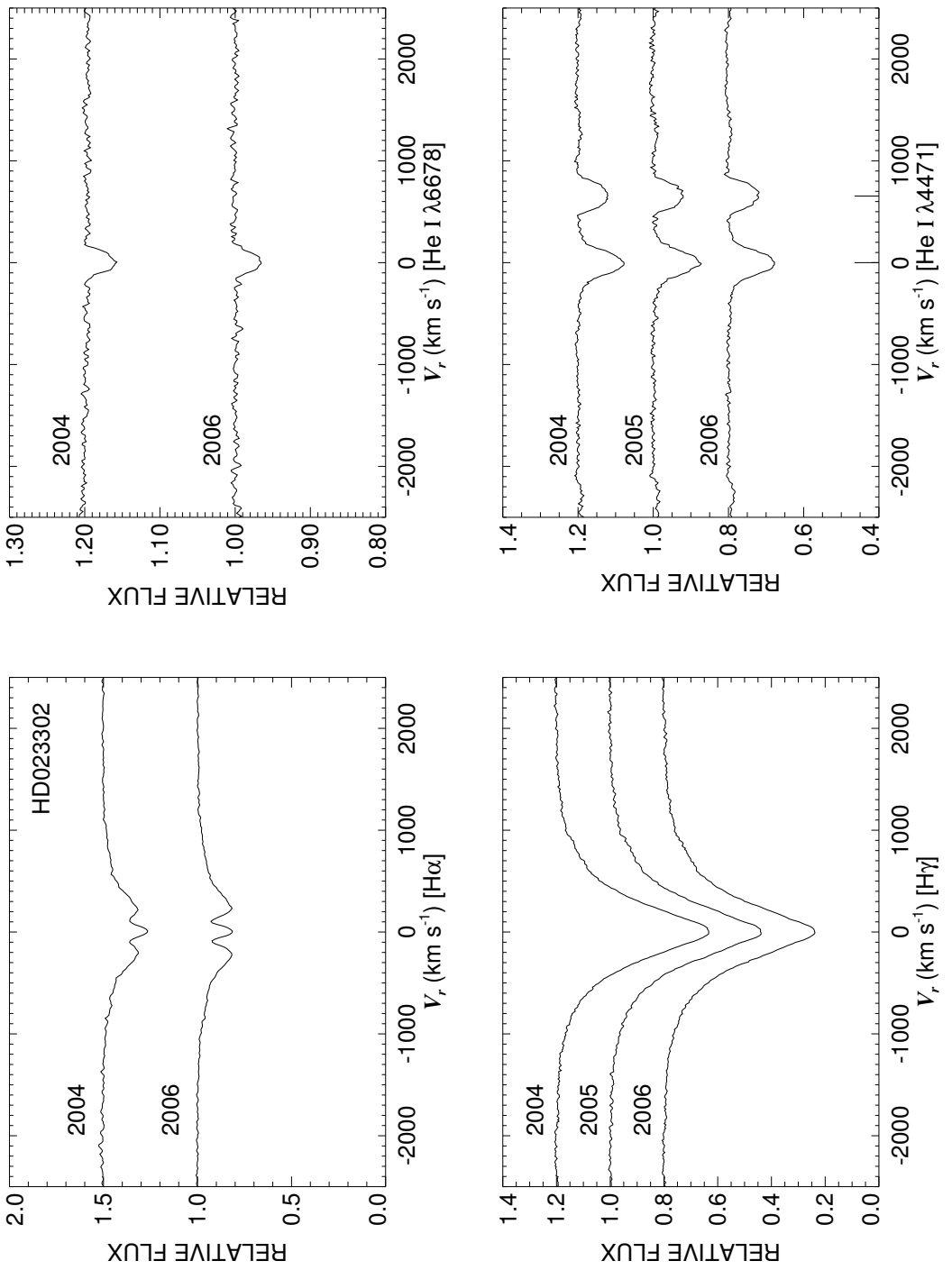

Figure C.31: A quadruple plot of HD023302 as described in §7.2.3 and Figure 7.6.

HD023478

NOT Classical Be Star - a dust disk

- Other Names: BD+31°649, HIP17631
- Spectral Type: B3 IVe:
- V magnitude: 6.71
- In WDS?: no
- Known spectroscopic binary?: yes - the central binary is actually resolved (yet not in WDS? Why?), see notes below.
- Velocity variations seen in these data?: no

	Hα	He I λ6678	Hγ	He I λ4471	Mg II λ4481	Fe II ccfs
Mean RV (km s^{-1})	26.5	22.1	22.5	-22.2	5.1	···
RV range (km s^{-1})	12.6 to 39.0	8.9 to 52.4	14.9 to 31.2	-28.6 to -15.3	2.4 to 7.8	···
RV change (km s^{-1})	26.4	43.5	16.3	13.3	5.4	···

- Shell classification: not normal, but did not correlate with Fe II
- Do shell features move with the star?:
- Notes on emission and absorption features: Hα looks very strange compared to classical Be stars.
- Other notes: This star is embedded in the young dusty cluster IC 348 and there is an image of a dust disk published in Nature (Kalas & Jewitt 1997) - it is bigger than that of β Pic (this one is ≈6000 AU). The central star is actually a resolved pair of stars that are both B5 (separation of 0.45 to 0.76 arcsec) (Eggen 1963) with an age of 6-7 × 10^6 y. Brunini (1998) found preliminary orbital elements using astrometric measurements - a period of 6000 to 7000 y, a separation of 364 AU and an inclination of 45°. The spectrum shows evidence of Si III that is only seen in hotter stars (late O/early B) so at least one of the two stars is likely hotter.

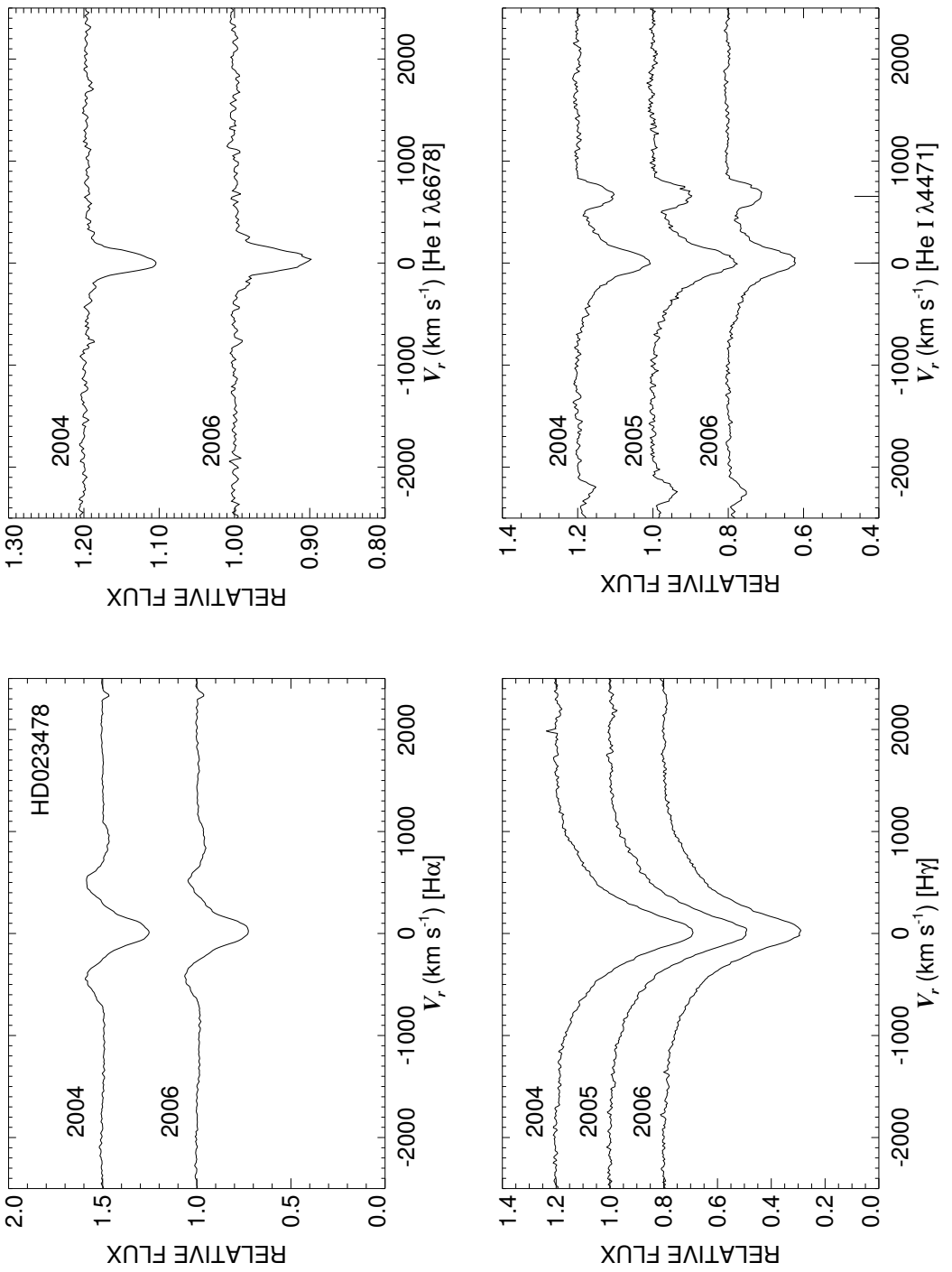

Figure C.32: A quadruple plot of HD023478 as described in §7.2.3 and Figure 7.6.

HD023480

Classical Be Star

- Other Names: HR 1156, 23 Tau, V971 Tau, Merope
- Spectral Type: B6.5 IVe
- V magnitude: 4.11
- In WDS?: yes, 14 and 13 mag companions 110 and 146 arcsec away (discovered in 1887)
- Known spectroscopic binary?: no
- Velocity variations seen in these data?: no

	Hα	He I λ6678	Hγ	He I λ4471	Mg II λ4481	Fe II ccfs
Mean RV (km s^{-1})	8.6	-4.1	19.3	-10.2	3.3	···
RV range (km s^{-1})	6.7 to 9.8	-15.6 to 7.1	16.5 to 21.8	-14.5 to -5.8	-4.3 to 8.0	···
RV change (km s^{-1})	3.1	22.7	5.3	8.7	12.3	···

- Shell classification: normal
- Notes on emission and absorption features: Hα decreases. He I λ6678 looks filled-in (esp. on right).
- Other notes:

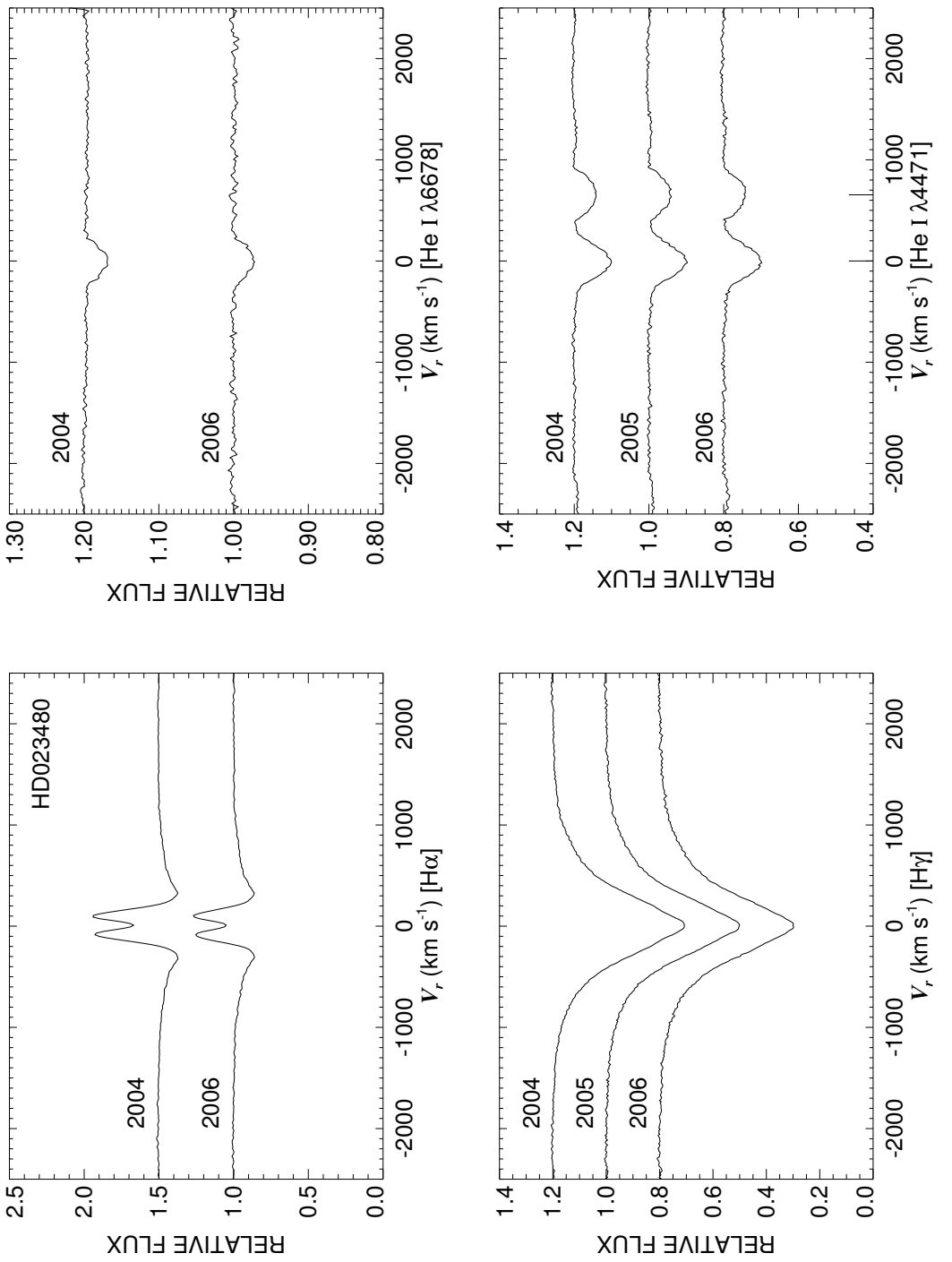

Figure C.33: A quadruple plot of HD023480 as described in §7.2.3 and Figure 7.6.

HD023552

Classical Be Star

- Other Names: HR 1160
- Spectral Type: B8 Vne
- V magnitude: 6.20
- In WDS?: yes - 11.2 mag companion 6.8 arcsec away (discovered in 1848)
- Known spectroscopic binary?: no
- Velocity variations seen in these data?: no

	Hα	He I λ6678	Hγ	He I λ4471	Mg II λ4481	Fe II ccfs
Mean RV (km s^{-1})	-15.6	-19.4	-20.9	-17.2	-19.2	···
RV range (km s^{-1})	-19.1 to -11.8	-30.1 to -12.1	-25.6 to -15.3	-20.4 to -14.0	-26.0 to -10.7	···
RV change (km s^{-1})	7.3	18.0	10.3	6.4	15.3	···

- Shell classification: normal
- Notes on emission and absorption features: Hα peaks change a bit.
- Other notes:

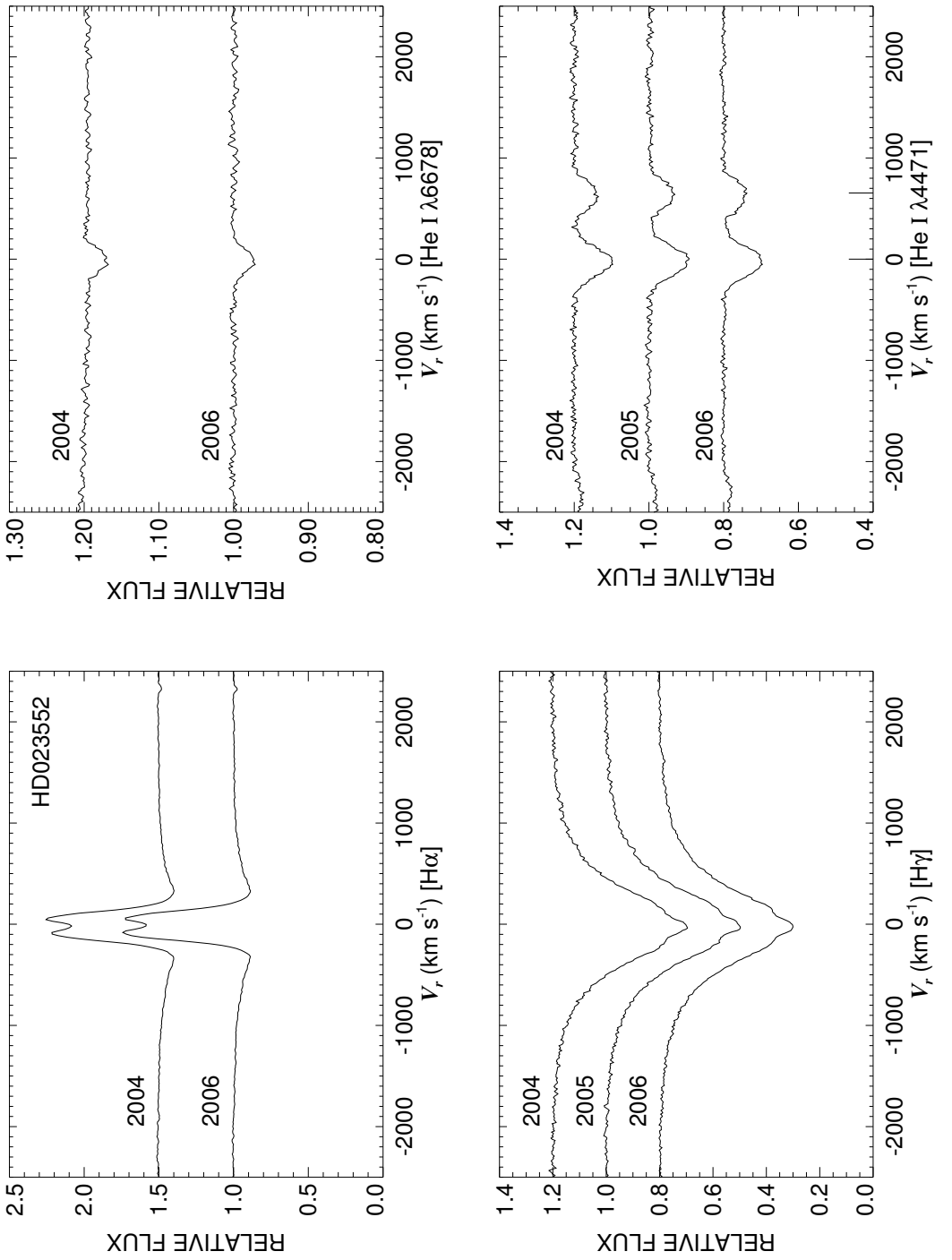

Figure C.34: A quadruple plot of HD023552 as described in §7.2.3 and Figure 7.6.

HD023630

Classical Be Star

- Other Names: HR 1165, η Tau, 25 Tau, Alcyone
- Spectral Type: B7 IIIe
- V magnitude: 2.80
- In WDS?: yes - A4 V 6.27 mag companion 117 arcsec away (discovered in 1836), an A7 V 8.22 mag companion 181 arcsec away and a 8.73 mag companion 191 arcsec away (both discovered in 1868) and 4 fainter companions (mag 15, 14, 11, 11) at 78, 143, 199 and 221 arcsec away (all 4 discovered in 1885).
- Known spectroscopic binary?: possibly - Harmanec (2001) reports a period of 4.1349 d found by others who suggest that period tentatively
- Velocity variations seen in these data?: no

	Hα	He I λ6678	Hγ	He I λ4471	Mg II λ4481	Fe II ccfs
Mean RV (km s^{-1})	7.7	-6.0	3.8	8.4	5.0	9.4
RV range (km s^{-1})	6.1 to 8.5	-19.6 to 31.5	1.2 to 6.8	6.2 to 11.6	0.9 to 10.2	-0.3 to 17.2
RV change (km s^{-1})	2.4	51.1	5.6	5.4	9.3	17.5

- Shell classification: squarish
- Do shell features move with the star?: N/A
- Notes on emission and absorption features: He I λ6678 appears filled in by emission
- Other notes: Has Hα interferometric measurements (Quirrenbach et al. 1997; Tycner et al. 2005).

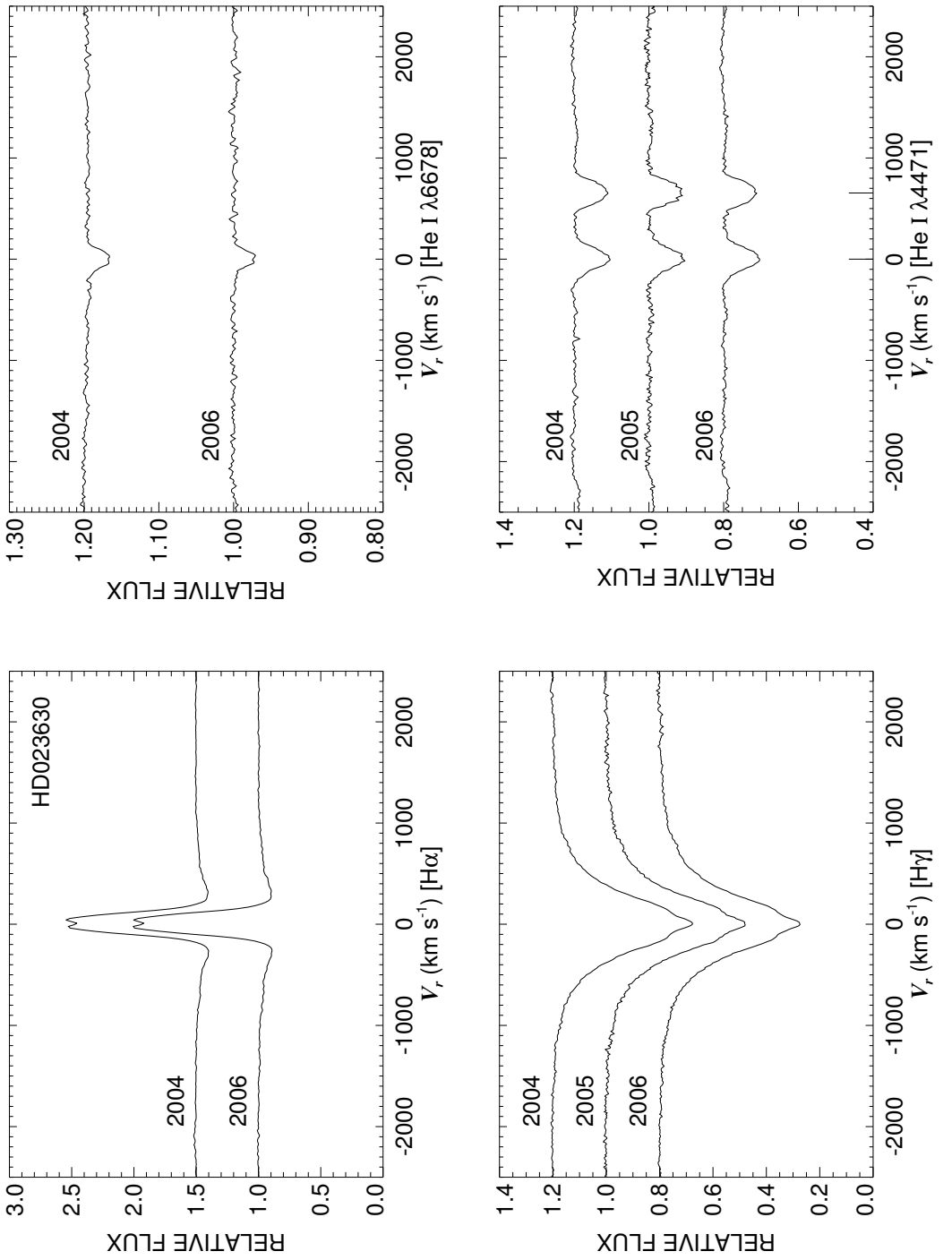

Figure C.35: A quadruple plot of HD023630 as described in §7.2.3 and Figure 7.6.

HD023800

Classical Be Star?

- Other Names:
- Spectral Type: B1.5 IVe
- V magnitude: 7.20
- In WDS?: no
- Known spectroscopic binary?: no
- Velocity variations seen in these data?: possibly

	Hα	He I λ6678	Hγ	He I λ4471	Mg II λ4481	Fe II ccfs
Mean RV (km s^{-1})	-12.6	-12.6	63.6	-31.4	-49.3	···
RV range (km s^{-1})	-32.9 to 12.4	-27.1 to -0.6	40.0 to 74.3	-45.0 to -22.5	-67.3 to -29.8	···
RV change (km s^{-1})	45.3	26.5	34.3	22.5	37.5	···

- Shell classification: normal
- Notes on emission and absorption features: Hα has an unusual shape not indicative of a classical Be star. Hγ has a really big, broad wing, caused by a blend with O 2 λ4349.
- Other notes: Percy et al. (2002) confirm this star is a short-period variable using Hipparcos photometry. 2MASS K observations show a big IR excess.

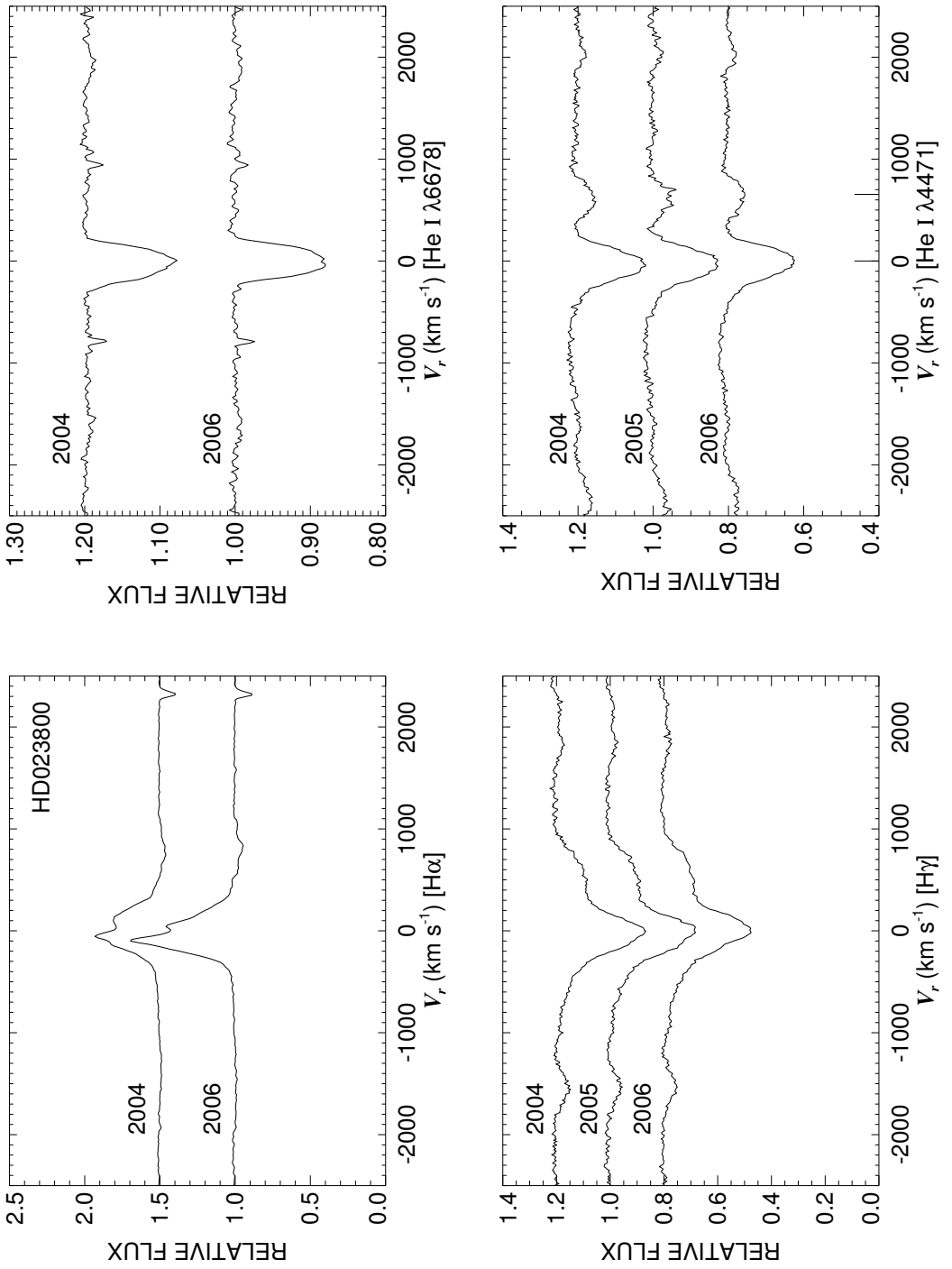

Figure C.36: A quadruple plot of HD023800 as described in §7.2.3 and Figure 7.6.

HD023862

Classical Be Star; Shell Star

- Other Names: HR 1180, 28 Tau, Pleione
- Spectral Type: B8 Vpe+sh
- V magnitude: 4.96
- In WDS?: yes - a speckle companion of unlisted magnitude 0.2 arcsec away (discovered in 1987) and 4 faint companions (mag 12, 10, 14, 15) at 168, 223, 144, and 97 arcsec away (all discovered in 1886).
- Known spectroscopic binary?: possibly - Harmanec (2001) reports a period of 218.0 d from others, but observes that the RV curve has a great deal of scatter
- Velocity variations seen in these data?: unknown

	Hα	He I λ6678	Hγ	He I λ4471	Mg II λ4481	Fe II ccfs
Mean RV (km s^{-1})	8.8	0.2	-1.5	-28.4	-7.7	-7.4
RV range (km s^{-1})	1.9 to 13.2	-29.9 to 43.1	-14.1 to 7.8	-71.4 to 9.5	-27.5 to 8.4	-42.3 to 8.2
RV change (km s^{-1})	11.3	73.0	21.9	80.9	35.9	50.4

- Shell classification: emission shell changes to strong absorption shell (see Fig. C.38)
- Do shell features move with the star?: N/A
- Notes on emission and absorption features: The Hα emission decreases, but the shell features dramatically strengthen at the same time. He I λ6678 becomes less filled in from 2004 to 2006.
- Other notes: This star is known to go through shell episodes periodically (Cramer et al. 1995).

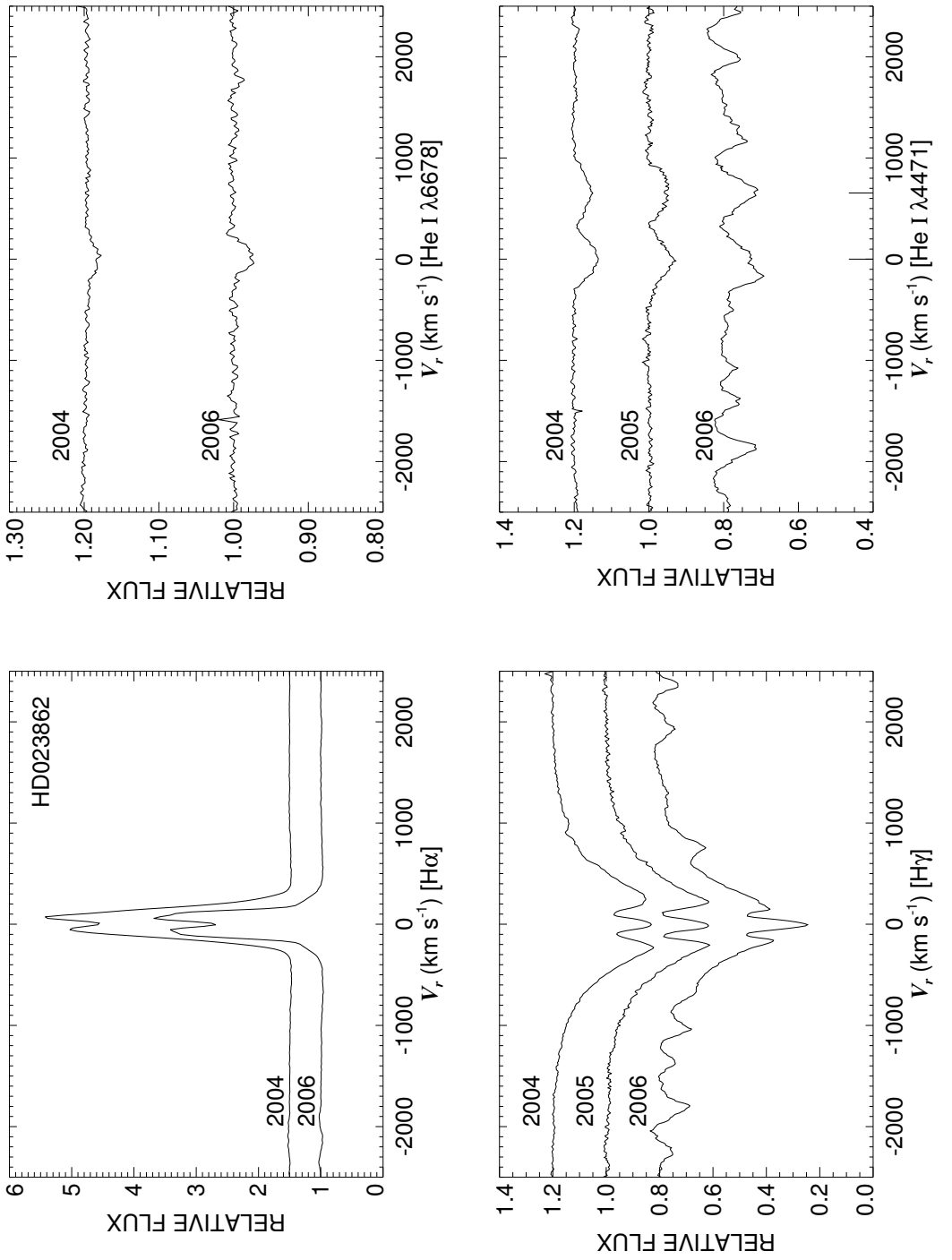

Figure C.37: A quadruple plot of HD023862 as described in §7.2.3 and Figure 7.6.

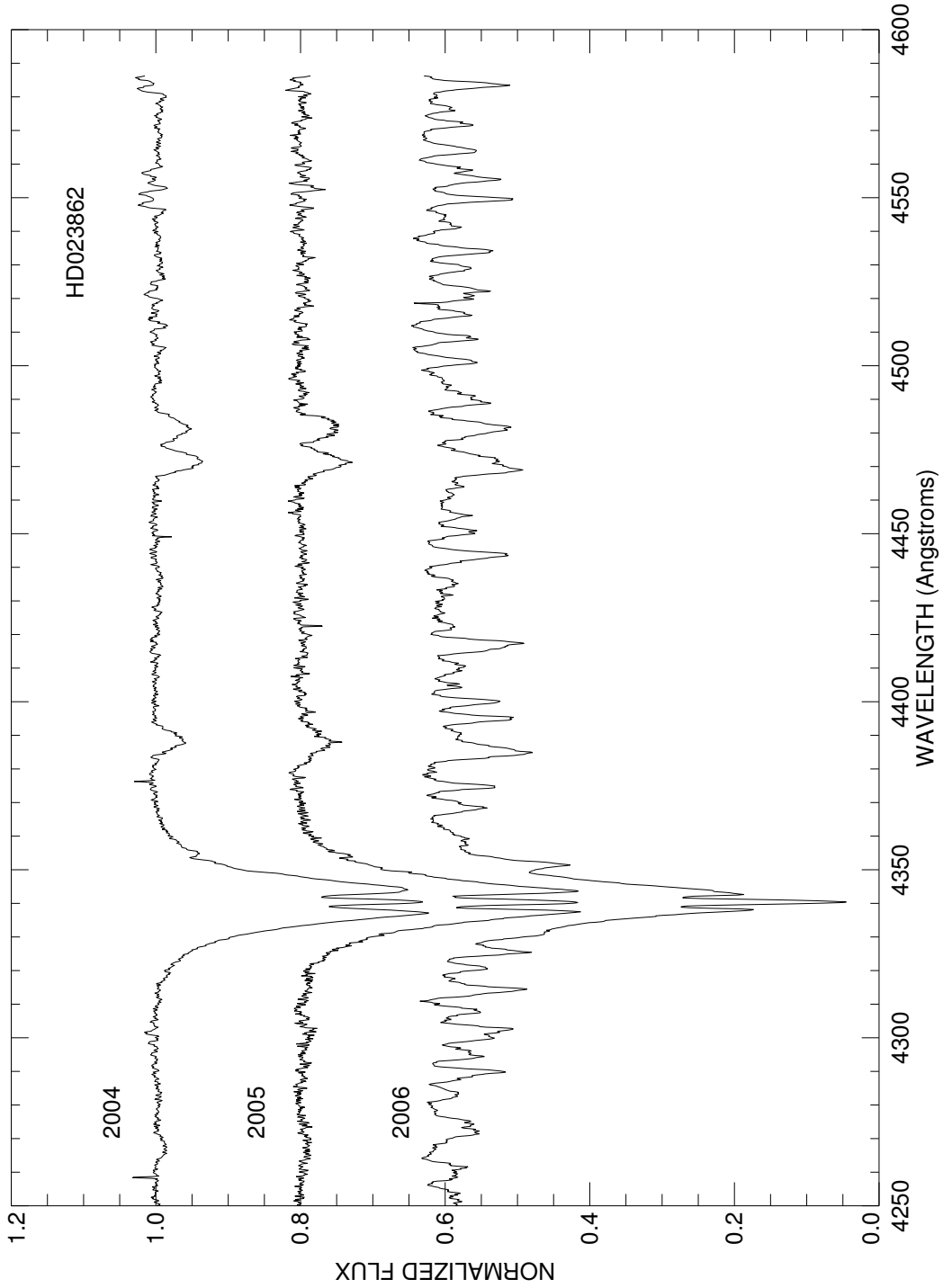

Figure C.38: A plot of the averages for each run in the blue region of HD023862. Each is labeled with the year of observation and they are offset from each other for clarity.

HD024479

Classical Be Star

- Other Names: HR 1204
- Spectral Type: B9.5Ve
- V magnitude: 4.89
- In WDS?: no
- Known spectroscopic binary?: no
- Velocity variations seen in these data?: no

	Hα	He I λ6678	Hγ	He I λ4471	Mg II λ4481	Fe II ccfs
Mean RV (km s^{-1})	-0.7	···	3.8	-30.1	-1.3	-7.0
RV range (km s^{-1})	-4.5 to 1.7	···	0.5 to 6.8	-35.1 to -18.8	-2.5 to 1.3	-10.3 to -5.5
RV change (km s^{-1})	6.2	···	6.3	16.3	3.8	4.8

- Shell classification: squarish (although they may be photospheric as the star is rather cool)
- Do shell features move with the star?: N/A
- Notes on emission and absorption features: Both helium lines are very small, mostly due to the relatively low temperature of this star.
- Other notes: This star is also plotted in Figure 7.3.

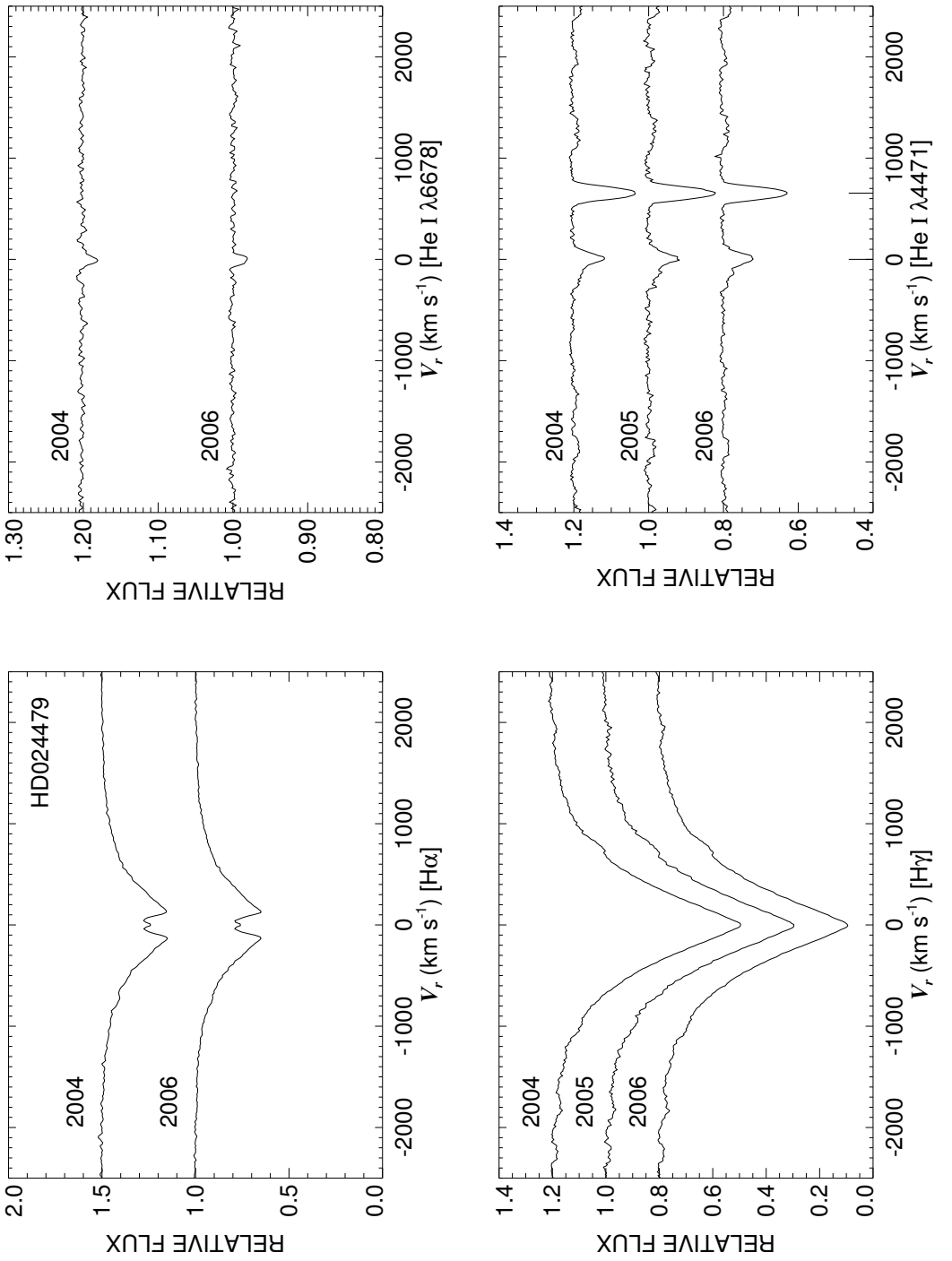

Figure C.39: A quadruple plot of HD024479 as described in §7.2.3 and Figure 7.6.

HD024534

Be X-ray Binary

- Other Names: HR 1209, X Per
- Spectral Type: O9.5 Vep
- V magnitude: 6.39
- In WDS?: yes - 12. mag companion 23 arcsec away (discovered in 1891)
- Known spectroscopic binary?: yes - in Chapter 6, I refer to the Delgado-Martí et al. (2001) period of 250.3 d (see Fig. C.41)
- Velocity variations seen in these data?: yes

	Hα	He I λ6678	Hγ	He I λ4471	Mg II λ4481	Fe II ccfs
Mean RV (km s^{-1})	-8.2	-11.7	-26.0	-70.3	···	-41.5
RV range (km s^{-1})	-9.4 to -6.3	-22.8 to 13.0	-31.4 to -17.0	-120.6 to -48.0	···	-53.5 to -22.2
RV change (km s^{-1})	3.1	35.8	14.4	72.6	···	31.3

- Shell classification: emission shell
- Do shell features move with the star?: difficult to tell
- Notes on emission and absorption features: Interesting morphology in both of the hydrogen and helium lines.
- Other notes: See Chapter 6

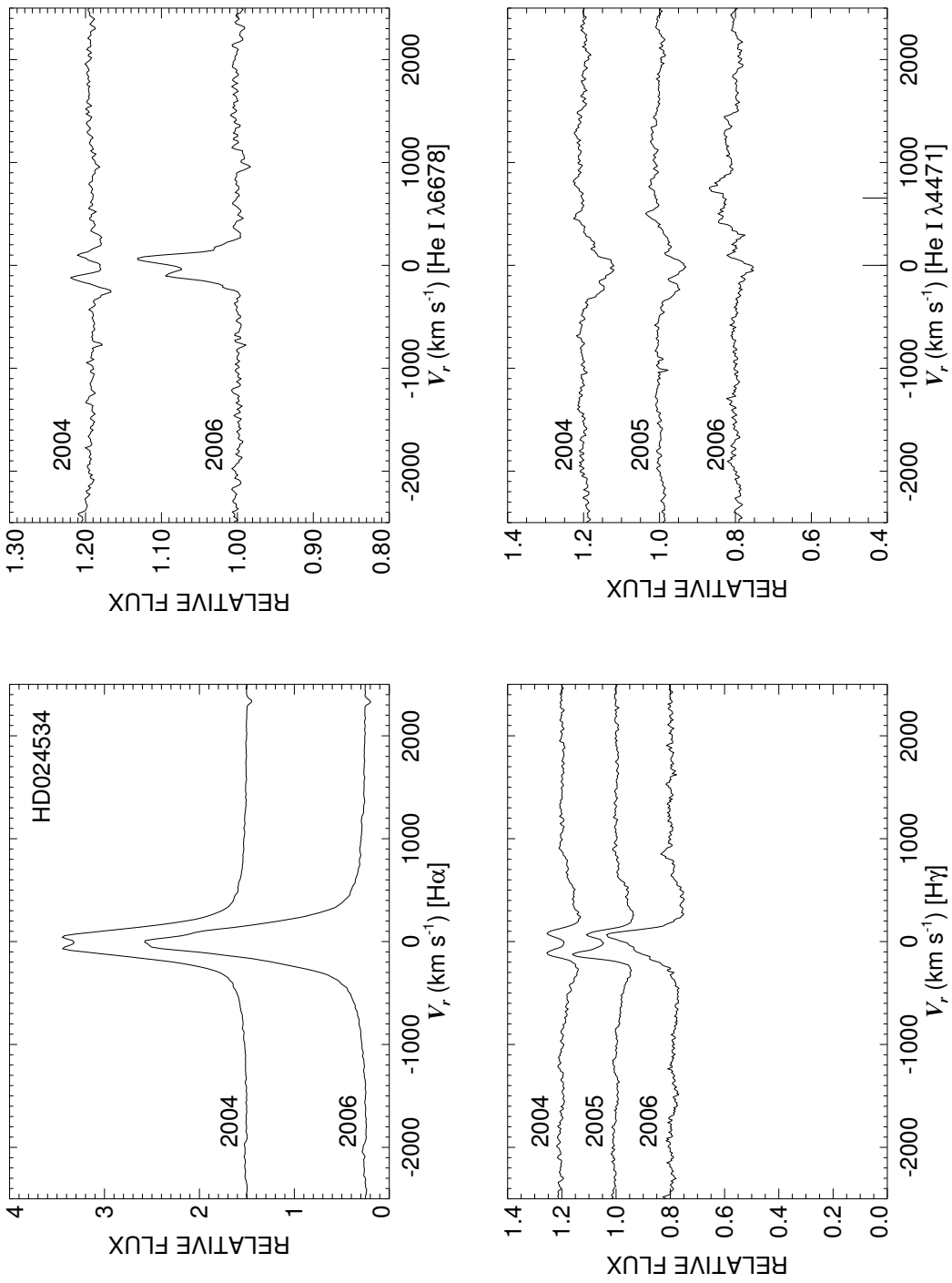

Figure C.40: A quadruple plot of HD024534 as described in §7.2.3 and Figure 7.6.

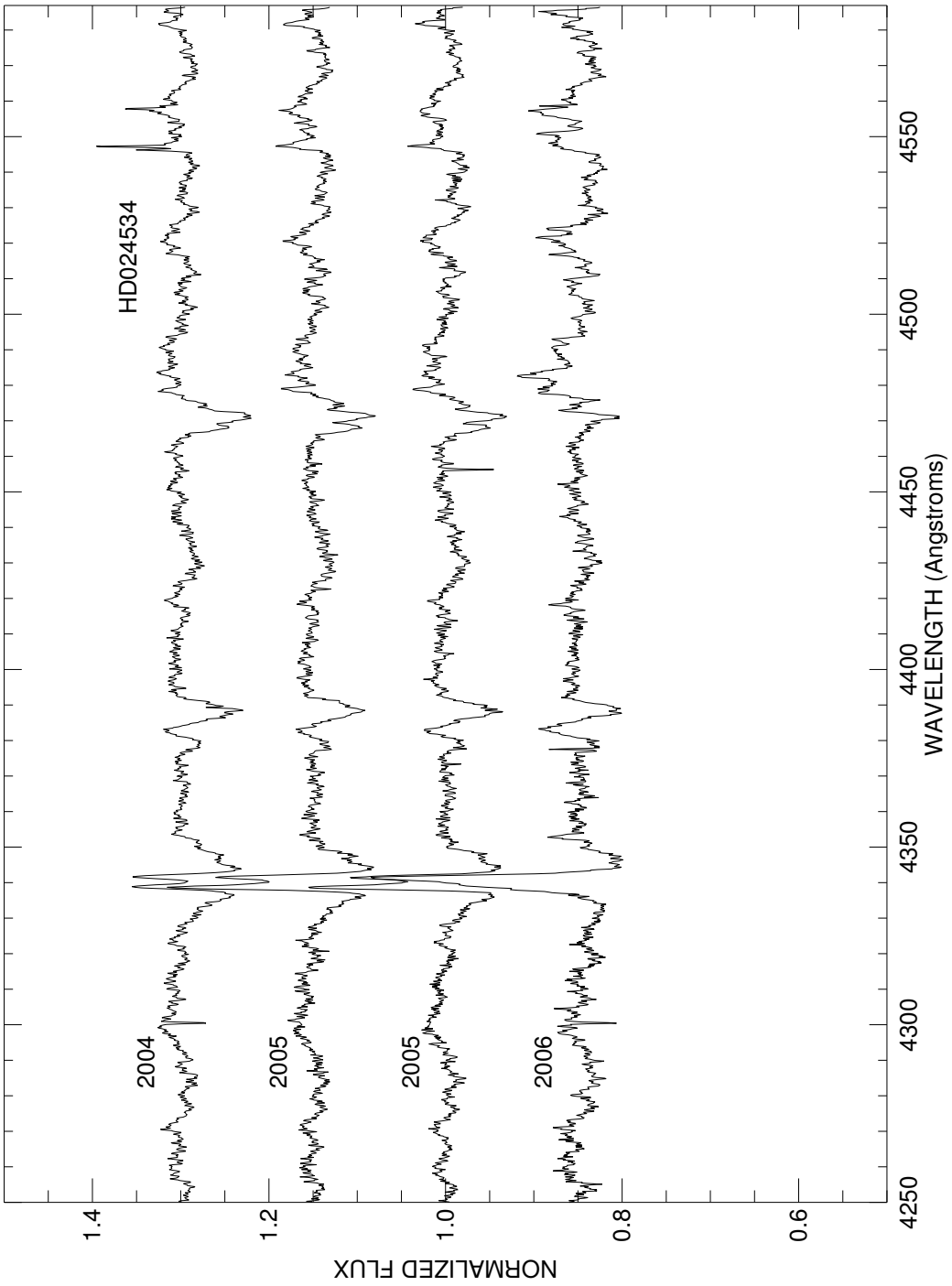

Figure C.41: A plot of all spectra of HD024534 in the blue region. Each is labeled with the year of observation and they are offset for clarity.

HD025799

NOT Be Star, Non-Radial Pulsator

- Other Names: V490 Per
- Spectral Type: B3 V
- V magnitude: 7.11
- In WDS?: no
- Known spectroscopic binary?: no
- Velocity variations seen in these data?: maybe (but could be NRP)

	Hα	He I λ6678	Hγ	He I λ4471	Mg II λ4481	Fe II ccfs
Mean RV (km s^{-1})	32.4	35.4	35.5	3.1	2.3	···
RV range (km s^{-1})	7.0 to 46.7	11.6 to 56.7	27.1 to 44.6	-2.2 to 7.6	-11.6 to 13.5	···
RV change (km s^{-1})	39.7	45.1	17.5	9.8	25.1	···

- Shell classification: normal
- Notes on emission and absorption features: Some evidence for NRP in Hα, He I λ6678, and Mg II λ4481.
- Other notes: SIMBAD lists it as an eclipsing binary however Morris et al. (1988) find it is a non-radial pulsator with a period of 0.9126 d (the light curve and velocity variations "cannot be explained by a binary star model"),

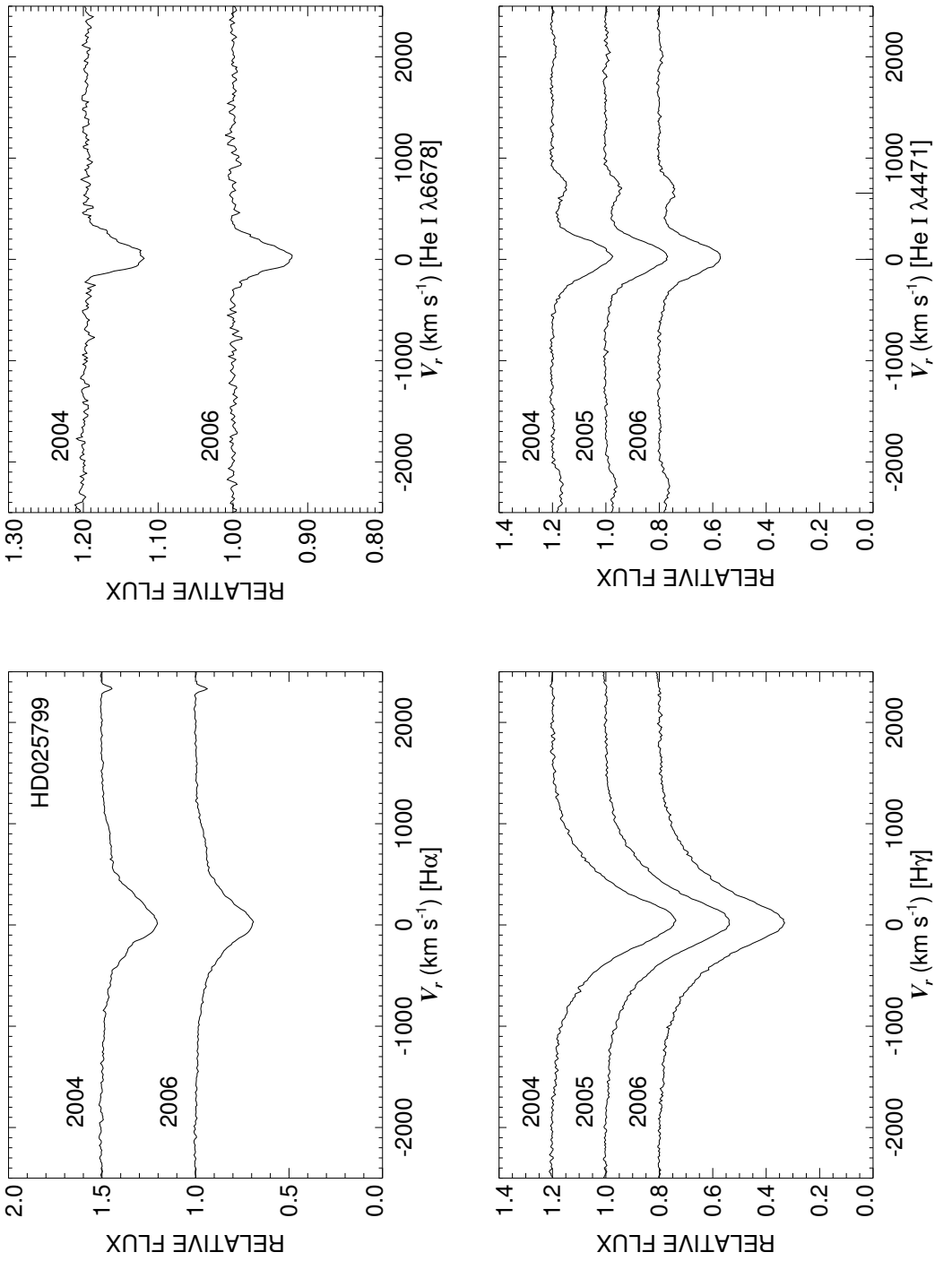

Figure C.42: A quadruple plot of HD025799 as described in §7.2.3 and Figure 7.6.

HD025940

Classical Be Star

- Other Names: HR 1273, 48 Per, MX Per
- Spectral Type: B4 Ve
- V magnitude: 3.96
- In WDS?: no
- Known spectroscopic binary?: possibly - Harmanec (2001) reports a period of 16.59594 d but thinks it needs to be confirmed
- Velocity variations seen in these data?: no

	Hα	He I λ6678	Hγ	He I λ4471	Mg II λ4481	Fe II ccfs
Mean RV (km s^{-1})	3.8	4.1	-1.9	6.6	-4.9	-10.6
RV range (km s^{-1})	2.1 to 5.3	-5.0 to 21.4	-6.5 to 2.0	4.1 to 10.8	-8.1 to -0.7	-14.6 to -7.2
RV change (km s^{-1})	3.2	26.4	8.5	6.7	7.4	7.4

- Shell classification: emission shell
- Do shell features move with the star?: N/A
- Notes on emission and absorption features: Big, single-peaked Hα emission. He I λ6678 appears filled in especially on the right.
- Other notes: This star has Hα interferometric observations (Quirrenbach et al. 1997). It is also plotted in Figure 7.4.

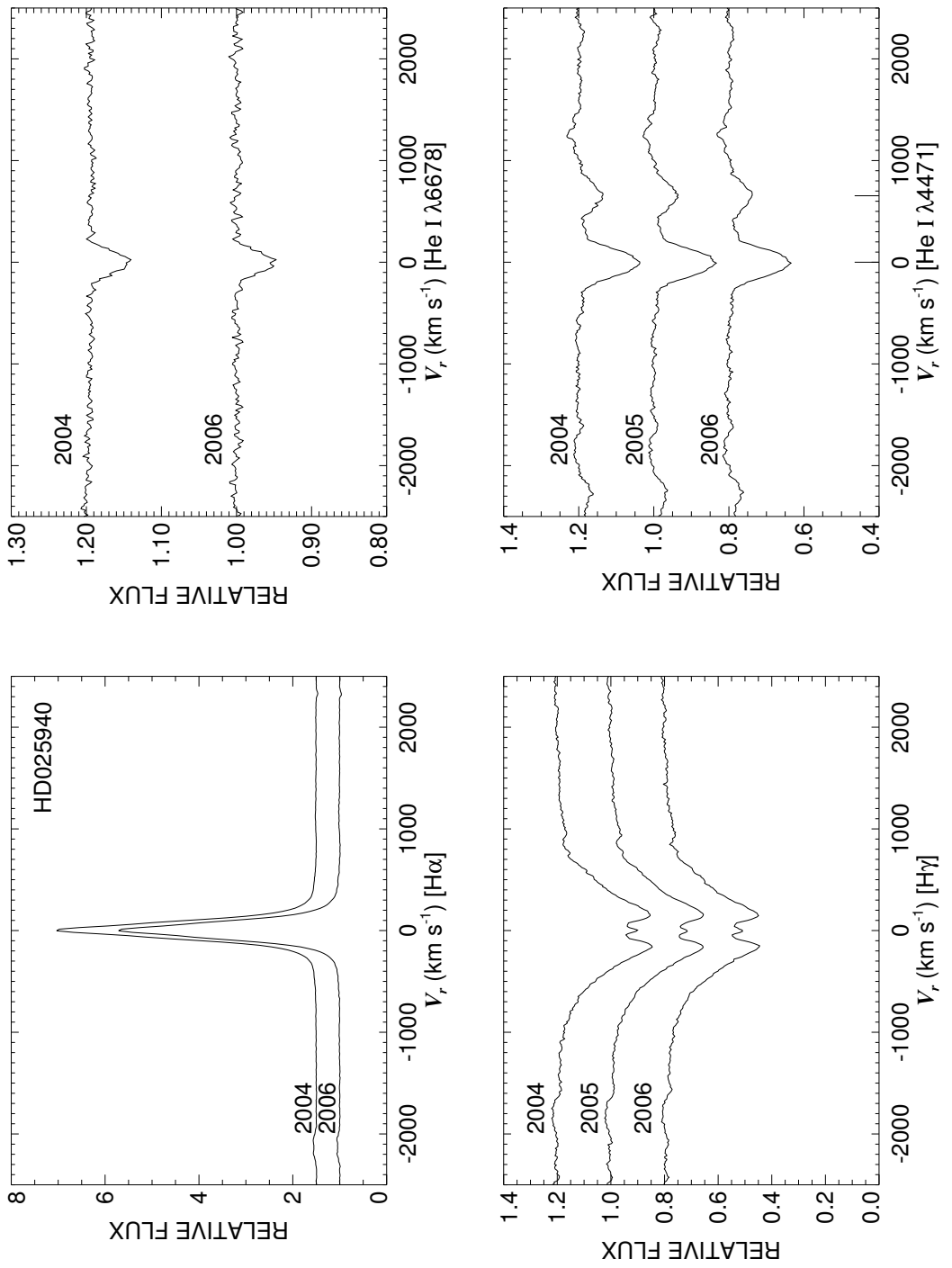

Figure C.43: A quadruple plot of HD025940 as described in §7.2.3 and Figure 7.6.

HD026670

NOT Be Star

- Other Names: HR 1305
- Spectral Type: B6 V
- V magnitude: 5.56
- In WDS?: no
- Known spectroscopic binary?: no
- Velocity variations seen in these data?: no

	Hα	He I λ6678	Hγ	He I λ4471	Mg II λ4481	Fe II ccfs
Mean RV (km s^{-1})	1.4	5.8	5.9	-19.6	-15.1	···
RV range (km s^{-1})	-2.3 to 7.8	-25.9 to 56.5	0.5 to 9.6	-21.7 to -17.9	-21.7 to -10.4	···
RV change (km s^{-1})	10.1	82.4	9.1	3.8	11.3	···

- Notes on emission and absorption features: He I λ6678 has RV variations, however, I beleive they are spurious as this star is a very fast rotator (so the line is broad and shallow).
- Other notes: Slettebak (1982) cannot find any emission but states that Appenzeller (1967) classifies it as B5nn(e) - however, no one has before or since. This star is also plotted in Figure 7.2.

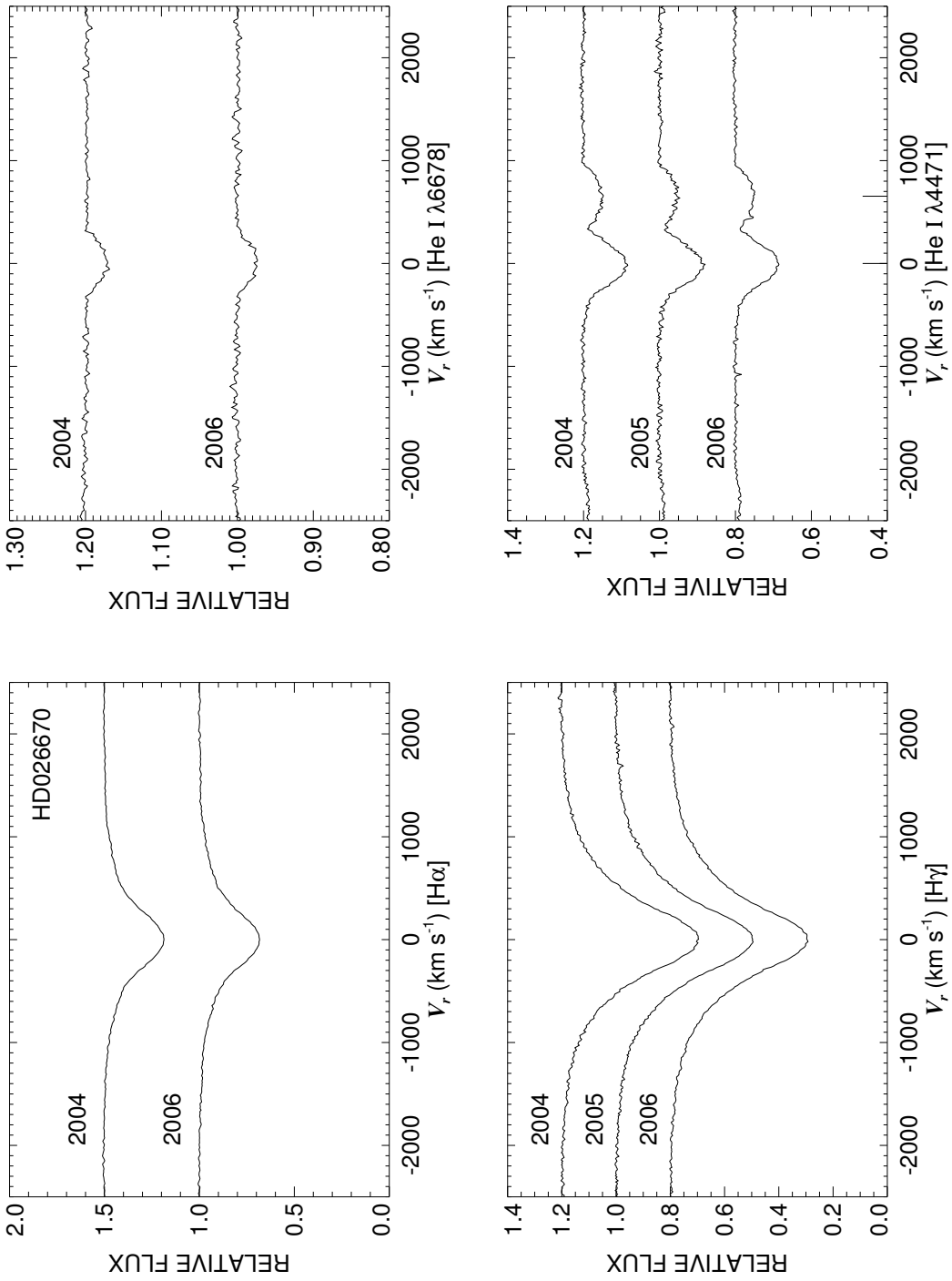

Figure C.44: A quadruple plot of HD026670 as described in §7.2.3 and Figure 7.6.

HD029866

Classical Be Star

- Other Names: HR 1500
- Spectral Type: B7.5 IVne
- V magnitude: 6.12
- In WDS?: no
- Known spectroscopic binary?: no
- Velocity variations seen in these data?: no

	Hα	He I λ6678	Hγ	He I λ4471	Mg II λ4481	Fe II ccfs
Mean RV (km s^{-1})	12.0	9.0	10.2	-10.8	-2.7	23.6
RV range (km s^{-1})	10.5 to 13.2	-0.4 to 49.1	5.3 to 16.1	-14.3 to -8.3	-14.8 to 6.4	11.8 to 28.0
RV change (km s^{-1})	2.7	49.5	10.8	6.0	21.2	16.2

- Shell classification: squarish
- Do shell features move with the star?: N/A
- Notes on emission and absorption features: Hα emission grows from 2004 to 2006. He I λ6678 is either rotationally broadened or filled in or both.
- Other notes: This star is also plotted in Figure 7.3.

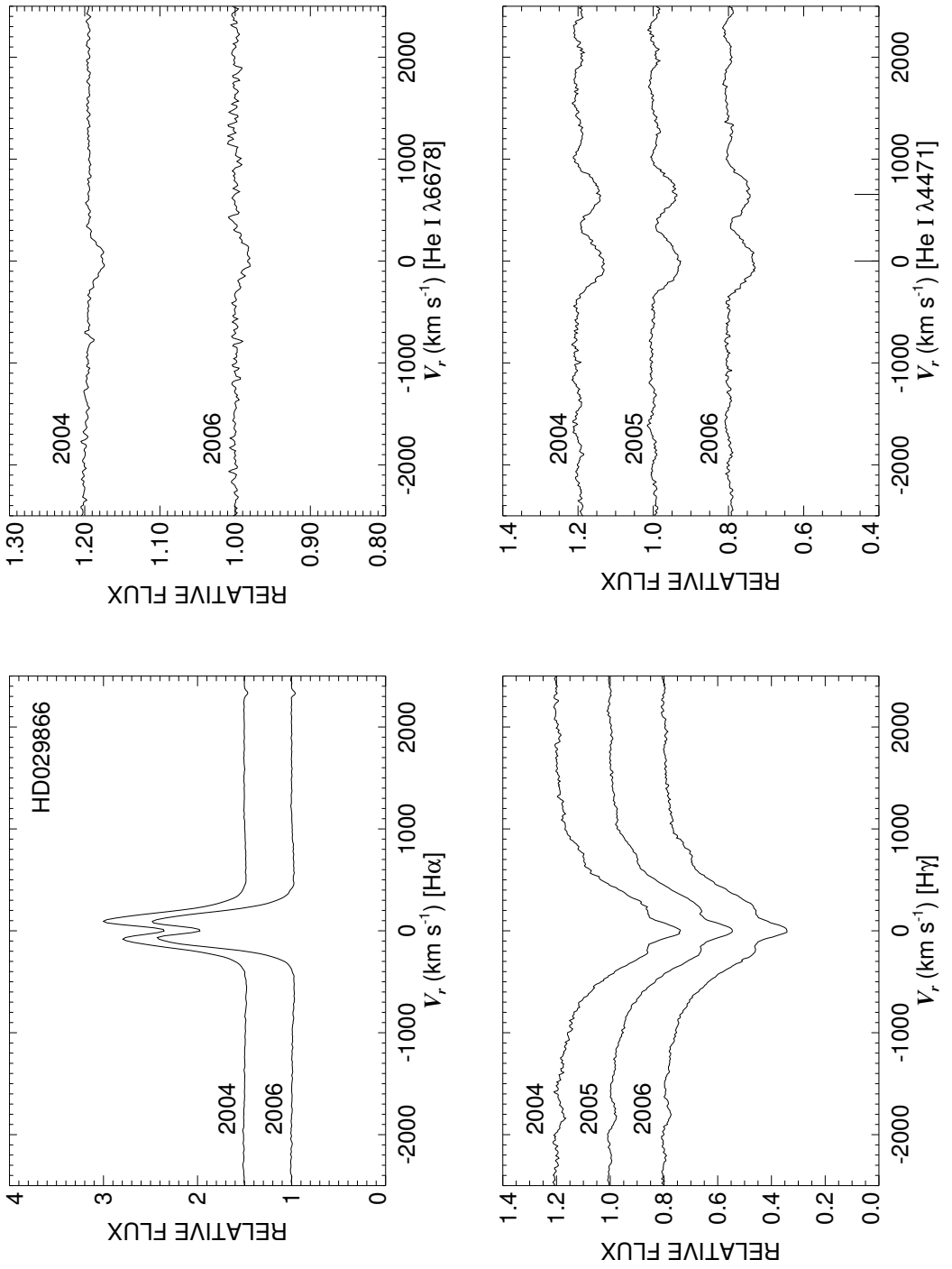

Figure C.45: A quadruple plot of HD029866 as described in §7.2.3 and Figure 7.6.

HD032343

Classical Be Star

- Other Names: HR 1622, 11 Cam, BV Cam
- Spectral Type: B3 Ve
- V magnitude: 5.03
- In WDS?: yes - K0 III 10.1 mag companion 178 arcsec away
- Known spectroscopic binary?: no
- Velocity variations seen in these data?: no

	Hα	He I λ6678	Hγ	He I λ4471	Mg II λ4481	Fe II ccfs
Mean RV (km s^{-1})	-8.2	-12.7	-18.1	-21.8	-9.6	-9.7
RV range (km s^{-1})	-9.1 to -7.2	-16.1 to -9.2	-21.4 to -14.0	-26.0 to -19.6	-14.2 to -6.0	-19.4 to 2.1
RV change (km s^{-1})	1.9	6.9	7.4	6.4	8.2	21.5

- Shell classification: emission shell
- Do shell features move with the star?: N/A
- Notes on emission and absorption features: Narrow lines indicate this is a pole-on star. Big Hα emission.
- Other notes: This star is also plotted in Figure 7.4.

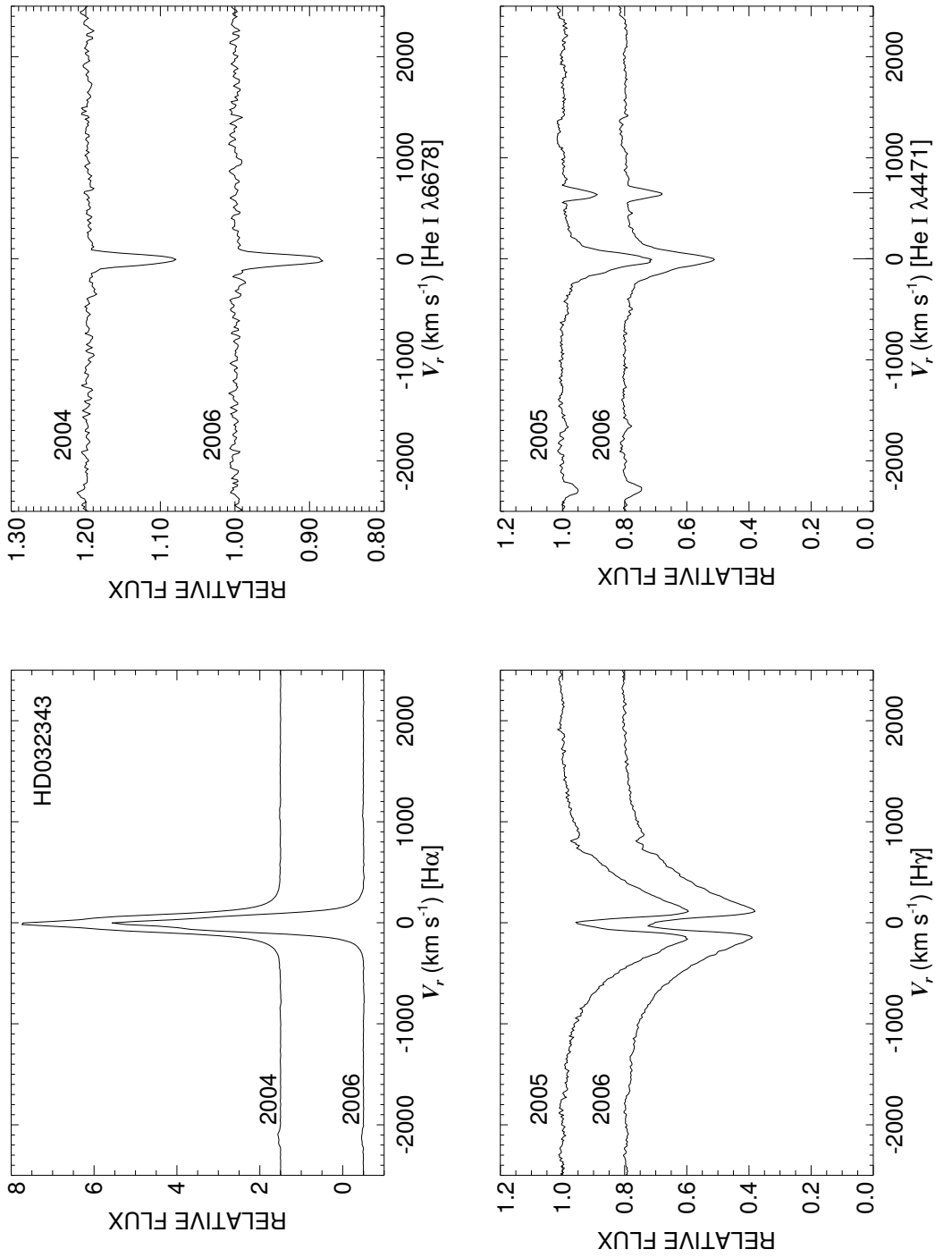

Figure C.46: A quadruple plot of HD032343 as described in §7.2.3 and Figure 7.6.

HD036576

Classical Be Star

- Other Names: HR 1858, 120 Tau
- Spectral Type: B1.5 IVe
- V magnitude: 5.67
- In WDS?: no
- Known spectroscopic binary?: no
- Velocity variations seen in these data?: very unlikely

	Hα	He I λ6678	Hγ	He I λ4471	Mg II λ4481	Fe II ccfs
Mean RV (km s^{-1})	45.8	33.3	57.1	15.4	···	-55.8
RV range (km s^{-1})	44.2 to 47.9	-14.1 to 160.9	49.0 to 68.5	2.1 to 26.5	···	-68.9 to -43.1
RV change (km s^{-1})	3.7	175.0	19.5	24.4	···	25.8

- Shell classification: emission shell
- Do shell features move with the star?: N/A
- Notes on emission and absorption features: Hα emission increases from 2004 to 2006. He I λ6678 and Mg II λ4481 both show emission horns (useless for RV studies).
- Other notes: The peaks of Hα and Hγ are opposite in 2006 (this may show the differences between asymmetries in the outer and inner disk) (see Fig. C.48).

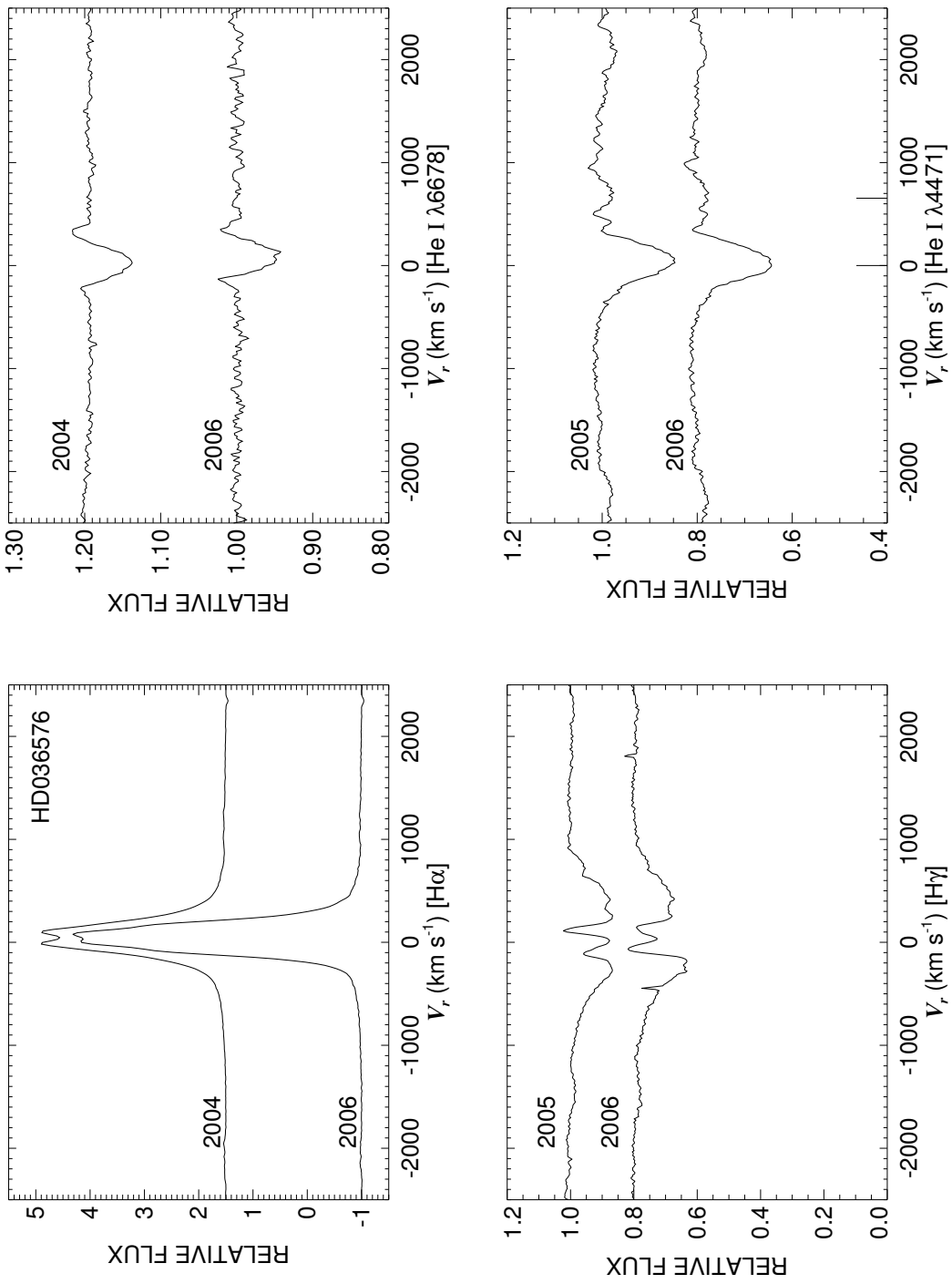

Figure C.47: A quadruple plot of HD036576 as described in §7.2.3 and Figure 7.6.

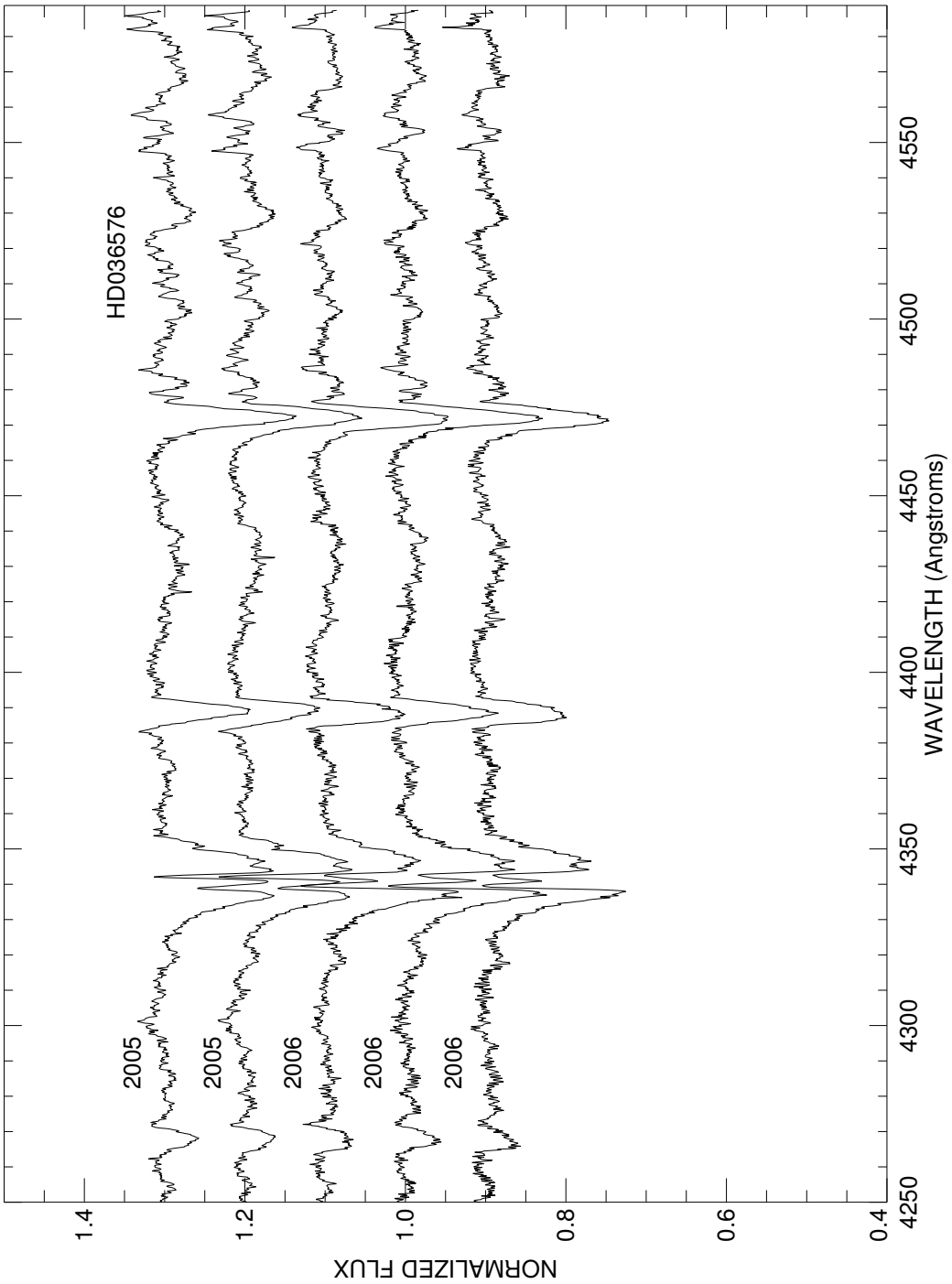

Figure C.48: A plot of all spectra of HD036576 in the blue region. Each is labeled with the year of observation and they are offset for clarity.

HD037202

Classical Be Star; Shell Star

- Other Names: HR 1910, 123 Tau, ζ Tau
- Spectral Type: B1 IVe+sh
- In WDS?: no
- V magnitude: 3.03
- Known spectroscopic binary?: yes - Harmanec (2001) reports a period of 132.97 d
- Velocity variations seen in these data?: yes

	Hα	He I λ6678	Hγ	He I λ4471	Mg II λ4481	Fe II ccfs
Mean RV (km s^{-1})	30.0	17.1	79.4	1.4	-22.4	-10.7
RV range (km s^{-1})	16.3 to 36.9	-7.9 to 31.5	61.7 to 99.1	-2.4 to 5.9	-42.1 to -7.2	-26.3 to -0.2
RV change (km s^{-1})	20.6	39.4	37.4	8.3	34.9	26.0

- Shell classification: emission shell
- Do shell features move with the star?: unknown
- Notes on emission and absorption features: Hα has an unusual shape (compared to other Be stars). Hγ, He I λ6678, and Mg II λ4481 are untrustworthy for RV studies (due to shell components) and He I λ4471 also looks "contaminated" so RV studies are problematic.
- Other notes: This star has interferometric observations in Hα (Quirrenbach et al. 1997; Tycner et al. 2005) and CHARA K$'$ (Gies et al. 2007). Tycner et al. (2004) determined there is no Roche lobe filling and hypothesize that the disk is truncated by graviational influence of the companion. This star is also plotted in Figure 7.3.

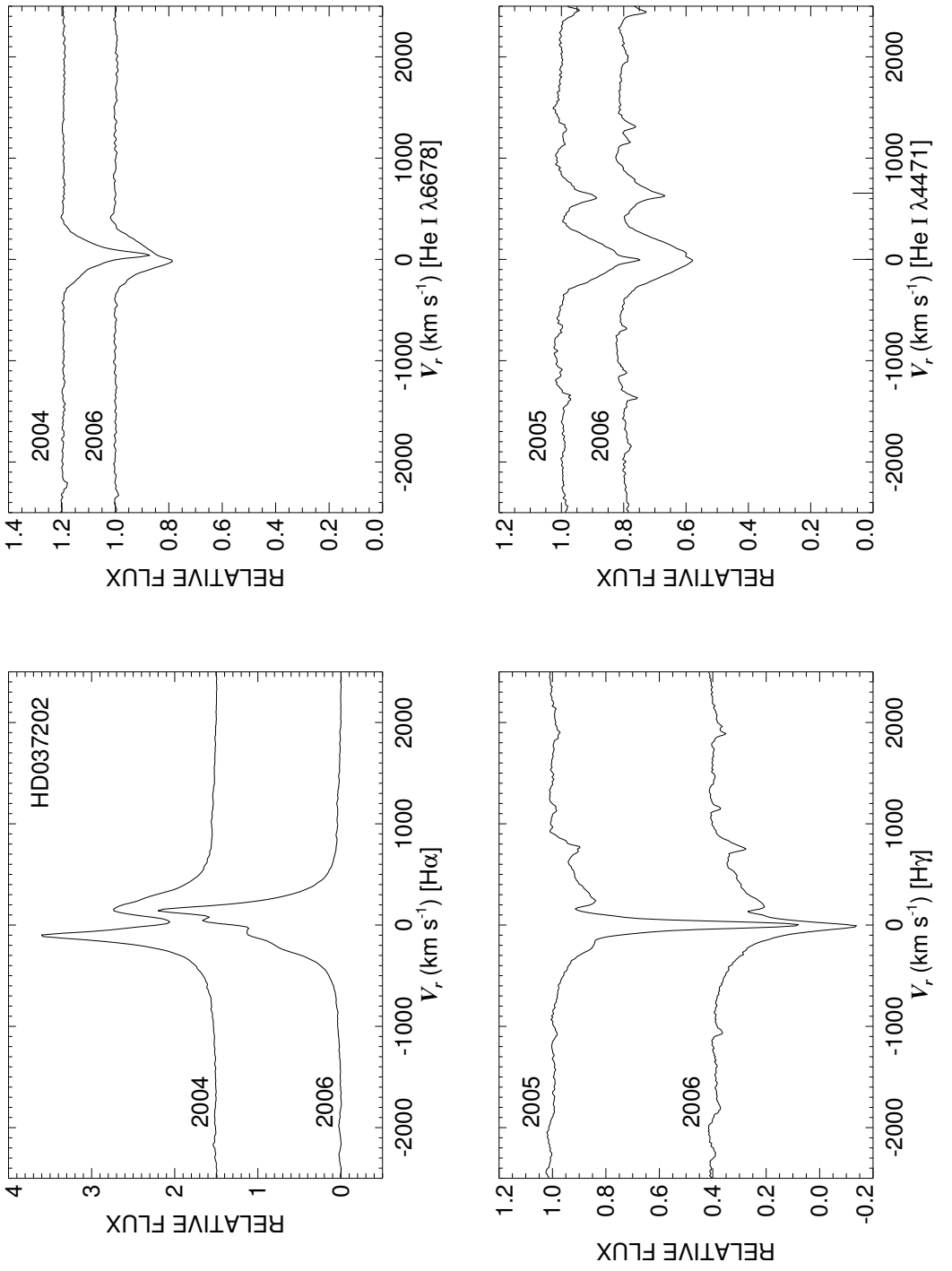

Figure C.49: A quadruple plot of HD037202 as described in §7.2.3 and Figure 7.6.

HD041335

Interacting Binary; Shell Star

- Other Names: HR 2142, V696 Mon
- Spectral Type: B2 Vne
- V magnitude: 5.25
- In WDS?: yes - 9.45 mag companion 0.6 arcsec away (discovered in 1991)
- Known spectroscopic binary?: yes - Peters (1976) finds a period of 80.860 d
- Velocity variations seen in these data?: unknown (see Fig. C.51)

	Hα	He I λ6678	Hγ	He I λ4471	Mg II λ4481	Fe II ccfs
Mean RV (km s^{-1})	46.7	31.2	40.0	41.1	-32.3	-9.8
RV range (km s^{-1})	45.8 to 50.1	7.0 to 49.7	30.7 to 54.4	37.2 to 44.9	-36.9 to -26.2	-17.8 to 1.0
RV change (km s^{-1})	4.3	42.7	23.7	7.7	10.7	18.8

- Shell classification: emission shell
- Do shell features move with the star?: N/A
- Notes on emission and absorption features: Hα increases from 2004 to 2006. The central absorption in Hγ increases throughout 2006. He I λ6678 may have an emission horn on the right. Mg II λ4481 is extremely difficult to see and measure.
- Other notes: Peters (1983) presents a model of this star which exhibits very regular shell phases as we (the observers) look through a gas stream resulting from the mass transfer in this system. This is not unlike what I found for RY Scuti in Chapter 2. Waters et al. (1991) hypothesizes the system is much like ϕ Per in that it has a hot subdwarf companion. This star is also plotted in Figure 7.4.

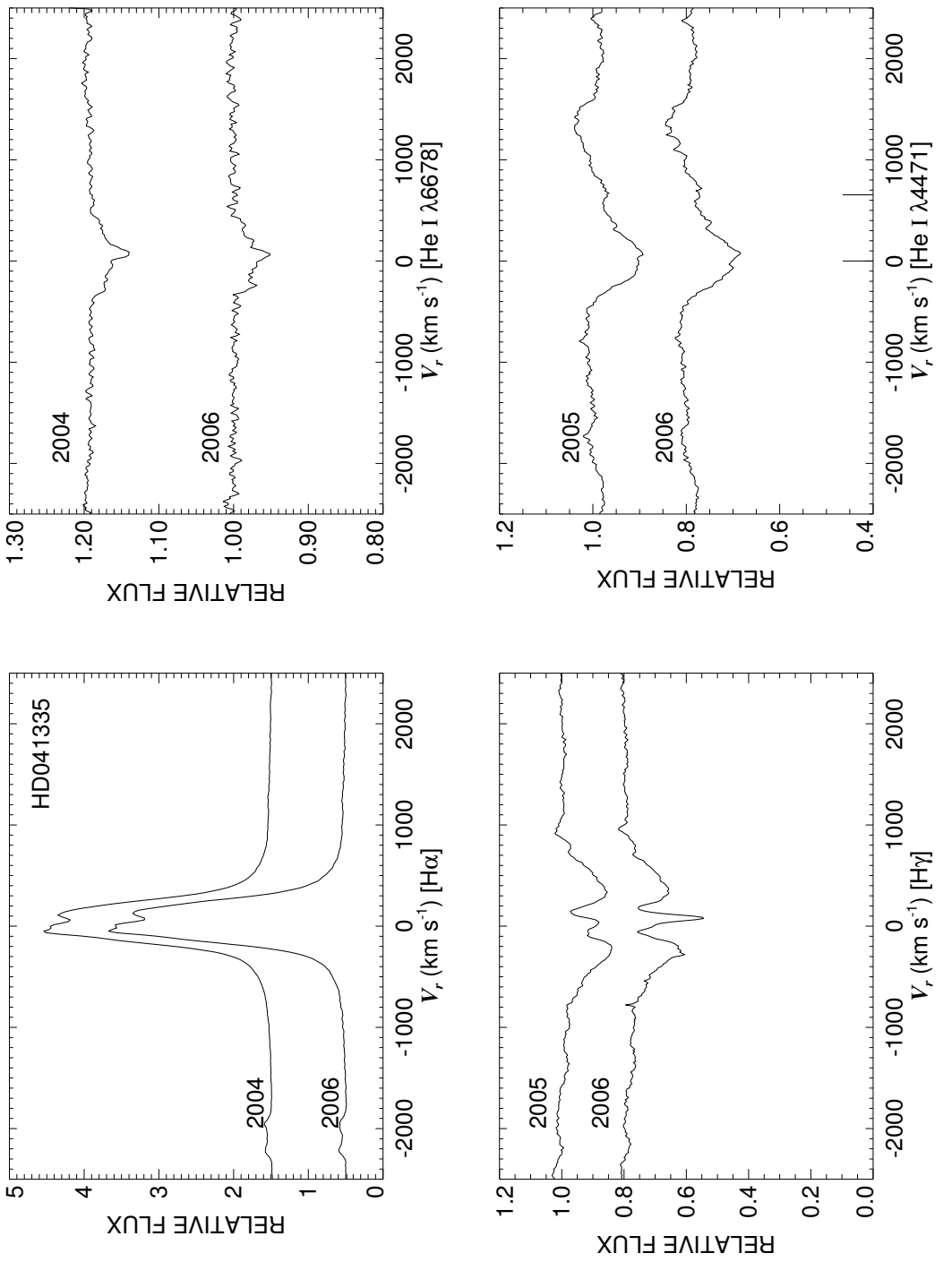

Figure C.50: A quadruple plot of HD041335 as described in §7.2.3 and Figure 7.6.

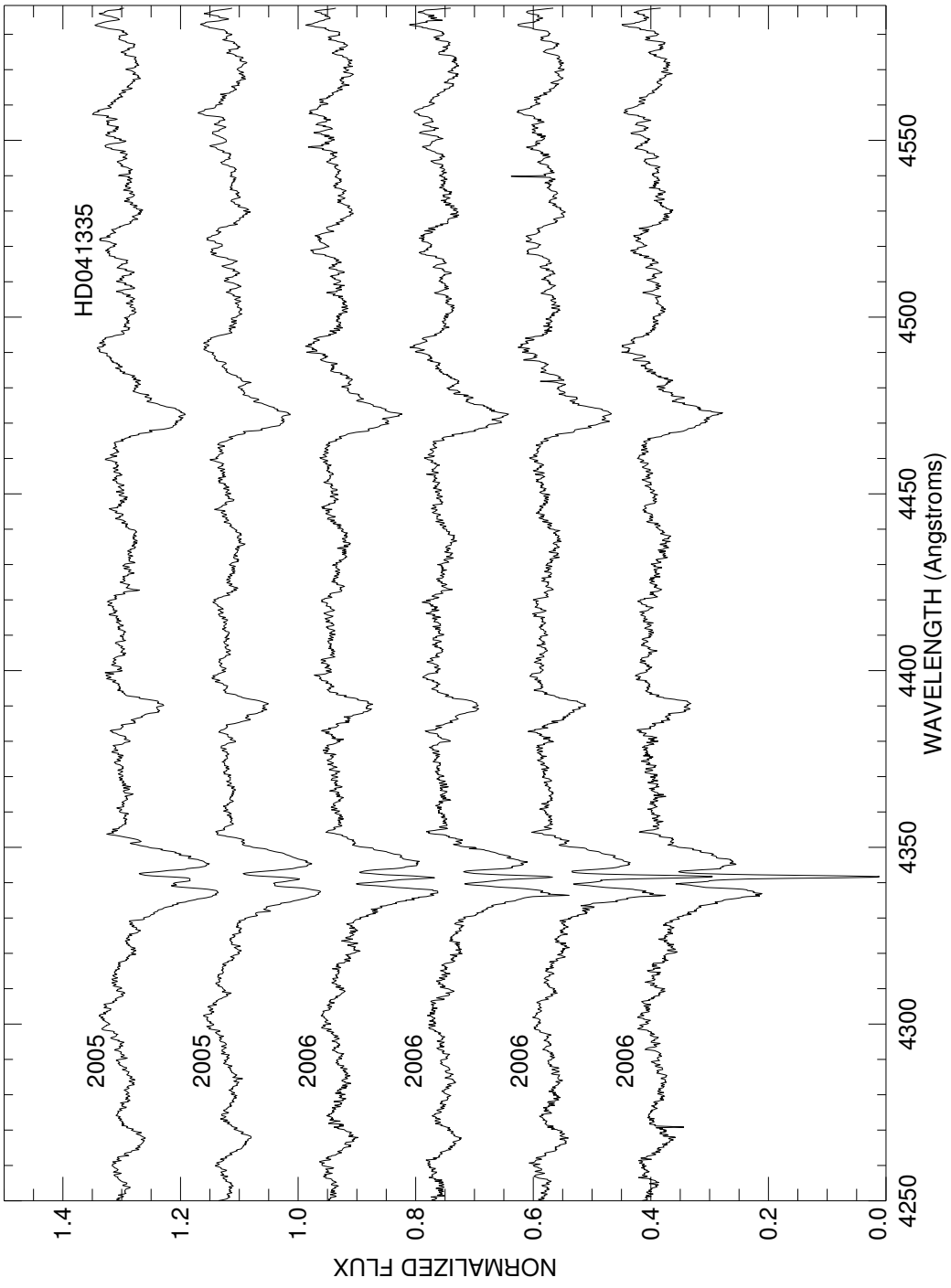

Figure C.51: A plot of all spectra of HD041335 in the blue region. Each is labeled with the year of observation and they are offset for clarity.

HD058715

Classical Be Star; Non-Radial Pulsator

- Other Names: HR 2845, β CMi, 3 CMi
- Spectral Type: B8 Ve
- V magnitude: 2.89
- In WDS?: yes - 6 faint (mag 13, 11.2, 11.1, 10.9, 12.5, 13.0) companions at 49, 103, 131, 138, 80, and 84 arcsec away (discovered in 1831, 1879, 1984)
- Known spectroscopic binary?: possibly - Harmanec (2001) reports a period of 218.498 d but states it needs additional verification
- Velocity variations seen in these data?: no

	Hα	He I λ6678	Hγ	He I λ4471	Mg II λ4481	Fe II ccfs
Mean RV (km s^{-1})	12.6	···	1.7	22.3	8.4	13.3
RV range (km s^{-1})	10.9 to 14.5	···	-2.7 to 5.6	17.7 to 27.0	5.6 to 10.6	7.3 to 16.2
RV change (km s^{-1})	3.6	···	8.3	9.3	5.0	8.9

- Shell classification: very mild squarish
- Do shell features move with the star?: N/A
- Notes on emission and absorption features: He I λ6678 is practically non-existant. There is a little bit of emission at the bottom of Hγ.
- Other notes: Rivinius et al. (2004) suggest it has a He star companion like ϕ Per, 59 Cyg, and HR2142. They also find evidence of profile variations suggesting NRP. This star has interferometric measurements in Hα (Tycner et al. 2005). It is also plotted in Figure 7.2.

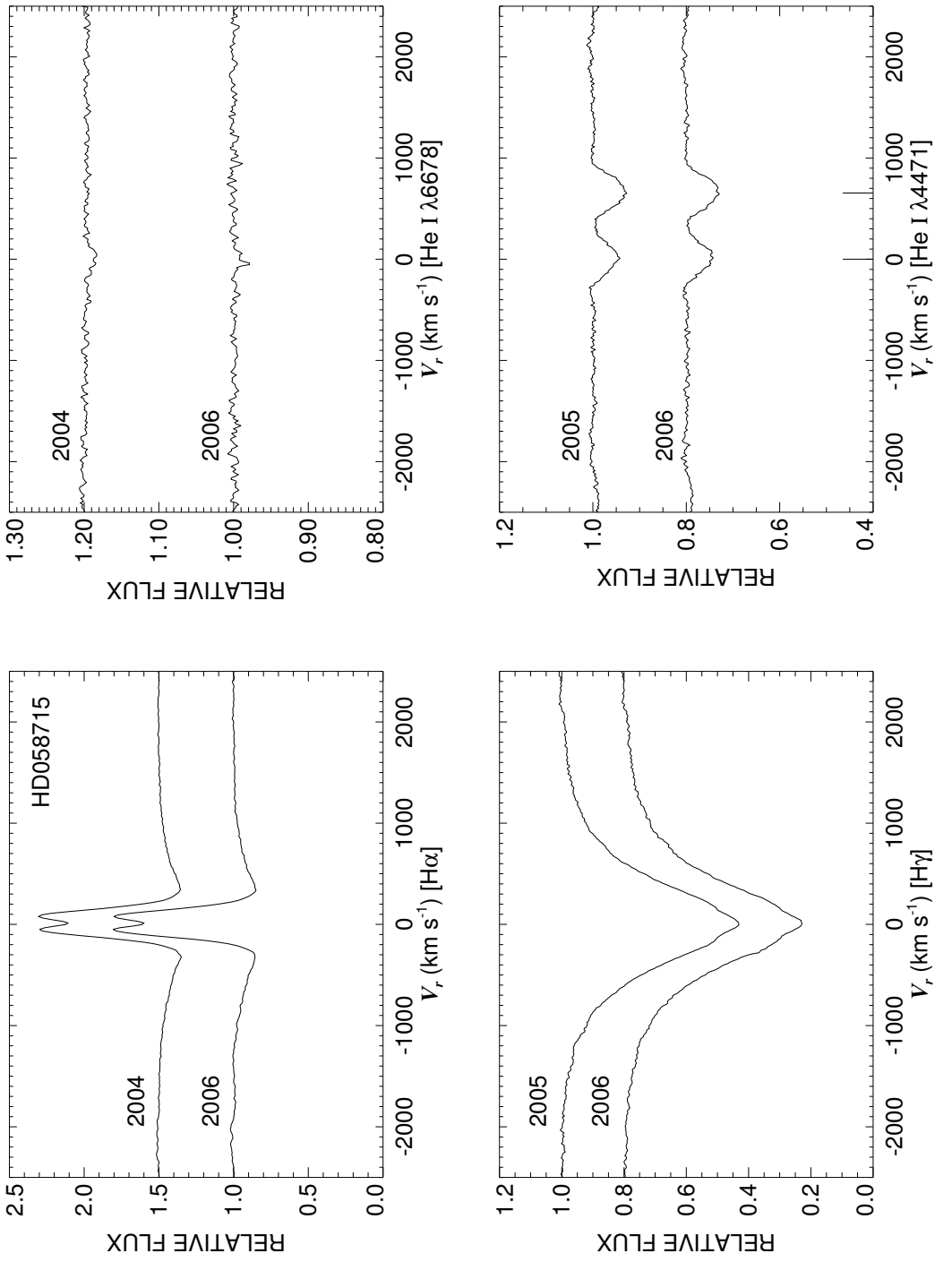

Figure C.52: A quadruple plot of HD058715 as described in §7.2.3 and Figure 7.6.

HD058978

Classical Be Star, Non-Radial Pulsator

- Other Names: HR 2855, FY CMa
- Spectral Type: B0.5 IVne+sh
- V magnitude: 5.61
- In WDS?: no
- Known spectroscopic binary?: yes - Rivinius et al. (2004) find a period of 37.26 d (however there is some uncertainty)
- Velocity variations seen in these data?: yes (esp. see Fig. C.54)

	Hα	He I λ6678	Hγ	He I λ4471	Mg II λ4481	Fe II ccfs
Mean RV (km s^{-1})	43.2	125.1	109.9	5.4	···	-22.8
RV range (km s^{-1})	35.6 to 52.3	-39.6 to 211.8	92.3 to 130.2	-31.6 to 26.7	···	-53.4 to 21.4
RV change (km s^{-1})	16.7	251.4	37.9	58.3	···	74.9

- Shell classification: emission shell
- Do shell features move with the star?: yes
- Notes on emission and absorption features: Hα looks somewhat unusual. He I λ6678 is completely odd (and filled in) and not trustworthy for RV studies. The absorption in Hγ gets deeper throughout 2006. He I λ4471 and Mg II λ4481 appear affected by shell features and/or emission.
- Other notes: Rivinius et al. (2004) find this star is likely analogous to ϕ Per (HD010516) in that it is a Be star orbited by an evolved hot subdwarf companion. They find it shows non-radial pulsations and is also like HD200120 (59 Cyg) and HD041335 (HR 2142).

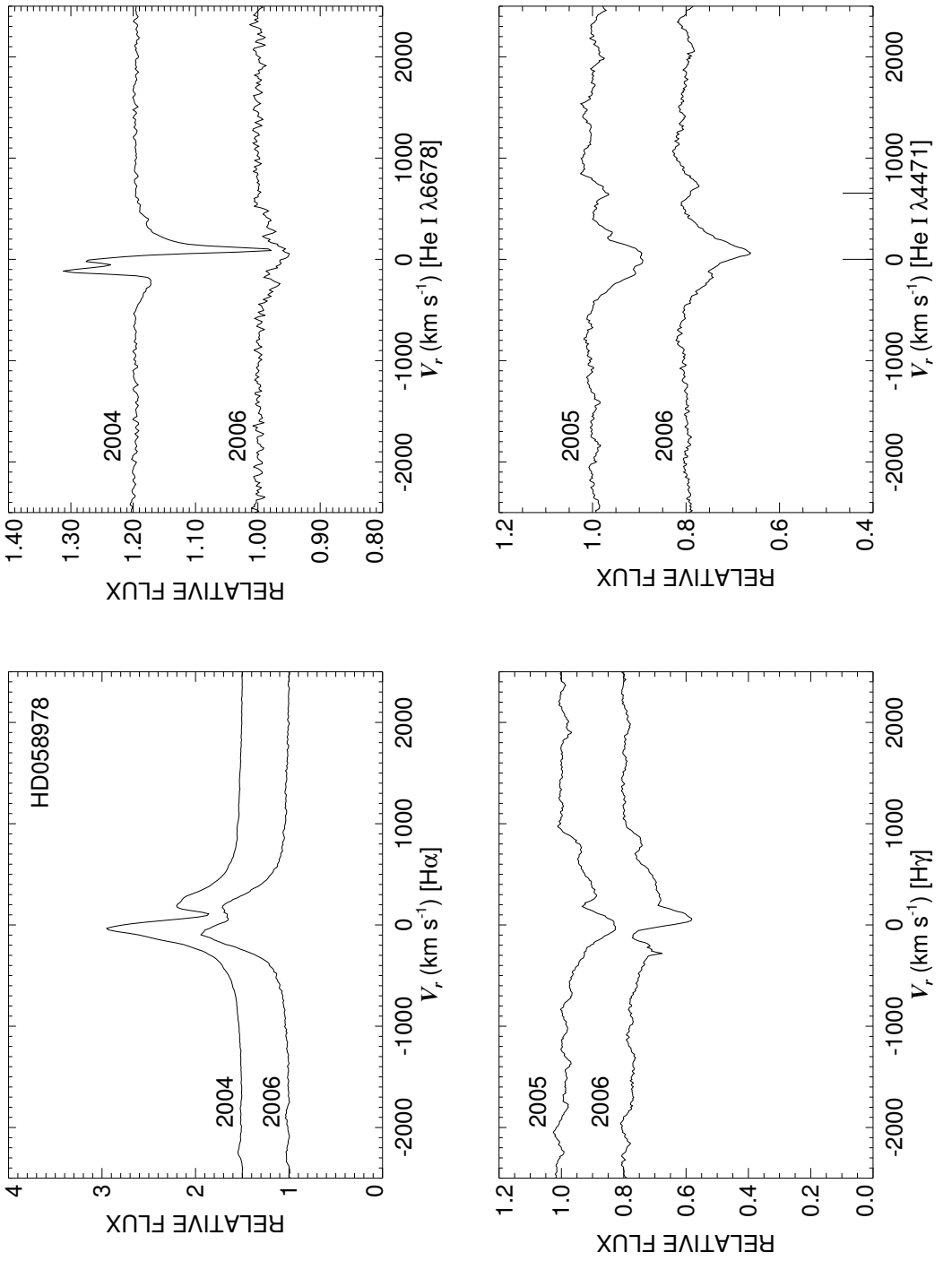

Figure C.53: A quadruple plot of HD058978 as described in §7.2.3 and Figure 7.6.

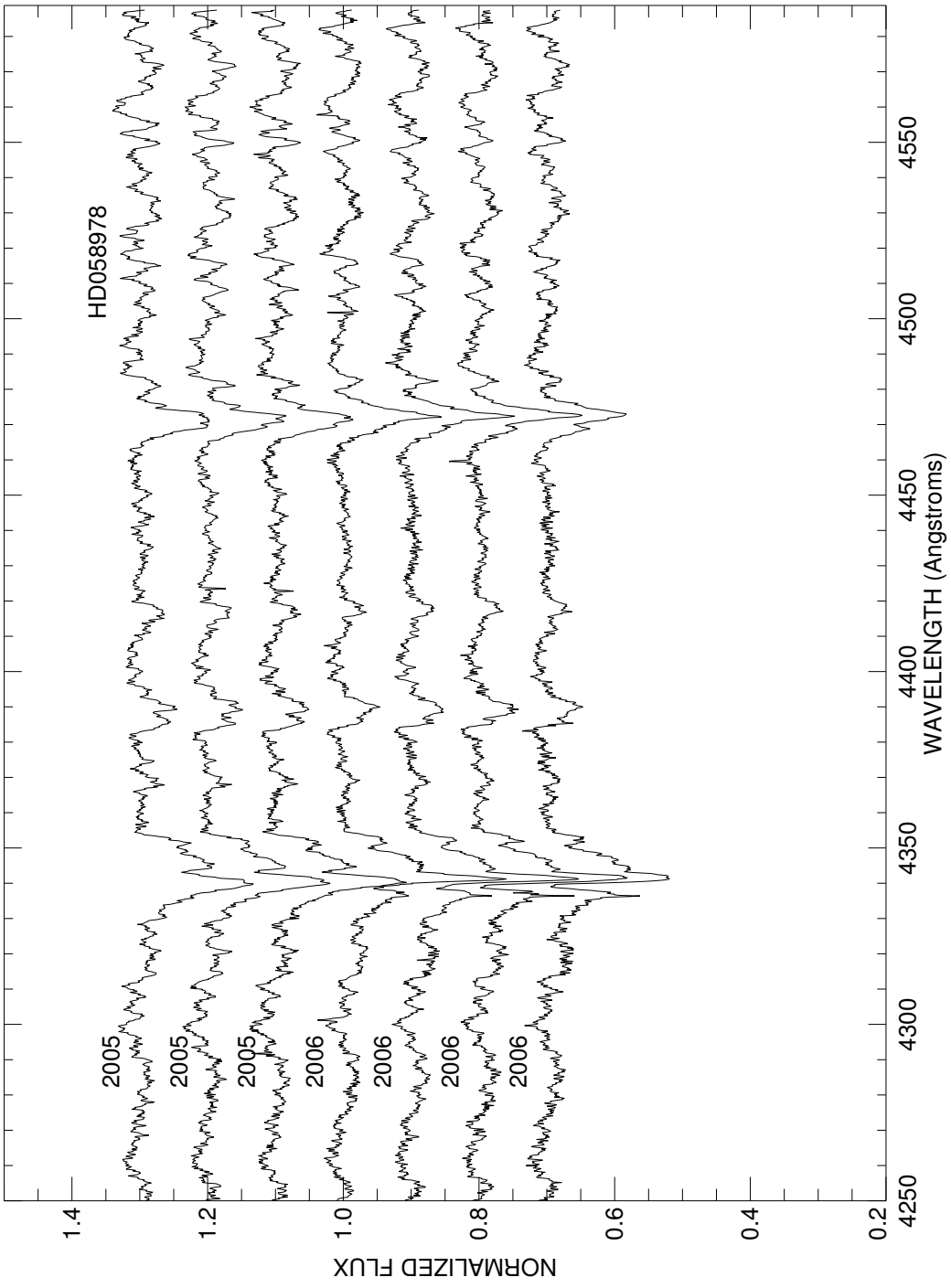

Figure C.54: A plot of all spectra of HD058978 in the blue region. Each is labeled with the year of observation and they are offset for clarity.

HD060855

Classical Be Star

- Other Names: HR 2921
- Spectral Type: B2 Ve
- V magnitude: 5.66
- In WDS?: yes - 2 fainter (mag 12.2 and 9.74) companions at 5.3 and 19.8 arcsec (discovered in 1928 abd 1830) along with 3 companions of unlisted magnitude at 150, 104, and 92 arcsec away (discovered in 1902 and 1983).
- Known spectroscopic binary?: no
- Velocity variations seen in these data?: yes

	Hα	He I λ6678	Hγ	He I λ4471	Mg II λ4481	Fe II ccfs
Mean RV (km s^{-1})	43.5	24.8	39.9	9.3	6.2	-78.5
RV range (km s^{-1})	39.6 to 50.0	-5.0 to 52.2	33.1 to 46.0	0.1 to 21.9	-9.2 to 30.6	-92.7 to -72.6
RV change (km s^{-1})	10.4	57.2	12.9	21.8	39.8	20.1

- Shell classification: emission shell
- Do shell features move with the star?: yes
- Notes on emission and absorption features: Big Hα emission. Both He I λ6678 and Mg II λ4481 have emission horns (and are therefore unreliable for RV studies). Hγ shows interesting morphology.
- Other notes: This star is also plotted in Figure 7.4.

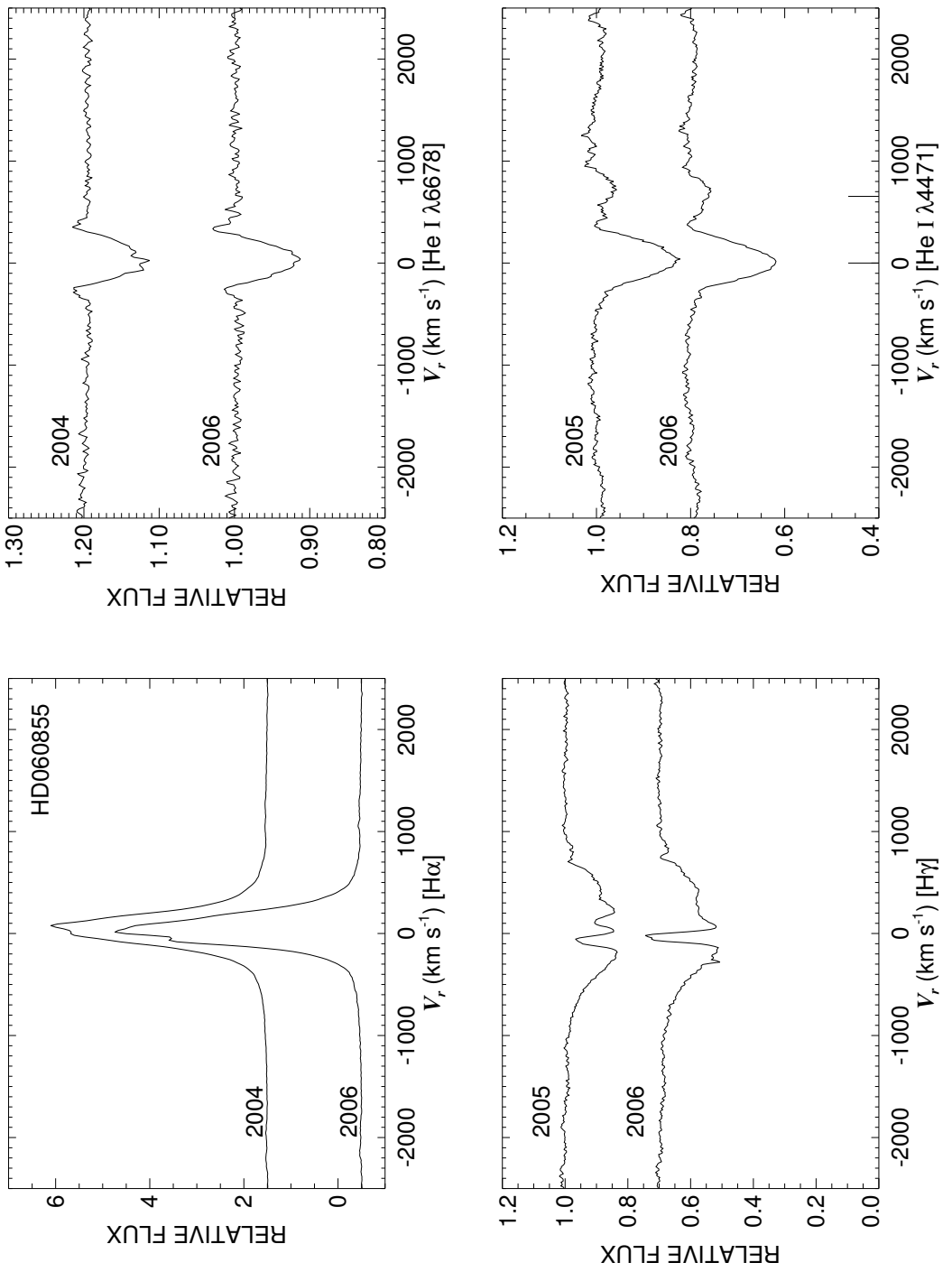

Figure C.55: A quadruple plot of HD060855 as described in §7.2.3 and Figure 7.6.

HD149757

Non-Radial Pulsator

- Other Names: HR 6175, 13 Oph, ζ Oph
- Spectral Type: O9 Ve
- V magnitude: 2.60
- In WDS?: no
- Known spectroscopic binary?: no
- Velocity variations seen in these data?: unknown as I only have one set of back to back spectra

	Hα	He I λ6678	Hγ	He I λ4471	Mg II λ4481	Fe II ccfs
Mean RV (km s^{-1})	-11.7	13.9	27.9	-19.5	-43.2	-142.2
RV range (km s^{-1})	-16.6 to -6.7	12.4 to 15.4	23.4 to 32.4	-19.9 to -19.2	-43.6 to -42.8	-145.3 to -139.2
RV change (km s^{-1})	9.9	3.0	9.0	0.7	0.8	6.2

- Shell classification: weak squarish
- Do shell features move with the star?: N/A
- Notes on emission and absorption features: Non-radial pulsations give rise to the velocity variations in all lines (incidentally there are only 2 red and 2 blue spectra).
- Other notes: This star was eliminated from statistical studies in Chapter 7 as it is an O star and a strange one at that.

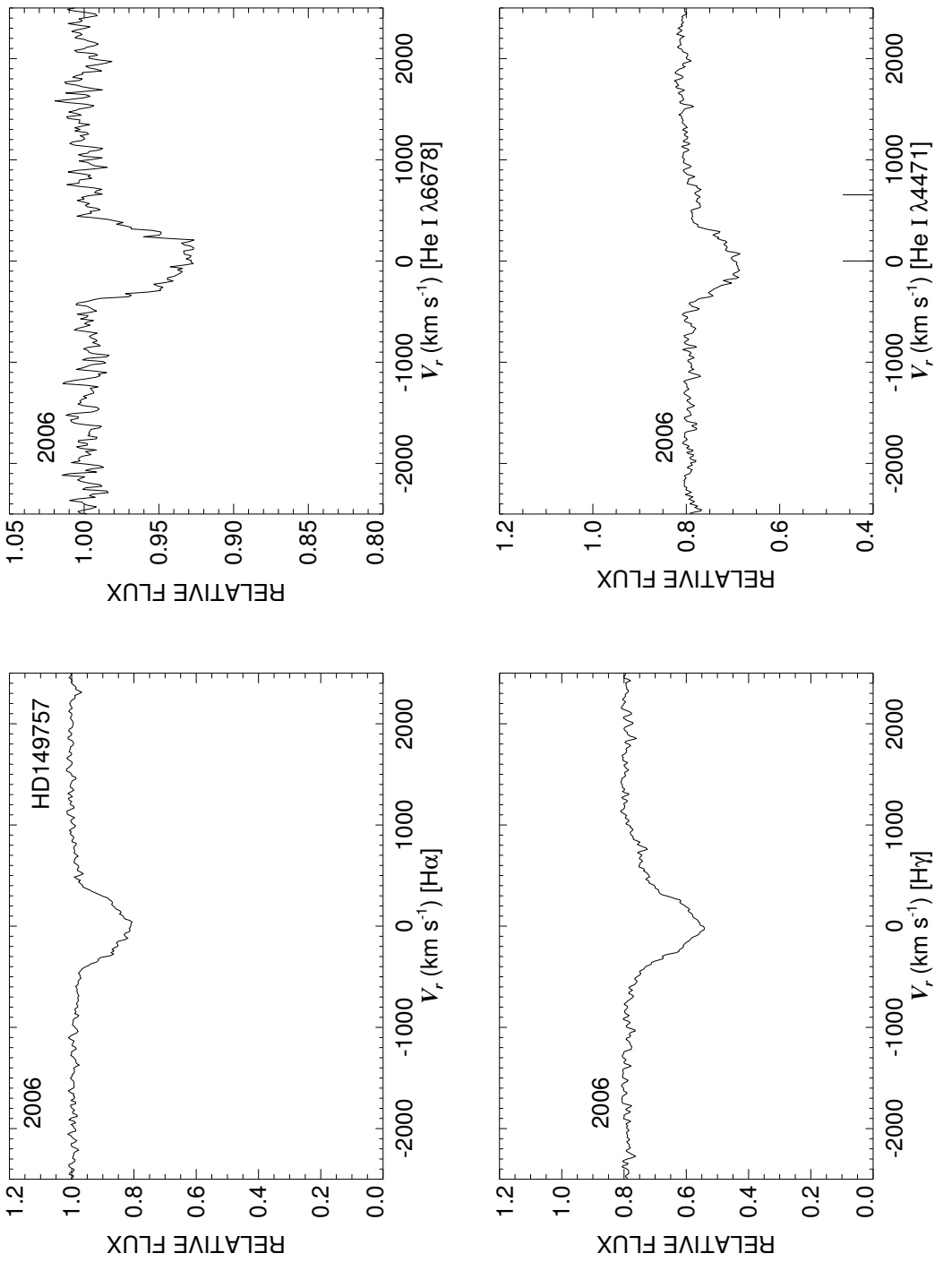

Figure C.56: A quadruple plot of HD149757 as described in §7.2.3 and Figure 7.6.

HD162428

Classical Be Star

- Other Names:
- Spectral Type: B7 IV/Ve
- V magnitude: 7.02
- In WDS?: yes - 8.85 mag companion at 6.3 arcsec away (discovered in 1830)
- Known spectroscopic binary?: no
- Velocity variations seen in these data?: maybe

	Hα	He I λ6678	Hγ	He I λ4471	Mg II λ4481	Fe II ccfs
Mean RV (km s^{-1})	-20.0	-58.3	-22.8	-36.3	-40.8	-19.6
RV range (km s^{-1})	-21.5 to -18.5	-90.3 to -26.3	-41.2 to -13.3	-45.6 to -21.0	-47.9 to -32.3	-34.6 to -12.0
RV change (km s^{-1})	3.0	64.0	27.9	24.6	15.6	22.6

Shell classification: squarish (increases from 2004 to 2006, see Fig C.58)

- Do shell features move with the star?: yes
- Notes on emission and absorption features: Hα strength increases from 2004 to 2006. He I λ6678 is filled in with emission (and unreliable).
- Other notes:

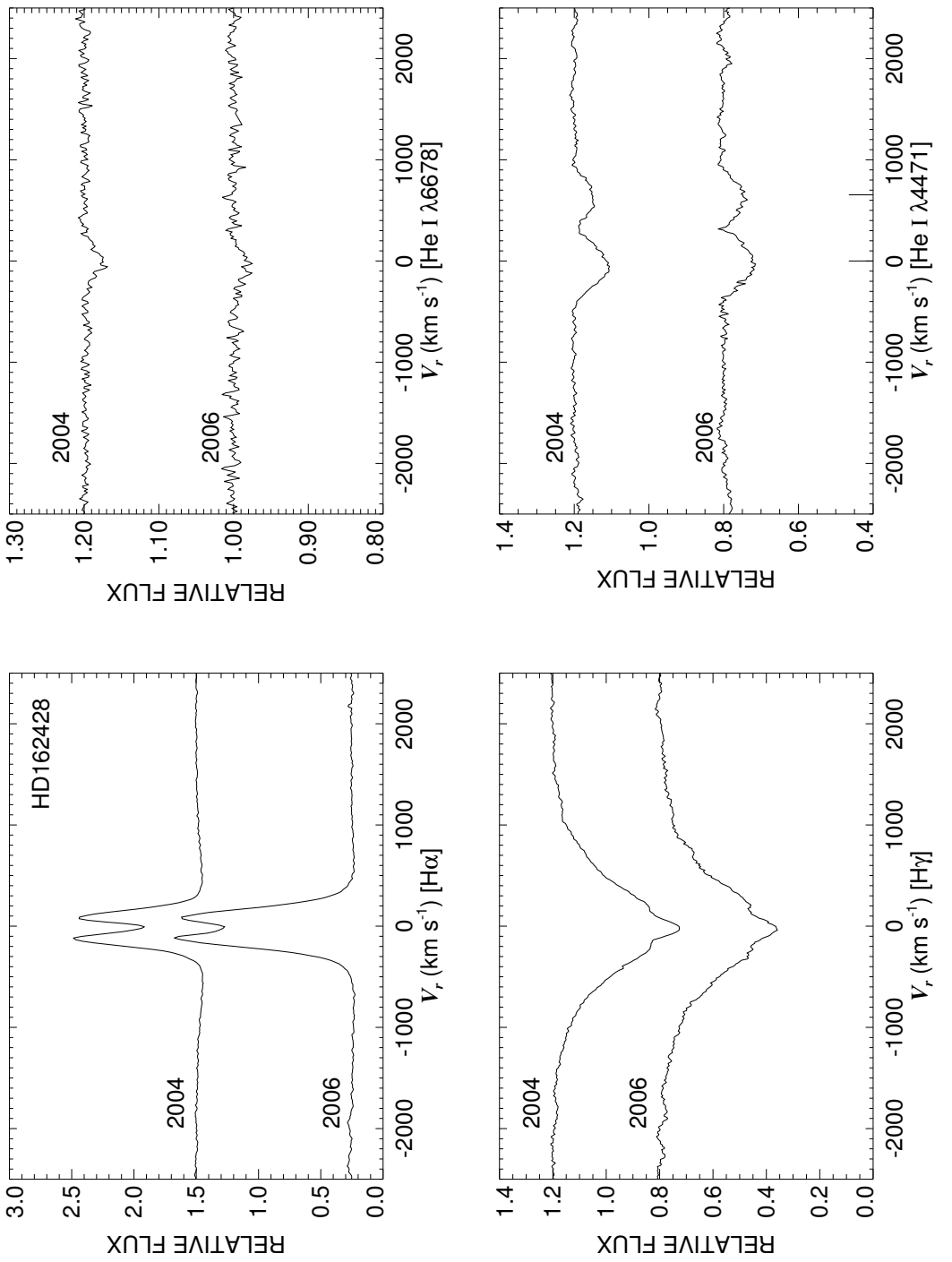

Figure C.57: A quadruple plot of HD162428 as described in §7.2.3 and Figure 7.6.

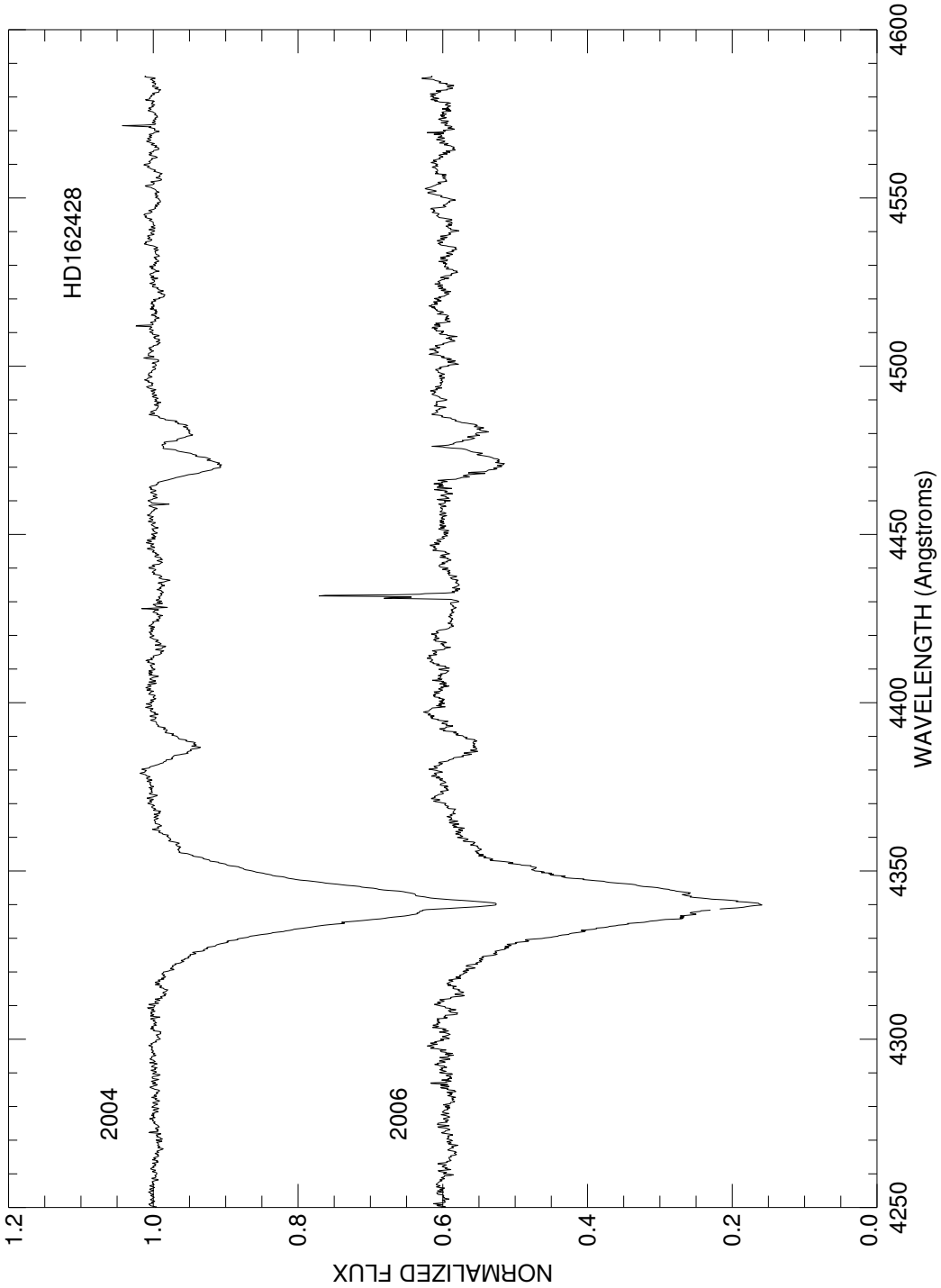

Figure C.58: A plot of the averages for each run in the blue region of HD162428. Each is labeled with the year of observation and they are offset from each other for clarity.

HD162732

Classical Be Star; Shell Star

- Other Names: HR 6664, V744 Her, 88 Her
- Spectral Type: B6 IVe+sh
- V magnitude: 6.65
- In WDS?: yes - 11.25 mag companion at 1.1 arcsec away (discovered in 1879)
- Known spectroscopic binary?: yes - Harmanec (2001) reports a period of 86.7221 d
- Velocity variations seen in these data?: likely not

	Hα	He I λ6678	Hγ	He I λ4471	Mg II λ4481	Fe II ccfs
Mean RV (km s^{-1})	-8.1	-24.3	-8.9	-65.9	-20.6	-6.0
RV range (km s^{-1})	-10.9 to -5.9	-31.3 to -20.2	-11.8 to -4.2	-72.4 to -59.5	-25.1 to -11.1	-9.0 to -0.8
RV change (km s^{-1})	5.0	11.1	7.6	12.9	14.0	8.2

- Shell classification: shell
- Do shell features move with the star?: N/A
- Notes on emission and absorption features: Hα has very strong central absorption and there are strong absorption shell features throughout both the red and blue spectra.
- Other notes: This star is also plotted in Figure 7.5.

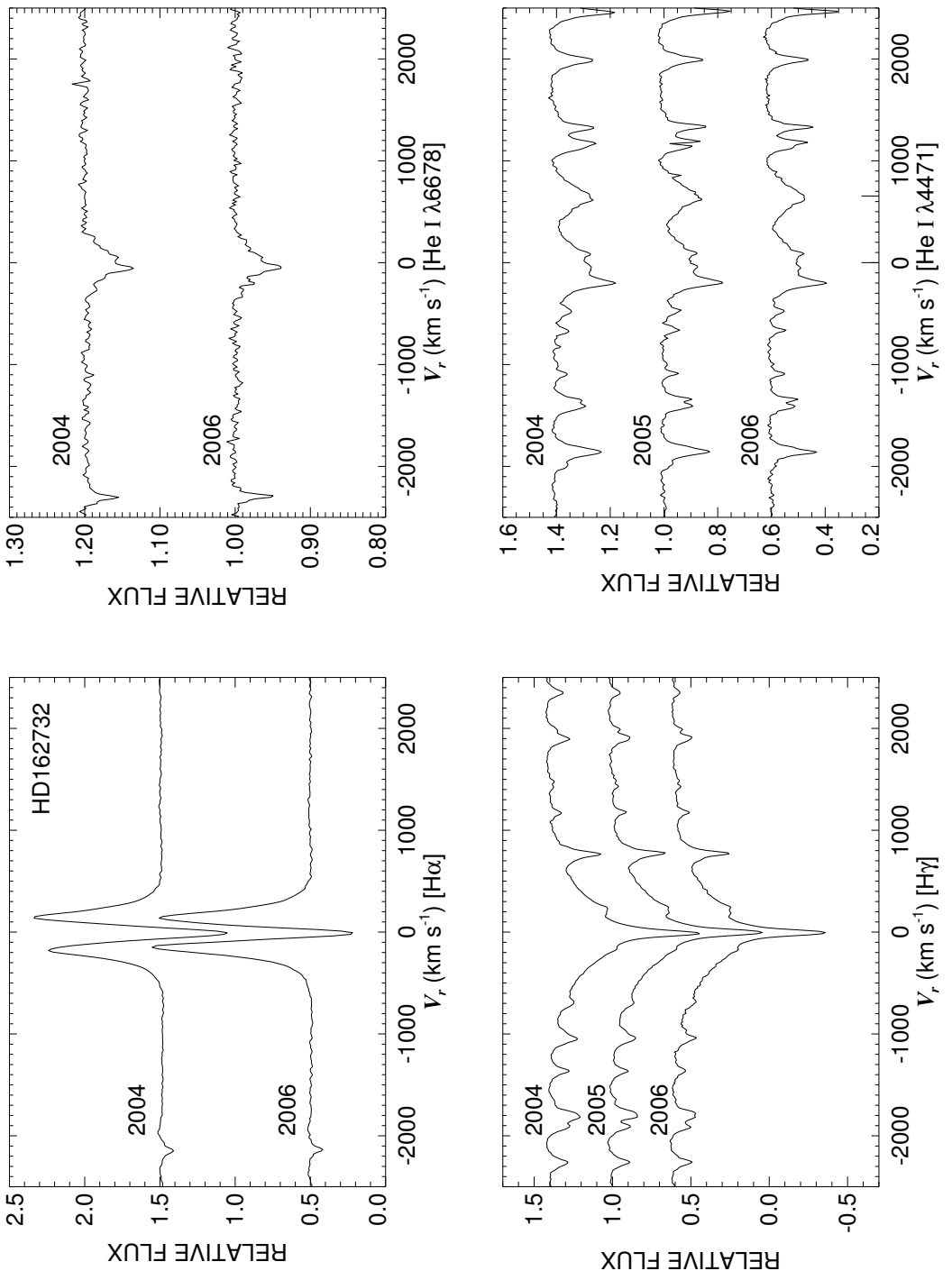

Figure C.59: A quadruple plot of HD162732 as described in §7.2.3 and Figure 7.6.

HD164284

Classical Be Star; Non-Radial Pulsator

- Other Names: HR 6712, 66 Oph, V2048 Oph
- Spectral Type: B2 IV/Ve+sh
- V magnitude: 4.68
- In WDS?: no
- Known spectroscopic binary?: yes - see notes below
- Velocity variations seen in these data?: very small if at all

	Hα	He I λ6678	Hγ	He I λ4471	Mg II λ4481	Fe II ccfs
Mean RV (km s^{-1})	-1.2	-4.1	18.9	-32.9	-44.4	-9.0
RV range (km s^{-1})	-2.4 to -0.3	-9.5 to 4.4	12.7 to 24.8	-36.7 to -28.5	-53.9 to -39.5	-44.9 to 16.8
RV change (km s^{-1})	2.1	13.9	12.1	8.2	14.4	61.8

- Shell classification: weak squarish
- Do shell features move with the star?: N/A
- Notes on emission and absorption features: He I λ6678 shows emission horns (unreliable for RV studies). Mg II λ4471 shows some weak features which may be indicative of companions (see below).
- Other notes: Rivinius et al. (2004) shows this star is a non-radial pulsator (their Fig. 4) and report periods of 0.25 and 0.45 d. They also report on the determination that this is a spectroscopic triple (but I cannot get to the reference) where a pair of late B/early A stars are seen. However, this pair orbits at a relatively considerable distance (and therefore won't influence the Be star).

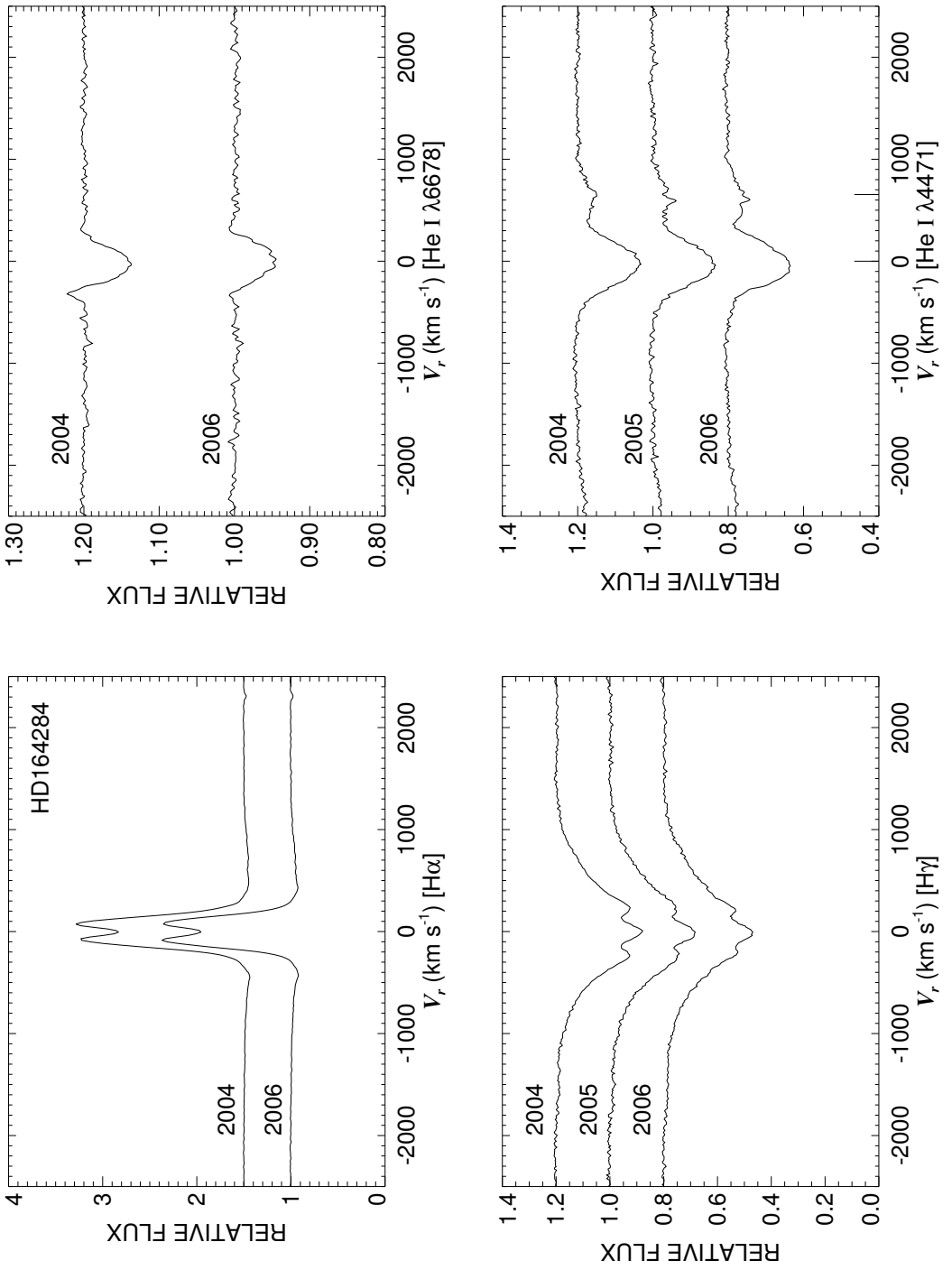

Figure C.60: A quadruple plot of HD164284 as described in §7.2.3 and Figure 7.6.

HD164447

Classical Be Star

- Other Names: HR 6720, V974 Her
- Spectral Type: B8 Vne
- V magnitude: 6.35
- In WDS?: no
- Known spectroscopic binary?: no
- Velocity variations seen in these data?: no

	Hα	He I λ6678	Hγ	He I λ4471	Mg II λ4481	Fe II ccfs
Mean RV (km s^{-1})	-38.5	-40.1	-39.5	-60.2	-48.3	-40.4
RV range (km s^{-1})	-42.4 to -36.3	-42.3 to -37.9	-42.6 to -34.6	-61.7 to -59.3	-49.5 to -47.1	-51.8 to -29.3
RV change (km s^{-1})	6.1	4.4	8.0	2.4	2.4	22.5

- Shell classification: squarish
- Do shell features move with the star?: N/A
- Notes on emission and absorption features: Both hydrogen lines show peak changing between runs.
- Other notes:

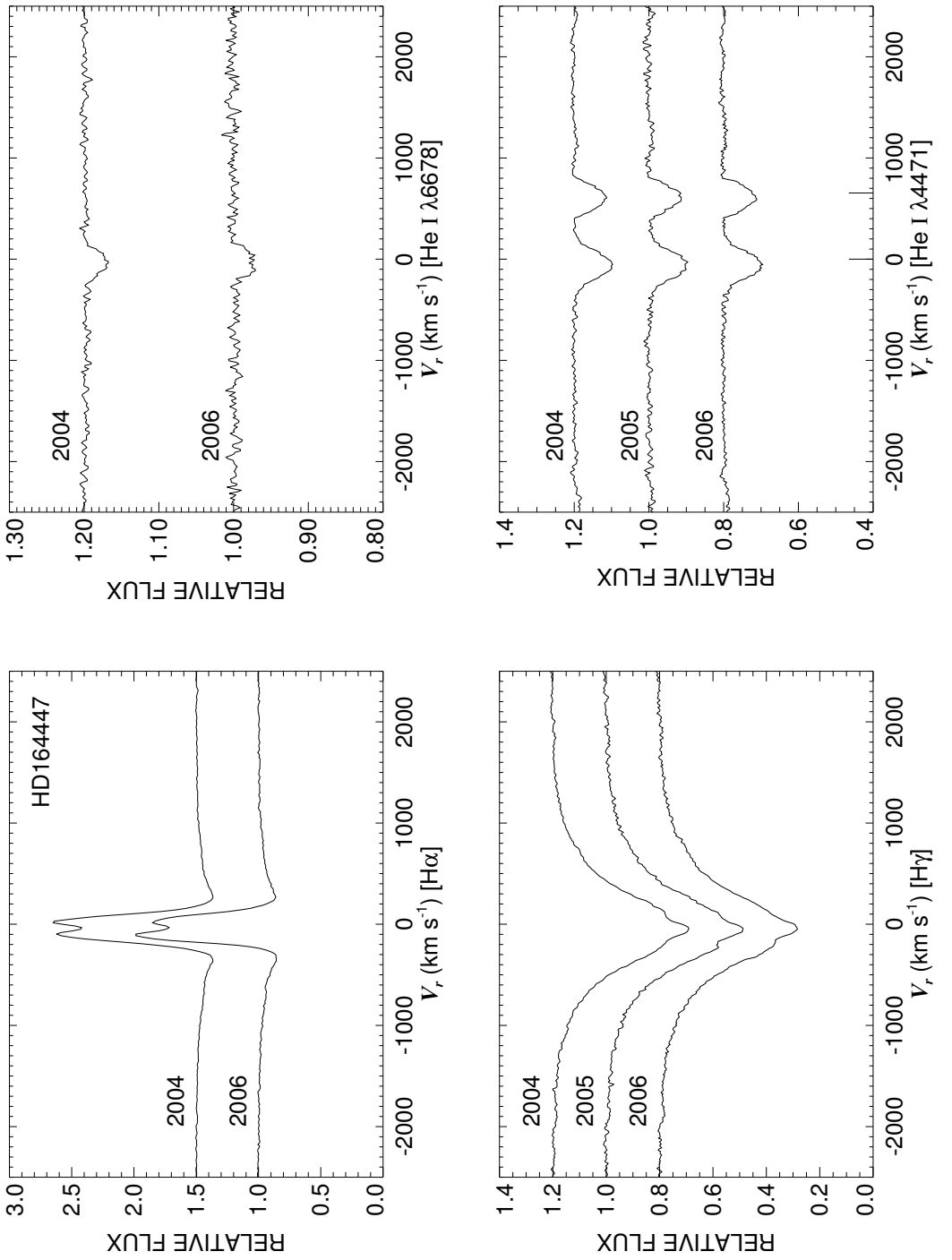

Figure C.61: A quadruple plot of HD164447 as described in §7.2.3 and Figure 7.6.

HD166014

Classical Be Star

- Other Names: HR 6779, *o* Her, 103 Her
- Spectral Type: B9.5 III
- V magnitude: 3.82
- In WDS?: yes - speckle companion of unlisted magnitude 0.1 arcsec away (discovered in 1981)
- Known spectroscopic binary?: no
- Velocity variations seen in these data?: no

	Hα	He I λ6678	Hγ	He I λ4471	Mg II λ4481	Fe II ccfs
Mean RV (km s^{-1})	-25.5	···	-13.0	···	-28.3	-17.8
RV range (km s^{-1})	-29.0 to -21.1	···	-14.3 to -10.6	···	-33.0 to -23.1	-21.8 to -14.4
RV change (km s^{-1})	7.9	···	3.7	···	9.9	7.4

- Shell classification: squarish (the shell features may be photospheric as this is a cool star)
- Do shell features move with the star?: N/A
- Notes on emission and absorption features: He I λ6678 and He I λ4471 practially non- existent as this star is cool and there is likely emission filling them in.
- Other notes: This star is also plotted in Figure 7.3.

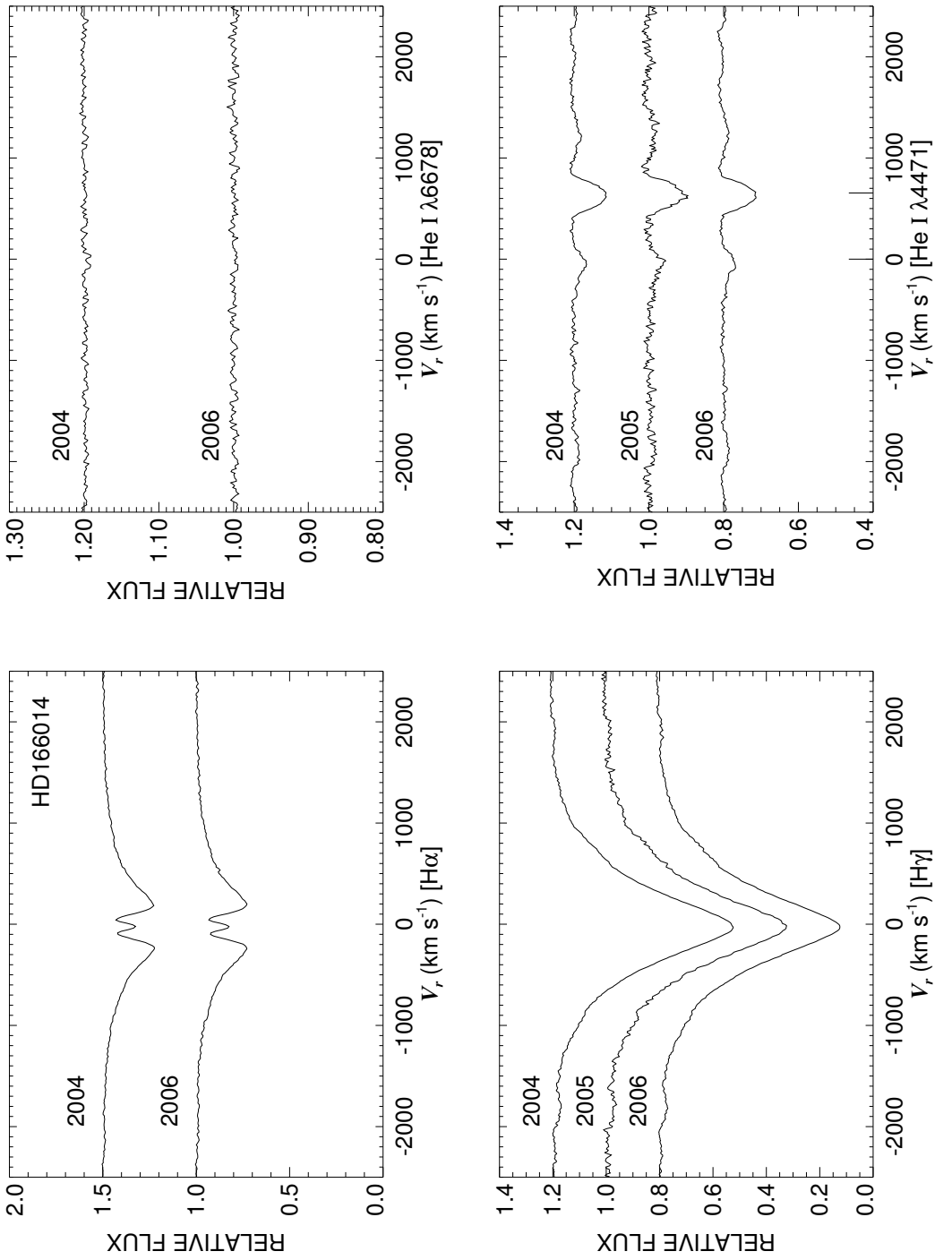

Figure C.62: A quadruple plot of HD166014 as described in §7.2.3 and Figure 7.6.

HD168797

Classical Be Star; Non-Radial Pulsator?

- Other Names: HR 6873, NW Ser
- Spectral Type: B3 Ve
- V magnitude: 6.09
- In WDS?: no
- Known spectroscopic binary?: no
- Velocity variations seen in these data?: yes (companion or NRP? - see Fig. C.64)

	Hα	He I λ6678	Hγ	He I λ4471	Mg II λ4481	Fe II ccfs
Mean RV (km s^{-1})	-13.5	-24.3	-8.4	-42.7	-47.7	···
RV range (km s^{-1})	-24.5 to -6.7	-30.1 to -13.5	-15.0 to 0.5	-49.0 to -38.2	-53.9 to -40.3	···
RV change (km s^{-1})	17.8	16.6	15.5	10.8	13.6	···

- Shell classification: normal
- Notes on emission and absorption features: Hα increases from 2004 to 2006. Line profile changes throughout the blue spectra.
- Other notes:

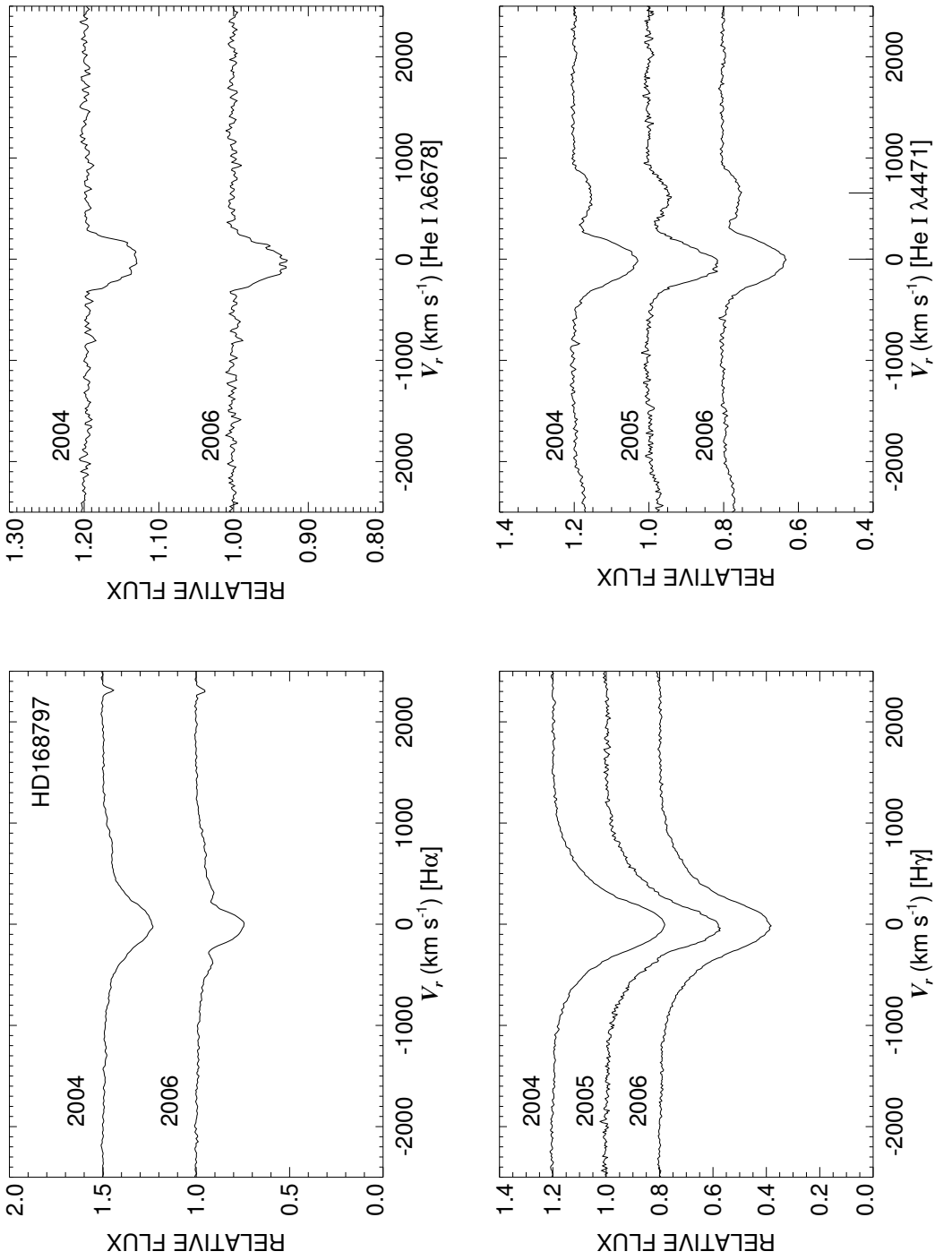

Figure C.63: A quadruple plot of HD168797 as described in §7.2.3 and Figure 7.6.

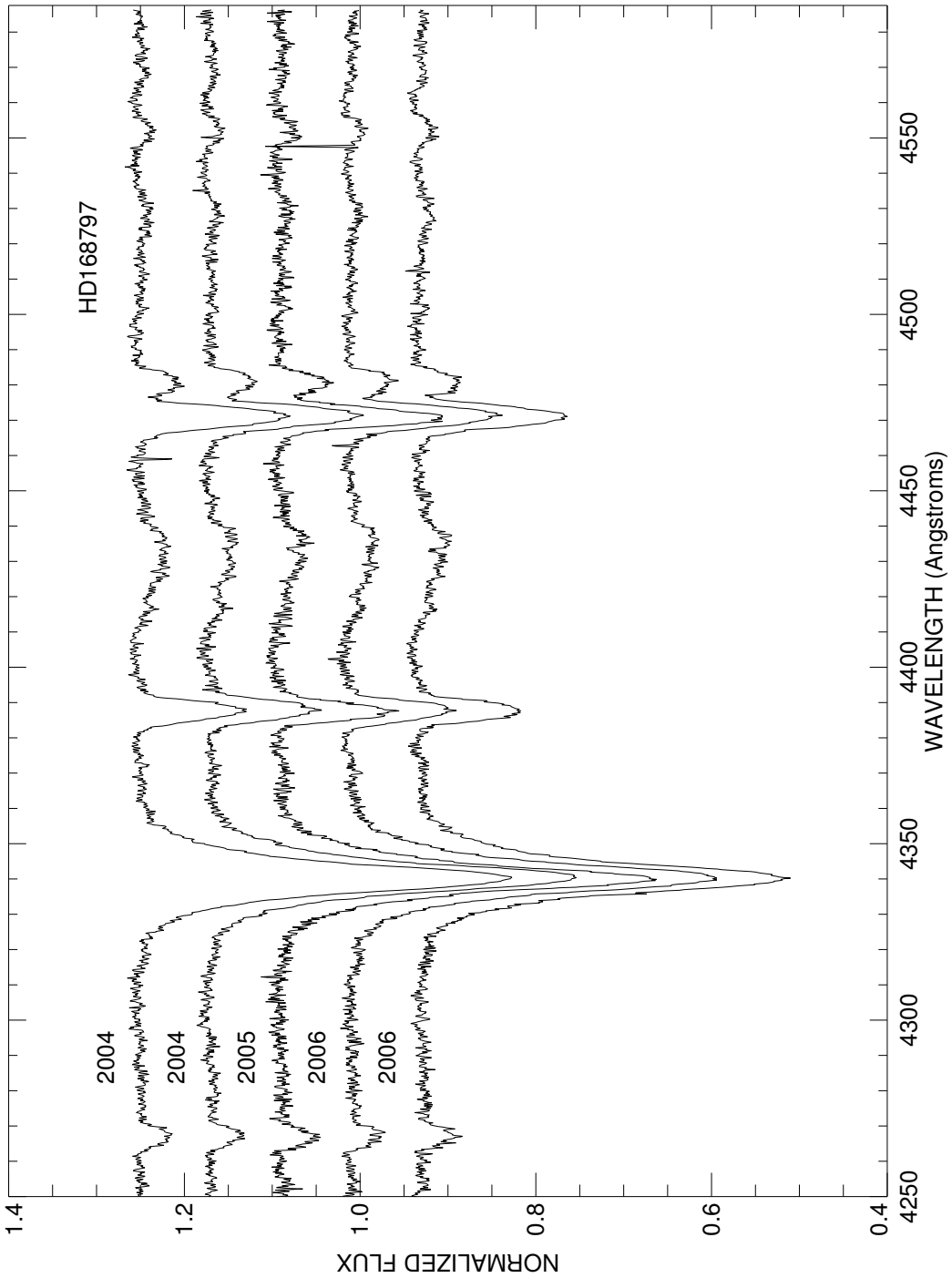

Figure C.64: A plot of all spectra of HD168797 in the blue region. Each is labeled with the year of observation and they are offset for clarity.

HD168957

Classical Be Star

- Other Names:
- Spectral Type: B4 Ve
- V magnitude: 6.89
- In WDS?: no
- Known spectroscopic binary?: no
- Velocity variations seen in these data?: no

	Hα	He I λ6678	Hγ	He I λ4471	Mg II λ4481	Fe II ccfs
Mean RV (km s^{-1})	-28.3	-30.7	-25.3	-38.8	-29.1	-27.0
RV range (km s^{-1})	-39.8 to -18.6	-31.3 to -29.8	-27.0 to -21.7	-40.5 to -37.9	-31.5 to -26.9	-29.3 to -24.7
RV change (km s^{-1})	21.2	1.5	5.3	2.6	4.6	4.6

- Shell classification: squarish (may be photospheric)
- Do shell features move with the star?: N/A
- Notes on emission and absorption features: The lines are very narrow (a sharp-lined B star).
- Other notes: While this star currently has no emission (and often shows none), there is evidence of emission in the past. For instance, in Marlborough & Peters (1986), they state this star had "strong emission" in 1974 according to private communication with Peters.

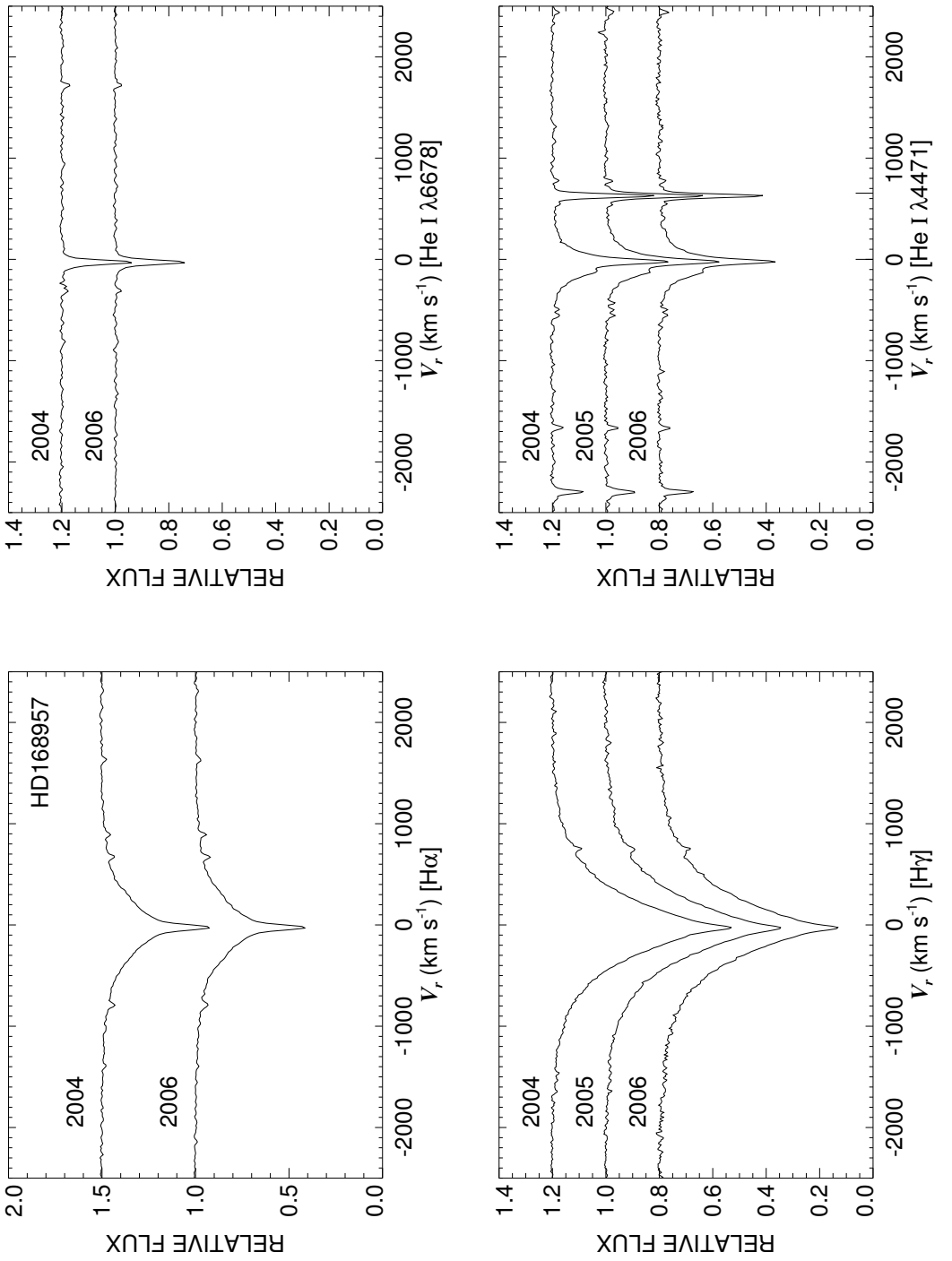

Figure C.65: A quadruple plot of HD168957 as described in §7.2.3 and Figure 7.6.

HD171406

Classical Be Star

- Other Names: HR 6971, V532 Lyr
- Spectral Type: B4 Ve
- V magnitude: 6.43
- In WDS?: no
- Known spectroscopic binary?: no (not published at least)
- Velocity variations seen in these data?: yes (see Fig C.67)

	Hα	He I λ6678	Hγ	He I λ4471	Mg II λ4481	Fe II ccfs
Mean RV (km s^{-1})	-8.0	-24.8	-10.8	-27.8	-25.0	-45.4
RV range (km s^{-1})	-22.4 to 1.2	-28.5 to -21.5	-22.2 to -4.6	-31.6 to -23.5	-30.4 to -20.5	-81.4 to -15.6
RV change (km s^{-1})	23.6	7.0	17.6	8.1	9.9	65.9

- Shell classification: normal
- Notes on emission and absorption features: Hα is in emission and increases from 2004 to 2006. The blue spectra show this is a composite spectrum.
- Other notes: This system is likely a Be star with a nearby very close binary system of perhaps A type stars that have a period of a few days. When these stars are together, the spectrum mimics that of a shell but when apart, it does not. This is previously unknown in the literature.

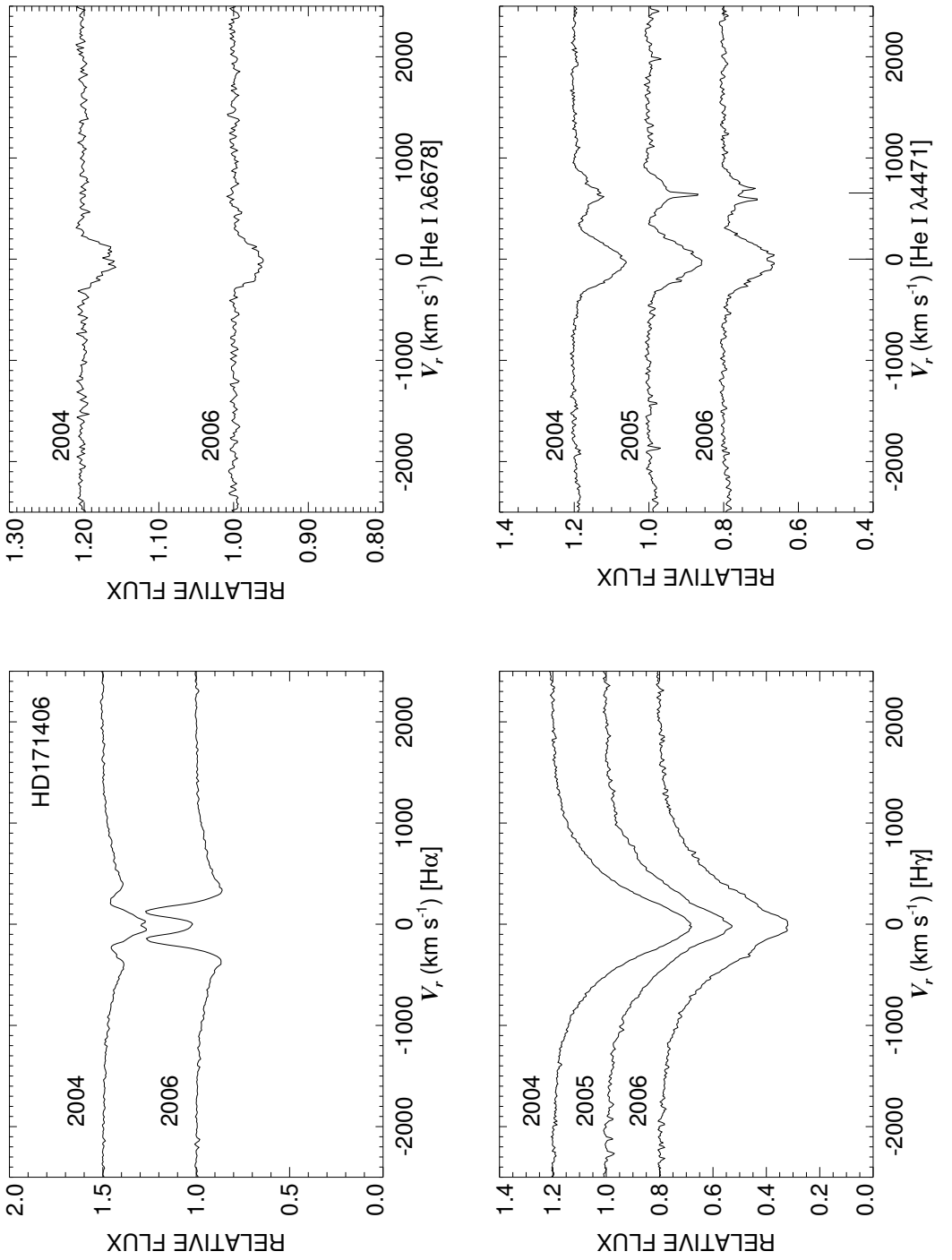

Figure C.66: A quadruple plot of HD171406 as described in §7.2.3 and Figure 7.6.

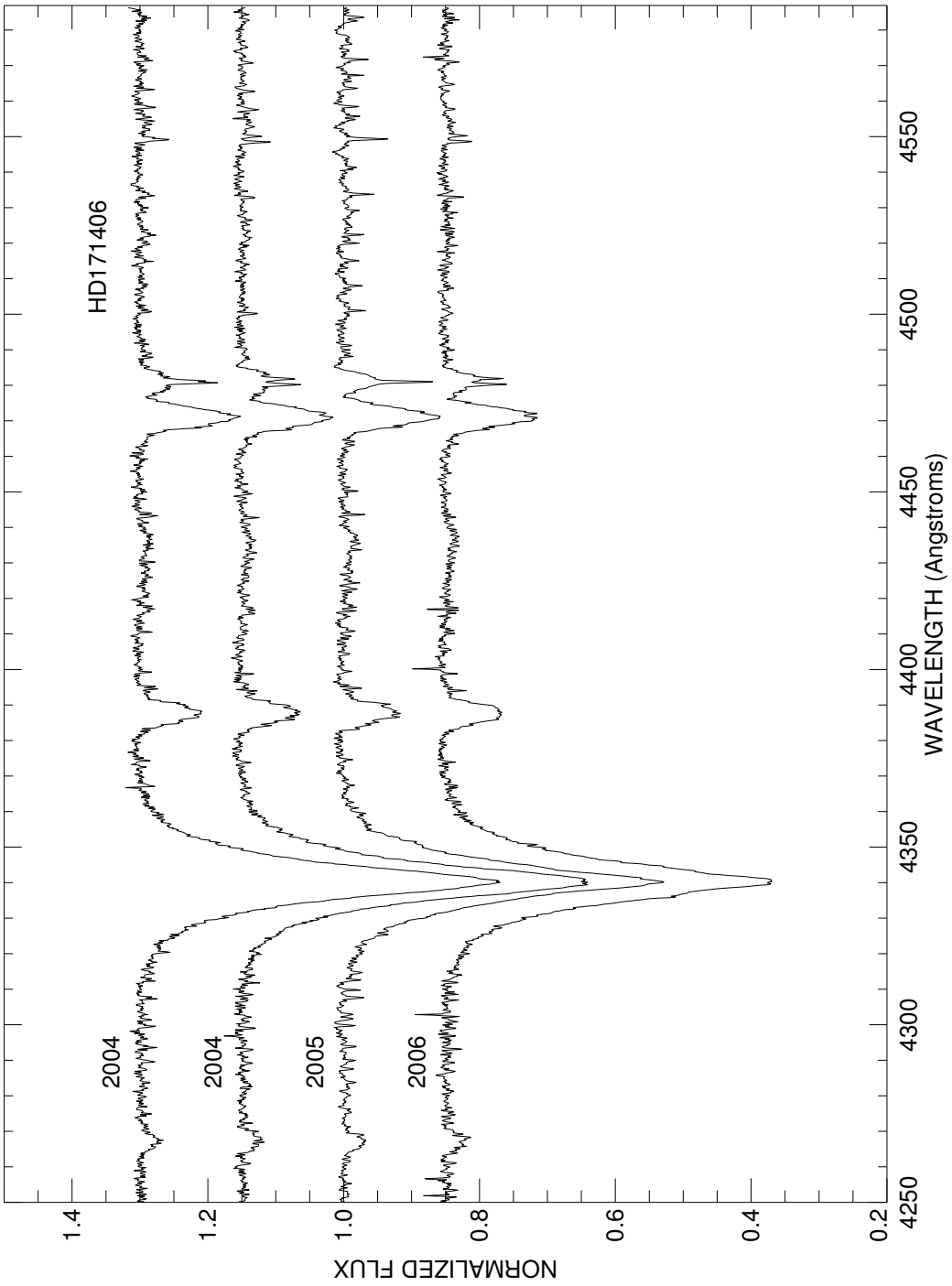

Figure C.67: A plot of all spectra of HD171406 in the blue region. Each is labeled with the year of observation and they are offset for clarity.

HD171780

Classical Be Star

- Other Names: HR 6984
- Spectral Type: B5 Vne
- V magnitude: 5.98
- In WDS?: yes - 9.47 mag companion 0.2 arcsec away (discovered in 1985)
- Known spectroscopic binary?: no
- Velocity variations seen in these data?: possible

	Hα	He I λ6678	Hγ	He I λ4471	Mg II λ4481	Fe II ccfs
Mean RV (km s^{-1})	-18.9	-27.9	-6.0	-41.6	-34.6	···
RV range (km s^{-1})	-19.9 to -17.1	-36.4 to -20.1	-11.3 to -0.5	-44.8 to -38.1	-41.2 to -23.3	···
RV change (km s^{-1})	2.8	16.3	10.8	6.7	17.9	···

- Shell classification: normal
- Notes on emission and absorption features: Hα decreases a great deal from 2004 to 2006.
- Other notes:

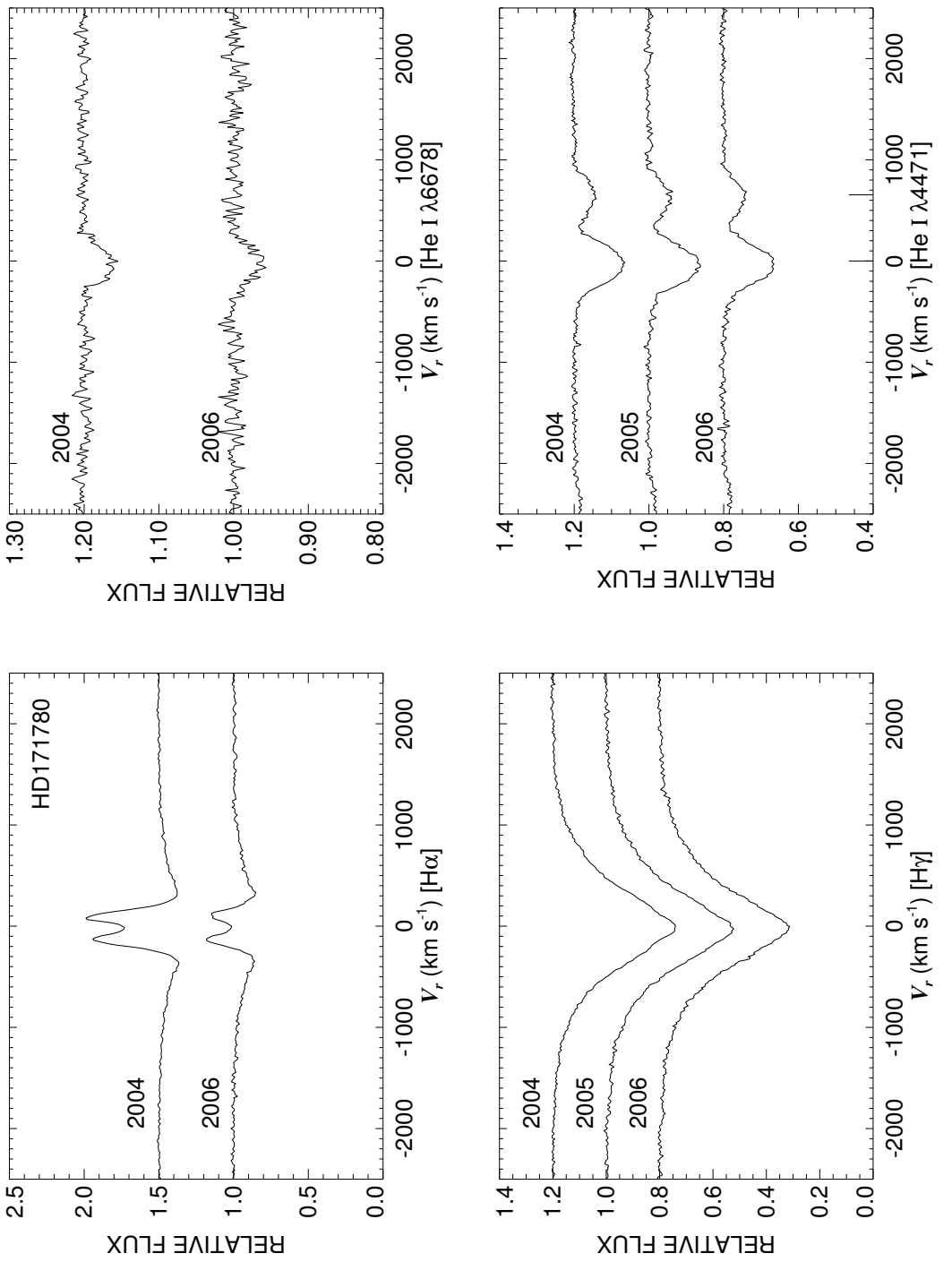

Figure C.68: A quadruple plot of HD171780 as described in §7.2.3 and Figure 7.6.

HD173370

Classical Be Star

- Other Names: HR 7040, 4 Aql
- Spectral Type: B9 Ve
- V magnitude: 4.96
- In WDS?: no
- Known spectroscopic binary?: no
- Velocity variations seen in these data?: no

	Hα	He I λ6678	Hγ	He I λ4471	Mg II λ4481	Fe II ccfs
Mean RV (km s^{-1})	-10.6	···	7.4	-23.0	-7.6	-7.1
RV range (km s^{-1})	-14.6 to -3.3	···	5.8 to 10.1	-29.3 to -15.4	-13.8 to -0.2	-27.9 to 23.3
RV change (km s^{-1})	11.3	···	4.3	13.9	13.6	51.1

- Shell classification: squarish
- Do shell features move with the star?: N/A
- Notes on emission and absorption features: He I λ6678 filled in by emission (as well as being weak due to the cool temperature of this star).
- Other notes:

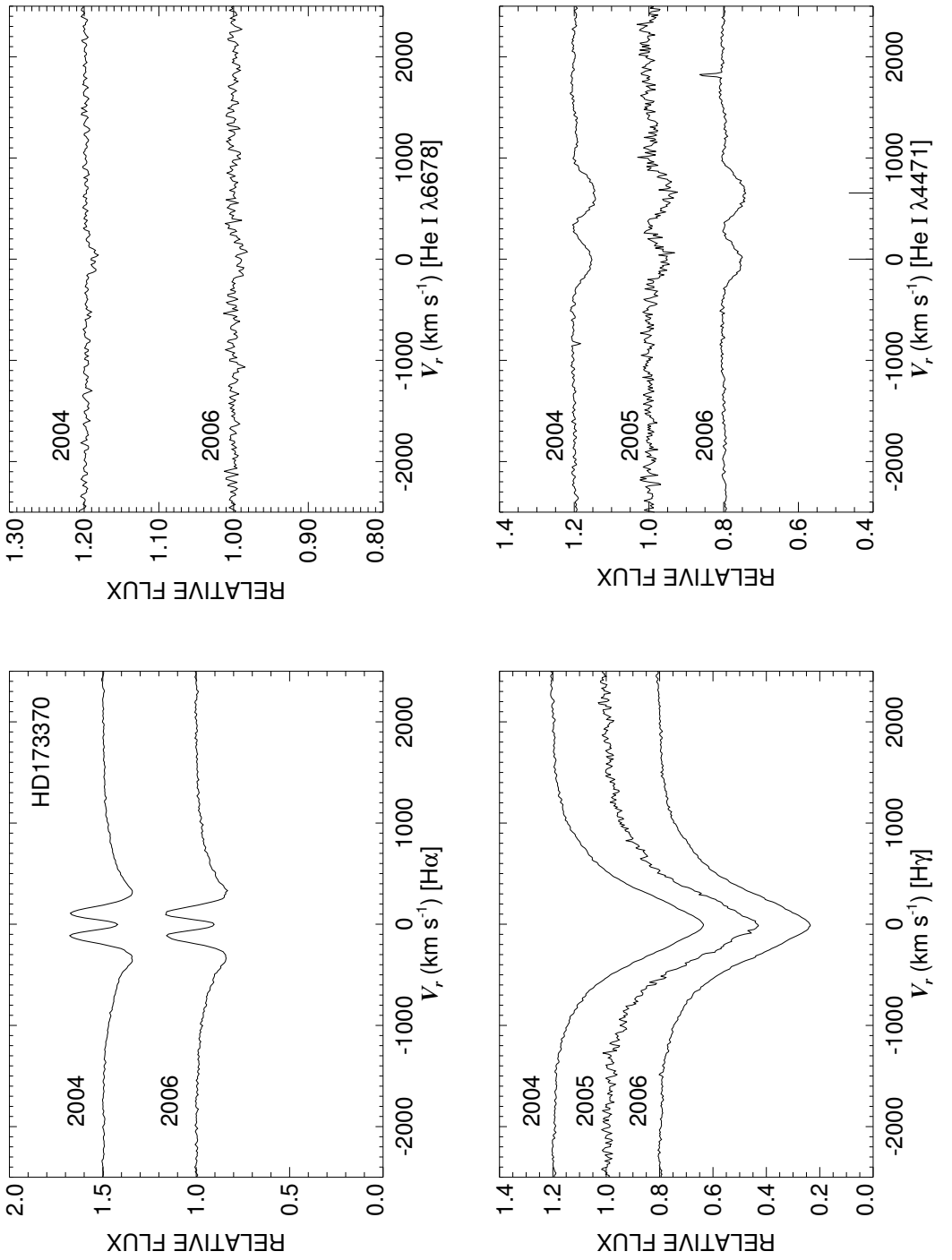

Figure C.69: A quadruple plot of HD173370 as described in §7.2.3 and Figure 7.6.

HD174237

Interacting Binary

- Other Names: HR 7084, CX Dra
- Spectral Type: B2.5 Ve
- V magnitude: 5.80
- In WDS?: no
- Known spectroscopic binary?: yes - Koubsky (1978) gives a period of 6.696 d and Horn et al. (1992) state the companion is an F5 III star overflowing its Roche lobe
- Velocity variations seen in these data?: yes (also see Fig C.71)

	Hα	He I λ6678	Hγ	He I λ4471	Mg II λ4481	Fe II ccfs
Mean RV (km s^{-1})	-2.1	36.9	24.5	-10.2	3.4	21.5
RV range (km s^{-1})	-10.4 to 4.4	-4.2 to 94.4	-9.6 to 66.6	-37.3 to 12.8	-9.2 to 32.9	-10.4 to 79.0
RV change (km s^{-1})	14.8	98.6	76.2	50.1	42.1	89.5

- Shell classification: weak squarish
- Do shell features move with the star?: yes?
- Notes on emission and absorption features: Hα has the shape common to interacting binaries (like RY Scuti, β Lyr, etc.) and the strength decreases from 2004 to 2006. He I λ6678 and Mg II λ4481 both show emission horns.
- Other notes: This is another star like RY Scuti - a messy system.

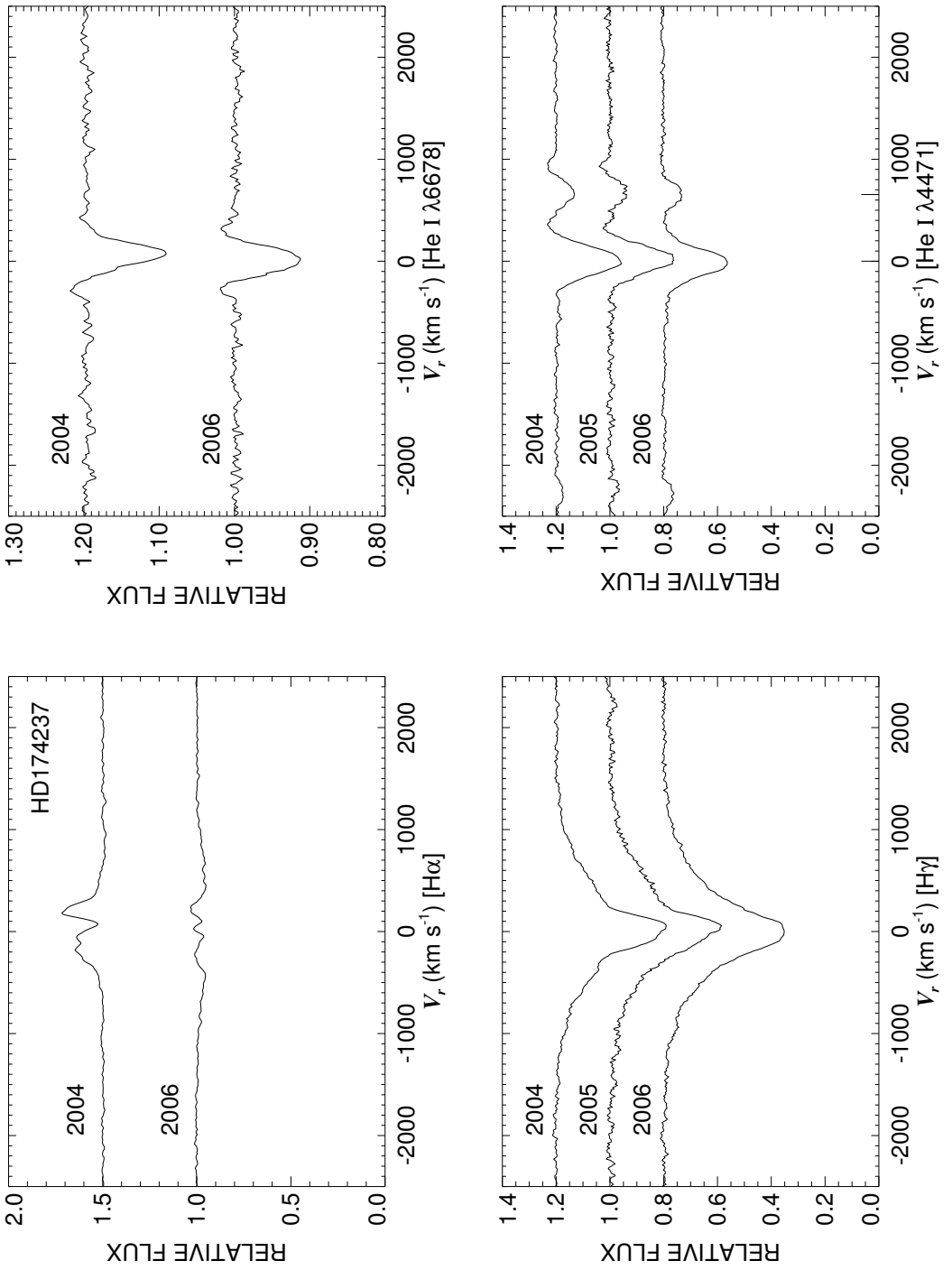

Figure C.70: A quadruple plot of HD174237 as described in §7.2.3 and Figure 7.6.

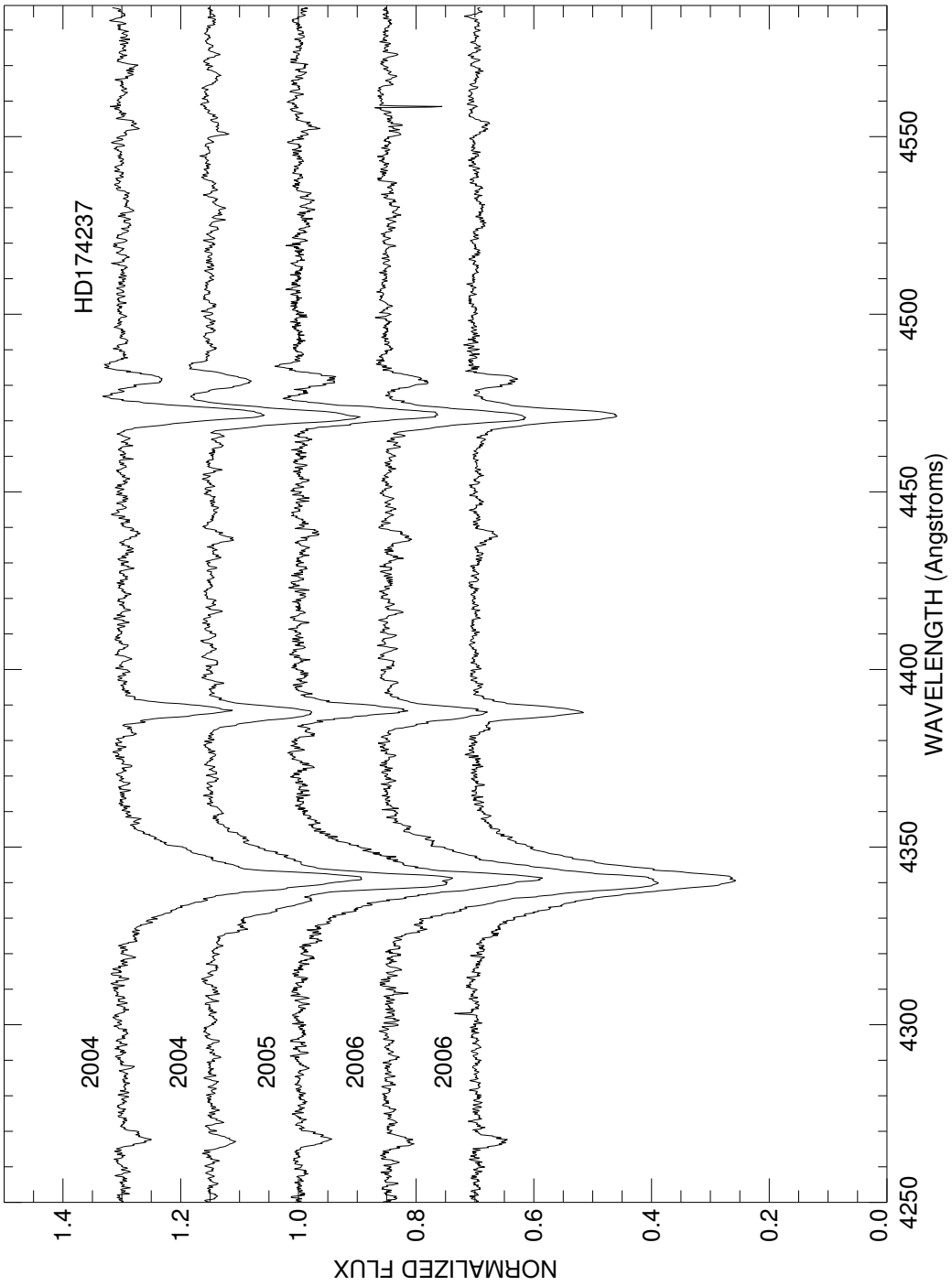

Figure C.71: A plot of all spectra of HD174237 in the blue region. Each is labeled with the year of observation and they are offset for clarity.

HD174638

Interacting Binary

- Other Names: HR 7106, β Lyr
- Spectral Type: B7 Ve
- V magnitude: 3.52
- In WDS?: yes - a 6.69 mag companion at 48 arcsec away (discovered in 1777) along with 4 fainter (13.0, 14.3, 10.14, 10.62) companions at 47, 80, 68, and 87 arcsec away (discovered in 1878, 1898, and 1834).
- Known spectroscopic binary?: yes - a very well known and well studied interacting binary (I refer to it often in Ch. 2) with a period of 12.935 d (Harmanec 2001) and an early B-type companion enshrouded in an accretion torus (Nazarenko & Glazunova 2006b)
- Velocity variations seen in these data?: yes (see Fig. C.73)

	Hα	He I λ6678	Hγ	He I λ4471	Mg II λ4481	Fe II ccfs
Mean RV (km s^{-1})	-18.4	···	-127.2	-187.1	-71.3	-64.7
RV range (km s^{-1})	-40.2 to 21.9	···	-257.0 to 209.1	-187.2 to -187.0	-267.2 to 141.1	-195.7 to 156.9
RV change (km s^{-1})	62.1	···	466.1	0.2	408.3	352.6

- Shell classification: squarish
- Do shell features move with the star?: yes and they move all over
- Notes on emission and absorption features: This interacting binary is transferring a great deal of mass and the system is leaky therefore the spectral features (esp. in the blue) look strange but also quite reminiscent of RY Scuti.
- Other notes: This is the star referred to often for models in Chapter 2. Notice that the Hα profile looks quite similar to RY Scuti (without the sharp nebular emission of course). As it is actively transferring mass from one star to another, it was eliminated from any statistical analysis in Chapter 7.

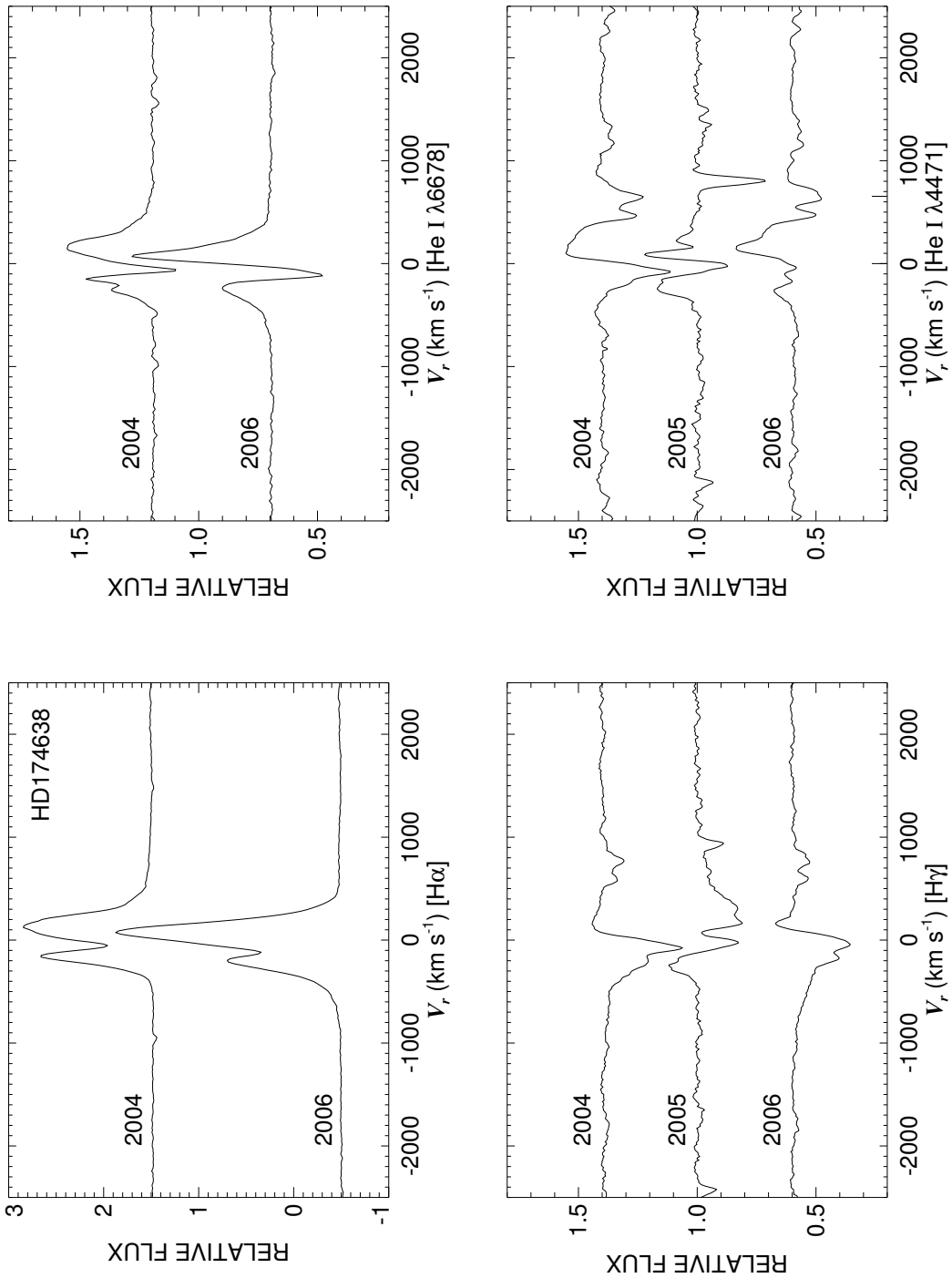

Figure C.72: A quadruple plot of HD174638 as described in §7.2.3 and Figure 7.6.

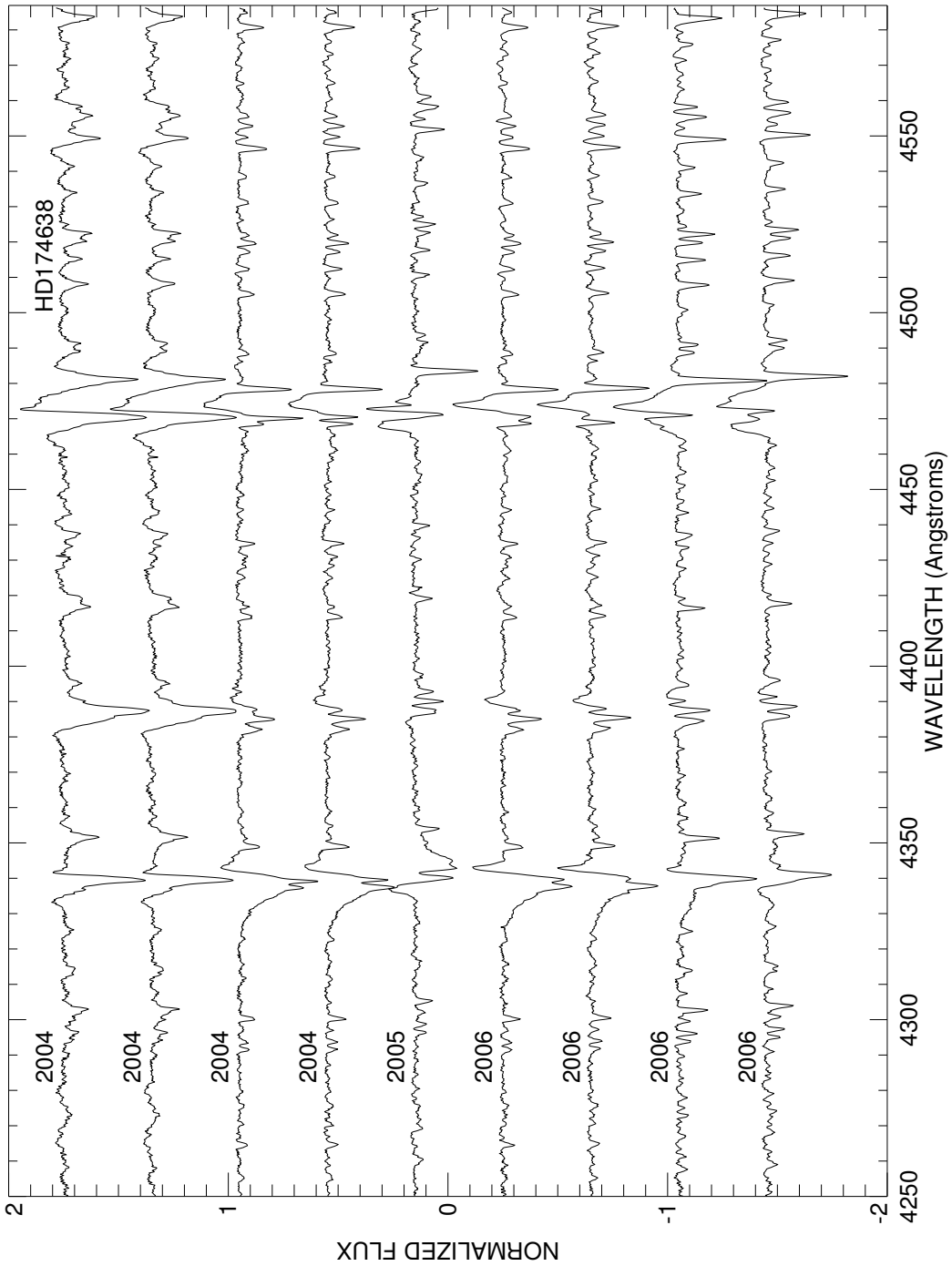

Figure C.73: A plot of all spectra of HD174638 in the blue region. Each is labeled with the year of observation and they are offset for clarity.

HD175863

Classical Be Star; Non-Radial Pulsator?

- Other Names:
- Spectral Type: B5 Ve
- V magnitude: 6.90
- In WDS?: no
- Known spectroscopic binary?: no
- Velocity variations seen in these data?: no

	Hα	He I λ6678	Hγ	He I λ4471	Mg II λ4481	Fe II ccfs
Mean RV (km s^{-1})	-15.7	-27.1	-14.8	-33.8	-19.3	···
RV range (km s^{-1})	-18.2 to -12.6	-28.0 to -26.2	-23.0 to -9.1	-35.8 to -31.9	-22.8 to -15.2	···
RV change (km s^{-1})	5.6	1.8	13.9	3.9	7.6	···

- Shell classification: normal
- Notes on emission and absorption features: Big decrease in Hα emission and a more modest decrease in the small amount of Hγ emission. He I λ6678 seems to have emission horns (esp. in 2004). The square shape of Mg II λ4481 in 2006 may indicate NRP (the asymmetry in other runs supports this too).
- Other notes:

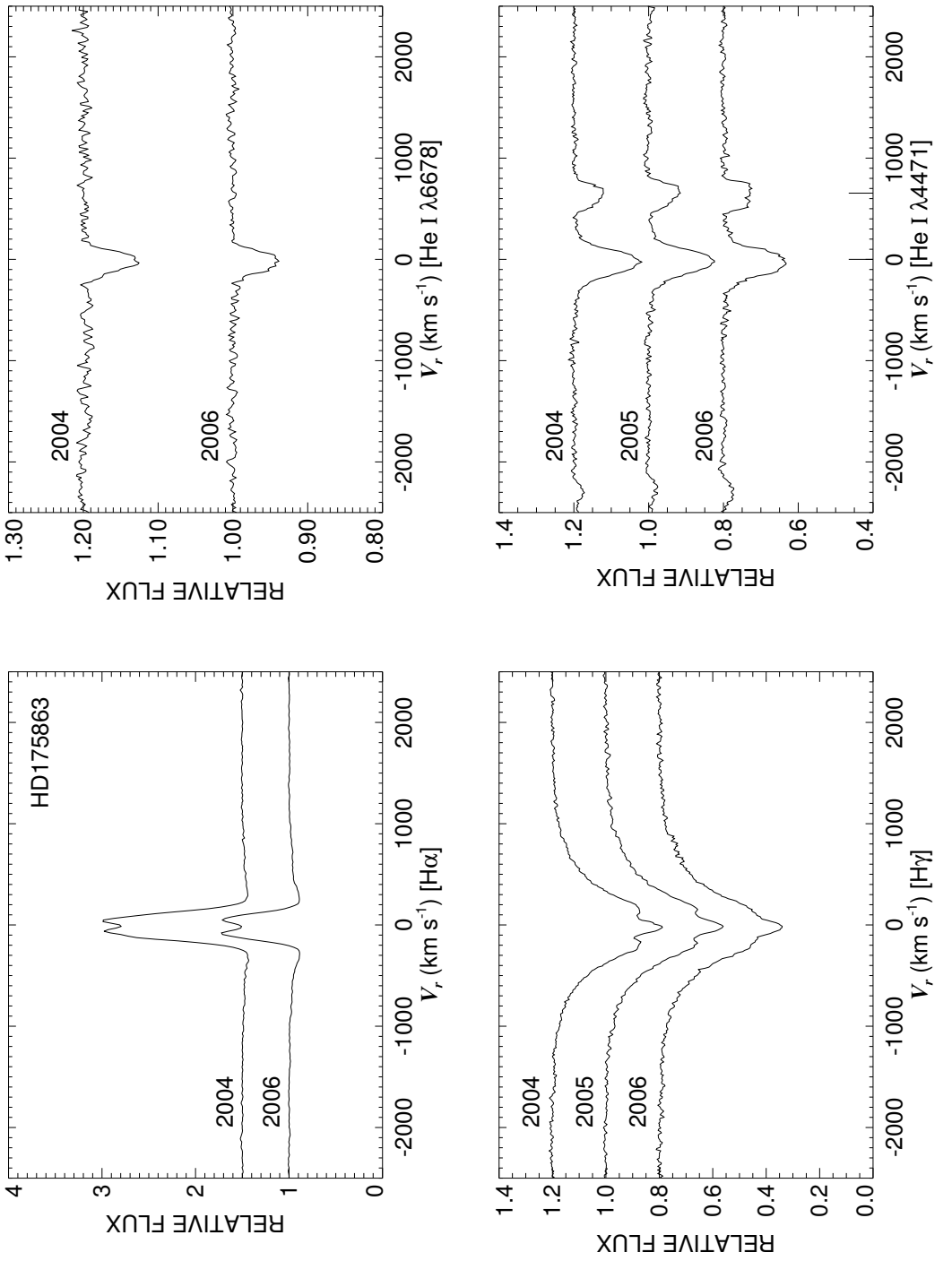

Figure C.74: A quadruple plot of HD175863 as described in §7.2.3 and Figure 7.6.

HD175869

Classical Be Star

- Other Names: HR 7158, 64 Ser
- Spectral Type: B8 IIIep
- V magnitude: 5.56
- In WDS?: no
- Known spectroscopic binary?: no
- Velocity variations seen in these data?: unlikely

	Hα	He I λ6678	Hγ	He I λ4471	Mg II λ4481	Fe II ccfs
Mean RV (km s^{-1})	-9.1	7.0	-7.6	-5.0	-10.2	1.4
RV range (km s^{-1})	-11.7 to -6.5	···	-12.5 to -4.4	-13.2 to 2.7	-15.9 to -6.8	-6.1 to 5.5
RV change (km s^{-1})	5.2	···	8.1	15.9	9.1	11.6

- Shell classification: squarish
- Do shell features move with the star?: N/A
- Notes on emission and absorption features: The helium lines are weak due to the cooler temperature of this star.
- Other notes: This star is also plotted in Figure 7.3.

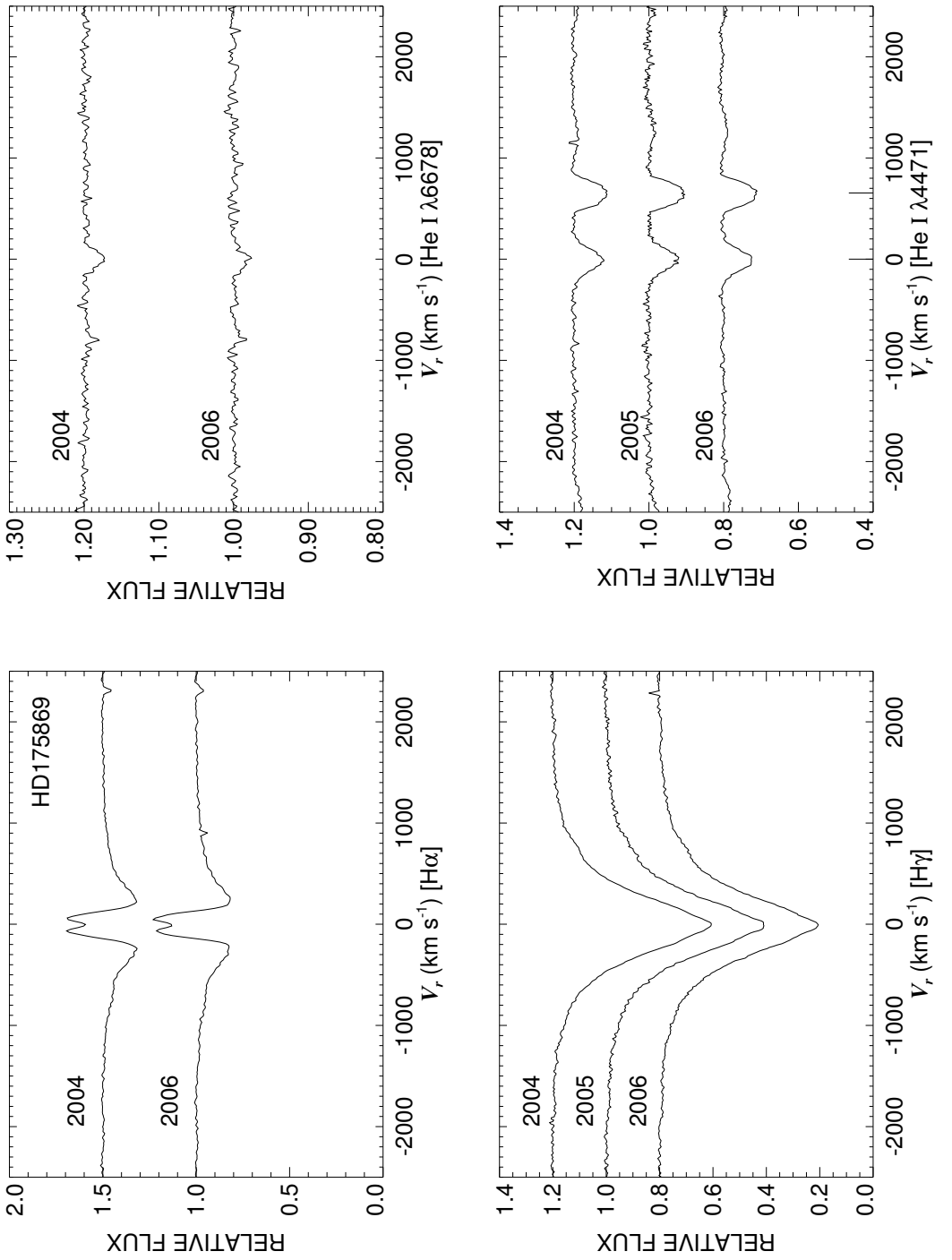

Figure C.75: A quadruple plot of HD175869 as described in §7.2.3 and Figure 7.6.

HD177648

Classical Be Star; Non-Radial Pulsator?

- Other Names:
- Spectral Type: B2 Ve
- V magnitude: 7.32
- In WDS?: yes - two companions, 8.57 and 8.46 mag 12.3 and 145 arcsec away (discovered in 1830 and 1889)
- Known spectroscopic binary?: no
- Velocity variations seen in these data?: yes (companion or NRP? - see Fig. C.77)

	Hα	He I λ6678	Hγ	He I λ4471	Mg II λ4481	Fe II ccfs
Mean RV (km s^{-1})	-8.8	-13.5	10.0	-29.5	-28.9	···
RV range (km s^{-1})	-9.9 to -6.7	-26.0 to 0.3	6.2 to 13.0	-46.0 to -20.9	-47.5 to -19.2	···
RV change (km s^{-1})	3.2	26.3	6.8	25.1	28.3	···

- Shell classification: normal
- Notes on emission and absorption features: Hα strength increases from 2004 to 2006. Emission horns in He I λ6678. The line profile changes could be the result of NRP.
- Other notes:

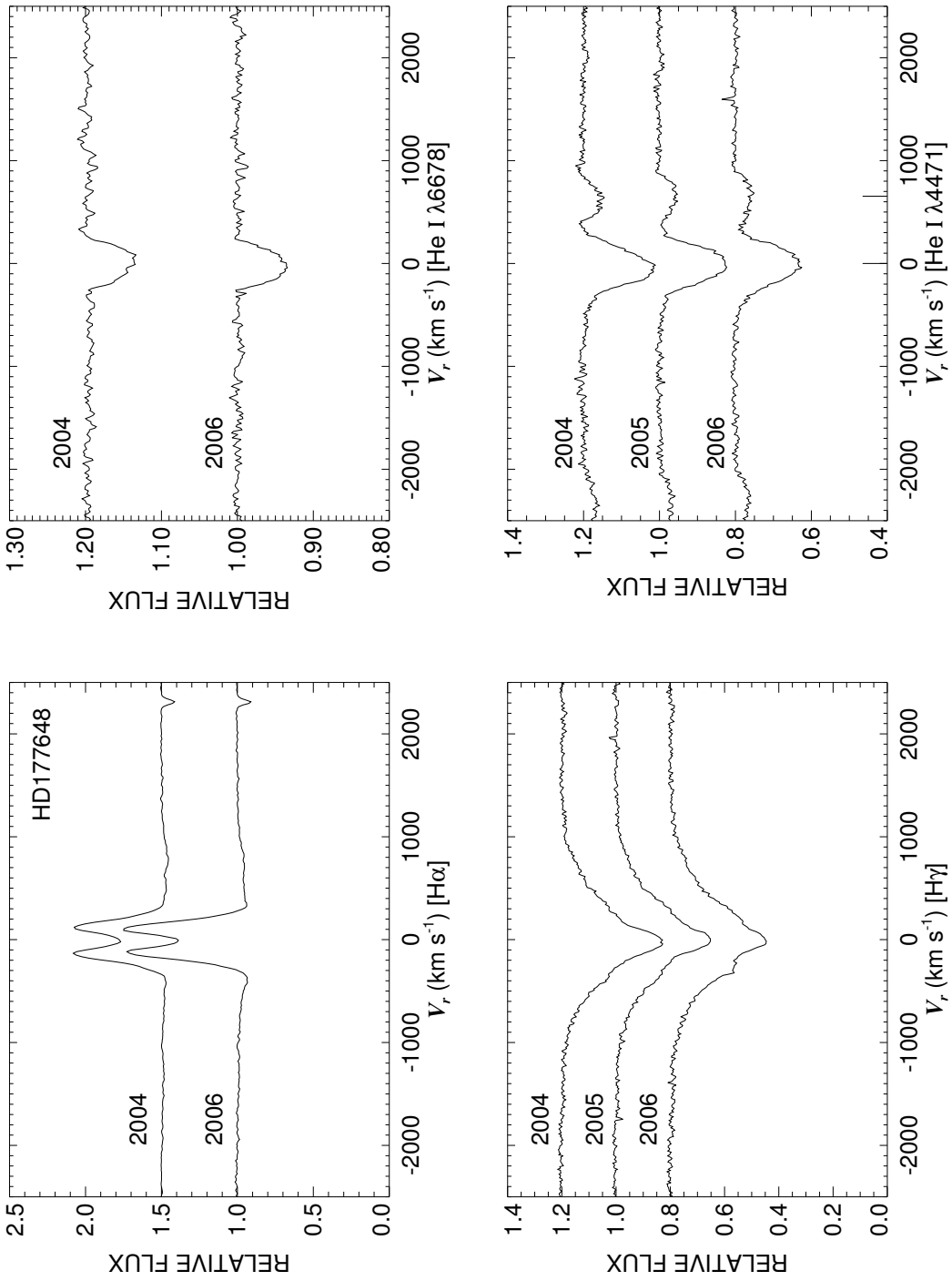

Figure C.76: A quadruple plot of HD177648 as described in §7.2.3 and Figure 7.6.

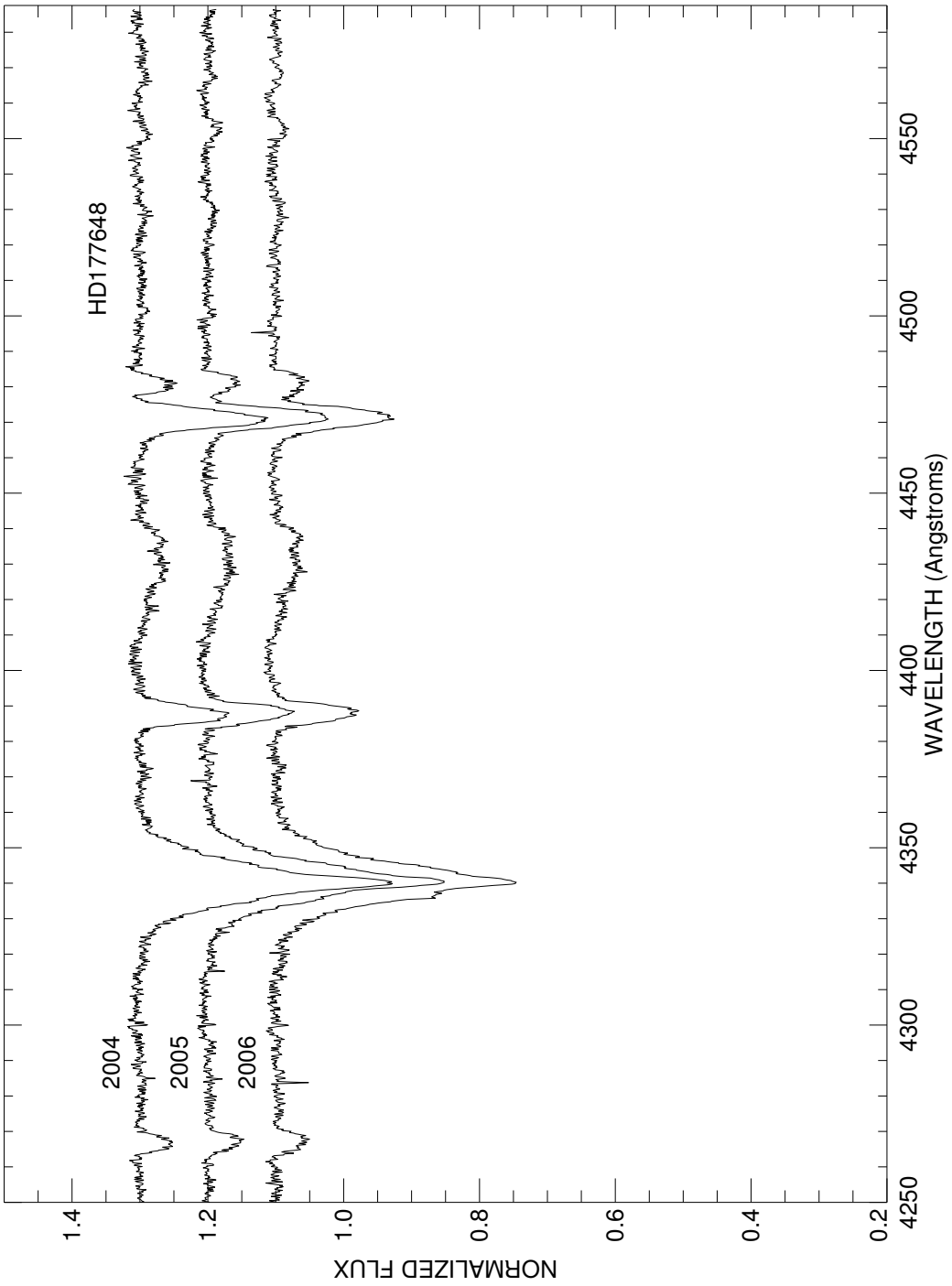

Figure C.77: A plot of all spectra of HD177648 in the blue region. Each is labeled with the year of observation and they are offset for clarity.

HD178475

Classical Be Star

- Other Names: HR 7262, ι Lyr, 18 Lyr
- Spectral Type: B5 V
- V magnitude: 5.14
- In WDS?: yes - 6.4 mag speckle companion 0.1 arcsec away (discovered in 1981)
- Known spectroscopic binary?: no
- Velocity variations seen in these data?: maybe

	Hα	He I λ6678	Hγ	He I λ4471	Mg II λ4481	Fe II ccfs
Mean RV (km s^{-1})	-20.6	-31.0	-3.3	-43.3	-33.3	-14.3
RV range (km s^{-1})	-22.8 to -18.2	-40.5 to -22.6	-16.5 to 17.7	-52.8 to -37.6	-36.3 to -27.6	-36.1 to 24.8
RV change (km s^{-1})	4.6	17.9	34.2	15.2	8.7	60.9

- Shell classification: squarish (changes - see Fig. C.79)
- Do shell features move with the star?: if it moves, then yes

  Notes on emission and absorption features: Hα decreases from 2004 to 2006 and so do the shell lines in the blue. There is a rather strange squarish feature in both He I λ6678 and Mg II λ4481 perhaps resulting from the speckle companion.

- Other notes:

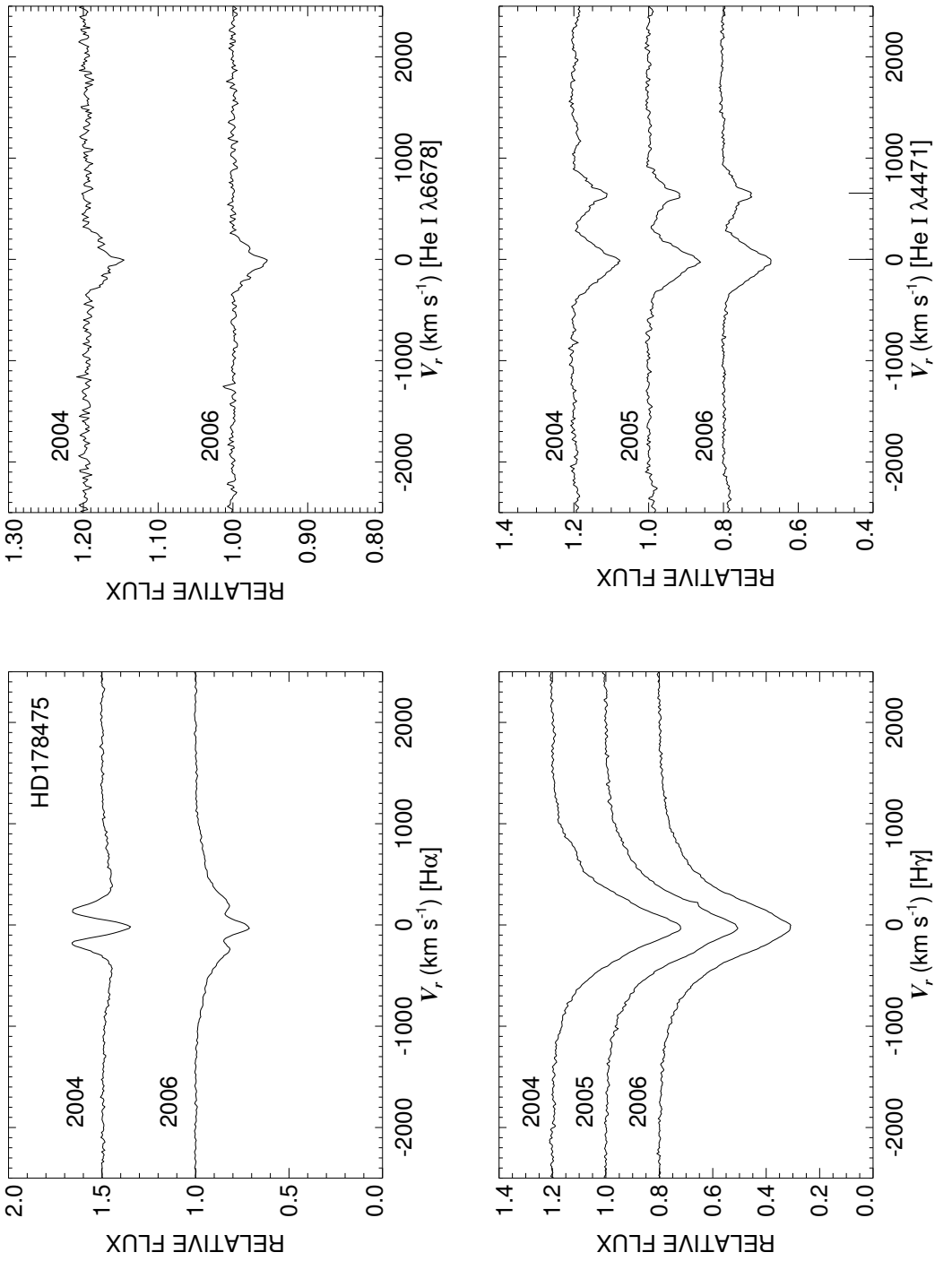

Figure C.78: A quadruple plot of HD178475 as described in §7.2.3 and Figure 7.6.

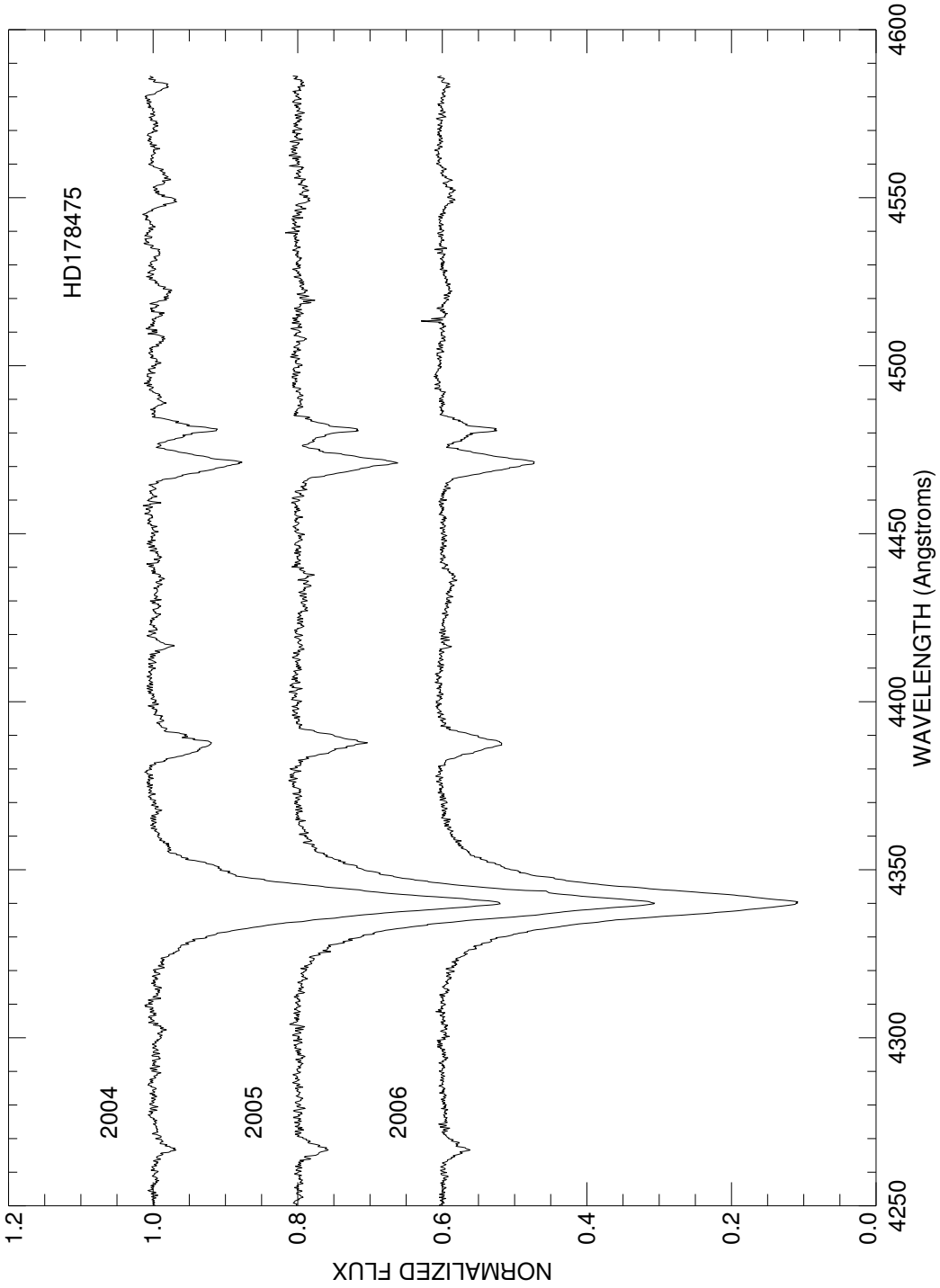

Figure C.79: A plot of the averages for each run in the blue region of HD178475. Each is labeled with the year of observation and they are offset from each other for clarity.

HD179343

Classical Be Star; Shell Star

- Other Names:
- Spectral Type: B9 V+sh
- V magnitude: 7.03
- In WDS?: yes - the AB pair is confusing - it is close (0.3 arcsec) and the components are mag 8 and 7.52 and discovered in 1890. There are 5 fainter companions to this pair (mag 11.2, 13.9, 13.1, 13.1, 10.2) at 13.3, 20.5, 25.9, 27.1, and 30.6 arcsec away (all discovered in 1890 except the last one, which was 1828).
- Known spectroscopic binary?: no
- Velocity variations seen in these data?: no

	Hα	He I λ6678	Hγ	He I λ4471	Mg II λ4481	Fe II ccfs
Mean RV (km s^{-1})	-8.9	-27.1	-6.8	-88.4	-14.5	-17.2
RV range (km s^{-1})	-9.7 to -8.2	-58.4 to -4.6	-7.5 to -6.0	-99.2 to -80.9	-23.5 to -9.1	-20.3 to -14.3
RV change (km s^{-1})	1.5	53.8	1.5	18.3	14.4	6.0

- Shell classification: shell
- Do shell features move with the star?: N/A
- Notes on emission and absorption features: Both hydrogen lines show strong central absorption. He I λ6678 is weak due to the cool temperature and emission filling it in.
- Other notes: This star is also plotted in Figure 7.5

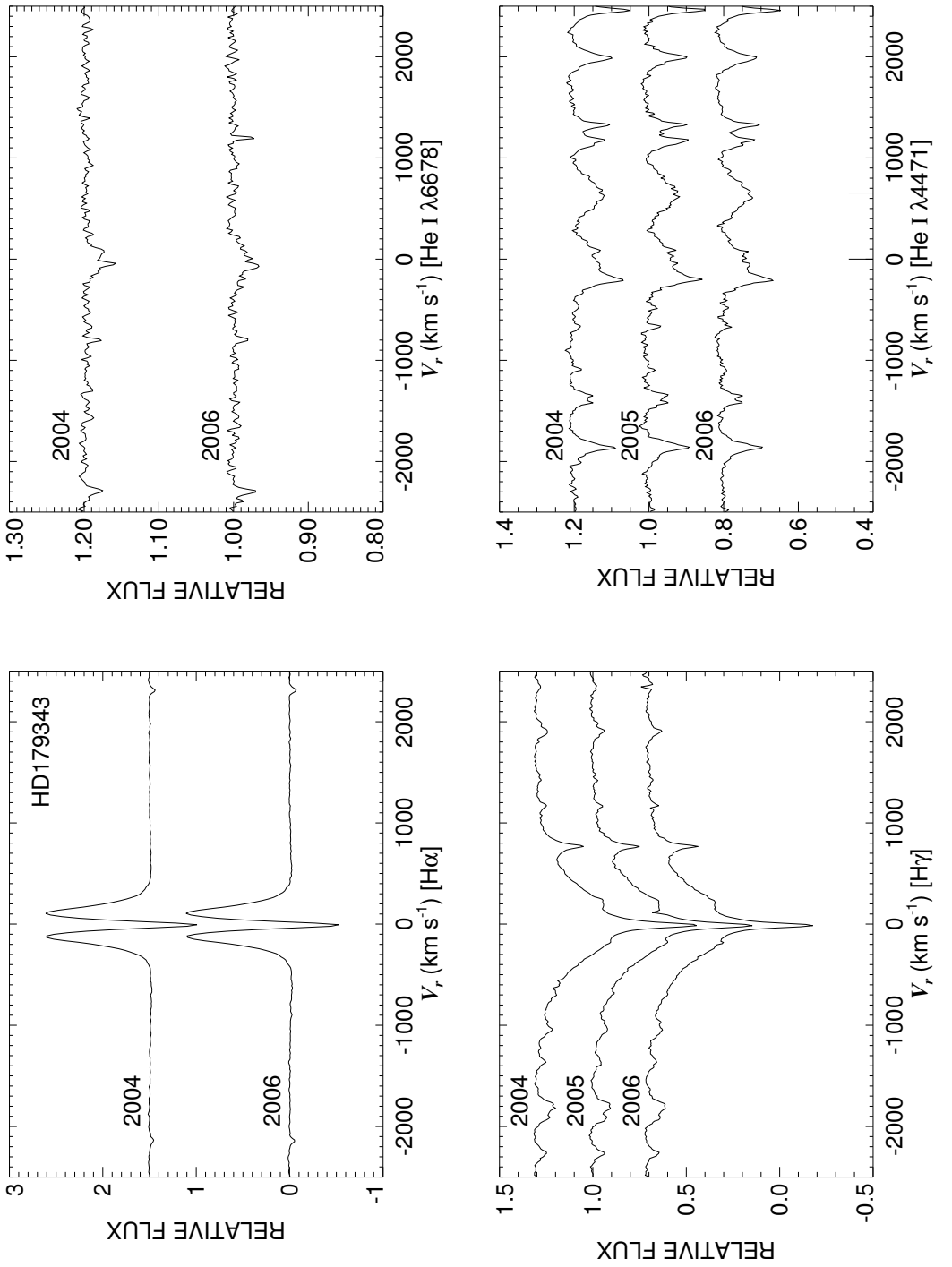

Figure C.80: A quadruple plot of HD179343 as described in §7.2.3 and Figure 7.6.

HD181409

NOT Be Star

- Other Names: HR 7335
- Spectral Type: B2 IVe
- V magnitude: 6.38
- In WDS?: no
- Known spectroscopic binary?: no
- Velocity variations seen in these data?: no

	Hα	He I λ6678	Hγ	He I λ4471	Mg II λ4481	Fe II ccfs
Mean RV (km s^{-1})	27.2	35.7	75.3	-2.4	2.4	···
RV range (km s^{-1})	22.9 to 32.7	32.5 to 38.9	64.9 to 78.7	-8.2 to 1.8	-1.3 to 7.6	···
RV change (km s^{-1})	9.8	6.4	13.8	10.0	8.9	···

- Notes on emission and absorption features: no emission
- Other notes: The original source of the emission classification is the Bright Star Catalogue but emission has not been seen since.

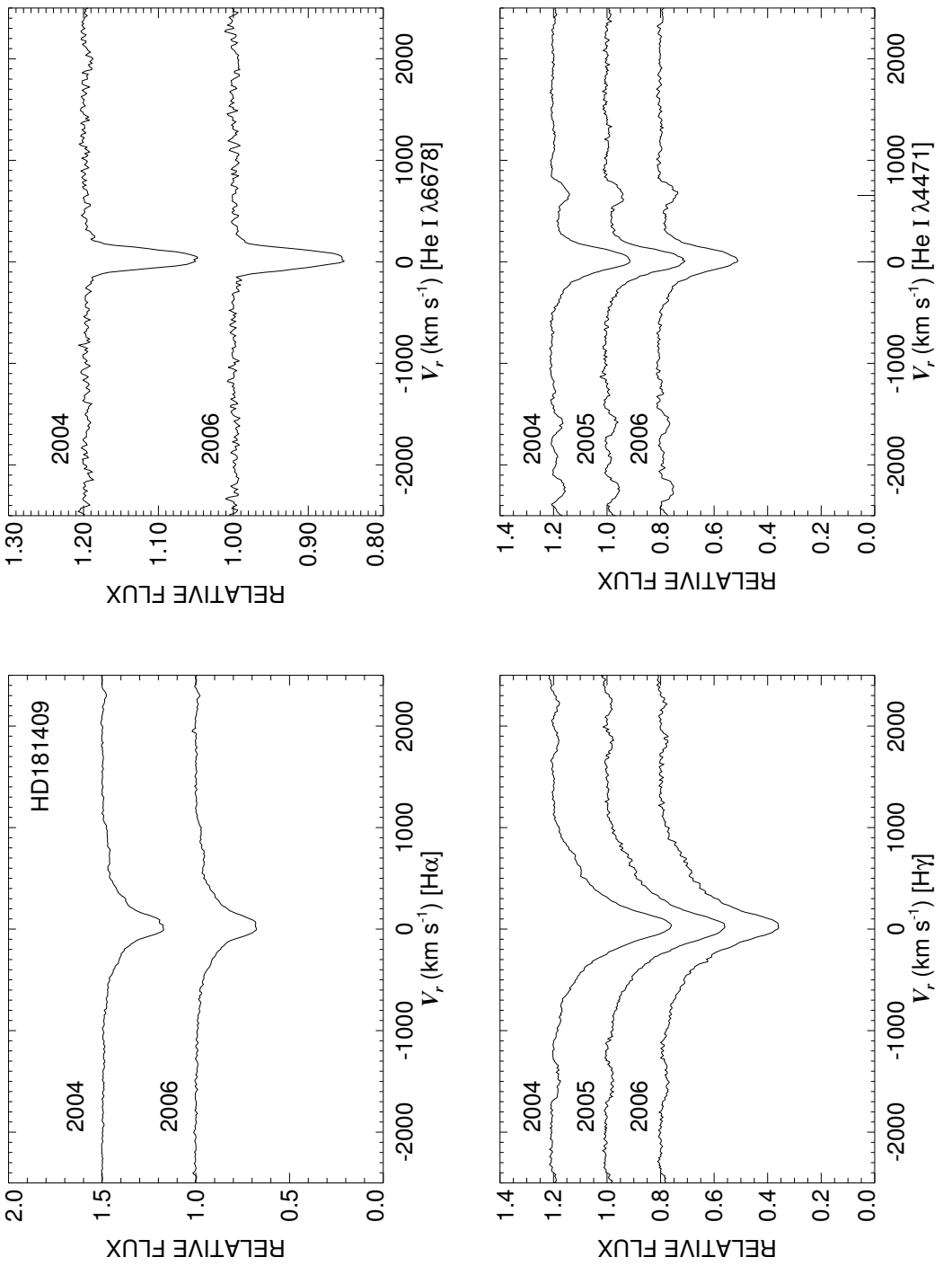

Figure C.81: A quadruple plot of HD181409 as described in §7.2.3 and Figure 7.6.

HD181615

Interacting Binary

- Other Names: HR 7342, υ Sgr
- Spectral Type: B2 Vpe
- V magnitude: 4.64
- In WDS?: no

  Known binary?: yes - this system seems to be similar to RY Scuti and Koubský et al. (2006) found a period of 137.9343 d in a very careful study
- Velocity variations seen in these data?: yes

	Hα	He I λ6678	Hγ	He I λ4471	Mg II λ4481	Fe II ccfs
Mean RV (km s^{-1})	···	-2.1	···	-20.5	-25.7	-138.9
RV range (km s^{-1})	···	-9.0 to 3.4	···	···	···	···
RV change (km s^{-1})	···	12.4	···	···	···	···

- Shell classification: shell (but it is photospheric)
- Do shell features move with the star?: unknown
- Notes on emission and absorption features: dominated by the hydrogen-deficient supergiant companion
- Other notes: This star was omitted from survey statistics in Chapter 7 as it is an interacting binary, not a classical Be star.

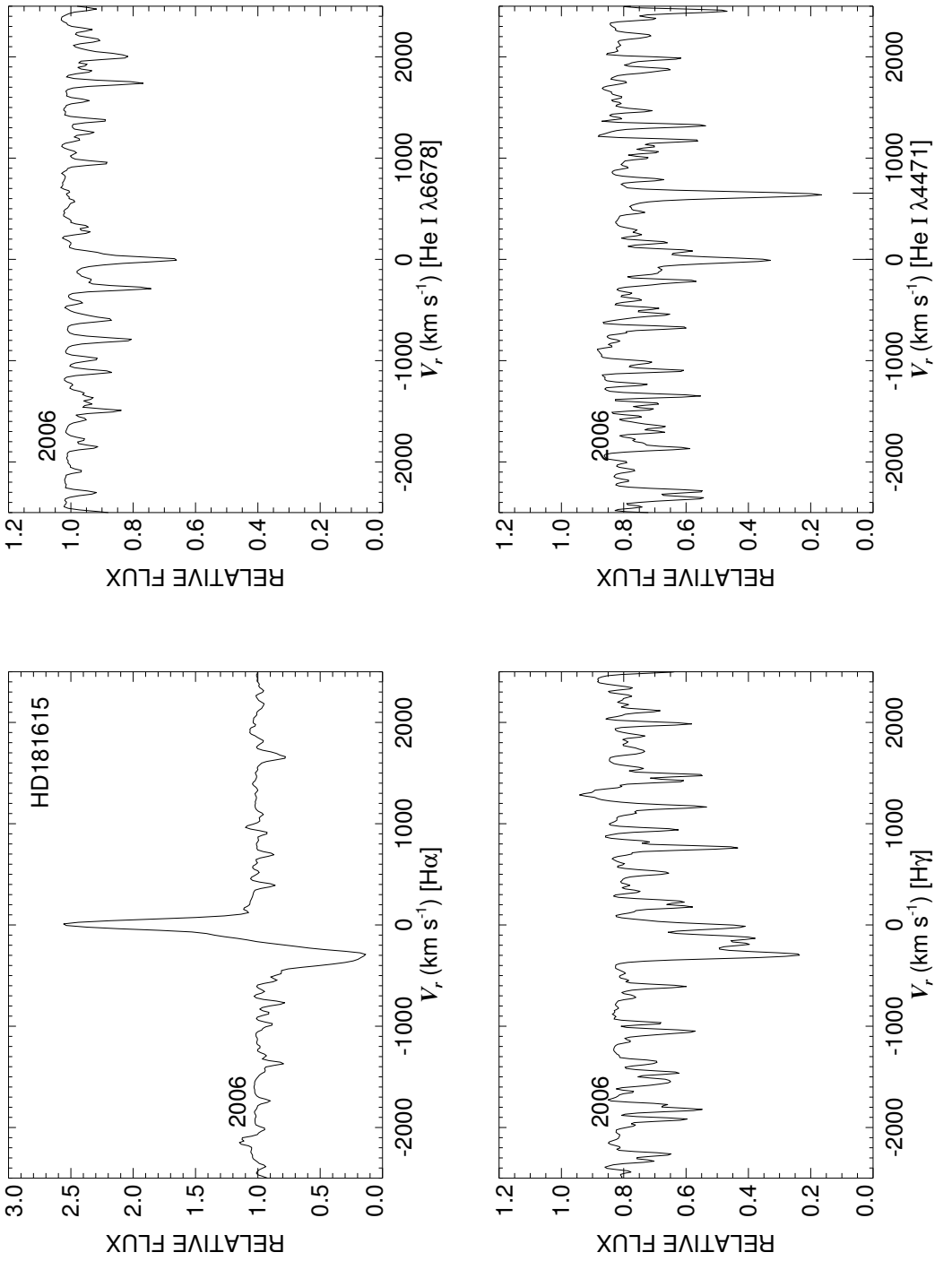

Figure C.82: A quadruple plot of HD181615 as described in §7.2.3 and Figure 7.6.

HD183362

Classical Be Star

- Other Names: HR 7403, V558 Lyr
- Spectral Type: B3 Ve+sh
- V magnitude: 6.17
- In WDS?: no
- Known spectroscopic binary?: no
- Velocity variations seen in these data?: possibly

	Hα	He I λ6678	Hγ	He I λ4471	Mg II λ4481	Fe II ccfs
Mean RV (km s^{-1})	-20.4	-22.9	-39.9	-33.7	-41.0	-24.0
RV range (km s^{-1})	-23.8 to -16.2	-48.0 to -5.5	-46.2 to -35.1	-37.8 to -30.5	-52.8 to -33.9	-30.0 to -20.1
RV change (km s^{-1})	7.6	42.5	11.1	7.3	18.9	9.9

- Shell classification: emission shell
- Do shell features move with the star?: if it moves, then yes
- Notes on emission and absorption features: The hydrogen lines show slight morphological changes and Hα strength increases from 2004 to 2006 while the emission in Hγ gets slightly smaller. He I λ6678 develops emission horns in 2006.
- Other notes: This star is also plotted in Figure 7.4.

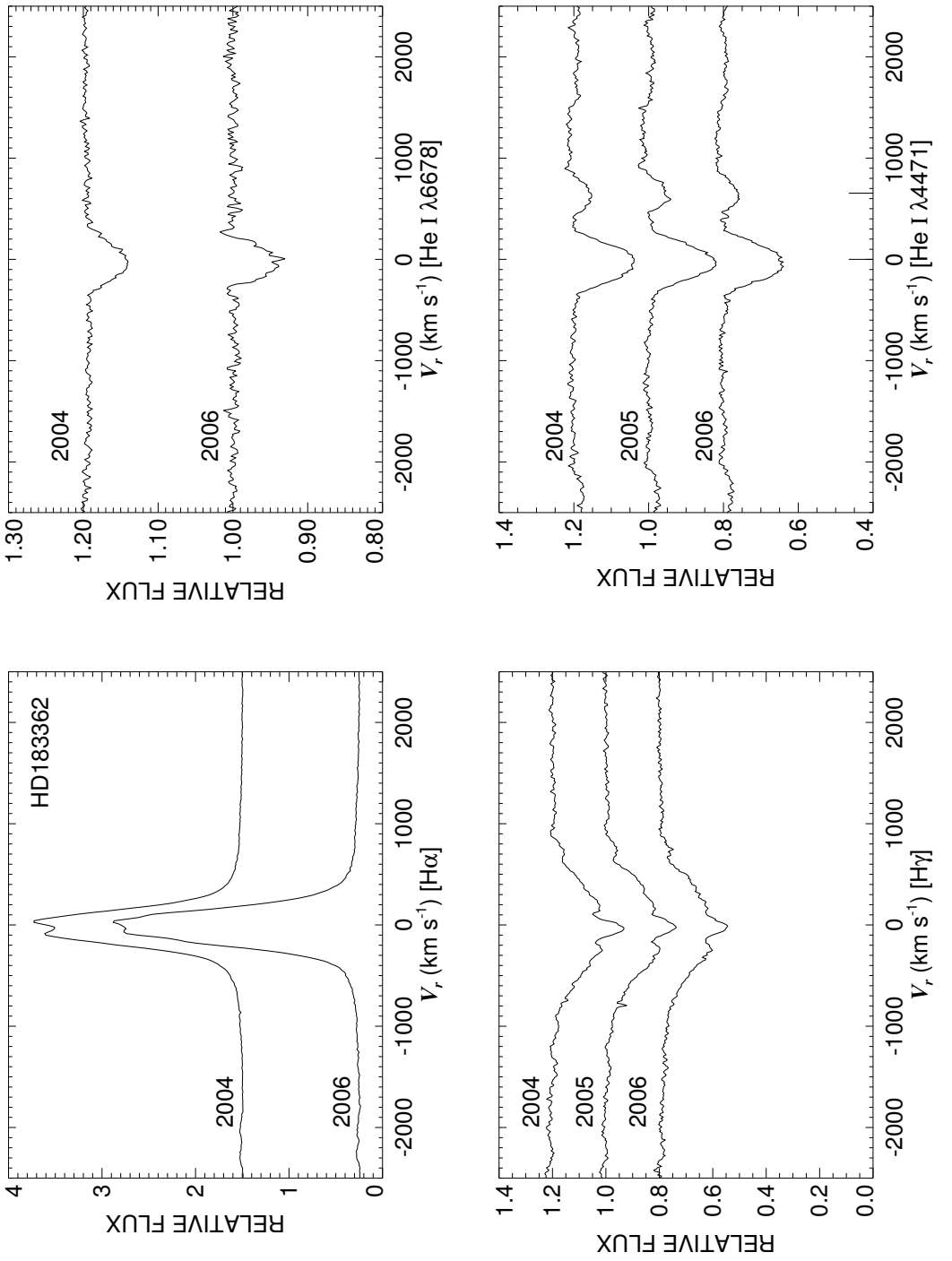

Figure C.83: A quadruple plot of HD183362 as described in §7.2.3 and Figure 7.6.

HD183656

Classical Be Star; Shell Star

- Other Names: HR 7415, V923 Aql
- Spectral Type: B6 Ve+sh
- V magnitude: 6.06
- In WDS?: no
- Known spectroscopic binary?: yes - Koubsky et al. (1989) found a period of 214.74 d
- Velocity variations seen in these data?: yes (see Fig. C.85)

	Hα	He I λ6678	Hγ	He I λ4471	Mg II λ4481	Fe II ccfs
Mean RV (km s^{-1})	-19.5	-20.2	-16.2	-52.4	-24.7	-27.8
RV range (km s^{-1})	-29.2 to -7.3	-35.7 to -6.8	-21.9 to -3.3	-62.5 to -45.0	-29.5 to -14.1	-56.4 to 18.0
RV change (km s^{-1})	21.9	28.9	18.6	17.5	15.4	74.4

- Shell classification: shell
- Do shell features move with the star?: yes
- Notes on emission and absorption features: Hα has a deep central self-absorption, the emission peaks switch, and the emission decreases slightly in strength in 2006. Shell features are visible throughout the spectra and "contaminate" the lines
- Other notes: Koubsky et al. (1989) performed a study of 60 years of data and find it very similar to HD037202 (ζ Tau). They also hypothesize it is an interacting binary.

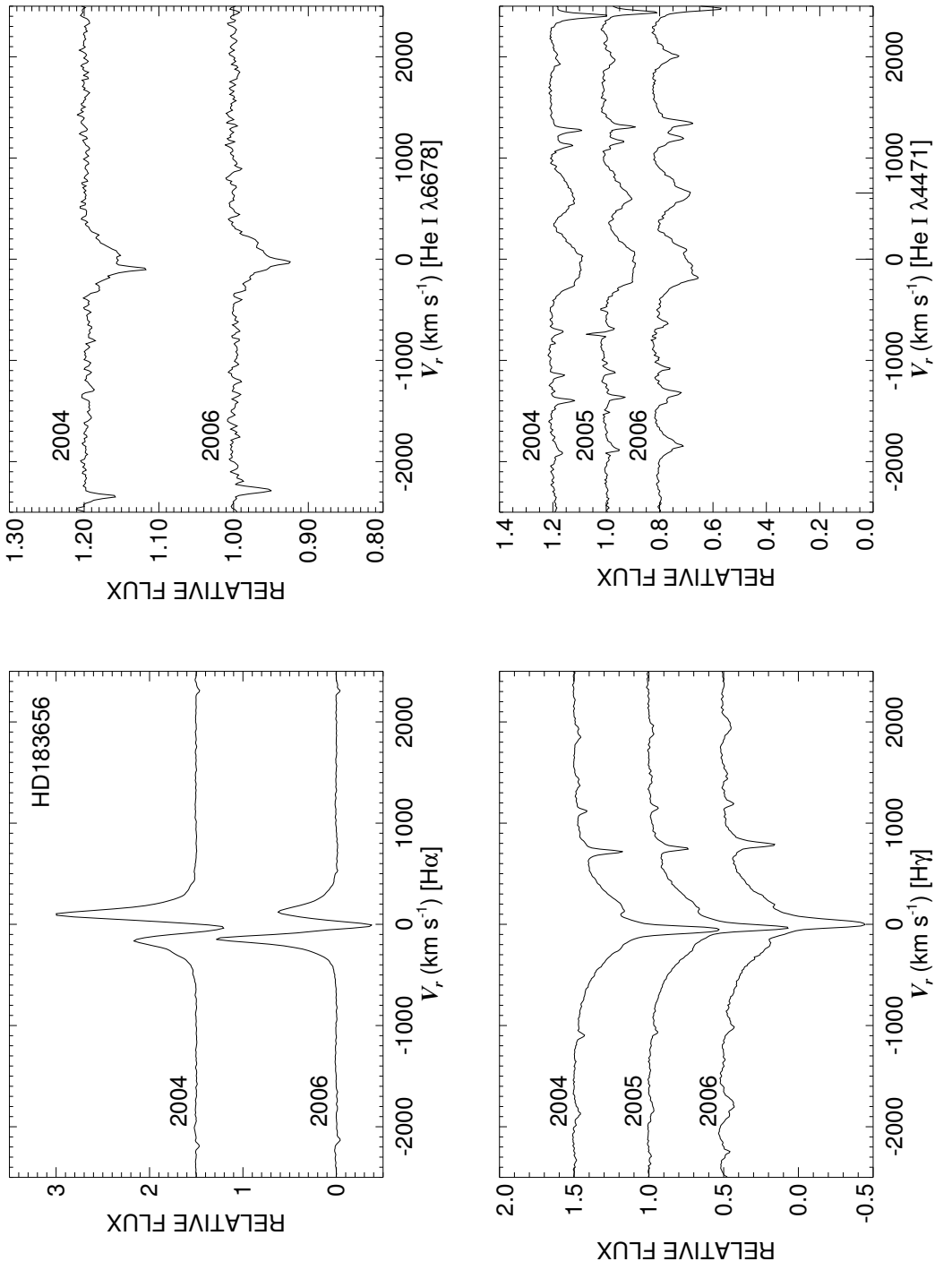

Figure C.84: A quadruple plot of HD183656 as described in §7.2.3 and Figure 7.6.

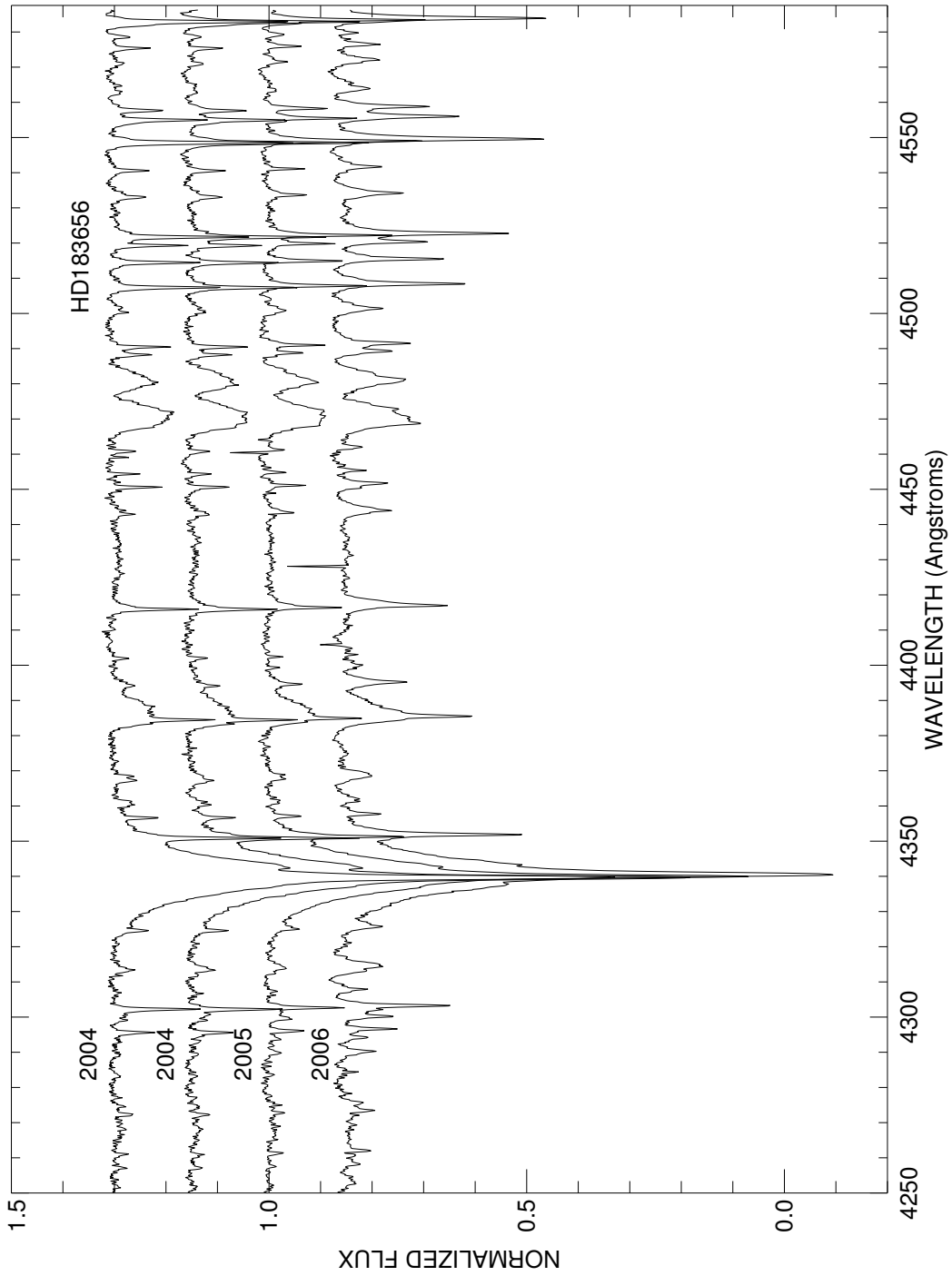

Figure C.85: A plot of all spectra of HD183656 in the blue region. Each is labeled with the year of observation and they are offset for clarity.

HD183914

Classical Be Star

- Other Names: HR 7418, 6 Cyg
- Spectral Type: B8 Ve
- V magnitude: 5.02
- In WDS?: no
- Known spectroscopic binary?: no
- Velocity variations seen in these data?: no

	Hα	He I λ6678	Hγ	He I λ4471	Mg II λ4481	Fe II ccfs
Mean RV (km s^{-1})	-18.8	1.8	-23.9	-10.1	-26.8	···
RV range (km s^{-1})	-20.2 to -16.5	···	-25.3 to -21.8	-16.5 to -5.6	-33.6 to -20.7	···
RV change (km s^{-1})	3.7	···	3.5	10.9	12.9	···

- Shell classification: normal
- Notes on emission and absorption features: He I λ6678 is extremely filled in (besides being weak due to coolness of the star).
- Other notes:

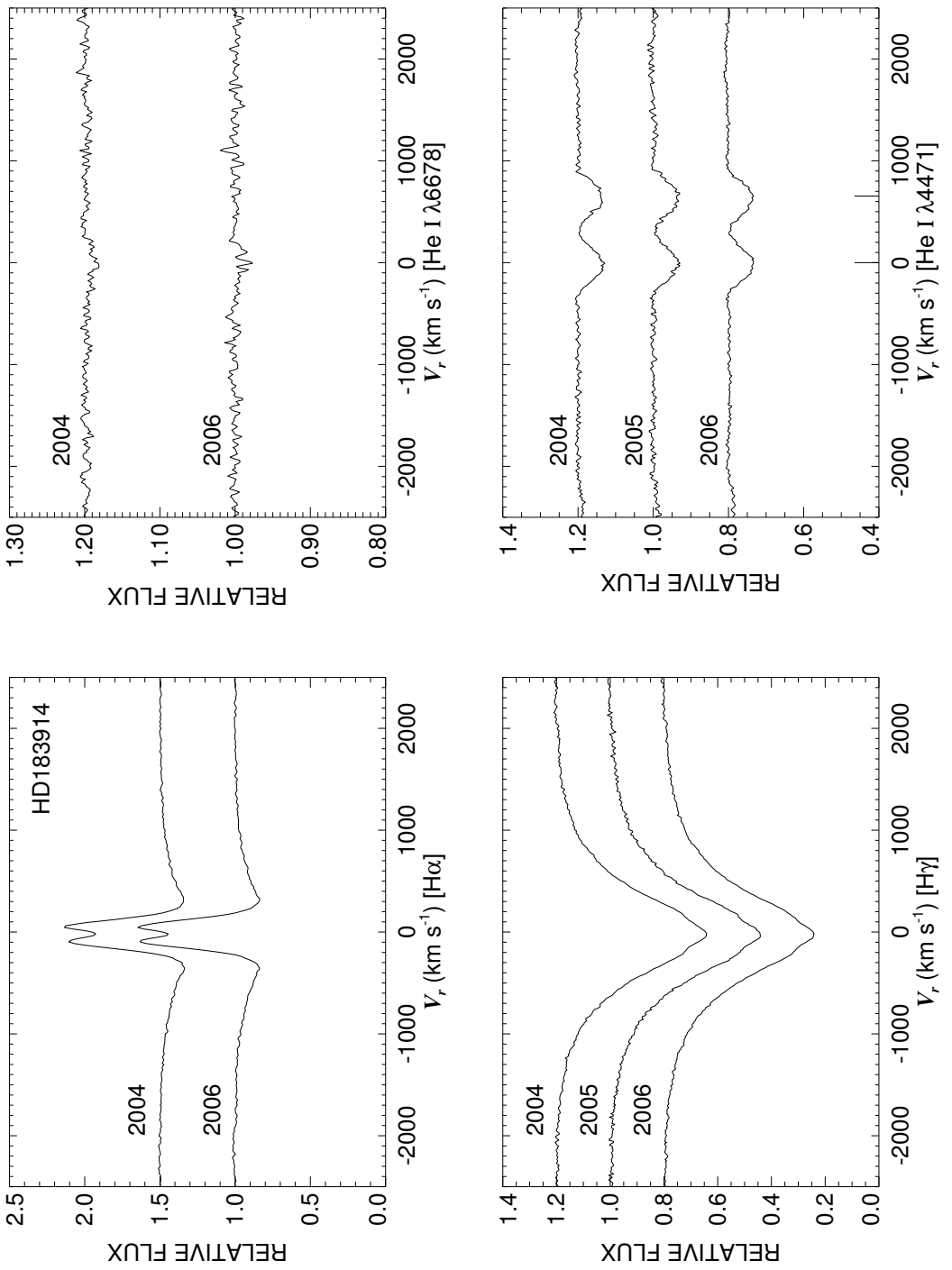

Figure C.86: A quadruple plot of HD183914 as described in §7.2.3 and Figure 7.6.

HD184279

Classical Be Star; Shell Star

- Other Names: V1294 Aql
- Spectral Type: B0.5 Ve+sh
- V magnitude: 6.98
- In WDS?: no
- Known spectroscopic binary?: no
- Velocity variations seen in these data?: yes (it's small)

	Hα	He I λ6678	Hγ	He I λ4471	Mg II λ4481	Fe II ccfs
Mean RV (km s^{-1})	-7.3	-18.6	65.8	-36.8	-60.8	-19.9
RV range (km s^{-1})	-9.6 to -4.8	-21.6 to -14.0	57.0 to 79.0	-40.0 to -34.3	-90.9 to -36.3	-23.1 to -16.6
RV change (km s^{-1})	4.8	7.6	22.0	5.7	54.6	6.5

- Shell classification: shell
- Do shell features move with the star?: yes
- Notes on emission and absorption features: Hα strength decreases markedly in 2006 and becomes distinctly double- peaked. Small emission surrounding the central Hγ absorption decreases from 2004 to 2006. He I λ6678 shows narrow shell absorption superposed on broad photospheric absorption.
- Other notes: This star is also plotted in Figure 7.5.

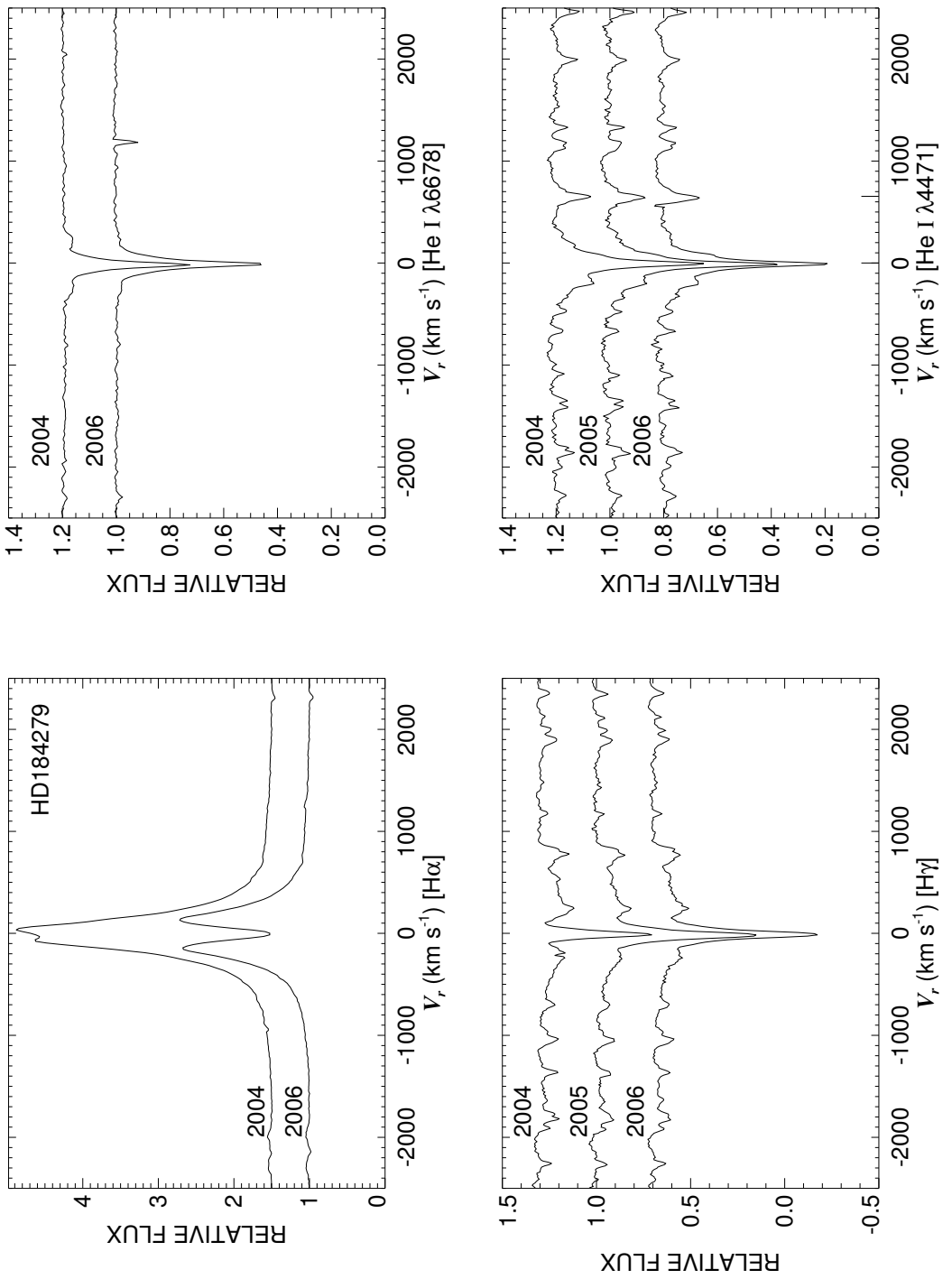

Figure C.87: A quadruple plot of HD184279 as described in §7.2.3 and Figure 7.6.

HD185037

Classical Be Star

- Other Names: HR 7457, 11 Cyg
- Spectral Type: B8 Vne
- V magnitude:
- In WDS?: no
- Known spectroscopic binary?: no
- Velocity variations seen in these data?: no

	Hα	He I λ6678	Hγ	He I λ4471	Mg II λ4481	Fe II ccfs
Mean RV (km s^{-1})	-19.8	9.4	-28.2	-7.9	-31.3	-9.1
RV range (km s^{-1})	-20.6 to -19.3	···	-30.6 to -25.9	-9.6 to -6.4	-39.9 to -23.9	-14.2 to -3.3
RV change (km s^{-1})	1.3	···	4.7	3.2	16.0	10.9

- Shell classification: squarish
- Do shell features move with the star?: N/A
- Notes on emission and absorption features: He I λ6678 is nearly completely filled in and weak (due to cool temperature).
- Other notes: This star is also plotted in Figure 7.3.

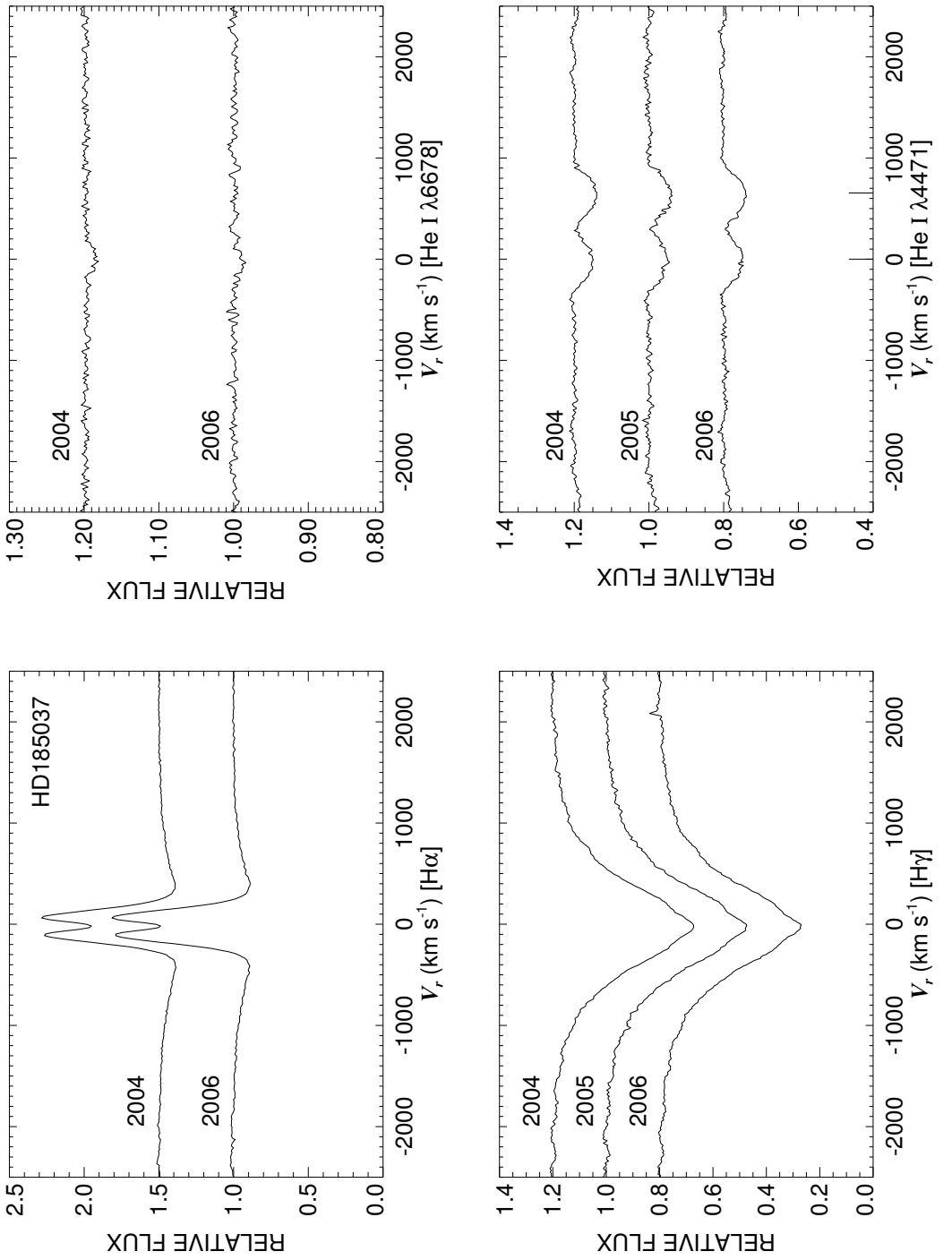

Figure C.88: A quadruple plot of HD185037 as described in §7.2.3 and Figure 7.6.

HD187567

Classical Be Star; Non-Radial Pulsator?

- Other Names: HR 7554, V1339 Aql
- Spectral Type: B2.5 IVe
- V magnitude: 6.39
- In WDS?: yes - a speckle companion of unlisted magnitude less than 0.1 arcsec away (discovered in 1985).
- Known spectroscopic binary?: yes - Harmanec (2001) reports a period of 1.2722 d
- Velocity variations seen in these data?: yes

	Hα	He I λ6678	Hγ	He I λ4471	Mg II λ4481	Fe II ccfs
Mean RV (km s^{-1})	-13.8	-36.7	-4.0	-23.8	-40.5	-23.0
RV range (km s^{-1})	-21.0 to -10.1	-55.4 to -6.9	-20.9 to 4.9	-32.0 to -15.5	-65.7 to -10.8	-40.5 to -3.5
RV change (km s^{-1})	10.9	48.5	25.8	16.5	54.9	37.0

- Shell classification: emission shell
- Do shell features move with the star?: yes
- Notes on emission and absorption features: Hα grows and the peaks switch. Hγ changes. Both He I λ6678 and Mg II λ4481 show emission horns on the right side (therefore affected RVs). He I λ4471 shows fast line profile variations that are indicative of either a close companion or NRP.
- Other notes:

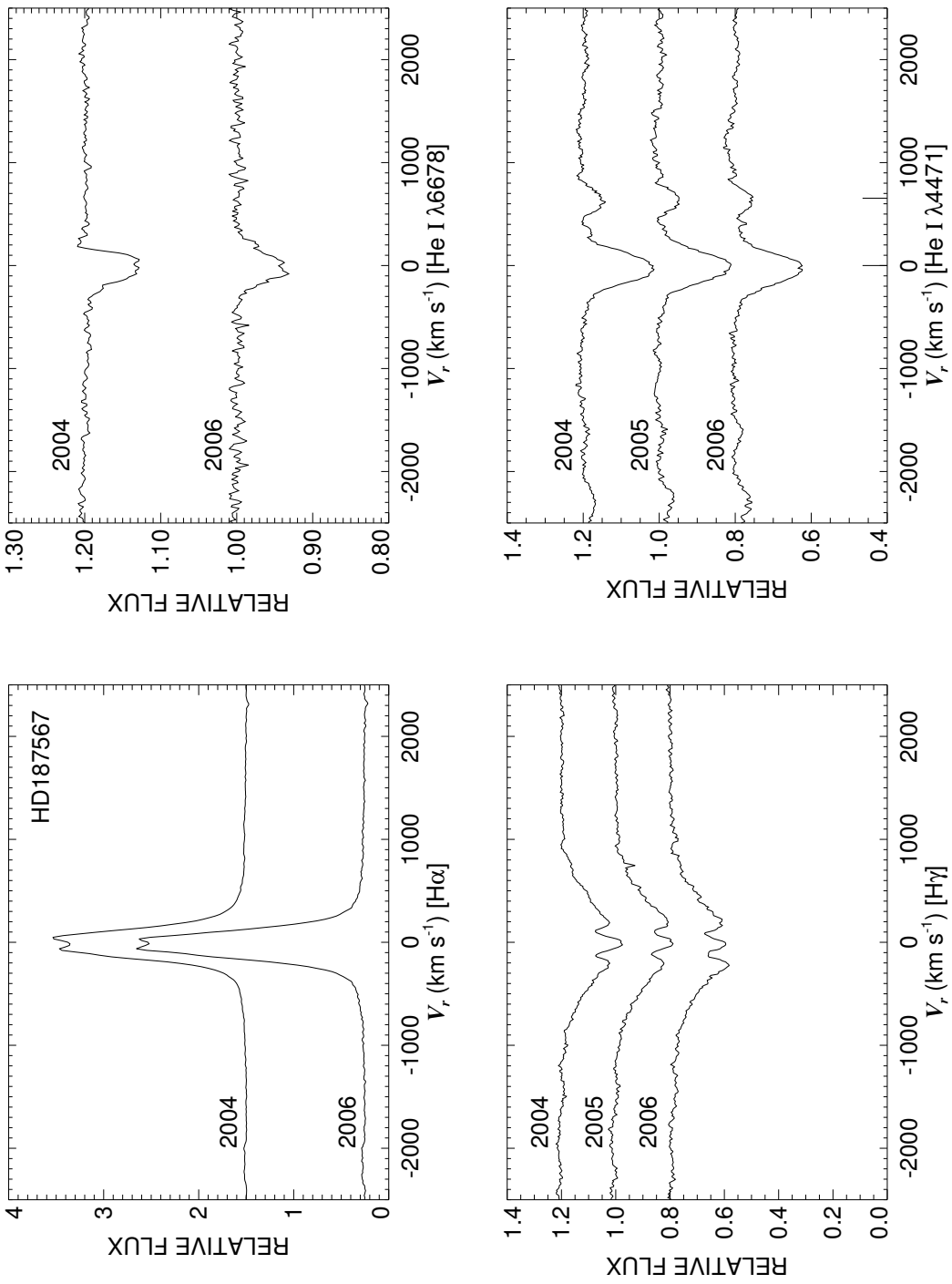

Figure C.89: A quadruple plot of HD187567 as described in §7.2.3 and Figure 7.6.

HD187811

Classical Be Star; Shell Star

- Other Names: HR 7565, 12 Vul
- Spectral Type: B2.5 Ve+sh
- V magnitude: 4.75
- In WDS?: no
- Known spectroscopic binary?: no
- Velocity variations seen in these data?: no

	Hα	He I λ6678	Hγ	He I λ4471	Mg II λ4481	Fe II ccfs
Mean RV (km s^{-1})	-19.9	-22.4	-13.9	-38.1	-42.0	···
RV range (km s^{-1})	-29.8 to -13.0	-24.9 to -19.4	-19.3 to -8.0	-40.1 to -35.5	-63.6 to -28.7	···
RV change (km s^{-1})	16.8	5.5	11.3	4.6	34.9	···

- Shell classification: has a very slight emission shell in 2004 then becomes normal (see Fig C.91)
- Do shell features move with the star?: N/A
- Notes on emission and absorption features: Hα emission strength decreases markedly in 2006. Emission horns in both He I λ6678 and Mg II λ4481 disappear after 2004. Hγ gains a little bit of emission in 2005 but has none in 2004 or 2006. The emission shell spectrum vanishes after 2004 as well.
- Other notes:

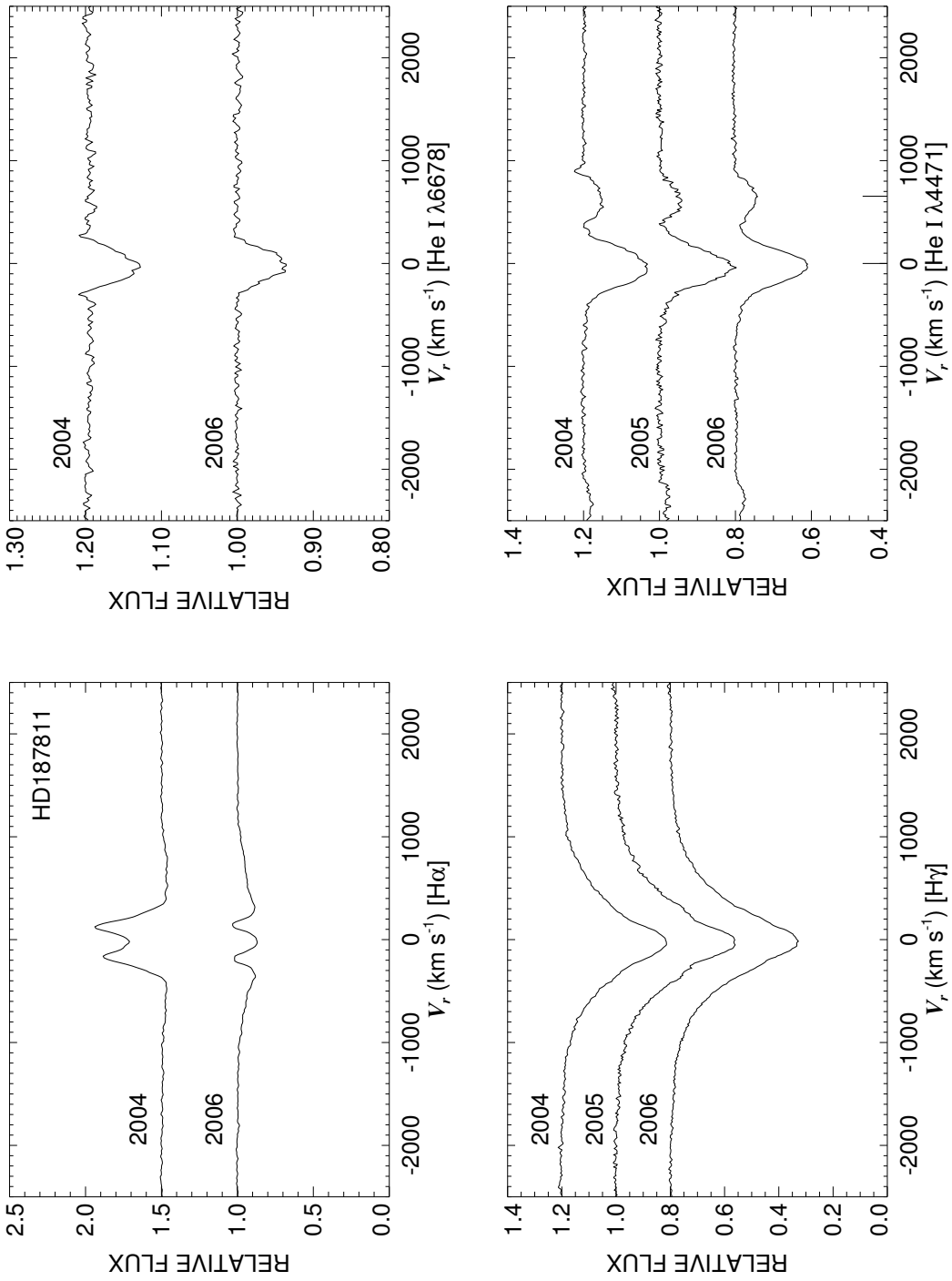

Figure C.90: A quadruple plot of HD187811 as described in §7.2.3 and Figure 7.6.

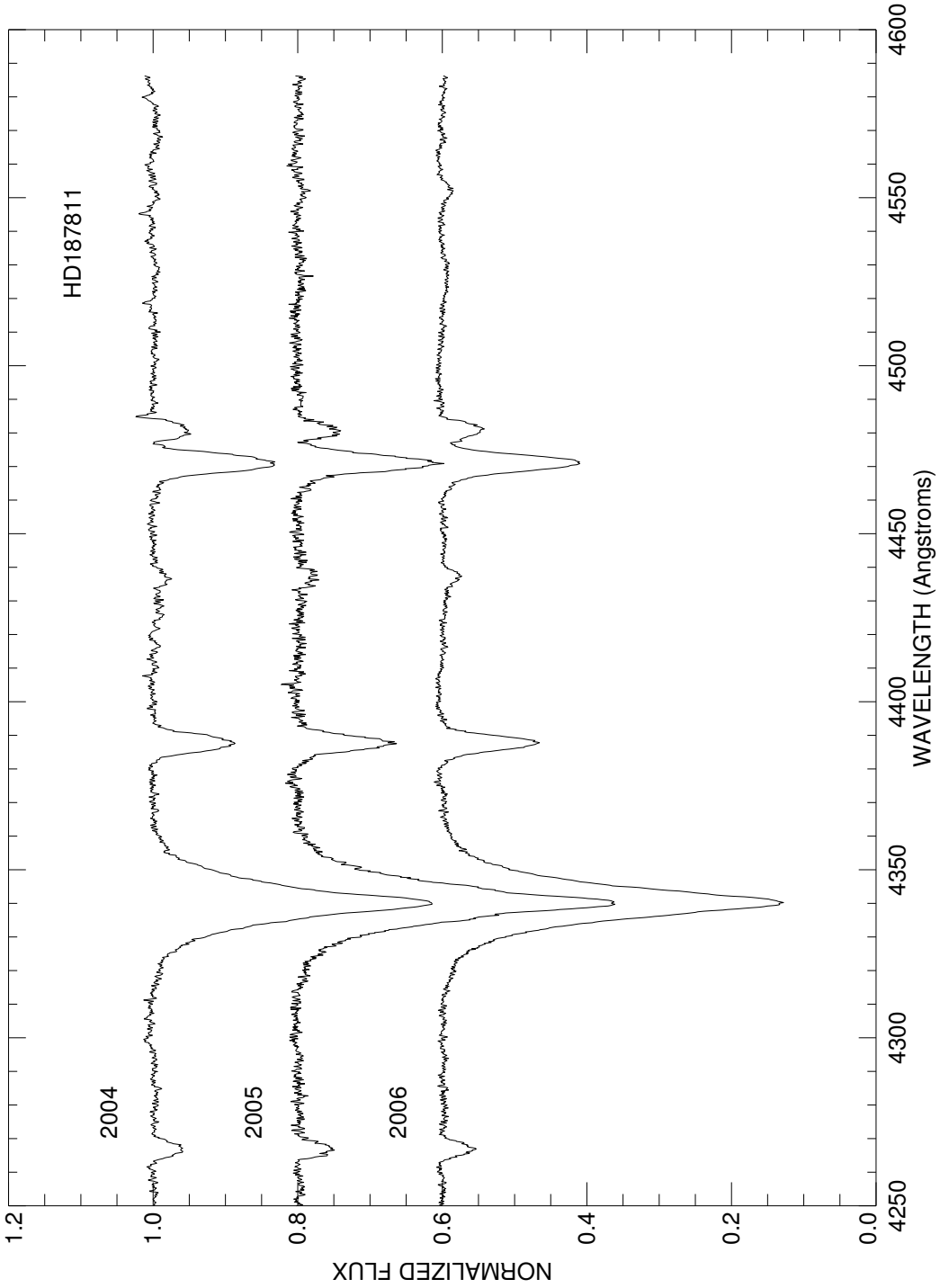

Figure C.91: A plot of the averages for each run in the blue region of HD187811. Each is labeled with the year of observation and they are offset from each other for clarity.

HD187851

Classical Be Star; Non-Radial Pulsator?

- Other Names: V396 Vul
- Spectral Type: B2 V
- V magnitude: 7.83
- In WDS?: yes - 10.4 mag companion 0.1 arcsec away (discovered in 1991)
- Known spectroscopic binary?: no
- Velocity variations seen in these data?: no

	Hα	He I λ6678	Hγ	He I λ4471	Mg II λ4481	Fe II ccfs
Mean RV (km s^{-1})	-18.1	-19.8	33.8	-16.6	-31.4	···
RV range (km s^{-1})	-37.5 to -0.4	-47.2 to -4.6	31.1 to 36.5	-22.3 to -9.1	-57.1 to -7.0	···
RV change (km s^{-1})	37.1	42.6	5.4	13.2	50.1	···

- Shell classification: normal
- Notes on emission and absorption features: Hα seems to have emission filling in the right side in 2004 and filling in both sides in 2006. He I λ6678 also shows emission filling in the right side. He I λ4471 may show evidence of NRP. Mg II λ4481 is very broad and shallow (therefor unreliable for RV studies).
- Other notes:

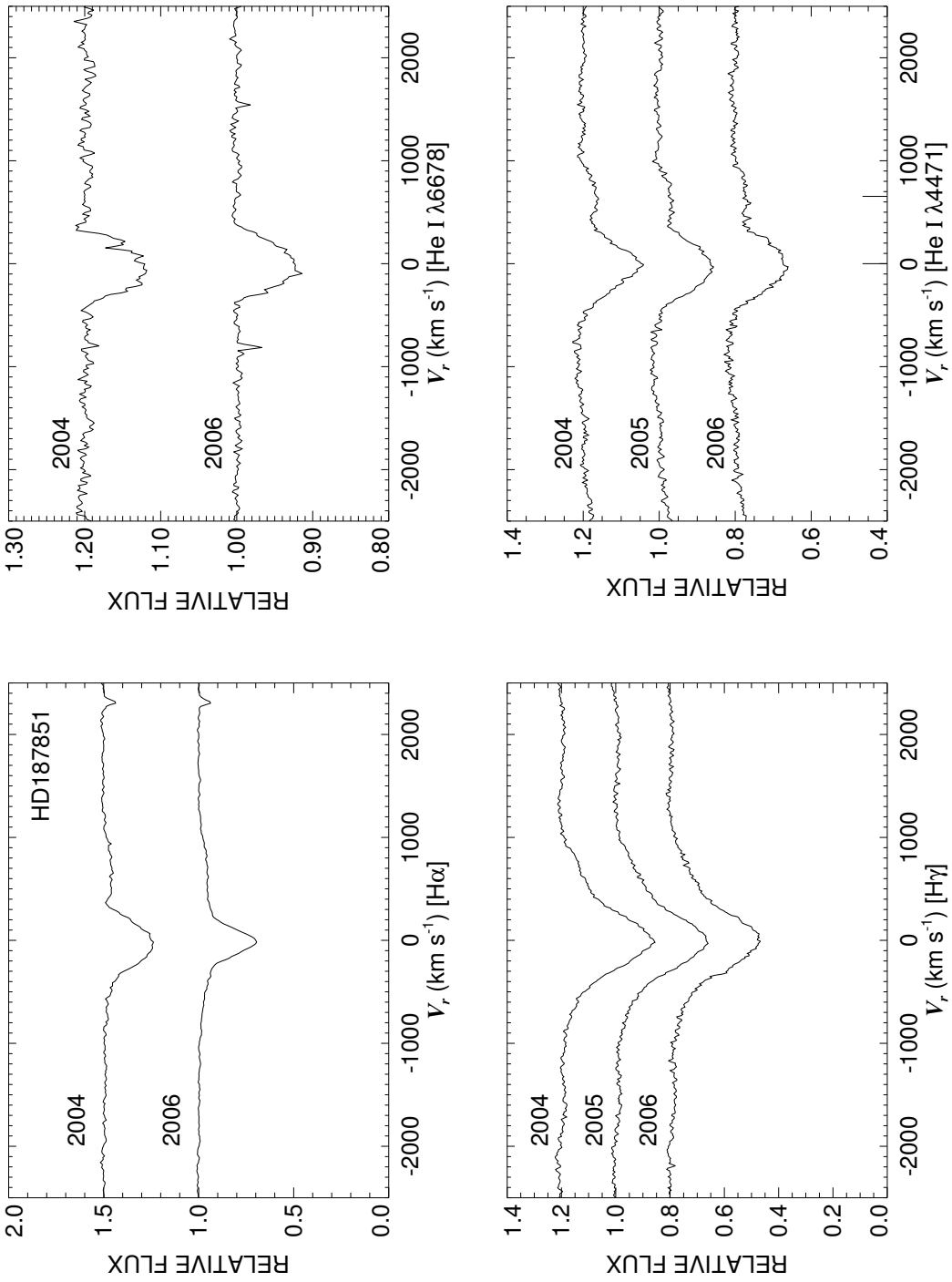

Figure C.92: A quadruple plot of HD187851 as described in §7.2.3 and Figure 7.6.

HD189687

Classical Be Star; Non-Radial Pulsator?

- Other Names: HR 7647, 25 Cyg, V1746 Cyg
- Spectral Type: B3 IVe
- V magnitude: 5.00
- In WDS?: no
- Known spectroscopic binary?: no
- Velocity variations seen in these data?: yes (see Fig. C.94)

	Hα	He I λ6678	Hγ	He I λ4471	Mg II λ4481	Fe II ccfs
Mean RV (km s^{-1})	-1.1	-6.9	3.6	-24.4	-17.8	···
RV range (km s^{-1})	-29.9 to 56.3	-19.4 to 1.3	-3.3 to 9.6	-31.8 to -15.9	-27.0 to -7.5	···
RV change (km s^{-1})	86.2	20.7	12.9	15.9	19.5	···

- Shell classification: normal
- Notes on emission and absorption features: Hα emission strength decreases, the peaks switch, and also has large RV variations (perhaps due to asymmetric disk structure?). The blue absorption lines all show line profile changes which may be indicative of NRP or a companion.
- Other notes:

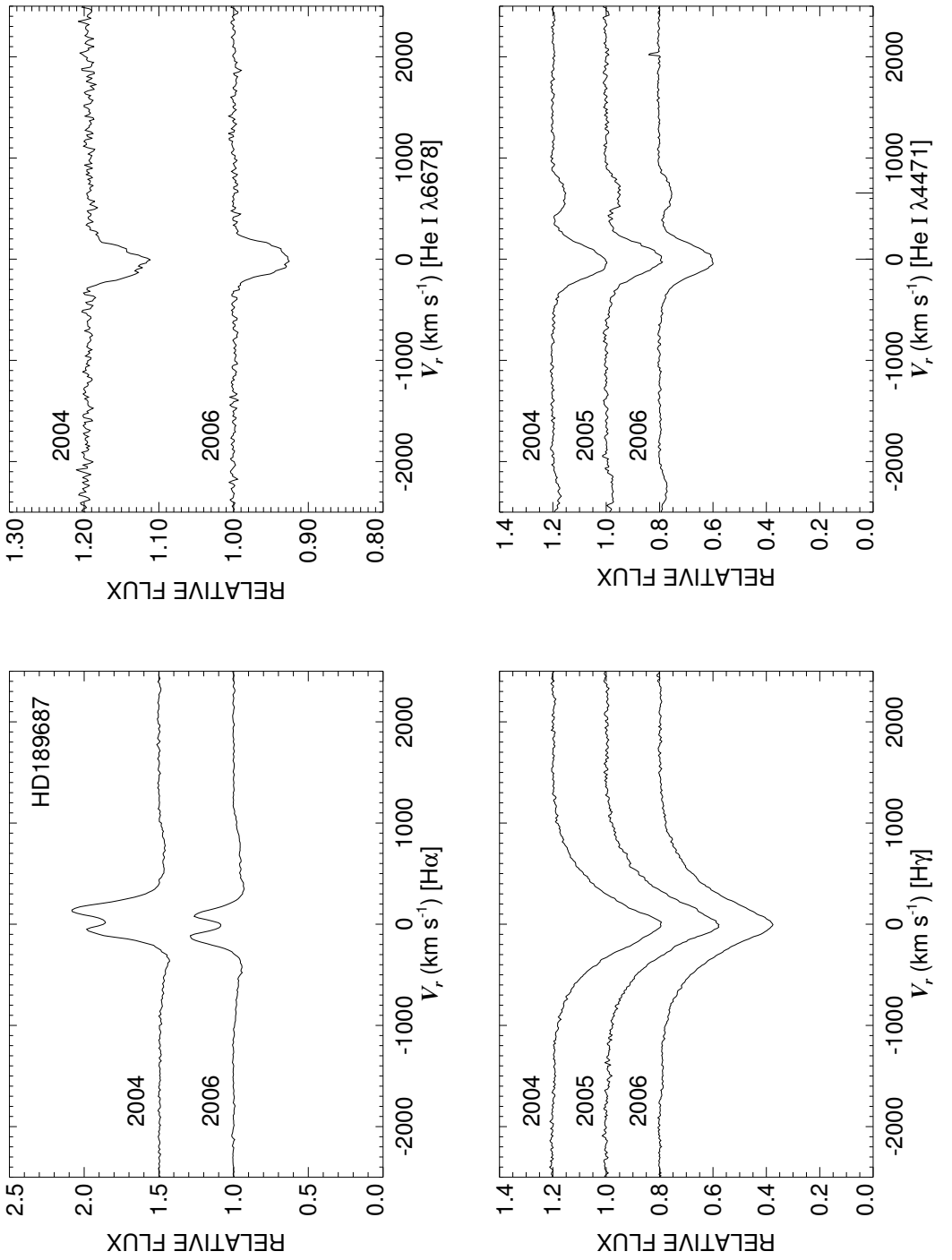

Figure C.93: A quadruple plot of HD189687 as described in §7.2.3 and Figure 7.6.

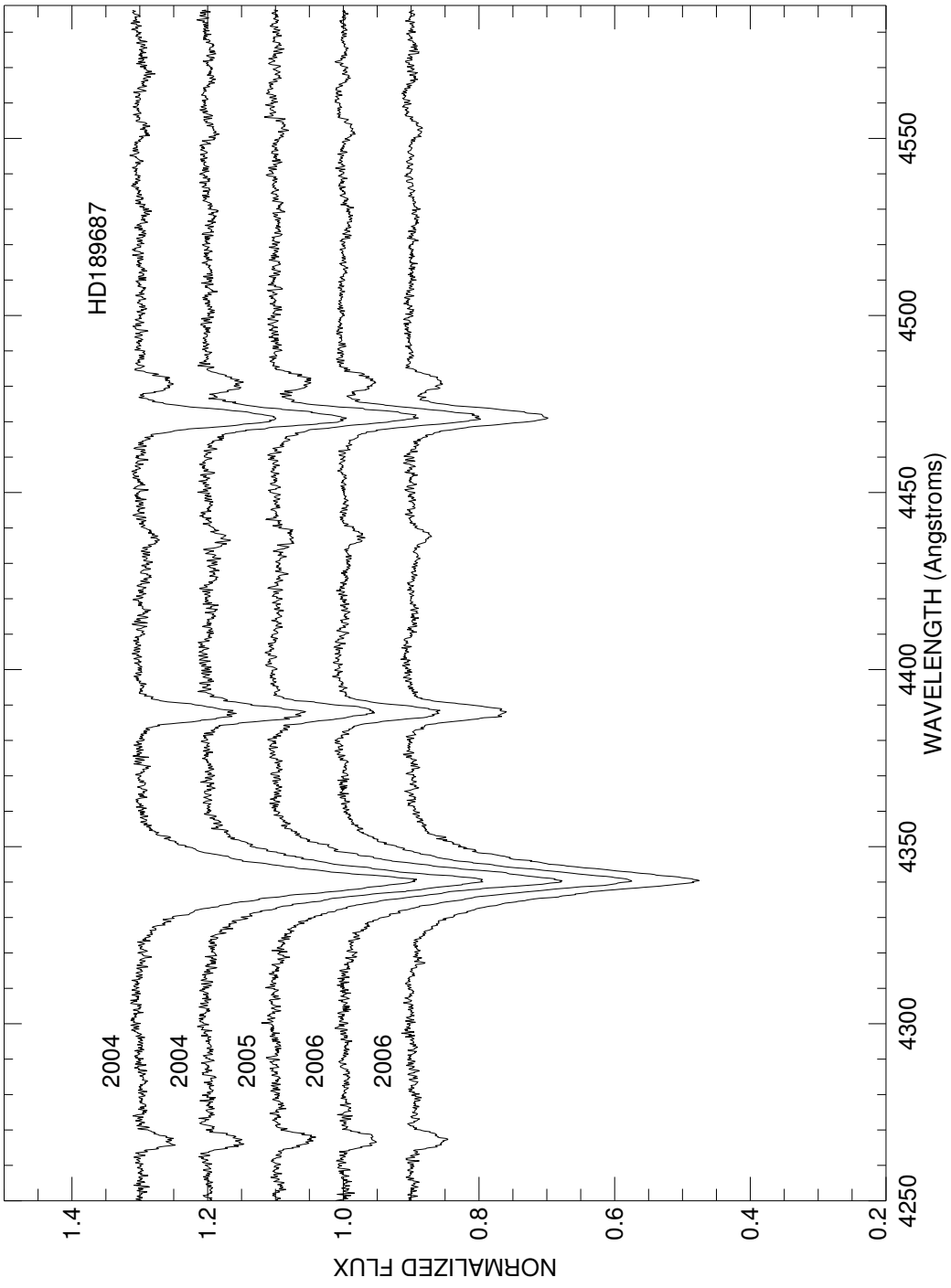

Figure C.94: A plot of all spectra of HD189687 in the blue region. Each is labeled with the year of observation and they are offset for clarity.

HD191610

Classical Be Star; Non-Radial Pulsator

- Other Names: HR 7708, 28 Cyg, V1624 Cyg
- Spectral Type: B3 IVe
- V magnitude: 4.79
- In WDS?: no
- Known spectroscopic binary?: no
- Velocity variations seen in these data?: no

	Hα	He I λ6678	Hγ	He I λ4471	Mg II λ4481	Fe II ccfs
Mean RV (km s^{-1})	-10.6	-25.2	1.8	-39.6	-37.2	···
RV range (km s^{-1})	-12.1 to -9.1	-47.9 to -13.4	-5.0 to 5.8	-46.4 to -31.7	-45.9 to -29.9	···
RV change (km s^{-1})	3.0	34.5	10.8	14.7	16.0	···

- Shell classification: normal
- Notes on emission and absorption features: Hα shows a marked decrease in 2006 and Hγ also shows a decrease in emission from 2004 to 2006. He I λ6678 shows a distinct emission horn on the right side and it disappears in 2006. The signature of NRP shows up in He I λ4471.
- Other notes: Rivinius et al. (2004) show the non-radial pulsations of this star (their Fig. 4) with a period of 0.64 d and this period was also found by Hahula & Gies (1994).

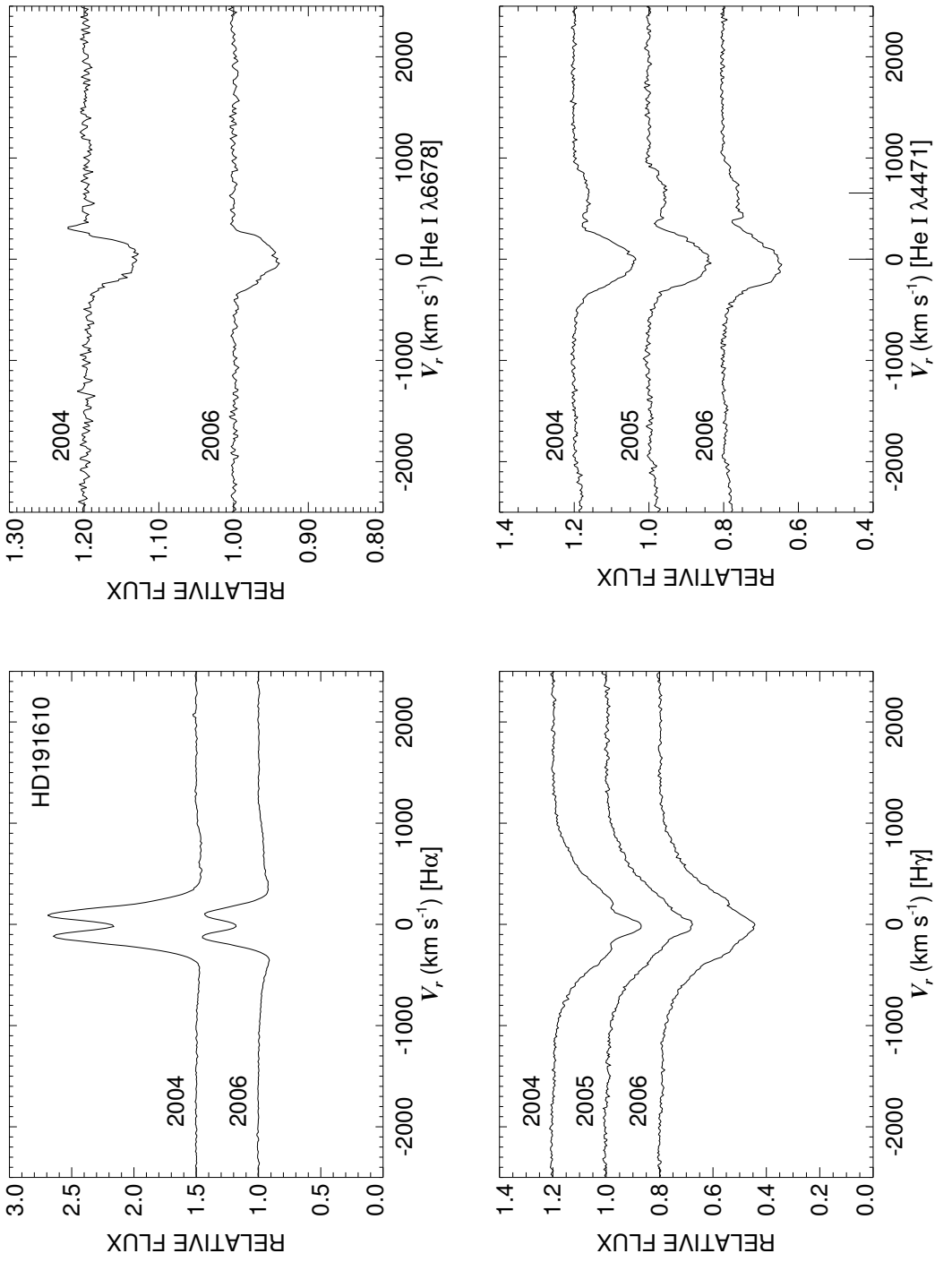

Figure C.95: A quadruple plot of HD191610 as described in §7.2.3 and Figure 7.6.

HD192044

Classical Be Star

- Other Names: HR 7719, 20 Vul
- Spectral Type: B7.5 Ve
- V magnitude: 5.79
- In WDS?: no
- Known spectroscopic binary?: no
- Velocity variations seen in these data?: unlikely

	Hα	He I λ6678	Hγ	He I λ4471	Mg II λ4481	Fe II ccfs
Mean RV (km s^{-1})	-21.6	-22.1	-36.8	-10.8	-27.8	-32.6
RV range (km s^{-1})	-22.0 to -21.3	-55.6 to 9.5	-39.8 to -33.7	-13.7 to -7.3	-33.6 to -24.9	-72.8 to -12.9
RV change (km s^{-1})	0.7	65.1	6.1	6.4	8.7	59.9

- Shell classification: weak emission shell
- Do shell features move with the star?: N/A
- Notes on emission and absorption features: He I λ6678 appears filled in on the right (as well as weak). Hγ shows changes.
- Other notes:

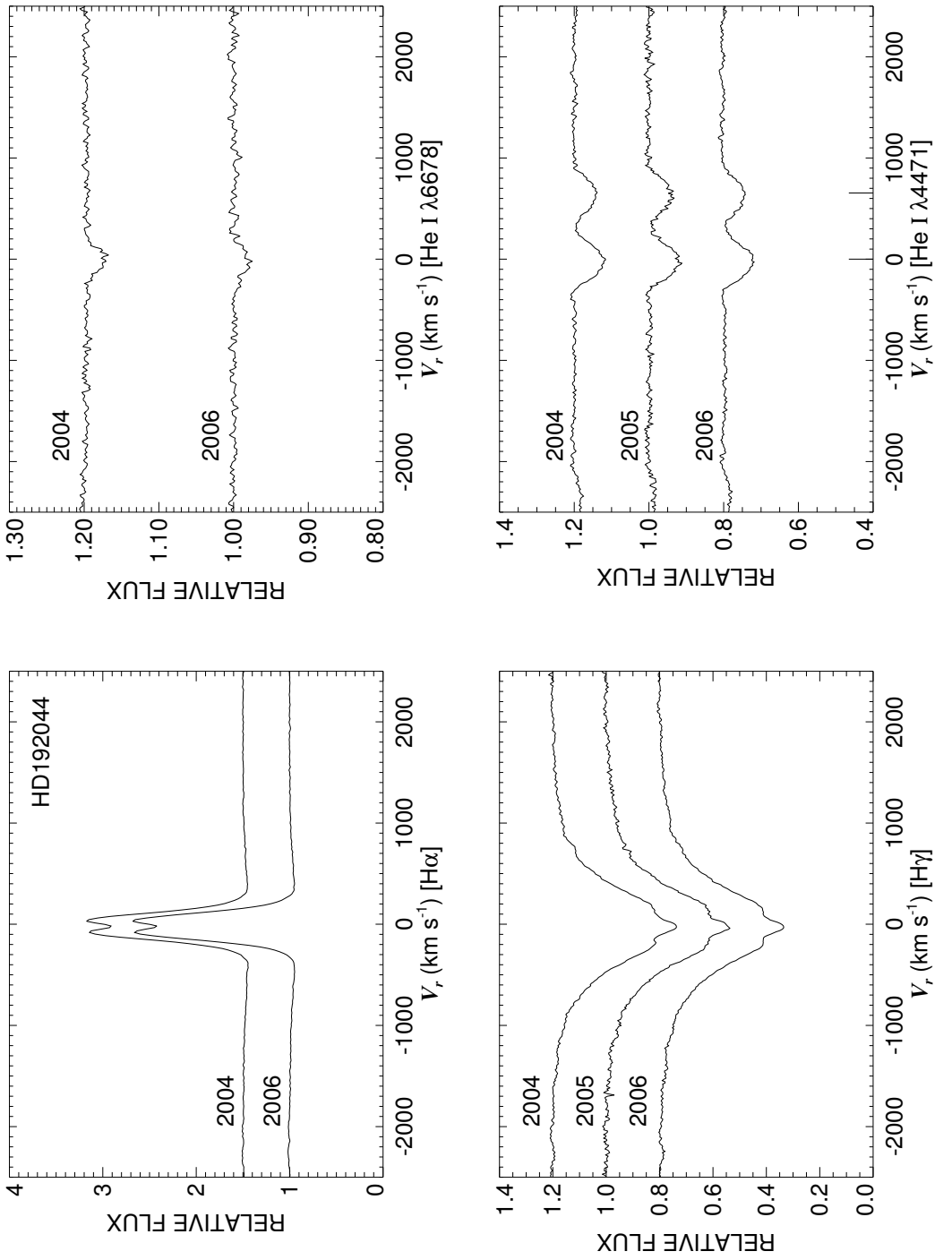

Figure C.96: A quadruple plot of HD192044 as described in §7.2.3 and Figure 7.6.

HD192445

Classical Be Star

- Other Names:
- Spectral Type: B2 Ve
- V magnitude:
- In WDS?: no
- Known spectroscopic binary?: no
- Velocity variations seen in these data?: yes (see Fig. C.98)

	Hα	He I λ6678	Hγ	He I λ4471	Mg II λ4481	Fe II ccfs
Mean RV (km s^{-1})	-17.8	-19.6	-11.1	-23.0	-76.0	48.3
RV range (km s^{-1})	-26.6 to -8.9	-25.7 to -8.5	-27.7 to -1.0	-25.7 to -20.0	-93.6 to -64.8	26.2 to 63.0
RV change (km s^{-1})	17.7	17.2	26.7	5.7	28.8	36.8

- Shell classification: emission shell
- Do shell features move with the star?: yes
- Notes on emission and absorption features: Huge Hα emission grows and merges into a single peak in 2006. Hγ shows changes (peaks switch and change size). Mg II λ4481 is very broad and therefore unreliable for RV studies. Examining Fig. C.98, the helium absorption line profiles change to one side or the other and the shell features shift in the same direction (therefore I suspect a spectroscopic binary rather than NRP).
- Other notes:

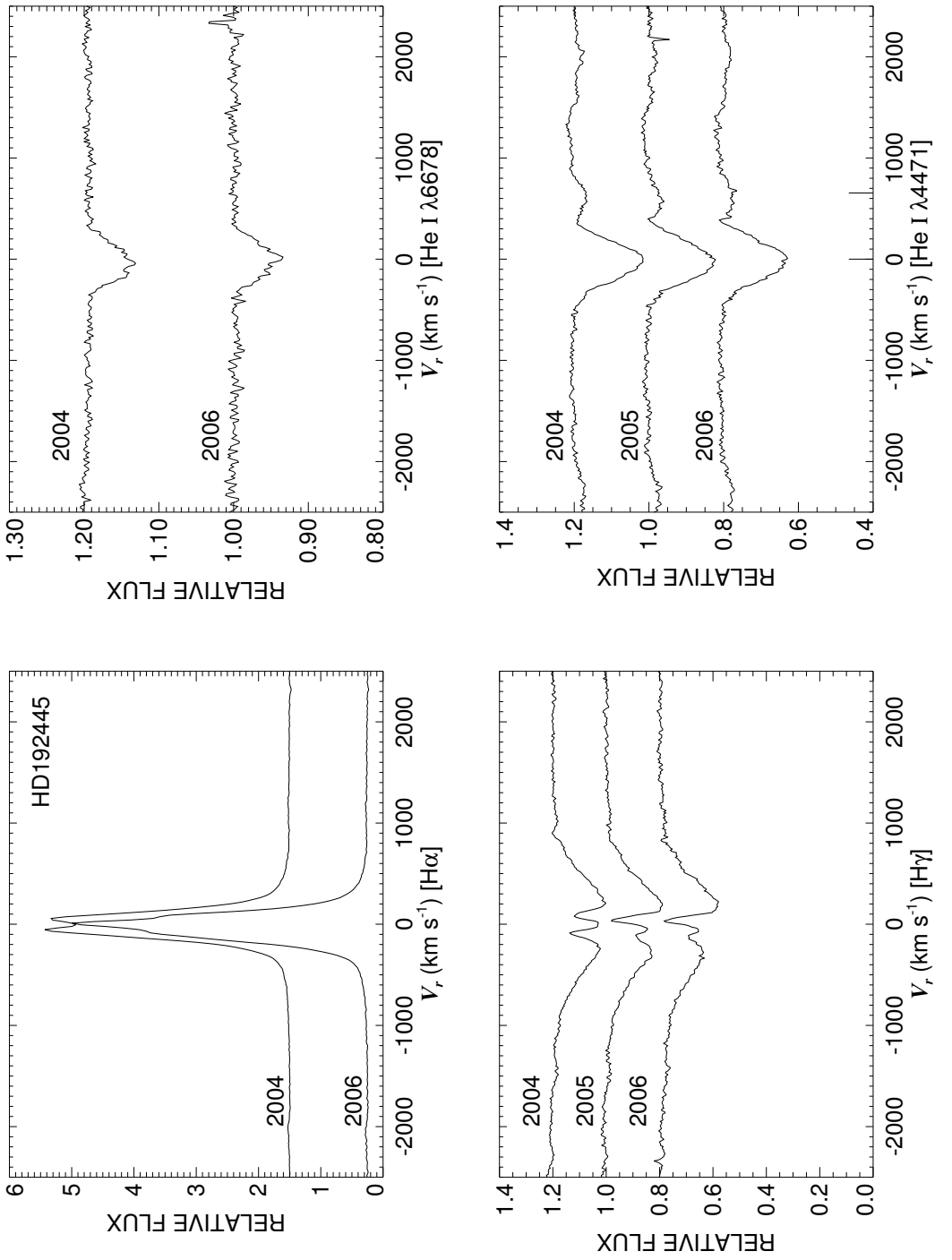

Figure C.97: A quadruple plot of HD192445 as described in §7.2.3 and Figure 7.6.

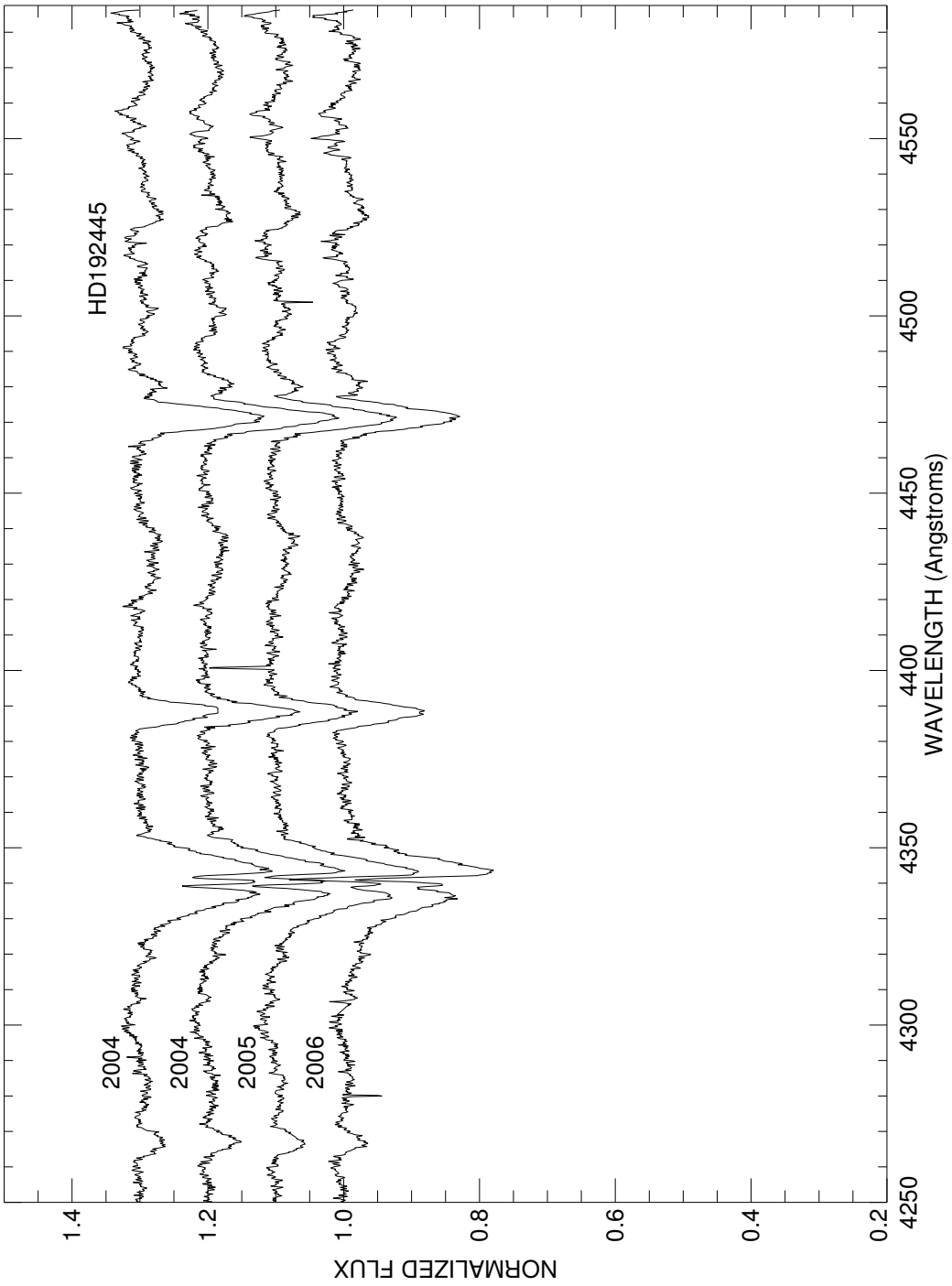

Figure C.98: A plot of all spectra of HD192445 in the blue region. Each is labeled with the year of observation and they are offset for clarity.

HD192685

Classical Be Star

- Other Names: HR 7739, QR Vul
- Spectral Type: B3 V
- V magnitude: 4.59
- In WDS?: yes - 7.55 and 9.7 mag companions 0.5 and 116 arcsec away (discovered in 1879 and 1912 respectively)
- Known spectroscopic binary?: no
- Velocity variations seen in these data?: unlikely

	Hα	He I λ6678	Hγ	He I λ4471	Mg II λ4481	Fe II ccfs
Mean RV (km s^{-1})	-8.2	-9.6	7.3	-19.6	-17.7	···
RV range (km s^{-1})	-10.8 to -5.1	-14.2 to -4.4	-4.1 to 11.8	-27.2 to -13.5	-24.8 to -12.6	···
RV change (km s^{-1})	5.7	9.8	15.9	13.7	12.2	···

- Shell classification: normal
- Notes on emission and absorption features: Nice appearance of Hα emission in 2006 (signifying disk building). Hγ shows some emission in 2005 but not 2004 or 2006. This may show there was an appearance of an inner Hγ-emitting disk and it propagated out to show Hα emission by 2006. Line profile changes in the helium and magnesium lines may signify NRP or that they are affected by the disk building.
- Other notes:

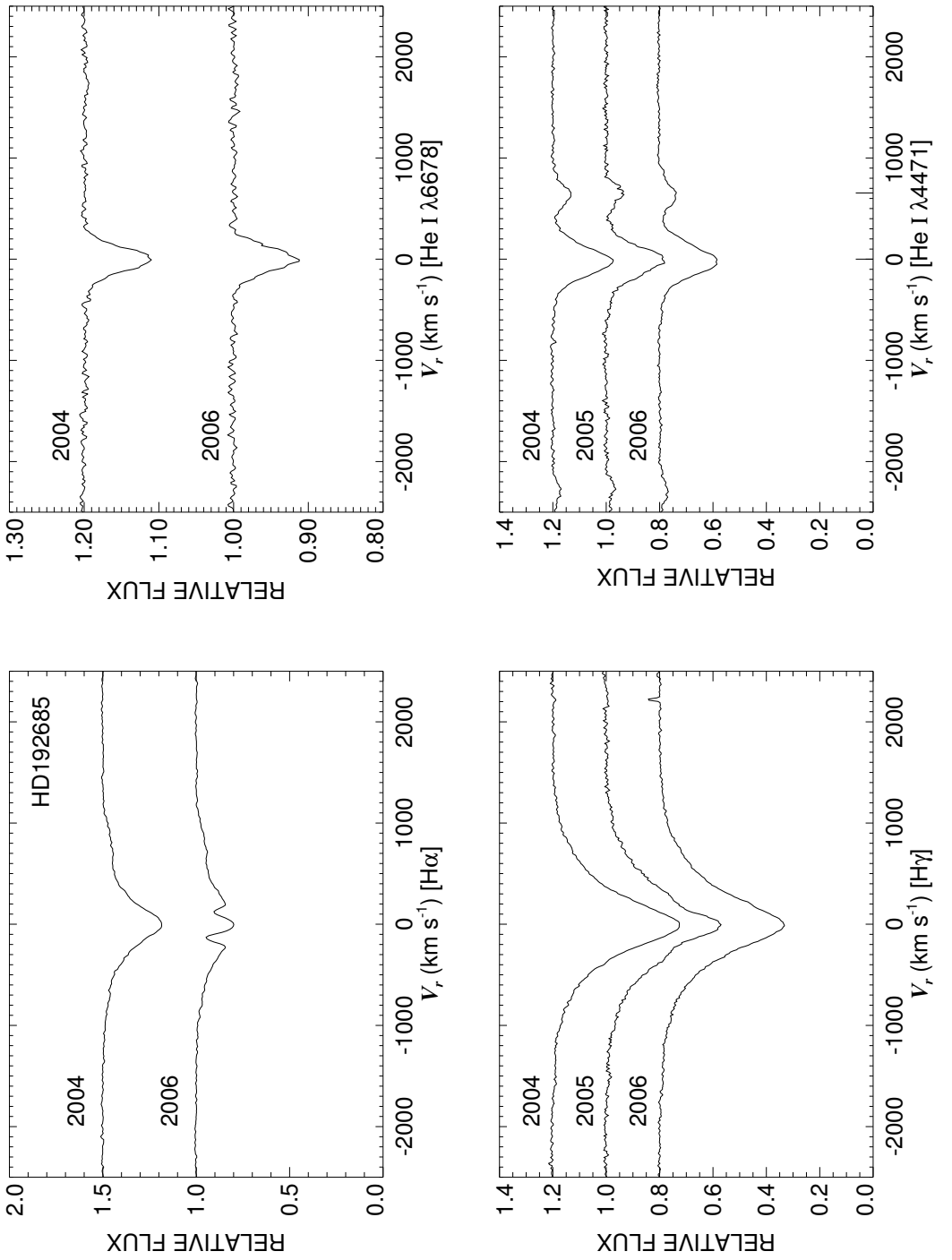

Figure C.99: A quadruple plot of HD192685 as described in §7.2.3 and Figure 7.6.

HD193009

Classical Be Star

- Other Names: V2113 Cyg
- Spectral Type: B1.5 Ve
- V magnitude: 7.25
- In WDS?: no
- Known spectroscopic binary?: no
- Velocity variations seen in these data?: yes (see Fig. C.101)

	Hα	He I λ6678	Hγ	He I λ4471	Mg II λ4481	Fe II ccfs
Mean RV (km s^{-1})	-8.7	18.7	17.8	-26.1	···	4.9
RV range (km s^{-1})	-16.1 to 0.5	-0.7 to 43.1	-14.5 to 54.7	-39.5 to -17.2	···	-22.9 to 41.6
RV change (km s^{-1})	16.6	43.8	69.2	22.3	···	64.5

- Shell classification: emission shell
- Do shell features move with the star?: yes
- Notes on emission and absorption features: Big Hα shows peak switching. He I λ6678 appears to have small emission horns. Hγ shows very fast peak switching (see the 2004 blue data) so the asymmetric disk seems to be rotating very quickly. Mg II λ4481 is shallow and blended. The absorption lines in the blue spectra show line profile changes and the emission shell spectrum shows shifts in the same direction.
- Other notes:

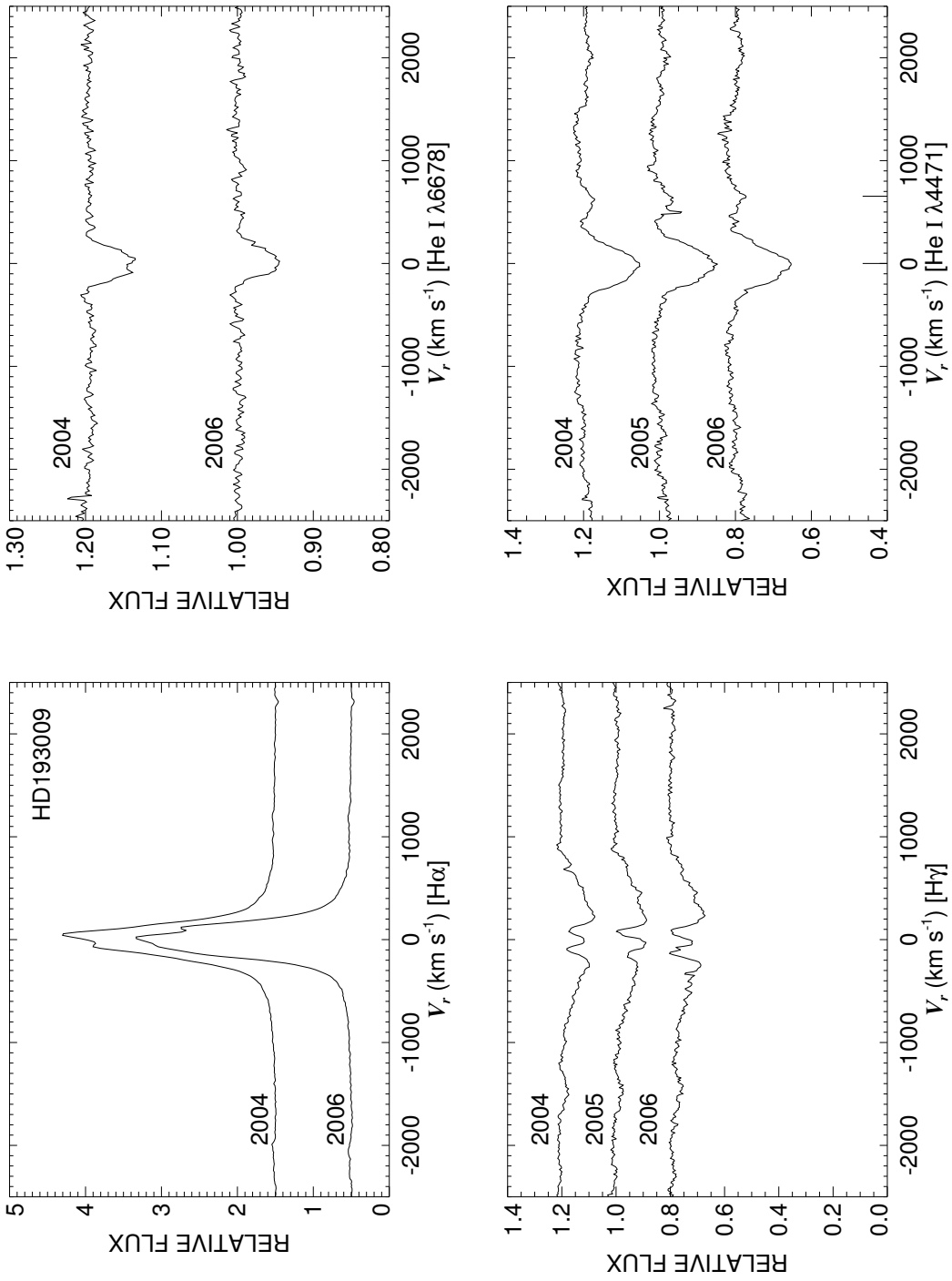

Figure C.100: A quadruple plot of HD193009 as described in §7.2.3 and Figure 7.6.

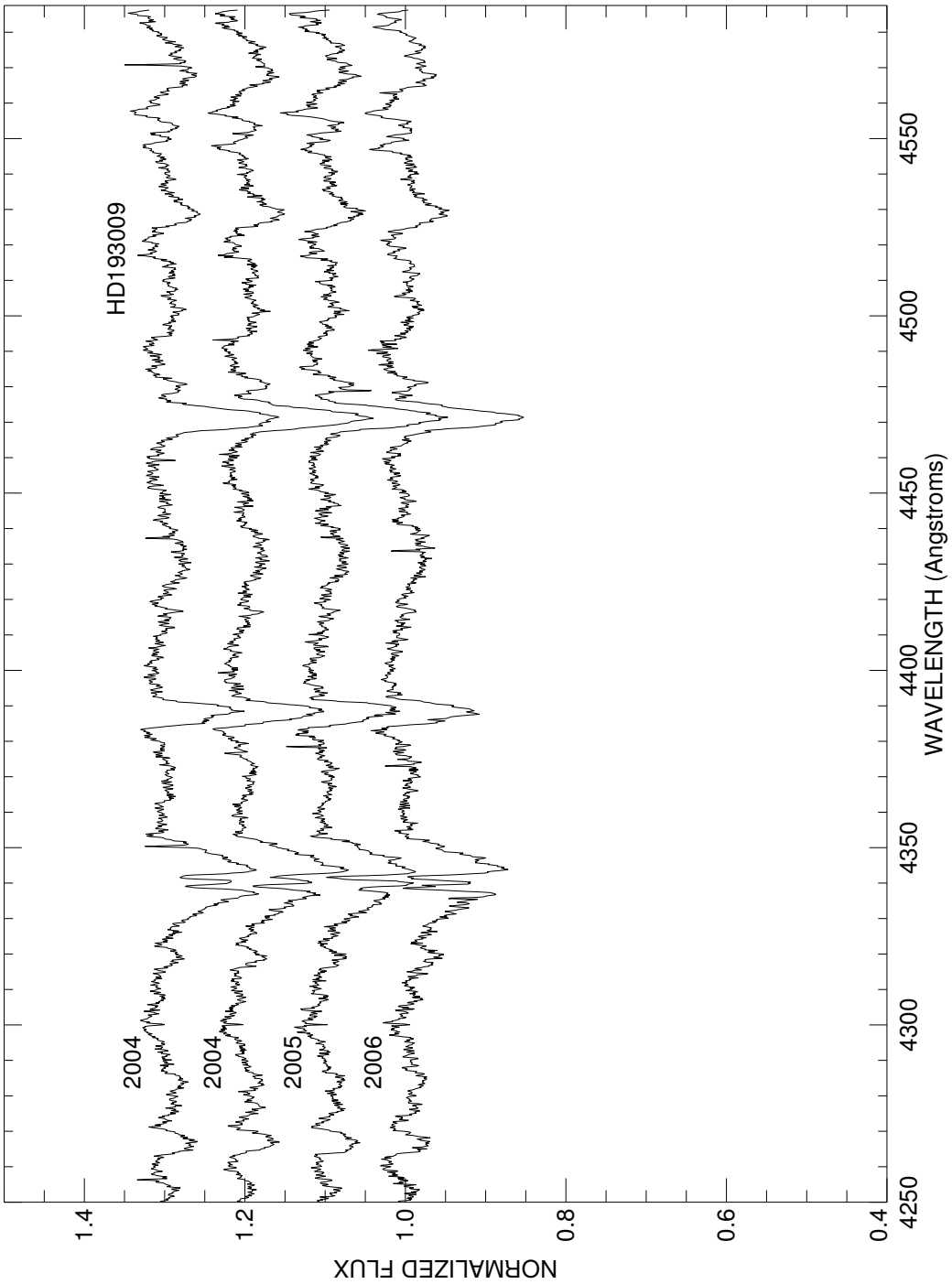

Figure C.101: A plot of all spectra of HD193009 in the blue region. Each is labeled with the year of observation and they are offset for clarity.

HD193182

Classical Be Star; Shell Star

- Other Names:
- Spectral Type: B7 IV/Ve+sh
- V magnitude: 6.48
- In WDS?: no
- Known spectroscopic binary?: no
- Velocity variations seen in these data?: no

	Hα	He I λ6678	Hγ	He I λ4471	Mg II λ4481	Fe II ccfs
Mean RV (km s^{-1})	-16.7	-28.5	-10.2	-99.3	-45.9	-20.8
RV range (km s^{-1})	-18.8 to -15.4	-40.2 to -24.8	-13.2 to -7.5	-101.6 to -97.5	-47.8 to -43.3	-21.5 to -20.1
RV change (km s^{-1})	3.4	15.4	5.7	4.1	4.5	1.4

- Shell classification: shell (VERY)
- Do shell features move with the star?: N/A
- Notes on emission and absorption features: Very strong central absorption in the hydrogen lines. These shell lines may be photospheric as this star is on the cool end of the B type.
- Other notes: This star is also plotted in Figure 7.5.

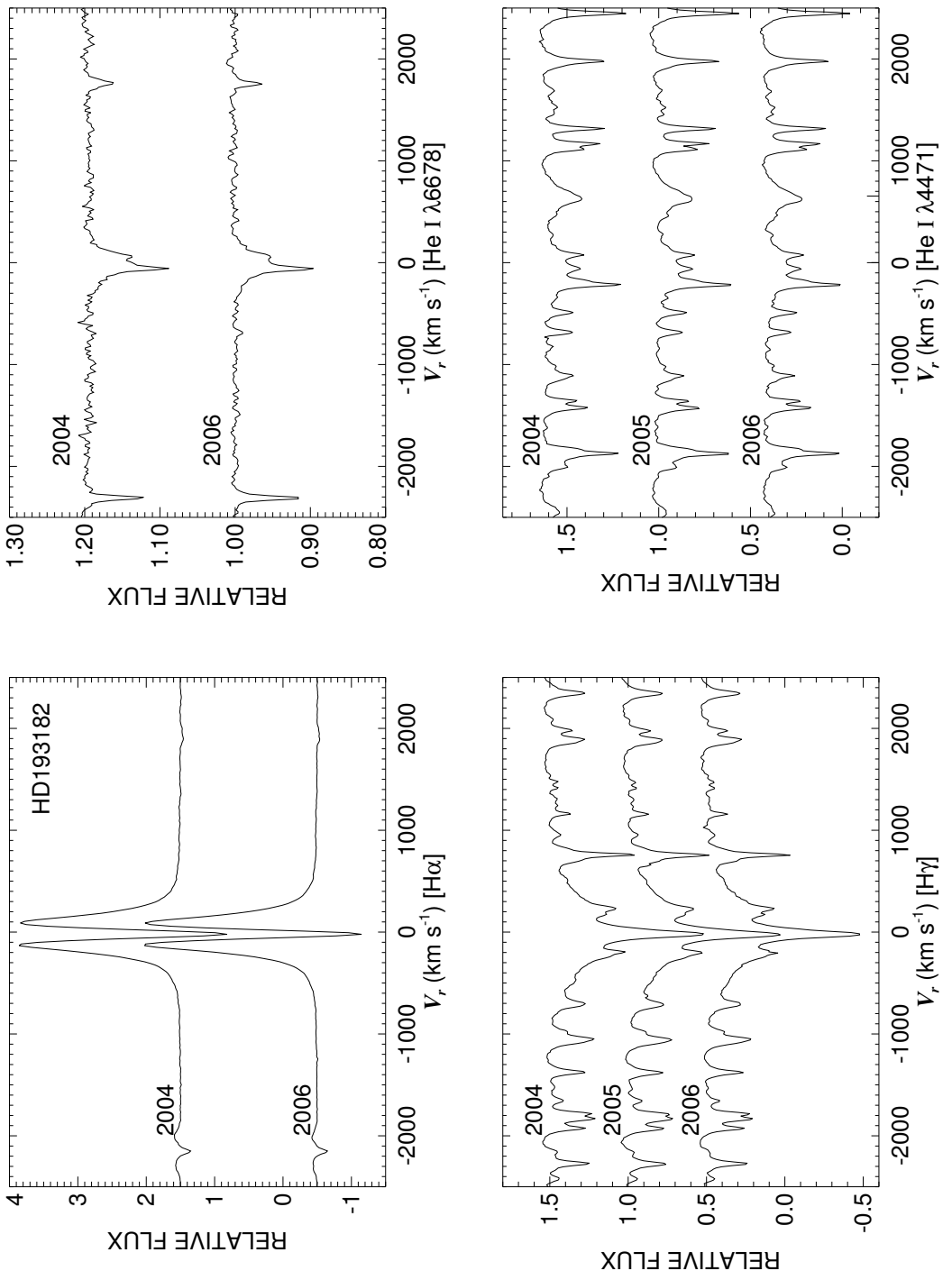

Figure C.102: A quadruple plot of HD193182 as described in §7.2.3 and Figure 7.6.

HD193911

Classical Be Star

- Other Names: HR 7789, 25 Vul
- Spectral Type: B8 IIIne+sh
- V magnitude: 5.43
- In WDS?: no
- Known spectroscopic binary?: no
- Velocity variations seen in these data?: unlikely

	Hα	He I λ6678	Hγ	He I λ4471	Mg II λ4481	Fe II ccfs
Mean RV (km s^{-1})	-3.3	-0.5	-8.8	-2.3	-8.7	-20.9
RV range (km s^{-1})	-4.1 to -2.8	-5.3 to 8.3	-11.4 to -7.6	-7.9 to 2.3	-14.6 to -4.8	-28.9 to -12.2
RV change (km s^{-1})	1.3	13.6	3.8	10.2	9.8	16.7

- Shell classification: weak emission shell
- Do shell features move with the star?: N/A
- Notes on emission and absorption features: He I λ6678 appears somewhat filled in (and has emission horns).
- Other notes: Despite the designation of "+sh," I find very little evidence for a shell spectrum at the current time. Perhaps it has shell episodes.

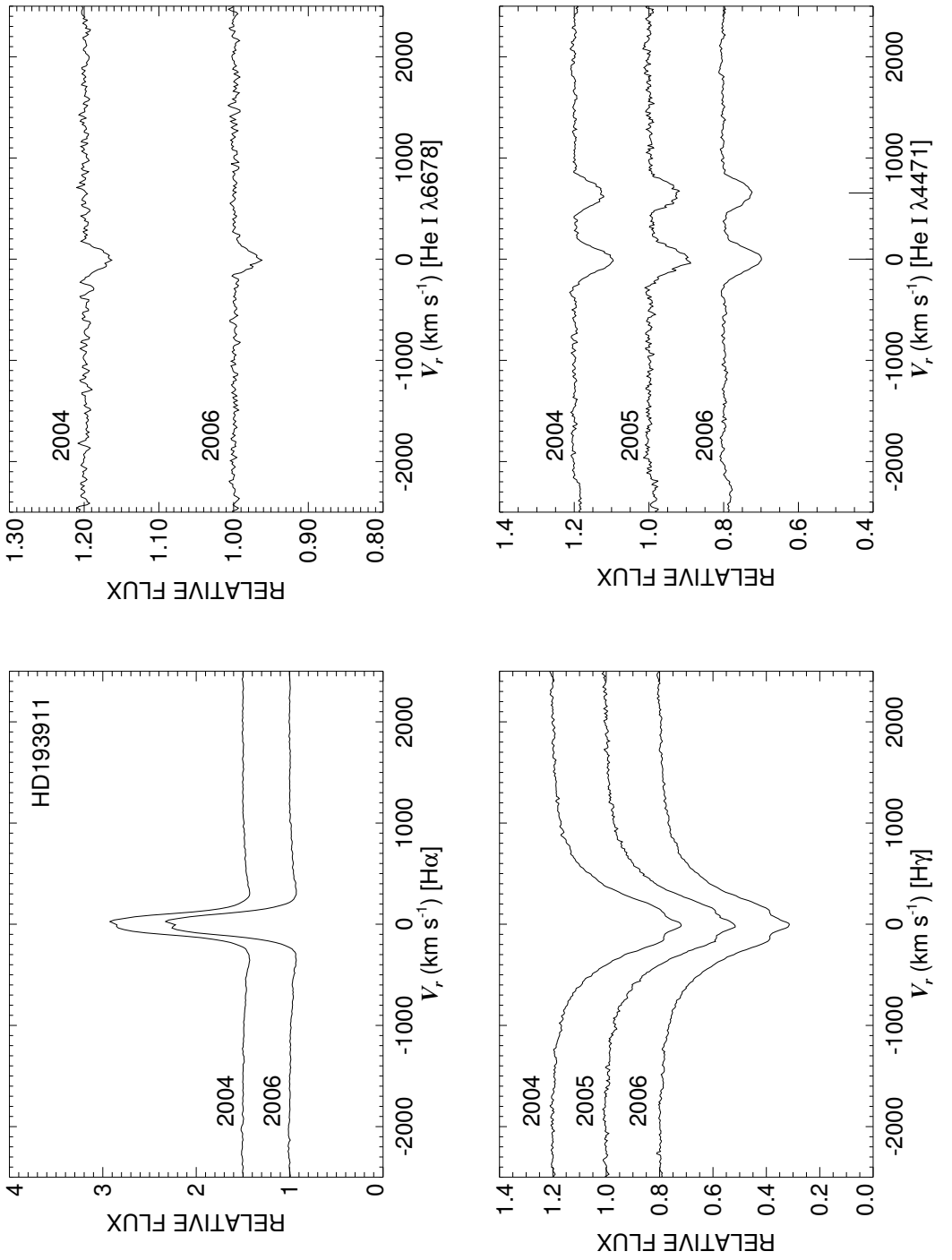

Figure C.103: A quadruple plot of HD193911 as described in §7.2.3 and Figure 7.6.

HD194244

Classical Be Star

- Other Names: HR 7803
- Spectral Type: B9 Ve
- V magnitude: 6.10
- In WDS?: no
- Known spectroscopic binary?: no
- Velocity variations seen in these data?: no

	Hα	He I λ6678	Hγ	He I λ4471	Mg II λ4481	Fe II ccfs
Mean RV (km s^{-1})	-19.3	···	-10.5	-44.3	-25.8	-0.4
RV range (km s^{-1})	-23.9 to -13.7	···	-12.7 to -8.9	-56.8 to -16.4	-29.1 to -24.0	-7.8 to 11.1
RV change (km s^{-1})	10.2	···	3.8	40.4	5.1	18.9

- Shell classification: squarish
- Do shell features move with the star?: N/A
- Notes on emission and absorption features: Helium lines are very weak or non-existent (filling and cool star). The shell features may be photospheric as the star is so cool.
- Other notes:

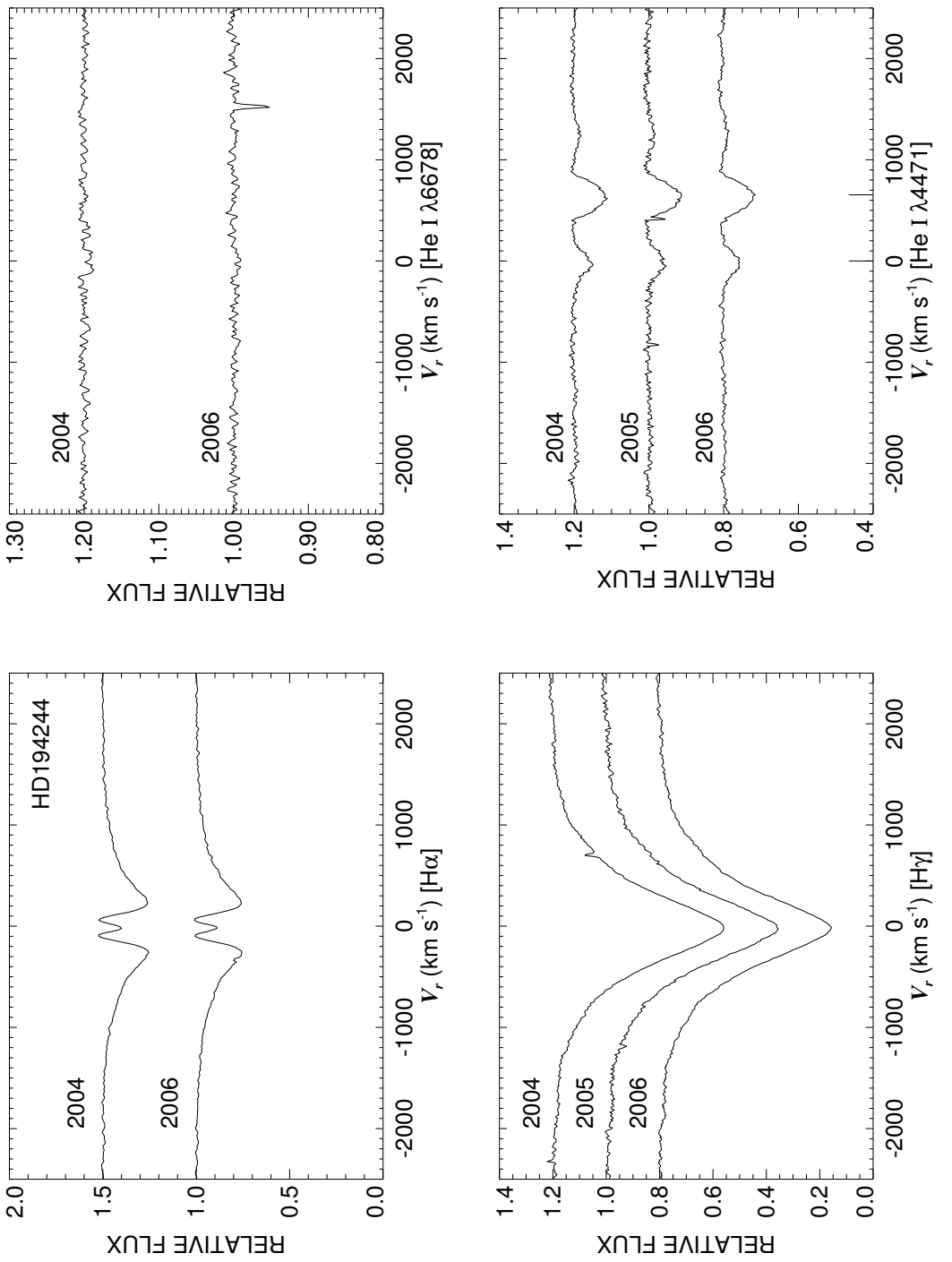

Figure C.104: A quadruple plot of HD194244 as described in §7.2.3 and Figure 7.6.

HD194335

Classical Be Star

- Other Names: HR 7807, V2119 Cyg
- Spectral Type: B2 IIIne
- V magnitude: 5.68
- In WDS?: no
- Known spectroscopic binary?: no
- Velocity variations seen in these data?: yes

	Hα	He I λ6678	Hγ	He I λ4471	Mg II λ4481	Fe II ccfs
Mean RV (km s^{-1})	-13.6	-22.0	6.8	-52.6	-103.3	51.9
RV range (km s^{-1})	-24.9 to -6.8	-32.1 to -2.1	-6.7 to 23.0	-59.9 to -39.3	-120.4 to -87.5	10.8 to 134.6
RV change (km s^{-1})	18.1	30.0	29.7	20.6	32.9	123.9

- Shell classification: emission shell
- Do shell features move with the star?: N/A
- Notes on emission and absorption features: Hα shows peak switching. He I λ6678 shows emission horns. Mg II λ4481 is very broad and quite blended.
- Other notes:

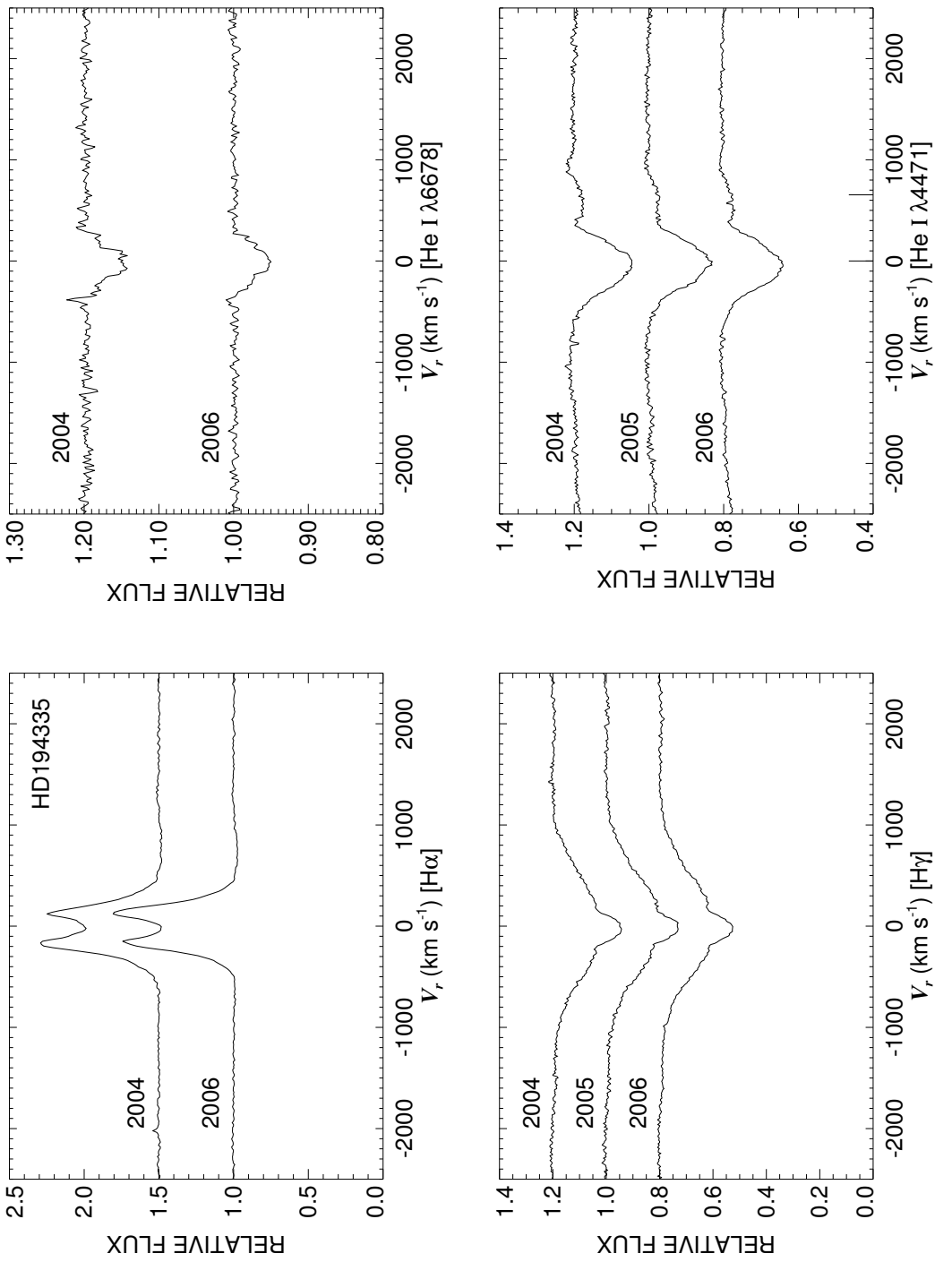

Figure C.105: A quadruple plot of HD194335 as described in §7.2.3 and Figure 7.6.

HD194883

Classical Be Star

- Other Names: V2120 Cyg
- Spectral Type: B2 Ve
- V magnitude: 7.32
- In WDS?: no
- Known spectroscopic binary?: no
- Velocity variations seen in these data?: maybe

	Hα	He I λ6678	Hγ	He I λ4471	Mg II λ4481	Fe II ccfs
Mean RV (km s^{-1})	-19.2	-27.1	-28.7	-26.0	-45.5	-44.2
RV range (km s^{-1})	-19.8 to -18.6	-30.4 to -24.1	-34.1 to -23.1	-28.3 to -24.9	-92.8 to -20.9	-62.4 to -20.4
RV change (km s^{-1})	1.2	6.3	11.0	3.4	71.9	42.0

- Shell classification: emission shell
- Do shell features move with the star?: if it moves, yes
- Notes on emission and absorption features: Large Hα emission. Both He I λ6678 and Mg II λ4481 show emission horns (therefore are unreliable for RV studies). Hγ shows changes.
- Other notes:

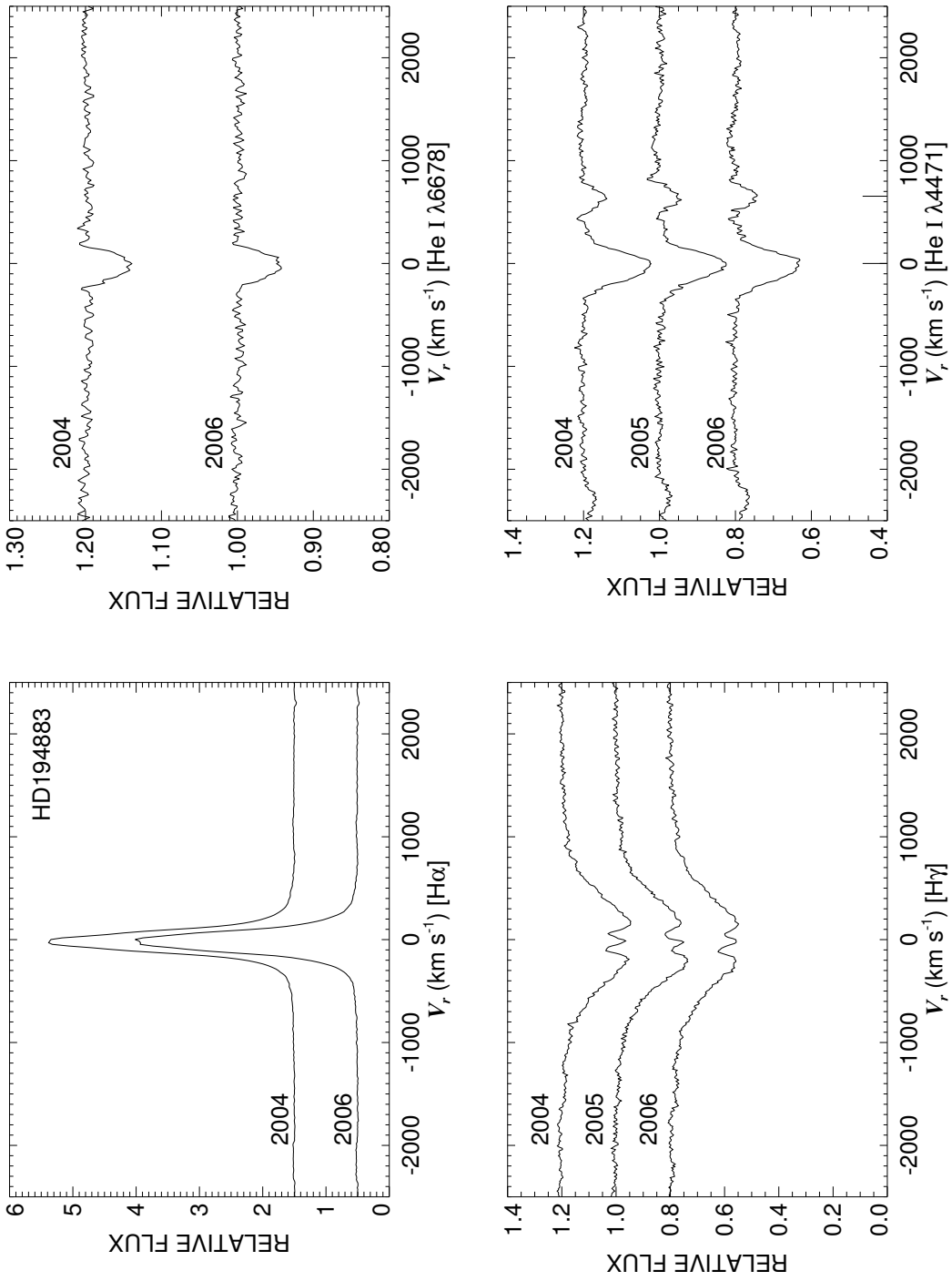

Figure C.106: A quadruple plot of HD194883 as described in §7.2.3 and Figure 7.6.

HD195325

Classical Be Star; Shell Star

- Other Names: HR 7836, 1 Del
- Spectral Type: B9e+sh
- V magnitude: 6.03
- In WDS?: yes - 8.02 and 14.1 mag companions 0.9 and 17.2 arcsec away (discovred in 1872 and 1885)
- Known spectroscopic binary?: no
- Velocity variations seen in these data?: no

	Hα	He I λ6678	Hγ	He I λ4471	Mg II λ4481	Fe II ccfs
Mean RV (km s^{-1})	-15.3	···	-8.9	-125.0	-16.4	-7.0
RV range (km s^{-1})	-22.3 to -4.0	···	-10.3 to -6.0	-130.8 to -119.5	-24.6 to -8.9	-7.8 to -6.3
RV change (km s^{-1})	18.3	···	4.3	11.3	15.7	1.5

- Shell classification: shell
- Do shell features move with the star?: N/A
- Notes on emission and absorption features: Strong central absorption in Hα. The helium lines are small and sharp (dominated by shell absorption). Mg II λ4481 appears broad (likely photospheric).
- Other notes: This star is also plotted in 7.5.

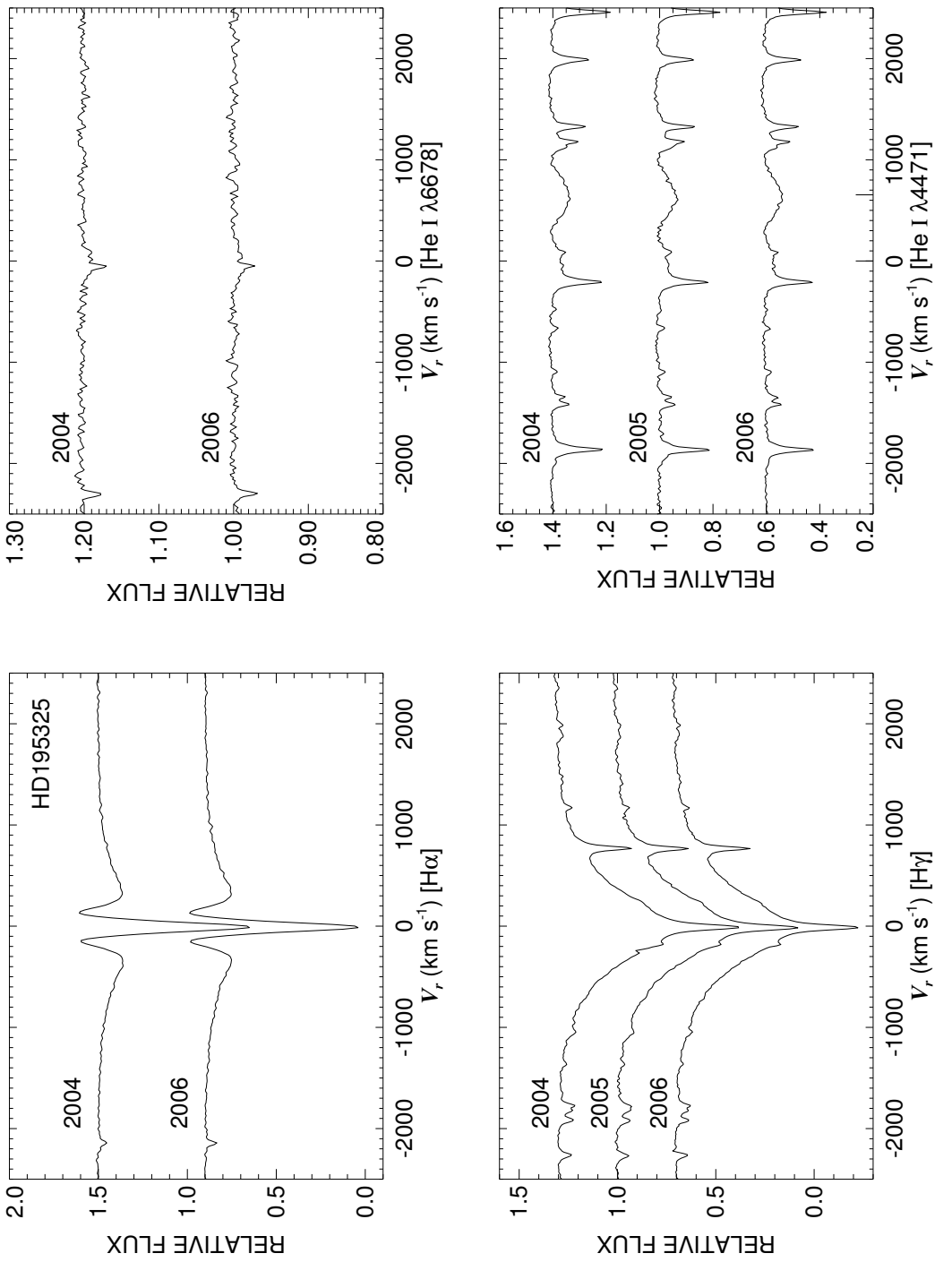

Figure C.107: A quadruple plot of HD195325 as described in §7.2.3 and Figure 7.6.

HD195554

Classical Be Star

- Other Names: HR 7843
- Spectral Type: B9 Vne
- V magnitude: 5.83
- In WDS?: yes - 8.84 mag companion 0.8 arcsec away (discovered in 1937)
- Known spectroscopic binary?: no
- Velocity variations seen in these data?: no

	Hα	He I λ6678	Hγ	He I λ4471	Mg II λ4481	Fe II ccfs
Mean RV (km s^{-1})	-19.1	···	-20.5	-37.9	-28.1	-11.2
RV range (km s^{-1})	-23.5 to -16.9	···	-25.0 to -18.5	-48.0 to -31.4	-31.7 to -23.9	-23.2 to 6.8
RV change (km s^{-1})	6.6	···	6.5	16.6	7.8	30.0

- Shell classification: squarish
- Do shell features move with the star?: N/A
- Notes on emission and absorption features: Hα peaks change. The helium lines are very weak (cool temperature and filling in).
- Other notes:

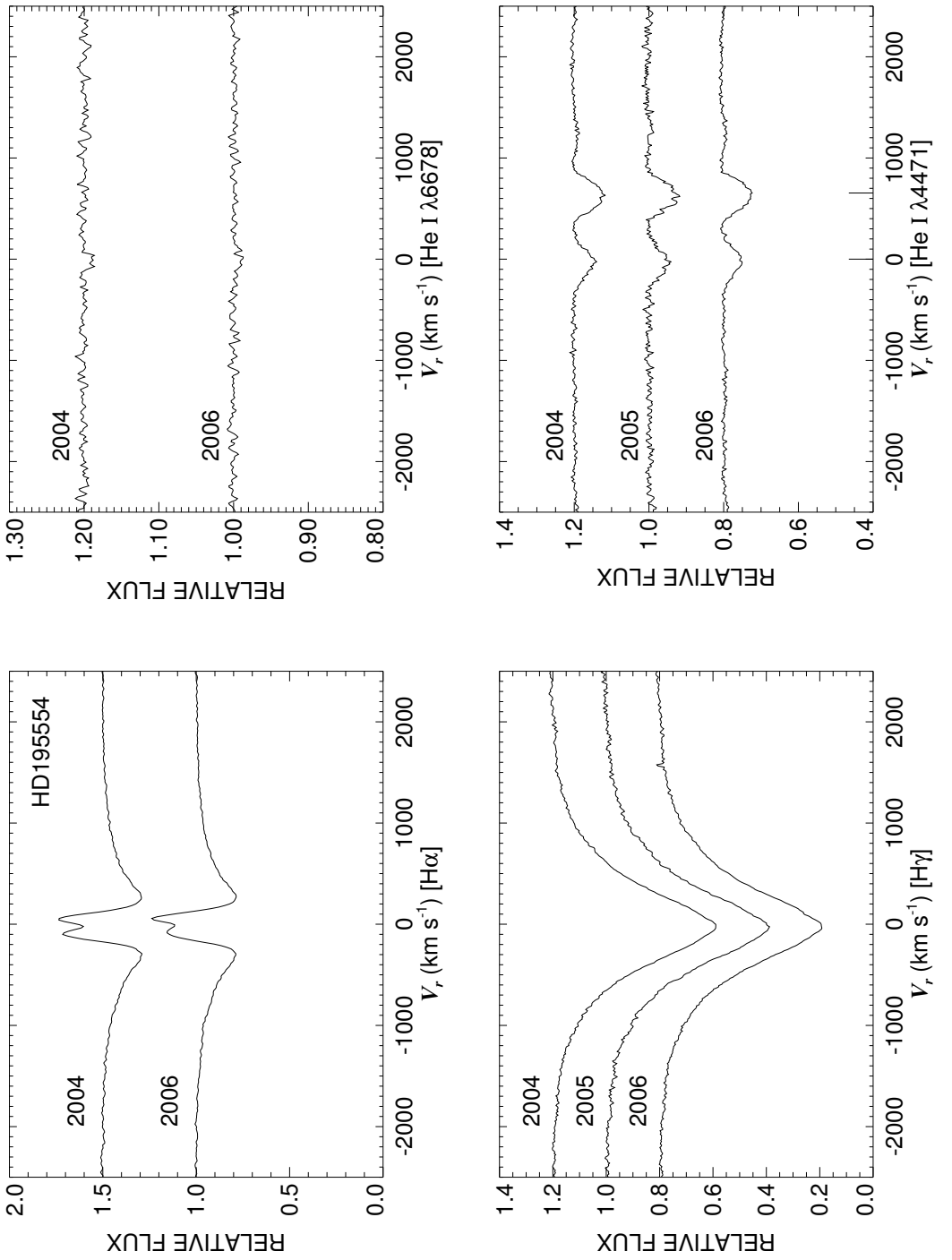

Figure C.108: A quadruple plot of HD195554 as described in §7.2.3 and Figure 7.6.

HD197419

Classical Be Star

- Other Names: HR 7927, V568 Cyg
- Spectral Type: B2 IV-Ve
- V magnitude: 6.51
- In WDS?: no
- Known spectroscopic binary?: no
- Velocity variations seen in these data?: no

	Hα	He I λ6678	Hγ	He I λ4471	Mg II λ4481	Fe II ccfs
Mean RV (km s^{-1})	-6.7	-5.2	-4.9	-33.8	-10.2	···
RV range (km s^{-1})	-7.3 to -6.2	-6.4 to -3.6	-9.3 to 0.2	-36.7 to -29.5	-11.8 to -9.1	···
RV change (km s^{-1})	1.1	2.8	9.5	7.2	2.7	···

- Shell classification: normal
- Notes on emission and absorption features: The narrowness of the lines suggests this star is nearly pole-on. There are line profile changes in the helium and magnesium lines (companion or NRP). In the 2005 Hγ spectrum, the protrusion on the left is likely a cosmic ray hit. To the right of Hα is the C II doublet.
- Other notes:

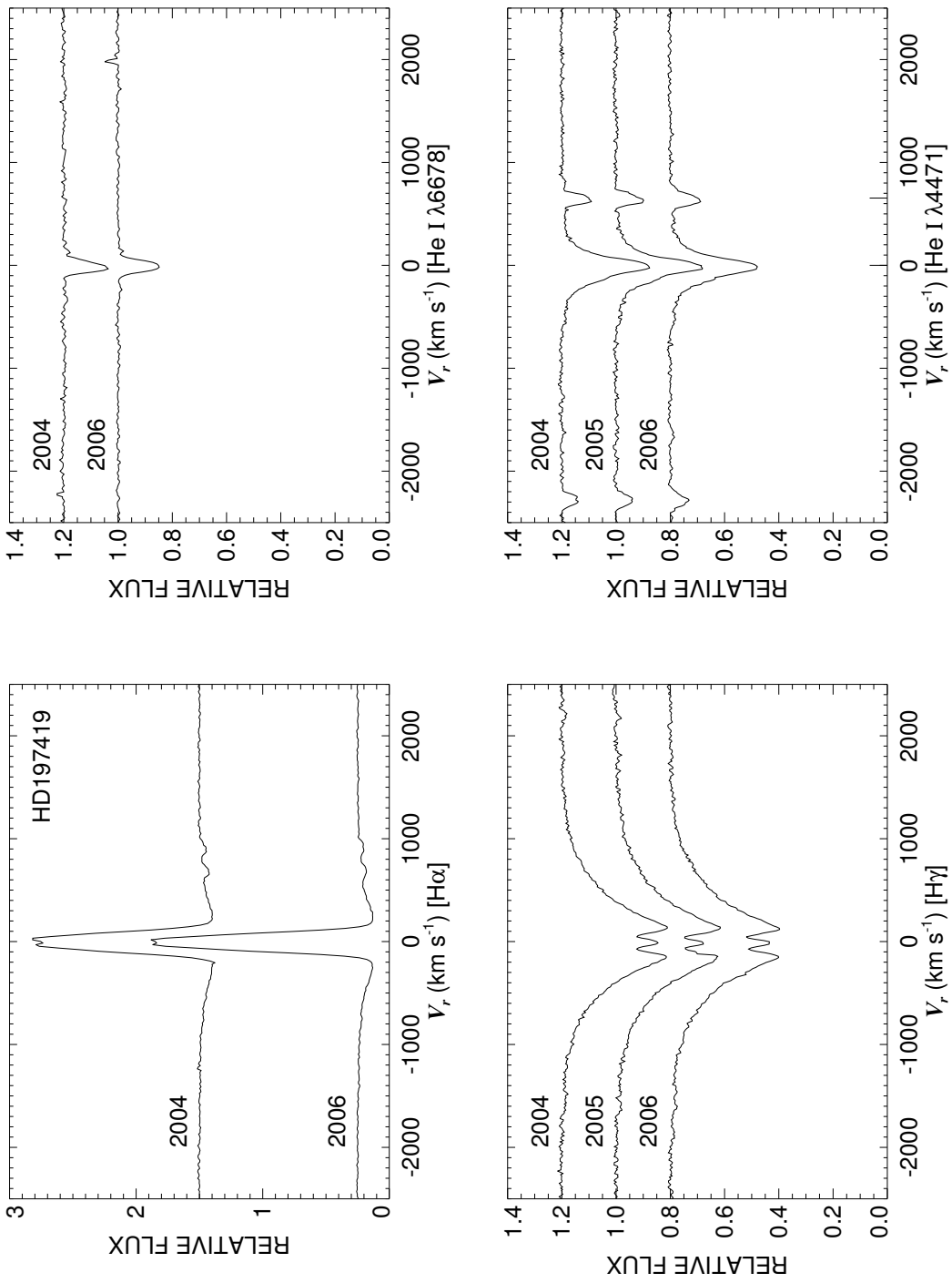

Figure C.109: A quadruple plot of HD197419 as described in §7.2.3 and Figure 7.6.

HD198183

Classical Be Star; Non-Radial Pulsator?

- Other Names: HR 7963, 54 Cyg, λ Cyg
- Spectral Type: B5 Ve
- V magnitude: 4.45
- In WDS?: yes - a 4.5 mag speckle companion less than 0.1 arcsec away (discovered in 1978) along with 6.26 and 9.65 mag companions 1.0 and 84 arcsec away (discovered in 1842 and 1834).
- Known spectroscopic binary?: no
- Velocity variations seen in these data?: yes (see Fig. C.111)

	Hα	He I λ6678	Hγ	He I λ4471	Mg II λ4481	Fe II ccfs
Mean RV (km s^{-1})	-19.5	-21.3	-15.0	-35.9	-26.8	24.8
RV range (km s^{-1})	-31.6 to -13.5	-27.3 to -15.9	-19.5 to -10.8	-39.1 to -31.3	-28.9 to -25.6	-1.1 to 40.2
RV change (km s^{-1})	18.1	11.4	8.7	7.8	3.3	41.3

- Shell classification: squarish
- Do shell features move with the star?: yes
- Notes on emission and absorption features: The tiny Hα emission increases in 2006. Rapid line profile changes in the blue spectra imply either a very close, rapidly orbiting companion or NRP. Or it could be a triple system with the stationary Be star and a nearby SB1.
- Other notes:

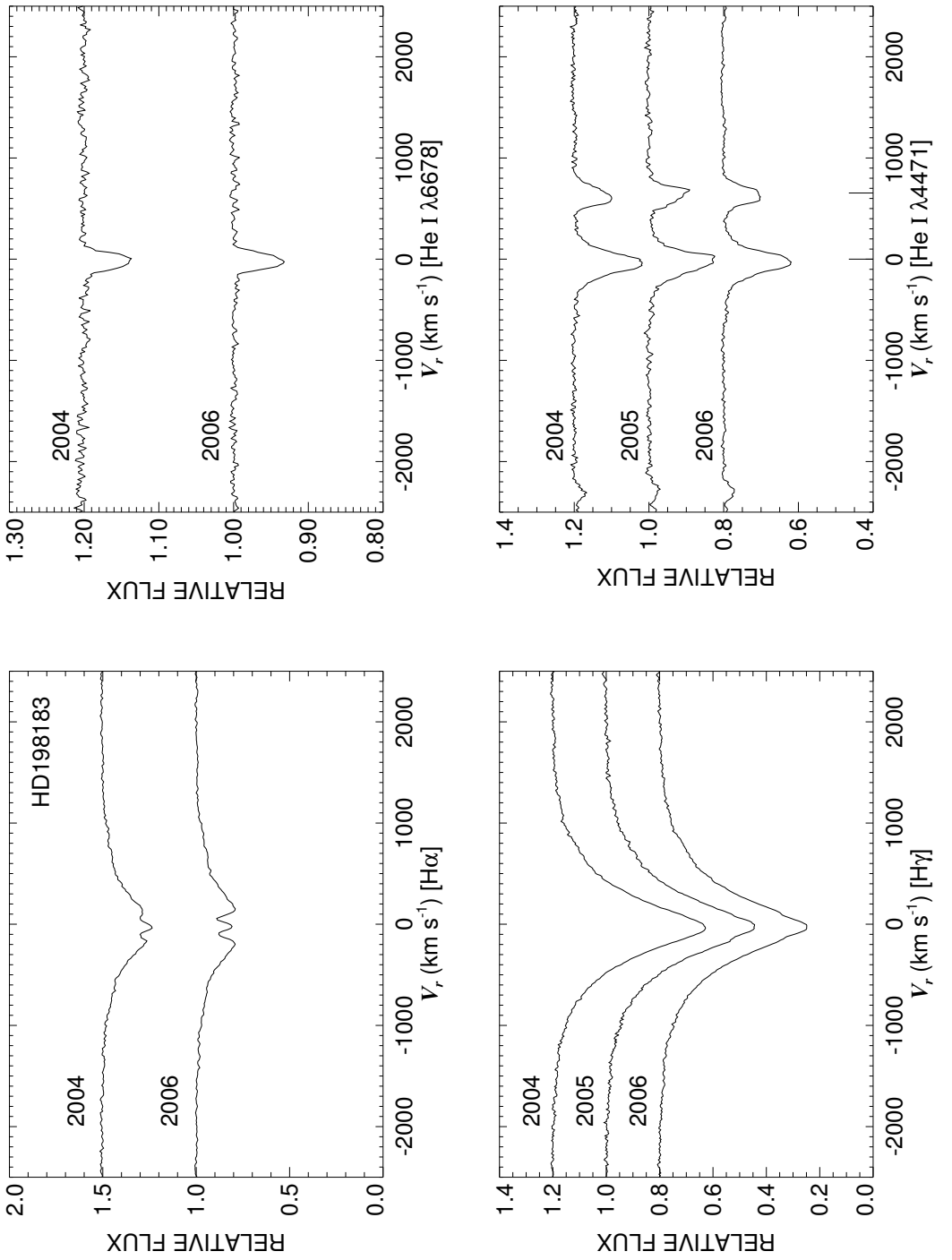

Figure C.110: A quadruple plot of HD198183 as described in §7.2.3 and Figure 7.6.

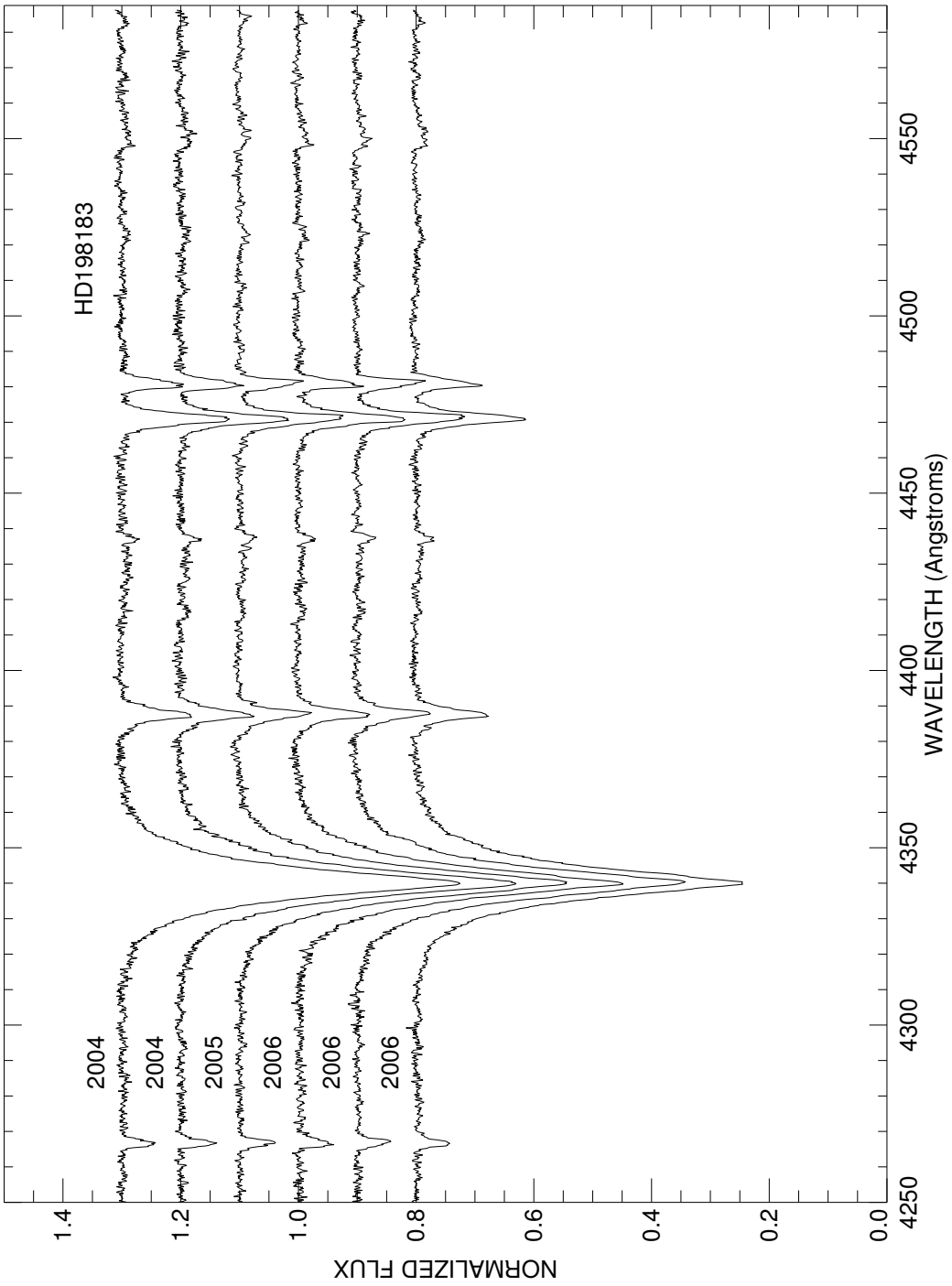

Figure C.111: A plot of all spectra of HD198183 in the blue region. Each is labeled with the year of observation and they are offset for clarity.

HD198625

Classical Be Star

- Other Names: HR 7983, V2136 Cyg
- Spectral Type: B4 Ve
- V magnitude: 6.27
- In WDS?: yes - 11.5 mag companion 18.6 arcsec away (discovered in 1875)
- Known spectroscopic binary?: no
- Velocity variations seen in these data?: maybe

	Hα	He I λ6678	Hγ	He I λ4471	Mg II λ4481	Fe II ccfs
Mean RV (km s^{-1})	-12.9	-3.4	-6.2	-32.2	-24.2	···
RV range (km s^{-1})	-16.6 to -7.9	-18.3 to 6.5	-11.3 to 1.1	-41.7 to -22.8	-37.7 to -11.0	···
RV change (km s^{-1})	8.7	24.8	12.4	18.9	26.7	···

- Shell classification: normal
- Notes on emission and absorption features: Hα shows a dramatic weakening in 2006. He I λ6678 has emission horns in 2004 and a right horn in 2006. In 2004, Hγ shows weak emission but it went away in 2005 and 2006 has a somewhat odd shape - perhaps filling in again? Mg II λ4481 is very broad and blended (somewhat unreliable for RV studies).
- Other notes: This star is also plotted in Figure 7.2.

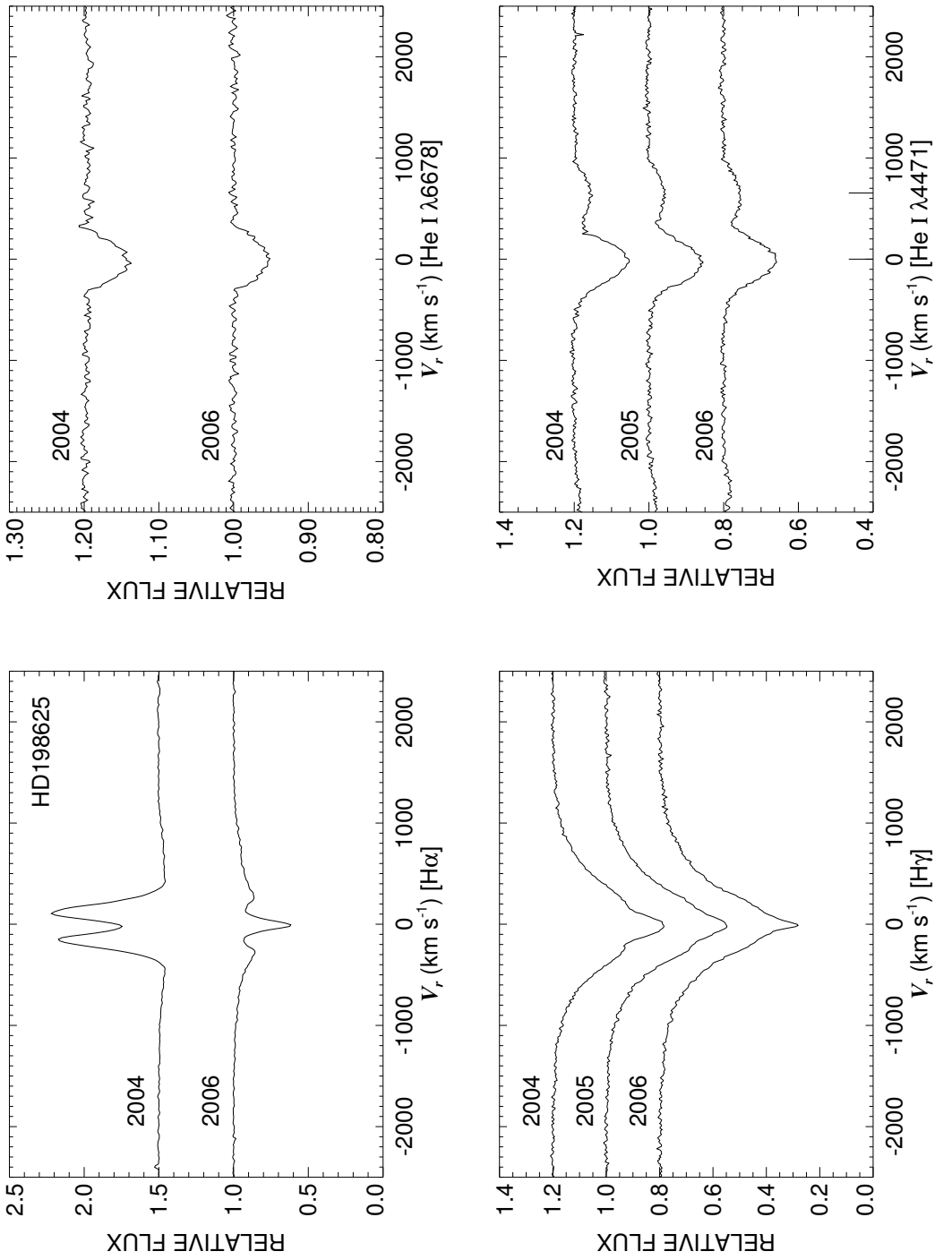

Figure C.112: A quadruple plot of HD198625 as described in §7.2.3 and Figure 7.6.

HD199218

Classical Be Star

- Other Names: HR 8009
- Spectral Type: B8 Vnne
- V magnitude: 6.61
- In WDS?: yes - 10.7 mag companion 5.8 arcsec away (discovered in 1848)
- Known spectroscopic binary?: no
- Velocity variations seen in these data?: no

	Hα	He I λ6678	Hγ	He I λ4471	Mg II λ4481	Fe II ccfs
Mean RV (km s^{-1})	-16.6	-35.6	-18.6	-37.3	-28.9	-12.4
RV range (km s^{-1})	-17.4 to -15.7	-69.9 to 10.4	-21.2 to -12.2	-38.8 to -36.4	-34.7 to -22.2	-15.1 to -8.9
RV change (km s^{-1})	1.7	80.3	9.0	2.4	12.5	6.2

- Shell classification: squarish
- Do shell features move with the star?: N/A
- Notes on emission and absorption features: Hα grows slightly in 2006. Both helium lines are shallow due to the cool nature of the star and due to rotational broadening.
- Other notes: This star is also plotted in Figure 7.3.

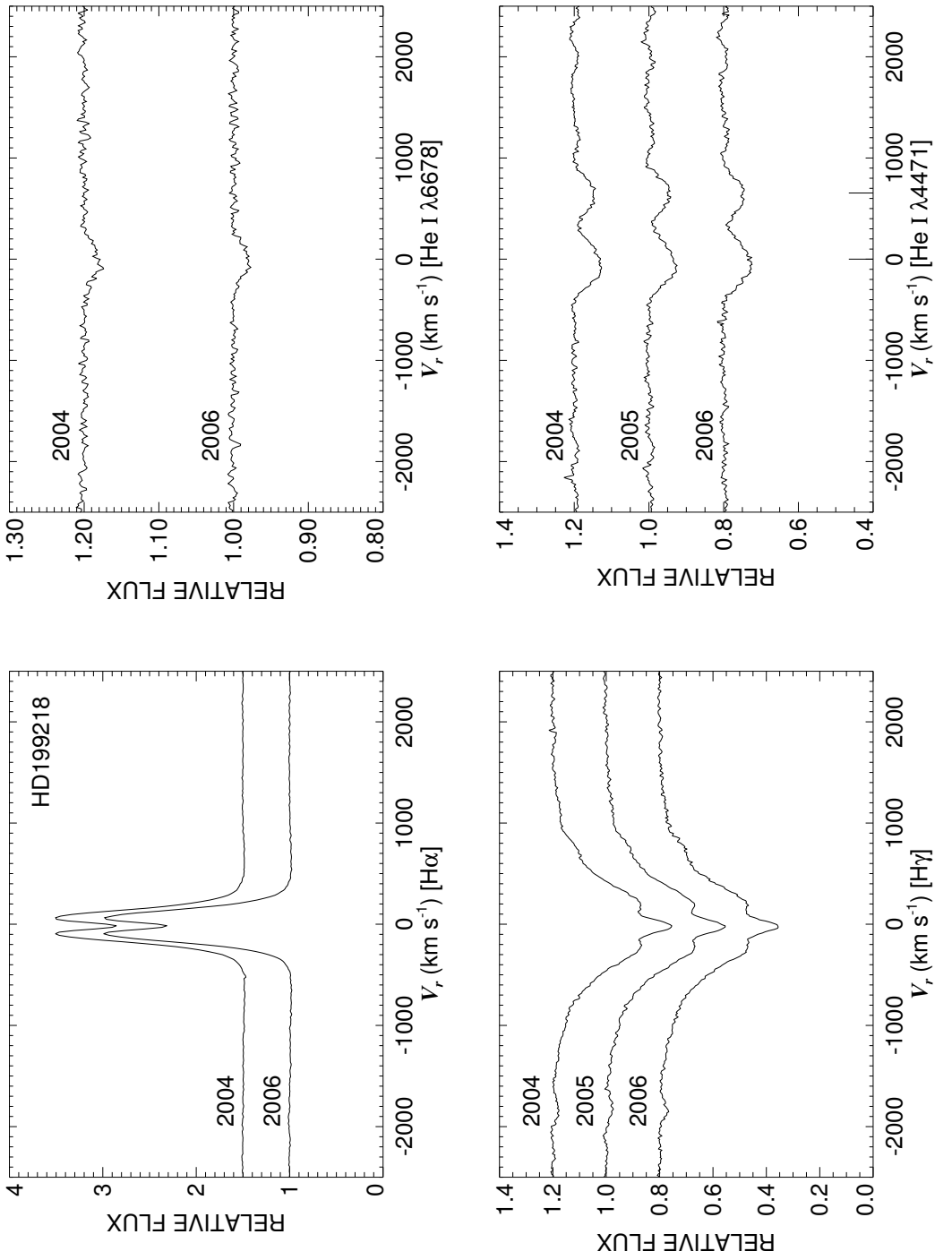

Figure C.113: A quadruple plot of HD199218 as described in §7.2.3 and Figure 7.6.

HD199356

Classical Be Star

- Other Names: V2139 Cyg
- Spectral Type: B2 IVe
- V magnitude: 7.29
- In WDS?: no
- Known spectroscopic binary?: no
- Velocity variations seen in these data?: no

	Hα	He I λ6678	Hγ	He I λ4471	Mg II λ4481	Fe II ccfs
Mean RV (km s^{-1})	-14.5	-5.8	-5.8	11.0	···	-9.2
RV range (km s^{-1})	-16.3 to -12.3	-21.4 to 15.8	-20.6 to 5.1	-12.7 to 24.2	···	-21.7 to -1.4
RV change (km s^{-1})	4.0	37.2	25.7	36.9	···	20.2

- Shell classification: emission shell
- Do shell features move with the star?: N/A
- Notes on emission and absorption features: Hα emission has a rather broad profile that changes. He I λ6678 is filled in with emission and is useless for RV studies. Hγ shows subtle changes in the central emission peaks. Mg II λ4481 is extremely broad as well as blended, therefore it is useless for RV studies.
- Other notes: This star is also plotted in Figure 7.4.

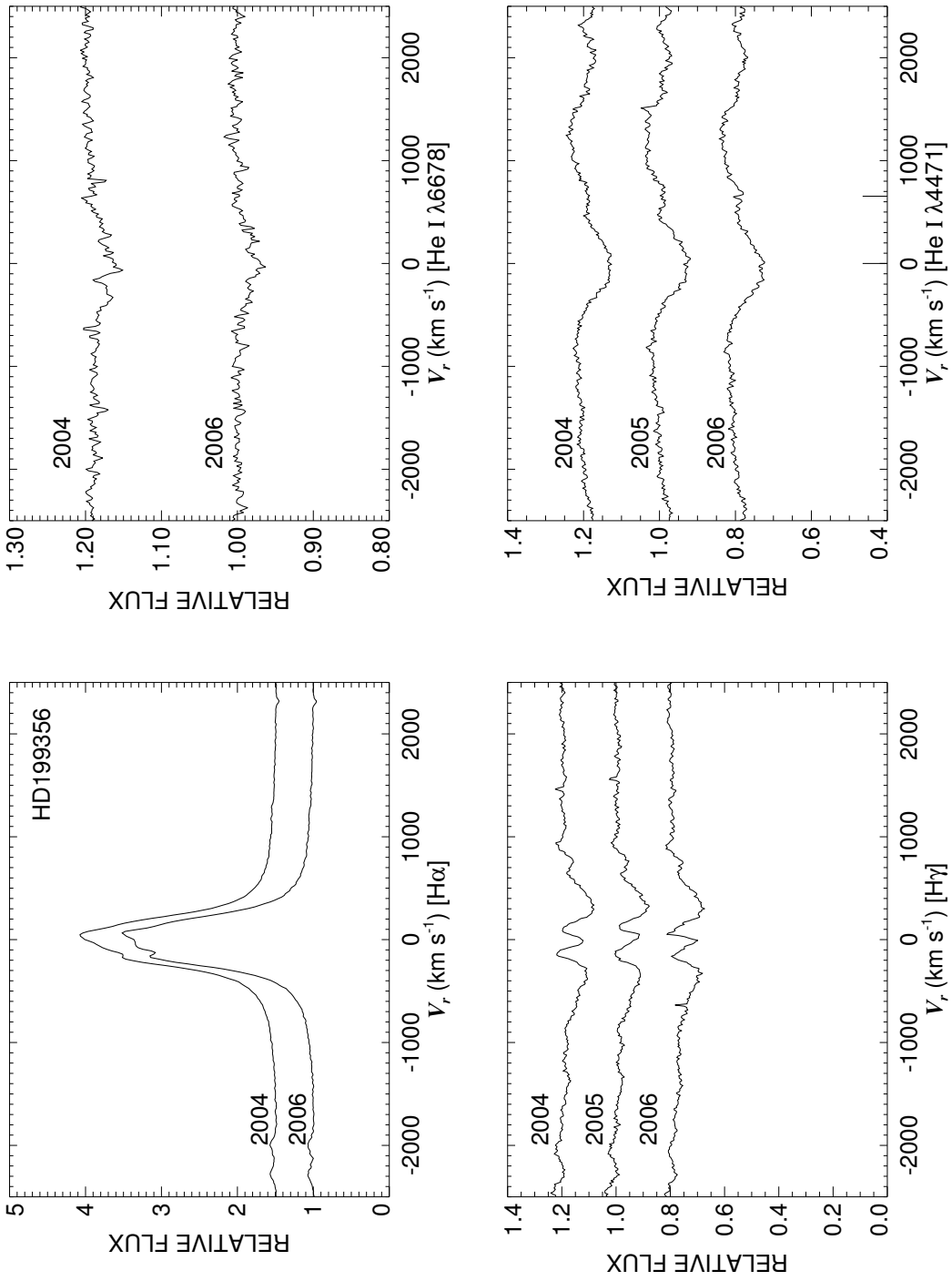

Figure C.114: A quadruple plot of HD199356 as described in §7.2.3 and Figure 7.6.

HD200120

Classical Be Star

- Other Names: HR 8047, 59 Cyg, V832 Cyg
- Spectral Type: B1.5 Ve+sh
- V magnitude: 4.69
- In WDS?: yes - a 7.64 mag companion 0.2 arcsec away (discovered in 1981) and 3 fainter companions (mag 9.43, 11.62, 11.20) at 20, 27, and 70 arcsec away (discovered in 1828 and 1899)
- Known spectroscopic binary?: yes - Rivinius & Štefl (2000) finds a period of 28.17 d
- Velocity variations seen in these data?: possibly

	Hα	He I λ6678	Hγ	He I λ4471	Mg II λ4481	Fe II ccfs
Mean RV (km s^{-1})	-5.9	138.1	26.3	8.8	···	-19.4
RV range (km s^{-1})	-9.3 to 5.1	125.5 to 150.7	16.9 to 36.1	-9.6 to 32.4	···	-41.7 to 4.7
RV change (km s^{-1})	14.4	25.2	19.2	42.0	···	46.5

- Shell classification: emission shell
- Do shell features move with the star?: yes
- Notes on emission and absorption features: Hα has an unusual shape (broad, peaks look strange). He I λ6678 is totally filled in and useless for RV studies. From 2004 to 2006, Hγ emission grows a little and it also shows rapid peak variations (see Fig. C.116) He I λ4471 has an asymmetric shape.
- Other notes: Maintz et al. (2005) report that this star is analogous to ϕ Per in that it is a Be star with a hot subdwarf companion. The Hα profile shape reminds me of HD023800 and HD058978 (FY CMa) as well as ϕ Per. This star is also plotted in Figure 7.4.

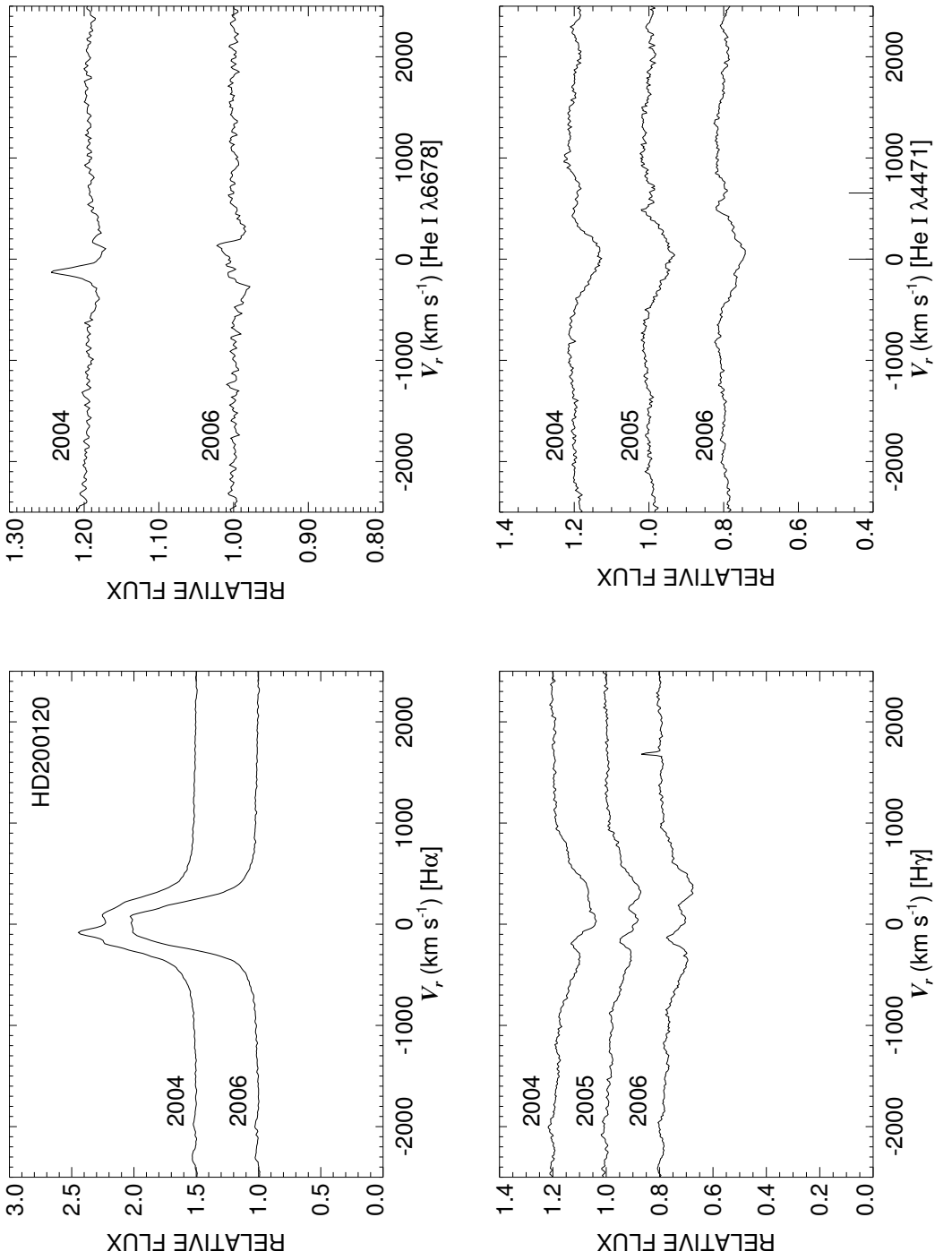

Figure C.115: A quadruple plot of HD200120 as described in §7.2.3 and Figure 7.6.

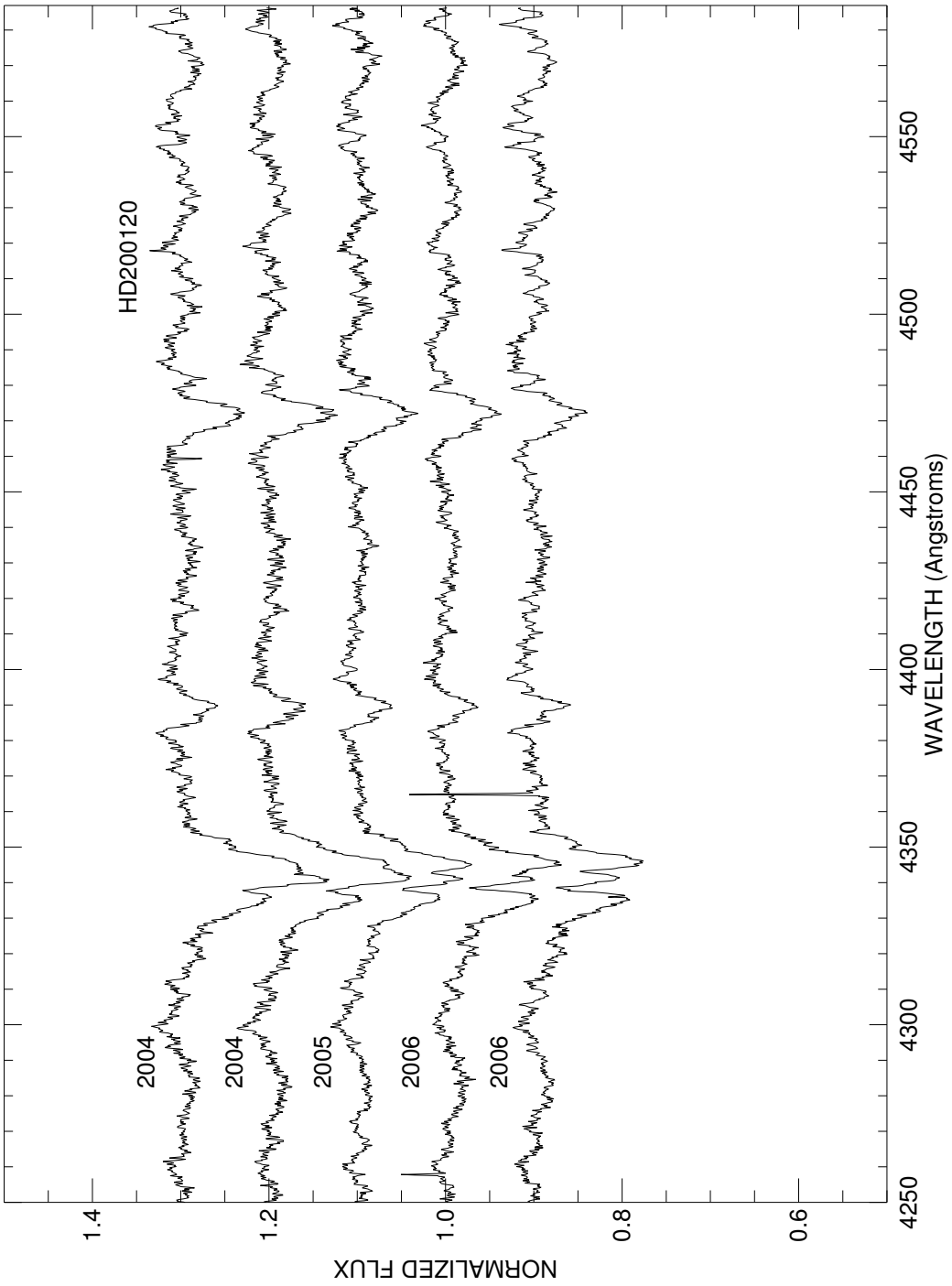

Figure C.116: A plot of all spectra of HD200120 in the blue region. Each is labeled with the year of observation and they are offset for clarity.

HD200310

Classical Be Star

- Other Names: HR 8053, 60 Cyg, V1931 Cyg
- Spectral Type: B1 Ve
- V magnitude: 5.21
- In WDS?: yes - 9.53 mag companion 2.9 arcsec away (discovered in 1848)
- Known spectroscopic binary?: yes - Harmanec (2001) gives a period of 146.6 d
- Velocity variations seen in these data?: yes

	Hα	He I λ6678	Hγ	He I λ4471	Mg II λ4481	Fe II ccfs
Mean RV (km s^{-1})	-20.8	-19.1	41.7	-30.4	-26.8	···
RV range (km s^{-1})	-25.9 to -17.5	-25.9 to -7.0	20.9 to 64.2	-40.9 to -22.6	-71.4 to 14.0	···
RV change (km s^{-1})	8.4	18.9	43.3	18.3	85.4	···

- Shell classification: normal
- Notes on emission and absorption features: Hα shows slight emission that broadens in 2006. All other lines are very broad! He I λ6678 shows emission horns (esp. in 2006). Hγ is greatly affected by a blend with O 2 λ4349. Mg II λ4481 is extremely broad and blended and is useless for RV studies.
- Other notes:

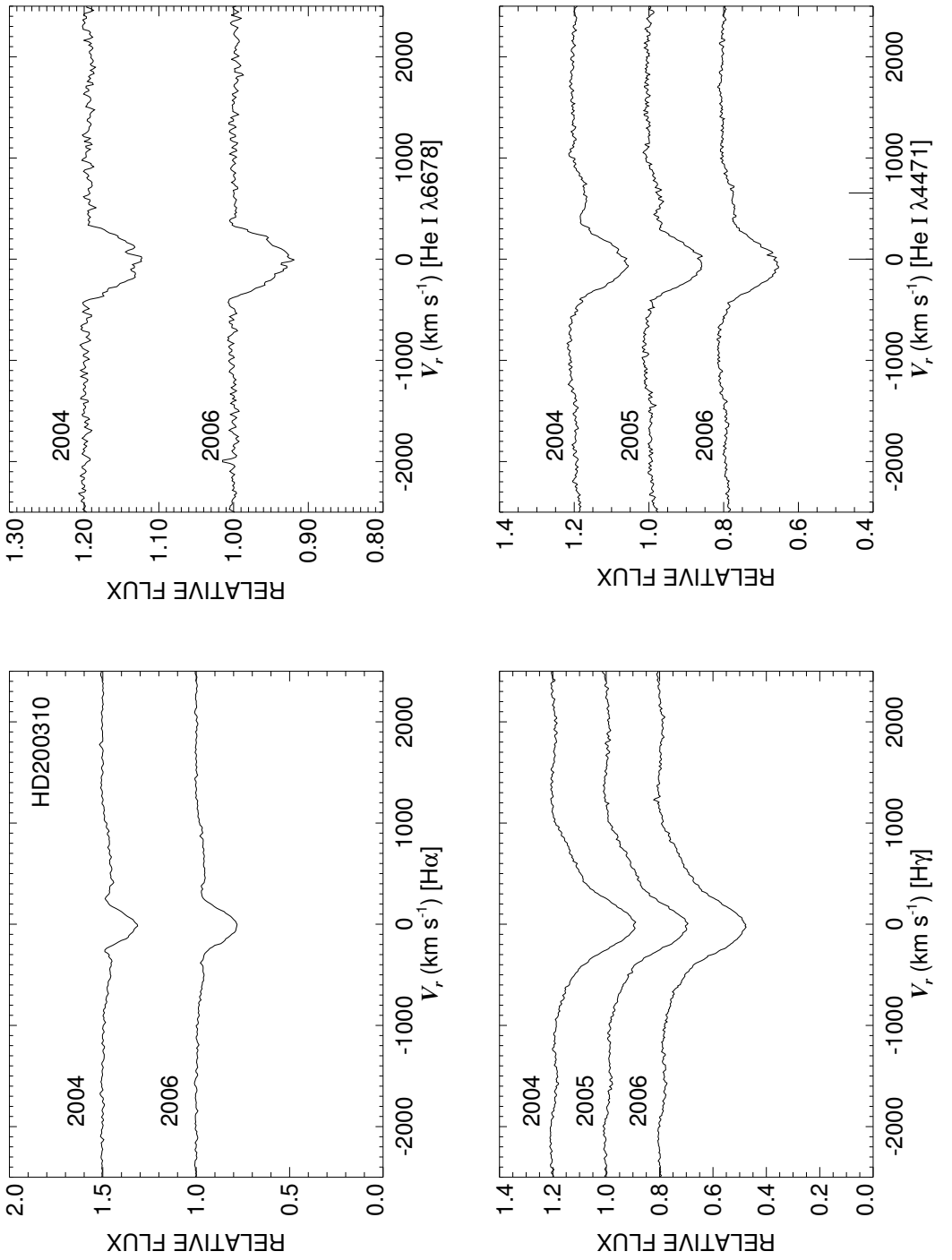

Figure C.117: A quadruple plot of HD200310 as described in §7.2.3 and Figure 7.6.

HD201522

Classical Be Star

- Other Names:
- Spectral Type: B7 IV
- V magnitude: 7.84
- In WDS?: no
- Known spectroscopic binary?: no
- Velocity variations seen in these data?: no (or if yes very small)

	Hα	He I λ6678	Hγ	He I λ4471	Mg II λ4481	Fe II ccfs
Mean RV (km s^{-1})	-4.6	-22.9	4.1	-16.0	-15.7	···
RV range (km s^{-1})	-9.4 to 0.7	-60.7 to -6.4	1.1 to 7.1	-18.1 to -13.4	-18.6 to -10.5	···
RV change (km s^{-1})	10.1	54.3	6.0	4.7	8.1	···

- Shell classification: normal
- Notes on emission and absorption features: He I λ6678 is unreliable for RV studies as it is filled in.
- Other notes: This star is also plotted in Figure 7.2.

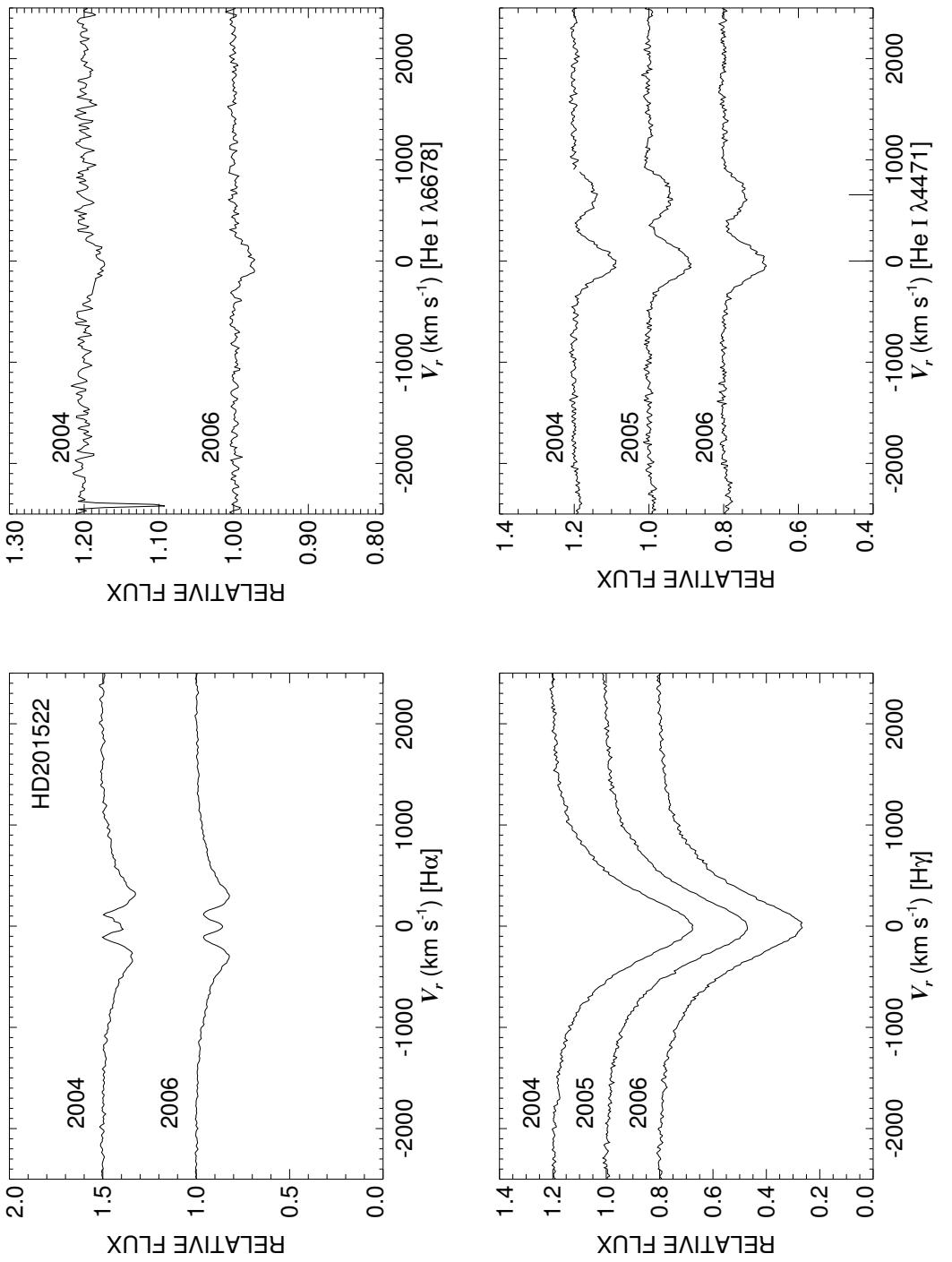

Figure C.118: A quadruple plot of HD201522 as described in §7.2.3 and Figure 7.6.

HD201733

Classical Be Star; Non-Radial Pulsator?

- Other Names: HR 8103, V2148 Cyg
- Spectral Type: B4 IVp
- V magnitude: 6.47
- In WDS?: no
- Known spectroscopic binary?: no
- Velocity variations seen in these data?: no

	Hα	He I λ6678	Hγ	He I λ4471	Mg II λ4481	Fe II ccfs
Mean RV (km s^{-1})	19.2	22.7	14.0	-5.2	13.9	···
RV range (km s^{-1})	14.4 to 21.8	-7.2 to 39.2	12.6 to 17.1	-7.1 to -0.8	4.6 to 33.7	···
RV change (km s^{-1})	7.4	46.4	4.5	6.3	29.1	···

- Shell classification: normal
- Notes on emission and absorption features: Despite a lack of shell features, Hα shows strong central absorption. The helium lines may show some evidence for NRP. Mg II λ4481 is very broad and very blended, thus it is useless for RV studies.
- Other notes:

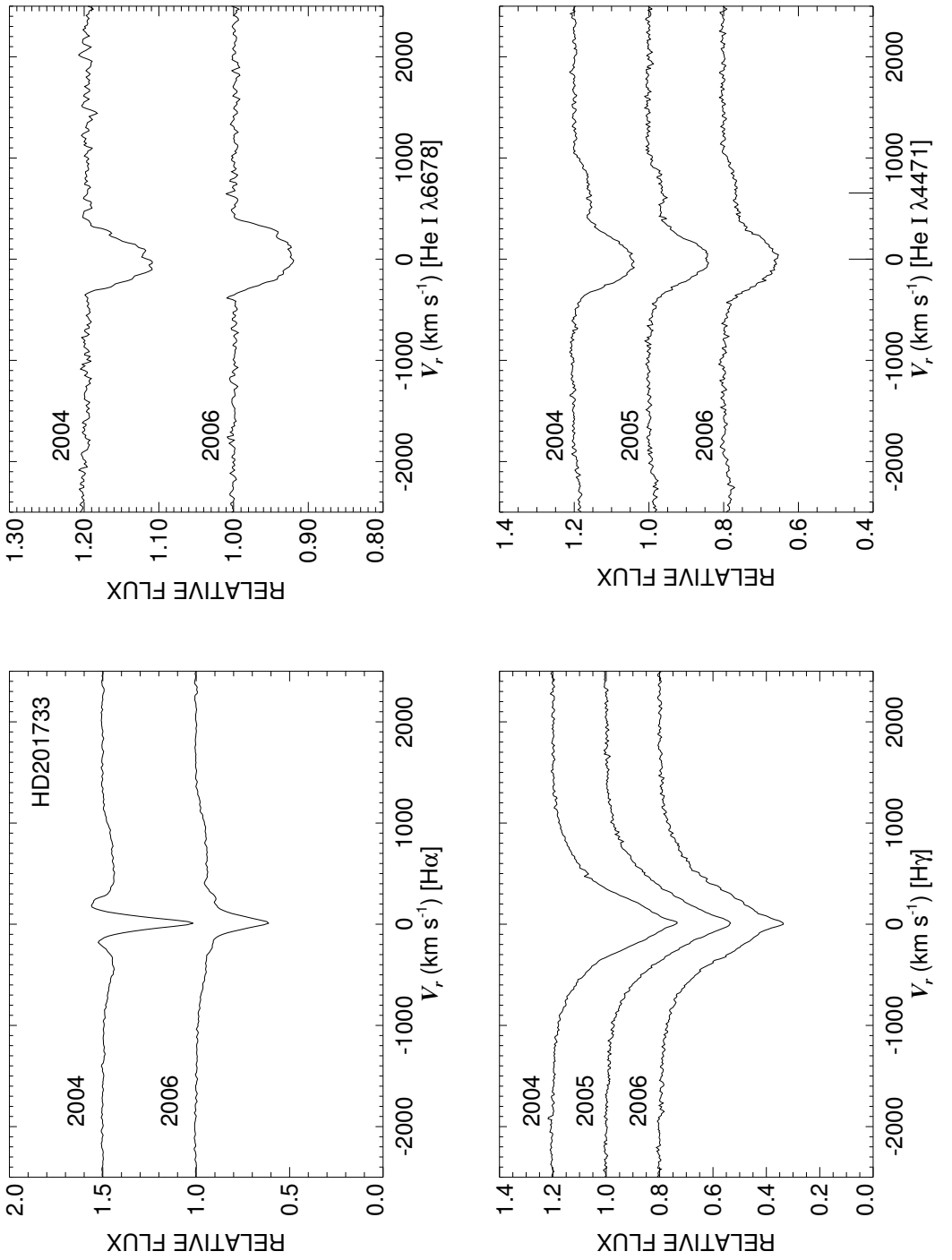

Figure C.119: A quadruple plot of HD201733 as described in §7.2.3 and Figure 7.6.

HD202904

Classical Be Star

- Other Names: HR 8146, 66 Cyg, υ Cyg
- Spectral Type: B2.5 Vne
- V magnitude: 4.32
- In WDS?: yes - 10.0, 9.95, and 12.0 mag companions 15.1, 21.8, and 57 arcsec away (discovered in 1849 and 1982)
- Known spectroscopic binary?: no
- Velocity variations seen in these data?: yes (see Fig. C.121)

	Hα	He I λ6678	Hγ	He I λ4471	Mg II λ4481	Fe II ccfs
Mean RV (km s^{-1})	-0.8	1.8	-7.5	-8.2	-6.8	-8.6
RV range (km s^{-1})	-3.9 to 1.7	-1.5 to 6.4	-16.0 to 4.8	-14.9 to 1.5	-44.6 to 8.8	-20.2 to 1.5
RV change (km s^{-1})	5.6	7.9	20.8	16.4	53.4	21.7

- Shell classification: emission shell (decreases by 2006)
- Do shell features move with the star?: yes
- Notes on emission and absorption features: Very large Hα emission. Both He I λ6678 and Mg II λ4481 show emission horns. Hγ shows rapid changes in peak morphology (see the 2004/6 data in Fig. C.121). The blue absorption line profiles morph in the same direction as the shell features shift.
- Other notes:

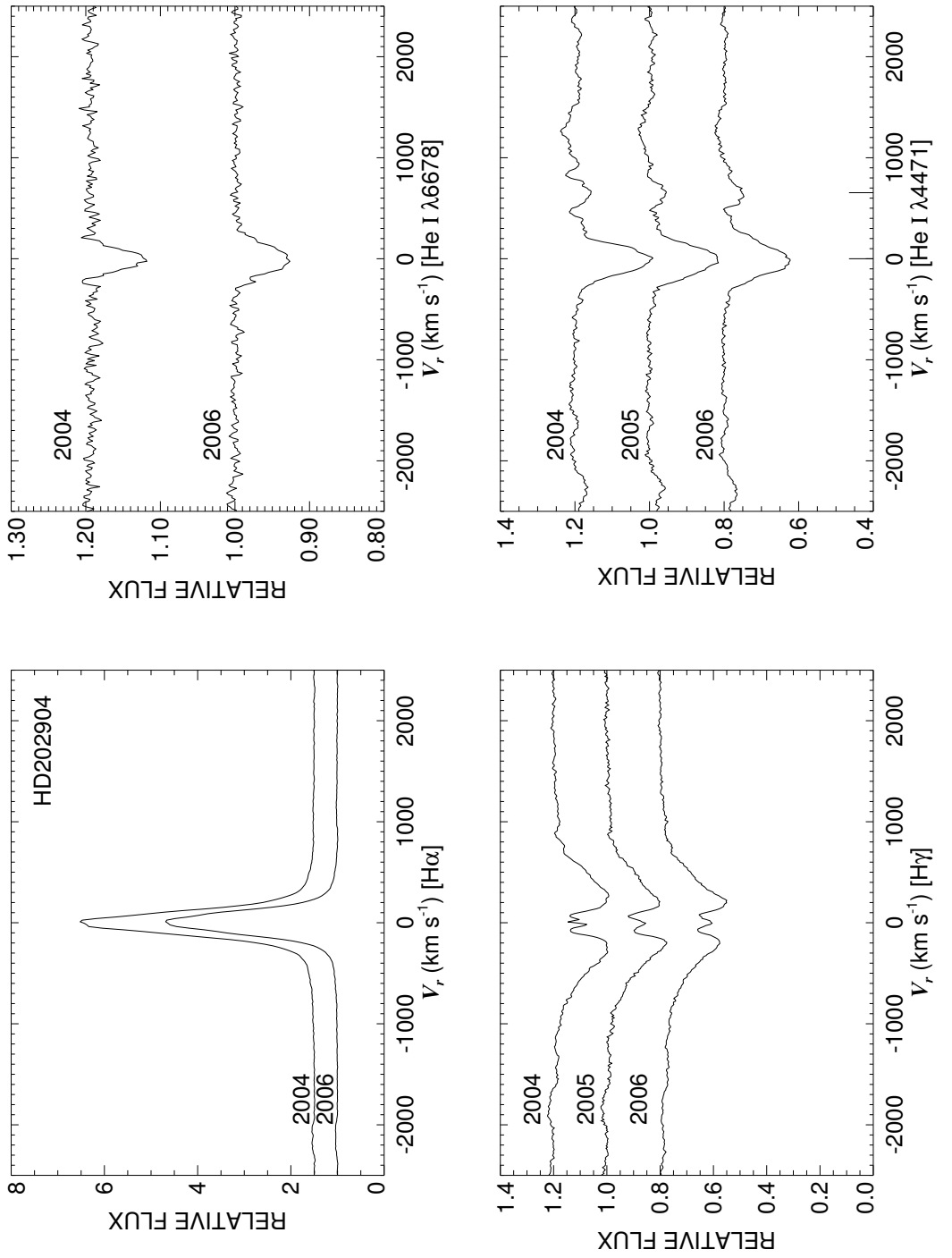

Figure C.120: A quadruple plot of HD202904 as described in §7.2.3 and Figure 7.6.

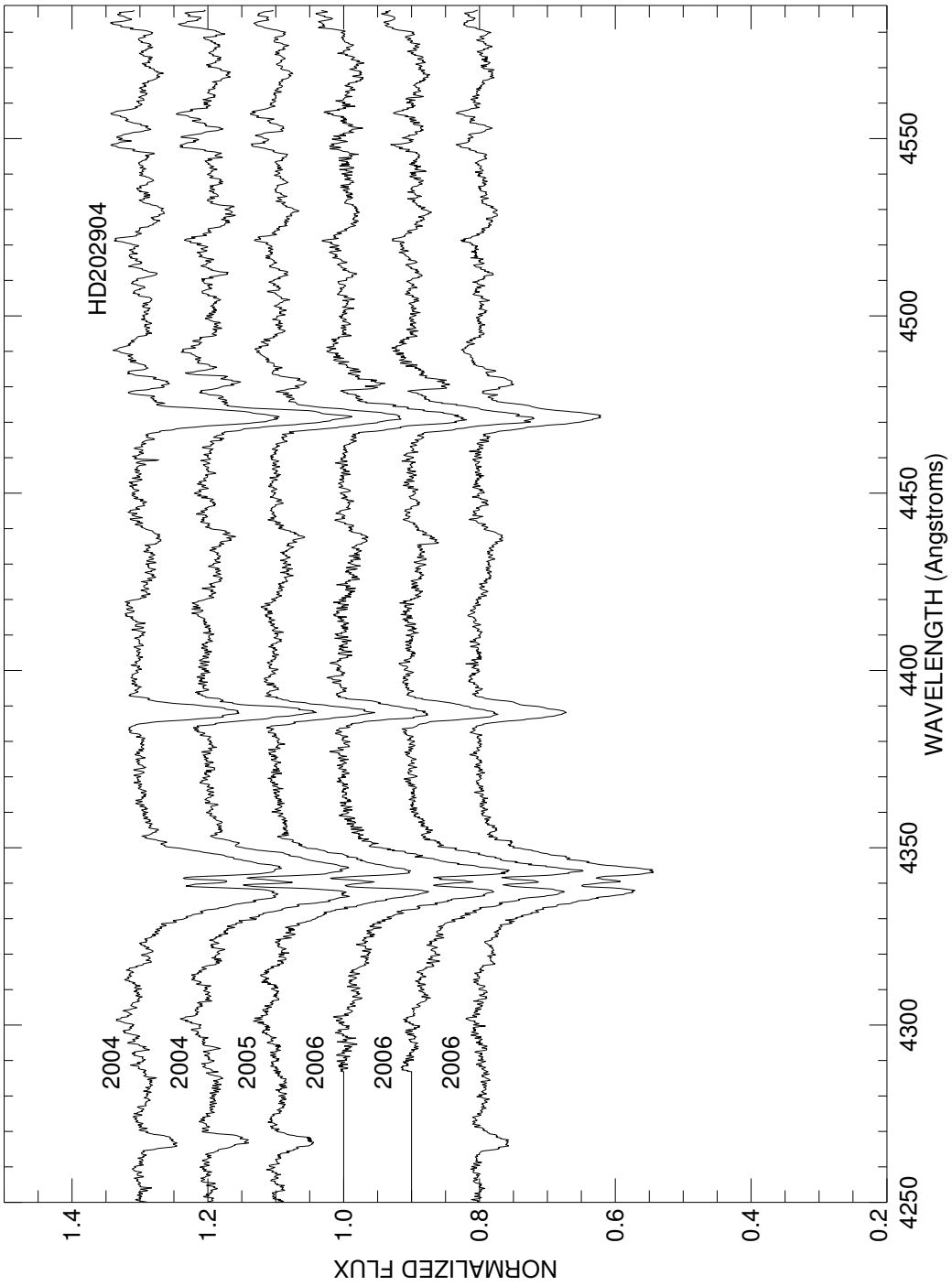

Figure C.121: A plot of all spectra of HD202904 in the blue region. Each is labeled with the year of observation and they are offset for clarity.

HD203025

Classical Be Star

- Other Names: HR 8153
- Spectral Type: B2 IIIe
- V magnitude: 6.58
- In WDS?: yes - 12 and 12.6 mag companions 4.0 and 68 arcsec away (discovered in 1889 and 1912)
- Known spectroscopic binary?: yes - it is a triple spectroscopic system as reported by Harmanec (2001) however there is some uncertainty here as one estimate came from 1926 and then other people did work but did not give details. Harmanec suggests a new campaign of spectroscopic and photometric study. Some periods suggested are 1.365, 3.183, 5.413, and 225.44 d.
- Velocity variations seen in these data?: yes (see Fig. C.123)

	Hα	He I λ6678	Hγ	He I λ4471	Mg II λ4481	Fe II ccfs
Mean RV (km s^{-1})	-15.9	-22.3	-7.3	-42.0	-50.7	···
RV range (km s^{-1})	-25.6 to -4.6	-31.4 to -4.9	-19.5 to 9.4	-56.2 to -23.9	-78.0 to -24.2	···
RV change (km s^{-1})	21.0	26.5	28.9	32.3	53.8	···

- Shell classification: normal
- Notes on emission and absorption features: Hα gets slightly weaker in 2006. He I λ6678 may have a red emission horn. All blue absorption lines show FAST radial velocity shifts (see the two 2004 spectra especially). Very distinct Si III $\lambda\lambda 4552, 4567, 4574$ features that move with the star (they are produced in hot stars).
- Other notes:

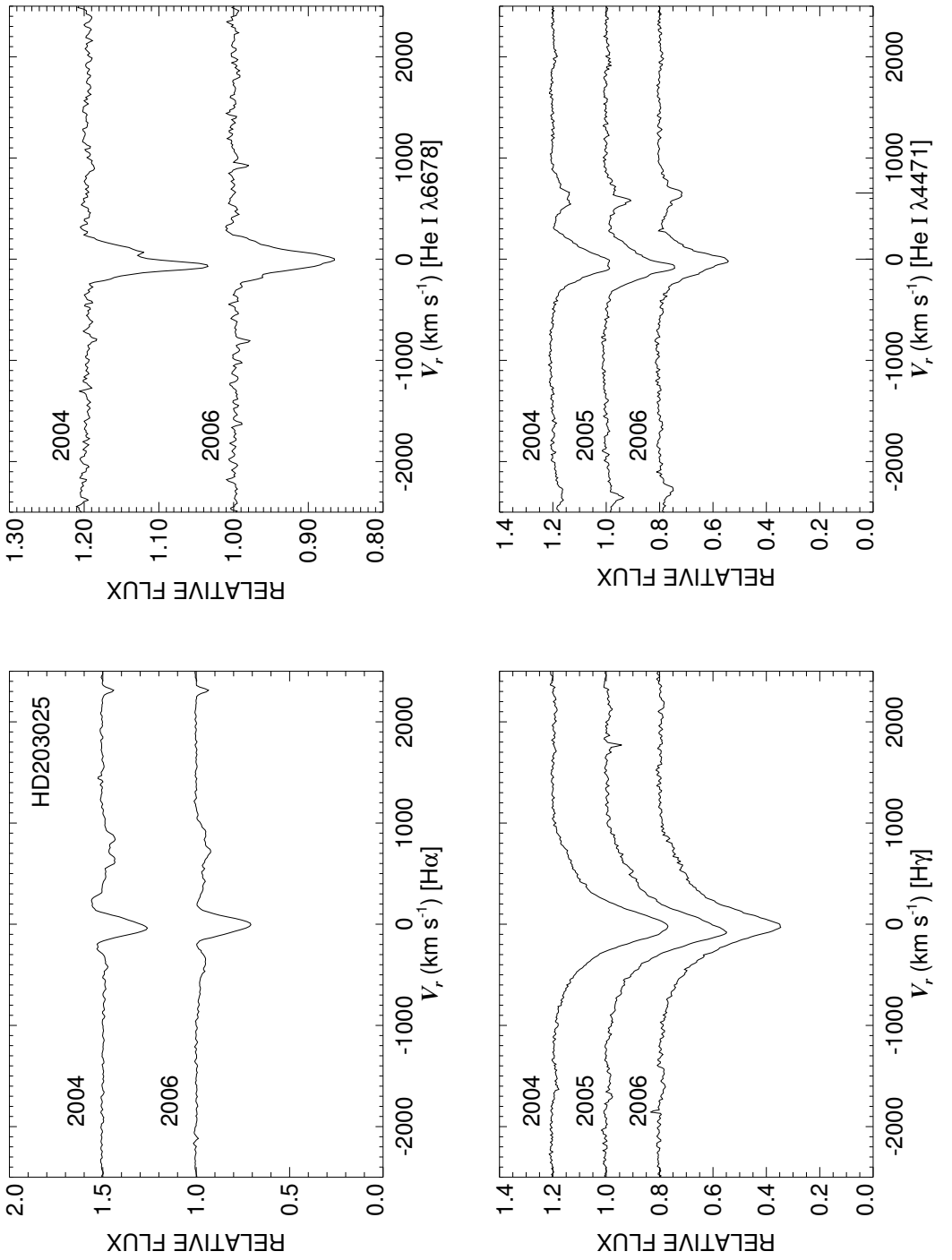

Figure C.122: A quadruple plot of HD203025 as described in §7.2.3 and Figure 7.6.

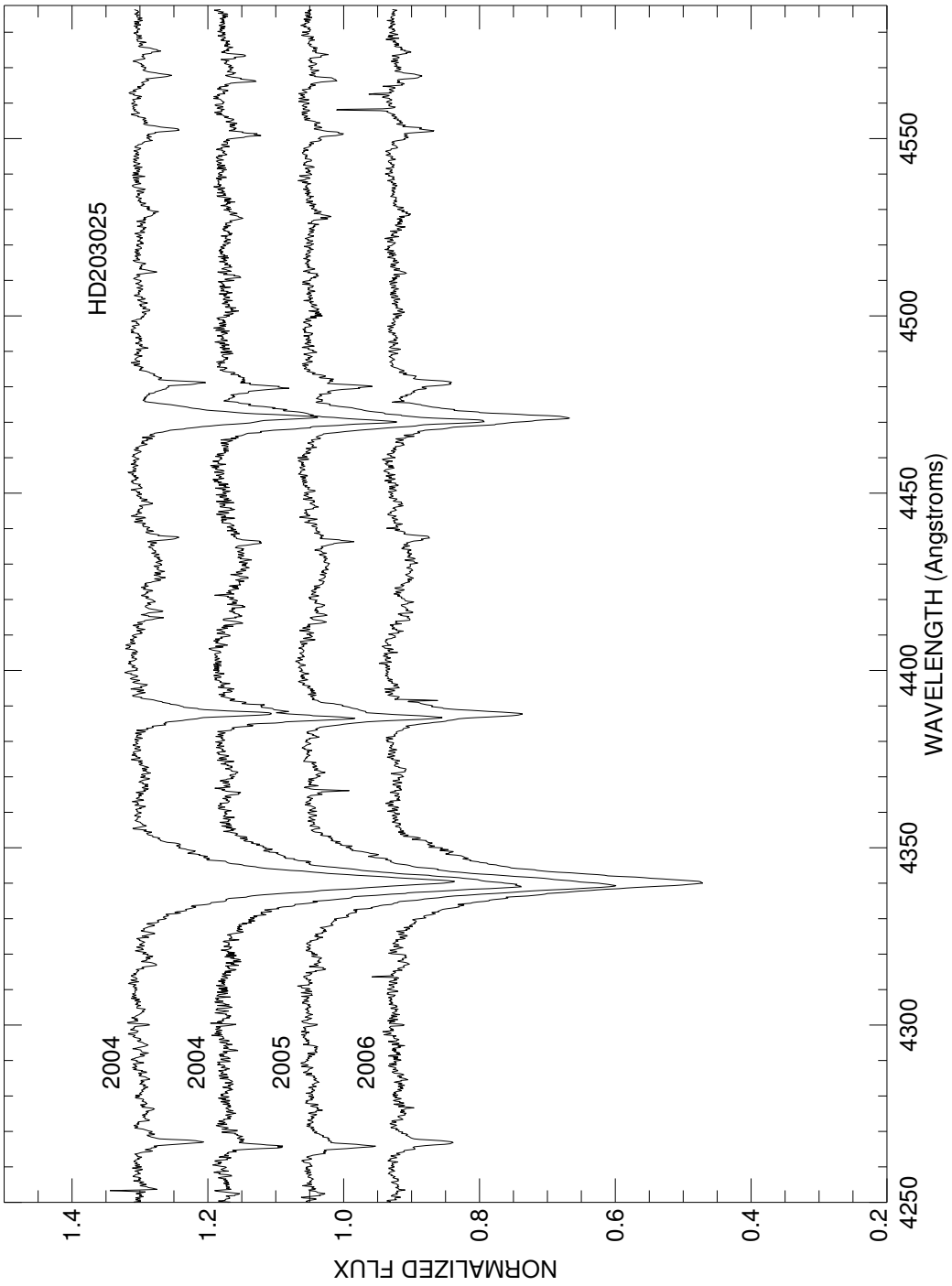

Figure C.123: A plot of all spectra of HD203025 in the blue region. Each is labeled with the year of observation and they are offset for clarity.

HD203064

NOT Be Star

- Other Names: HR 8154, 68 Cyg
- Spectral Type: O7.5 III((f))
- V magnitude: 4.98
- In WDS?: no
- Known spectroscopic binary?: no
- Velocity variations seen in these data?: no

	Hα	He I λ6678	Hγ	He I λ4471	Mg II λ4481	Fe II ccfs
Mean RV (km s^{-1})	-1.0	132.1	18.4	20.6	···	···
RV range (km s^{-1})	-8.1 to 6.1	123.5 to 143.3	10.9 to 21.4	13.9 to 25.4	···	···
RV change (km s^{-1})	14.2	19.8	10.5	11.5	···	···

- Shell classification: normal
- Notes on emission and absorption features: no emission currently visible. The large RV value for He I λ6678 is due to a blend with He II λ6683. Mg II λ4481 is practically non-existent (as is often the case in such hot stars).
- Other notes: According to an excellent study by Negueruela et al. (2004), this star is "at best, a very mild member of the [Oe] class." The first (and only to date) report of emission was from Wilson (1958). This star was eliminated from all statistics in Chapter 7 (on the grounds it is not an emission star and it is an O star).

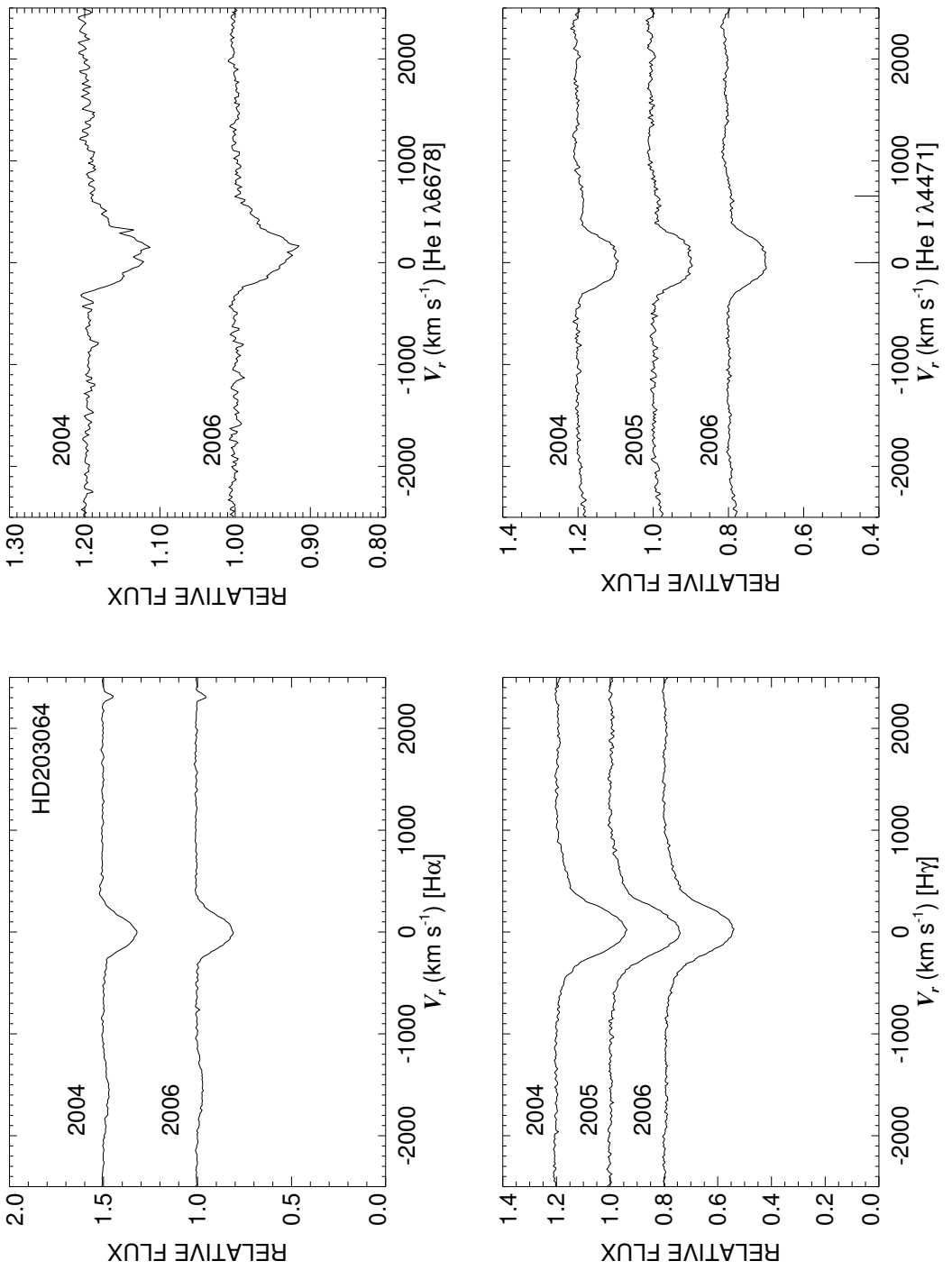

Figure C.124: A quadruple plot of HD203064 as described in §7.2.3 and Figure 7.6.

HD203374

Classical Be Star

- Other Names:
- Spectral Type: B0 IVpe
- V magnitude: 6.91
- In WDS?: yes - a 9.12 mag speckle companion 0.3 arcsec away (discovered in 1991) and 10.30 and 12.7 mag companions 45 and 2.8 arcsec away from the speckle pair (discovered in 1902)
- Known spectroscopic binary?: no
- Velocity variations seen in these data?: yes?? (Hα line)

	Hα	He I λ6678	Hγ	He I λ4471	Mg II λ4481	Fe II ccfs
Mean RV (km s^{-1})	-21.4	···	56.7	-27.4	···	-36.8
RV range (km s^{-1})	-31.5 to -16.2	···	31.1 to 80.1	-44.7 to -10.7	···	-47.0 to -32.5
RV change (km s^{-1})	15.3	···	49.0	34.0	···	14.5

- Shell classification: emission shell
- Do shell features move with the star?: yes
- Notes on emission and absorption features: Very strong Hα emission that has a distinct RV shift (despite nothing else showing that kind of shift - it could be asymmetry in the disk). Unusually strong emission in both He I λ6678 and Hγ. Hγ shows morphological changes. Emission horns also present in Mg II λ4481 (line almost totally filled in).
- Other notes: This star is also plotted in Figure 7.4.

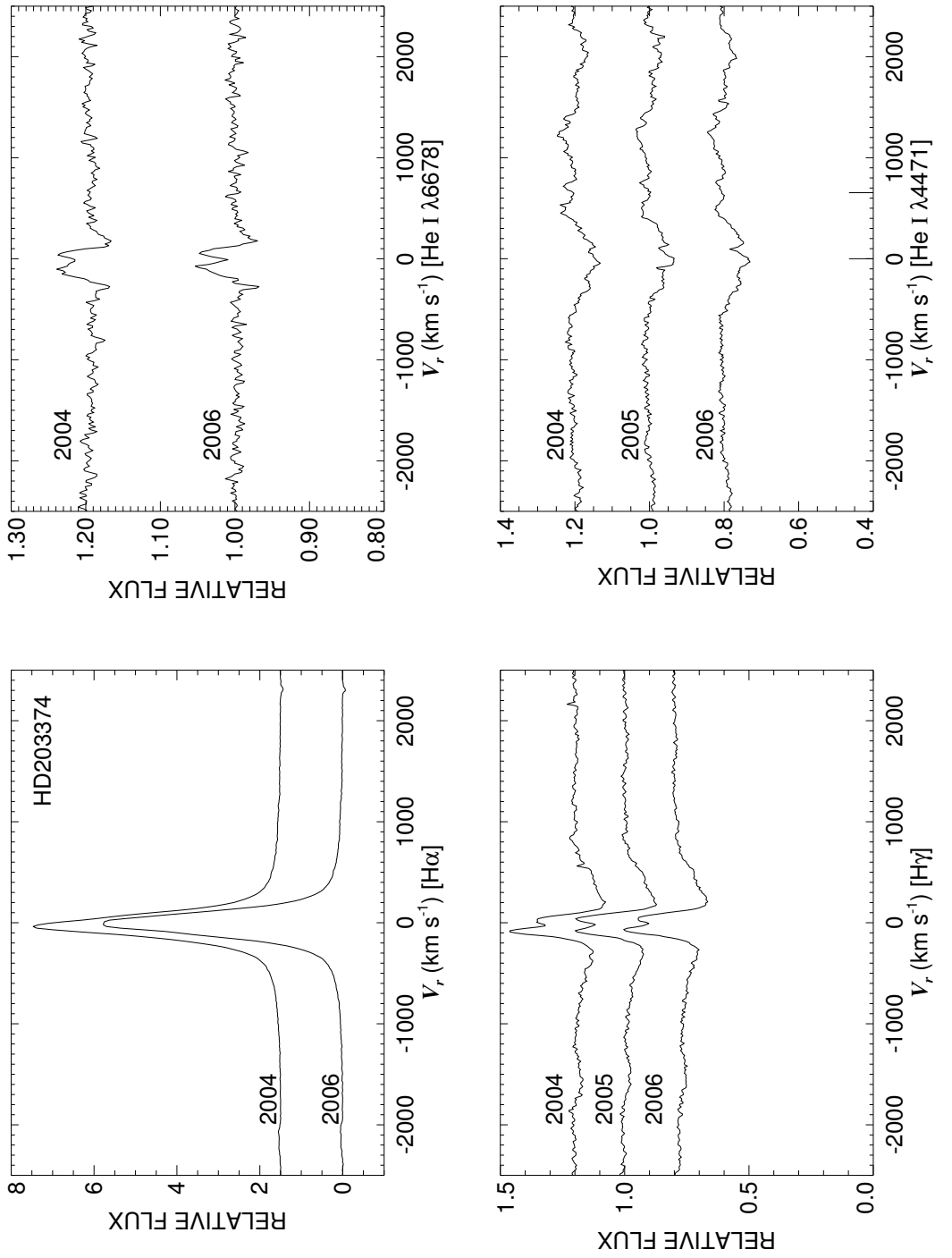

Figure C.125: A quadruple plot of HD203374 as described in §7.2.3 and Figure 7.6.

HD203467

Classical Be Star; Non-Radial Pulsator?

- Other Names: HR 8171, 6 Cep, V382 Cep
- Spectral Type: B2.5 Ve+sh
- V magnitude: 5.13
- In WDS?: no
- Known spectroscopic binary?: yes and no - Harmanec (2001) reports that a period of 2.4389 d exists, but even the person who found that thinks the period is a result of rapid line-profile changes rather than orbital motion.
- Velocity variations seen in these data?: yes (companion or NRP?)

	Hα	He I λ6678	Hγ	He I λ4471	Mg II λ4481	Fe II ccfs
Mean RV (km s^{-1})	-11.9	-31.2	-8.1	-10.8	-5.8	-22.1
RV range (km s^{-1})	-14.3 to -9.9	-35.7 to -27.9	-19.3 to 0.7	-17.0 to -5.9	-18.2 to 1.6	-44.5 to -7.2
RV change (km s^{-1})	4.4	7.8	20.0	11.1	19.8	37.3

- Shell classification: emission shell
- Do shell features move with the star?: they don't move, so I suspect NRP for the velocity variations in the blue features.
- Notes on emission and absorption features: Very strong Hα emission. Hγ emission is stronger in 2005 than 2004/6. Emission horns in Mg II λ4481. Blue absorption lines (esp. He I λ4471 and Mg II λ4481) show rapid profile changes (NRP?).
- Other notes:

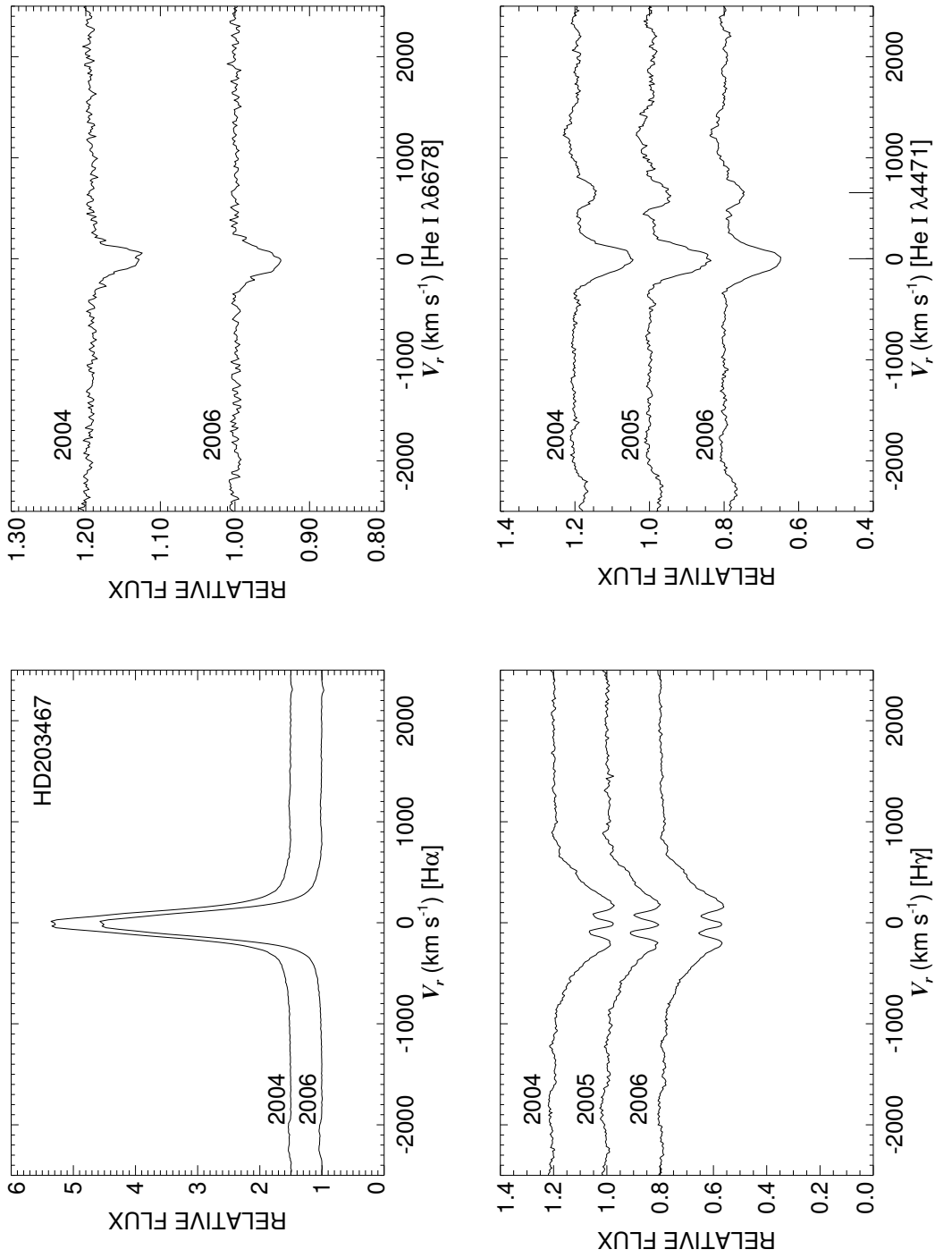

Figure C.126: A quadruple plot of HD203467 as described in §7.2.3 and Figure 7.6.

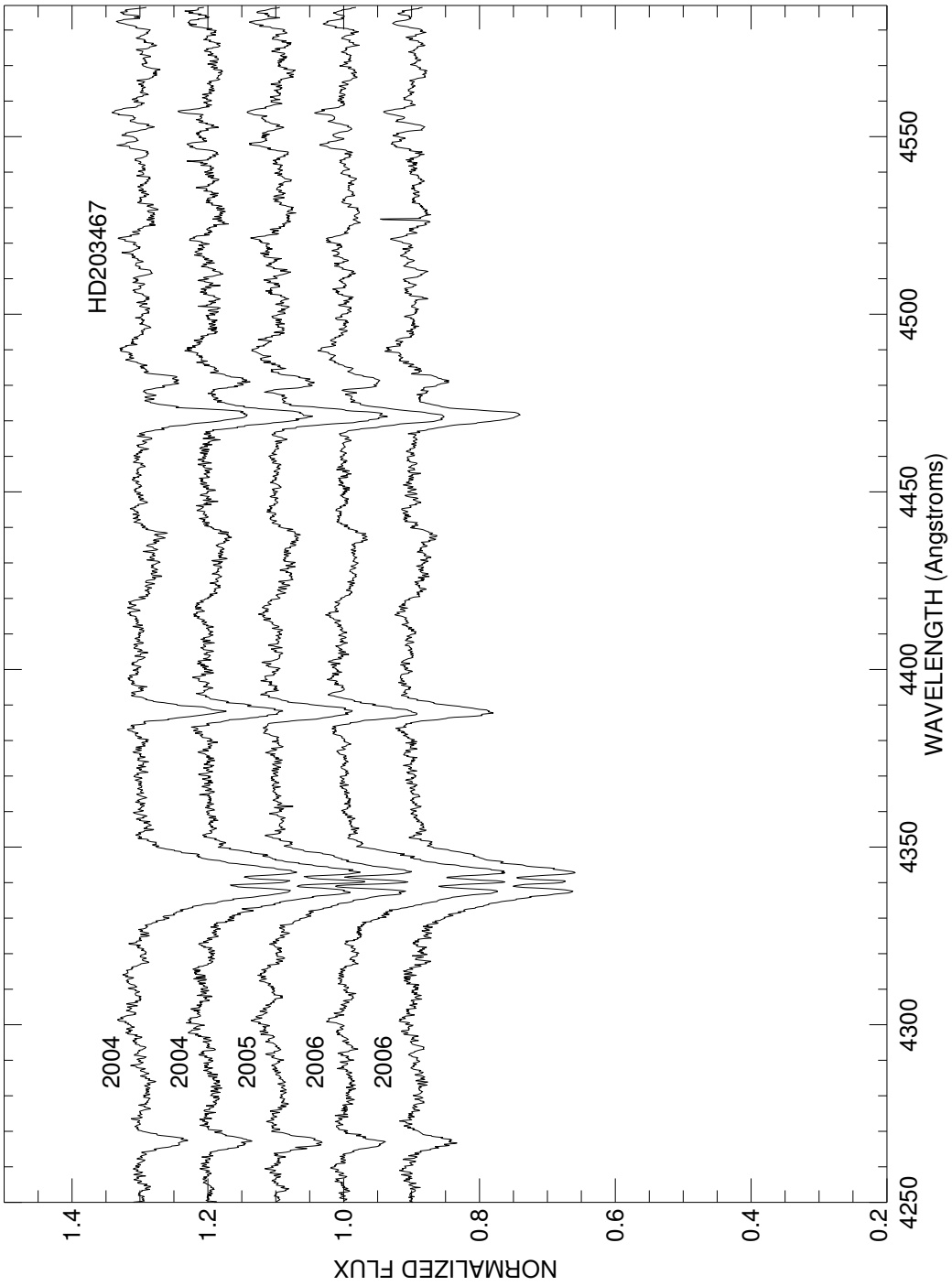

Figure C.127: A plot of all spectra of HD203467 in the blue region. Each is labeled with the year of observation and they are offset for clarity.

HD203699

Classical Be Star

- Other Names:
- Spectral Type: B3 IV
- V magnitude: 6.75
- In WDS?: no
- Known spectroscopic binary?: no
- Velocity variations seen in these data?: no

	Hα	He I λ6678	Hγ	He I λ4471	Mg II λ4481	Fe II ccfs
Mean RV (km s^{-1})	0.5	-0.6	3.3	-8.2	-5.2	-2.4
RV range (km s^{-1})	-0.7 to 1.2	-8.0 to 5.4	1.4 to 4.8	-10.2 to -3.8	-11.8 to 2.0	-22.6 to 10.2
RV change (km s^{-1})	1.9	13.4	3.4	6.4	13.8	32.8

- Shell classification: emission shell (decreases from 2004 to 2006 - see Fig. C.129)
- Do shell features move with the star?: N/A
- Notes on emission and absorption features: Strong Hα emission. Emission horns in He I λ6678 and Mg II λ4481 disappear by 2006 (like the shell features).
- Other notes:

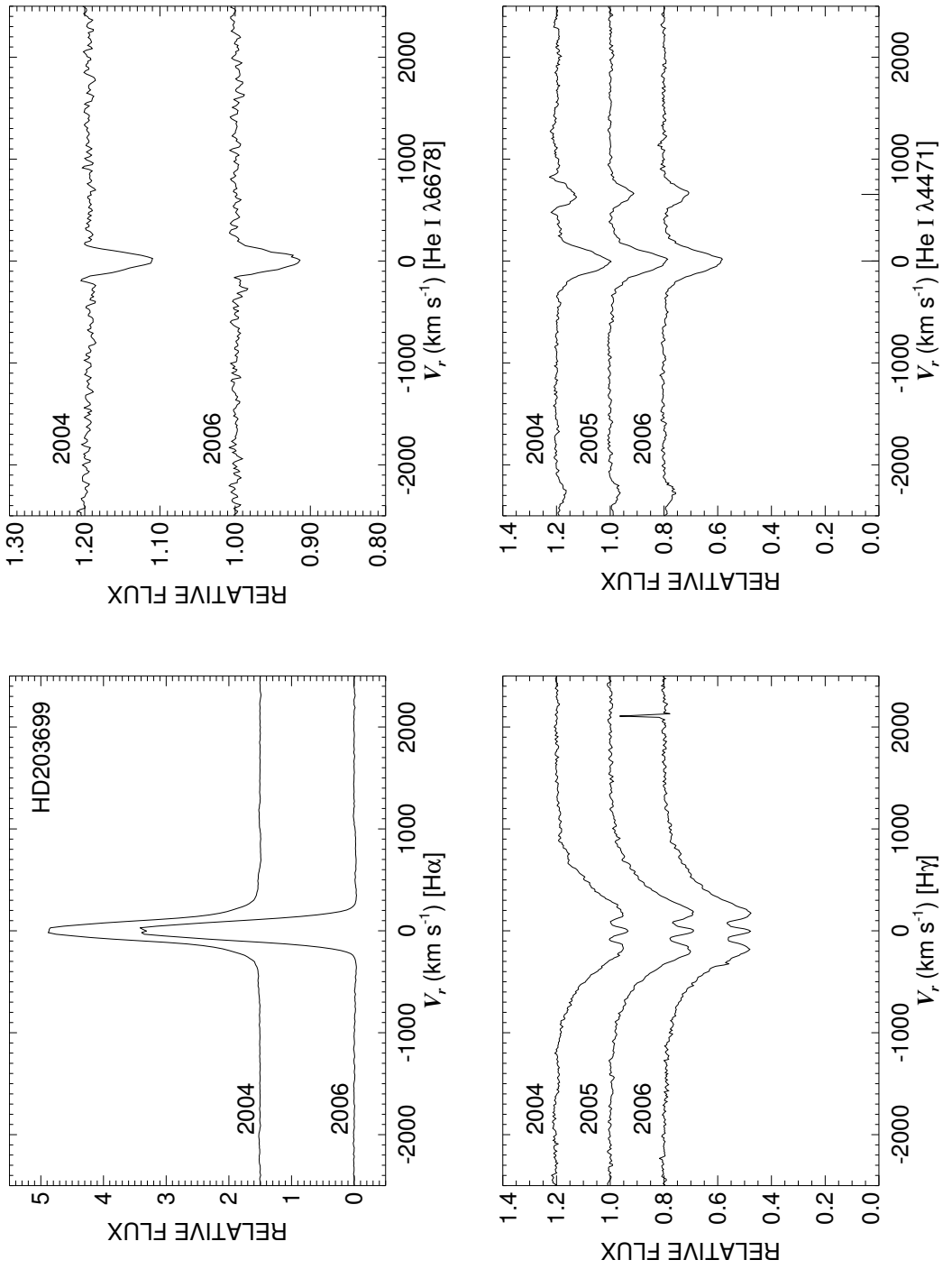

Figure C.128: A quadruple plot of HD203699 as described in §7.2.3 and Figure 7.6.

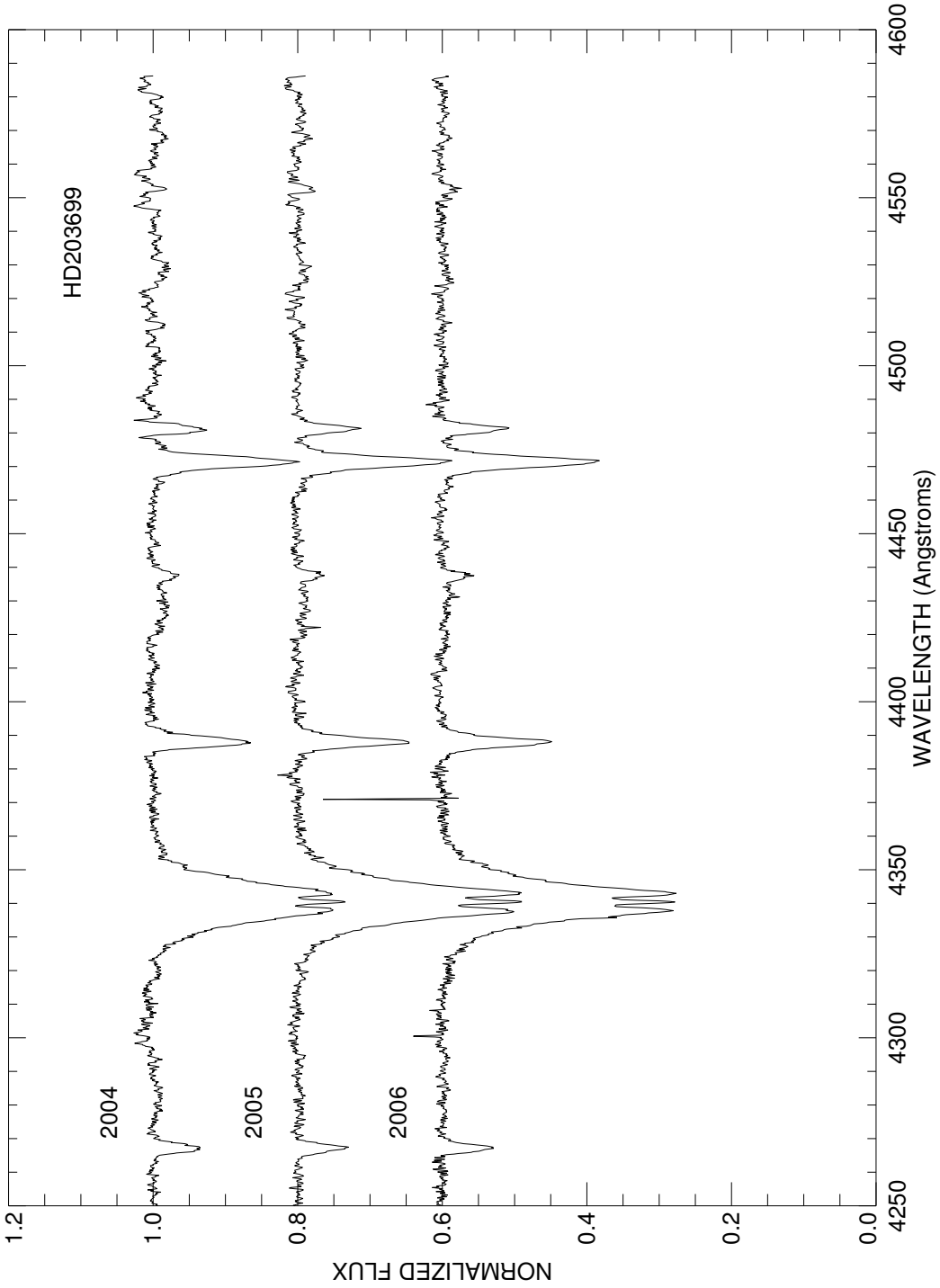

Figure C.129: A plot of the averages for each run in the blue region of HD203699. Each is labeled with the year of observation and they are offset from each other for clarity.

HD203731

Classical Be Star

- Other Names: V2153 Cyg
- Spectral Type: B1 Vne
- V magnitude: 7.67
- In WDS?: no
- Known spectroscopic binary?: no
- Velocity variations seen in these data?: possibly

	Hα	He I λ6678	Hγ	He I λ4471	Mg II λ4481	Fe II ccfs
Mean RV (km s^{-1})	-24.3	-11.2	-0.6	-49.0	-55.0	-40.4
RV range (km s^{-1})	-32.0 to -12.1	-60.7 to 15.4	-14.2 to 19.8	-53.0 to -41.0	-109.5 to 17.2	-58.8 to -17.9
RV change (km s^{-1})	19.9	76.1	34.0	12.0	126.7	40.9

- Shell classification: emission shell
- Do shell features move with the star?: if it is moving then yes
- Notes on emission and absorption features: Strong, broad Hα emission that grows (and merges into one peak) in 2006. Emission horns in He I λ6678 and Mg II λ4481 (therefore unreliable RV measurements). Big morphological changes in Hγ emission.
- Other notes: This star is also plotted in Figure 7.4. It has only 19 references in SIMBAD (very small relatively) and has no papers written on just it.

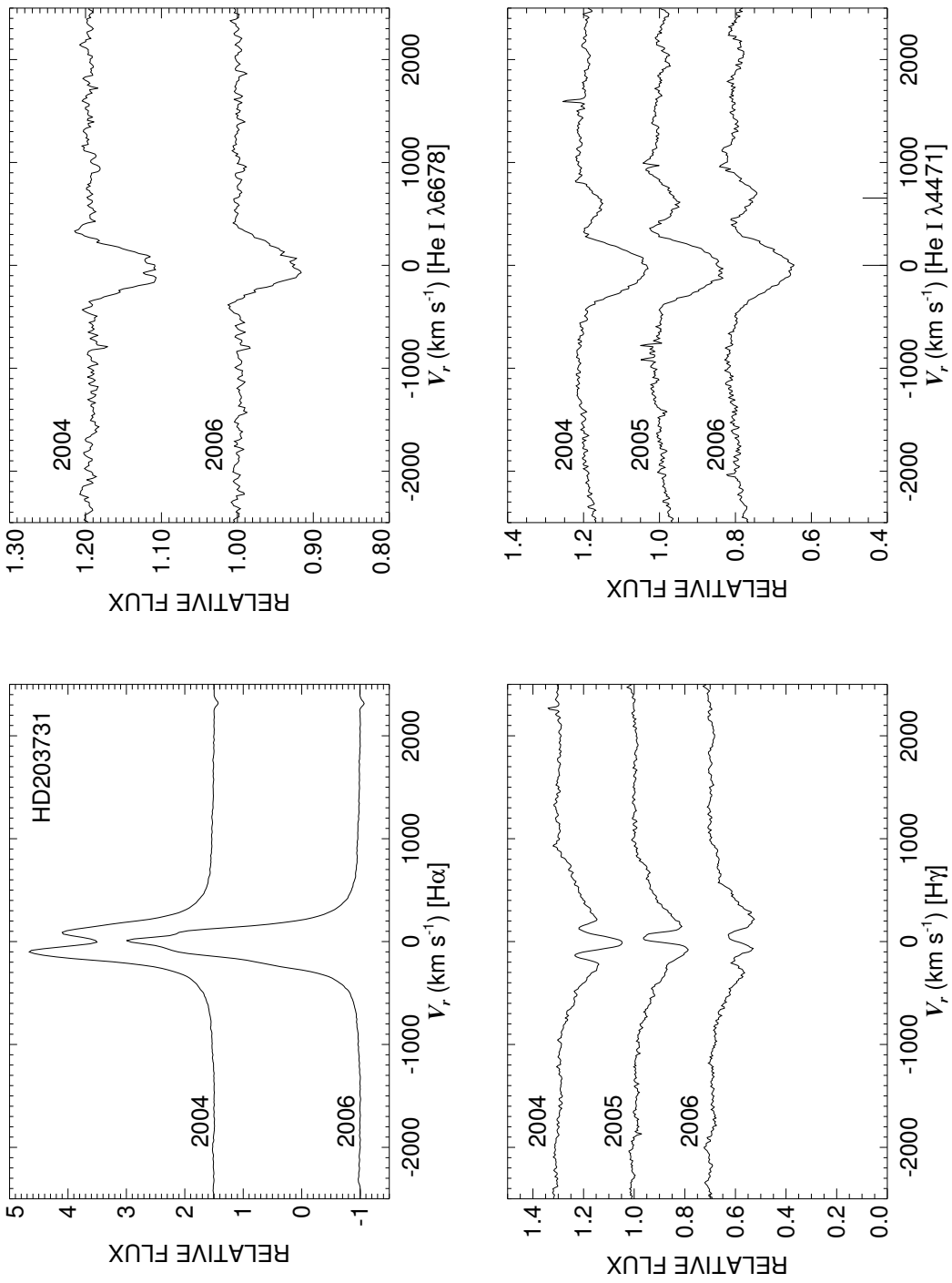

Figure C.130: A quadruple plot of HD203731 as described in §7.2.3 and Figure 7.6.

HD204116

Classical Be Star

- Other Names: V2155 Cyg
- Spectral Type: B1 Ve
- V magnitude: 7.99
- In WDS?: no
- Known spectroscopic binary?: no
- Velocity variations seen in these data?: no

	Hα	He I λ6678	Hγ	He I λ4471	Mg II λ4481	Fe II ccfs
Mean RV (km s^{-1})	-11.9	-43.5	48.4	-54.6	···	-37.1
RV range (km s^{-1})	-12.5 to -11.3	-49.0 to -37.9	41.8 to 54.7	-55.1 to -53.8	···	-42.5 to -32.6
RV change (km s^{-1})	1.2	11.1	12.9	1.3	···	9.9

- Shell classification: emission shell
- Do shell features move with the star?: N/A
- Notes on emission and absorption features: Very strong Hα emission. He I λ6678 is filled in. Emission in Hγ gets weaker from 2004 to 2006 and it also switches peaks. He I λ4471 appears affected by something (emission, absorption, NRP, by a companion)? Mg II λ4481 shows emission horns.
- Other notes: This star is also plotted in Figure 7.4.

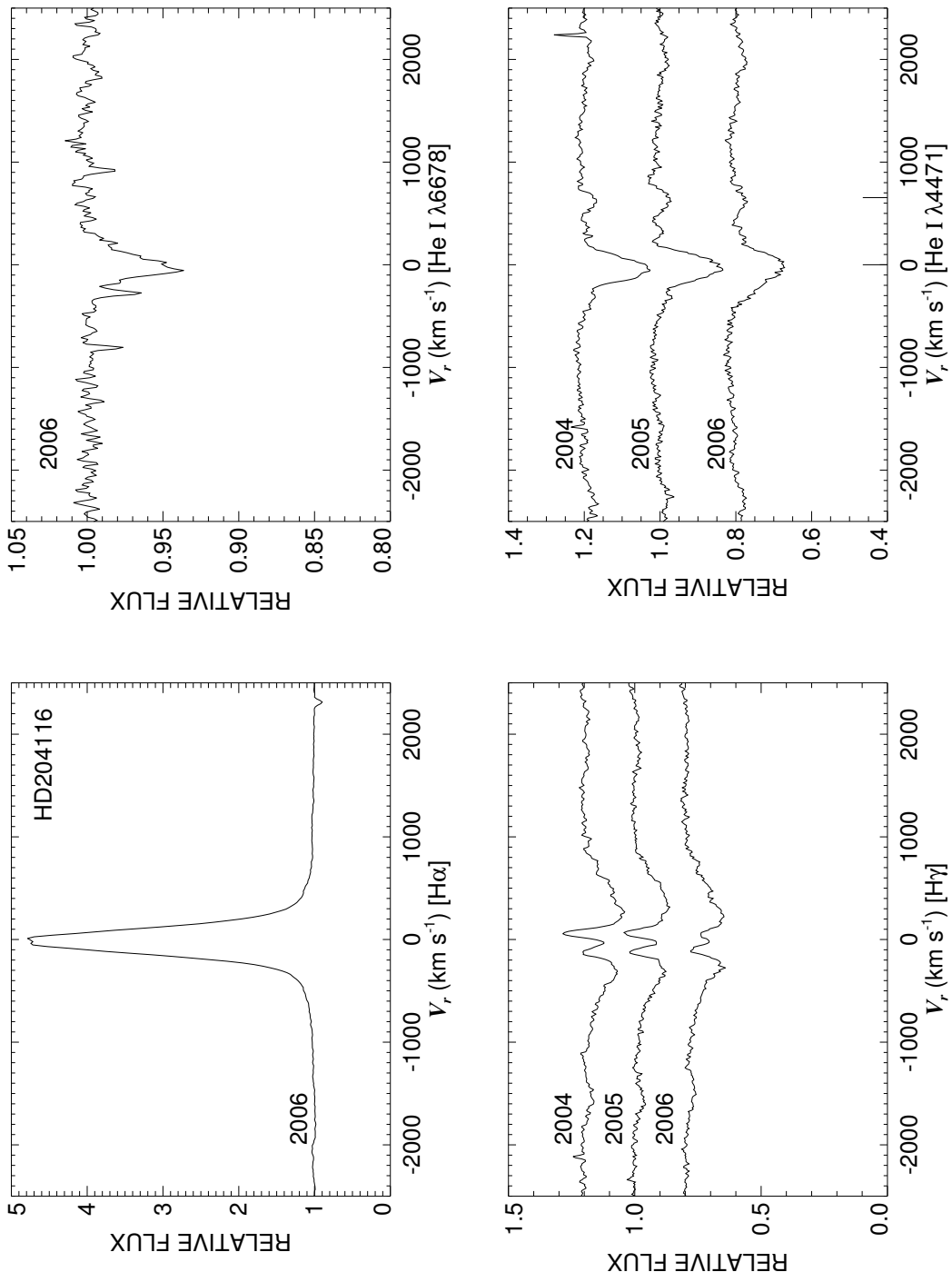

Figure C.131: A quadruple plot of HD204116 as described in §7.2.3 and Figure 7.6.

HD204722

Classical Be Star

- Other Names: V2162 Cyg
- Spectral Type: B2 Ve
- V magnitude: 7.61
- In WDS?: No
- Known spectroscopic binary?: no
- Velocity variations seen in these data?: maybe

	Hα	He I λ6678	Hγ	He I λ4471	Mg II λ4481	Fe II ccfs
Mean RV (km s^{-1})	-21.2	57.8	15.8	-44.2	-51.1	-20.6
RV range (km s^{-1})	-33.5 to -0.2	-36.4 to 126.6	6.5 to 33.5	-55.0 to -35.8	···	-46.6 to -3.0
RV change (km s^{-1})	33.3	163.0	27.0	19.2	···	43.6

- Shell classification: emission shell
- Do shell features move with the star?: if it moves then yes
- Notes on emission and absorption features: Pretty strong Hα emission (it grows in 2006) that also exhibits peak switching. He I λ6678 shows a distinct left emission horn in 2006. Distinct peak changes in Hγ emission.
- Other notes: This star is also plotted in Figure 7.4.

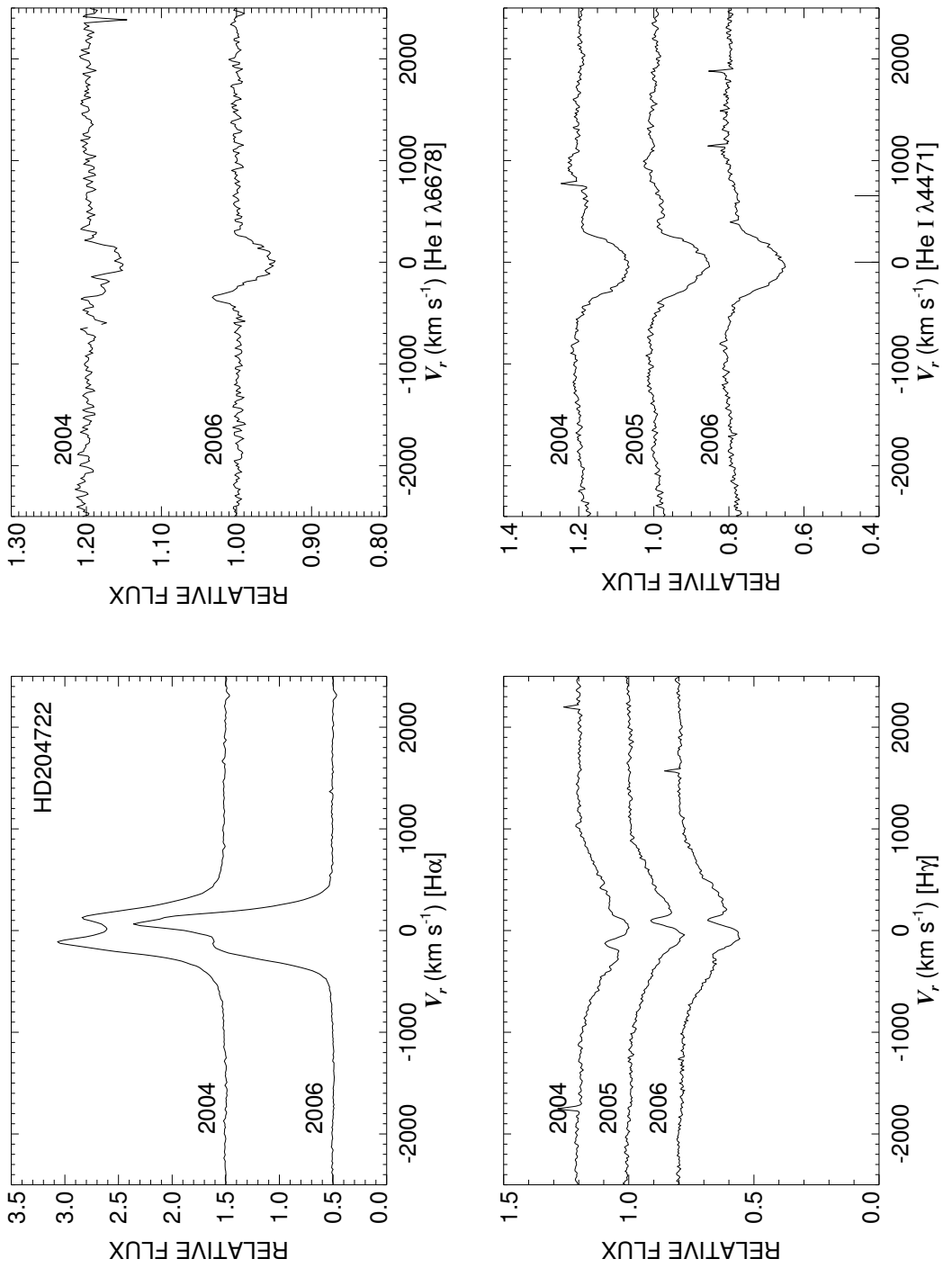

Figure C.132: A quadruple plot of HD204722 as described in §7.2.3 and Figure 7.6.

HD204860

Classical Be Star

- Other Names: V2163 Cyg
- Spectral Type: B4 Ve
- V magnitude: 6.90
- In WDS?: no
- Known spectroscopic binary?: no
- Velocity variations seen in these data?: possibly

	Hα	He I λ6678	Hγ	He I λ4471	Mg II λ4481	Fe II ccfs
Mean RV (km s^{-1})	-2.5	-17.6	-3.5	-20.9	-12.4	0.9
RV range (km s^{-1})	-10.2 to 4.6	-28.5 to -12.7	-11.3 to 5.7	-30.5 to -16.1	-22.9 to -2.0	-9.1 to 26.3
RV change (km s^{-1})	14.8	15.8	17.0	14.4	20.9	35.4

- Shell classification: squarish (big increase in 2005 but decreases again - see Fig. C.134)
- Do shell features move with the star?: can't tell
- Notes on emission and absorption features: Hα undergoes a big increase and has a quite strong central absorption. Mg II λ4481 deepens when the shell features deepen.
- Other notes:

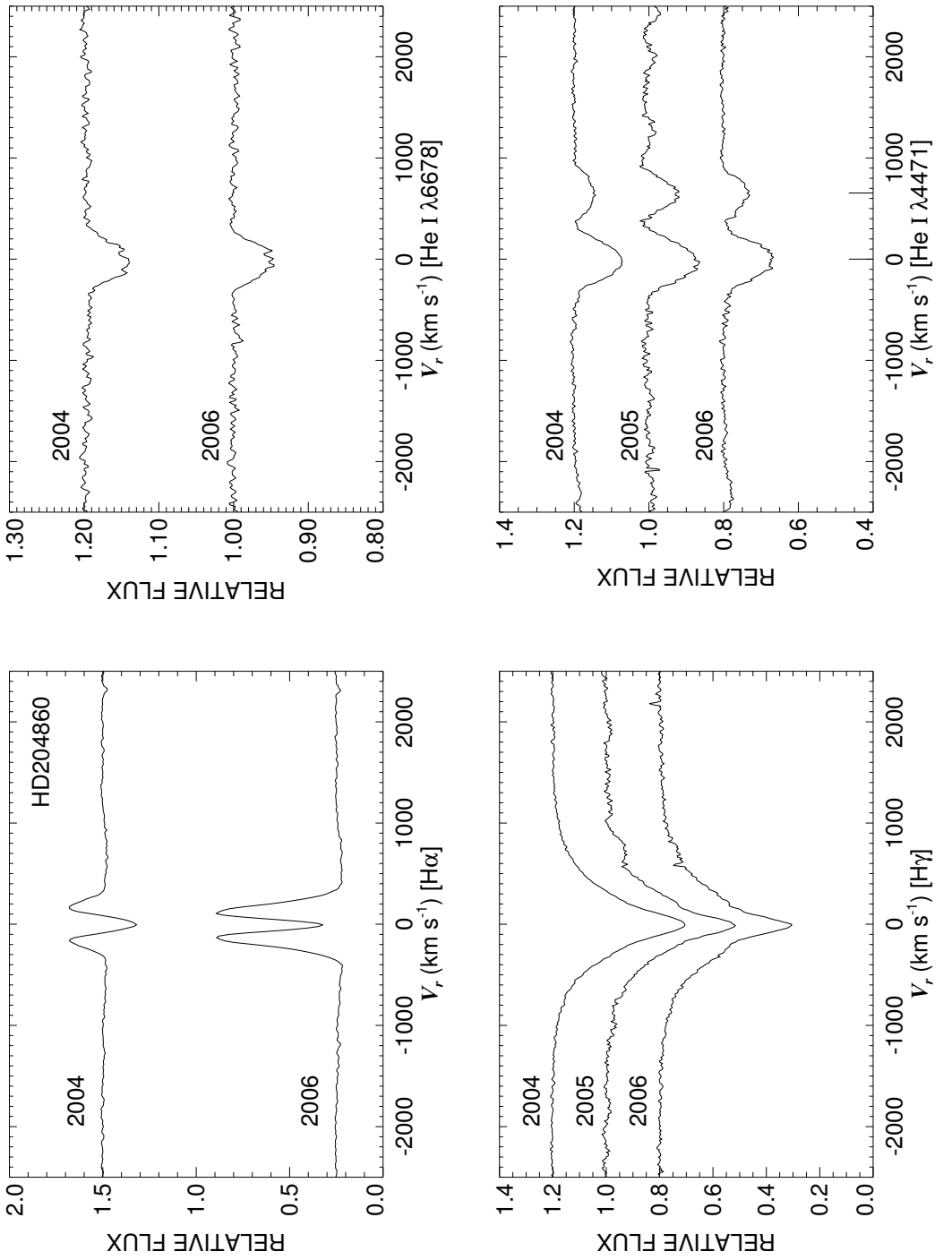

Figure C.133: A quadruple plot of HD204860 as described in §7.2.3 and Figure 7.6.

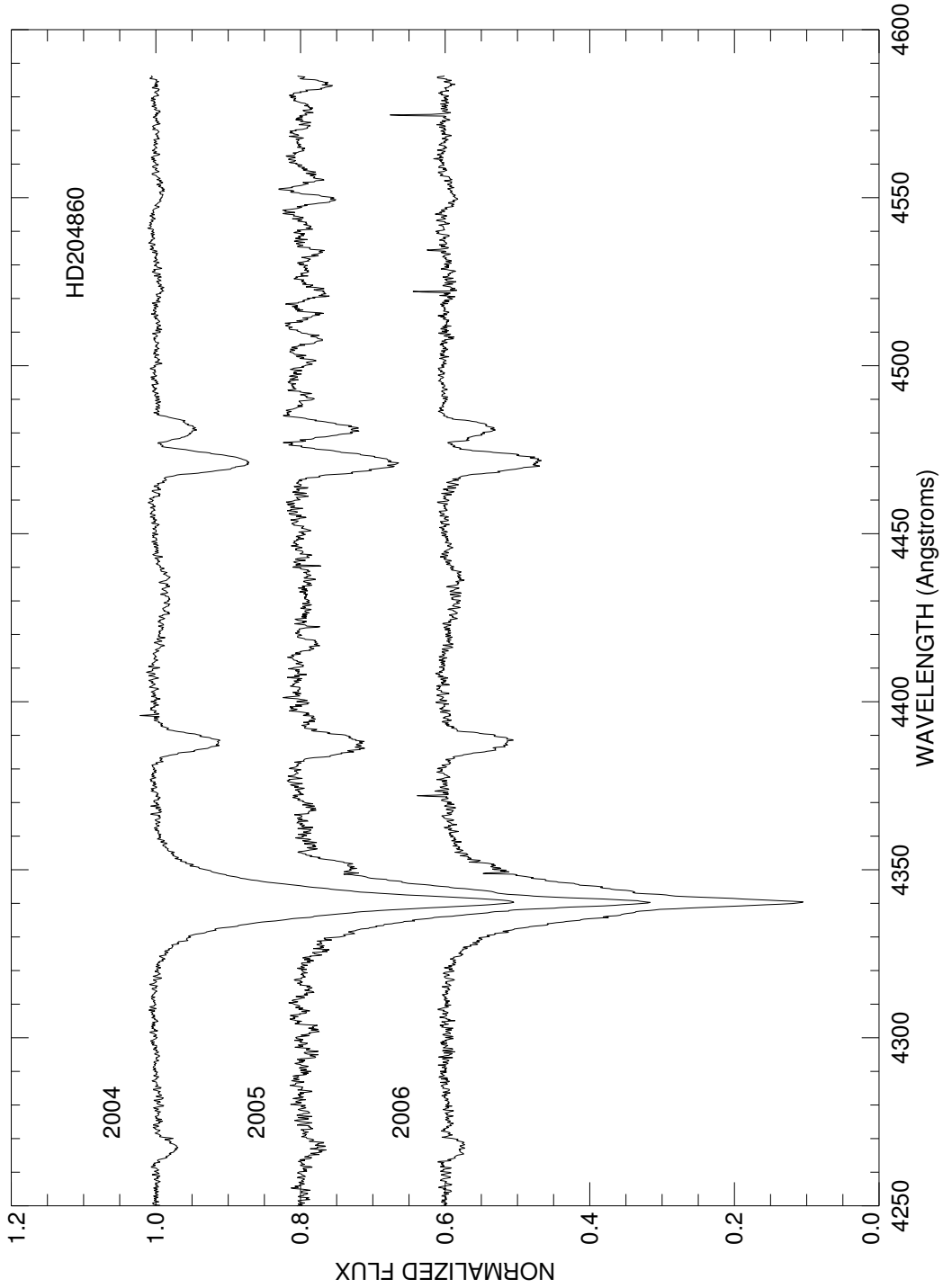

Figure C.134: A plot of the averages for each run in the blue region of HD204860. Each is labeled with the year of observation and they are offset from each other for clarity.

HD205060

Classical Be Star

- Other Names:
- Spectral Type: B6 Ve
- V magnitude: 7.18
- In WDS?: no
- Known spectroscopic binary?: no
- Velocity variations seen in these data?: yes (see Fig. C.135)

	Hα	He I λ6678	Hγ	He I λ4471	Mg II λ4481	Fe II ccfs
Mean RV (km s^{-1})	1.7	-31.5	-8.5	-17.3	-4.3	-10.6
RV range (km s^{-1})	-10.7 to 8.3	-48.9 to -9.7	-14.7 to -4.4	-22.6 to -9.1	-12.7 to 1.8	-32.0 to 32.0
RV change (km s^{-1})	19.0	39.2	10.3	13.5	14.5	64.1

- Shell classification: squarish
- Do shell features move with the star?: yes
- Notes on emission and absorption features: Hα grows slightly in 2006 and exhibits RV variations (shifted to the right). He I λ6678 appears filled in.
- Other notes: This star is also plotted in Figure 7.3.

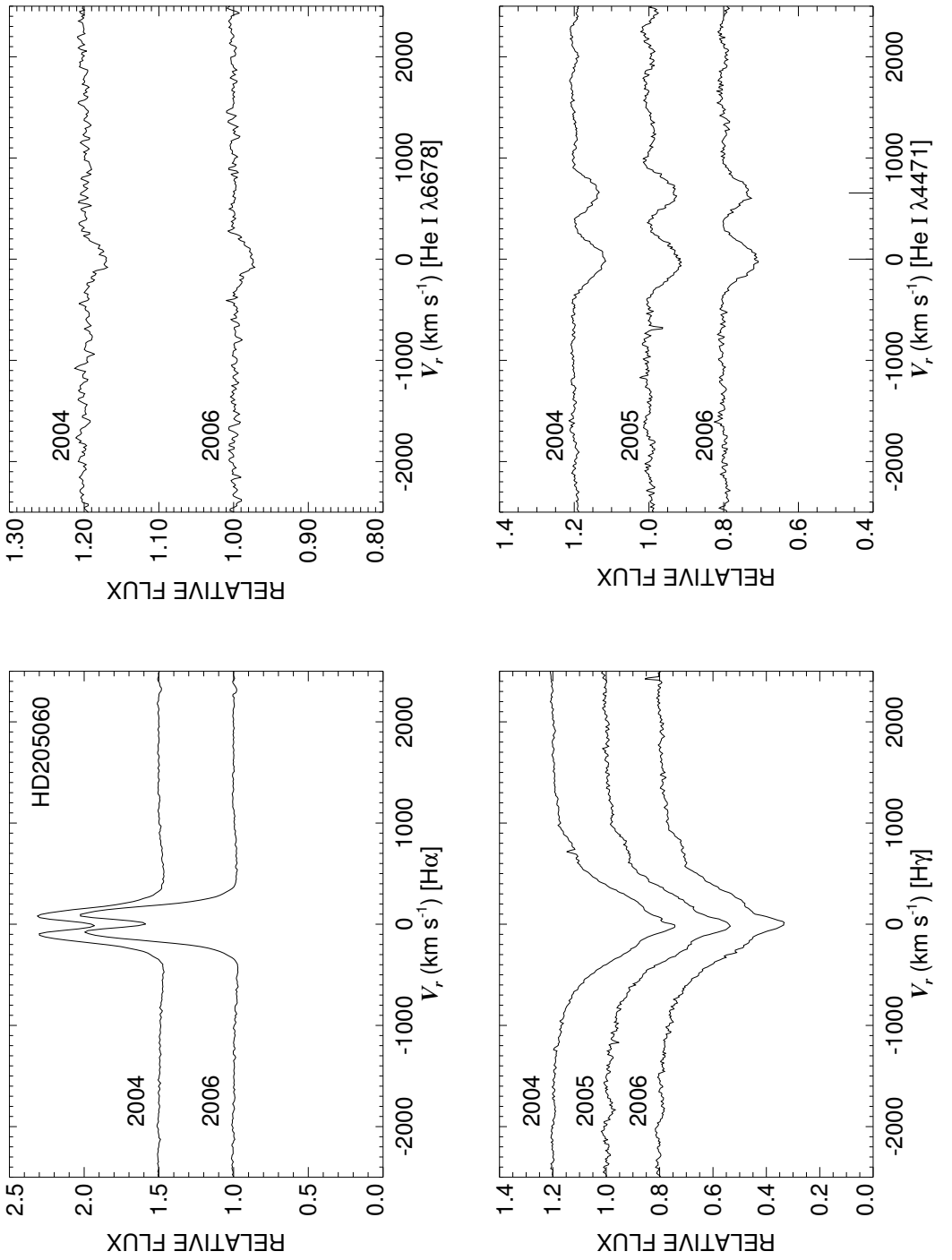

Figure C.135: A quadruple plot of HD205060 as described in §7.2.3 and Figure 7.6.

HD205551

Classical Be Star

- Other Names: HR 8259
- Spectral Type: B9 IIIe
- V magnitude: 6.14
- In WDS?: no
- Known spectroscopic binary?: no
- Velocity variations seen in these data?: no

	Hα	He I λ6678	Hγ	He I λ4471	Mg II λ4481	Fe II ccfs
Mean RV (km s^{-1})	-23.1	-12.4	-23.8	-28.4	-26.5	-24.4
RV range (km s^{-1})	-24.9 to -20.6	···	-27.0 to -20.6	-31.1 to -24.4	-27.4 to -25.2	-28.3 to -16.4
RV change (km s^{-1})	4.3	···	6.4	6.7	2.2	11.8

- Shell classification: squarish (may be photospheric)
- Do shell features move with the star?: N/A
- Notes on emission and absorption features: He I λ6678 appears filled in (weak anyway due to star temperature).
- Other notes:

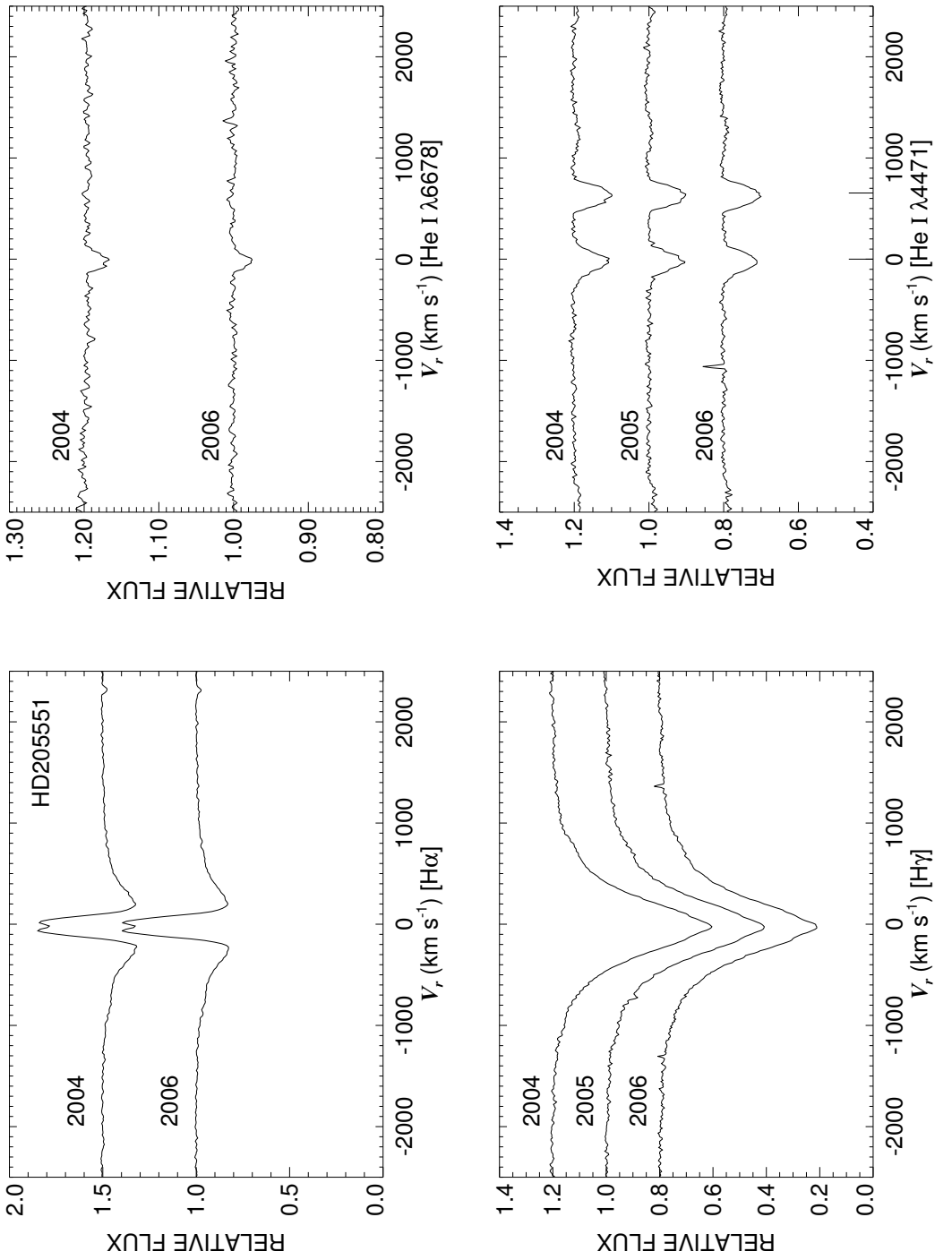

Figure C.136: A quadruple plot of HD205551 as described in §7.2.3 and Figure 7.6.

HD206773

Classical Be Star

- Other Names:
- Spectral Type: B0 Vpe
- V magnitude: 7.06
- In WDS?: no
- Known spectroscopic binary?: no
- Velocity variations seen in these data?: no

	Hα	He I λ6678	Hγ	He I λ4471	Mg II λ4481	Fe II ccfs
Mean RV (km s^{-1})	-2.1	···	69.5	-69.8	···	···
RV range (km s^{-1})	-8.0 to 1.2	···	49.1 to 89.3	-78.9 to -49.2	···	···
RV change (km s^{-1})	9.2	···	40.2	29.7	···	···

- Shell classification: normal
- Do shell features move with the star?: N/A
- Notes on emission and absorption features: Hα emission is broad and shows some changes in shape. He I λ6678 has a great deal of emission. Hγ velocities are unreliable with the way the emission is filling in the line. He I λ4471 is rather small (hot star) and Mg II λ4481 is practically non-existent.
- Other notes:

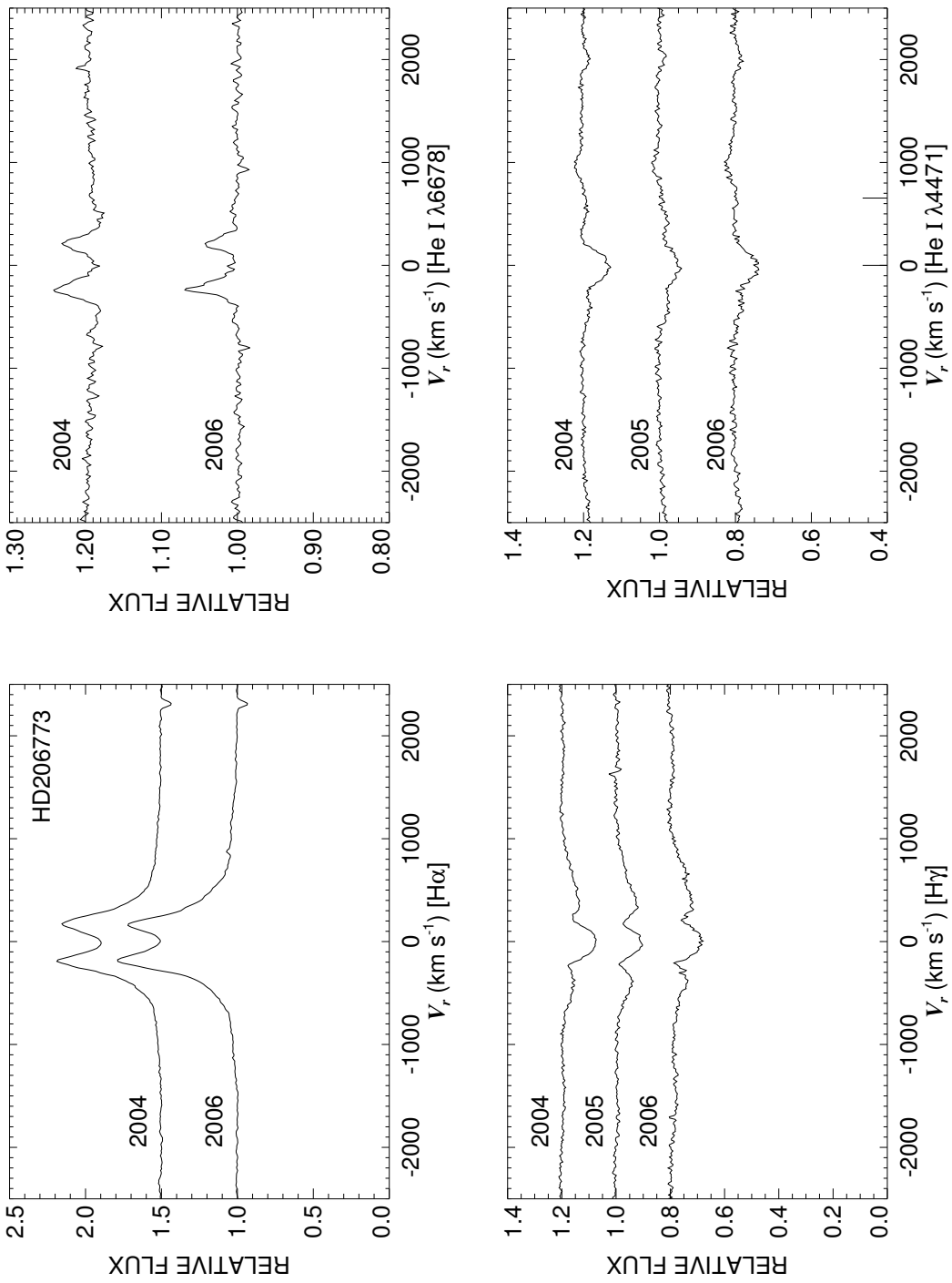

Figure C.137: A quadruple plot of HD206773 as described in §7.2.3 and Figure 7.6.

HD207232

Classical Be Star

- Other Names:
- Spectral Type: B7 V
- V magnitude: 6.96
- In WDS?: no
- Known spectroscopic binary?: no
- Velocity variations seen in these data?: no

	Hα	He I λ6678	Hγ	He I λ4471	Mg II λ4481	Fe II ccfs
Mean RV (km s^{-1})	-15.5	-19.6	-25.4	-54.2	-29.7	-28.1
RV range (km s^{-1})	-18.5 to -13.0	-31.9 to -2.5	-41.8 to -11.5	-58.6 to -47.8	-35.7 to -24.9	-35.7 to -7.4
RV change (km s^{-1})	5.5	29.4	30.3	10.8	10.8	28.3

- Shell classification: squarish (gets deeper in 2005 and stays that way - see Fig. C.139)
- Do shell features move with the star?: N/A
- Additional plot because: intensity of shell features changes over course of observations
- Notes on emission and absorption features: He I λ6678 filled in (emission hump on right).
- Other notes:

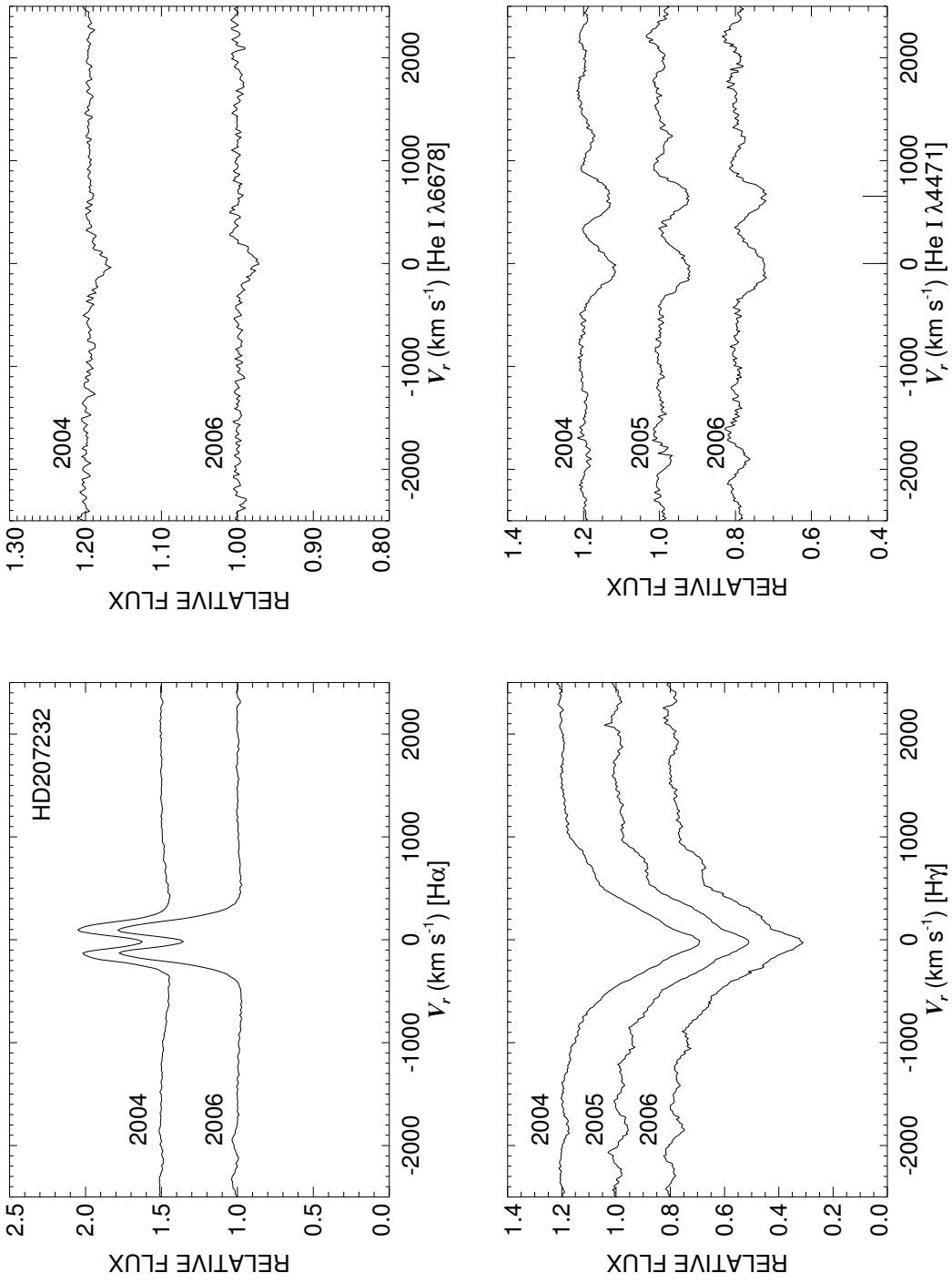

Figure C.138: A quadruple plot of HD207232 as described in §7.2.3 and Figure 7.6.

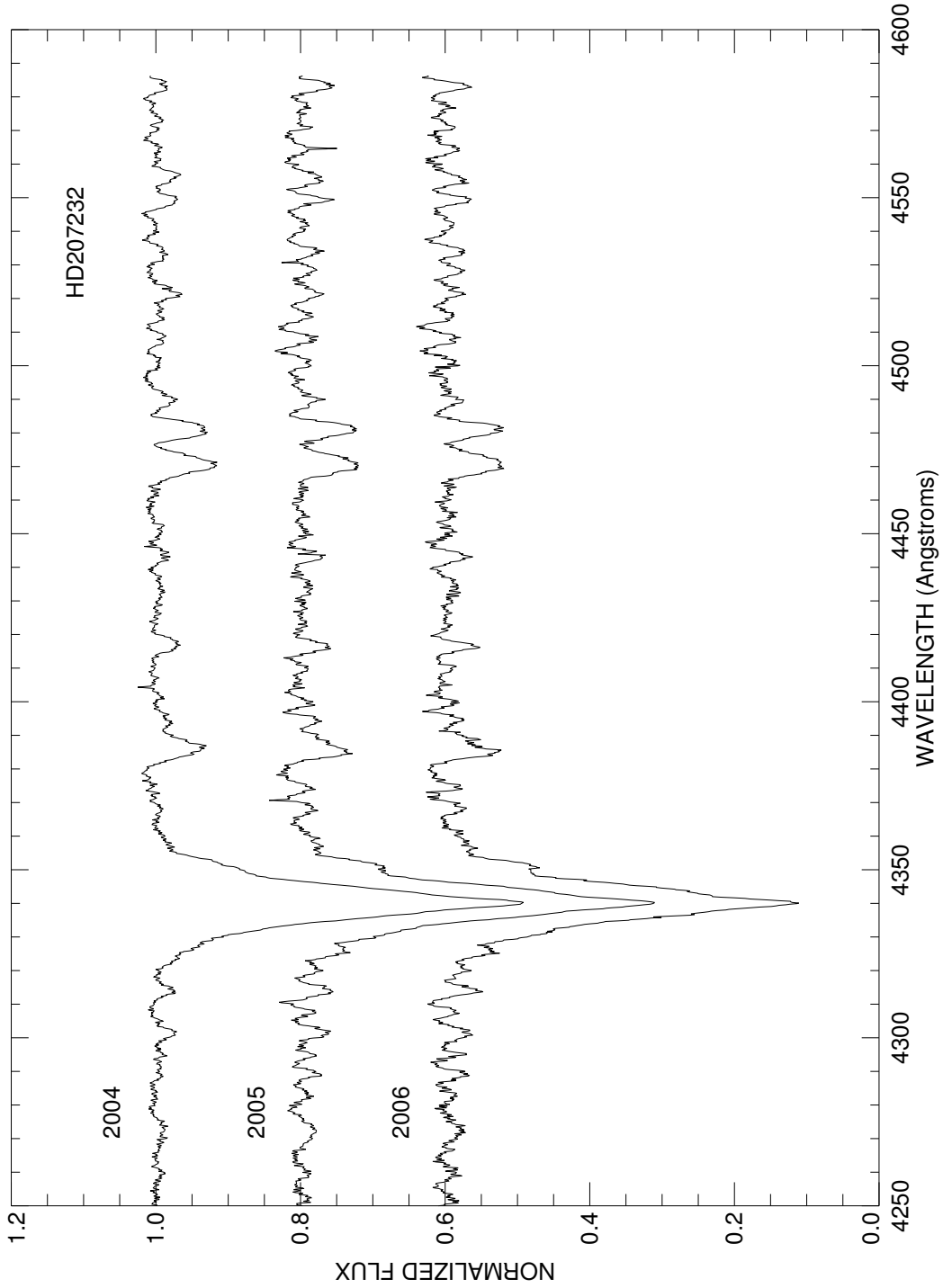

Figure C.139: A plot of the averages for each run in the blue region of HD207232. Each is labeled with the year of observation and they are offset from each other for clarity.

HD208057

NOT Be Star

- Other Names: HR 8356, 16 Peg, OQ Peg
- Spectral Type: B3 Ve
- V magnitude: 4.92
- In WDS?: no
- Known spectroscopic binary?: no
- Velocity variations seen in these data?: no

	Hα	He I λ6678	Hγ	He I λ4471	Mg II λ4481	Fe II ccfs
Mean RV (km s^{-1})	-24.5	-20.9	-14.2	-30.9	-17.8	···
RV range (km s^{-1})	-32.7 to -19.7	-30.2 to -16.8	-18.0 to -11.8	-34.3 to -26.3	-22.1 to -13.1	···
RV change (km s^{-1})	13.0	13.4	6.2	8.0	9.0	···

- Notes on emission and absorption features: No emission seen.
- Other notes: This star first classified as a B3 e star by Merrill & Burwell (1943). However, NO ONE has seen any emission since (I found nine other researchers who published that they didn't see emission, just absorption).

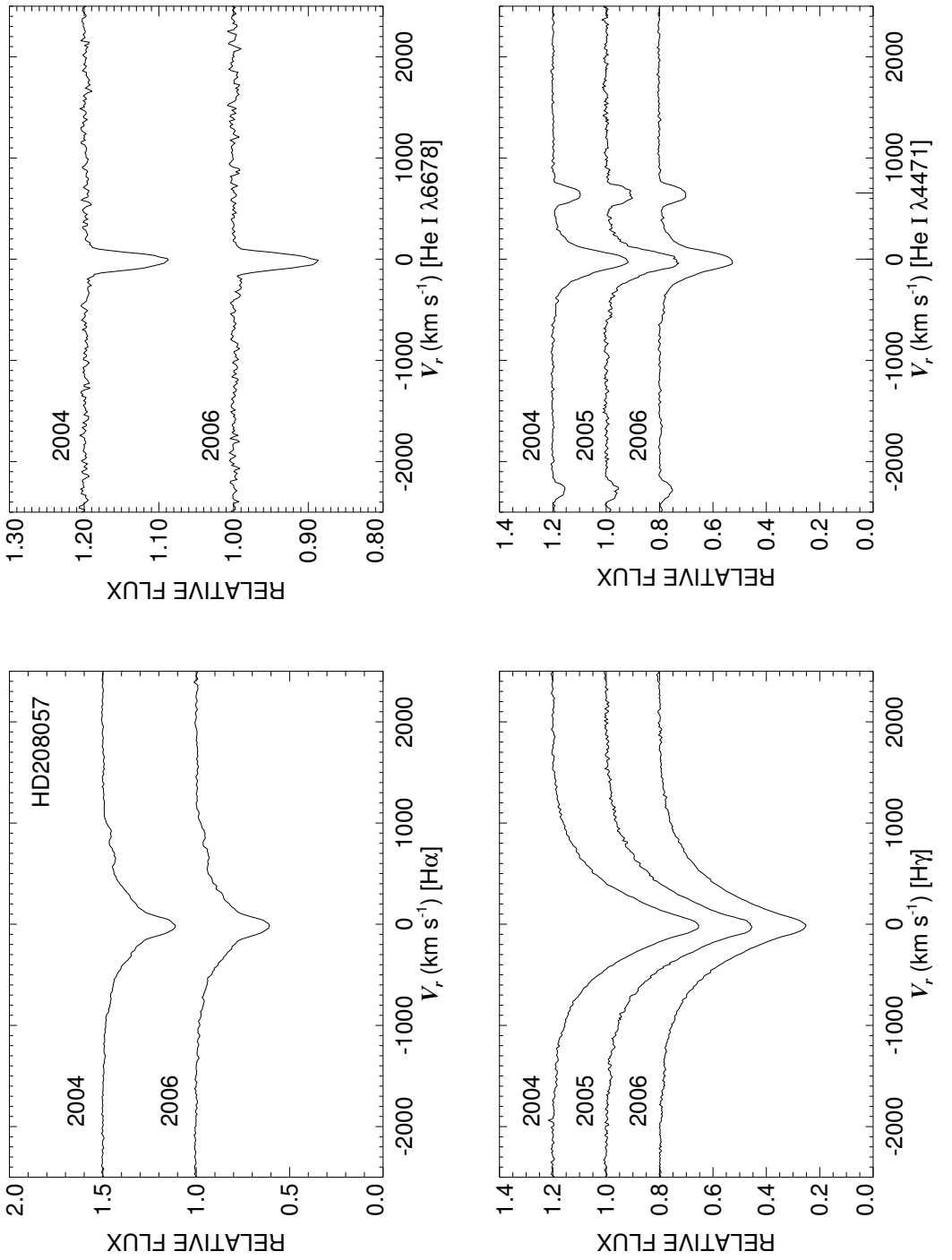

Figure C.140: A quadruple plot of HD208057 as described in §7.2.3 and Figure 7.6.

HD208392

Classical Be Star; Non-Radial Pulsator

- Other Names: EM Cep
- Spectral Type: B1 IIIe
- V magnitude: 7.20
- In WDS?: no
- Known spectroscopic binary?: no
- Velocity variations seen in these data?: yes (NRP?)

	Hα	He I λ6678	Hγ	He I λ4471	Mg II λ4481	Fe II ccfs
Mean RV (km s^{-1})	-15.5	-20.2	112.0	-23.3	-62.0	···
RV range (km s^{-1})	-20.2 to -10.8	-35.0 to -12.5	98.9 to 119.9	-25.4 to -21.5	-73.9 to -50.1	···
RV change (km s^{-1})	9.4	22.5	21.0	3.9	23.8	···

- Shell classification: normal
- Notes on emission and absorption features: No emission currently seen. All spectral features show line profile changes.
- Other notes: This star was first reported to have an emission line of medium intensity in 1931 and 1932 (see Harmanec 1984) and Bidelman (1988) states "Aug. 11, '72 plate shows a fairly strong self-reversal at Hα." This star is listed in SIMBAD as an "eclipsing binary of β Lyr type" however this is incorrect according to spectroscopic studies by Hilditch, McLean, & Reid (1982) and Harmanec (1984). Harmanec points out that while there are periodic light variations with two maxima and two minima (like an eclipsing system), there are no radial velocity variations as required for an eclipsing contact binary. Hilditch et al. suggest the variations are caused by non-radial pulsation or possibly a starspot. They also point out that a long-period binary is not ruled out.

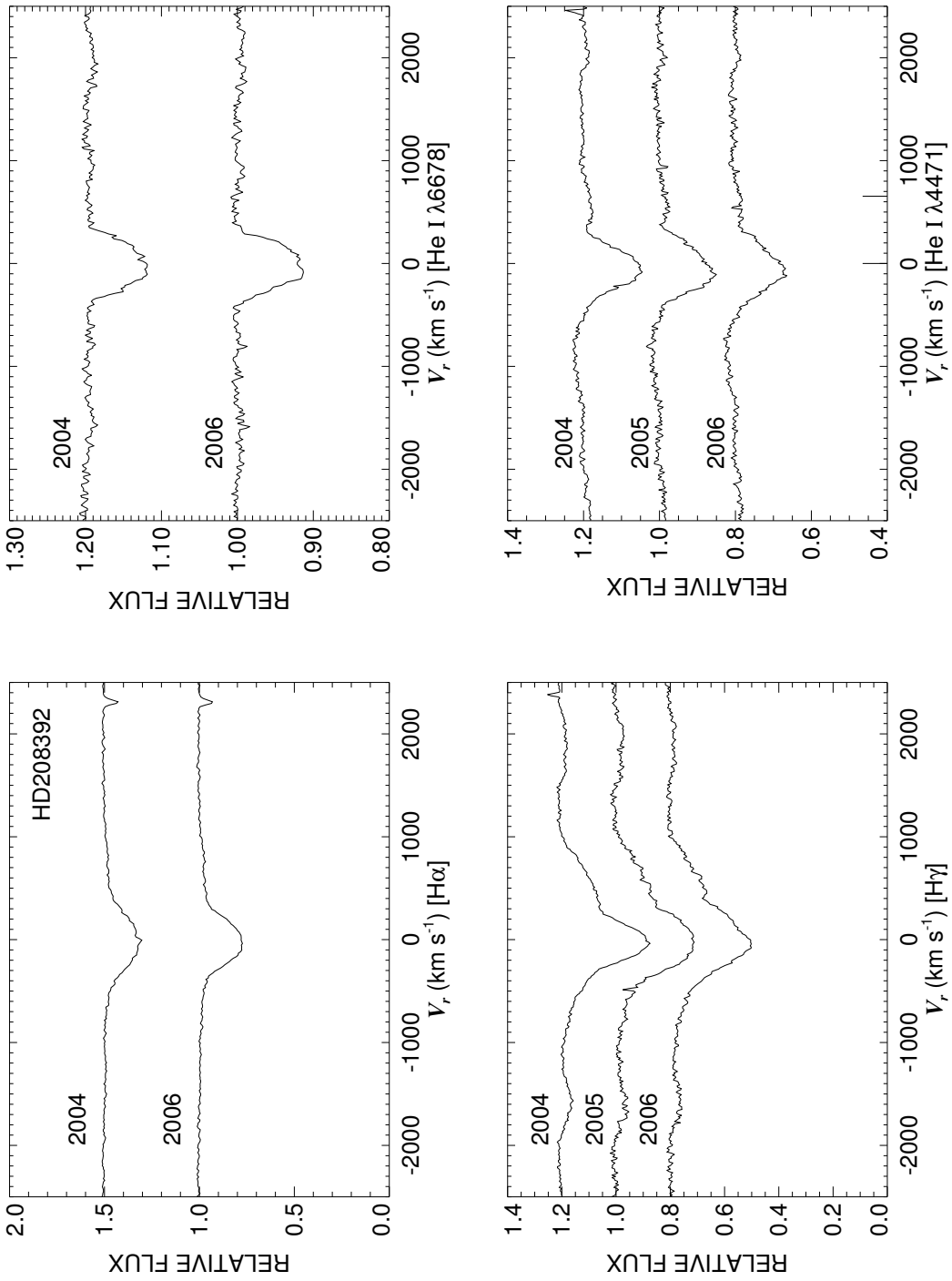

Figure C.141: A quadruple plot of HD208392 as described in §7.2.3 and Figure 7.6.

HD208682

Classical Be Star; Non-Radial Pulsator?

- Other Names: HR 8375
- Spectral Type: B2.5 Ve+sh
- V magnitude: 5.84
- In WDS?: yes - 8.17 mag companion 1.1 arcsec away (discovered in 1847)
- Known spectroscopic binary?: no
- Velocity variations seen in these data?: maybe

	Hα	He I λ6678	Hγ	He I λ4471	Mg II λ4481	Fe II ccfs
Mean RV (km s^{-1})	-4.1	-11.1	19.5	-31.9	-35.8	···
RV range (km s^{-1})	-17.9 to 11.7	-19.9 to 3.1	9.7 to 33.0	-35.5 to -22.9	-43.5 to -25.5	···
RV change (km s^{-1})	29.6	23.0	23.3	12.6	18.0	···

- Shell classification: normal
- Notes on emission and absorption features: Hα appears to have some emission in 2004 as it looks wider in 2006. He I λ6678 may show NRP. Mg II λ4481 is very broad and blended.
- Other notes: This star does not look like it has much emission right now, but it has had large emission in the past, as well as shell features - emission profiles may be found in Figure 7 of Fontaine et al. (1982).

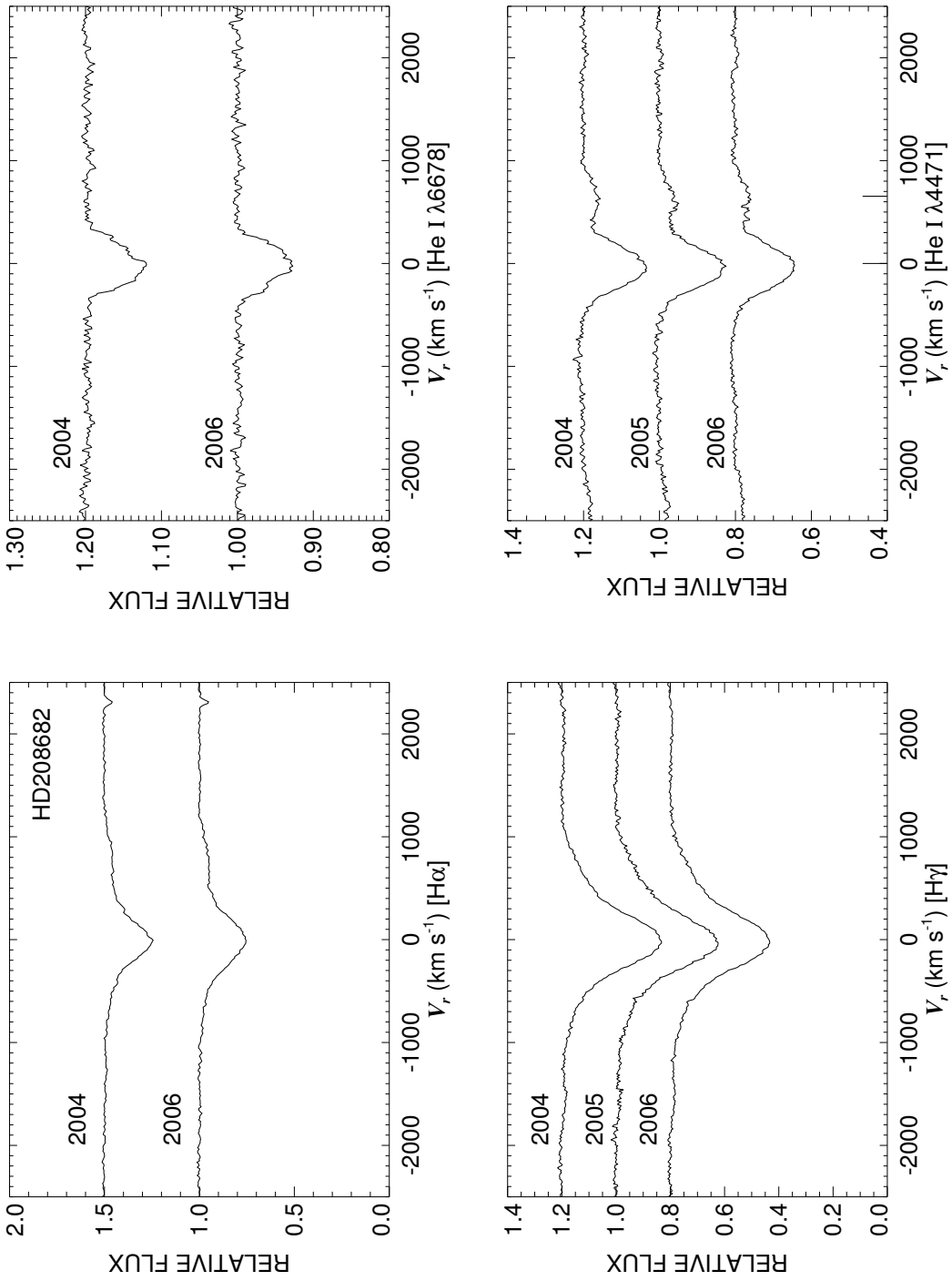

Figure C.142: A quadruple plot of HD208682 as described in §7.2.3 and Figure 7.6.

HD210129

Classical Be Star

- Other Names: HR 8438, 25 Peg
- Spectral Type: B7 Vne
- V magnitude: 5.70
- In WDS?: no
- Known spectroscopic binary?: no
- Velocity variations seen in these data?: no

	Hα	He I λ6678	Hγ	He I λ4471	Mg II λ4481	Fe II ccfs
Mean RV (km s^{-1})	-56.8	-60.2	-62.1	-58.7	-55.3	-45.6
RV range (km s^{-1})	-57.8 to -56.4	-81.3 to -48.0	-69.4 to -56.3	-64.9 to -53.5	-59.0 to -49.7	-74.7 to 6.1
RV change (km s^{-1})	1.4	33.3	13.1	11.4	9.3	80.8

- Shell classification: emission shell (weak but grows slightly in 2005/6 - see Fig. C.144)
- Do shell features move with the star?: N/A
- Notes on emission and absorption features: Hα emission strengthens a great deal in 2006. He I λ6678 is filled in with emission (and has horns). Hγ emission increases slightly in 2005 and in 2006. The shell features grow with the Hα emission.
- Other notes:

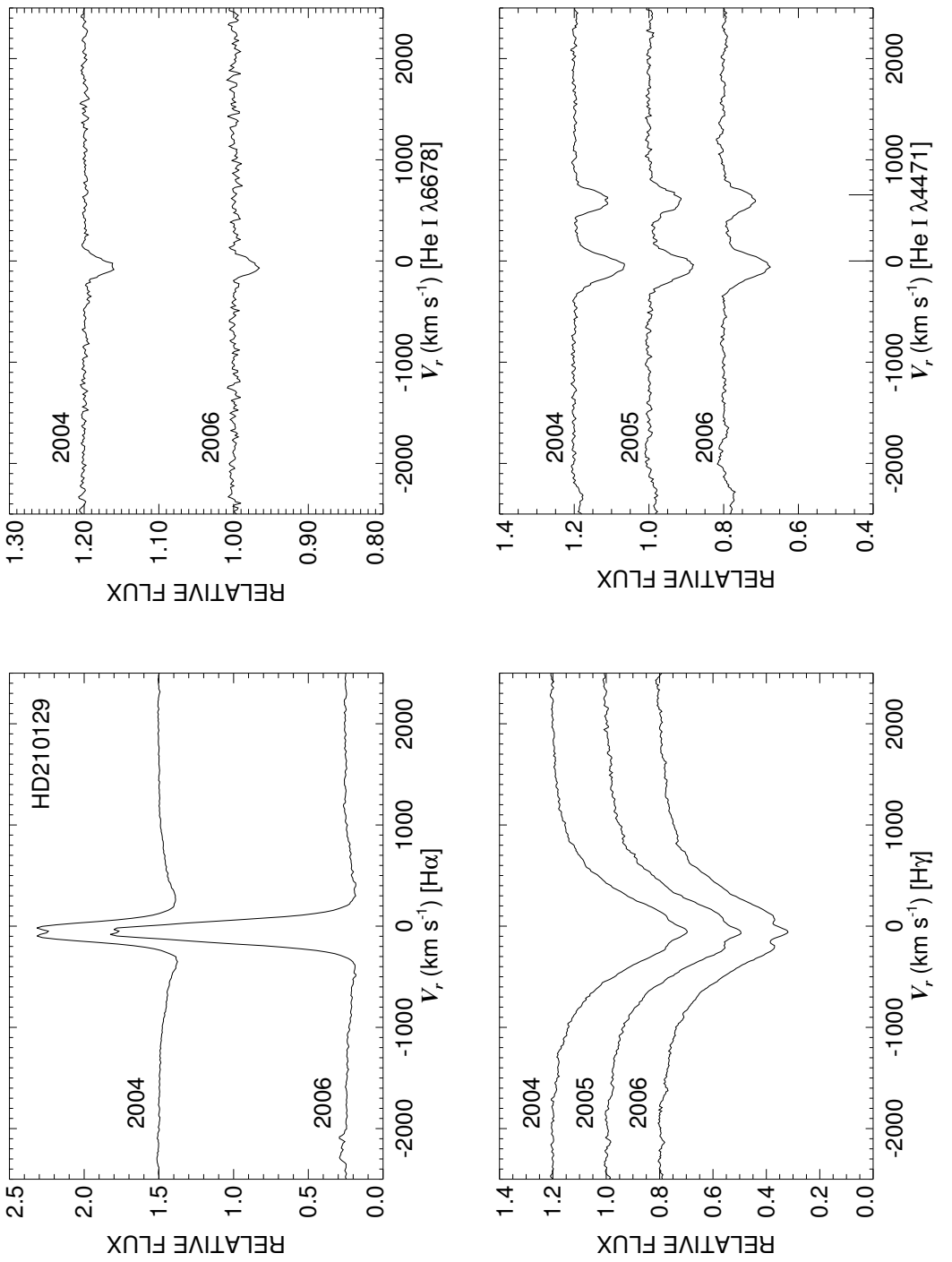

Figure C.143: A quadruple plot of HD210129 as described in §7.2.3 and Figure 7.6.

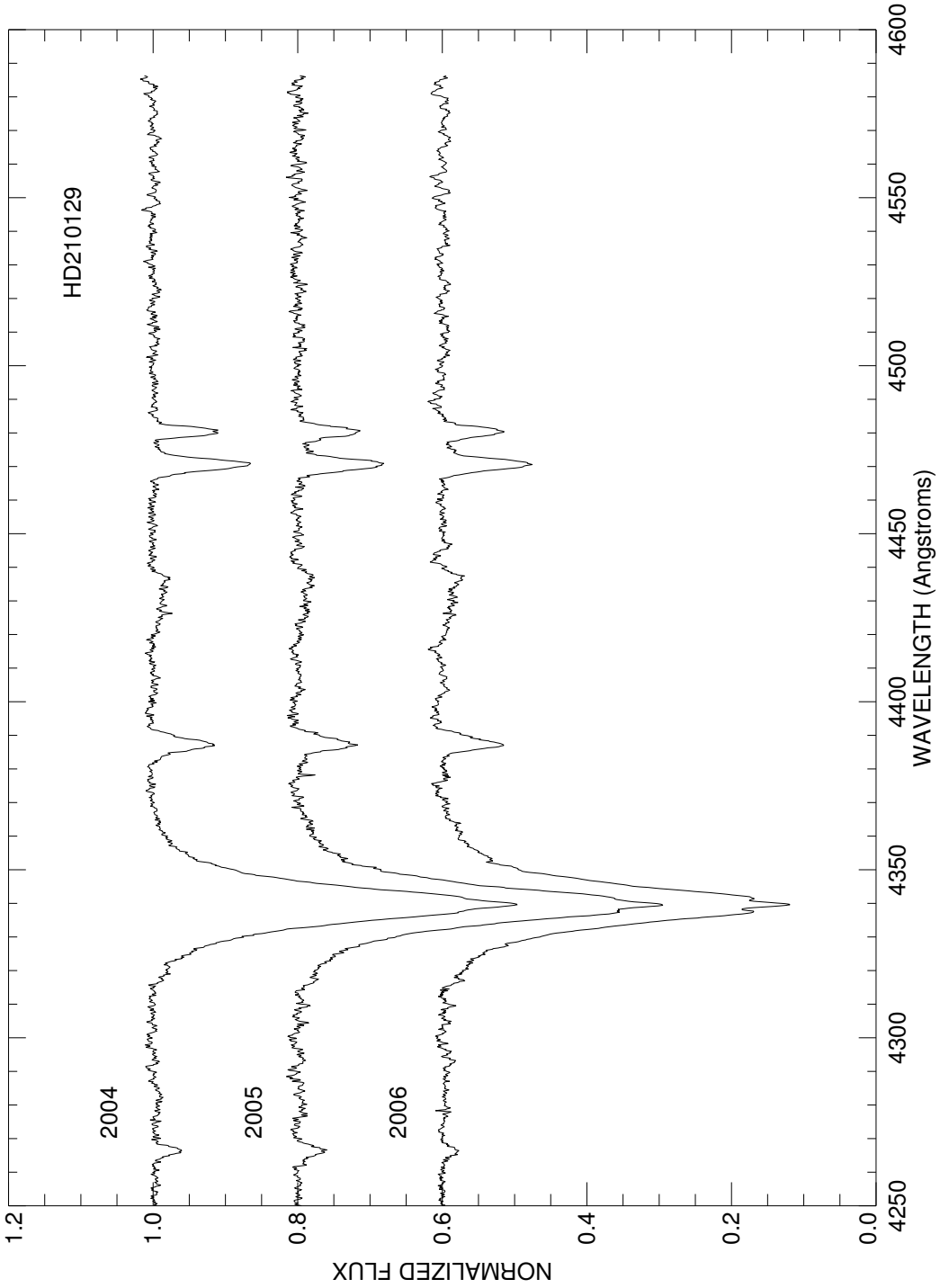

Figure C.144: A plot of the averages for each run in the blue region of HD210129. Each is labeled with the year of observation and they are offset from each other for clarity.

HD212044

Classical Be Star

- Other Names: V357 Lac
- Spectral Type: B0 Ve
- V magnitude: 7.02
- In WDS?: no
- Known spectroscopic binary?: no
- Velocity variations seen in these data?: yes (see Fig. C.146)

	Hα	He I λ6678	Hγ	He I λ4471	Mg II λ4481	Fe II ccfs
Mean RV (km s^{-1})	-13.3	-33.5	51.7	-56.9	···	-32.6
RV range (km s^{-1})	-16.2 to -10.2	-34.6 to -32.4	25.2 to 75.0	-93.3 to -22.9	···	-51.5 to -11.4
RV change (km s^{-1})	6.0	2.2	49.8	70.4	···	40.1

- Shell classification: emission shell (disappears in 2006!)
- Do shell features move with the star?: yes
- Notes on emission and absorption features: Hα grows a great deal in 2006. Hγ shows extremely rapid peak changes in 2004 (both 2006 spectra are from one night) but does not grow like Hα does. Stong emission horns appear in both He I λ6678 and Mg II λ4481 (useless for radial velocity studies). All absorption lines in the blue show line profile variations (perhaps from a companion as the features do move or maybe NRP). The strong silicon lines ($\lambda\lambda 4552, 4567, 4574$) of a hot star are fully revealed after the shell goes away.
- Other notes:

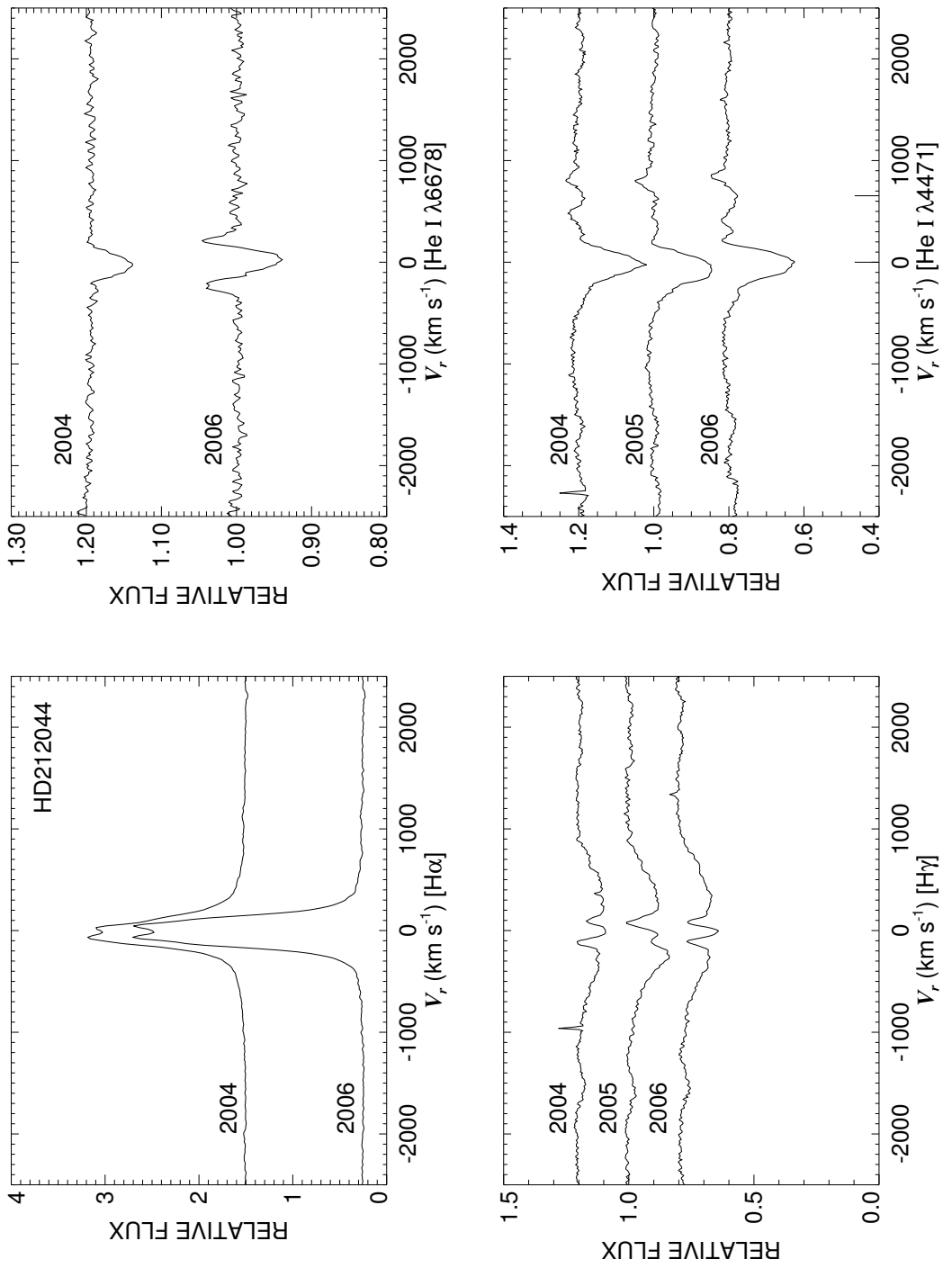

Figure C.145: A quadruple plot of HD212044 as described in §7.2.3 and Figure 7.6.

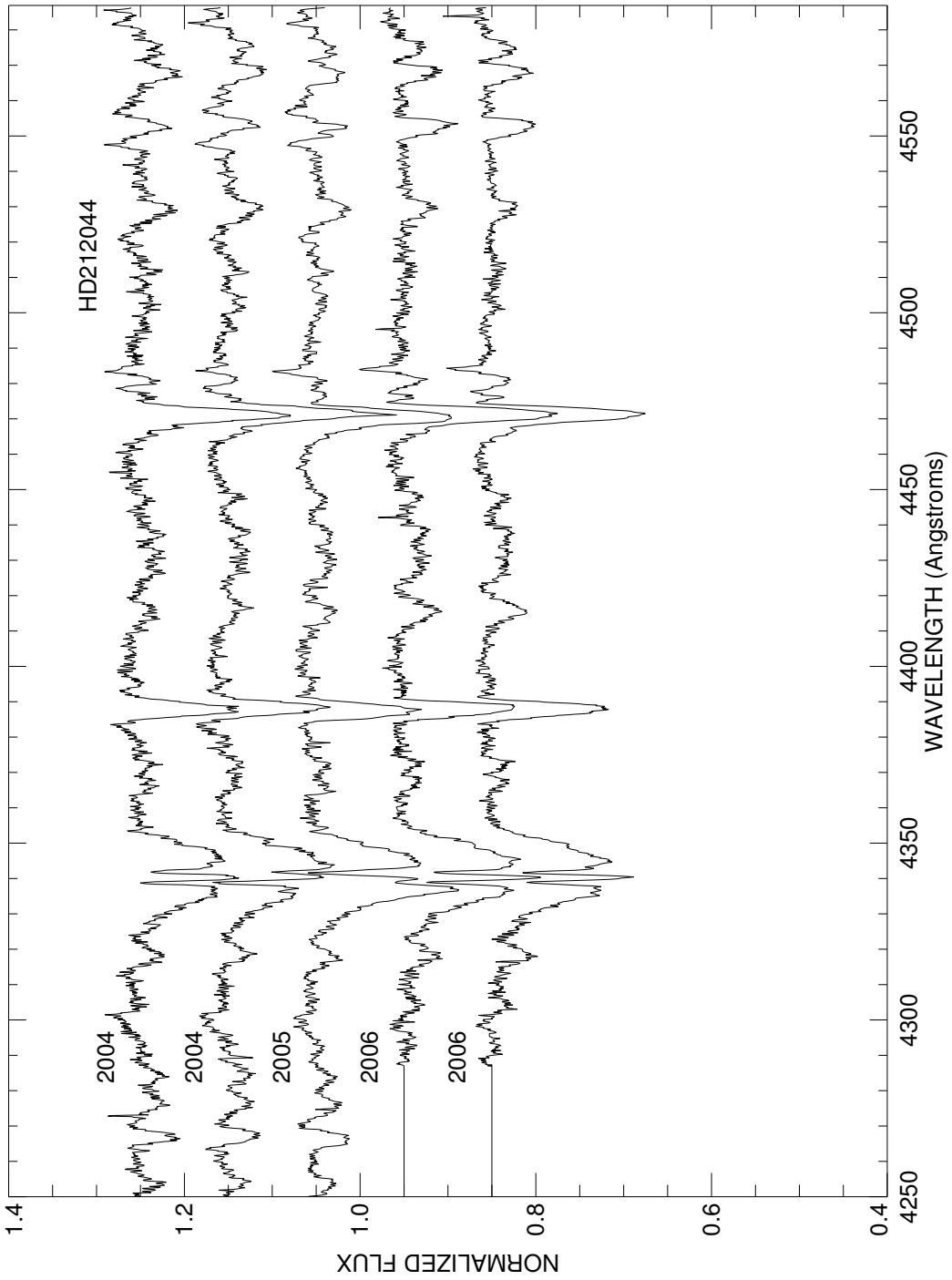

Figure C.146: A plot of all spectra of HD212044 in the blue region. Each is labeled with the year of observation and they are offset for clarity.

HD212076

Classical Be Star; Non-Radial Pulsator

- Other Names: HR 8520, 31 Peg, IN Peg
- Spectral Type: B1.5 Vne
- V magnitude: 4.72
- In WDS?: no
- Known spectroscopic binary?: no
- Velocity variations seen in these data?: no

	Hα	He I λ6678	Hγ	He I λ4471	Mg II λ4481	Fe II ccfs
Mean RV (km s^{-1})	10.6	13.7	39.0	-13.9	···	10.1
RV range (km s^{-1})	9.0 to 12.5	-10.1 to 30.6	23.3 to 51.1	-22.6 to -6.4	···	4.0 to 18.5
RV change (km s^{-1})	3.5	40.7	27.8	16.2	···	14.5

- Shell classification: emission shell
- Do shell features move with the star?: N/A
- Notes on emission and absorption features: Very large Hα emission that strengthens considerably in 2006. Hγ emission also exhibits a relatively considerable increase into 2006. Emission horns seen in both He I λ6678 and Mg II λ4481 (both are therefore unreliable in RV studies). He I λ4471 may also have some emission filling it in.
- Other notes: Rivinius et al. (2004) shows non-radial pulsations in their Fig. 5 with a tentative period of 0.724 d. This star is also plotted in Figure 7.4.

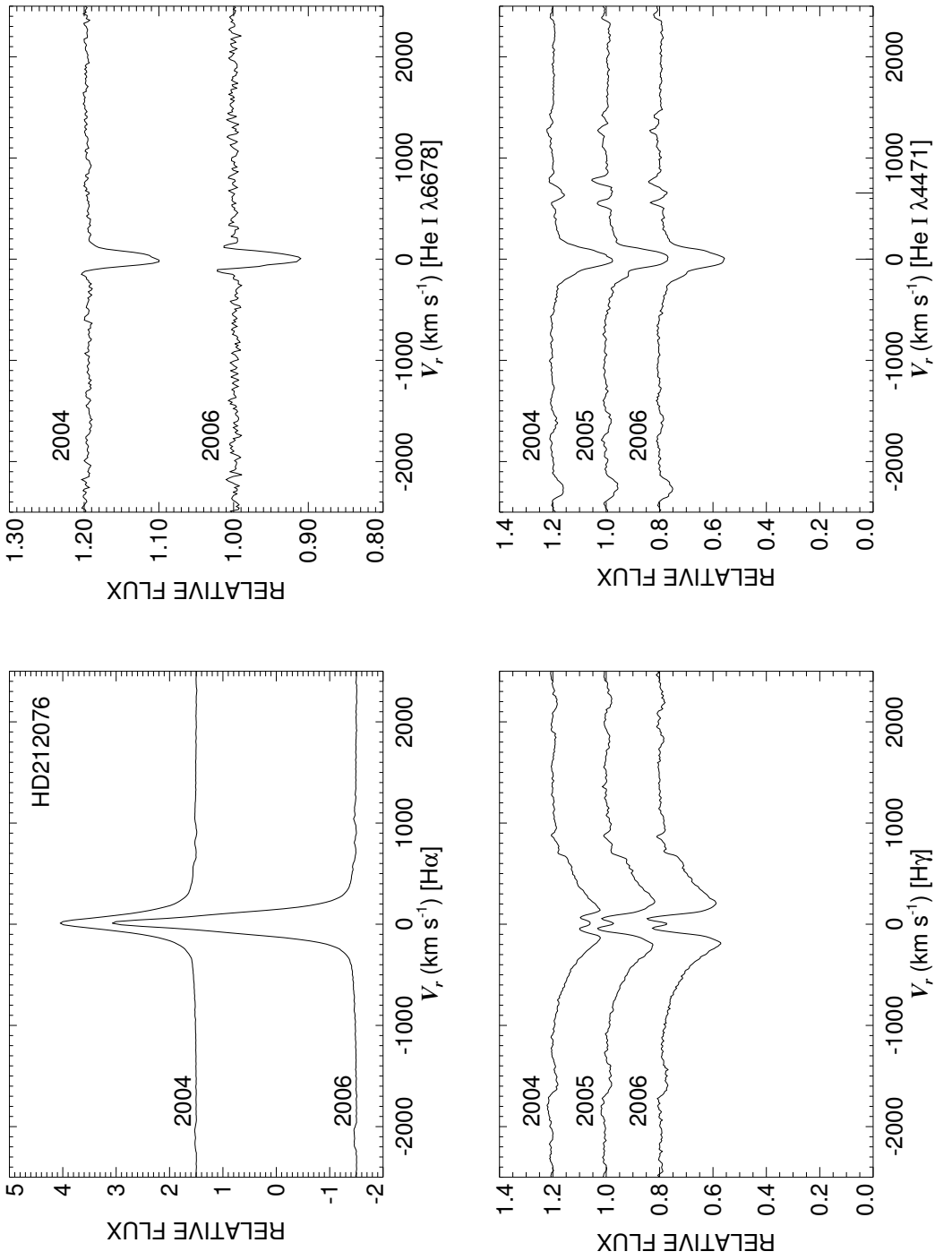

Figure C.147: A quadruple plot of HD212076 as described in §7.2.3 and Figure 7.6.

HD212571

Classical Be Star; Non-Radial Pulsator

- Other Names: HR 8539, 52 Aqr, π Aqr
- Spectral Type: B1 Ve+sh
- V magnitude: 4.62
- In WDS?: no
- Known spectroscopic binary?: yes - while it is distinctly a non-radial pulsator (see §7.7), it seems to have a binary period as found by Bjorkman et al. (2002) of 84 days. Also see the following figures.
- Velocity variations seen in these data?: yes (see Figs. C.149, C.150 , and C.151)

	Hα	He I λ6678	Hγ	He I λ4471	Mg II λ4481	Fe II ccfs
Mean RV (km s^{-1})	-2.3	-14.0	109.7	-43.5	-89.1	···
RV range (km s^{-1})	-12.5 to 6.9	-34.7 to -1.0	91.5 to 147.0	-51.7 to -31.6	-121.3 to -64.4	···
RV change (km s^{-1})	19.4	33.7	55.5	20.1	56.9	···

- Shell classification: not an Fe II shell
- Notes on emission and absorption features: Hα emission strength decreases slightly in 2006. Emission wings in He I λ6678 increase markedly in 2006. All spectral features show the marching bumps of non-radial pulsation (esp. see C II λ4267, He I $\lambda\lambda$4388, 4471, 6678, O II λ4415 and Si III $\lambda\lambda$4552, 4567, 4574).
- Other notes: This star is discussed in more detail in §7.7.

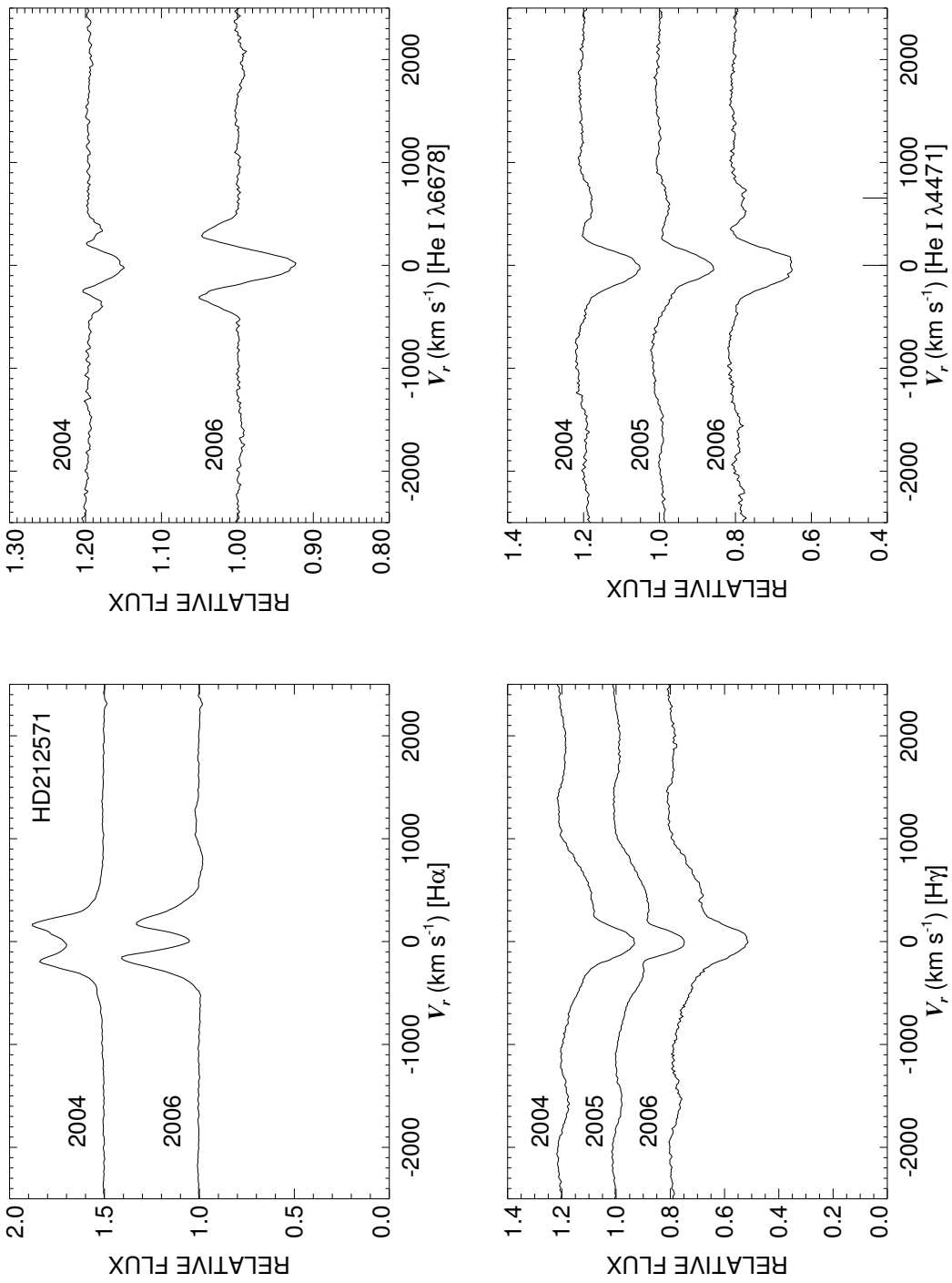

Figure C.148: A quadruple plot of HD212571 as described in §7.2.3 and Figure 7.6.

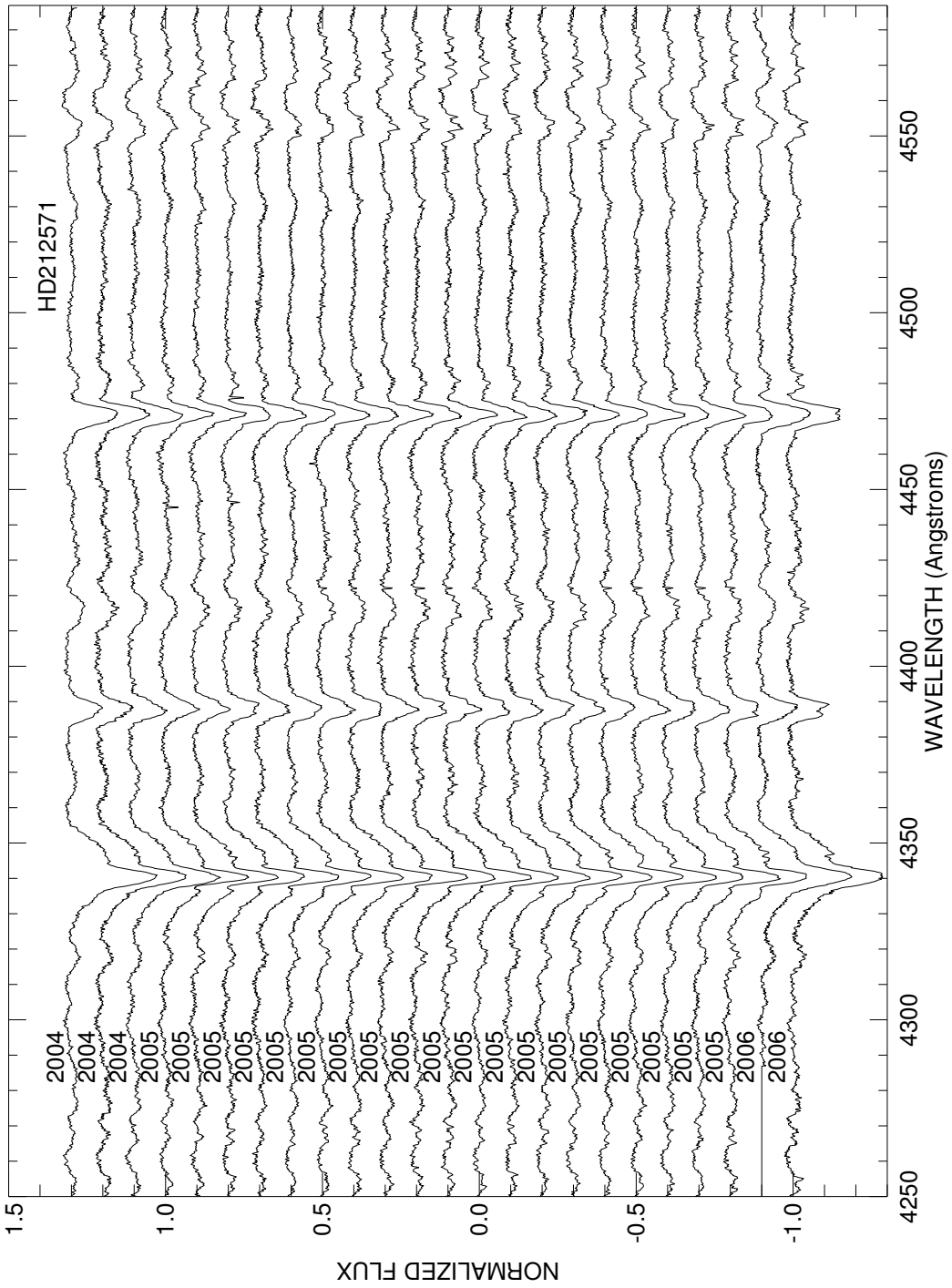

Figure C.149: A plot of all spectra of HD212571 in the blue region. Each is labeled with the year of observation and they are offset for clarity.

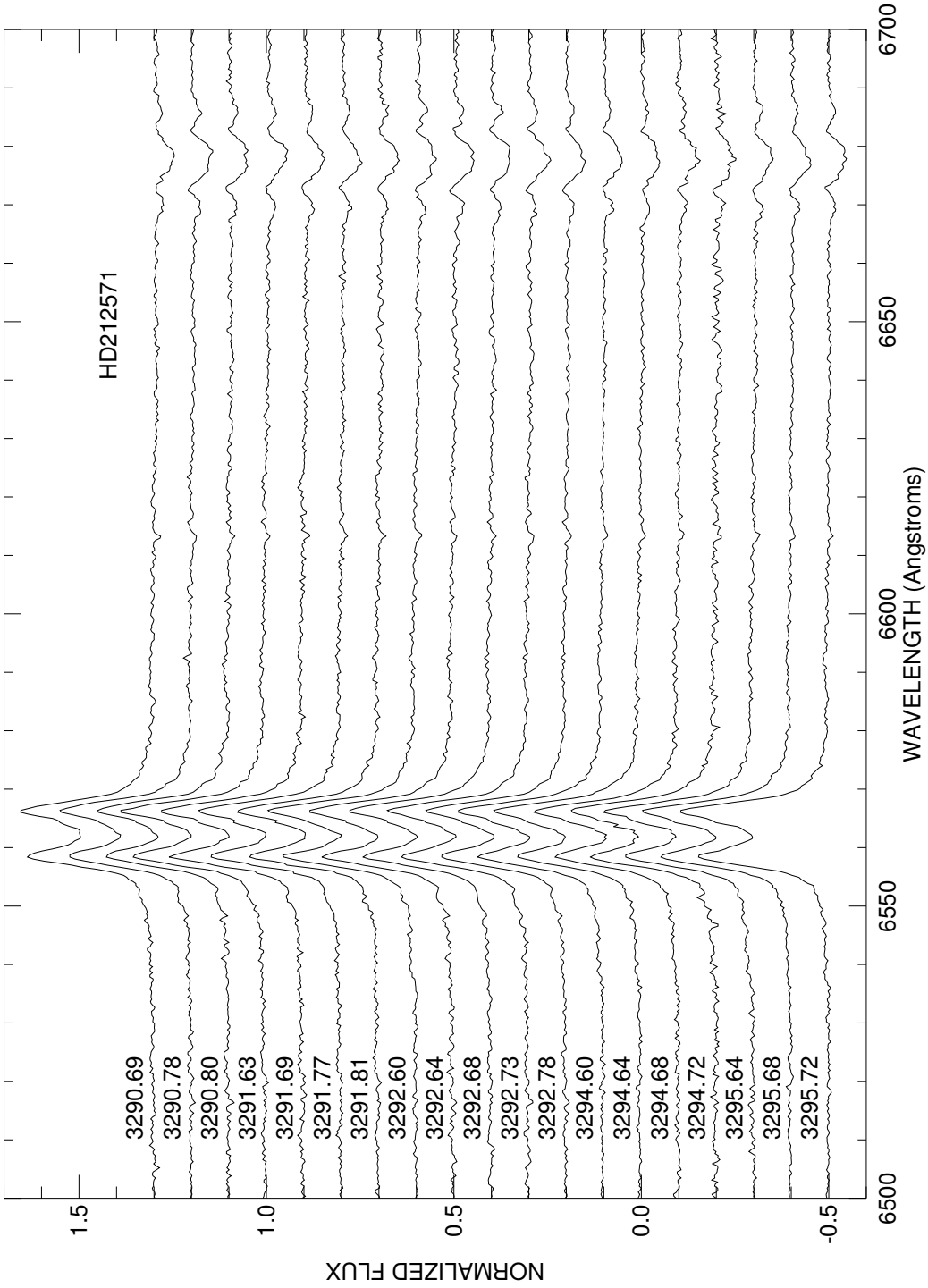

Figure C.150: All red spectra of HD212571 for the 2004 observing run. Each spectrum is labeled with HJD-2450000. and is offset for clarity

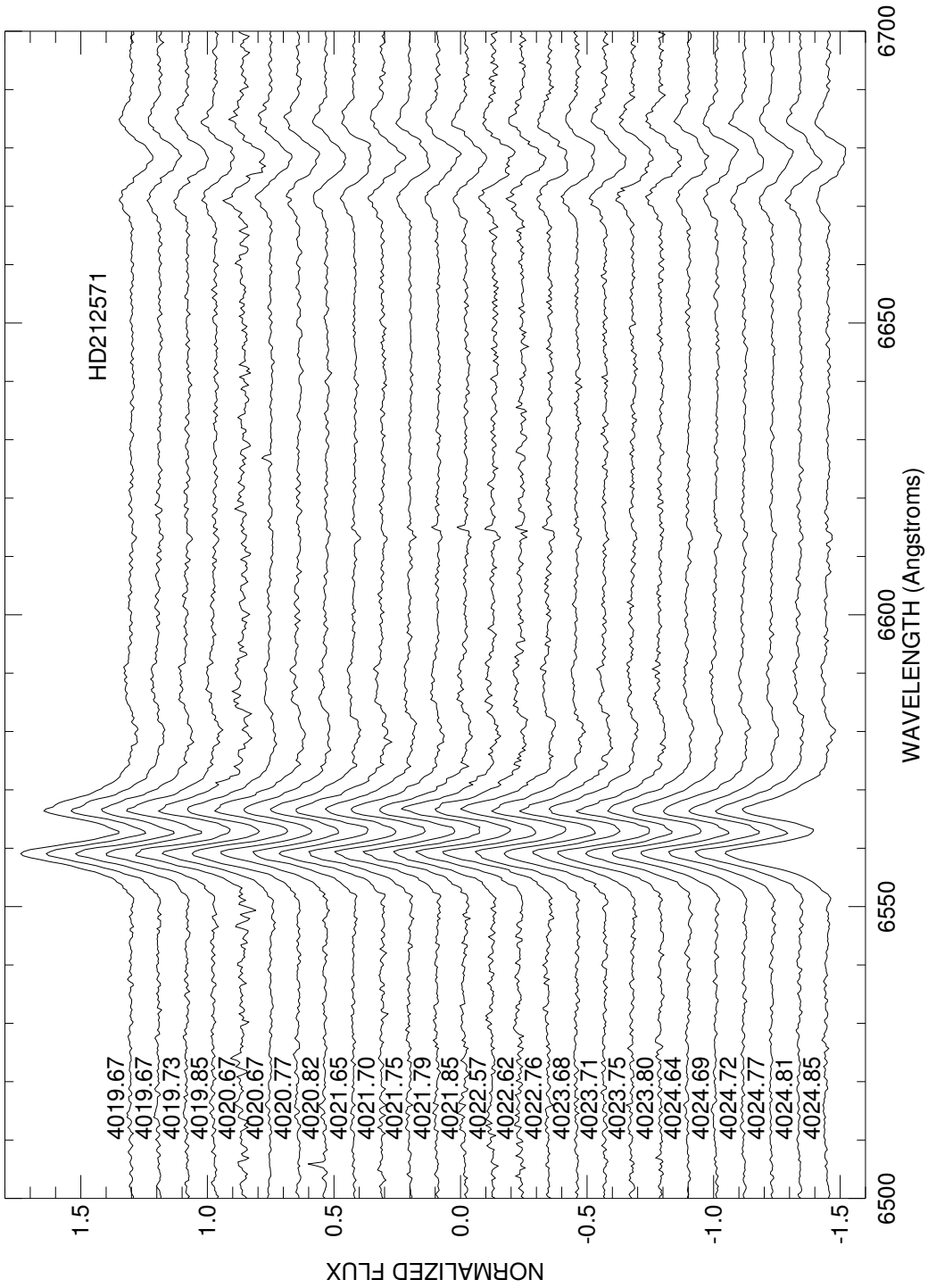

Figure C.151: All red spectra of HD212571 for the 2006 observing run. Each spectrum is labeled with HJD-2450000. and is offset for clarity

HD212791

Classical Be Star; Non-Radial Pulsator?

- Other Names: V408 Lac
- Spectral Type: B6e
- V magnitude: 7.98
- In WDS?: no
- Known spectroscopic binary?: no
- Velocity variations seen in these data?: yes (NRP?)

	Hα	He I λ6678	Hγ	He I λ4471	Mg II λ4481	Fe II ccfs
Mean RV (km s^{-1})	-11.6	-13.7	-8.0	-34.6	-20.6	···
RV range (km s^{-1})	-11.9 to -11.3	-16.5 to -10.9	-10.6 to -4.9	-37.6 to -31.6	-24.2 to -15.8	···
RV change (km s^{-1})	0.6	5.6	5.7	6.0	8.4	···

- Shell classification: normal
- Notes on emission and absorption features: Emission in Hα shows a very distinct decrease. Hγ emission decreases from 2004 to 2006 and the peaks change. Line profile changes in He I λ6678, He I λ4471, and Mg II λ4481 could be indicative of NRP.
- Other notes:

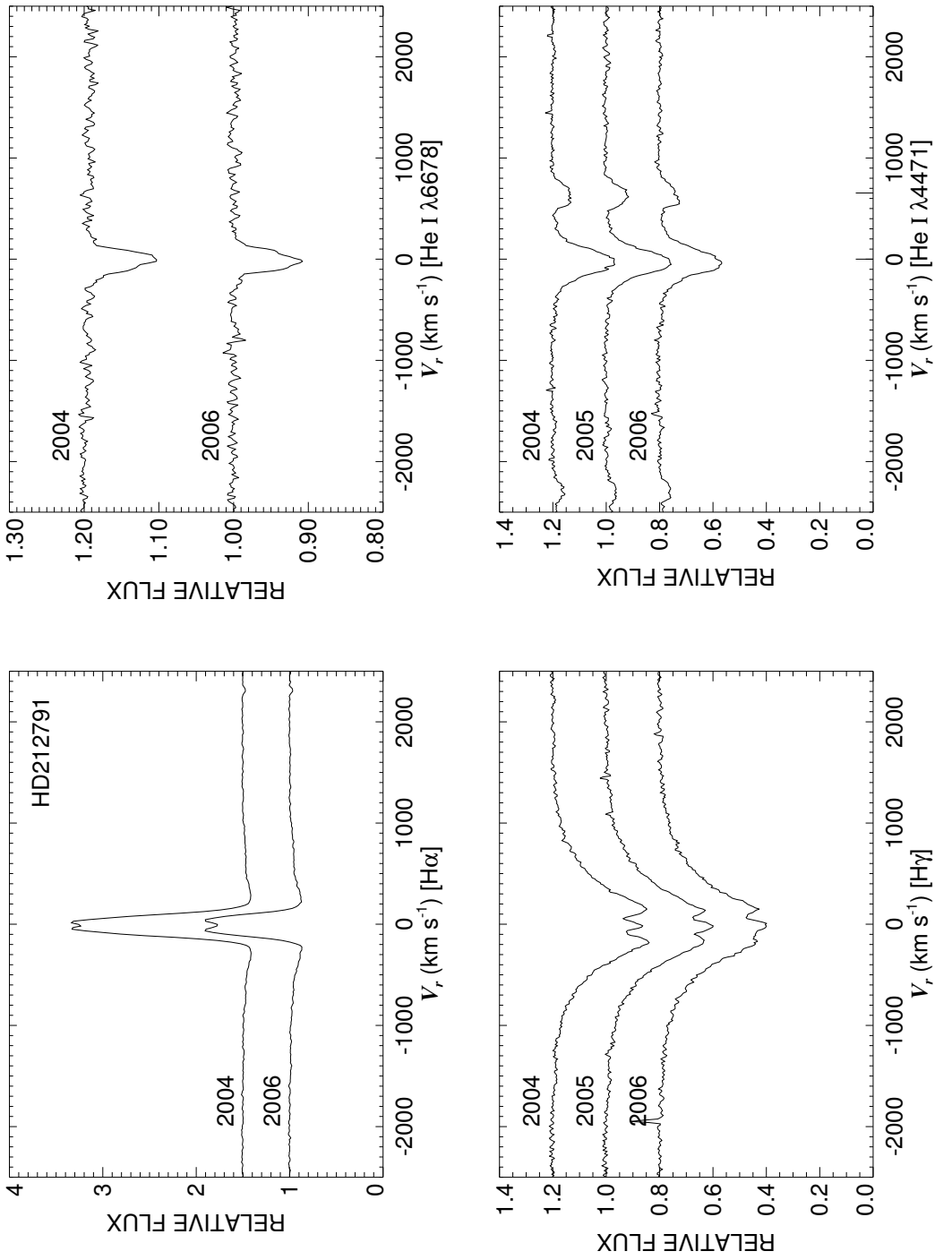

Figure C.152: A quadruple plot of HD212791 as described in §7.2.3 and Figure 7.6.

HD214167

NOT a Be Star

- Other Names: 8 Lac B
- V magnitude: 6.32
- Spectral Type: B1 V
- In WDS?: yes - it is paired with the next star in this appendix (HD214168), a comparable 6.29 mag B5 star 23 arcsec away (discovered in 1782). This particular star has a speckle companion of unlisted magnitude less than 0.1 arcsec away (discovered in 1985) and 4 fainter (mag 10.5, 9.08, 7.25, 13.6) companions 48, 81, 339, and 79 arcsec away (discovered in 1886, 1823, 1895 and 2005).
- Known spectroscopic binary?: no
- Velocity variations seen in these data?:

	Hα	He I λ6678	Hγ	He I λ4471	Mg II λ4481	Fe II ccfs
Mean RV (km s^{-1})	-14.4	-10.5	-5.2	-39.5	-26.4	···
RV range (km s^{-1})	-24.1 to -2.2	-14.0 to -6.5	-8.1 to -0.3	-40.0 to -38.6	-32.1 to -23.6	···
RV change (km s^{-1})	21.9	7.5	7.8	1.4	8.5	···

- Notes on emission and absorption features: No emission, a slow rotator.
- Other notes: This star is notoriously confused with the comparable magnitude close neighbor and Be star HD214168. It is only through confusion that this star was ever declared a Be star in the literature. I eliminated this star from statistics in Chapter 7.

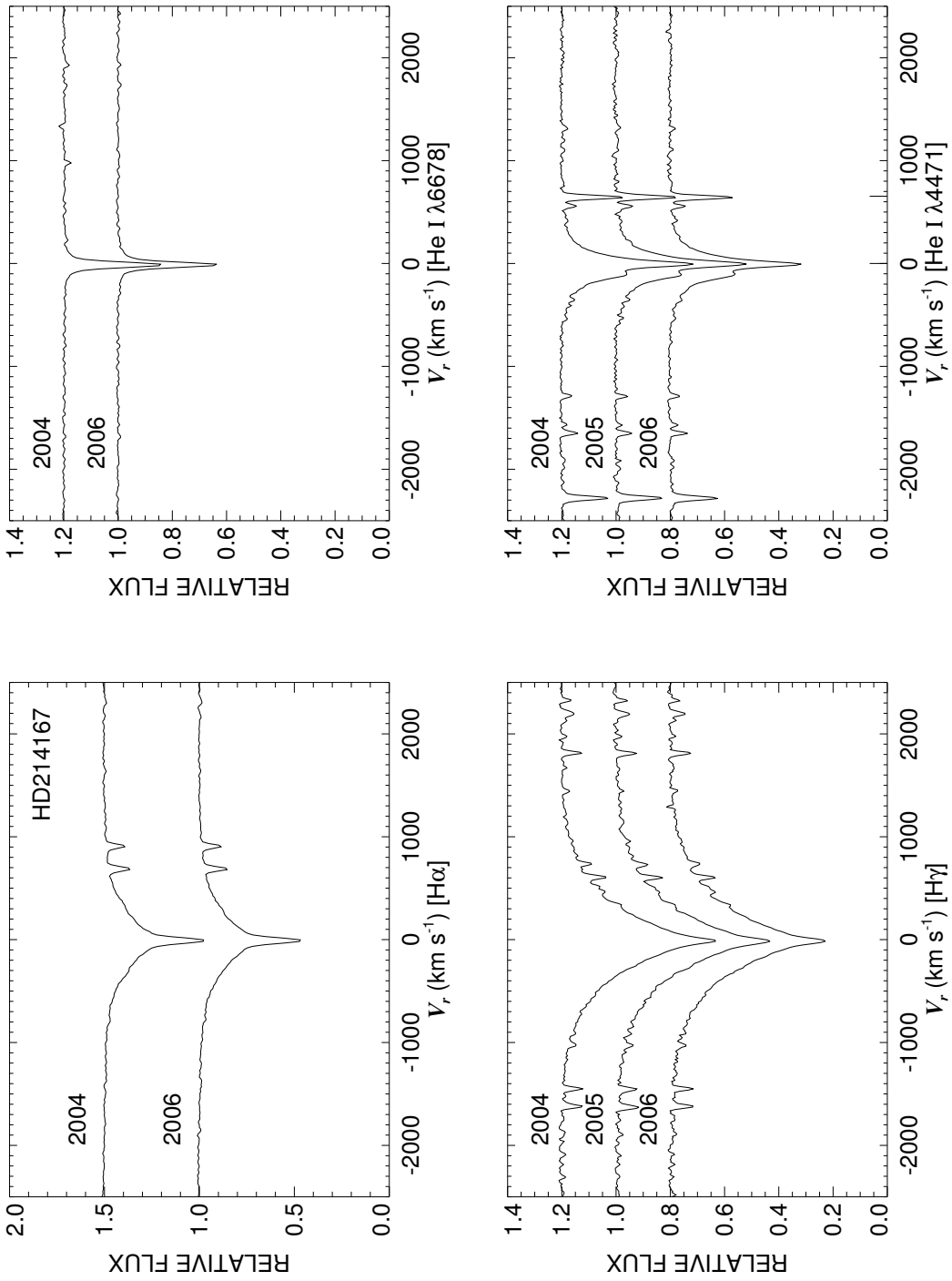

Figure C.153: A quadruple plot of HD214167 as described in §7.2.3 and Figure 7.6.

HD214168

Be Star

- Other Names: HR 8603, 8 Lac A
- Spectral Type: B1 Ve
- V magnitude: 5.58
- In WDS?: yes with its close companion HD214167 (the previous star in this appendix). The same companions as HD214167 are present, but there are 4 additional ones listed (mag 10.3, 8.5, 7.25, 10.0) at 29, 65, 320 and 128 arcsec away (discovered in 1830, 1823, 1880, and 1913). It could be that these are just re-labelled companions listed for HD124167.
- Known spectroscopic binary?: no
- Velocity variations seen in these data?: no

	Hα	He I λ6678	Hγ	He I λ4471	Mg II λ4481	Fe II ccfs
Mean RV (km s^{-1})	0.7	-5.8	18.1	-34.2	-72.8	···
RV range (km s^{-1})	-18.8 to 20.8	-24.2 to 12.0	7.3 to 26.6	-37.3 to -30.8	-82.1 to -63.9	···
RV change (km s^{-1})	39.6	36.2	19.3	6.5	18.2	···

- Shell classification: very very weak emission shell
- Notes on emission and absorption features: The strong Hα emission shows morphological changes (that result in shifts of the radial velocity of the wings). The emission peaks in Hγ also exhibit peak shifting and match with the peak location for Hα. He I λ6678 shows very small emission wings (unreliable for RV studies). Mg II λ4481 is very broad and blended (therefore untrustworthy for RV studies). Only the broad He I λ4471 line does not appear affected by emission (but it likely is anyway).
- Other notes: This star is notoriously confused with its close neighbor HD214167 (which is not a Be star, but is a narrow-lined B star). Another plot of this star is shown in Figure 7.4.

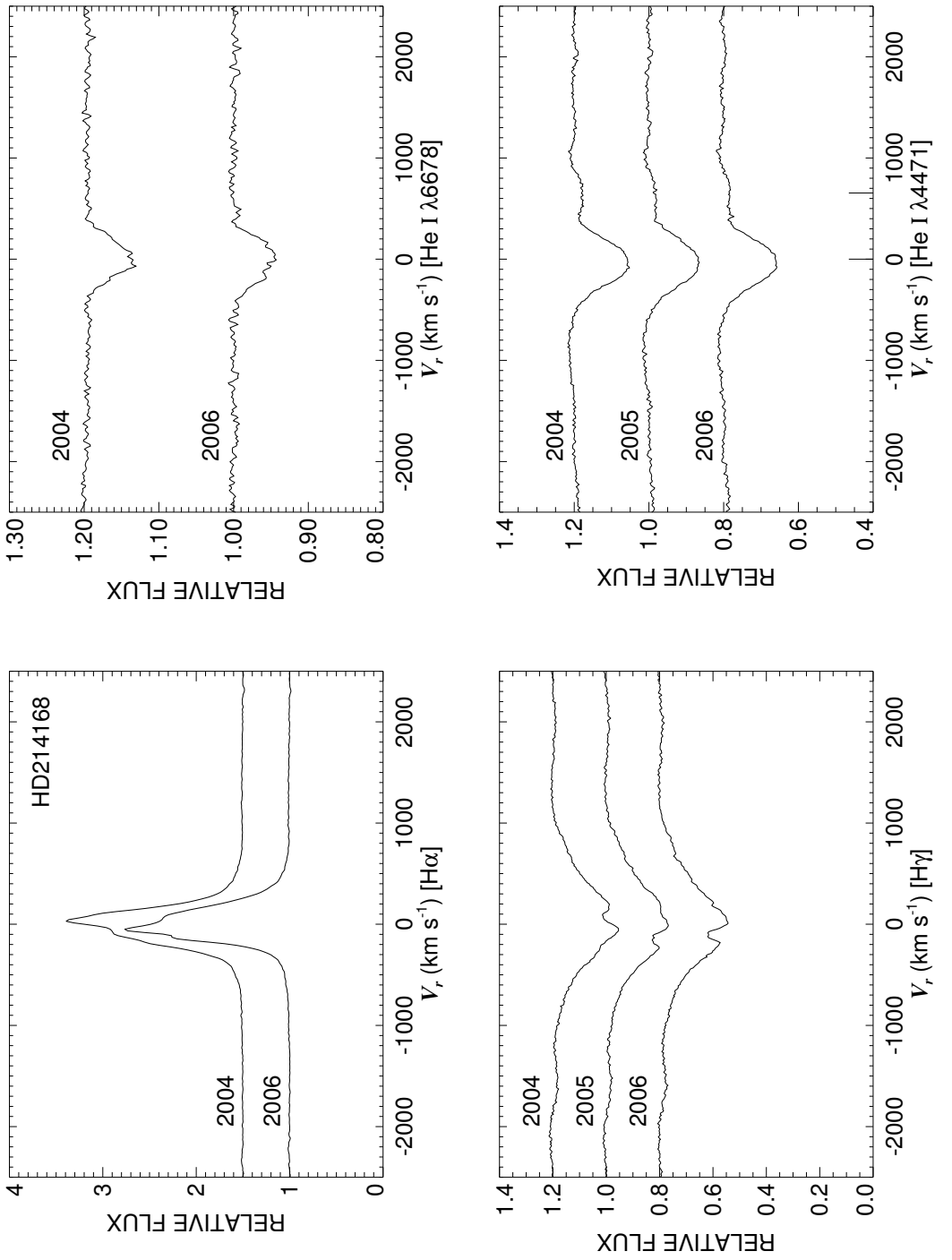

Figure C.154: A quadruple plot of HD214168 as described in §7.2.3 and Figure 7.6.

HD216057

Classical Be Star

- Other Names: HR 8682
- Spectral Type: B5 Vne
- V magnitude: 6.04
- In WDS?: no
- Known spectroscopic binary?: no
- Velocity variations seen in these data?: no

	Hα	He I λ6678	Hγ	He I λ4471	Mg II λ4481	Fe II ccfs
Mean RV (km s^{-1})	0.9	-0.5	-0.0	-22.7	-17.3	···
RV range (km s^{-1})	-2.0 to 5.6	-0.5 to -0.4	-4.6 to 4.6	-28.0 to -16.6	-20.5 to -10.9	···
RV change (km s^{-1})	7.6	0.1	9.2	11.4	9.6	···

- Shell classification: normal
- Notes on emission and absorption features: This broad-lined (thus fast rotating) star shows very weak Hα emission.
- Other notes: This star is also plotted in the "normal" Figure 7.2.

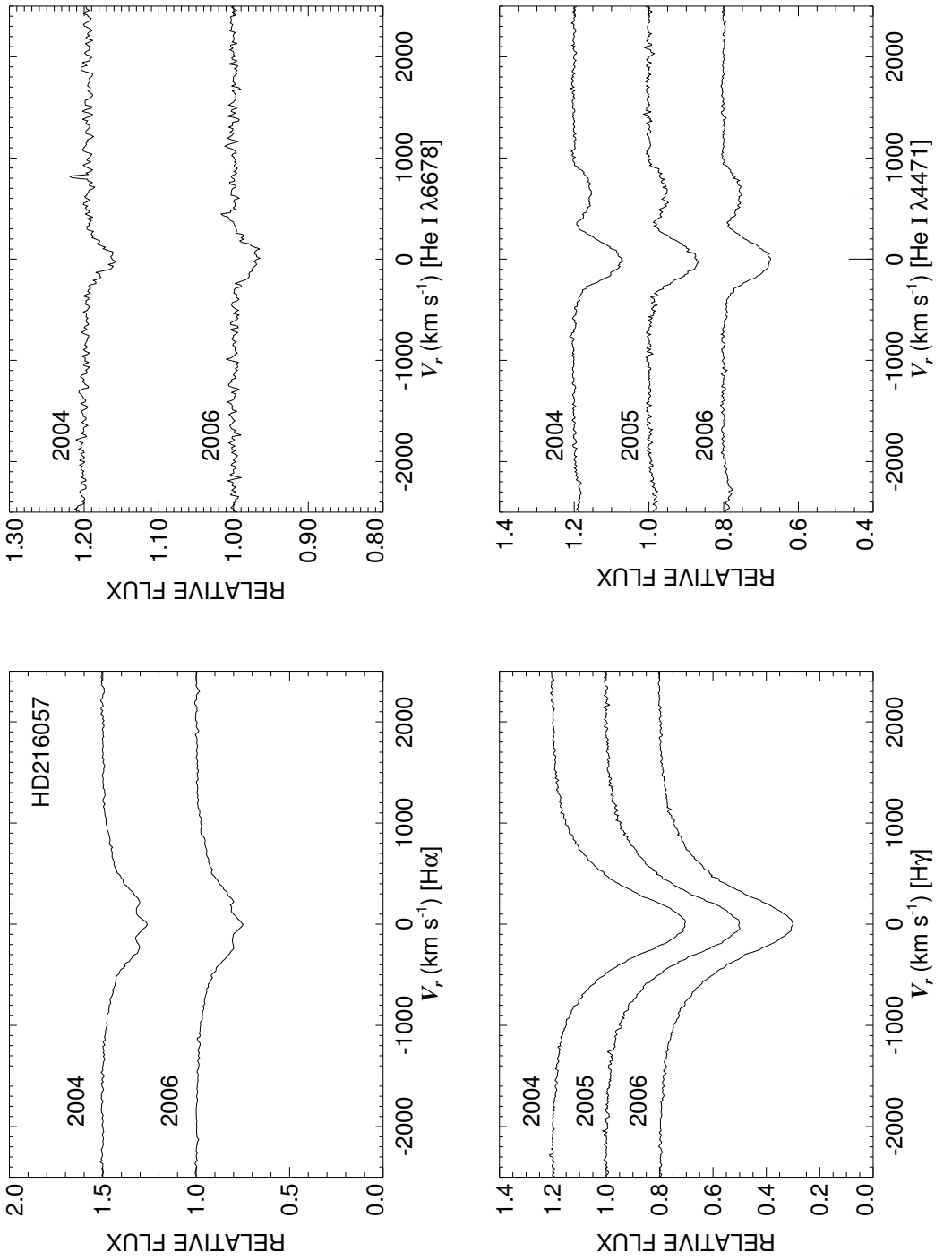

Figure C.155: A quadruple plot of HD216057 as described in §7.2.3 and Figure 7.6.

HD216200

Interacting Binary

- Other Names: HR 8690, 14 Lac, V360 Lac
- Spectral Type: B3 IV:e
- V magnitude: 5.98
- In WDS?: yes - 9.36 mag companion 0.4 arcsec away (discovered in 1985)
- Known spectroscopic binary?: yes - both components are seen in the spectrum (the secondary is an F9 IV star) and the period is 10.0854 d (Hill et al. 1997)
- Velocity variations seen in these data?: yes (see Fig. C.157)

	Hα	He I λ6678	Hγ	He I λ4471	Mg II λ4481	Fe II ccfs
Mean RV (km s^{-1})	-20.4	-24.3	-1.5	-38.6	-7.5	19.1
RV range (km s^{-1})	-52.3 to 16.6	-69.6 to 39.3	-18.3 to 27.3	-58.2 to -3.7	-31.7 to 15.0	-143.1 to 155.5
RV change (km s^{-1})	68.9	108.9	45.6	54.5	46.7	298.6

- Shell classification: composite
- Do shell features move with the star?: no - composite spectrum
- Notes on emission and absorption features: The wings of Hα are filled in with emission. Both He I λ6678 and Mg II λ4481 show emission horns. The whole blue spectrum shows evidence of the orbital motions of both stars.
- Other notes: Linnell et al. (2006) state this system is analogous to CX Dra (HD174237) except at a lower inclination, find it to be a "double-contact" system, and find evidence for circumstellar matter moving with the primary (the Be star).

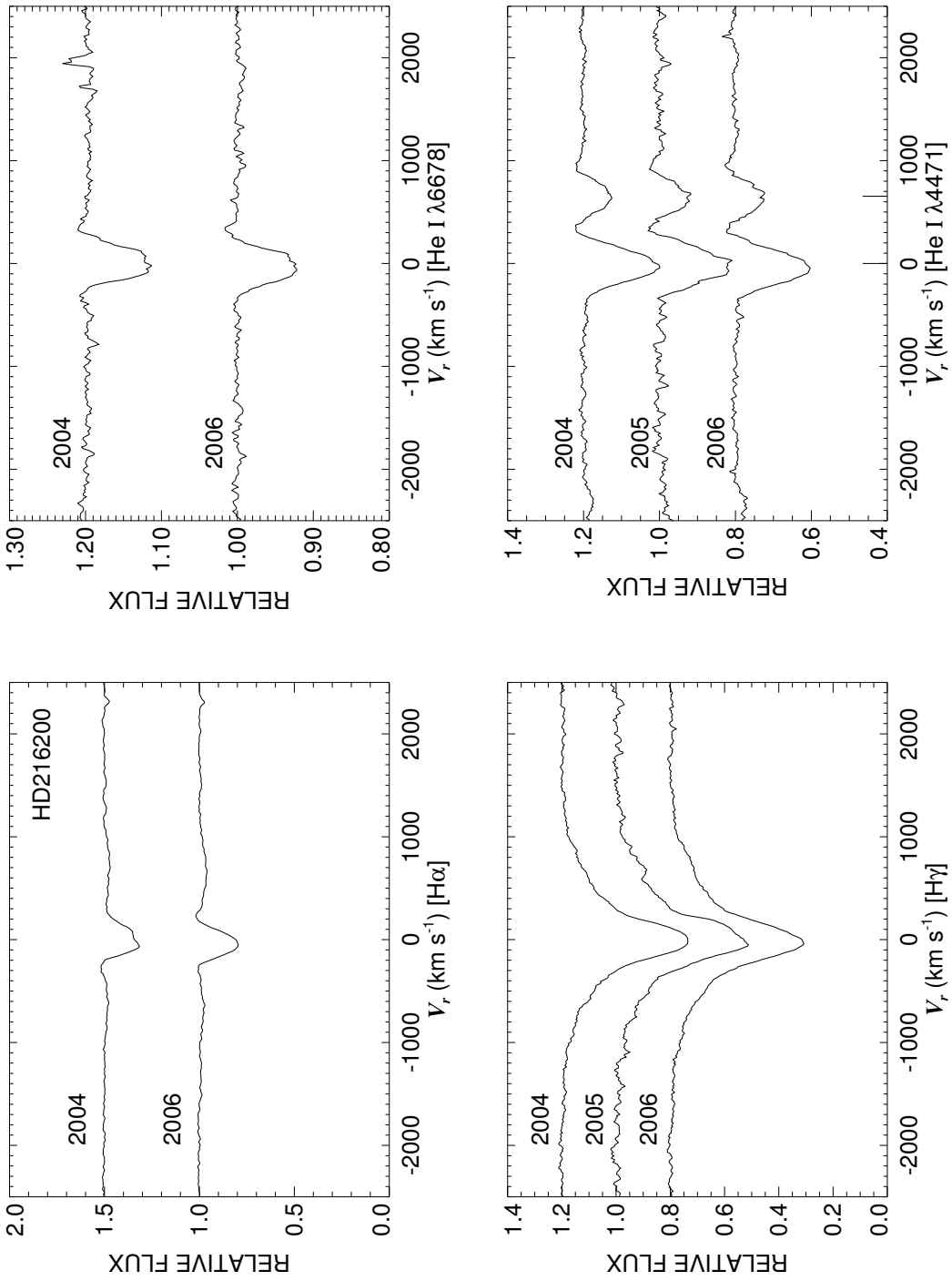

Figure C.156: A quadruple plot of HD216200 as described in §7.2.3 and Figure 7.6.

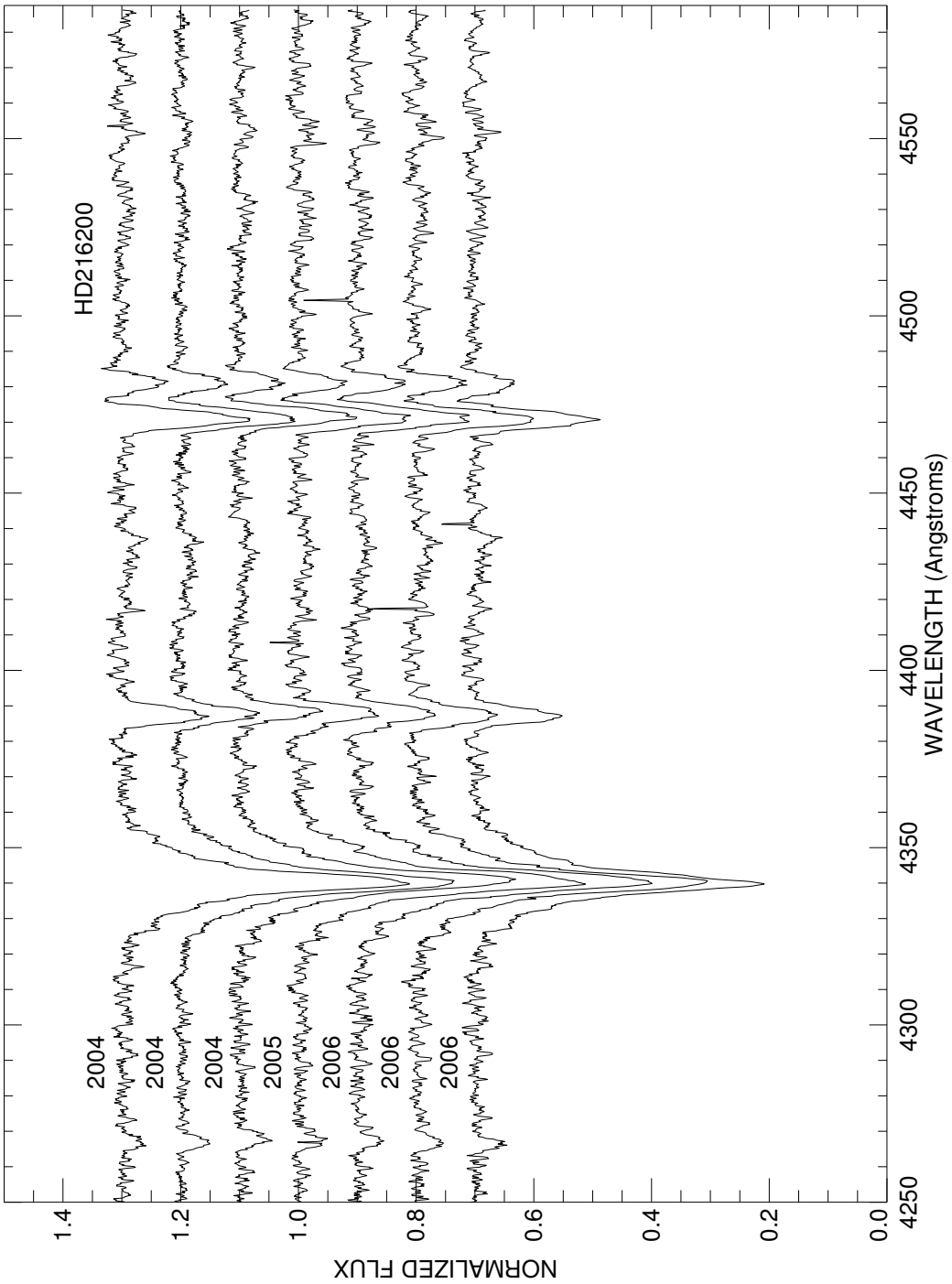

Figure C.157: A plot of all spectra of HD216200 in the blue region. Each is labeled with the year of observation and they are offset for clarity.

HD217050

Classical Be Star, Shell Star

- Other Names: HR 8731, EW Lac
- Spectral Type: B3.5 IIIpe+sh
- V magnitude: 5.33
- In WDS?: no
- Known spectroscopic binary?: no
- Velocity variations seen in these data?: yes (see Fig. C.159)

	Hα	He I λ6678	Hγ	He I λ4471	Mg II λ4481	Fe II ccfs
Mean RV (km s^{-1})	-12.3	-11.1	-4.8	-31.0	-9.8	7.2
RV range (km s^{-1})	-14.8 to -7.3	-25.9 to 25.0	-10.7 to 3.1	-39.5 to -16.8	-42.2 to 29.7	-24.8 to 45.3
RV change (km s^{-1})	7.5	50.9	13.8	22.7	71.9	70.1

- Shell classification: shell (very deep! get deeper in 2006)
- Do shell features move with the star?: yes
- Notes on emission and absorption features: Hα shows a very strong central absorption as well as showing peak morphology. All lines are affected by shell features and show the same velocity variation.
- Other notes:

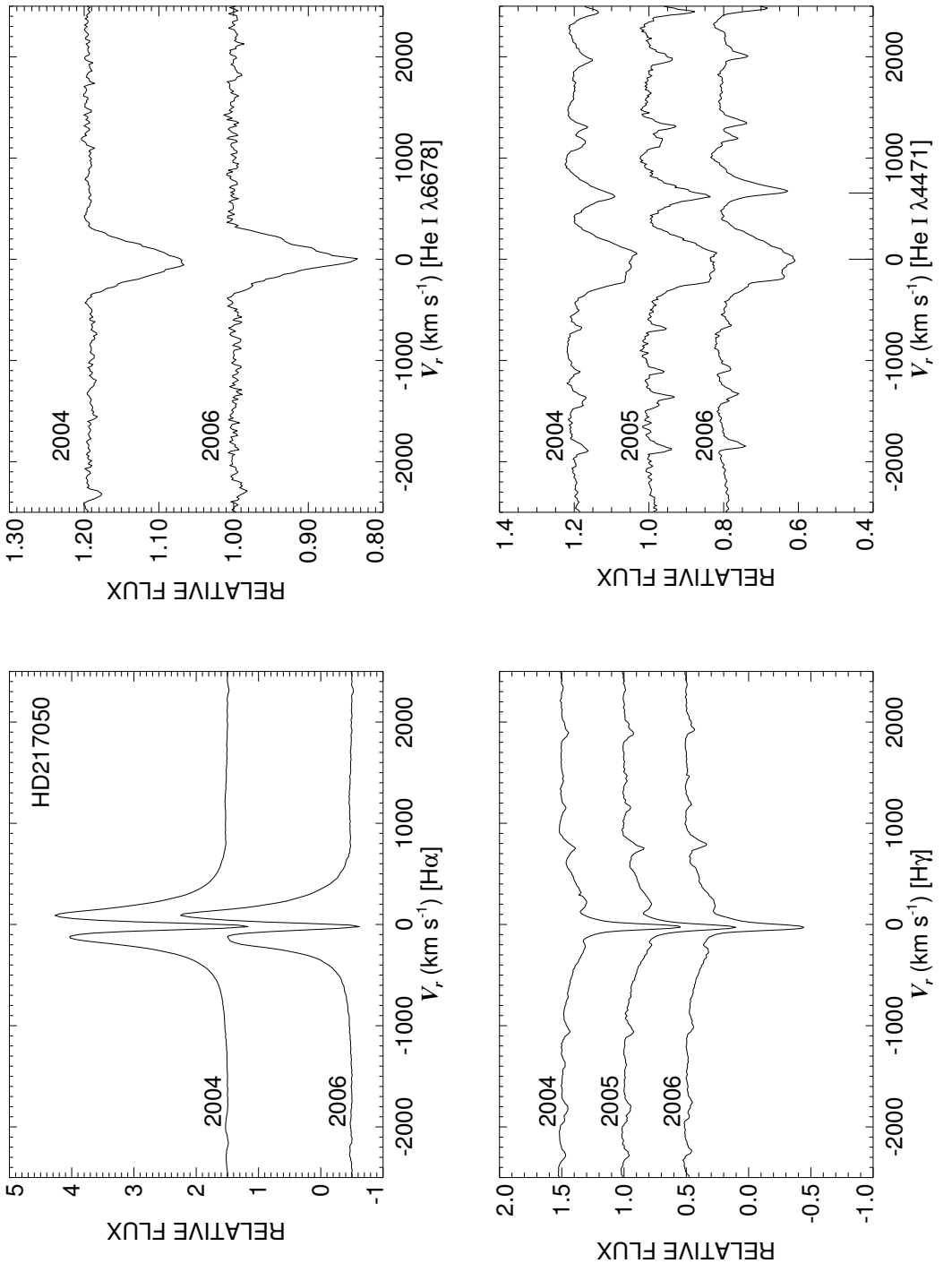

Figure C.158: A quadruple plot of HD217050 as described in §7.2.3 and Figure 7.6.

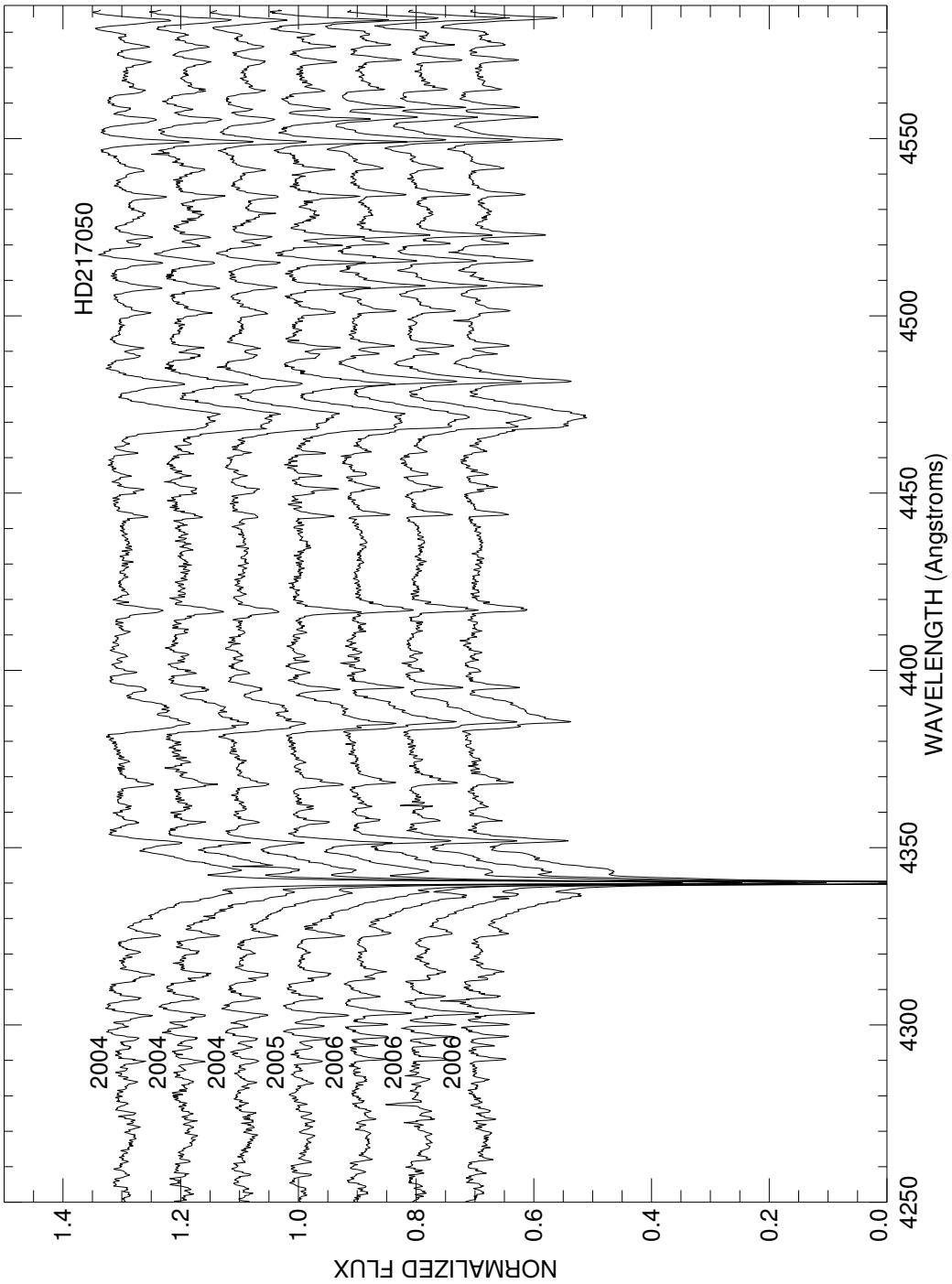

Figure C.159: A plot of all spectra of HD217050 in the blue region. Each is labeled with the year of observation and they are offset for clarity.

HD217543

Classical Be Star, Non-Radial Pulsator

- Other Names: HR 8758
- Spectral Type: B3.5 Vpe
- V magnitude: 6.44
- In WDS?: no
- Known spectroscopic binary?: no
- Velocity variations seen in these data?: yes (see Fig. C.161)

	Hα	He I λ6678	Hγ	He I λ4471	Mg II λ4481	Fe II ccfs
Mean RV (km s^{-1})	-4.5	-26.3	-9.9	-21.7	8.2	···
RV range (km s^{-1})	-10.2 to 3.0	-29.8 to -20.9	-15.5 to -5.0	-30.8 to -7.4	-10.7 to 24.2	···
RV change (km s^{-1})	13.2	8.9	10.5	23.4	34.9	···

- Shell classification: normal
- Notes on emission and absorption features: Hα wings are filled-in in 2004 and develops into peaks in 2006. He I λ6678 has an emission horn in 2004 but not in 2006 and also shows variations that may be the result of emission filling or NRP. Hγ gets sharper in 2006. The broad blue absorption lines show line profile variations consistant with NRP. Mg II λ4481 is very broad and blended (therefore unreliable). C II λ4267 develops an emission horn in 2006.
- Other notes:

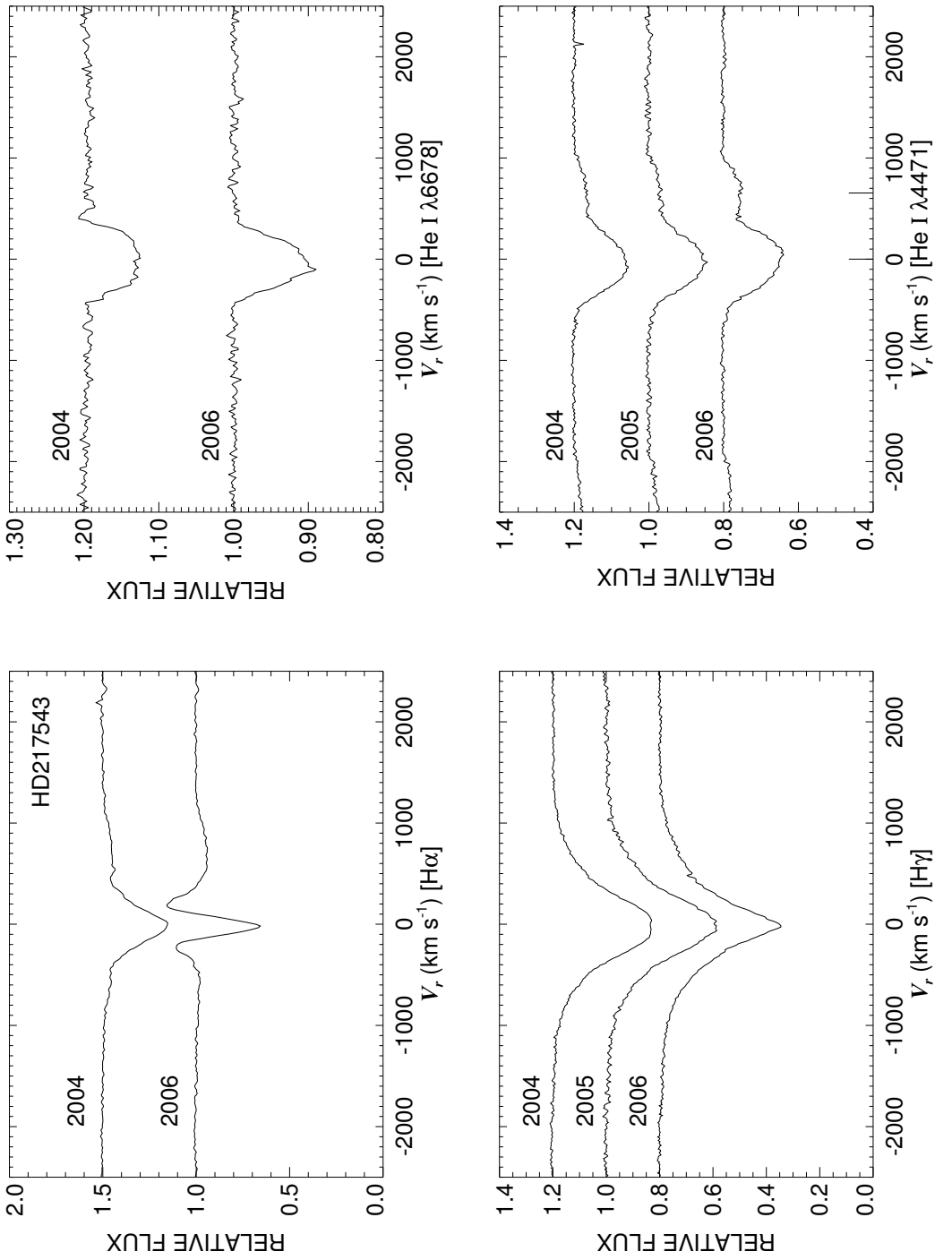

Figure C.160: A quadruple plot of HD217543 as described in §7.2.3 and Figure 7.6.

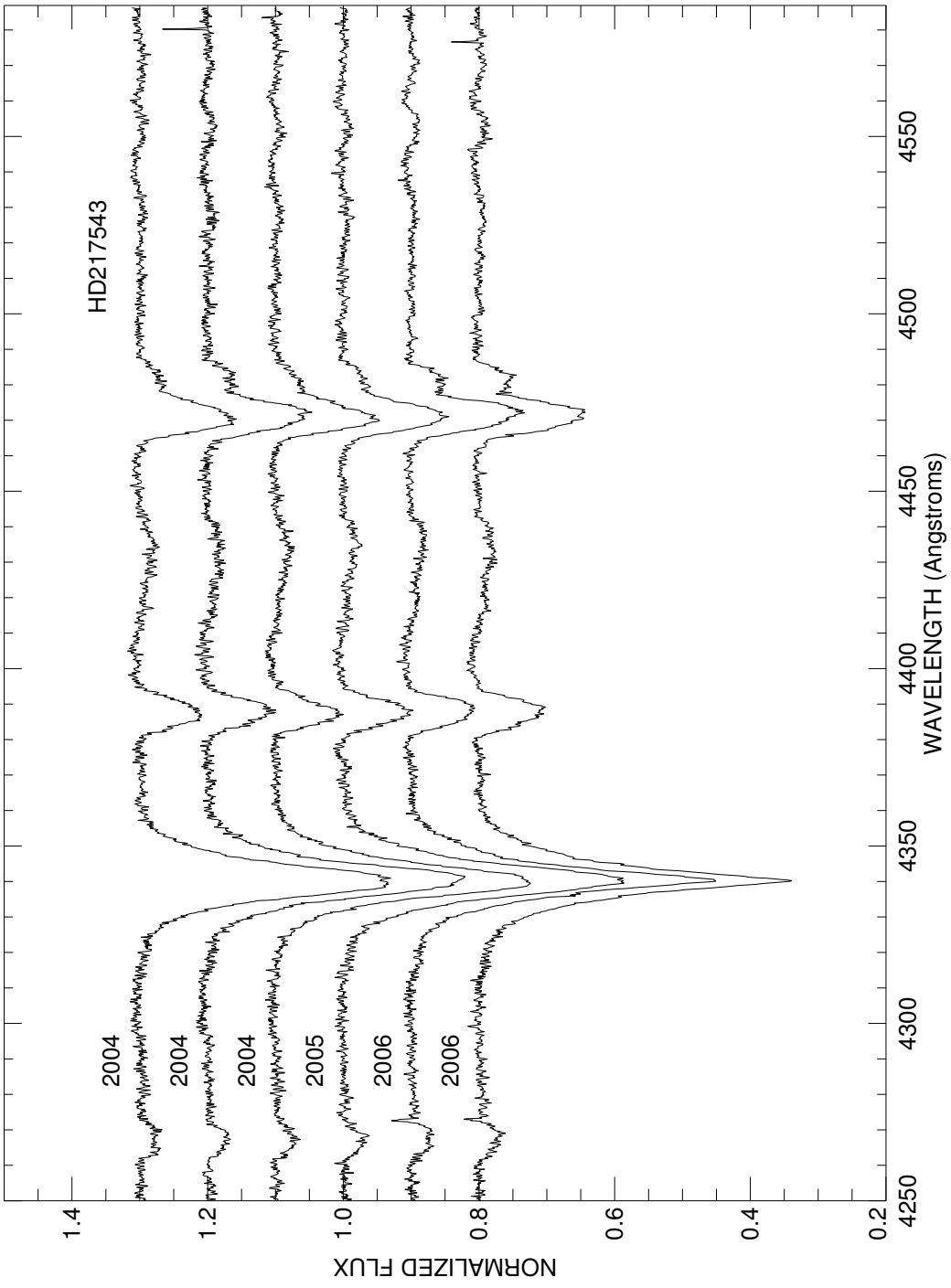

Figure C.161: A plot of all spectra of HD217543 in the blue region. Each is labeled with the year of observation and they are offset for clarity.

HD217675

Classical Be Star; Non-Radial Pulsator

- Other Names: HR 8762, *o* And, 1 And
- Spectral Type: B6 IIIpe+sh
- V magnitude: 3.55
- In WDS?: yes - a speckle companion of unlisted magnitude less than 0.1 arcsec away (discovered in 1975) along with a 6.03 mag companion 0.1 arcsec away (discovered in 1949)
- Known spectroscopic binary?: yes - see notes below
- Velocity variations seen in these data?: yes (NRP? - see Fig. C.163)

	Hα	He I λ6678	Hγ	He I λ4471	Mg II λ4481	Fe II ccfs
Mean RV (km s^{-1})	-3.6	-20.2	-12.3	-24.6	-16.3	···
RV range (km s^{-1})	-11.6 to 7.2	-32.3 to -9.2	-15.1 to -7.8	-28.7 to -20.3	-22.5 to -6.7	···
RV change (km s^{-1})	18.8	23.1	7.3	8.4	15.8	···

- Shell classification: normal
- Notes on emission and absorption features: Hα shows emission wings in 2004 but the wings weaken in 2004. Hγ is sharp-lined in 2004 but widens toward 2006. The blue absorption lines show line profile variations indicative of NRP and/or a composite spectrum. Mg II λ4481 especially shows sharp rapidly moving components (this could show the close binary mentioned in the notes below).
- Other notes: Rivinius et al. (2004) show the non-radial pulsations in their Fig. 6 with a period of 0.694 d (although they point out there is a photometric period of 1.58 d). They also state that this star is a spectroscopic triple where a close pair of late B/early A stars are seen in spectral lines but this pair is not orbiting close enough to affect the Be star.

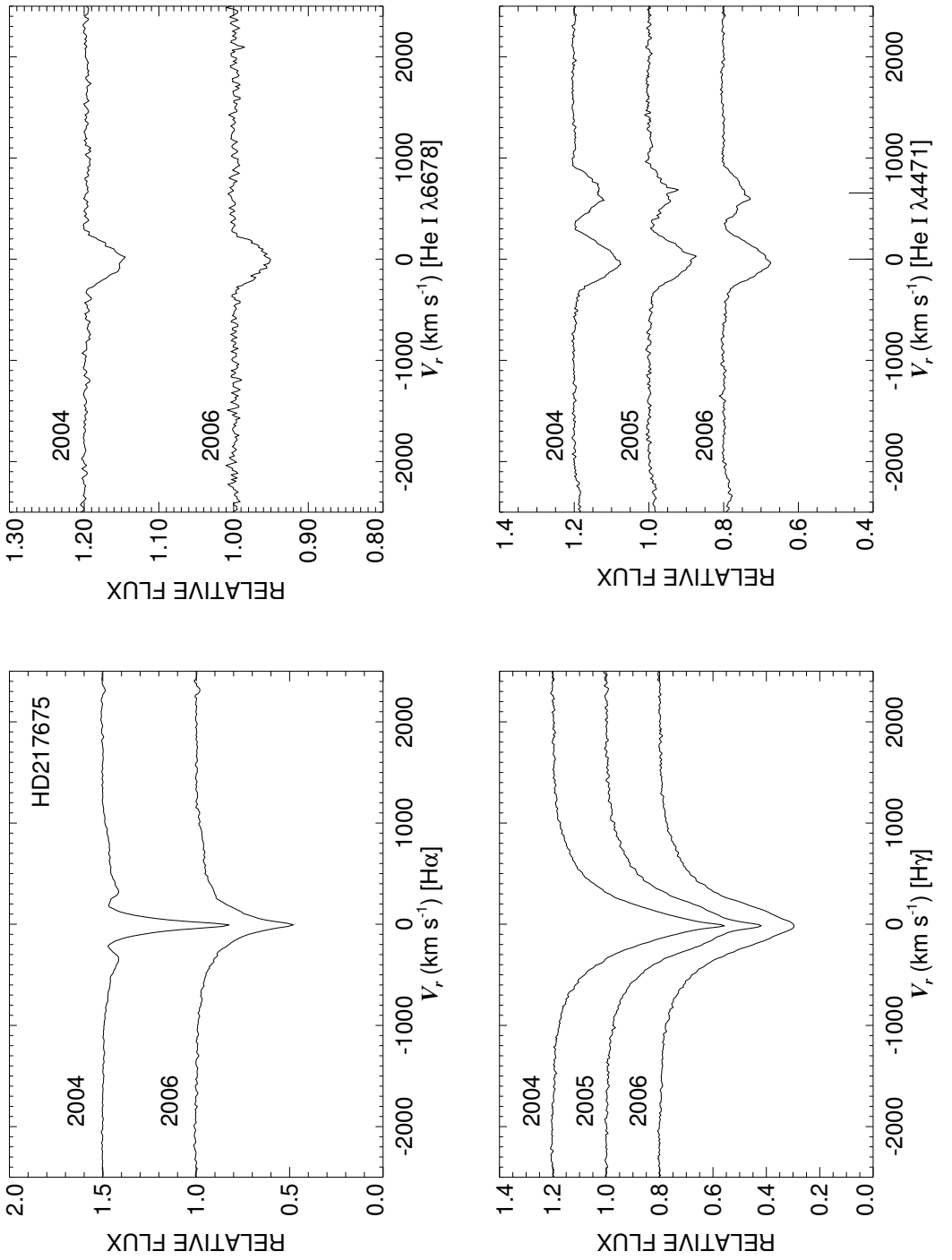

Figure C.162: A quadruple plot of HD217675 as described in §7.2.3 and Figure 7.6.

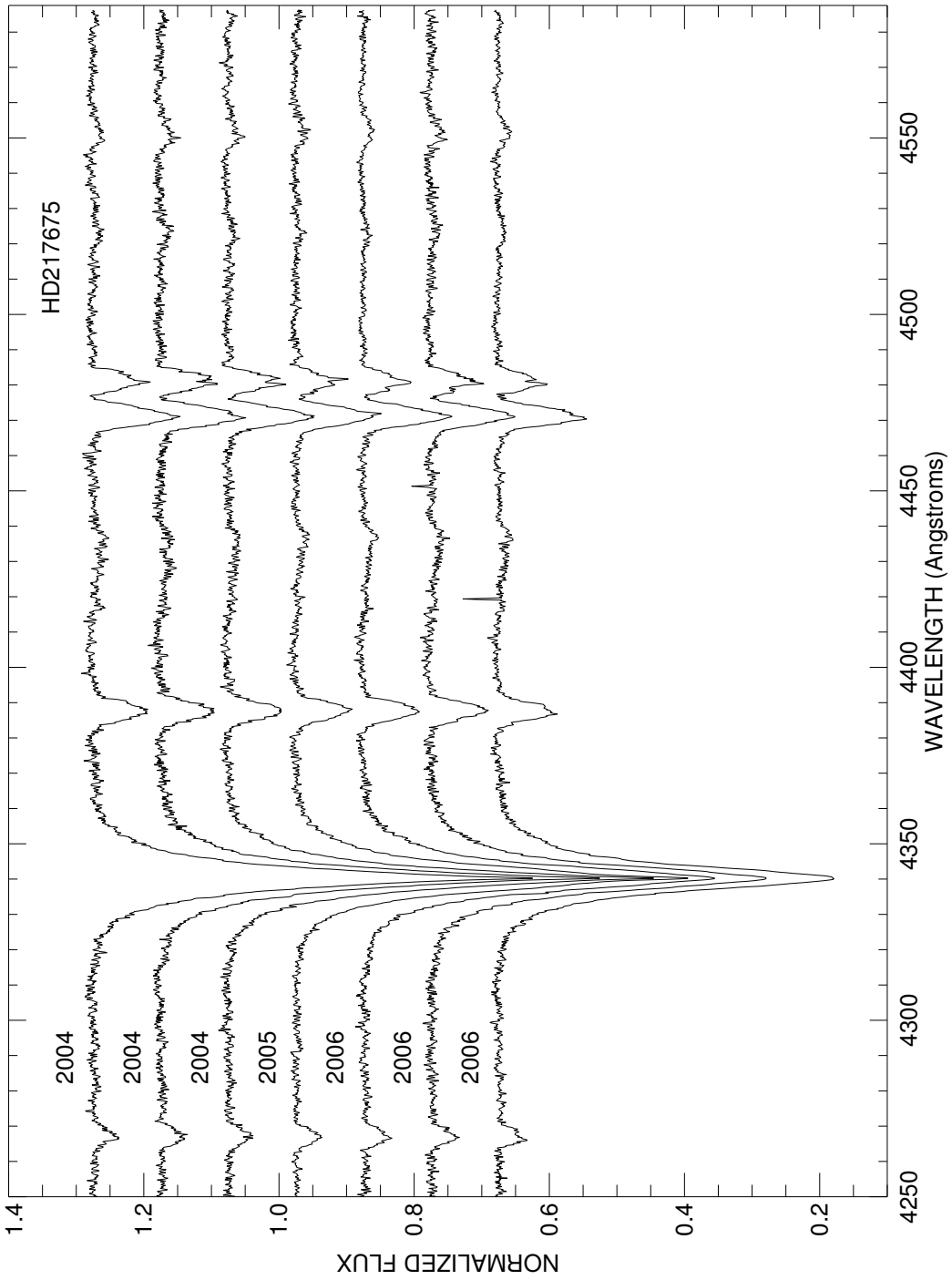

Figure C.163: A plot of all spectra of HD217675 in the blue region. Each is labeled with the year of observation and they are offset for clarity.

HD217891

Classical Be Star

- Other Names: HR 8773, β Psc, 4 Psc
- Spectral Type: B5 Ve
- V magnitude: 4.37
- In WDS?: no
- Known spectroscopic binary?: no
- Velocity variations seen in these data?: perhaps very small

	Hα	He I λ6678	Hγ	He I λ4471	Mg II λ4481	Fe II ccfs
Mean RV (km s^{-1})	5.7	5.1	1.1	-0.2	3.8	···
RV range (km s^{-1})	4.8 to 6.2	-4.6 to 13.7	-2.2 to 3.4	-5.1 to 4.0	-0.8 to 7.9	···
RV change (km s^{-1})	1.4	18.3	5.6	9.1	8.7	···

- Shell classification: normal
- Notes on emission and absorption features: Likely a pole-on Be star as the lines are so narrow. Emission in both Hα and Hγ decreases in 2006. He I λ6678 may be slightly filled in with emission.
- Other notes:

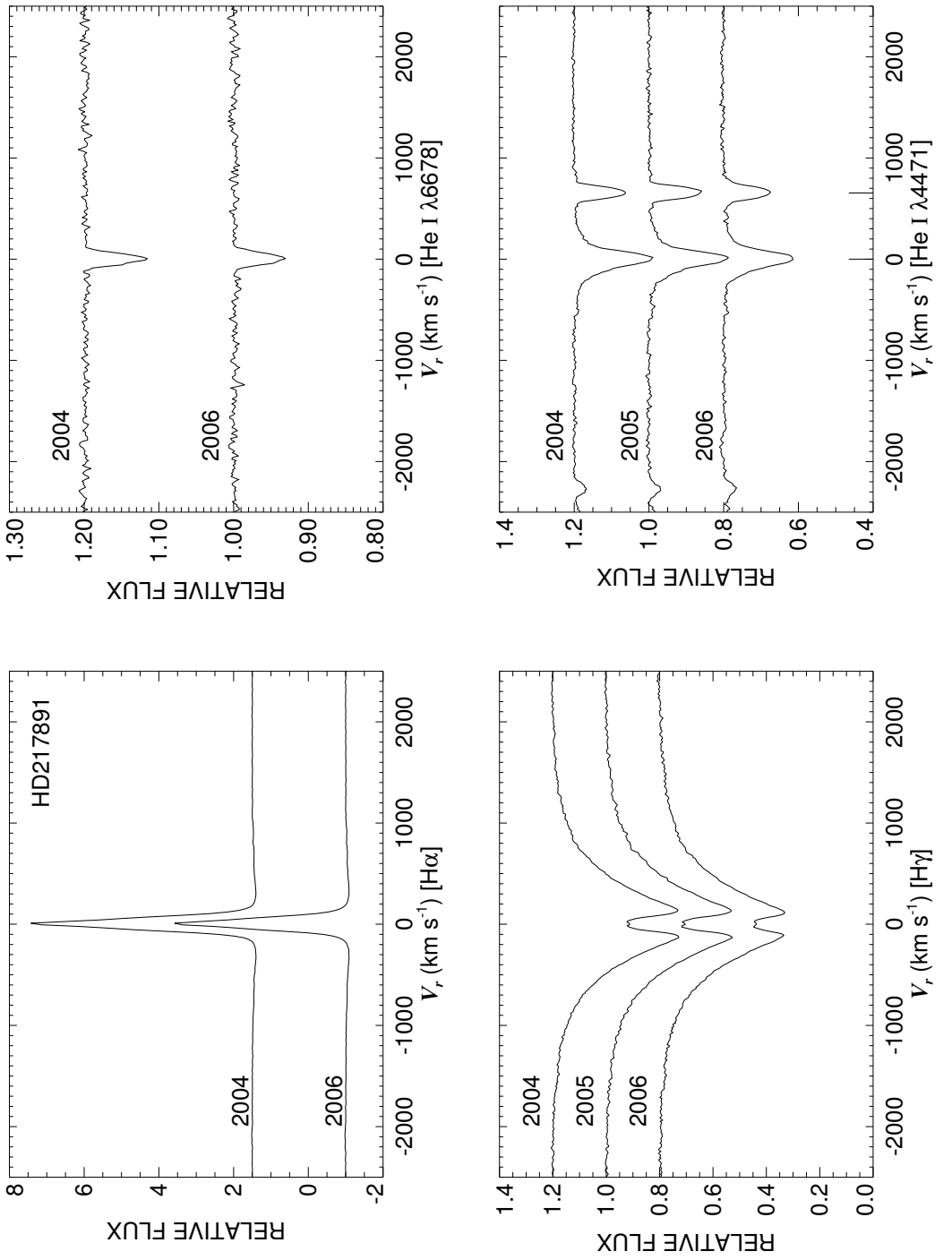

Figure C.164: A quadruple plot of HD217891 as described in §7.2.3 and Figure 7.6.

HD218393

Interacting Binary

- Other Names: KX And
- Spectral Type: B2 IIIne
- V magnitude: 7.41
- In WDS?: no
- Known spectroscopic binary?: yes - analogous to RY Scuti, it has a period of 38.918 d (Štefl et al. 1990) and the secondary is a K0 II star filling its Roche lobe (Floquet et al. 1995) (see Fig. C.166)
- Velocity variations seen in these data?: yes

	Hα	He I λ6678	Hγ	He I λ4471	Mg II λ4481	Fe II ccfs
Mean RV (km s^{-1})	17.3	-155.2	-128.0	-107.7	-40.0	-4.0
RV range (km s^{-1})	8.7 to 22.8	-191.6 to -114.4	-184.9 to -105.2	-140.4 to -94.4	-69.6 to -10.3	-14.3 to 4.9
RV change (km s^{-1})	14.1	77.2	79.7	46.0	59.3	19.3

- Shell classification: composite
- Notes on emission and absorption features: The interacting nature of this system affects the entire spectrum.
- Other notes: This star is a good representative of the class of W Serpentis stars (of which RY Scuti is a member) (Tarasov 2000). As it is such a good representative of interacting binaries, it was eliminated from all statistics in Chapter 7.

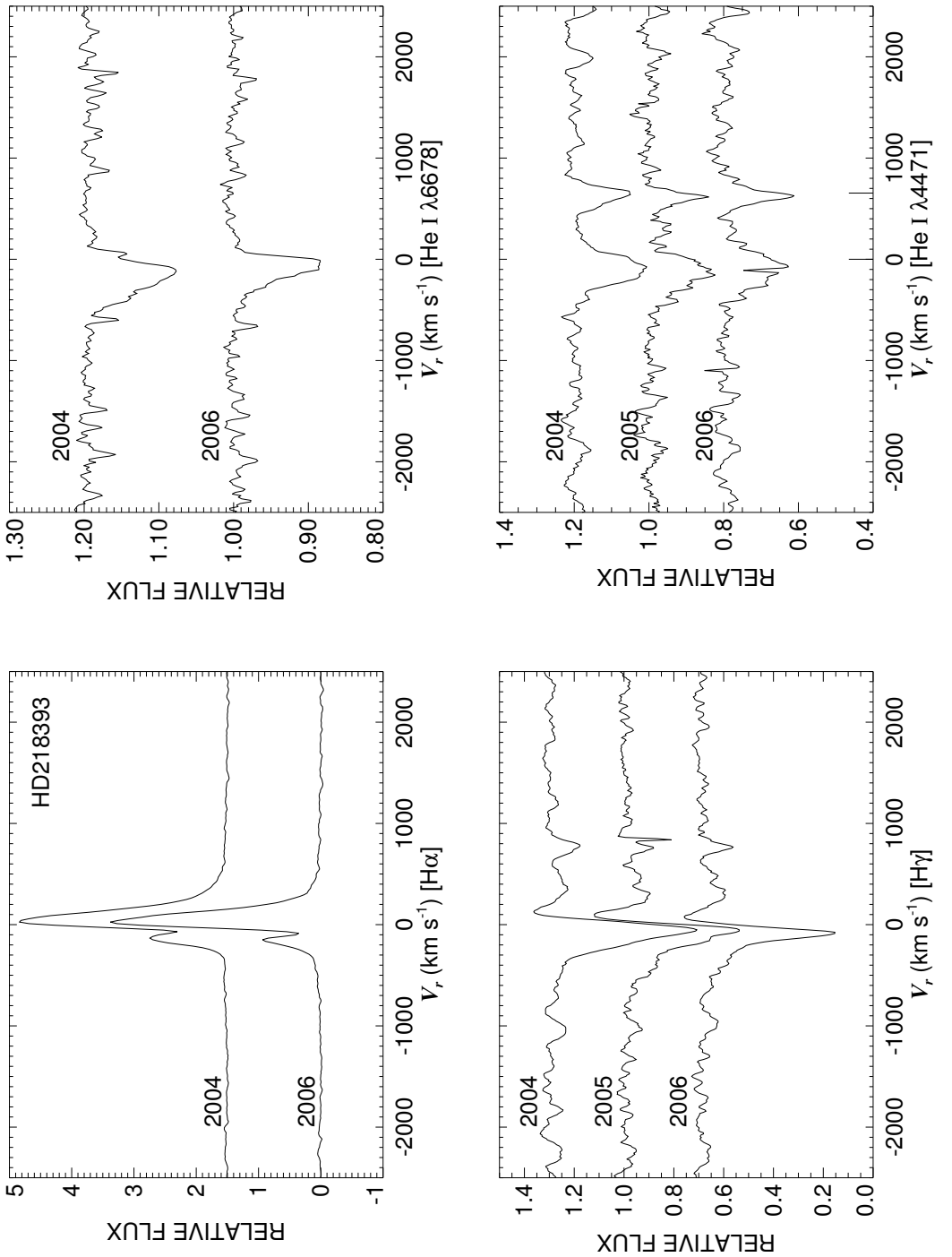

Figure C.165: A quadruple plot of HD218393 as described in §7.2.3 and Figure 7.6.

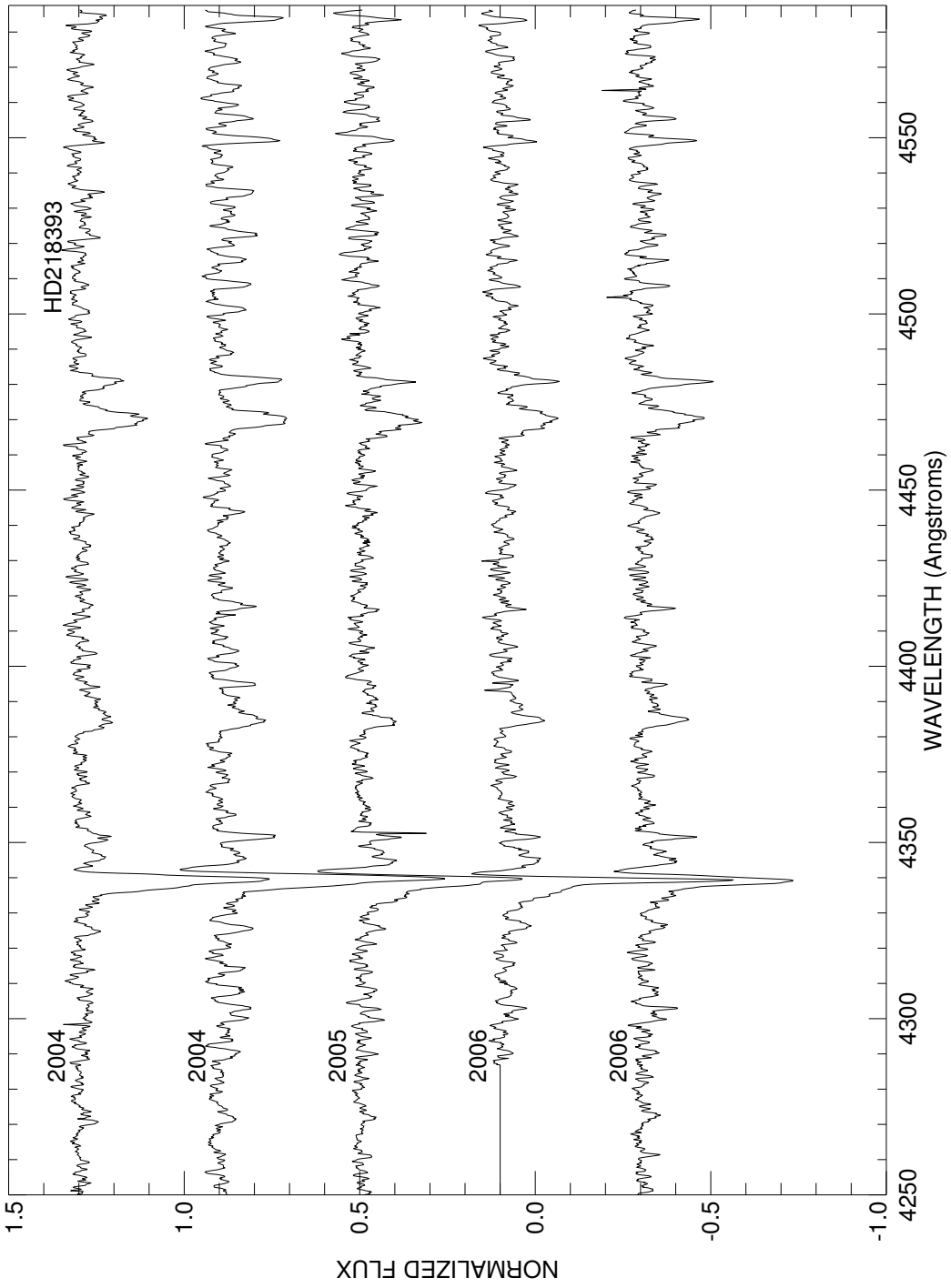

Figure C.166: A plot of all spectra of HD218393 in the blue region. Each is labeled with the year of observation and they are offset for clarity.

HD218674

Classical Be Star; Non-Radial Pulsator

- Other Names: KY And
- Spectral Type: B3 IV/Ve+sh
- V magnitude: 6.71
- In WDS?: no
- Known spectroscopic binary?: no
- Velocity variations seen in these data?: yes (see Fig. C.168)

	Hα	He I λ6678	Hγ	He I λ4471	Mg II λ4481	Fe II ccfs
Mean RV (km s^{-1})	-15.2	-30.2	-6.2	-27.9	-32.4	-12.0
RV range (km s^{-1})	-18.3 to -7.5	-59.3 to -7.0	-18.3 to 7.0	-37.0 to -8.7	-45.7 to -17.8	-18.6 to -4.0
RV change (km s^{-1})	10.8	52.3	25.3	28.3	27.9	14.6

- Shell classification: very weak squarish (they disappear in 2006)
- Notes on emission and absorption features: Hα emission strength decreases slightly. Hγ moves around. All absorption lines (both red and blue) show evidence for NRP as well as perhaps binarity.
- Other notes: Hahula & Gies (1994) (among others) find this star is a non-radial pulsator with a period of 0.79 d. Pavlovski & Ruzic (1988) looked for multi-periodic variability but their search was inconclusive.

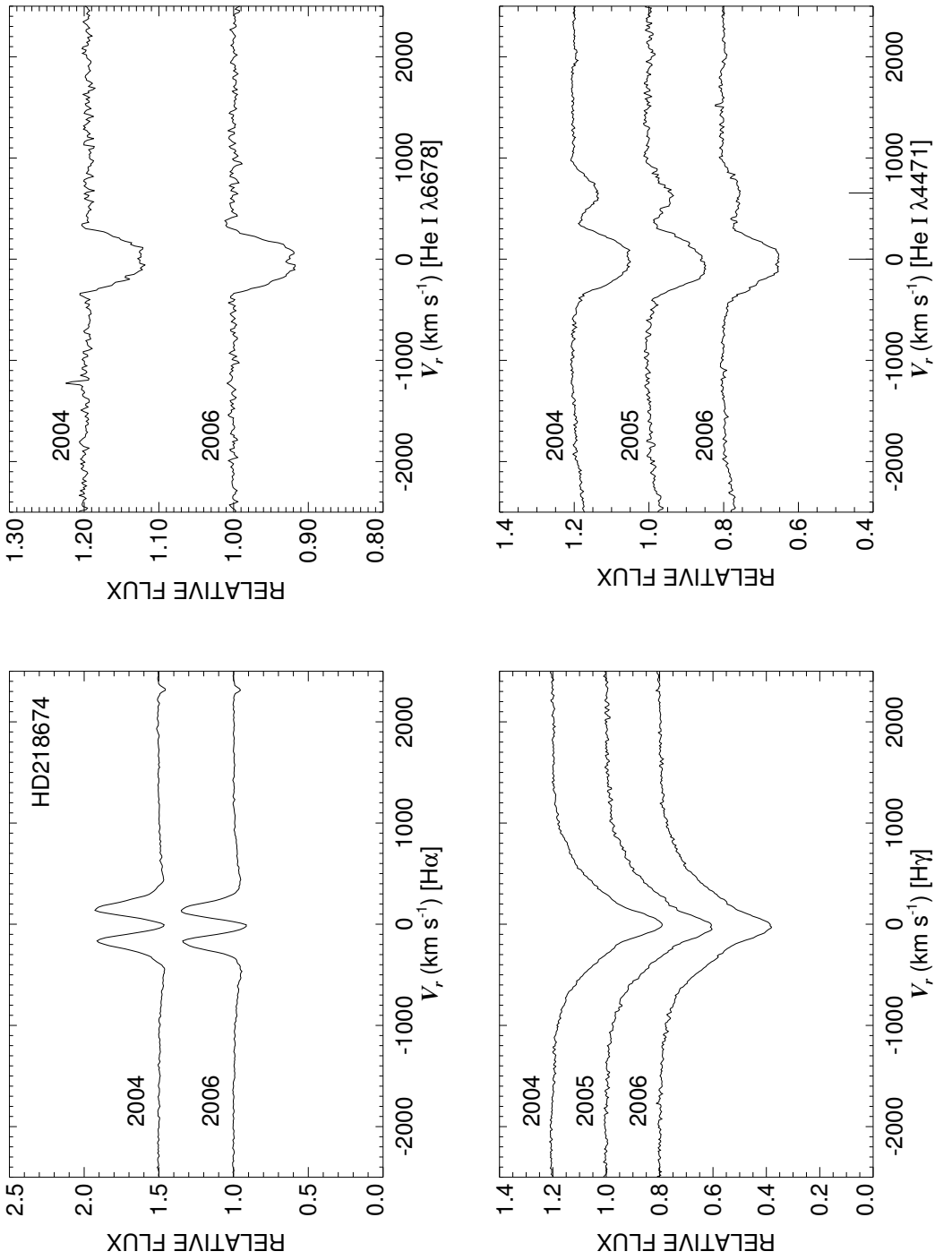

Figure C.167: A quadruple plot of HD218674 as described in §7.2.3 and Figure 7.6.

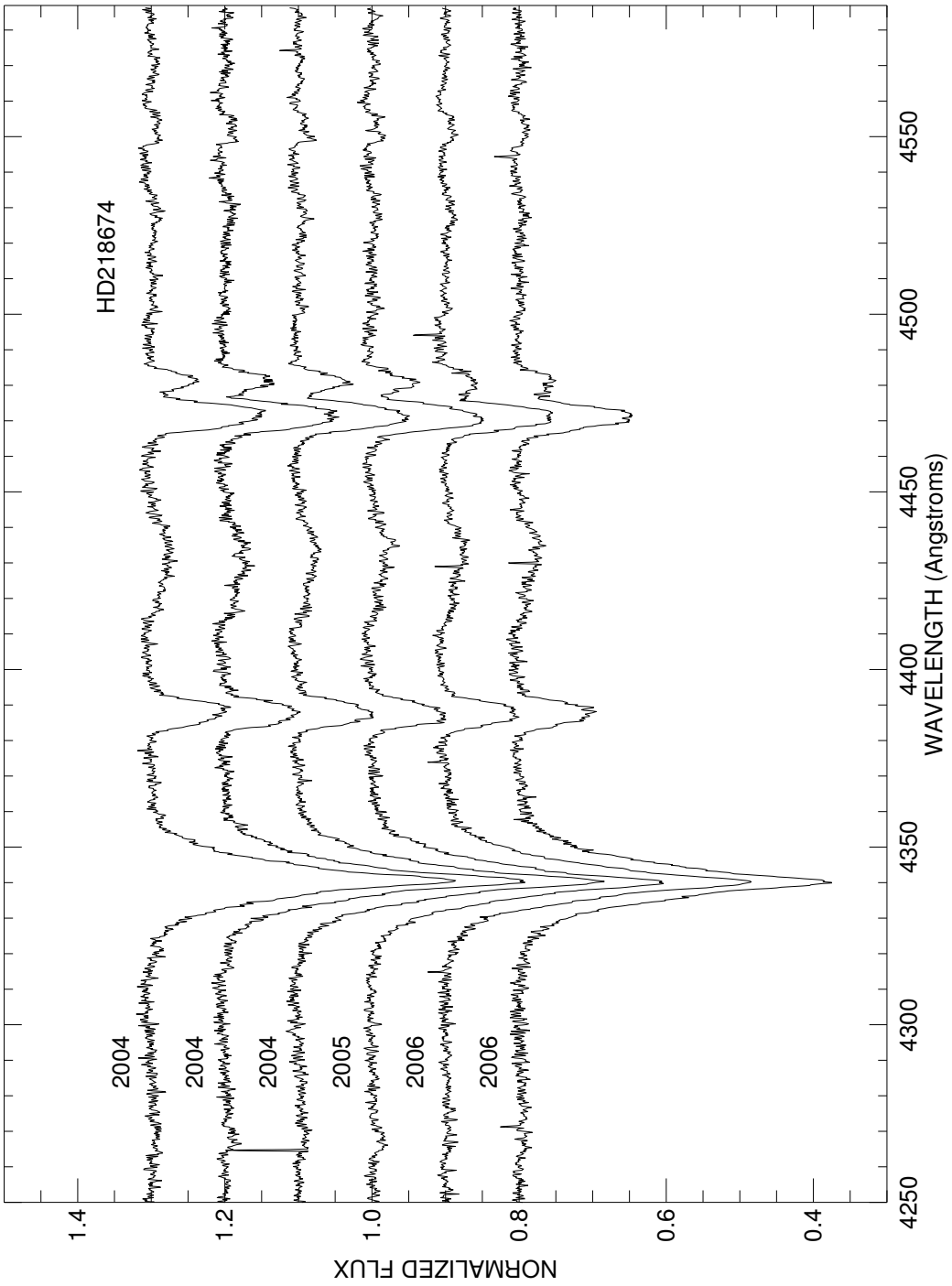

Figure C.168: A plot of all spectra of HD218674 in the blue region. Each is labeled with the year of observation and they are offset for clarity.

HD224544

Classical Be Star

- Other Names: HR 9068
- Spectral Type: B6 IVe+sh
- V magnitude: 6.40
- In WDS?: no
- Known spectroscopic binary?: no
- Velocity variations seen in these data?: maybe slight (NRP?)

	Hα	He I λ6678	Hγ	He I λ4471	Mg II λ4481	Fe II ccfs
Mean RV (km s^{-1})	-8.3	-14.7	-6.0	-34.0	-27.7	···
RV range (km s^{-1})	-10.3 to -7.0	-32.2 to -2.1	-11.3 to -0.5	-38.6 to -30.9	-34.6 to -21.5	···
RV change (km s^{-1})	3.3	30.1	10.8	7.7	13.1	···

- Shell classification: normal (at this time)
- Notes on emission and absorption features: No emission at this time. He I λ6678 exhibits a rather strange profile - it is not rounded in 2004 (NRP?).
- Other notes: This IS a Be star - for instance, Andrillat (1983) show a double-peaked spectrum (somewhat similar to that of HD023480).

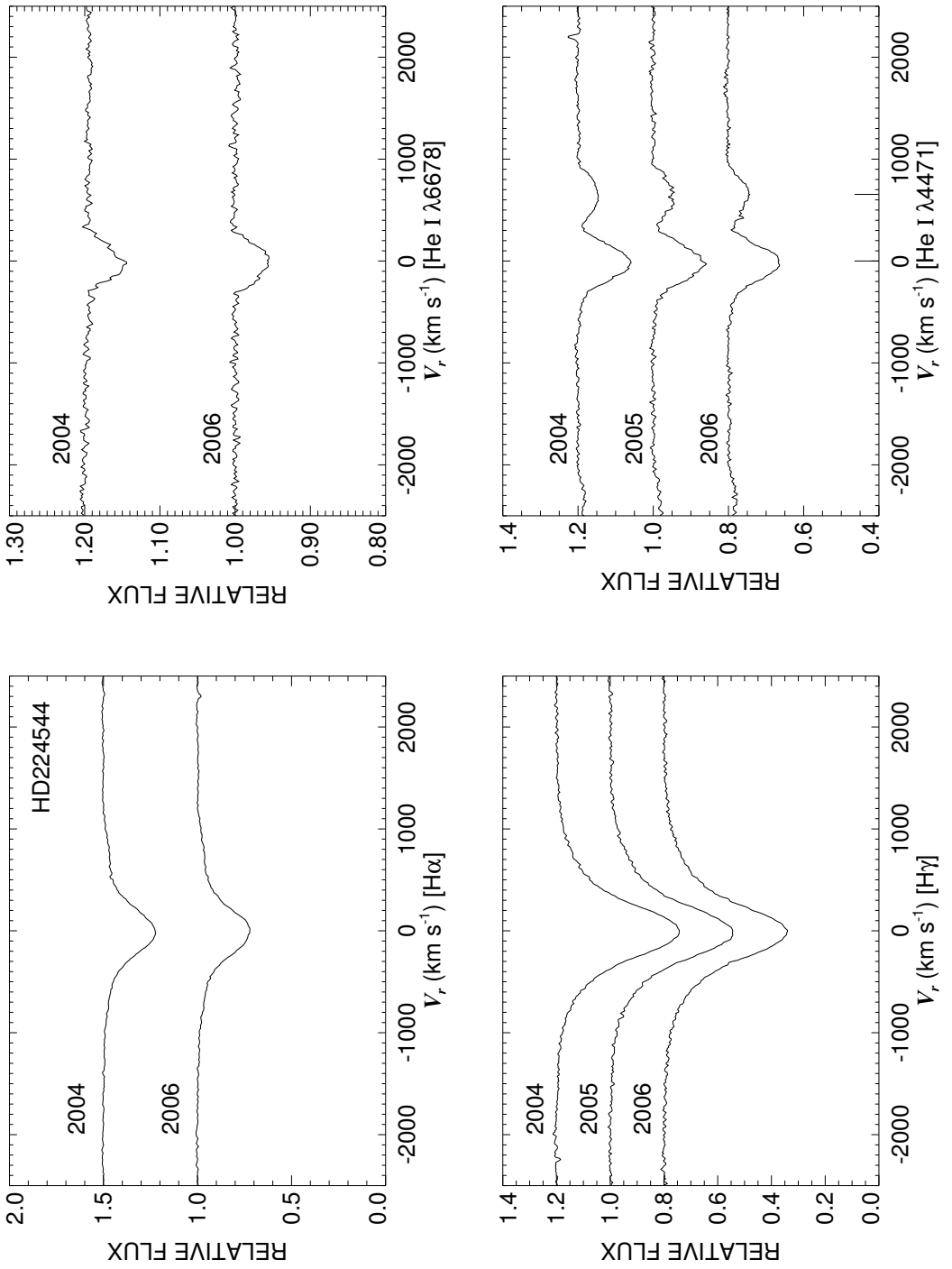

Figure C.169: A quadruple plot of HD224544 as described in §7.2.3 and Figure 7.6.

HD224559

Classical Be Star

- Other Names: HR 9070, LQ And
- Spectral Type: B3.5 Vne
- V magnitude: 6.45
- In WDS?: no
- Known spectroscopic binary?: possibly - Harmanec (2001) reports a period of 7.41 d but this star exhibits period light changes of 0.619 d (and that period is a resonance thereof).
- Velocity variations seen in these data?: perhaps very small

	Hα	He I λ6678	Hγ	He I λ4471	Mg II λ4481	Fe II ccfs
Mean RV (km s^{-1})	-2.0	-3.3	-22.7	-2.8	-16.8	-0.4
RV range (km s^{-1})	-3.4 to -0.8	-13.3 to 9.5	-27.6 to -15.6	-7.2 to 0.7	-24.2 to -10.0	-17.0 to 20.6
RV change (km s^{-1})	2.6	22.8	12.0	7.9	14.2	37.6

- Shell classification: emission shell (but looks squarish)
- Do shell features move with the star?: if it moves, then yes
- Notes on emission and absorption features: Strong Hα emission that grows in 2006. He I λ6678 seems shallow and filled in (unreliable). Mg II λ4481 is very broad and blended (likely unreliable).
- Other notes: This star is also plotted in Figure 7.3.

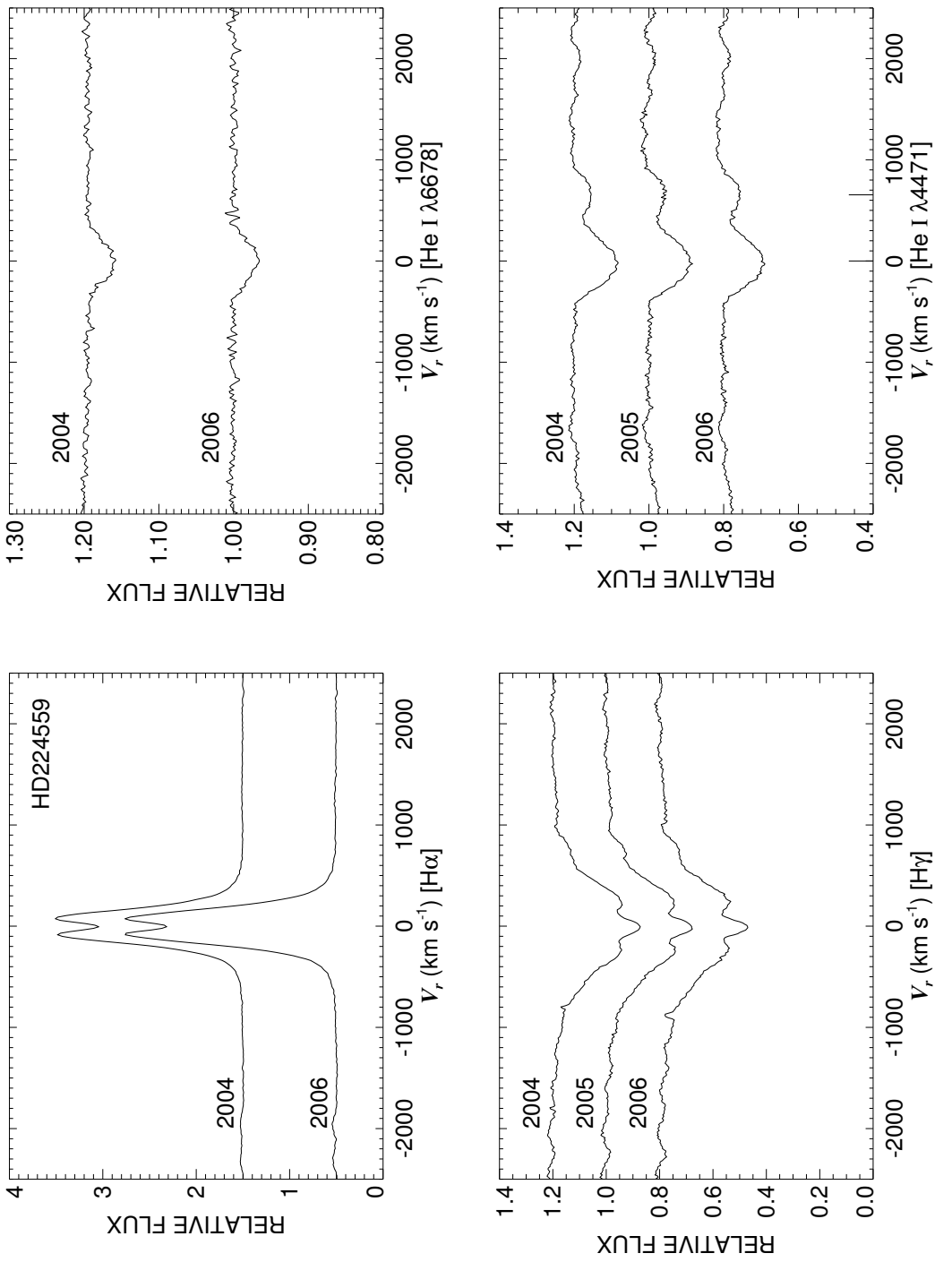

Figure C.170: A quadruple plot of HD224559 as described in §7.2.3 and Figure 7.6.

HD225095

Classical Be Star

- Other Names:
- Spectral Type: B2 IVne
- V magnitude: 7.91
- In WDS?: no
- Known spectroscopic binary?: no
- Velocity variations seen in these data?: no

	Hα	He I λ6678	Hγ	He I λ4471	Mg II λ4481	Fe II ccfs
Mean RV (km s^{-1})	-29.8	-60.7	44.3	-53.2	···	-33.3
RV range (km s^{-1})	-34.7 to -25.9	-132.4 to 11.1	19.6 to 62.1	-66.2 to -40.2	···	-38.6 to -28.9
RV change (km s^{-1})	8.8	143.5	42.5	26.0	···	9.7

- Shell classification: emission shell
- Do shell features move with the star?: N/A
- Notes on emission and absorption features: The already big Hα emission grows in 2006 and Hγ emission also increases from 2004 to 2006. The emission peaks in Hγ do morph and change in relative strength. He I λ6678 is slightly filled-in in 2004 and develops emission horns in 2006. Mg II λ4481 is all emission.
- Other notes: This star is also plotted in Figure 7.4.

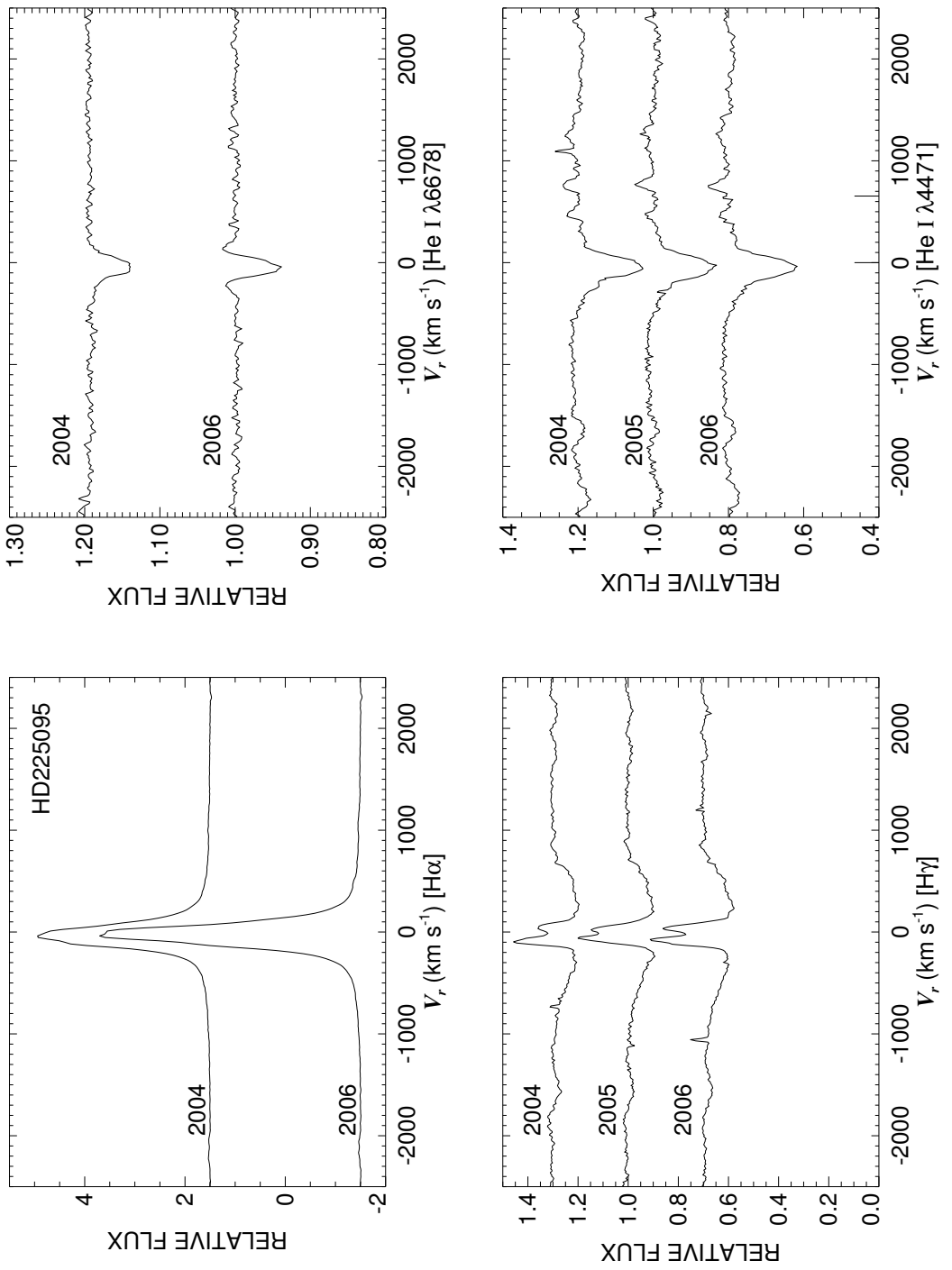

Figure C.171: A quadruple plot of HD225095 as described in §7.2.3 and Figure 7.6.